Nucleic Acids and Molecular Biology 29

Jørgen Kjems
Elena Ferapontova
Kurt V. Gothelf *Editors*

Nucleic Acid Nanotechnology

Springer

Nucleic Acids and Molecular Biology

Volume 29

Series Editor
Janusz M. Bujnicki
International Institute of Molecular
and Cell Biology
Laboratory of Bioinformatics and
Protein Engineering
Trojdena 4
02-109 Warsaw
Poland

For further volumes:
http://www.springer.com/series/881

Jørgen Kjems • Elena Ferapontova •
Kurt V. Gothelf
Editors

Nucleic Acid Nanotechnology

Springer

Editors
Jørgen Kjems
Center for DNA Nanotechnology,
Interdisciplinary Nanoscience Center
and Department of Molecular Biology
University of Aarhus
Aarhus C
Denmark

Kurt V. Gothelf
Center for DNA Nanotechnology,
Interdisciplinary Nanoscience Center
and Department of Chemistry
Aarhus University
Aarhus C
Denmark

Elena Ferapontova
Center for DNA Nanotechnology,
Interdisciplinary Nanoscience Center
Aarhus University
Aarhus C
Denmark

ISSN 0933-1891 ISSN 1869-2486 (electronic)
ISBN 978-3-642-38814-9 ISBN 978-3-642-38815-6 (eBook)
DOI 10.1007/978-3-642-38815-6
Springer Heidelberg New York Dordrecht London

Library of Congress Control Number: 2013951331

Printed on acid-free paper

Springer is part of Springer Science+Business Media (www.springer.com)

Foreword

What is nucleic acid nanotechnology? We read much about "nanotechnology" these days, both in the technical literature and in the popular press. The prefix "nano" in "nanotechnology" means 10^{-9}, a billionth, and implies something very small. In fact, relative to the chemical world, "nano" actually means something that is somewhat larger than the usual scale. A billionth of a meter is the length of about half a dozen chemical bonds between atoms, not a single bond. The usual components brought to mind when "nanotechnology" is mentioned are carbon-based materials, such as fullerenes (buckyballs), carbon nanotubes, or graphene, or metallic (often gold) and semiconducting nanoparticles, such as CdSe. Except for the particles, the relationship of these species to "nano" is not immediately obvious. Indeed, except when trying to increase one's prominence or funding, one doesn't often describe organic molecules as "nanocomponents," even though they fit the size range very nicely.

So why "nucleic acid" nanotechnology? The nanometer scale is indeed an appropriate scale for talking about "nucleic acids" nanotechnology, because nucleic acid double helices are about 2 nm wide. However, focusing on size when discussing nucleic acid nanotechnology really leads in the wrong direction. The key quality of nucleic acids is not their size but *their information content*. This feature is central to the roles of DNA and RNA in biological systems, and it is the vital component that distinguishes them from the other polymers that occur in both living and man-made systems. Although the most prominent aspect of nucleic acids in biology is their ability to code for proteins, RNA, at least, is well known to form complex tertiary structures from linear molecules. The ability to program the formation from nucleic acids of branched molecules at the secondary structure level and also to program their intermolecular interactions (Seeman 1982) has led to a new field which today is called "nucleic acid nanotechnology." The field has been growing since 1982, but its expansion has been particularly dramatic in the twenty-first century.

The goals of nucleic acid nanotechnology are very broad, and they are certainly not limited to biological applications. The initial target of the field was the formation of robust 3D crystals to solve the "crystallization problem" of macromolecular

crystallography (Seeman 1982). However, while awaiting the realization of this aim (Zheng et al. 2009), numerous other milestones have been achieved, and other new directions have been enunciated. These have included the construction of DNA objects (Chen and Seeman 1991), 2D lattices (Winfree et al. 1998), nanomechanical devices (Mao et al. 1999), robots (Sherman and Seeman 2004), and assembly lines (Gu et al. 2010). IT-related systems have been an intrinsic part of nucleic acid nanotechnology for over 25 years (Robinson and Seeman 1987). Adleman's Hamiltonian Path experiment (Adleman 1994) first brought DNA to the experimental consciousness of computer scientists, and Winfree's proposal of algorithmic assembly (Winfree 1998) similarly added logical operations to the notion of nanoscale self-assembly. Since its origination in the early 1980s, one of the most important developments in the area is undoubtedly Paul Rothemund's expansion of the scale of target objects through the use of DNA origami (Rothemund 2006). Peng Yin et al.'s follow-up of scaffold-free large-object construction nicely complements Rothemund's advance (Wei et al. 2012). The other key breakthrough in nucleic acid nanotechnology was the development of isothermal strand displacement by Yurke et al. (2000); as a consequence of this development, robust sequence-specific (i.e., programmable) devices have been developed (Yan et al. 2002) and significantly more complex computations have been undertaken successfully (Qian and Winfree 2011).

The central strength of nucleic acid nanotechnology is its ability to *use the chemical information contained in programmed DNA and RNA sequences to organize matter*, either DNA itself or other chemical species. We see numerous examples in this volume, which is a compendium of recent advances in the field, including the application of modern instrumentation to the analysis of constructs. However, the book goes beyond these topics, to extend nucleic acid nanotechnology to biological applications as well.

Without the development of single-molecule methods, many of the achievements of nucleic acid technology would have proved impossible to characterize. In the first chapter, Lei Liu, Flemming Besenbacher, and Ming Dong use a key nanoscale instrument, the scanning tunneling microscope, to examine the fundamental reaction of nucleic acid nanotechnology and the association of base pairs. Single-molecule experiments are often regarded as another component of "nanotechnology": In the second chapter, Rebecca Bolt Ettlinger, Michael Askvad Sørensen, and Lene Broeng Oddershede apply this force spectroscopy to nucleic acids. Similarly, in the third chapter, Sofie L. Kragh and Victoria Birkedal describe applications of single-molecule FRET to DNA nanotechnology.

From the foregoing, it is clear that self-assembly is a key component of nucleic acid nanotechnology. In the fourth chapter, Abhijit Rangnekar and Thomas H. LaBean summarize the long history of DNA tile-based self-assemblies and suggest how they may be applied in the future, both for object and lattice construction. In the fifth chapter, Angela Edwards and Hao Yan provide an extensive introduction of the state of the art of DNA origami and its applications. The sixth chapter, by Chunhua Liu and Andrew D. Ellington, summarizes recent developments in DNA nanotechnology and addresses its potential applications in drug delivery, analysis

and diagnosis, electronics, and photovoltaics, showing how technology can result from a system originally thought to be relevant only to biology. The use of DNA, fundamentally a nanoscale system, to aid in the construction of molecules on the scale of organic chemistry (DNA-templated synthesis) is treated in the seventh chapter, contributed by Christian B. Rosen, Thomas Tørring, and Kurt V. Gothelf. The eighth chapter, by Zhen-gang Wang and Baoquan Ding, discusses the applications of DNA-based nanomechanical devices.

The last section of the book returns DNA to its biological roots but with a nanotechnological slant. The ninth chapter by Eveline Edith Salcher and Ernst Wagner is concerned with the encapsulation of oligonucleotides for therapeutic purposes; it details the nature of the issues involved in this activity. In the tenth chapter, Günter Mayer, Monika Pofahl, Katia M.U. Schöler, and Silvana Haßel discuss the applications of aptamers for the therapeutic purposes, including modifications and cell targeting. Slaven Garaj discusses the use of nanopores for the central purpose of DNA sequencing in the eleventh chapter; the target here is the least expensive genome, and the chapter covers both the advances and challenges confronting the field. In the final chapter, Alfredo de la Escosura-Muñiz and Arben Merkoçi discuss the use of nanomaterials in DNA sensing, with the goal of integrated chip technologies.

In summary, Jørgen Kjems, Elena Ferapontova, and Kurt V. Gothelf, the editors of this book, have provided the reader with an accessible entry to the area of nucleic acid nanotechnology. In addition, they have included developments that go well beyond a simple introduction. The work in this field was available a decade ago to those following the output of only a few laboratories. However, it has grown so much that it is no longer possible for even the experts in the area to keep abreast of the developments that are occurring. This volume will certainly assist in that effort.

New York, NY Nadrian C. Seeman

References

Adleman L (1994) Molecular computation of solutions to combinatorial problems. Science 266:1021–1024

Chen J, Seeman NC (1991) The synthesis from DNA of a molecule with the connectivity of a cube. Nature 350:631–633

Gu H, Chao J, Xiao SJ, Seeman NC (2010) A proximity-based programmable DNA nanoscale assembly line. Nature 465:202-205

Mao C, Sun W, Shen Z, Seeman NC (1999) A DNA nanomechanical device based on the B-Z transition. Nature 397:144–146

Qian L, Winfree E (2011) Scaling up digital circuit computation with DNA strand displacement cascades. Science 332:1196–1201

Robinson BH, Seeman NC (1987) The design of a biochip: a self-assembling molecular-scale memory device. Protein Eng 1:295–300

Rothemund PWK (2006) Scaffolded DNA origami for nanoscale shapes and patterns. Nature 440:297–302

Seeman NC (1982) Nucleic acid junctions and lattices. J Theor Biol 99:237–247
Sherman WB, Seeman NC (2004) A precisely controlled DNA bipedal walking device. Nano Lett 4:1203–1207
Wei B, Dai M, Yin P (2012) Complex shapes self-assembled from single-stranded DNA tiles. Nature 485:623–627
Winfree E (1998) Algorithmic self-assembly of DNA. Ph.D. Thesis, Caltech
Winfree E, Liu F, Wenzler LA, Seeman NC (1998) Design and self-assembly of two-dimensional DNA crystals. Nature 394:539–544
Yan H, Zhang X, Shen Z, Seeman NC (2002) A robust DNA mechanical device controlled by hybridization topology. Nature 415:62–65
Yurke B, Turberfield AJ, Mills AP Jr, Simmel FC, Newmann JL (2000) A DNA-fuelled molecular machine made of DNA. Nature 406:605–608
Zheng J, Birktoft JJ, Chen Y, Wang T, Sha R, Constantinou PE, Ginell SL, Mao C, Seeman NC (2009) From molecular to macroscopic via the rational design of a self-assembled 3D DNA crystal. Nature 461:74–77

Preface

Fifty-one years passed since James Watson, Francis Crick, and Maurice Wilkins were awarded the Nobel Prize in physiology or medicine for their 1953 discovery that deoxyribonucleic acid, DNA, consists of two twisted oligonucleotide chains that are held together in an antiparallel fashion by highly specific oligonucleotide base pair interactions. This discovery opened a new era in biology, genetics, medicine, biotechnology, and biochemistry and provided further basis for studying and manipulating the biological processes—molecular biology science. It dramatically changed our understanding of the molecular basis of genes, genetic diseases, and the inheritance passage of genetic material from one generation to another.

Later, new powerful physical–chemical tools for synthesis, manipulation, and visualization of nucleoacids at atomic level enabled functional studies and control nucleic acids organization and function at a nanoscale level. Now, at the 60th anniversary of the discovery of the double helix, the combination of nucleic acid chemistry and nanotechnology created a new challenging direction of research called Nucleic Acid Nanotechnology, which has tremendously improved our knowledge and control of basic biological processes and enabled novel biotechnological applications in many fields including food and pharmaceutical industries, medicine, agriculture, forensics, material engineering, and computation. The necessity of a book, where the latest achievements in this rapidly expanding area of research are summarized, is evident and timely.

This book contains 12 chapters, written by the leading world's scientists in the field of DNA and RNA nanotechnology. It represent a diverse collection of reviews devoted to basic directions in this area, from single nucleotides and single nucleic acid molecule studies and characterization to the design and synthesis of more complex DNA- and RNA-based systems and their application in nanomechanics, nanomedicine, and nanobiosensing. We believe that this book provides both a solid background knowledge for those who are not directly in the field of the research and advanced knowledge for those who are interested in the more detailed and practical information on the methods and the latest achievements in this field. We are very thankful to all the authors contributing to this book and to Prof. Janusz Bujnicki, the Editor of the "Nucleic Acids and Molecular Biology" series, for challenging us to

edit this book and Dr. Ursula Gramm, Springer, for her constant support and assistance during the editing procedure.

Aarhus, Denmark
April, 2013

Jørgen Kjems
Elena Ferapontova
Kurt Gothelf

Contents

Part I
Single RNA/DNA Molecule Interactions

Chapter 1
Self-Assembly of DNA Bases via Hydrogen Bonding Studied by Scanning Tunneling Microscopy

Lei Liu, Flemming Besenbacher, and MingDong Dong

Abstract Nature is the master of self-assembly, and in biological system, a great many of hierarchical structures of biomolecules including DNA, peptide, and protein are attributed to the self-assembly from molecular level to nanoscale. One successful example is inspired by nature; DNA can be an excellent agent to self-assemble into the desirable amazing two-dimensional and three-dimensional nanostructures in a well-ordered manner by specific hydrogen bonding interactions between the DNA bases. Therefore, the self-assembly of DNA bases has played a significant role in constructing the hierarchical nanostructures, and maybe they are also the key to the earliest appearance of life. In this chapter, we will study on DNA base self-assembly by scanning tunneling microscopy (STM) at the liquid/solid interface and present the nanoscale patterns that can be created by assembly of the individual DNA base (G, guanine; C, cytosine; A, adenine; T, thymine) and coabsorption of DNA complementary bases (G-C and A-T) based on the specific hydrogen bond interactions. Scanning tunneling microscopy is the powerful technique to visualize atomic-scale structure with submolecular resolution. At the liquid/solid interface, one can be in the ambient condition that is more close to the physiological environment rather than the extreme condition in vacuum system. On the other hand, the influence of the various types of intermolecular interactions is revealed such as hydrogen bond, stacking interaction, *etc*. Therefore, the utilization of STM at liquid/solid interface has the good advantage to investigate the DNA base self-assemblies on the surface, and the variety of novel two-dimensional nanostructure-based DNA base assemblies will be introduced in this chapter.

L. Liu • F. Besenbacher • M. Dong (✉)
iNANO Center, Aarhus University, Gustav Wieds vej 14, Building 1590, 8000 Aarhus, Denmark

CDNA Center, Aarhus University, Gustav Wieds vej 14, Building 1590, 8000 Aarhus, Denmark
e-mail: dong@inano.au.dk

J. KJEMS et al. (eds.), *Nucleic Acid Nanotechnology*, Nucleic Acids and Molecular Biology 29, DOI 10.1007/978-3-642-38815-6_1,

Furthermore, the theoretical calculation will also provide the assembly models of DNA base to make better understanding of the mechanism of self-assembly of DNA bases.

Contents

1.1 The Role of Hydrogen Bond in the Self-Assembly of DNA Bases

Self-assembly involves the organization of molecules into highly ordered structures through specific, local interactions among the components, without any external direction (Whitesides et al. 1991). Weak interactions, such as van der Waals, electrostatic, and π–π interactions, as well as hydrogen bonding, can lead to all kinds of challenging self-assembled nanostructures. The self-assembly as a strategy not only involves atoms and molecules but spans a wide range of nano- and microscopy structures. The most important is that it plays a key role in nature. It is widely accepted that self-assembly processes are common throughout nature and technology (Whitesides and Grzybowski 2002). Nature is the master of self-assembly. In biological system, the hierarchical structures of many biomolecules including DNA, peptide, and protein are attributed to self-assembly from molecular level to nanoscale. Peptides with specific amino acid sequences are capable of self-assembling into hierarchical structure with important biological functions (Zhao and Zhang 2006; Liu et al. 2011a). DNA is an ideal molecule that is allowed to form target-assembling structures based on the specificity of the base paring. Self-assembly also gives contribution to microscale structure formation spontaneously such as cell wall. It draws from the variety of examples in biology for inspiration, and self-assembly could be one of the most important strategies utilized in biology or material science for development of complex, functional structures. By studying the self-assembly behaviors of biological molecules in model system, questions of real biological significance can be addressed.

An efficient approach for combining molecular building blocks into artificial structures with desired functions is molecular self-assembly and self-organization

by specific interactions mainly including van der Waals, electrostatic, and π–π interactions, especially hydrogen bonding. In some macromolecules, hydrogen bonding exists widely between the parts of the same macromolecule and causes it to fold into a specific shape and determines the molecular or biochemical role. It is therefore significant for hydrogen bonding as the main driving force to construct the assembly structure not only in biological system but in material science.

A hydrogen bond is defined as the kind of attractive interaction of a hydrogen atom and an electronegative atom including oxygen, nitrogen, or fluorine, which is from other molecules or functional groups. Hydrogen bonding is a kind of non-covalent interaction rather than a chemical bond but is an important aspect concerning molecular self-assembly. The term hydrogen bond was used for the first time in 1930s to discuss the $[H:F:H]^-$ ion in Pauling's paper "The Nature of Chemical Bond" (1931) (Pauling 1992). Now it is known to be one of the most important concepts in supramolecular chemistry and molecular biology. Hydrogen bonds can be divided, according to the bond energy, into strong (15–40 kcal/mol), moderate (4–15 kcal/mol), and weak bonds (1–4 kcal/mol)(Bernstein et al. 1995). Strong hydrogen bonds are formed by chemical groups in which there is a deficiency of electron density in the donor group or an excess of electron density in the acceptor group. Moderate hydrogen bonds are formed generally by neutral donor and acceptor groups. Weak hydrogen bonds are formed when the hydrogen atom is bonded to a slightly more neutral atom relative to hydrogen. Hydrogen bonds are highly selective and directional, though moderately strong, and they have been extensively applied to direct the molecular ordering structures.

The self-assembly of DNA bases is the extreme system representing the hydrogen bond interaction. The formation of double-helical DNA structure is mainly due to the hydrogen bonds of complementary bases. Furthermore, in DNA nanotechnology, the complementary base pairing resulting from the specific hydrogen bonds is utilized to create desirable two-dimensional (2D) (Winfree et al. 1998; Rothemund 2006) or even three-dimensional (3D) nanostructures (Douglas et al. 2009) in a well-controlled manner. Therefore, the self-assembly of these bases will play an important role in constructing the hierarchical nanostructures and maybe is the key to the earliest appearance of life. Basically, upon the rule discovered by Watson and Crick around 54 years ago, a simple set of base pairing were proposed for the four nucleic acid (NA) bases: guanine (G), cytosine (C), adenine (A), and thymine (T). However, it is important to note that the NA bases are not exclusive in their binding behaviors. For example, at least 28 possible base-pairing motifs exist to involve the hydrogen bond forming during the four nature bases. These NA base binding modes can also play a significant role in NA self-assembly process and even in biological system. Besides, these single NA bases have the ability to form 1D or 2D supramolecular nanostructures, when deposited onto various surfaces, which was explored in UHV system. To understand the DNA replication mechanism in future details, it is a plausible way to simplify the study by choosing the model system. In this chapter, we approach self-assembly of nucleic acid (NA) bases based on hydrogen bonds by means of scanning tunneling microscopy (STM) at ambient condition. The novel assembling structures of pure NA

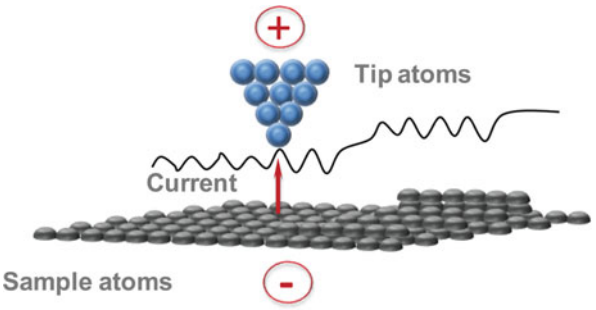

Fig. 1.1 Schematic diagram of STM setup

bases and complementary bases will be introduced on liquid/solid interface, respectively. Combining the DFT theoretical calculation, it is clearly presented how the NA bases will be able to self-assemble into the diversity of nanopatterns on the surface by the intermolecular hydrogen bonding of NA bases.

1.2 Scanning Tunneling Microscopy Applied in Studying DNA Base Assembly

1.2.1 The Principle of STM

STM is a powerful technique for imaging surfaces at the atomic level. It was invented in the early 1980s by the Nobel Prize winners Binning and Rohrer at the IBM research facilities in Zurich (Binnig and Rohrer 1982; Binning et al. 1982). The basic operation of STM is illustrated in Fig. 1.1. The microscope probes the surface with very sharp tip which is usually produced by mechanical cutting of a platinum/iridium (Pt/Ir) wire or chemical etching of tungsten (W) wire. The tip is moved in x, y, and z directions with the aid of a piezoelectric actuator that shrinks, expands, or bends, according to the electrical potentials applied to its electrodes. The tip can move over a few micrometers with the accuracy down to 1 % of an Ångstrom with this actuator. When a potential difference is applied between the tip and the sample, an electrical current will flow with the distance closing between the tip and the sample (Fig. 1.1).

Recently, STM has become a more and more powerful technique for studying the organic molecule (Yang and Wang 2009) and biomolecules (Liu et al. 2009, 2011a, b; Ma et al. 2009) at the interface due to their high structural resolution and the adapting for the variety of environments including vacuum system and solid/liquid interface. The assembly of DNA bases on the surface as the model system was widely studied by STM to address the significant question in biological system. It can be revealed and visualized by STM study how DNA bases self-assemble into supramolecular structures on the surface.

1.2.2 Sample Preparation and STM Operation

In STM study, all the samples have to be deposited on the surface. Generally, highly oriented pyrolytic graphite (HOPG) was selected to be the surface. All the NA bases (G, Sigma Aldrich, 98 % purity; C, Sigma Aldrich, 97 % purity; A, Sigma Aldrich, 99 % purity; T, Sigma Aldrich, 98 % purity) were dissolved into polar 1-octanol (Sigma Aldrich, 99.5 % purity). To obtain the assembling structure of NA bases, a drop of each NA bases solution was applied to a fresh cleaved HOPG (grade ZYA, reliability and quality BV, the Netherlands) surface, followed by annealing at 50°C for 1 h. The STM experiments were performed under ambient conditions at the liquid/solid interface with a commercial Digital Instruments Nanoscope IV Multimode SPM system (Bruker Company). STM tips were mechanically cut from a 0.25 mm Pt/Ir (80/20) and tested on HOPG. All STM images were recorded in the constant-current mode under different tunneling conditions (tunneling current range is 0.5–1 nA and tunneling bias is 0.5–0.8 V), with the sample positively biased. The STM scanner was calibrated from images of clean HOPG using the scanning probe image processor (SPIP™) software (Image metrology Aps, Lyngby, Denmark). Correlation averaging method from SPIP software was used to deal with STM images. In correlation averaging a template area is defined, and an average is performed over the N ($N = 100$) equivalently sized regions in the image that provide a best match to this template. Theoretical simulations of the structures were performed within the framework of the self-consistent charge density-functional-based tight binding (SCC-DFTB) method. In the calculations, all involved atoms were fully relaxed without constraints.

1.3 Self-Assembled Structures of Individual DNA Bases (G, C, A, T)

The stabilization of DNA double-helical structure is mainly due to the predominant hydrogen bonding between nucleic acid (NA) bases (Watson and Crick 2003). Although there are not huge structural differences between NA bases, it is obvious for the chemistry and electronic properties in different NA bases. Furthermore, it is a great challenge to understand the mechanisms behind the assembly of DNA bases and their complexes with amino acids, proteins, and with more complicated biological systems. Therefore, it is really of great importance to study self-assemblies of NA bases molecules as a means of exploring inter- and intramolecular hydrogen bonding properties between them. In addition to the recognition processes in complementary base pairing that are mediated by hydrogen bonding, the self-complementary interactions between NA bases have been observed in DNA molecules (Arnott 1984) and solid supports (Perdigao et al. 2006; Otero et al. 2005; McNutt et al. 2003). In recent, a variety of binding possibilities between NA bases dimers were well investigated by theoretical calculations (Kelly

et al. 2005a, b; Kelly and Kantorovich 2006). Dimer formation is the key component to construct two-dimensional (2D) supramolecular structures on surface, and it will also uncover the variety of interaction mechanism between the DNA bases. It is widely explored by STM that NA bases are capable of self-assembling into a diversity of structures on many different surfaces and under variable conditions (Furukawa et al. 2000, 2001; Kawai et al. 1997; Nishimura et al. 2002; Sowerby and Heckl 1998, Wandlowski et al. 1996). One that the STM studies of NA bases at the liquid/solid interface has the advantages that the liquid can in principle provide molecules with a certain degree of freedom during the physisorption process and prevent any extra force during thermal deposition (particular in case of UHV-STM) and finally avoid contamination of the sample due to exposure to air (particular in case of air-STM). It is therefore that a wide range of organic molecules have been investigated at liquid/solid interfaces based on NA bases that can potentially be used for the supramolecular chemistry, molecular crystal, surface functionalization, and biosensor (Winfree et al. 1998; Fritz et al. 2000; Samori and Zuccheri 2005). Moreover, the study of the self-assembly of NA bases by STM could also give a better understanding of the forces at play that are necessary for creating 2D patterns on surface. In this section, we provide the introduction of 2D supramolecular structures based on individual NA bases (G, guanine; C, cytosine; A, adenine; T, thymine) that have been created at the 1-octanol/HOPG interface. The theoretical modeling provides a convincing rationale for the formation of these 2D patterns based on DNA base pairing.

1.3.1 STM Study on Self-Assembly of Individual Nucleic Acid Bases

NA bases (G, guanine; C, cytosine; A, adenine; T, thymine) are the basic components which are able to generally form the specific hydrogen bond following the base paring rule in DNA molecule. However, in some cases, these NA bases could also self-assemble into dimer by the hydrogen bond between themselves.

Subsequent STM imaging at the liquid/solid interface revealed the gradual formation of well-ordered domains of NA base molecules (Fig. 1.2). The high-resolution images of individual NA base self-assemblies present the well-ordered adlayers. Lattice parameters of observed different adlayer structures are summarized in Table 1.1. The guanine molecules (Fig. 1.2a) present the 2D network structures with a determined unit cell, where the lattice constants $a = 0.64 \pm 0.07$ nm, $b = 0.68 \pm 0.07$ nm, and $\alpha = 90.1 \pm 2.6°$. The cytosine molecule shows the parallel chain alignment with a determined unit cell, where lattice constants $a = 0.82 \pm 0.08$ nm, $b = 0.53 \pm 0.06$ nm, and $\alpha = 77.3 \pm 2.3°$ (Fig. 1.2b). The adenine molecules could also self-assemble into the stable 2D network arrangement with the determined unit cell including $a = 0.8 \pm 0.1$ nm, $b = 2.2 \pm 0.2$ nm, and $\alpha = 76.0 \pm 2.3°$ (Fig. 1.2c). The self-assembling structure

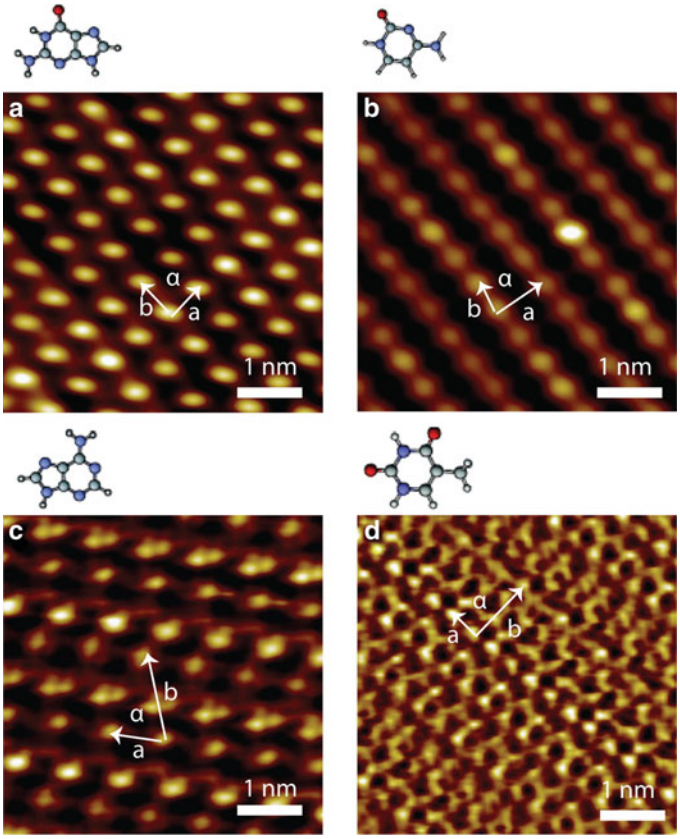

Fig. 1.2 The typical STM images of the pure NA bases adsorbed at the 1-octanol/HOPG interface. (**a**) Guanine, (**b**) cytosine, (**c**) adenine, and (**d**) thymine. Scan size: 5 nm × 5 nm, I_{set} = 500–1,000 pA, V_{bias} = 500–800 mV

Table 1.1 Comparison of the lattice parameters of the observed different assembly structures of NA bases as derived from the analysis of the STM images

	a (nm)	*b* (nm)	*α* (deg)
Pure G	0.64 ± 0.07	0.68 ± 0.07	90.1 ± 2.6
Pure C	0.82 ± 0.08	0.53 ± 0.06	77.3 ± 2.3
Pure A	0.80 ± 0.10	2.20 ± 0.20	76.0 ± 2.3
Pure T	0.80 ± 0.10	1.50 ± 0.20	87.0 ± 2.5

of adenine molecules is also reported on Ag-terminated Si (111) by hydrogen bond packing (Perdigao et al. 2006). The thymine molecules present the chain arrangement. The lattice constants include $a = 0.8 \pm 0.1$ nm, $b = 1.5 \pm 0.2$ nm, and $\alpha = 87.0 \pm 2.5^{\circ}$ (Fig. 1.2d). The chain arrangement was proposed by previous theoretical calculation (Kelly and Kantorovich 2006).

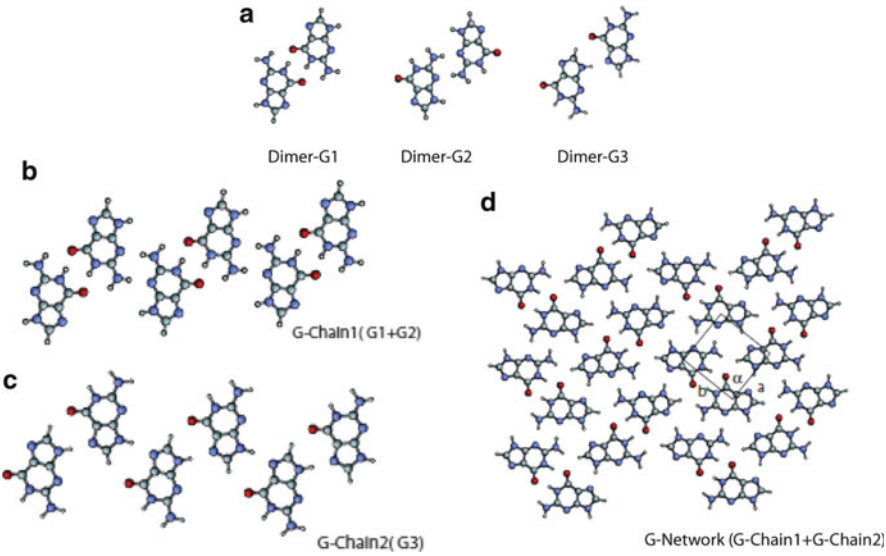

Fig. 1.3 Structural models of guanine molecules. (**a**) Three kinds of guanine dimers (dimer-G1, dimer-G2, and dimer-G3). (**b**) G-chain 1 formed by alternating dimer-G1 and dimer-G2. (**c**) G-chain2 was consisted of alternating dimer-G3. (**d**) The calculated network formed by combination of G-chain 1 and G-chain 2

1.3.1.1 G-Dimer and G-Network Structure

All the pure NA bases presented the chain arrangement that consists of NA hydrogen-bonded dimer, based on the analysis of the STM images, and further these chains propagate into well-ordered 2D supramolecular networks. To understand the basis of the formation of these 2D supramoleculear networks, theoretical simulations were performed using the SCC-DFTB method. In the calculation, all possible dimers were considered and were assumed to adopt planar geometries, but only some combinations play a significant role in the ordering of molecular self-assemblies on the surface due to many configurations with low binding energy. Most energetically favorable combinations of stabilized dimer were shown for each of the NA bases based on calculation (Fig. 1.3). Three types of energetically favorable G-dimers and two types of G-chain structures are presented in Fig. 1.3. G-chain 1 was composed of alternating dimer-G1 and dimer-G2, while G-chain 2 was formed by alternating dimer-G3, respectively. To construct the 2D supramolecular network corresponding to the G monolayer observed in STM image, the chain structures that combine G-chain 1 and G-chain 2 shown above can be used to construct the 2D network.

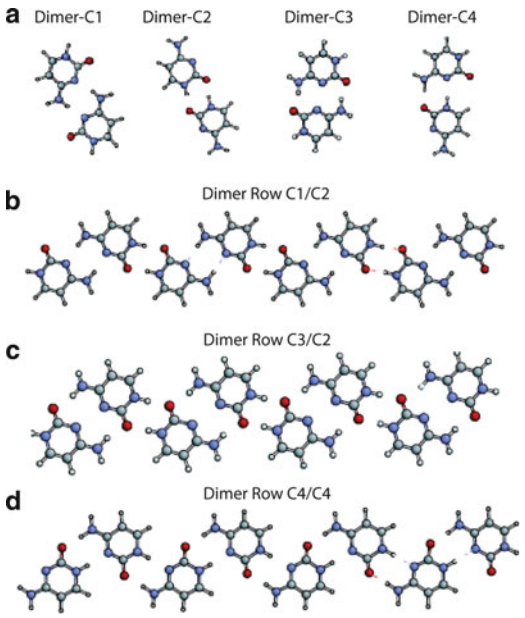

Fig. 1.4 Structural models of cytosine molecules. (**a**) Four kinds of cytosine dimers from SCC-DFTB calculations (dimer-C1, dimer-C2, dimer-C3, and dimer-C4). (**b**) C-chain 1 was constructed by alternating dimer-C1 and dimer-C2. (**c**) C-chain 2 was formed by alternating dimer-C2 and dimer-C3. (**d**) C-chain 3 was formed by alternating dimer-C4

1.3.1.2 C-Dimer and C-Chain Structure

There are four different types of C-dimers with different binding energies in the construction of cytosine-assembling structures. These dimers are involved in the formation of three types of C-chain structures. C-chain 1 was formed by alternating dimer-C1 and dimer-C2, C-chain 2 was constructed by alternating dimer-C2 and dimer-C3, and C-chain 3 was composed of alternating dimer-C4. It is clearly shown that parallel chain arrangements are formed in STM image based on one of the possible types of C-chain which is illustrated in Fig. 1.4. It seems that the bind energies are close, among the three proposed chain models; however, model C-chain 3 is to be more consistent with the unit cell parameters obtained from STM image, and C-chain structures are stabilized by van der Waals interaction.

1.3.1.3 A-Dimer and G-Chain Structure

Adenine is another NA base that involves the hydrogen bond interaction forming. Three possible types of A-dimers with different binding energies (dimer-A1 $>$ A2 $>$ A3), and two types of A-chain structures are presented in Fig. 1.5. It is obtained from the analysis of calculation results that A-chain 1 was formed by alternating dimer-A1 and dimer-A2, and A-chain 2 was constructed by alternating dimer-A3, respectively. The binding energy of A-chain 1 is higher than the one of A-chain 2. It is clearly presented that in STM image adenines are capable of self-assembling into parallel chain arrangement. However, from STM experiment result and SCC-DFTB

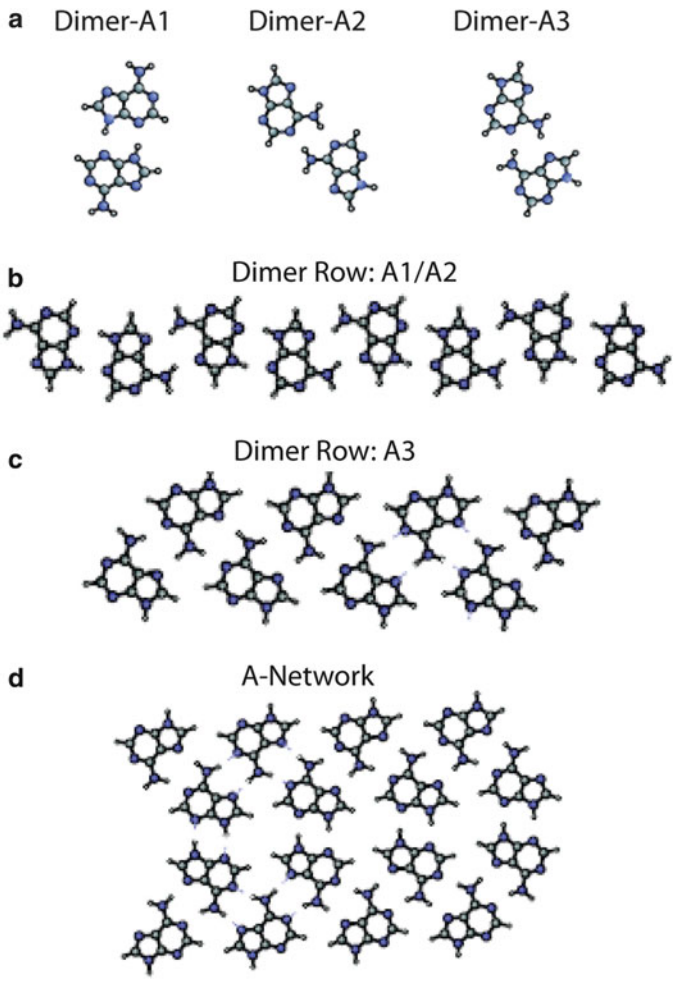

Fig. 1.5 Structural models of adenine molecules. (**a**) Three kinds of adenine dimers (dimer-A1, dimer-A2, and dimer-A3). (**b**) A-chain 1 was formed by alternating dimer-A1 and dimer-A2. (**c**) A-chain 2 was formed by alternating dimer-A3. (**d**) The calculated network was constructed by identical parallel A-chain 2 that can then form hydrogen bonds by the dimer-A1 configuration

calculation, A-chain 2 is more consistent with the STM image, although the A-chain 1 has a higher binding energy than the A-chain 2. It is suggested that some other more factors affect the forming of final stable adenine-assembling structures. Due to the most energetically favorable dimer (dimer-A1) involved to construct the intermolecular hydrogen bonds between two A-chains 2, it is therefore plausible that A-chain 2 is more matched with STM image since the binding energy of optimize model of A network is larger than the one of A-chain 1.

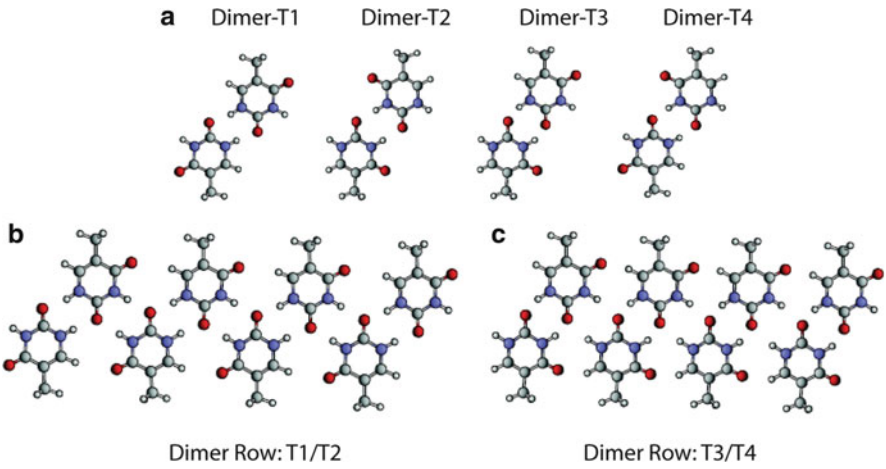

Fig. 1.6 Structural models of thymine molecules. (**a**) Four kinds of thymine dimers (dimer-T1, dimer-T2, dimer-T3, and dimer-T4). (**b**) T-chain 1 was formed by alternating dimer-T1 and dimer-T2. (**c**) T-chain 2 was constructed by alternating dimer-T3 and dimer-T3

1.3.1.4 T-Dimer and T-Chain Structure

Thymine is also a very important NA base involving the formation of hydrogen bond. In general, by calculation, four different types of T-dimer (almost the similar binding energy) and two types of T-chain structure formed based on the proposed T-dimer were obtained (Fig. 1.6). T-chain 1 was formed by alternating dimer-T1 and dimer-T2. T-chain 2 was constructed by alternating dimer-T3 and dimer-T4, respectively. Compared to T-chain 1, T-chain 2 has the similar hydrogen bond motifs and similar binding energies with T-chain 1 based on the proposed model. Therefore, both models could match the assembly structure obtained by STM. However, a high degree of diffusion dynamics is observed upon adsorption of T-molecule on HOPG, which suggests that both kinds of chains arrangements are likely to be present in the adsorption process. It is the reason that the destabilization of the T-network is mainly due to the transition between the two types of chain conformations.

There exist certain similarities in the 2D supramolecular structures observed for G and A, and similarly between T and C, respectively. The 2D supramolecular networks based on G and A have the similar hydrogen bonding dimer construction, whereas the parallel chain structure constructed by T and C involves the hydrogen bond dimer chains and van der Waals interaction between the chains. In conclusion, well-ordered assembling structures were constructed by pure NA bases at the liquid/solid interface. The network structures were commensurate with the energetically favorable network determined by the theoretical calculations. It is suggested from NA base-assembling structures and theoretical calculation that NA dimers construct the base chain and further that the chains result in the formation of 2D network by either intermolecular hydrogen bond or van der Waals interaction. An

understanding of the properties of adsorbed NA base at the liquid/solid interface is of high interest to both surface and synthesis. A variety of applications involving hydrogen bond-mediated supramolecular chemistry and biotechnology could be based on the NA base dimerization.

1.4 Self-Assembled Structure of Complementary Base (G-C, A-T)

DNA as the essential building block for life is very important and it plays a significant role in cell biology. The specific molecular interaction between DNA results in the precision and efficiency of its self-assembling into double helices and further more fascinating nanostructures. These designable and predictable DNA self-assembling nanostructures are mainly due to using NA base sequence to encode instruction (Winfree et al. 1998). The complementary base pairing via the hydrogen bonds in the double-helical DNA structure is of utmost importance. It is therefore very important and valuable to investigate the assembling structure of pure DNA bases by specific hydrogen bond interaction. The adsorption of pure DNA base molecules on flat surfaces makes the DNA base structure accessible to exploration by STM, which will provide the visualization at molecular or submolecular level resolution and get insight into the base self-assembly. In the last session, we have already introduced the self-assembly of individual NA bases. Four NA bases (A, T, G, C) could be able to self-assemble into base network or base arrangement structures. In this session, we provide STM visualization of a well-ordered assembling structure formed by coadsorption of the complementary bases G-C and A-T at the liquid/solid interface, respectively.

1.4.1 Self-Assembled Structure of Complementary Base G-C

The hydrogen bond between the guanine and cytosine is one kind of NA base complementary pairing. Guanine and cytosine are capable of assembling into G-dimer and C-dimer further forming the G- and C-chains based on the intermolecular hydrogen bond interaction. The coadsorption of G and C on the surface will lead to the hybrids by the specific hydrogen bond that G-C complementary pairing. The typical STM image of well-ordered adlayer is presented in Fig. 1.7 (Xu et al. 2006). A distinct double-row structure is obviously observed, which is ascribed to aligned GC pairs. The hybrids of G and C on the surface are different from the assembling structure formed by pure base G and C molecules. In the coadsorption of G and C on the surface, three distinct domains can be identified, which are marked in I, II, and III. Domains I and II are composed of assembling bases with the feature aligned into straight and parallel rows. The quality of

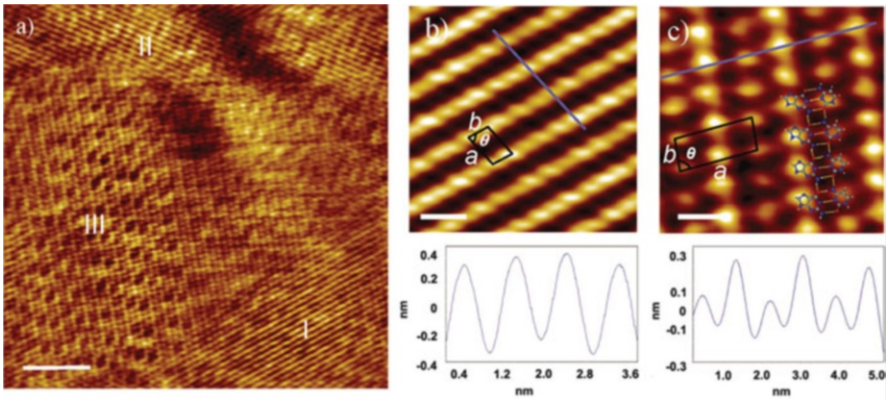

Fig. 1.7 Coadsorption of guanine and cytosine at the 1-octanol/HOPG interface. (**a**) Typical STM image presenting three domains, marked with I, II, and III. Scan size: 50 nm × 50 nm. (**b**) Correlation-averaged magnified image of structure of domain I, 5 nm × 5 nm, a unit cell is indicated. There is a line profile on the *bottom* of (**b**) along the *blue line* in the *top* of STM image. (**c**) Correlation-averaged magnified image of structure of domain III, 5 nm × 5 nm, a unit cell is indicated. *Bottom*: Height profile along the *blue line* in the *top* of panel. The structural model is superimposed on the STM image. $I_{set} = 549$ pA, $V_{bias} = 750$ mV (**a–c** are reproduced with the permission from Xu et al. 2006, Copyright 2006, American Chemistry Society)

Table 1.2 Comparison of lattice parameters for the different assembly structures of G, C, and G-C from the analysis of STM images

	a (nm)	b (nm)	θ (deg)
Domain I and II	0.87 ± 0.09	0.45 ± 0.05	76.7 ± 2.2
Domain III	1.71 ± 0.18	0.69 ± 0.07	84.1 ± 2.4
Pure cytosine	0.82 ± 0.08	0.53 ± 0.06	77.3 ± 2.3
Pure guanine	0.64 ± 0.07	0.68 ± 0.07	90.1 ± 2.6

Table is reproduced with the permission from Xu et al. (2006), Copyright 2006, American Chemistry Society

high-resolution structure with molecular contrast can be improved by performing correlation averaging. The periodicity of domain I/II is presented in Table 1.2. The parameter of the unit cell of domain I/II is determined to be $a = 0.87 \pm 0.09$ nm, $b = 0.45 \pm 0.05$ nm, and $\theta = 77.3 \pm 2.3°$. The structure of domain I/II is in agreement with the structure formed by pure cytosine (Fig. 1.2b). The lattice parameters of domain I/II are mostly similar to the ones of pure C-assembling structures. It is therefore concluded that domains I and II are formed by cytosine molecule alone. Compared to the previous STM images of pure C and G assemblies, the structure of domain III is distinct from them. It is indeed the mixed phase consisting of both C and G molecules. Within domain III, the periodic molecular arrangement alternates between rows of high and low protrusions (Fig. 1.7c). The G and C form the heterodimers aligned into rows. The lattice parameters are determined to be $a = 1.71 \pm 0.18$ nm, $b = 0.69 \pm 0.07$ nm, and

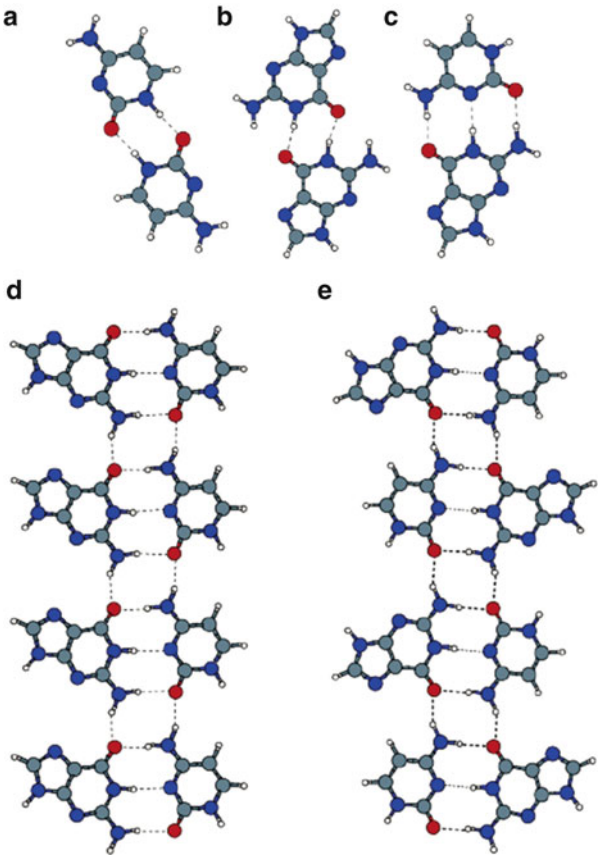

Fig. 1.8 Structural model. (**a**) C-dimer, (**b**) G-dimer, (**c**) GC dimer, (**d**) chain of GC dimers. (**e**) Chain of GCGC quartet was formed by alternating GC dimers (**a–c** are reproduced with the permission from Xu et al. 2006, Copyright 2006, American Chemistry Society)

$\theta = 84.1 \pm 2.4°$. To obtain insight into the underlying molecule–molecule interaction, theoretical modeling based on the self-consistent charge density functional-based tight binding method was performed. It is obtained that the planar structures for homodimers of G and C are the lowest energy configuration with the binding energies of 0.4 eV (CC) and 0.5 eV (GG), which is presented in Fig. 1.8a, b, respectively. The optimum heterodimer is definitely a Watson–Crick GC pair (Fig. 1.8c), which is found to be with a considerably higher binding energy of 0.9 eV. It is therefore plausible that a GC dimer is the most preferential complex to form. GC dimer could also arrange into a row with an optimized model (Fig. 1.8d). The periodicity along the model structure is 0.74 nm, consistent with the 0.69 ± 0.07 nm that is determined from experiment. It is proved that experiment and theoretical model have a good agreement. The intermolecular hydrogen bonds in fact stabilize the row structure by GC dimers. The dimer–dimer interaction energy was obtained by calculating the binding energy per GC dimer. It is proved that the binding energies for row segments with n GC dimers increase

monotonically toward the limit for an infinite chain. It is the main reason why the GC dimer could further assemble into the structures. It is also found that there exist so-called GCGC quartet formation in four-stranded DNA quadruplexes due to the interaction between G and C (Leonard et al. 1995). The quartet structure can be realized from the model of Fig. 1.8d by rotating the GC dimer by 180° around the surface normal each second, resulting in the optimized structure shown in Fig. 1.8e. An oscillatory behavior with maxima for row segments with an even number of GC dimers is presented by calculating, and it proves that a closed quartet structure forming is preferable. Although the quartet row structure (G and C molecules alternate along the row direction) is found from the calculation, which is slightly (0.1 eV per dimer) more stable than the dimer row observed by STM (Fig. 1.7c), it appears to be inconsistent with the experiment. It is true that STM could not capture the configuration of GC pair with the lowest binding energy, and however, it also shows the possible assembling structure by G and C. Possibly, the destabilization at the experiment coverage of GC row structure is mainly due to the absence of quartet chains.

The investigation of adsorption and coadsorption structures formed by NA base guanine and cytosine at the liquid/solid interface studied by STM prove revealed that hydrogen bond of G and C as well as between the GC dimers will mainly contribute to the formation of double-row structures assembled by guanine and cytosine.

1.4.2 Self-Assembled Structure of Complementary Base TA

To the similarity of the supramolecular structures assembled by G and C by hydrogen bond interaction, thymine and adenine are also capable of creating the assembling structures on liquid/solid interface. The high-resolution STM image of A and T mixture is presented to be a well-ordered molecular pattern that is significantly different from the assembling structures by pure adenine and thymine molecule (Fig. 1.2c, d). In the mixture phase of A and T (Fig. 1.9), two different coexisting features are obviously revealed: (1) rows that contain cyclic structure (indicated with red rectangles) and which are separated by (2) single chains that contain only bright spots (indicated with yellow ovals) (Mamdouh et al. 2006). The assembly structures of pure A and T have no quartet cyclic feature, compared to the mixed phase of A and T. In addition, calculation proves that when four A molecules approach to each other, dimer-A forming is favorable, and when two dimers A bind together, the orientation of the A-A dimer will be altered from one row to another, which is shown in Fig. 1.2c, resulting in the network forming without the quartet cycles. Similarly, no T quartet cyclic structure was observed, and the calculation showed that T-T dimer formation is preferred over T quartet cyclic structures. It is therefore clear that the quartet cyclic structure is resulting from co-assemblies of A and T.

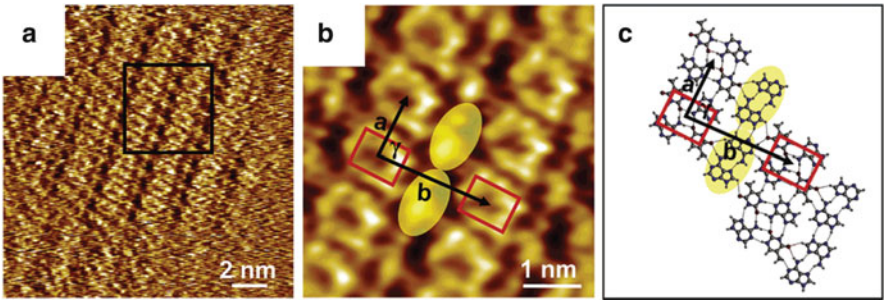

Fig. 1.9 (**a**) STM image of A and T mixture at the 1-octanol/HOPG interface. (**b**) A correlation-averaged zoom-in image of the part indicated in image (**a**) by a *black square*. (**c**) The calculated model: each cycle is formed by four molecules 2A + 2T, resulting in the reverse Hoogsteen A-T-A-T quartets adjacent to homochiral chains of A-A dimer. Cycle is indicated by *red rectangles*, and the unit cell is indicated in *black* (**a–c** are reproduced with the permission from Leonard et al. 1995, Copyright 2006, American Chemistry Society)

Table 1.3 Comparison of lattice parameters for the different assembly structures of A, T, and A-T from the analysis of STM images

	a (nm)	*b* (nm)	γ (deg)
Pure adenine (A)	0.8 ± 0.1	2.2 ± 0.2	76.0 ± 2.3
Pure thymine (T)	0.8 ± 0.1	1.5 ± 0.2	87.0 ± 2.5
Mixture A + T	1.0 ± 0.2	2.3 ± 0.2	88.0 ± 2.0

Table is reproduced with the permission from Leonard et al. (1995), Copyright 2006, American Chemistry Society

When two mixed A-T heterodimers approach each other, binding occurs between the A-T heterodimers leading to the quartet cycle formation, which was observed by STM; the unit cell of assembling structure is showed in Table 1.3. Due to the mixing molar ratio (350A:1T), more A molecules are involved in the assembly than T molecules. T molecules are mainly involved in the formation of A-T-A-T quartets. However, more adenine molecules by A-A dimers are suggested to consist of the single chains that bind to the A-T-A-T quartets to stabilize the whole network, which was also observed by STM (Fig. 1.9a, b). To identify which proposed model of quartet is more suitable for the molecular network assembled by A and T which is presented in STM image, all kinds of quartet models in addition of a single chain A-dimers were proposed in Fig. 1.10. Except the reverse Hoogsteen A-T-A-T quartet model, all other calculated models are not reasonable and not suitable for the structures in STM image. When two quartets approach each other along unit cell vector *a*, no binding occurs between the quartets along the unit cell vector *a* and between the quartets and the A-dimer chains along unit cell vector *b*. Therefore, only reverse Hoogsteen (Zain and Sun 2003) A-T-A-T quartets separated by homochiral chains of A-A dimer represent the best model according to the contrast of the STM image, the size, and shape of quartet cycles and single chains, binding energies between the quartets, as well as between the homochiral chains by A-A dimers. The binding energy of this most stable overall molecular

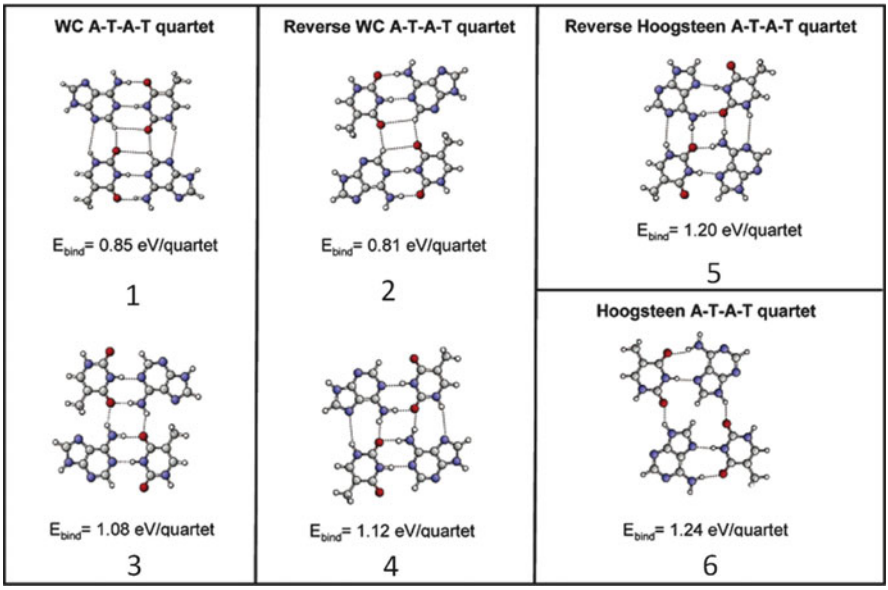

Fig. 1.10 A-T-A-T quartets and their calculated binding energies. Numbers are used to identify between the A-A, T-T, and A-T dimers and the A-T-A-T quartets (figure is reproduced with the permission from Leonard et al. 1995, Copyright 2006, American Chemistry Society)

network is 2.03 eV (per one A-T-A-T quartet + one A-A dimer in the unit cell). The unit cell from calculations is determined to be $a = 1.0 \pm 0.2$ nm, $b = 2.3 \pm 0.2$ nm, and $\gamma = 88.0 \pm 2.0^{\circ}$ which is in good agreement with STM findings. Furthermore, in the reverse Hoogsteen quartet, eight hydrogen bonds exist, whereas there are only two hydrogen bonds between two reverse Hoogsteen A-T-A-T quartets along the unit cell vector a (Fig. 1.9c).

In general, combining STM study and the theoretical calculation, the assembly structures by adenine and thymine molecules are investigated. The reverse Hoogsteen A-T-A-T quartets separated by homochiral chains of A-dimers were constructed initially; further, they self-assembled into an overall stabilization of a molecular network. The cyclic features constructed by A and T mixture are closely correlated to the structure so-called quadruplexes that consist of only one type of DNA bases, or a mixture of complementary DNA bases, which is found in biological system including replication, transcription, and recombination to telomere function (Lamond 2002).

1.5 Conclusion and Perspectives

We have introduced novel 2D supramolecular nanostructures assembled by DNA complementary bases on surface. DNA bases have the versatility to self-assemble into a wide variety of nanoscale-patterned structures. The pure guanine and adenine

are able to assemble into molecular network pattern on the surface by hydrogen bond interaction; cytosine and thymine are capable of constructing the molecular chain structure. However, the self-assembling nanostructures formed by the mixture of G-C and A-T are significantly different from the previous one by pure DNA bases. In the G-C system, they could construct the periodic molecular arrangement alternates between rows of high and low protrusions. Compared to G-C mixture, the self-assembling structures by A-T are more complicated. The reverse Hoogsteen A-T-A-T quartets separated by homochiral chains of A-dimers were constructed initially; further, they self-assembled into an overall stabilization of a molecular network. The observation and understanding of these novel nanoscale patterns formed from complementary DNA bases on an inorganic substrate are not least interesting from the perspective that molecular organization at interfaces, but are useful for targeting biological molecules by using some pattern structure. Furthermore, the study of self-assemblies of nucleic acid base molecules is of great use for the future to understand the mechanisms behind the assemblies of DNA bases and their complexes with amino acids and protein or more complex biological system.

Acknowledgments The authors acknowledge financial support from the Centre for DNA Nanotechnology and Danish-Chinese Centre for Self-Assembly and Function of Molecular Nanostructures on Surfaces from iNANO through the Danish National Research Foundation and Carlsberg Foundation. M.D. acknowledges the support from the STENO Independent Research grant and Young Investigator Program of Villum Kann Rasmussen Foundation.

References

Arnott S (1984) Sprung from chain. Nature 312:174–174

Bernstein J, Davis RE, Shimoni L et al (1995) Patterns in hydrogen bonding – functionality and graph set analysis in crystals. Angew Chem Int Ed 34:1555–1573

Binnig G, Rohrer H (1982) Scanning tunneling microscopy. Helv Phys Acta 55:726–735

Binning G, Rohrer H, Gerber C et al (1982) Surface studies by scanning tunneling microscopy. Phys Rev Lett 49:57–61

Douglas SM, Dietz H, Liedl T et al (2009) Self-assembly of DNA into nanoscale three-dimensional shapes. Nature 459:414–418

Fritz J, Baller MK, Lang HP et al (2000) Translating biomolecular recognition into nanomechanics. Science 288:316–318

Furukawa M, Tanaka H, Kawai T (2000) Formation mechanism of low-dimensional superstructure of adenine molecules and its control by chemical modification: a low-temperature scanning tunneling microscopy study. Surf Sci 445:1–10

Furukawa M, Tanaka H, Kawai T (2001) The role of dimer formation in the self-assemblies of DNA base molecules on Cu(111) surfaces: a scanning tunneling microscope study. J Chem Phys 115:3419–3423

Kawai T, Tanaka H, Nakagawa T (1997) Low dimensional self-organization of DNA-base molecules on Cu(111) surfaces. Surf Sci 386:124–136

Kelly REA, Kantorovich LN (2006) Homopairing possibilities of the DNA base thymine and the RNA base uracil: an ab initio density functional theory study. J Phys Chem B 110:2249–2255

Kelly REA, Lee YJ, Kantorovich LN (2005a) Homopairing possibilities of the DNA base adenine. J Phys Chem B 109:11933–11939

Kelly REA, Lee YJ, Kantorovich LN (2005b) Homopairing possibilities of the DNA bases cytosine and guanine: an ab initio DFT study. J Phys Chem B 109:22045–22052
Lamond AI (2002) Swimming lessons. Nature 417:383–383
Leonard GA, Zhang S, Peterson MR et al (1995) Self-association of a DNA loop creates a quadruplex – crystal-structure of D(Gcatgct) at 1.8-angstrom resolution. Structure 3:335–340
Liu L, Zhang L, Mao XB et al (2009) Chaperon-mediated single molecular approach toward modulating a beta peptide aggregation. Nano Lett 9:4066–4072
Liu L, Busuttil K, Zhang S et al (2011a) The role of self-assembling polypeptides in building nanomaterials. Phys Chem Chem Phys 13:17435–17444
Liu L, Zhang L, Niu L et al (2011b) Observation of reduced cytotoxicity of aggregated amyloidogenic peptides with chaperone-like molecules. ACS Nano 5:6001–6007
Ma XJ, Liu L, Mao XB et al (2009) Amyloid beta (1-42) folding multiplicity and single-molecule binding behavior studied with STM. J Mol Biol 388:894–901
Mamdouh W, Dong MD, Xu SL et al (2006) Supramolecular nanopatterns self-assembled by adenine-thymine quartets at the liquid/solid interface. J Am Chem Soc 128:13305–13311
McNutt A, Haq S, Raval R (2003) RAIRS investigations on the orientation and intermolecular interactions of adenine on Cu(110). Surf Sci 531:131–144
Nishimura M, Tanaka H, Kawai T (2002) Structure of linear double-stranded deoxyribonucleic acid adsorbed on Cu(111) surfaces: a low-temperature scanning tunneling microscopy study. Jpn J Appl Phys 41:7510–7511
Otero R, Schock M, Molina LM et al (2005) Guanine quartet networks stabilized by cooperative hydrogen bonds. Angew Chem Int Ed 44:2270–2275
Pauling L (1992) The nature of the chemical-bond – 1992. J Chem Educ 69:519–521
Perdigao LMA, Staniec PA, Champness NR et al (2006) Experimental and theoretical identification of adenine monolayers on Ag-terminated Si(111). Phys Rev B 73 195423(1–7)
Rothemund PWK (2006) Folding DNA to create nanoscale shapes and patterns. Nature 440:297–302
Samori B, Zuccheri G (2005) DNA codes for nanoscience. Angew Chem Int Ed 44:1166–1181
Sowerby SJ, Heckl WM (1998) The role of self-assembled monolayers of the purine and pyrimidine bases in the emergence of life. Orig Life Evol Biosph 28:283–310
Wandlowski T, Lampner D, Lindsay SM (1996) Structure and stability of cytosine adlayers on Au (111): an in-situ STM study. J Electroanal Chem 404:215–226
Watson JD, Crick FHC (2003) Molecular structure of nucleic acids – a structure for deoxyribose nucleic acid. Revista De Investigacion Clinica 55:108–109 (Reprinted from Nature, vol 171, pg 737–738, 1953)
Whitesides GM, Grzybowski B (2002) Self-assembly at all scales. Science 295:2418–2421
Whitesides GM, Mathias JP, Seto CT (1991) Molecular self-assembly and nanochemistry – a chemical strategy for the synthesis of nanostructures. Science 254:1312–1319
Winfree E, Liu FR, Wenzler LA et al (1998) Design and self-assembly of two-dimensional DNA crystals. Nature 394:539–544
Xu SL, Dong MD, Rauls E et al (2006) Coadsorption of guanine and cytosine on graphite: ordered structure based on GC pairing. Nano Lett 6:1434–1438
Yang YL, Wang C (2009) Hierarchical construction of self-assembled low-dimensional molecular architectures observed by using scanning tunneling microscopy. Chem Soc Rev 38:2576–2589
Zain R, Sun JS (2003) Do natural DNA triple-helical structures occur and function in vivo? Cell Mol Life Sci 60:862–870
Zhao XJ, Zhang SG (2006) Molecular designer self-assembling peptides. Chem Soc Rev 35:1105–1110

Chapter 2
Force Spectroscopy of DNA and RNA: Structure and Kinetics from Single-Molecule Experiments

Rebecca Bolt Ettlinger, Michael Askvad Sørensen, and Lene Broeng Oddershede

Abstract Force spectroscopy of individual DNA and RNA molecules provides unique insights into the structure and mechanics of these for life so essential molecules. Observations of DNA and RNA molecules one at a time provide spatial, structural, and temporal information that is complementary to the information obtained by classical ensemble methods. Single-molecule force spectroscopy has been realized only within the last decades, and its success is crucially connected to the technological development that has allowed single-molecule resolution. This chapter provides an introduction to in vitro force spectroscopy of individual DNA and RNA molecules including the most commonly used techniques, the theory and methodology necessary for understanding the data, and the exciting results achieved. Three commonly used single-molecule methods are emphasized: optical tweezers, magnetic tweezers, and nanopore force spectroscopy. The theory of DNA stretch and twist under tension is described along with related experimental examples. New principles for extracting kinetic and thermodynamic information from nonequilibrium data are outlined, and further examples are given including the opening of DNA and RNA structures to reveal their energy landscape. Finally, future perspectives for force spectroscopy of DNA and RNA are offered.

Contents

R.B. Ettlinger • L.B. Oddershede (✉)
The Niels Bohr Institute, University of Copenhagen, Copenhagen, Denmark
e-mail: rebecca@nbi.dk; oddershede@nbi.dk

M.A. Sørensen
The Department of Biology, University of Copenhagen, Copenhagen, Denmark
e-mail: mas@bio.ku.dk

J. KJEMS et al. (eds.), *Nucleic Acid Nanotechnology*, Nucleic Acids and Molecular Biology 29, DOI 10.1007/978-3-642-38815-6_2,

Nomenclature

ΔG	Gibbs free energy change
$\Delta G^{\ddagger}$	Activation energy
CFT	Crooks fluctuation theorem
dsDNA	Double-stranded DNA
EWLC	Extensible worm-like chain model
FJC	Freely jointed chain model
JE	Jarzynski equality
$k(F)$	Rate of transition at force F
k_0	Rate of transition at zero force
K_0	Elasticity
L_c	Contour length
L_p	Persistence length
MT	Magnetic tweezers
NFS	Nanopore force spectroscopy
OT	Optical tweezers
ssDNA	Single-stranded DNA
TWLC	Twistable worm-like chain model
WLC	Worm-like chain model
$x^{\ddagger}$	Distance to the transition state

2.1 Introduction

The response of single DNA and RNA molecules to force helps reveal their structure and the transitions they undergo when experiencing mechanical stress. In essence, molecular force spectroscopy probes how molecules comply with tension. Experimenters uncover molecular response over a range of pulling forces or a range of degrees of twist. They may also study the molecular response at a constant force for an extended period of time. The results provide information about the mechanical deformation that DNA and RNA may experience in other contexts, e.g., due to enzyme binding, artificial manipulation, or strand separation during cell division. This makes molecular force spectroscopy a crucial tool in nucleic acids nanotechnology.

The present chapter focuses on in vitro single-molecule force spectroscopy investigations of DNA and RNA. Examples include stretch-induced melting of double-stranded DNA (Sect. 2.3.1), mapping the energy landscape of DNA hairpins (Sect. 2.5.2), and exploring how mRNA pseudoknots unfold (Sect. 2.5.3). One major field not covered here is the use of force spectroscopy to examine the action of enzymatic complexes such as RNA polymerase and ribosomes on polynucleic acids. Recent reviews of this area have been made by, e.g., Bryant et al. (2012) and Lavelle et al. (2011). Another field omitted here is in vivo single-molecule force spectroscopy, which has recently been reviewed by Oddershede (2012).

Early pulling experiments on individual molecules of DNA and RNA have shown that the intrinsic nature of these polymers is more like that of a "worm-like chain," i.e., a continually flexible elastic cord, than a "freely jointed chain" with stiff linkers oriented at random (Bustamante et al. 1994). The flexibility and elasticity of single-stranded RNA and single- and double-stranded DNA (ssDNA and dsDNA) have been evaluated (Mangeol et al. 2011; Chen et al. 2012; Wang et al. 1997), and DNA response to twist and the coupling between stretching and twisting have been quantified (Gore et al. 2006; Gross et al. 2011). Further experiments have extensively probed the overstretching transition of double-stranded DNA where a 70 % increase in length is suddenly observed at high force; the exact force at which the transition takes place varies, e.g., with pH (Cluzel et al. 1996; Williams et al. 2001).

Force spectroscopy has further been used to illuminate patterns of bond breakage and formation, as pulling can alter the chemical structure of the molecule being examined. Classical studies include the unzipping of the strands of dsDNA and the unfolding of RNA hairpins, both of which are accompanied by identifiable changes in molecular extension directly related to the number of base pairs opening (Essevaz-Roulet et al. 1997; Liphardt et al. 2001). Data on transition forces and molecular extension at a given force have allowed evaluation of the brittleness and strength of the structure being pulled. These data also provide access to the rate of formation and dissociation at zero force (Liphardt et al. 2001) and the Gibbs free energy change of the transition (Liphardt et al. 2002; Collin et al. 2005).

The following section introduces the three most commonly used methods for force spectroscopy of DNA and RNA: optical tweezers, magnetic tweezers, and nanopore force spectroscopy. Section 2.3 of this chapter describes the characterization of DNA response to stretch and twist, while Sects. 2.4 and 2.5 lay out the principles developed within the last 15 years to extract kinetic and thermodynamic parameters from transition data. Several notable experimental results are shown. Finally, Sect. 2.6 provides a summary and perspectives on what to expect from force spectroscopy of DNA and RNA in the coming years.

2.2 Commonly Used Methods

Three main methods of molecular force spectroscopy are described in this section: optical tweezers, magnetic tweezers, and nanopore force spectroscopy (OT, MT, and NFS). When using optical and magnetic tweezers, the experimenter applies force to the molecule under investigation by tethering it between extremities such as artificial beads that can be manipulated with the instrument. Calibration allows conversion of the measurement output to force. In nanopore force spectroscopy, a difference in electrical potential pulls single molecules across a membrane, requiring no external attachment of the molecule under investigation, but also providing no direct measurement of the magnitude of the force. The three approaches are illustrated in Fig. 2.1 and compared in Table 2.1.

Other force spectroscopy techniques that have been applied to DNA and RNA include atomic force microscopy (AFM) (Strunz et al. 1999), microneedle manipulation (Essevaz-Roulet et al. 1997), and application of flow to tethered molecules (Perkins et al. 1997). AFM most efficiently probes at higher forces than the structural transitions of polynucleic acids and is more commonly used to investigate protein filaments. Microneedle manipulation gives access to lower forces than AFM, but accurate measurements are difficult to obtain. Application of flow allows measurement of both molecular extension and molecular flexibility in a buffer that is easily exchanged, but force is not easily measured, and manipulative control is limited (Bustamante et al. 2000).

2.2.1 Optical Tweezers

An optical trap captures nanometer to micrometer-sized objects such as cells or highly refractive beads through the induction of an electrical dipole by a tightly focused laser beam. The interaction can be viewed as a balance between the scattering and gradient forces exerted by the laser. The scattering force pushes the object in the direction of the light's propagation, while the gradient force pulls it towards the point of greatest light intensity. A full analysis of these forces requires calculations which take into account the exact shape and size of the object

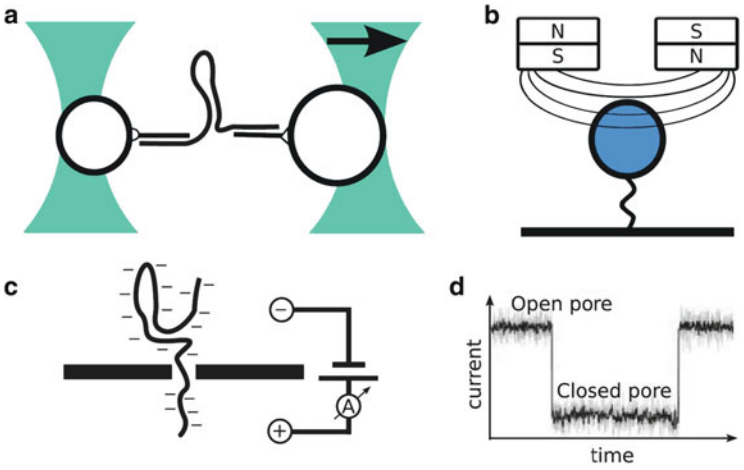

Fig. 2.1 Force spectroscopy methods. (**a**) Dual beam optical tweezers for pulling a single-stranded polynucleic acid hairpin. The single-stranded DNA or RNA molecule is attached to two single-stranded DNA handles via base pairing. The DNA handles are attached through linker molecules to the beads. (**b**) Simple magnetic tweezers for pulling and twisting a polynucleic acid attached through linkers to the sample chamber surface and to a magnetic bead. Figure inspired by de Vlaminck and Dekker (2012). (**c**) Nanopore force spectroscopy for investigating the structure of a single-stranded polynucleic acid. The electrical field across the membrane exerts a force on the negatively charged DNA or RNA molecule. The current through the membrane is monitored (**d**) as DNA passes and the amount of time that the pore is closed (the passage time) is used to characterize the unfolding of the single-stranded structure. Figure inspired by Dudko et al. (2010)

Table 2.1 Characteristics of the most common molecular force spectroscopy methods

	Typical force	Stiffness	Spatial resolution	Twist	Usage
OT	0.1–200 pN	0.005–1 pN/nm	0.1 nm	With permanent dipole in handles	Lateral and axial pull. Handles needed
MT	0.001–20 pN	$\approx 10^{-6}$ pN/nm	1 nm	Yes	Axial pull, torque measurement Magnetic handles needed
NFS	1–30 pN (solid-state nanopore)	≈0.2 pN/mV (solid-state nanopore) (Keyser et al. 2006)	NA	No	Axial pull across a membrane. No handles. No direct force/distance measurement

OT optical tweezers, *MT* magnetic tweezers, *NFS* nanopore force spectroscopy

(Rohrbach 2005). Here we will simply note that the force created by a focused laser with a Gaussian intensity profile can stably hold an object with an index of refraction larger than that of the surrounding medium. The trapping potential is

approximately harmonic with $F = -\kappa x$, where F is the force of the trap on the object, κ the trap stiffness, and x the displacement of the object from the trap center. The potential is strongest for objects about the size of the wavelength of the laser, often about 1 μm, and can extend several hundred nanometers, exerting forces of more than 100 pN.

A typical optical tweezers setup consists of a laser implemented in an inverted microscope which focuses the trapping laser on the sample using the microscope objective. The position of the object in the trap can be monitored either by video microscopy or by collecting the laser light by a condenser and focusing it onto a photodiode. The trap may be moved with optical devices such as galvanic mirrors or acousto-optical deflectors. In some cases, the trapping beam is split into several independently controlled traps. Calibration is based on measurement of the constrained Brownian motion of the bead in the trap, sometimes combined with drag measurements. This allows conversion of the voltage output from the photodiodes to precise measurements of position and force (Gittes and Schmidt 1998).

In force spectroscopy experiments, the DNA or RNA molecule under investigation is attached by linkers such as biotin–streptavidin or digoxigenin–antidigoxigenin bindings to two optically trapped beads, to a trapped bead and a surface, or to a trapped bead and a bead held by a micropipette. During experiments, the surface, the micropipette, or one of the optical traps may be moved in a controlled fashion in order to extend the molecule and apply force. Most often the force is either changed at an approximately constant rate (force ramp) or held constant by a feedback system.

The precise nature of the attachment between the molecule and the bead must be taken into account in interpretation of the results. For instance, rotational constraint can be crucial for the molecule's response to stretch. This may be determined by whether dsDNA is attached to the beads or to the surface by both strands or only by one strand (see Sect. 2.3.1). Single-stranded DNA or RNA under investigation is commonly attached by base pairing to single-stranded handles, which again are attached to linkers and beads (Fig. 2.1a). Any significant stretching of these handles must be included in the data analysis. This is especially relevant when evaluating, for instance, changes in molecular extension.

Long handles can make experimentation easier because the two points of attachment are better separated spatially, thus reducing surface interactions. Larger separation also reduces dual trap interference. Short handles on the other hand reduce noise and the contribution of handle stretching.

Optical tweezers are usually used for pulling experiments in which force is applied parallel to the axis between the two molecular points of attachment. In the last 10 years, however, optical torque wrenches have been introduced. These use polarized light to turn birefringent particles and thus twist molecules in the plane perpendicular to the direction of propagation of the laser (La Porta and Wang 2004). In combination with other techniques, optical tweezers thus enable a wide range of investigations into polynucleic acids and their interactions with other components of the cell. A review of the diverse capabilities and applications of optical tweezers in biomedicine is provided by Stevenson et al. (2010).

2.2.2 Magnetic Tweezers

The simplest magnetic tweezers consist of two movable magnets mounted above a sample chamber. The magnetic field creates a force on a magnetic bead, which can be moved relative to the sample chamber surface by moving either the chamber or the magnets. Torque can be applied by using paramagnetic beads, since the magnetic field induced in a paramagnet is stronger along one axis, which will align to the magnetic field. This ability to apply torque is a key advantage of magnetic tweezers. Another important property is that in contrast to optical tweezers, the force of magnetic tweezers does not change appreciably with bead movement in the trap. Thus, the force on the bead is more or less constant despite changes in, e.g., molecular extension. The near-constant magnetic field also means that magnetic tweezers exert force on all magnetic particles in the sample at the same time.

For force spectroscopy experiments, the molecule is frequently tethered between a magnetic bead and the sample chamber surface (Fig. 2.1b). The magnetic tweezers are usually built into a microscope, and detection of changes in extension of the molecule is done using CCD cameras. These cameras track the interference pattern created by the bead's motion with respect to the microscope focus. The CCD output is calibrated with a series of images of the bead at known z-heights above the sample chamber surface.

Force calibration is done by monitoring the Brownian motion of the tethered bead and invoking the equipartition theorem while applying knowledge of the extension of the molecule from the CCD images. To do this, the tether is treated as a pendulum with a lateral stiffness constant α_x, so that $\alpha_x = F_z/L$, where F_z is the upward force on the bead and L is the length of the tether (Neuman and Nagy 2008). The energy of the particle is related to the average bead displacement from the center of its movement by $k_B T = \alpha_x <x^2>$, where k_B is the Boltzmann constant and T the temperature, so that $F_z = Lk_B T/<x^2>$.

The magnitude of the torque applied to twist the molecule a given number of turns cannot be directly measured in most magnetic tweezers setups. However, using new techniques that allow almost unconstrained turning of the molecule, experimenters have been able to measure torque by measuring the average motion of fluorescent beads attached to the molecule or of marker beads attached to the magnetic bead. These and other recent technical advances in magnetic tweezers are reviewed by de Vlaminck and Dekker (2012).

2.2.3 Nanopore Force Spectroscopy

Nanopore force spectroscopy (NFS) is intrinsically different from OT and MT force spectroscopy because force is applied electrically rather than mechanically. Therefore, force is applied diffusely to the entire molecule rather than at a single point.

In a typical DNA or RNA NFS experiment, a nanopore just large enough for the passage of single-stranded DNA or RNA is located in a membrane that separates two buffer reservoirs (Fig. 2.1c). The pore may be either biological, e.g., an α-hemolysin pore in a lipid membrane, or solid state, e.g., etched in a silicon-based membrane. A voltage is applied across the membrane, and the current due to ion flow through the pore is measured. If a DNA or RNA molecule enters the pore, the current changes due to the change in ion flow (Fig. 2.1d). After a characteristic time, the molecule is pulled across the membrane by the voltage drop because both DNA and RNA have a net negative charge under physiological buffer conditions. The time that the DNA or RNA molecule takes to pass the membrane is monitored. The passage time data are used to extract kinetic parameters of the structural change, such as hairpin unfolding, that occurs while the molecule passes through the pore.

Unlike OT and MT force spectroscopy, NFS does not allow for direct measurement of force. However, the technique can be combined with optical trapping for accurate force measurements. Alternatively, one may approximate the force by calculating the estimated charge on the molecule, since $F = q_{\text{eff}}E$, where F is the force on the molecule, q_{eff} is the effective charge of the molecule inside the pore, and E is the electric field across the pore. Keyser et al. (2006) combined optical trapping and nanopore force spectroscopy and found $q_{\text{eff}} \approx 0.25Q$ for a variety of buffer strengths, where Q is the bare DNA charge.

NFS may allow easier access to large amounts of single-molecule force spectroscopy data than OT or MT, since it may be more efficient to coerce molecules through a membrane ion channel than to capture them one at a time with optical or magnetic traps. The high throughput of the technique has already proven useful in validating new theory for extracting kinetic rates of DNA hairpin unfolding (Sect. 2.4.3; Dudko et al. 2010).

2.3 Stretching DNA and RNA

How does DNA conform to force along its length and how elastic is it? Does the double-stranded helix unwind as it is pulled? And how do single-stranded DNA and RNA differ from double-stranded molecules in their response to tension?

The answers have important implications both for direct manipulation of DNA in nanotechnological applications and for understanding the action of DNA-modifying molecular motors that locally bend or stretch the molecule as they progress along their template. DNA stretching and twisting have therefore been investigated experimentally in vitro since the mid-1990s. Curves of applied force versus molecular end-to-end distance (Fig. 2.2a) show that dsDNA may be extended almost without resistance from an initially randomly coiled position until it approaches its contour length, L_c. The contour length is the molecule's extension when completely straightened but not stretched. Near the contour length, more and more force must be applied to further extend the molecule. Surprisingly, however,

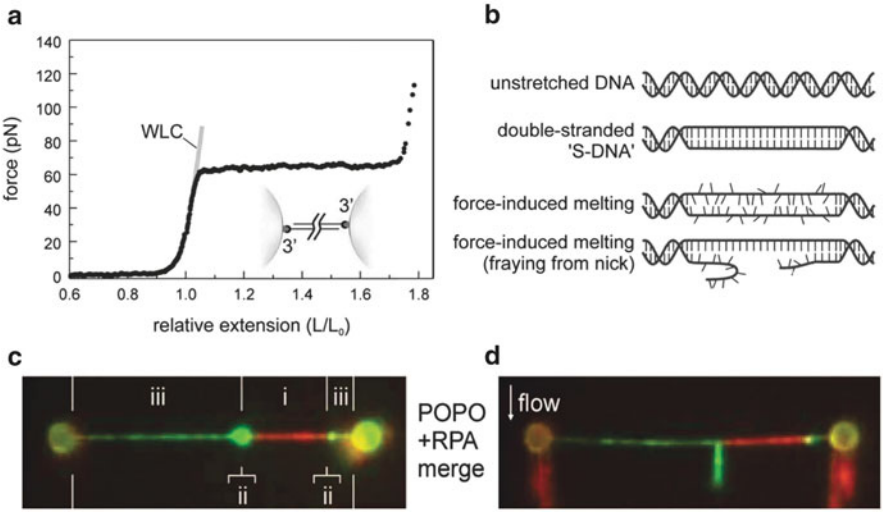

Fig. 2.2 dsDNA force–extension behavior: (**a**) Force–extension curve showing the overstretching transition at 65 pN for rotationally unconstrained dsDNA. The DNA is attached at the 3′ end of each strand as indicated in the *inset*. L_0 is the contour length, called L_c in the remainder of this chapter. (**b**) Hypothesized DNA conformations during the overstretching transition. (**c**) Overstretched λ-DNA held between two optically trapped beads. Attachment to beads as shown in *inset* in (**a**); note that the DNA is free to rotate. The same DNA is shown in (**c**) and (**d**). *Red*: dsDNA labeled with the fluorescent dsDNA-intercalator POPO-3. *Green*: ssDNA labeled by enhanced green fluorescent protein-tagged replication protein A (eGFP-RPA). (**d**) Flow is applied perpendicular to the extended molecule so that ssDNA is clearly seen flowing away from the remaining dsDNA. Reproduced with permission from van Mameren et al. (2009)

at high force, the force–extension curve of dsDNA displays an overstretching plateau at which the molecule can be lengthened by about 70 % beyond its contour length with very little resistance.

If the molecule is free to rotate, e.g., if the beads are attached only to one strand at each end of the double-stranded DNA, the overstretching plateau occurs at about 65 pN. In contrast, if the molecule is rotationally constrained because both strands are attached at both ends, the overstretching plateau occurs at around 110 pN (Leger et al. 1999).

2.3.1 The Nature of Overstretched DNA

The nature of the DNA structure at the overstretching plateau in the dsDNA force–extension curve has been the subject of controversy for over a decade. Two possibilities were put forward (Fig. 2.2b): (1) that the overstretching results from unwinding of the original double helix structure of dsDNA (B-DNA), creating a

ladder-like double-stranded structure ("S-DNA") (Cluzel et al. 1996), and (2) that the base pairs connecting the double strands of the B-DNA melt, creating two single strands (Williams et al. 2001).

These discussions were significantly advanced in 2009 by van Mameren et al. The group performed a series of pulling experiments combining optical tweezers and fluorescence imaging. Using a range of fluorescent markers that bind only to either double- or single-stranded DNA, and using two different methods of DNA attachment, they were able to show that the overstretching transition for rotationally unconstrained DNA at 65 pN occurs due to melting of the dsDNA strand into ssDNA (Fig. 2.2c, d). The melting was shown to initiate at a free end of the dsDNA or at a nicked site. Additionally, the group showed that if the dsDNA was rotationally constrained, then the overstretching plateau occurred at 110 pN.

The investigation and discussion of the structure of overstretched dsDNA is ongoing, and Zhang et al. (2012) recently showed that the nature of the DNA formed during the transition is dependent on temperature, buffer strength, and DNA base composition. The group observed two different types of overstretching transitions near 65 pN in rotationally unconstrained DNA. One corresponds to the melting into single strands observed by van Mameren et al. (2009) and occurs at relatively high temperatures (generally room temperature or above), low GC content, and/or low salt concentrations. The other transition, which occurs at lower temperatures, higher salt concentrations, and/or higher GC content, appears to correspond to a transition from B-DNA to a structure which is yet not structurally characterized but where the two strands of the original B-DNA do stay closely associated.

The experiments by van Mameren et al. (2009) were carried out at salt concentrations up to 150 mM NaCl, which corresponds to the observation of Zhang et al. (2012) that a melting transition occurs for dsDNA with up to 50 % GC content when pulled at room temperature in a buffer with less than 150 mM NaCl.

2.3.2 *Models of DNA Stretch*

To describe the force–extension properties of dsDNA at low forces, the worm-like chain (WLC) model is often used (Bustamante et al. 1994; Collin et al. 2005). This model treats the DNA as a rope or an electrical cord which at forces below about 10 pN can be stretched entropically (i.e., by changing its state of disorder without changing the internal energy or other enthalpy components). An interpolation formula for the WLC model uses the contour length, L_c, along with the characteristic persistence length, L_p, to predict the end-to-end distance, x, at a particular pulling force, F (Marko and Siggia 1995):

$$F = \frac{k_B T}{L_p}\left[\frac{1}{4(1 - x/L_c)^2} - \frac{1}{4} + \frac{x}{L_c}\right] \tag{2.1}$$

The persistence length, L_p, indicates how easily the polymer is bent at a given temperature. It is directly proportional to the polymer's flexural rigidity, κ_f, and inversely proportional to temperature: $L_p = \kappa_f/k_BT$. The flexural rigidity, κ_f, is the product of Young's modulus, Y, a property that describes the inherent material stiffness, and the inertial cross section, J, which relates purely to the polymer's geometry (Boal 2002).

To better describe the behavior of dsDNA at pulling forces above 10 pN, the WLC model has been modified by the addition of a parameter characterizing the enthalpic elasticity, K_0, in the extensible worm-like chain (EWLC) model (Wang et al. 1997). This incorporates the stretching ability of the polymer's intrinsic structure. Both the WLC and the EWLC models have been used to characterize the stretching of ssDNA and RNA as well as dsDNA, though ssDNA is sometimes described by the freely jointed chain model and its true behavior may be a hybrid of EWLC and FJC behavior (Rouzina and Bloomfield 2001). Single-stranded molecules are more flexible than dsDNA with correspondingly lower L_p, but they are approximately as elastic, showing about the same K_0. For dsDNA, $L_p \approx 47$ nm, while for single-stranded RNA, $L_p \approx 1.5$ nm (Mangeol et al. 2011). The values vary with buffer strength, and while, for instance, $L_p \approx 0.75$ nm has been found for ssDNA in 150 mM NaCl by Smith et al. (1996), a range between 1 and 6 nm have been found for ssDNA using different measurement techniques in other buffers, mainly weaker ones. To complicate the picture, addition of divalent cations, e.g., magnesium, appears to increase the persistence length much more dramatically than increasing monovalent salt concentration (Chen et al. 2012; Bizarro et al. 2012).

Recently, the EWLC model for dsDNA has been improved for forces above 35 pN by taking into account the coupling between twist and stretch that occurs for rotationally unconstrained DNA as further discussed in Sect. 2.3.4. The twistable worm-like chain (tWLC) model fits the force–extension data accurately up to the overstretching plateau at about 65 pN, as seen in Fig. 2.3a. In addition to L_c, L_p, and K_0, the model incorporates the DNA's twist rigidity, C, and an empirically derived function, $g(F)$, describing the coupling of twist and stretch to predict the force–extension curve. The tWLC model is formulated as (Gross et al. 2011)

$$x = L_c\left(1 - \frac{1}{2}\sqrt{\frac{k_BT}{FL_p}} + \frac{FC}{-g(F)^2 + K_0C}\right) \tag{2.2}$$

Importantly, the family of WLC models can only be applied when the contour length is much longer than the persistence length ($L_c \gg L_p$). The contour length of a dsDNA base pair at zero force is about 0.28 nm while that of a single-strand nucleotide is about 0.59 nm (Hansen et al. 2007). Thus, for the WLC models to apply, the dsDNA in question must be much longer than 150 base pairs.

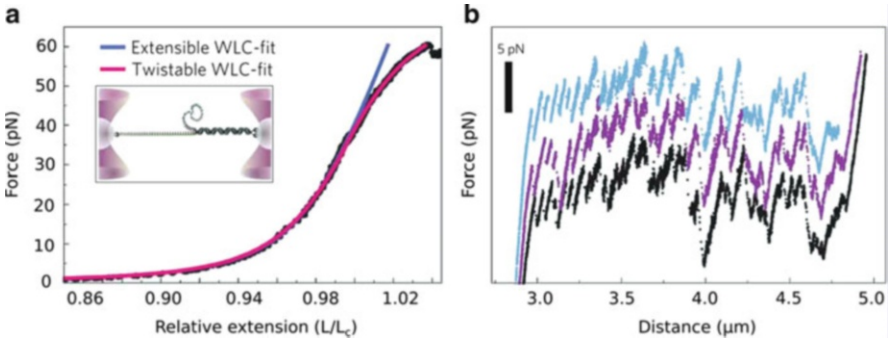

Fig. 2.3 Twistable worm-like chain and sawtooth pattern during the overstretching transition. (**a**) tWLC model versus data. The experimental values of pulling force versus molecular extension (*black*) are compared to the extensible worm-like chain model (*blue*) and the twistable worm-like chain model (*pink*). *Inset*: pulling geometry. The dsDNA is attached to bead handles at three sites. (**b**) Sawtooth unfolding pattern at the 65 pN overstretch plateau during three different pulls, see Sect. 2.3.3. The dsDNA is attached as in the *inset* of (**a**) so that only one strand has a free end. Figures from Gross et al. (2011)

For single-stranded RNA and DNA, on the other hand, the minimum length for applying the WLC models is equivalent to less than ten nucleotides.

2.3.3 DNA Unzipping

Early single-molecule DNA investigations showed that a sequence-dependent sawtooth pattern occurs in the force–extension curve when a long piece of dsDNA is unzipped by a force perpendicular to the helix (Essevaz-Roulet et al. 1997). Unzipping occurs at forces of about 10–15 pN, much lower than the forces required for overstretching when dsDNA is pulled along the length of the helix. The peaks in the unzipping sawtooth pattern are correlated with GC-rich areas in the dsDNA because GC base pairs are stronger than AT base pairs, requiring more force to open. Thus, researchers found that dsDNA unzipping occurs in bursts at high speed in AT-rich regions and lower speed in the GC-rich regions.

Sawtooth patterns are also observed during overstretching when force is applied parallel to the helical direction, supporting the hypothesis described in the previous section (Sect. 2.3.1) that the overstretching plateau represents base pairs melting. Recent experiments by Gross et al. (2011) further corroborate this explanation by showing that the sawtooth patterns observed during overstretching at room temperature and low salt concentration (50 mM NaCl) are reproducible and sequence correlated just like those seen in unzipping experiments (Fig. 2.3b). This reproducible slip-stick behavior of melting dsDNA is most clearly visible in experiments when only a single end of the tethered dsDNA is free; hence, the melting into ssDNA will initiate from this point only, as in the inset in Fig. 2.3a.

2.3.4 DNA Twist

The twist-stretch coupling function $g(F)$ was first quantified by monitoring the torque on the DNA together with the change in length of the molecule using magnetic torque tweezers (Gore et al. 2006). Remarkably, DNA at first overwinds when stretched: the helix winds more closely as the molecule is lengthened, conserving volume. If pulled by forces stronger than 30 pN, the DNA eventually does unwind as it lengthens further.

Conversely, if the dsDNA is overwound by torque, it stretches. Twisting the molecule, one complete rotation causes it to lengthen by approximately 0.5 nm. This lengthening continues until eventually, with increased winding at constant force, the DNA shortens as might be expected because supercoiling is induced in the double-stranded structure (Gore et al. 2006).

Generally, if dsDNA is strongly over- or underwound at low force, it forms writhes and plectonemes (supercoils), resulting in shorter molecular extension (Strick et al. 1998). An overview of the research on the transitions that DNA undergoes when over- or underwound has been laid out by Bryant et al. (2012).

2.3.5 Higher-Order DNA Structure

The packaging of DNA in chromatin is a major topic of single-molecule research, recently reviewed by Killian et al. (2012). Chromatin is a higher-order DNA structure composed of dsDNA wrapped around histone proteins in tight bundles called nucleosomes. Force spectroscopy techniques have been used to probe how dsDNA is bound to individual histones, how nucleosomes are distributed along the DNA, and how series of nucleosomes are arranged in relation to each other in the chromatin fiber.

An example of such a study is the use of magnetic tweezers by Kruithof et al. (2009) to deduce the folding geometry of nucleosome-bound DNA in chromatin. The group calibrated the magnitude of the force applied by the magnetic tweezers at different heights relative to the sample chamber and were therefore able to measure the response of the chromatin at different forces. They used this ability to investigate the force response of two different types of chromatin fibers. Both types of fibers were previously known to wrap into a structure with a diameter of about 30 nm, but the spatial arrangement of the nucleosomes within the fibers was debated. One type of fiber had a nucleosome repeat length of 197 base pairs; the other had a nucleosome repeat length of 167 base pairs. The nucleosome repeat length is the number of base pairs per nucleosome, some of which is DNA is wrapped around the histone complex and some of which may constitute linker DNA between the histones. In nature a variety of different repeat lengths are found. A repeat length of 197 base pairs allows for an average amount of linker DNA, while 167 base pairs allow for no linker DNA at all. How could these two types of fiber wrap into apparently similar structures?

To investigate this, chromatin fibers were attached between the chamber surface and a magnetic bead and stretched. The results showed that both types of chromatin fiber stretch gradually up to a force of about 4–6 pN. Above this force, the force–extension curve displays a plateau, which the group attributed to the disruption of nucleosome–nucleosome interactions, i.e., dissociation of the fiber.

Focusing on the slope of the curve before the nucleosome dissociation plateau, the group was able to show that the chromatin fibers behaved like Hookean springs and that fibers with normal-length linker DNA had lower stiffness and were shorter than fibers lacking linker DNA. This led the group to conclude that with normal-length linkers, chromatin forms a single-helix coil, while without linkers it forms a stacked zigzag coil. The softer of the two types of coil will stretch and contract more with thermal fluctuations than the stiffer type of fiber, possibly allowing for different types of interactions with chromatin-modifying proteins. The group expects that both types of structure and possibly others will occur naturally (Kruithof et al. 2009).

2.4 Kinetics

Molecular force spectroscopy is often used to investigate structural changes from one molecular state to another, e.g., the opening and closing of DNA or RNA hairpins. As such experiments inevitably involve a force acting on the molecule of interest, traditional equilibrium thermodynamics is inadequate to describe the process. Recent advances in nonequilibrium thermodynamics are, however, providing tools to extract thermodynamic constants from nonequilibrium experiments. The following section describes a theoretical framework that can be used to find the kinetic transition rates and the brittleness of the investigated molecule. In Sect. 2.5, we outline recently discovered thermodynamic principles that allow quantification of the Gibbs free energy change from nonequilibrium data and give access to the profile of the energy landscape.

2.4.1 Rate of Transition and Molecular Brittleness

Investigating molecular structure with optical or magnetic tweezers by applying either a constantly increasing force (force ramp) or a constant force to a single molecule usually results in data series of transition forces or waiting times, respectively. Both types of experiments measure the change in extension of the molecule due to a structural transition. From the distribution of forces or waiting times, information may be extracted about the rate of opening at different forces, $k(F)$, with the rate of opening at zero force, k_0, especially of interest. From the change in extension, the number of base pairs or single nucleotides involved in the transition may be calculated, see Fig. 2.4b for an example.

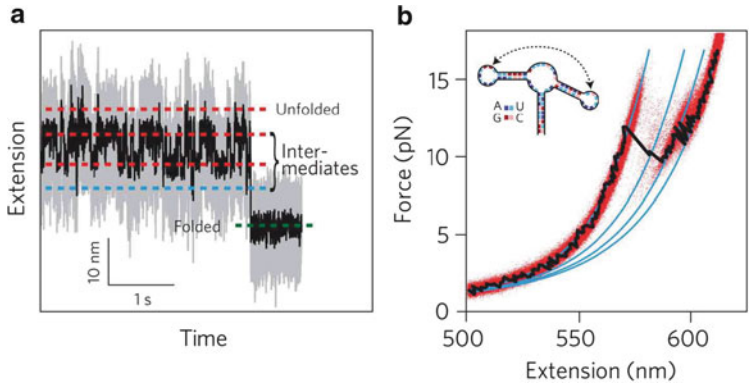

Fig. 2.4 Data from unfolding a riboswitch aptamer (more details on the experiment are given in Sect. 2.5.2): (**a**) Constant-force OT data. The aptamer hops between unfolded, folded, and intermediate states with different molecular extensions. (**b**) 700 overlaid force–extension curves from OT force-ramp experiments (data *red*, average *black*). Intermediate states corresponding to different (*blue*) equilibrium WLC stretch curves are evident. *Inset*: expected closed state of the aptamer. The *arrow* indicates expected interaction between the two hairpin loops. Reproduced with permission from Gupta et al. (2011)

Nanopore experiments for investigating molecular structure do not directly yield force or distance measurements. However, the series of waiting times between molecule insertion and molecule passage through the membrane likewise yield the rate of reaction.

Data on changes in extension may be used to identify intermediate states. In constant-force experiments, several distinct equilibrium molecular lengths corresponding to different molecular states may be directly observed (Fig. 2.4a). Similarly, in force-ramp experiments, it may be clear that the molecule is passing between several equilibrium force–extension curves. In this case intermediate states are most clearly seen by aligning many curves of force versus molecular extension (Fig. 2.4b). Curves corresponding to different molecular states may be distinguished by fitting to extension curves for folded, intermediate, or unfolded configurations. The curves are modeled by using the appropriate stretching model for the force regime being probed, i.e., the worm-like chain model or the twistable worm-like chain model, as described in Sect. 2.3. When a sudden change in molecular extension occurs, the unfolding/refolding length may be related to the number of nucleotides being exposed/folded away using the same theory.

Since the most commonly applied kinetic theories are valid only for two-state transitions, intermediate states should in principle be identified from the raw data before the kinetic analysis. Assuming that different types of transitions can be separated into distributions, the waiting times or transition force data for each sub-transition are then usually analyzed separately.

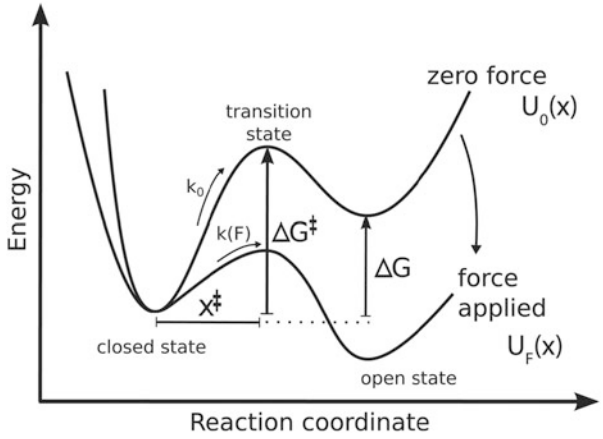

Fig. 2.5 Generic energy landscape profile along an arbitrary reaction coordinate for a two-state system with an open and a closed state separated by an energy barrier. The barrier is characterized by $x^\ddagger$, the distance from the closed state to the transition state, and $\Delta G^\ddagger$, the energy of activation along the reaction coordinate. ΔG is the Gibbs free energy change of the transition, which is independent of the reaction coordinate. k_0 and $k(F)$ are the rates of reaction at zero force and force F, respectively. The energy surface, $U_0(x)$, is in effect tilted by the potential energy added by the application of force, turning it into an energy surface $U_F(x)$. During a typical pulling experiment, the reaction coordinate, x, corresponds to, e.g., the position of the optical trap or the extension of the molecule. Figure inspired by Dudko et al. (2006)

For a simple two-state transition, several models exist for finding $k(F)$ from the distribution of unfolding forces. The most common approach is based on Bell's formula (Bell 1978):

$$k(F) = k_0 \mathrm{e}^{Fx^\ddagger/(k_\mathrm{B}T)} \tag{2.3}$$

Here, k_B is the Boltzmann constant and T the temperature as before, while $x^\ddagger$ is a quantity called the "distance to the transition state," which is a "distance" in the energy landscape of the molecule between a closed state and the energy barrier to an open state. The transition state is located at the top of the energy barrier. If $x^\ddagger$ is measured along a coordinate of molecular extension (or the coordinate of trap position), $Fx^\ddagger$ is the energy required for the molecule to reach the transition state. Bell's formula is thus very similar to the Arrhenius equation, which is obtained by replacing $Fx^\ddagger$ by E in Eq. (2.3).

Figure 2.5 illustrates an energy landscape with a certain distance, $x^\ddagger$, to the transition state. Here, the profile of an energy landscape surface at zero force, $U_0(x)$, varies along an arbitrary reaction coordinate, and the distance to the transition state, $x^\ddagger$, is simply a distance along this virtual coordinate between the original (closed) state and the transition state. Similarly, the energy of activation, $\Delta G^\ddagger$, quantifies the energy difference between the closed and transition states at zero force. Like the

zero-force rate of transition, k_0, the values of $x^\ddagger$ and $\Delta G^\ddagger$ depend on the reaction coordinate along which the energy profile is drawn (Dudko et al. 2008).

When the reaction coordinate is the molecular extension, $x^\ddagger$ is a useful measure of the brittleness of the molecule: it directly shows how much the molecule can be deformed before it switches from one state to another. A small value of $x^\ddagger$ indicates a brittle molecule, while a larger value indicates a more compliant one. An example of a reaction wherein molecular extension is directly correlated to molecular state is the unzipping of a DNA or RNA hairpin. Simple RNA and DNA hairpins have generally been found to be less brittle than complex structures such as RNA pseudoknots (see Sect. 2.5.3). For DNA hairpins, $x^\ddagger$ has been found in the range of 2–20 nm (Woodside et al. 2006), increasing with the length of the hairpin stem. A simple RNA hairpin and an RNA hairpin with a side branch likewise had $x^\ddagger$ of about 12 nm, while a more complex RNA hairpin structure stabilized by magnesium ions had $x^\ddagger$ of only 1.6 nm (Liphardt et al. 2001). For RNA pseudoknots, values of $x^\ddagger$ have been found as low as 0.2 nm (Hansen et al. 2007).

2.4.2 *Extension and Molecular States*

When DNA or RNA hairpins are unzipped, the transition generally takes place in a single clear "hop" in the extension-time series of a constant-force experiment (Fig. 2.4a) or a clear "rip" in the force extension curve derived from a force-ramp experiment (Fig. 2.4b). During each rip or hop, base pairs are opened in quick succession from the base of the helix to yield a fully unfolded structure. For this type of reaction, $x^\ddagger$ truly corresponds to a change in the end-to-end extension of the molecule, corresponding to a number of opened base pairs. Since $x^\ddagger$ measures the distance between the closed state and the energy barrier, the physical location of the energy barrier can be found by translating $x^\ddagger$ into base pair length, taking into account the stretching of the molecule at the transition force by using the theory described in Sect. 2.3 (Woodside et al. 2006).

However, an intrinsic problem with looking at energy landscapes along the coordinate of molecular extension is that in some cases, several different molecular states might be associated with a single molecular extension. This occurs if other thermodynamic variables are more important for determining the state of the molecule than its extension. In such cases the folding pathway of the molecule might not scale linearly with molecular extension in the way that polynucleic acid hairpin unwinding does, and application of force may in fact make a molecular transition less likely to occur (Dudko et al. 2008). This might be the case, e.g., for a polynucleic acid wound around itself or around another molecule: pulling may tighten the winding, making a transition to the open state less likely, at least up to a certain force level.

2.4.3 Kinetic Parameters from Force Data

For force-ramp experiments, where the force is increased over time at a constant loading rate, r, an expression may be derived from Eq. (2.3) for k_0 and $x^{\ddagger}$ in terms of the probability, P, that the molecule has not yet undergone a transition. In the derivation it is assumed that the transition is a first-order two-state reaction, so that the survival probability of the initial molecular state is an exponential function of time. This assumption requires that the force is increased slowly enough for the transition rate to depend directly on the force, i.e., a quasi-adiabatic transition (Dudko et al. 2008). The expression is (Hummer and Szabo 2003)

$$r \ln P = -\frac{k_0 k_B T}{x^{\ddagger}} \left(e^{F x^{\ddagger}/(k_B T)} - 1 \right) \tag{2.4}$$

With this expression, using the known loading rate and the empirical probability distribution of transition forces, one can plot $r \ln P$ against F (the forces at which molecular transitions are observed) and fit Eq. (2.4) to the data to obtain estimates of k_0 and $x^{\ddagger}$. Note that $p(F)$ depends on r, so that the average unfolding force increases with the loading rate (Dudko et al. 2010).

For constant-force experiments, finding k_0 and $x^{\ddagger}$ requires finding the transition frequency (i.e., the inverse of the average waiting times between transitions) for a range of forces. A fit is then made directly to Bell's formula [Eq. (2.3)] to find the parameters k_0 and $x^{\ddagger}$, as done, e.g., in the classical study of RNA hairpins by Liphardt et al. (2001).

2.4.4 Expanded Kinetic Theory

Although the approach presented in Sect. 2.4 above is useful, its assumptions are unlikely to be true in single-molecule experiments. In recent theoretical work, Dudko, Hummer, and Szabo (2006) have incorporated a more accurate assumption about the energy landscape: as the force increases, the whole "energy landscape" of the structure changes, including $x^{\ddagger}$, as illustrated in Fig. 2.5. To allow for this, the researchers explicitly introduce a theoretical free energy surface $U_F(x)$ along the pulling coordinate x:

$$U_F(x) = U_0(x) - Fx,$$

where $U_0(x)$ is the free energy surface at zero force expressed by one of several simple geometric formulas and Fx is the potential applied by pulling the molecule along the coordinate x. Two possible shapes of $U_0(x)$ are shown in Fig. 2.6: cusp shaped and linear cubic. The cusp shape derives from a parabolic function with a vertical drop-off beyond the energy barrier at $x^{\ddagger}$, while the linear-cubic shape is a

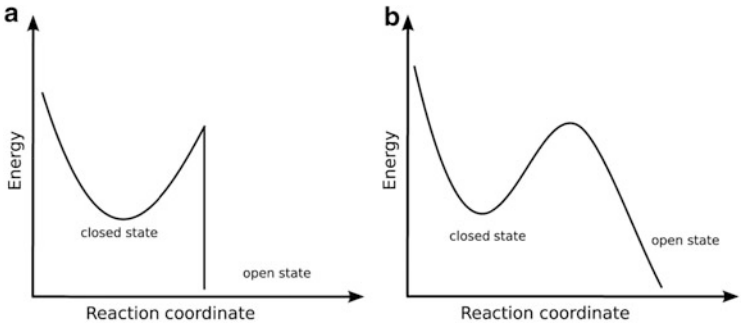

Fig. 2.6 Free energy surfaces $U_0(x)$ at zero force: (**a**) Cusp-shaped energy landscape consisting of a parabolic function with a vertical drop-off beyond the energy barrier at $x^{\ddagger}$. (**b**) Linear-cubic energy landscape consisting of a cubic function with an asymptotically linear drop-off beyond the energy barrier. Energy profile functions are defined in Dudko et al. (2006)

cubic function with a valley at the initial state and an asymptotically linear drop-off beyond the energy barrier.

Assuming that $U_0(x)$ is shaped like one of the two functions shown in Fig. 2.6, an analytical expression can be found for the transition rate, $k(F)$, at force F (Dudko et al. 2006):

$$k(F) = k_0 \left(1 - \frac{\upsilon F x^{\ddagger}}{\Delta G^{\ddagger}}\right)^{1/(\upsilon-1)} \mathrm{e}^{\Delta G^{\ddagger}\left[1-(1-\upsilon F x^{\ddagger}/\Delta G^{\ddagger})^{1/\upsilon}\right]} \tag{2.5}$$

where $\Delta G^{\ddagger}$ as above is the apparent energy of activation and ν is a parameter describing U_0. Setting $\nu = 1/2$ corresponds to the cusp-shaped U_0 energy landscape, $\nu = 2/3$ corresponds to the linear cubic. Both shapes imply that there is no return across the energy barrier once the molecule has passed $x^{\ddagger}$. This closely resembles the assumption of a first-order transition made to derive Eq. (2.4). Indeed, setting $\nu = 1$, Eq. (2.5) reduces to Eq. (2.4). To find k_0, $x^{\ddagger}$, and $\Delta G^{\ddagger}$, Eq. (2.5) can be fitted to empirical values for $k(F)$ (constant-force experiments) or to values of $k(F)$ calculated from an empirical estimate of $p(F)$, the probability distribution for transition at different forces (force-ramp experiments) (Dudko et al. 2008).

Because there are three unknowns in the fit and because a pooling of data is needed to empirically estimate $k(F)$ over a range of forces, a large number of data points are needed. Nonetheless, Dudko et al. (2007) have successfully applied the theory to experimental data for unzipping of DNA hairpins using nanopore force spectroscopy as outlined in Sect. 2.2.3. One advantage of this method is that it makes more accurate assumptions than Bell's formula about the distance to the transition state for high force transitions.

2.5 Nonequilibrium Thermodynamics

Within the last 15 years, new thermodynamics theories have enabled the derivation of the Gibbs free energy change, ΔG, from nonequilibrium nanoscale experiments. The relation first discovered is the Jarzynski equality (JE) (Jarzynski 1997), which links the work spent to drive a system from an initial to a final state to the Gibbs free energy difference between the two states:

$$\overline{\exp\left(-\frac{W_i}{k_B T}\right)} = \exp\left(-\frac{\Delta G}{k_B T}\right) \tag{2.6}$$

Here W_i is the work measured for either a forward or a reverse transition (e.g., either the work required to open a DNA hairpin or the work gained when it reanneals). Note that the left-hand side of Eq. (2.6) is an average over many measurements of the transition work, W_i. The equality requires that the transition being measured, whether forward or reverse, begins and ends in thermodynamic equilibrium.

The second relation is the Crooks Fluctuation Theorem (CFT). The Jarzynski equality, presented 2 years before the CFT, may easily be derived from the CFT. The CFT states (Crooks 1999; Collin et al. 2005)

$$\frac{P_F(W)}{P_R(-W)} = e^{(W-\Delta G)/k_B T} \tag{2.7}$$

where W is the amount of work done on the construct, $P_F(W)$ is the probability of the amount of work W being exerted by the system on the construct during the forward transition, $P_R(-W)$ is the probability of the amount of work W being absorbed by the system during the reverse transition, and ΔG as above is the reversible change in the Gibbs free energy of the construct between the initial and the final state.

The CFT applies under the following assumptions:

- The state in which the forward transition begins must be the same as the state in which the reverse transition ends and vice versa.
- The transition, though overall irreversible, must be microscopically reversible: At any moment, if the velocity were reversed, the system would be just as likely to move in the reverse direction as it was to move in the forward direction with the original velocity.

The latter condition means that at any given moment, the forward reaction is indistinguishable from the reverse reaction. This is true even though overall, when looking at many irreversible forward and backward reactions, there is hysteresis in the system as in Fig. 2.7, i.e., the forward and reverse reactions on average require and return different amounts of energy.

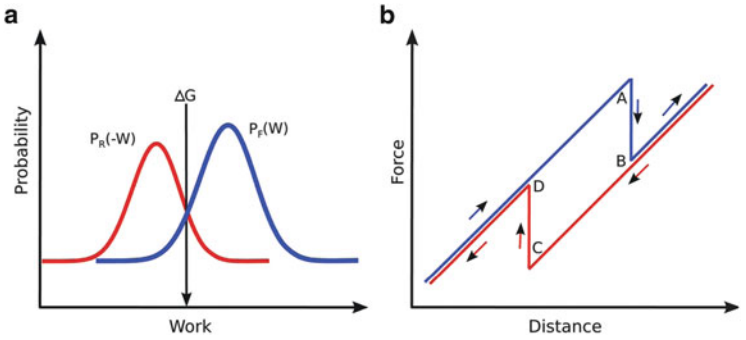

Fig. 2.7 Illustration of the Crooks fluctuation theorem. (**a**) The Crooks fluctuation theorem states that the Gibbs free energy change, ΔG, of an irreversible transition is equal to the work value where the forward and reverse transition work distributions intersect. The work distributions need not be Gaussian distributions. (**b**) Irreversible transition during a force-ramp molecule pulling experiment. The model curve shows force versus distance moved by the system (e.g., the optical trap, magnetic tweezers, or sample chamber). *Blue*: forward reaction. *Red*: reverse reaction. The transition takes place during the zip from A to B and the zip from C to D. The area under the *curve* in the direction of the *arrows* corresponds to the work performed on the system

The CFT implies immediately from Eq. (2.7) that at the point where $P_{\mathrm{F}}(W) = P_{\mathrm{R}}(-W)$, $W = \Delta G$, as shown in Fig. 2.7a. Thus, even though the reaction is irreversible, ΔG for the reversible transition can be found directly from the intersection of the empirical probability distributions of work for the forward and reverse transitions. Note that $P_{\mathrm{F}}(W)$ and $P_{\mathrm{R}}(-W)$ are not always Gaussian, although they may often be approximated by Gaussian curves when the transition is close to equilibrium. If the transition were reversible, $P_{\mathrm{F}}(W)$ and $P_{\mathrm{R}}(-W)$ would overlap and both center on ΔG. The further the reaction is from equilibrium, the more heat is dissipated and the less $P_{\mathrm{F}}(W)$ and $P_{\mathrm{R}}(-W)$ overlap, making it more difficult to find their intersection. However, using Bennett's acceptance ratio, it can still be done (Collin et al. 2005).

Compared to the CFT, the Jarzynski equality has the advantage that it requires data for transitions only in one direction. The disadvantage, which is quite substantial, is that since it averages exponential functions, the smallest work values influence the result the most. Very large numbers of measurements are required to give good statistics, and the further the process is from equilibrium, the more data are required. In practice, Jarzynski noted, it would probably be very hard to obtain enough data if the heat dissipation is more than about $k_{\mathrm{B}}T$ (Jarzynski 1997). Ritort et al. (2002) have calculated that if the dissipation is more than about 5 $k_{\mathrm{B}}T$, more than 1,000 experimental repetitions are needed. However, a better estimate may be obtained if the Jarzynski equality is used on both unfolding and refolding work distributions and the two are averaged, as done by Collin et al. (2005).

2.5.1 Work Measurement in Practice

To apply the JE and CFT, the work is generally calculated from the force applied to the system times the distance moved by the system. For single-trap optical tweezers experiments, this should be done by integrating the force along the axis of the distance moved by the instrument, i.e., the area under the curve in Fig. 2.7b. The distance moved by the system is the distance moved by the trap, the sample chamber surface, or a bead held in a pipette (Mossa et al. 2009). For experiments where the instrument controls force rather than distance (e.g., magnetic tweezers experiments), molecular extension should be integrated along the force axis.

Integration of the force along distance moved by the instrument is usually not equivalent to integration along the axis of molecular extension because molecular extension fluctuates, e.g., with the movement of the bead in the trap. However, the error from integrating along the axis of molecular extension is reduced to essentially nothing if the data are sufficiently smoothed. Mossa et al. (2009) find that the error in ΔG calculated with the CFT can be up to about 10 % if the area under the force–extension curve is used as the work rather than the area under the force–distance curve. Conversely, the correctly calculated ΔG (using the work under the force–distance curve in the CFT) necessarily contains a contribution from the bead movement in the trap, which should be subtracted if the aim is to find ΔG for the molecule only (Mossa et al. 2009). Finding this correction requires data with very low noise, which necessitates very short molecular handles and a very well-aligned system where the force on the molecule can be measured with extremely high precision (Alemany et al. 2012). Work derived as the area under the force–extension curve requires no such correction and as mentioned above may yield reasonable results when the data are smoothed.

In either case, to apply the CFT, the integral of each experimental force–distance or force–extension curve is calculated between a starting force corresponding to the lowest transition force observed and an ending force corresponding to the highest transition force observed (Collin et al. 2005). For the JE, the entire curve should be integrated, as the transition must start and end in equilibrium.

Apart from contributions from bead movement, the work found from integrating the force–distance or force–extension curve for a pulling experiment also often contains a substantial component from stretching the DNA or RNA under investigation. Applying the JE or the CFT to this work results in a ΔG value that includes the change in internal energy required for pure stretching. If the aim is to find ΔG for only a transition between distinct chemical states (e.g., hairpin unzipping), the work used to stretch the structure and any handles must be subtracted. This is done by calculating the theoretical value of the stretching work using the appropriate stretch model for the type of polymer and the force regime in question (see Sect. 2.3). The assumption is that the model describes the stretching well and that the stretch and relax are reversible on the timescales of the experiment. When both double- and single-stranded polynucleic acids are involved, the contribution from stretching each of these types of polymer is added in sequence (Collin et al. 2005).

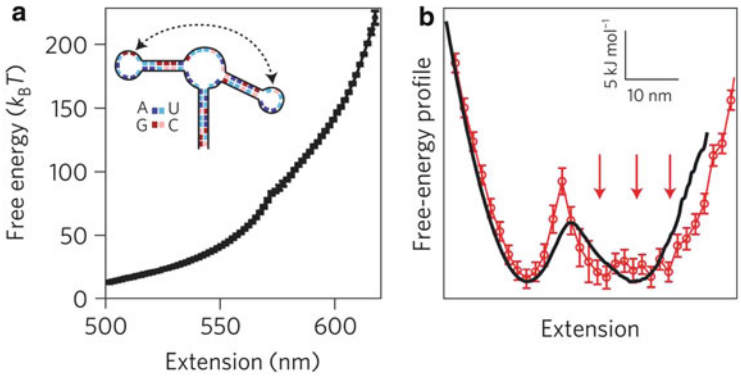

Fig. 2.8 Mapping the energy landscape of a riboswitch aptamer (data samples shown in Fig. 2.4): (**a**) Zero-force energy profile of the aptamer calculated from nonequilibrium experimental data. *Inset*: expected closed state of the molecule, also shown in Fig. 2.4b. The *arrow* shows expected interaction between the two hairpin loops. (**b**) Energy profile tilted by a force so that the closed and open states are approximately in equilibrium. *Black*: profile calculated from equilibrium (constant-force) measurements. *Red*: profile calculated from nonequilibrium (force-ramp) measurements. *Arrows*: possible intermediate states. Reproduced with permission from Gupta et al. (2011)

Note that the method is vulnerable to error arising from the estimate of the stretch contribution, especially for structures being unfolded far from equilibrium, since the stretch correction is larger in that case. The error also increases for small structures, since the WLC stretching models assume $L_c \gg L_p$.

2.5.2 *Intermediate States in the Energy Landscape*

Since the Jarzynski equality requires only that the system being measured starts or ends in equilibrium, it can be used to calculate the energy required to reach any nonequilibrium state. This means that the JE can be used to map the full energy landscape profile of a nonequilibrium transition, as originally suggested by Hummer and Szabo (2001). For pulling experiments, the mapping immediately yields the energy profile along the coordinate of pulling distance, but it can be transformed into a profile along the coordinate of molecular extension using several different methods (Hummer and Szabo 2010). To exploit the full data set when data for both forward and reverse transitions are available, energy profile mapping can also be done using the CFT; one method has been presented by Minh and Adib (2008).

The Hummer–Szabo method was first applied to RNA hairpin data by Liphardt et al. (2002) in their demonstration of the validity of the Jarzynski equality. Recently, Gupta et al. (2011) used the same principle to find the energy landscape profile of a DNA hairpin and an RNA riboswitch aptamer from force-ramp experiments. Figure 2.8 shows the experimental energy landscape profiles calculated for the riboswitch. The group employed optical tweezers in a geometry much

like the one shown in Fig. 2.1a. From constant-force and force-ramp data, they had seen that intermediate states existed in the energy landscape (data shown in Fig. 2.4). Figure 2.8a displays the calculated energy profile at zero force, illustrating how similar the intermediate states are in potential energy: they are not even visible as bumps in the energy profile along the coordinate of molecular extension. Figure 2.8b shows the energy profile when the aptamer is held at constant force near equilibrium between the open and closed states. The arrows in the figure indicate that at least three different states may be reached once the main energy barrier between the closed and the open state is passed. Comparing Figs. 2.8a and 2.8b, it becomes clear how the application of force tilts the energy landscape so that states that are highly unfavorable at zero force become favorable.

One main achievement of Gupta et al. (2011) is that the group was able to validate their nonequilibrium energy profile against an energy profile calculated with a more data-intensive approach involving equilibrium measurements. Gupta et al. (2011) found that the nonequilibrium approach yielded more information about intermediate states. The black curve in Fig. 2.8b shows the energy profile reconstruction from equilibrium data, which does not show any intermediate states. In contrast, the red curve from the nonequilibrium data does hint at possible intermediate states (arrows).

Note that the energy landscapes in Fig. 2.8 include the free energy used to stretch the dsDNA handles attached to the RNA riboswitch aptamer. To find the energy landscape of the aptamer, the free energies of the aptamer and the handles can be deconvolved; this was done by Woodside et al. (2006) in calculations of the equilibrium energy landscape of DNA hairpin unfolding. Hummer and Szabo (2010) suggest that alternatively one may approximate the handles as harmonic springs whose energy can be subtracted if their stiffness can be estimated.

Building on these advances, a thermodynamic approach developed by Junier et al. (2009) directly addresses the possibility that the molecule may be in many different states during experiment. This Expanded Fluctuation Theorem builds on the CFT by allowing calculation of transition energies even when the initial and final states of the molecule in a series of pulling experiment are not always the same, but rather represent a range of possible states including intermediates. The Expanded Fluctuation Theorem has recently been applied to data for DNA hairpin unfolding to reveal the energy of formation of a variety of intermediate states (Alemany et al. 2012). A prerequisite for the application of the theorem is a subtle determination of the populations of molecules corresponding to different intermediate states. This requires very low noise data, in the case of Alemany et al. (2012) attained using constructs with extremely short handles.

2.5.3 mRNA Pseudoknot Kinetics

Messenger RNA (mRNA) pseudoknots are secondary structures on mRNA that influence protein synthesis through their ability to sometimes shift the ribosomal

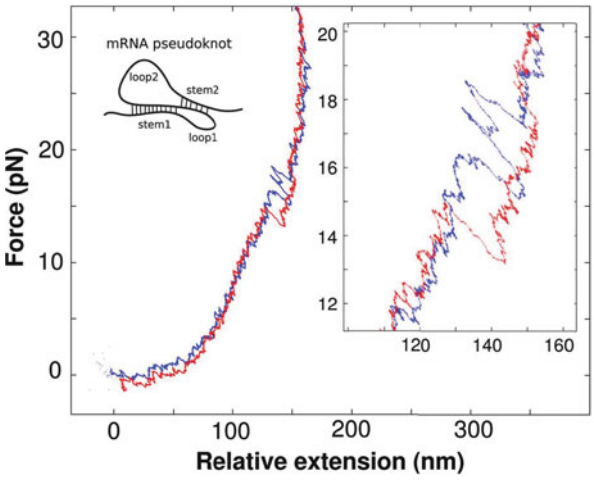

Fig. 2.9 Force versus molecular extension for an mRNA sequence containing a pseudoknot. Pulling experiment with two optical traps; the single-stranded mRNA containing the pseudoknot sequence was hybridized to DNA handles linked to polystyrene beads in the traps by biotin–streptavidin and digoxigenin–antidigoxigenin bonds. *Blue*: moving the beads apart, extending the molecule. *Red*: relaxing. *Left inset*: schematic structure of an mRNA pseudoknot. *Right inset*: zoom of the region in which the unfolding and refolding transitions take place

reading frame (see general pseudoknot structure in Fig. 2.9, left inset). This means that two different proteins can be produced from a single mRNA sequence, one frameshifted, one not. How efficient a given pseudoknot is at inducing frameshift may depend on sequence-correlated structural characteristics, but how exactly sequence relates to 3-D structure and to frameshifting is currently unclear. Several attempts to uncover the relationship between frameshift efficiency and mechanical properties have been made using optical tweezers; yet controversy remains in the literature regarding the deciding factors for pseudoknot strength (Ritchie et al. 2012). Nonetheless, mechanical strength and frameshift efficiency may be correlated at least within certain regimes and pseudoknot families (Hansen et al. 2007; Chen et al. 2009).

In contrast to experimental unfolding and refolding of hairpins, where opening and closing transitions generally happen in single clear steps, pseudoknot unfolding traces often display several unfolding or refolding steps of various sizes, which are clear indications of intermediate states (Fig. 2.9). A focus of pseudoknot investigations has therefore been the elucidation of intermediate steps and possible folding pathways for the mRNA sequence. OT investigations of mRNA pseudoknots have usually been force-ramp experiments, where the molecule is pulled at a constant rate, revealing how much force is needed to open the molecular structure and at which force it re-forms. Figure 2.9 shows a typical force–extension curve for an mRNA molecule expected to form a pseudoknot. Clear unfolding and

refolding events are observed, including unfolding and refolding to an intermediate state around 18 pN.

A pseudoknot usually consists of two loops and two stems that are interlinked. The steps observed in unfolding transitions may therefore correspond either to the full pseudoknot unfolding into single-stranded mRNA or to a single loop and stem opening, forming an intermediate structure. As described in Sect. 2.4.1, the length that the structure unfolds or refolds is a signature of how many base pairs are opened or closed during a transition, indicating which structural transition takes place. In Fig. 2.9, the largest transition steps are about 13–16 nm, but the expected unfolding length of the pseudoknot at these forces is expected to be at least 25 nm. Thus, the steps in the figure may all represent transitions to or from an intermediate state. For instance, it may be that the structure being opened is not a pseudoknot but a hairpin-like formation made up of one stem and one loop of the predicted pseudoknot, an explanation which corresponds well to the relatively low force observed for the transitions. In the presence of magnesium ions (as in the experiment shown in Fig. 2.9), pseudoknots often unfold at forces in the range of 20–50 pN.

Like hairpin investigations, pulling experiments with pseudoknots have been used to investigate the brittleness and the energy of formation of the structures observed using the theory described in Sects. 2.4 and 2.5. Frameshift-inducing pseudoknots are often strong, brittle structures, but the sequences capable of forming such pseudoknots also often form intermediate, weaker, and more pliable structures (Chen et al. 2009); as described, this may be the case in Fig. 2.9. Such intermediates may interfere less with the translating ribosomes, offering a possible reason why frameshifting does not always occur.

2.6 Summary and Outlook

Force spectroscopy has opened up a multifaceted toolbox for investigating the response of DNA and RNA to mechanical perturbation. Optical and magnetic tweezers, nanopore force spectroscopy, and combinations hereof, sometimes integrated with fluorescence measurements or the application of flow, allow researchers to stretch, twist, unzip, or relax single molecules, quantifying their direct response to force. The aim is often to understand the response of polynucleic acids to physiological or artificial conditions such as temperature, buffer, reactants, or mechanical strain. Induction of changes in conformation allows identification of intermediate states and calculation of energies of formation and transition rates.

This chapter describes the typical methods and fundamental areas of research in DNA and RNA force spectroscopy. The research areas include model description and understanding of the twist and stretch of double-stranded DNA, as well as analysis of energy changes, kinetic rates, and other energy landscape features characterizing force-induced structural changes in RNA and DNA.

Outside of the subjects covered here, a large field of research employs force spectroscopy to examine the interactions of polynucleic acids with transcription and translation factors, with histones and nucleosomes, with the enzymatic machinery of the cell, and with other DNA- and RNA-modifying proteins. This field is constantly growing, and in the coming years we may expect investigations not only of the effect of single polynucleic acid modifying ligands and molecular motors, e.g., a single ribosome moving on a piece of mRNA, but also of the collective action of several molecular motors and/or polynucleic acid modifying ligands. Already, the compound action of two RNA polymerases has been followed in vitro (Jin et al. 2010).

Another frontier is in vivo testing of DNA and RNA response to mechanical manipulation. Optical and magnetic tweezers are both able to act upon objects within living cells, and in vivo experiments have already been carried out to measure the action of molecular motors such as kinesins, which take part in chromosome segregation during cell division. Though challenges remain in how to internalize probe beads into cells and ensure specific single-molecule attachment, polynucleic acids and their associated molecular machinery may soon be measured in their native biological environment (Oddershede 2012). Alongside such in vivo experiments, in vitro research will continue to explore the effects of buffer, temperature, and other environmental factors on DNA and RNA structure and transitions.

To assist investigations, continued improvement of technical capabilities may be expected in coming years, allowing trapping of smaller items, application of higher force, measurements with higher precision, and more widespread mixing of techniques. Combinations of optical and magnetic tweezers (Crut et al. 2007), optical tweezers and nanopores (Keyser et al. 2006), and fluorescence in conjunction with either OT, MT, or NFS (van Mameren et al. 2009; Gore et al. 2006; McNally et al. 2010) have already been demonstrated. Some fluorescent molecules are even able to act directly as probes of force or distance; these properties are used, e.g., in fluorescence resonance energy transfer (FRET) measurements (Iwai and Uyeda 2008; Chen et al. 2012).

Rapid theoretical development is also taking place. In coming years we may thus better understand how kinetic data from force spectroscopy experiments can illuminate the entire energy landscape of the molecule. Molecules being altered by enzymes or undergoing structural transformations due to temperature or pressure fluctuations may pass along entirely different energy landscape profiles than the same molecule when exposed to tension along a single dimension. Yet Dudko et al. (2011) have already shown that under certain conditions, kinetic data obtained from force spectroscopy experiments provide general information about the underlying molecular energy landscape.

Additionally, we expect continued refinement of data processing for all force spectroscopy techniques, e.g., in eliminating handle effects for optical and magnetic tweezers results and accounting for nanopore interaction with polynucleic acid sequence. Methodological advances may also allow simpler elucidation of

intermediate states from limited data and from experiments where the molecules may not all start out in the same state.

In conclusion, force spectroscopy has already provided detailed knowledge on the properties of double- and single-stranded DNA, of the strength and force response of DNA and RNA hairpins, and of the folding of more complex structures. In coming years, probing of DNA, RNA, and associated molecules by force will continue to provide new insights into the core mechanisms of molecular biology.

References

Alemany A, Mossa A, Junier I, Ritort F (2012) Experimental free-energy measurements of kinetic molecular states using fluctuation theorems. Nat Phys 8:688–694

Bell GI (1978) Models for the specific adhesion of cells to cells. Science 200(4342):618–627

Bizarro CV, Alemany A, Ritort F (2012) Non-specific binding of Na^+ and Mg^{2+} to RNA determined by force spectroscopy methods. Nucleic Acids Res 40(14):6922–6935

Boal DH (2002) Mechanics of the cell. Cambridge University Press, Cambridge

Bryant Z, Oberstrass FC, Basu A (2012) Recent developments in single-molecule DNA mechanics. Curr Opin Struct Biol 22(3):304–312

Bustamante C, Marko JF, Siggia ED, Smith SB (1994) Entropic elasticity of λ-phage DNA. Science 265(5178):1599–1600

Bustamante C, Macosko JC, Wuite GJL (2000) Grabbing the cat by the tail: manipulating molecules one by one. Nat Rev Mol Cell Biol 1(2):130–136

Chen G, Chang K, Chou M, Bustamante C, Tinoco I Jr (2009) Triplex structures in an RNA pseudoknot enhance mechanical stability and increase efficiency of -1 ribosomal frameshifting. Proc Natl Acad Sci USA 106(31):12706–12711

Chen H, Meisburger SP, Pabit SA, Sutton JL, Webb WW, Pollack L (2012) Ionic strength-dependent persistence lengths of single-stranded RNA and DNA. Proc Natl Acad Sci USA 109(3):799–804

Cluzel P, Lebrun A, Heller C, Lavery R, Viovy J, Chatenay D, Caron F (1996) DNA: an extensible molecule. Science 271(5250):792–794

Collin D, Ritort F, Jarzynski C, Smith SB, Tinoco I Jr, Bustamante C (2005) Verification of the Crooks fluctuation theorem and recovery of RNA folding free energies. Nature 437:231–234

Crooks GE (1999) Entropy production fluctuation theorem and the nonequilibrium work relation for free energy differences. Phys Rev E 60(3):2721–2726

Crut A, Koster DA, Seidel R, Wiggins CH, Dekker NH (2007) Fast dynamics of supercoiled DNA revealed by single-molecule experiments. Proc Natl Acad Sci USA 104(29):11957–11962

de Vlaminck I, Dekker C (2012) Recent advances in magnetic tweezers. Annu Rev Biophys 41:453–472

Dudko OK, Hummer G, Szabo A (2006) Intrinsic rates and activation free energies from single-molecule pulling experiments. Phys Rev Lett 96:108101

Dudko OK, Mathé J, Szabo A, Meller A, Hummer G (2007) Extracting kinetics from single-molecule force spectroscopy: nanopore unzipping of DNA hairpins. Biophys J 92 (12):4188–4195

Dudko OK, Hummer G, Szabo A (2008) Theory, analysis, and interpretation of single-molecule force spectroscopy experiments. Proc Natl Acad Sci USA 105(41):15755–15760

Dudko OK, Mathé J, Meller A (2010) Nanopore force spectroscopy tools for analyzing single biomolecular complexes. Methods Enzym 475:565–589

Dudko OK, Graham TGW, Best RB (2011) Locating the barrier for folding of single molecules under an external force. Phys Rev Lett 107:208301

Essevaz-Roulet B, Bockelmann U, Heslot F (1997) Mechanical separation of the complementary strands of DNA. Proc Natl Acad Sci USA 94(22):11935–11940

Gittes F, Schmidt CH (1998) Signals and noise in micromechanical measurements. In: Sheetz MP (ed) Laser tweezers in cell biology, vol 55, Methods in cell biology. Academic, San Diego, pp 129–156

Gore J, Bryant Z, Nöllmann M, Le MU, Cozzarelli NR, Bustamante C (2006) DNA overwinds when stretched. Nature 442(7104):836–839

Gross P, Laurens N, Oddershede LB, Bockelmann U, Peterman EJL, Wuite GJL (2011) Quantifying how DNA stretches, melts and changes twist under tension. Nat Phys 7 (9):731–736

Gupta AN, Vincent A, Neupane K, Yu H, Wang F, Woodside MT (2011) Experimental validation of free-energy-landscape reconstruction from non-equilibrium single-molecule force spectroscopy measurements. Nat Phys 7(8):631–634

Hansen TM, Reihani SNS, Oddershede LB, Sørensen MA (2007) Correlation between mechanical strength of messenger RNA pseudoknots and ribosomal frameshifting. Proc Natl Acad Sci USA 104(14):5830–5835

Hummer G, Szabo A (2001) Free energy reconstruction from nonequilibrium single-molecule pulling experiments. Proc Natl Acad Sci USA 98(7):3658–3661

Hummer G, Szabo A (2003) Kinetics from nonequilibrium single-molecule pulling experiments. Biophys J 85(1):5–15

Hummer G, Szabo A (2010) Free energy profiles from single-molecule pulling experiments. Proc Natl Acad Sci USA 107(50):21441–21446

Iwai S, Uyeda TQP (2008) Visualizing myosin-actin interaction with a genetically-encoded fluorescent strain sensor. Proc Natl Acad Sci USA 105(44):16882–16887

Jarzynski C (1997) Nonequilibrium equality for free energy differences. Phys Rev Lett 78:2690–2693

Jin J, Bai L, Johnson DS, Fulbright RM, Kireeva ML, Kashlev M, Wang MD (2010) Synergistic action of RNA polymerases in overcoming the nucleosomal barrier. Nat Struct Mol Biol 17 (6):745–752

Junier I, Mossa A, Manosas M, Ritort F (2009) Recovery of free energy branches in single molecule experiments. Phys Rev Lett 102:070602

Keyser UF, Koeleman BN, Van Dorp S, Krapf D, Smeets RMM, Lemay SD, Dekker NH, Dekker C (2006) Direct force measurements on DNA in a solid-state nanopore. Nat Phys 2(7):473–477

Killian JL, Sheinia MY, Wang MD (2012) Recent advances in single molecule studies of nucleosomes. Curr Opin Struct Biol 22:80–87

Kruithof M, Chien FT, Routh A, Logie C, Rhodes D, van Noort J (2009) Single-molecule force spectroscopy reveals a highly compliant helical folding for the 30-nm chromatin fiber. Nat Struct Mol Biol 16(5):534–540

La Porta A, Wang MD (2004) Optical torque wrench: angular trapping, rotation, and torque detection of quartz microparticles. Phys Rev Lett 92:190801

Lavelle C, Praly E, Bensimon D, Le Cam E, Croquette V (2011) Nucleosome remodeling machines and other molecular motors observed at the single molecule level. FEBS J 298 (19):3596–3607

Leger JF, Romano G, Sarkar A, Robert J, Bourdieu L, Chatenay D, Marko JF (1999) Structural transitions of a twisted and stretched DNA molecule. Phys Rev Lett 83(5):1066–1069

Liphardt J, Onoa B, Smith SB, Tinoco I Jr, Bustamante C (2001) Reversible unfolding of single RNA molecules by mechanical force. Science 292(5517):733–737

Liphardt J, Dumont S, Smith SB, Tinoco I Jr, Bustamante C (2002) Equilibrium information from nonequilibrium measurements in an experimental test of Jarzynski's equality. Science 296:1832–1835

Mangeol P, Bizebard T, Chiaruttini C, Dreyfus M, Springer M, Bockelmann U (2011) Probing ribosomal protein–RNA interactions with an external force. Proc Natl Acad Sci USA 108 (45):18272–18276

Marko JF, Siggia ED (1995) Stretching DNA. Macromolecules 28(26):8759–8770
McNally B, Singer A, Zhiliang Y, Yingjie S, Zhipeng W, Meller A (2010) Optical recognition of converted DNA nucleotides for single-molecule DNA sequencing using nanopore arrays. NanoLetters 10:2237–2244
Minh DDL, Adib AD (2008) Optimized free energies from bidirectional single-molecule force spectroscopy. Phys Rev Lett 100(18):180602
Mossa A, de Lorenzo S, Huguet JM, Ritort F (2009) Measurement of work in single-molecule pulling experiments. J Chem Phys 130:234116
Neuman KC, Nagy A (2008) Single-molecule force spectroscopy: optical tweezers, magnetic tweezers and atomic force microscopy. Nat Methods 5(6):491–505
Oddershede LB (2012) Force probing of individual molecules inside the living cell is now a reality. Nat Chem Biol 8:879–886
Perkins T, Smith D, Chu S (1997) Single polymer dynamics in an elongational flow. Science 276 (5321):2016–2021
Ritchie DB, Foster DAN, Woodside MT (2012) Programmed -1 frameshifting efficiency correlates with RNA pseudoknot conformational plasticity, not resistance to mechanical unfolding. Proc Natl Acad Sci USA 109(40):16167–16172
Ritort F, Bustamante C, Tinoco I Jr (2002) A two-state kinetic model for the unfolding of single molecules by mechanical force. Proc Natl Acad Sci USA 99(21):13544–13548
Rohrbach A (2005) Stiffness of optical traps: quantitative agreement between experiment and electromagnetic theory. Phys Rev Lett 95:168102
Rouzina I, Bloomfield VA (2001) Force-induced melting of the DNA double helix 1. Thermodynamic analysis. Biophys J 80(2):882–893
Smith SB, Cui Y, Bustamante C (1996) Overstretching B-DNA: the elastic response of individual double stranded and single stranded DNA molecules. Science 271(5250):795–797
Stevenson DJ, Gunn-Moore F, Dholakia K (2010) Light forces the pace: optical manipulation for biophotonics. J Biomed Opt 15(2):041503
Strick T, Allemand J-F, Bensimon D, Croquette V (1998) The behavior of supercoiled DNA. Biophys J 74:2016–2028
Strunz T, Oroszlan K, Schäfer R, Güntherodt HJ (1999) Dynamic force spectroscopy of single DNA molecules. Proc Natl Acad Sci USA 96(20):11277–11282
van Mameren J, Gross P, Farge G, Hooijman P, Modesti M, Falkenberg M, Wuite GJL, Peterman EJG (2009) Unraveling the structure of DNA during overstretching by using multicolor, single-molecule fluorescence imaging. Proc Natl Acad Sci USA 106(43):18231–18236
Wang MD, Yin H, Landick R, Gelles J, Block SM (1997) Stretching DNA with optical tweezers. Biophys J 72(3):1335–1346
Williams MC, Wenner JR, Rouzina I, Bloomfield VA (2001) Effect of ph on the overstretching transition of double-stranded DNA: evidence of force-induced DNA melting. Biophys J 80 (2):874–881
Woodside MT, Behnke-Parks WM, Larizadeh K, Travers K, Herschlag D, Block SM (2006) Nanomechanical measurements of the sequence-dependent folding landscapes of single nucleic acid hairpins. Proc Natl Acad Sci USA 103(16):6190–6195
Zhang X, Chen H, Fu H, Doyle PS, Yan J (2012) Two distinct overstretched DNA structures revealed by single-molecule thermodynamics measurements. Proc Natl Acad Sci USA 109 (21):8103–8108

Chapter 3
The Power of Single-Molecule FRET Microscopy Applied to DNA Nanotechnology

Sofie L. Kragh and Victoria Birkedal

Abstract Single-molecule Förster resonance energy transfer (FRET) microscopy is a powerful technique to study structural dynamics of nucleic acid molecular structures. This short review gives an overview of the method and of its principles. Then it describes different experimental implementations of single-molecule FRET microscopy and their respective advantages. Finally, we discuss applications of the method in DNA nanotechnology. Two areas will be highlighted: 1) the investigation of the local structure and dynamics of functional DNA-based structures, and 2) the use of DNA as a template for precise fluorophore positioning for controlling and engineering energy transfer pathways.

Contents

S.L. Kragh
Interdisciplinary Nanoscience Center (iNANO), Aarhus University, Gustav Wieds vej 14, Building 1590, 8000 Aarhus, Denmark

V. Birkedal (✉)
Interdisciplinary Nanoscience Center (iNANO), Aarhus University, Gustav Wieds vej 14, Building 1590, 8000 Aarhus, Denmark

CDNA Center, Aarhus University, Gustav Wieds vej 14, Building 1590, 8000 Aarhus, Denmark
e-mail: vicb@inano.au.dk

J. KJEMS et al. (eds.), *Nucleic Acid Nanotechnology*, Nucleic Acids and Molecular Biology 29, DOI 10.1007/978-3-642-38815-6_3,

3.1 Introduction

DNA nanotechnology enables the design and self-assembly of artificial nucleic acid molecular structures and devices (Bath and Turberfield 2007; Seeman 2010; Krishnan and Simmel 2011; Pinheiro et al. 2011). The structures span in size from a few nanometers to hundreds of nanometers and can consist of the self-assembly of several hundreds of individual DNA strands (Rothemund 2006; Shih and Lin 2010; Wei et al. 2012). Nucleic acid molecular structures can be designed to undergo structural changes and show movement, and one of the goals of DNA nanotechnology is to make artificial molecular machines that are able to function autonomously or in response to external signals. A recent review on molecular nucleic acid devices can be found in Krishnan and Simmel (2011); examples of such structures are hairpins that can serve as molecular switches and beacons and DNA walkers that can transport cargo or information from one point to another. These structures have in common that they are designed to change their conformation dynamically to perform a certain function.

There are a number of methods that enable the study of structure and movement of nucleic acid-based molecular machines. Traditional biochemical experiments can give a view of sample assembly and heterogeneity. To obtain further details on the structure and function, it can be an advantage to be able to sort out well-assembled molecules from the different self assembled structures that can form in solution. However, purification can be a difficult step. A number of single-molecule techniques, which allow the imaging of one molecule at a time, can give a view of molecular heterogeneity and allow studying a given subpopulation without the need of advanced purification. Amongst them are atomic force microscopy (AFM), electron microscopy, and single-molecule fluorescence microscopy. A number of recent reviews address the applications of these techniques to DNA nanotechnology (Birkedal et al. 2011; Jungmann et al. 2012; Rajendran et al. 2012). In brief, AFM gives high-resolution pictures mostly of two-dimensional structures, and fast AFM can also follow dynamic movement with a resolution below 10 nm and an imaging speed of several frames per second (Ando et al. 2008; Endo et al. 2012). Electron microscopy images are 2D projections of the studied object, and through single particle reconstruction analysis methods, these allow for the reconstruction of a 3D model of the studied structures. In principle, time-resolved structure determination is possible (Fischer et al. 2010); however, these experiments are challenging. A number of single-molecule fluorescence microscopy techniques have contributed to the field of DNA nanotechnology, including super-resolution microscopy and single-molecule Förster/fluorescence resonance energy transfer (FRET)

microscopy. Super-resolution microscopy allows for the imaging of DNA nanostructures (Huang et al. 2009; Steinhauer et al. 2009; Schoen et al. 2011); however, dynamic information is currently limited to a few seconds per image (Zhu et al. 2012). FRET microscopy at the single-molecule level permits to have a detailed view of molecular conformation heterogeneity and follow conformation changes with a fast time resolution. It will be the subject of this review. There are a number of existing good reviews and protocols for the technique, for example, Roy et al. (2008) and Zhao and Rueda (2009). This short review intends to give an overview of the basic principles of FRET and of the advantages of single-molecule FRET microscopy with respect to ensemble FRET experiments. We will discuss the different available experimental implementations of single-molecule FRET microscopy and then turn to applications in the framework of DNA nanotechnology. There, we will highlight two topics: FRET studies of the structural dynamics of advanced DNA structures and the use of DNA nanotechnology to control energy transfer pathways.

3.2 FRET

The FRET mechanism describes the non-radiative energy transfer from a fluorescent donor dye molecule to an acceptor molecule. The stronger the energy transfer effect, the less fluorescence is emitted by the donor. The energy transfer efficiency E is very sensitive to the distance between the donor/acceptor molecules, Fig. 3.1, and is given by:

$$E = \frac{1}{\left(1 + \frac{R}{R_0}\right)^6}, \tag{3.1}$$

where R is the distance between the donor and acceptor molecules and R_0 is the Förster radius. The E value is comprised in the interval [0, 1], where a high FRET efficiency value means that the two probes are close to each other and $E = 0.5$ for $R = R_0$. R_0 is given by:

$$R_0 = \left[8.79 \times 10^{-5} \cdot (\kappa^2 \cdot n^{-4} \cdot \Phi_D \cdot J(\lambda))\right]^{1/6} \text{ Å}, \tag{3.2}$$

where the integral $J(\lambda)$ calculates the spectral overlap between donor fluorescence and acceptor absorption, Φ_D is the donor quantum yield, n is the refractive index, and κ^2 is a geometric factor with values from 0 to 4 that depends on the average relative dipole–dipole orientation of the two fluorophores. For freely rotating fluorophores, κ^2 takes the value 2/3.

The value of the FRET efficiency E can be determined by fluorescence spectroscopy. Measuring the fluorescence of the donor in the absence and in the presence of

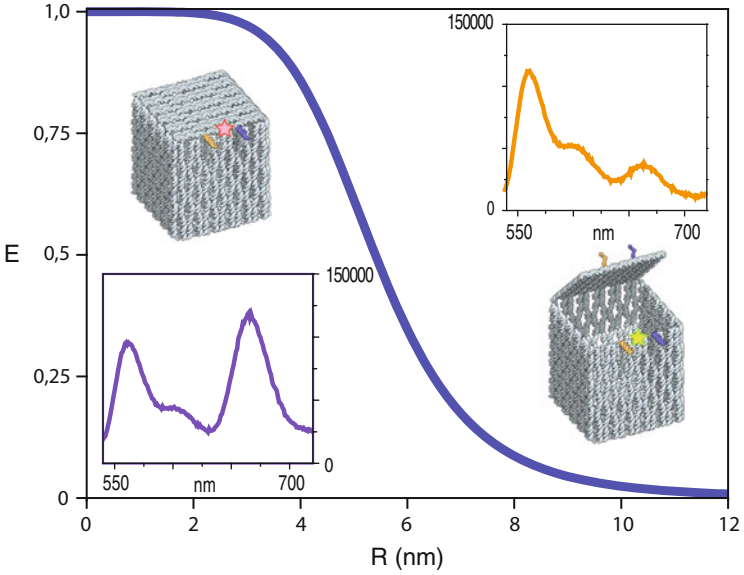

Fig. 3.1 Dependence of the FRET efficiency on the distance between the two dyes R (with $R_0 = 5.4$ nm). The *insets* illustrate that when the two dyes are far away from each other, strong donor fluorescence is observed (*right side* of the figure), while if the dyes are close to each other, energy transfer occurs and the intensity of donor fluorescence decreases and acceptor fluorescence appears, if the acceptor can emit light (*left side* of the figure). This is illustrated both by schematics of a DNA box structure in an open and closed state (Andersen et al. 2009) and by the observed corresponding fluorescence spectra showing donor and acceptor fluorescence after donor excitation. Some parts of this figure are reproduced with permission from Andersen et al. (2009)

an acceptor molecule yields either the respective fluorescence intensities I_D and I_{DA} or the respective fluorescence lifetimes τ_D and τ_{DA} from which E is obtained by:

$$E = 1 - \frac{I_{DA}}{I_D} \text{ or } E = 1 - \frac{\tau_{DA}}{\tau_D}. \tag{3.3}$$

The FRET efficiency can also be determined by using the acceptor fluorescence through a modified version of the previous equation, which takes into account the fact that the donor and acceptor fluorophores have different fluorescence quantum yields:

$$E = \frac{I_{AD}}{I_{AD} + \gamma \cdot I_{DA}} \quad \text{with } \gamma = \frac{\Phi_A \cdot \eta_A}{\Phi_D \cdot \eta_D}. \tag{3.4}$$

I_{AD} is the acceptor fluorescence in the presence of a donor and after donor excitation. γ takes into account the different donor and acceptor quantum yields and detection efficiencies, Φ_D, Φ_A and η_D, η_A, respectively.

There are several other methods that can be used to determine the FRET efficiency, including the Ratio A method, which uses a combination of absorption and fluorescence measurements or methods based on the measurement of polarization anisotropy (Clegg 1992).

3.3 Beyond the Ensemble Average: Single-Molecule FRET Techniques

Ensemble FRET experiments can provide valuable information; they, however, report on the average value of all conformations present in a sample. Single-molecule fluorescence microscopy, on the other side, allows measuring each molecule independently and provides information beyond the ensemble average. It gives access to information on dynamic processes and relaxation pathways without the difficult task of synchronizing all molecules together. It also provides a view of the sample conformational heterogeneity and allows sorting out subpopulations of interest so that their behavior can be followed specifically. Thus, information can be obtained that pertains only to the relevant subpopulation of molecules.

Using visible light, the diffraction limit is much bigger than a single molecule. Therefore, to be able to image a single molecule, low sample concentrations, in the 10–100 pM range, are usually used for single-molecule measurements with fluorescence microscopy. Two different microscopy techniques can be used for single-molecule FRET experiments: either based on confocal or wide-field microscopy. In both experiments, donor and acceptor fluorescence intensities are measured for each molecule individually. The FRET efficiency is usually calculated through Eq. (3.4).

3.3.1 Confocal Microscopy

In confocal-based single-molecule FRET microscopy, the incoming laser light is tightly focused at the excitation spot, which is in the femtoliter range. Signals are recorded from molecules that are freely diffusing through the excitation spot. The time resolution of a measurement can be very fast, in the picosecond and microsecond range; however, the total observation time is limited by the diffusion time of the molecule to about 1–10 ms. Figure 3.2a shows the schematic configuration of a confocal microscope for single-molecule FRET measurements. Burst analysis of the fluorescence of freely diffusing molecules can resolve the FRET efficiencies of DNA structures (Lee et al. 2005b). For observation times longer than about 10 ms, molecules need to be immobilized on the cover slip surface, and scanning confocal microscopy allows measuring conformational dynamics of each immobilized molecule one by one. This leads to time-consuming experiments when following the

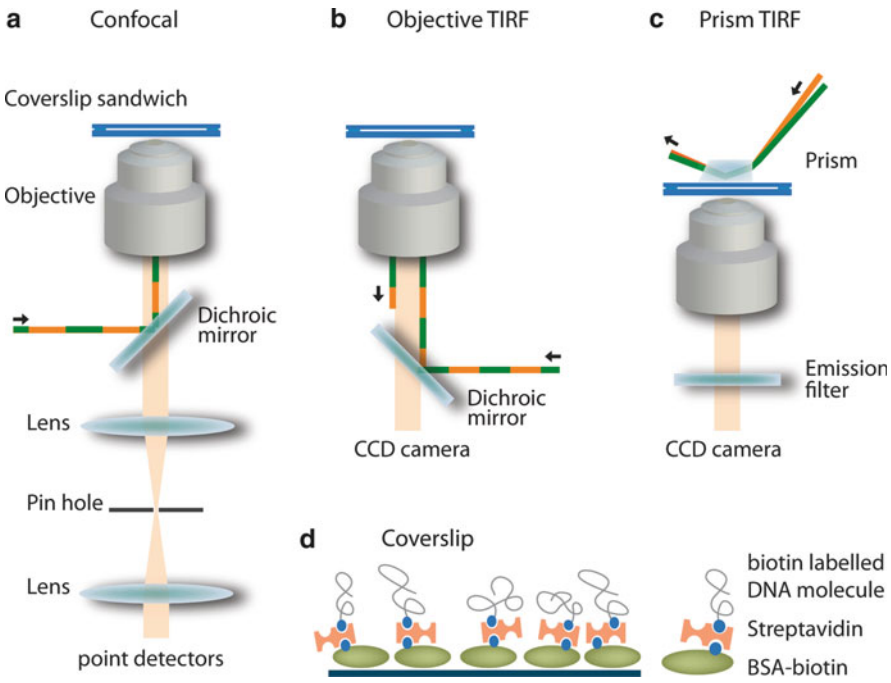

Fig. 3.2 Different types of single-molecule FRET microscopes. (**a**) Confocal geometry: the two lasers (light and dark gray lines and *red* and *green lines* in the colored online figure) are sent through the microscope objective and focused on the same spot. If using alternating-laser excitation, the alternating period is typically in the tens of microseconds range. Fluorescence (from molecules freely diffusing in the focal excitation spot) is collected through the objective, filtered by several filters, and also spatially filtered by the confocal pinhole then sent to several Avalanche Photodiodes point detectors. (**b**) Objective TIRF geometry: to achieve TIRF excitation, the two lasers are displaced relative to the optical axis when entering the microscope objective. The period for alternating lasers excitation is typically in the tens of milliseconds range. Fluorescence from the surface-immobilized molecules is filtered and separated in an acceptor and a donor fluorescence channel and imaged with a sensitive CCD camera. (**c**) Prism TIRF configuration: it is almost the same experimental configuration as for objective TIRF, except that the excitation is coupled through a prism to excited immobilized molecules on the top cover slip of the sample sandwich. Fluorescence is collected as in (**b**). (**d**) Schematic view of immobilized molecules on a cover slip surface using biotin–streptavidin interaction

longtime dynamics of each molecule individually. This inconvenience has been overcome in some cases by automating the microscope for these measurements (Sabanayagam et al. 2004).

3.3.2 Wide-Field Microscopy

Wide-field single-molecule FRET microscopy allows measuring a large number of immobilized molecules simultaneously. Fluorecence excitation can be limited to a

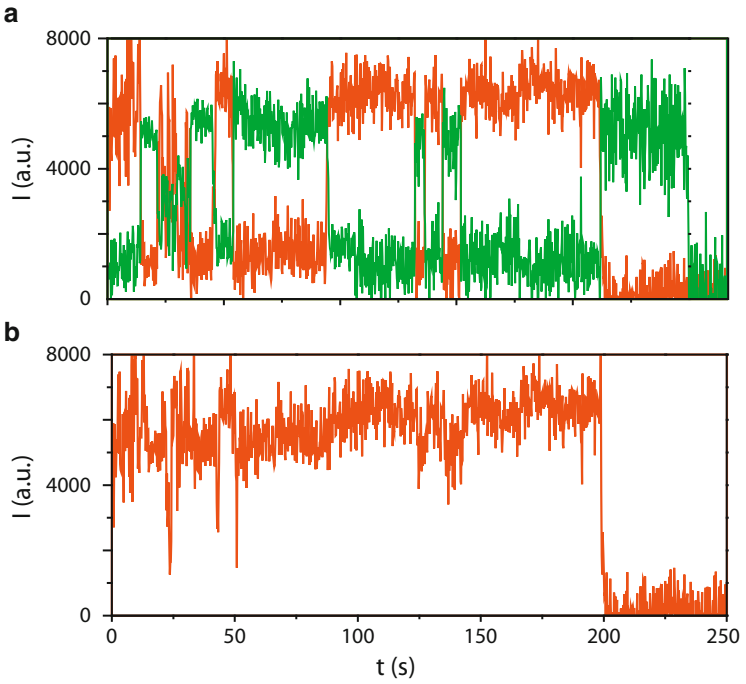

Fig. 3.3 Typical fluorescence time traces of a doubly labeled surface-immobilized DNA molecule showing the integrated fluorescence intensity of one molecule as a function of time. (**a**) Integrated donor (*green*) and acceptor (*red*) fluorescence intensity following donor excitation as a function of time. (**b**) Integrated acceptor fluorescence intensity following acceptor excitation as a function of time. Both the donor and acceptor molecule are seen to bleach in a single step, indicating that the signal originates from a single molecule. The donor and acceptor fluorescence intensity in (**a**) are anticorrelated, while fluorescence intensity in (**b**) is constant, indicating that the observed slow changes in fluorescence intensity in (**a**) do not originate from fluorescence blinking but are related to conformation changes of the molecule

small region close to the sample surface by the use of total internal reflection. This excitation method helps suppressing fluorescence background, which may be important as single-molecule signals are weak. Figures 3.2b and 3.2c schematically show the experimental configuration of a TIRF wide-field microscope for single-molecule FRET measurements. The time resolution of a measurement is limited to around 1–10 ms. However, depending on dye photobleaching, the same molecule can be followed for several minutes to tens of minutes (Holden et al. 2010). Figure 3.3a shows an example of donor and acceptor fluorescence time traces of an immobilized DNA molecule after donor excitation. The dye fluorescence longevity and stability before photobleaching can be chemically enhanced by oxygen scavenging and triplet-state quencher cocktails (Vogelsang et al. 2008; Dave et al. 2009). Proper immobilization and surface passivation is important and can

be a difficult problem. In the simplest case, streptavidin–biotin interaction can be used for molecule immobilization. Surfaces can also be passivated by PEG molecules, or the molecules of interest can be encapsulated into lipid vesicles. The challenges of surface passivation and molecule immobilization for single-molecule FRET experiments have recently been reviewed in Lamichhane et al. (2010).

3.3.3 *Alternate Laser Excitation and Multiparameter Fluorescence Detection*

Single-molecule FRET experiments are sensitive to artifacts related to the photophysical stability of the dyes used for labeling. Photoblinking of the acceptor fluorophore, i.e., transition to a dark state of the fluorophore, can be mistaken for a loss of FRET, and dynamic changes in the fluorescence can be mistakably interpreted as dynamic conformation changes. Monitoring dye integrity can be done by the Alternating Laser Excitation (ALEX) technique where donor excitation is rapidly alternated by direct acceptor excitation (Kapanidis et al. 2004; Lee et al. 2005b). Figure 3.3 shows examples of fluorescence time traces of an immobilized DNA molecule using the ALEX technique. The acceptor photostability can be directly monitored as shown in Fig. 3.3b. Using the acceptor fluorescence intensity after direct acceptor excitation I_{AA}, the label stoichiometry S can be determined and is given by:

$$S = \frac{I_{AD} + \gamma \cdot I_{DA}}{I_{AD} + \gamma \cdot I_{DA} + I_{AA}}. \tag{3.5}$$

DNA structures labeled only with a donor will have $S = 1$ and $E = 0$, and acceptor-only species $S = 0$. Single structures with both fluorescent labels will have an S value determined by the ratio of the two lasers excitation intensities, which is usually chosen close to 0,5. Single-molecule data can be shown as a 2D SE diagram, Fig. 3.4, thus allowing identification of the different subpopulations. ALEX allows distinguishing and selecting subpopulations of interest based on their FRET efficiency, on label stoichiometry, and on dye photophysics. ALEX can be used both with confocal and wide-field microscopy.

On top of the fluorescence intensity of the donor and acceptor labels, it is also possible to measure the fluorescence lifetime and anisotropy. These parameters can be simultaneously detected and analyzed using a technique known as multiparameter fluorescence detection (MFD) (Sisamakis et al. 2010). The technique allows for a detailed assessment of possible artifacts that can affect the interpretation of FRET measurements.

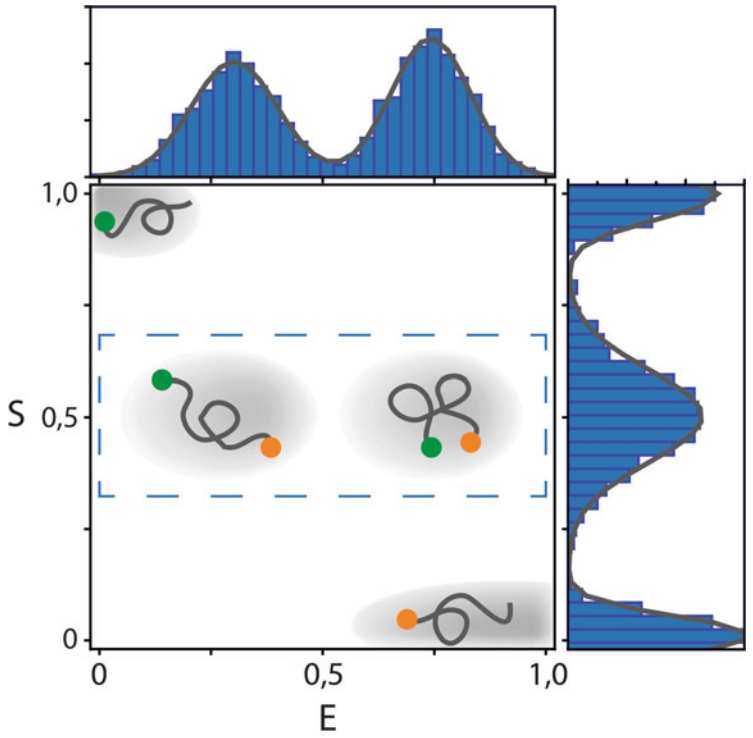

Fig. 3.4 Schematic SE diagram showing four different populations: molecules labeled with donor only and acceptor only appear at $S = 1$ and $S = 0$, respectively, and doubly labeled molecules with high or low FRET appear at $S = 0{,}5$. The *upper graph* shows the corresponding FRET histogram which only includes data from the doubly labeled molecules, which are highlighted by a *dashed box*. The *graph* to the *right* shows the S histogram of all data

3.3.4 Multicolor FRET

The use of several FRET pairs can allow for the observation of correlated changes in complex molecular dynamics or in multicomponents binding interactions. Three-color FRET with three different fluorophores has first been demonstrated at the single-molecule level in 2004 on studies of DNA Holliday junctions where the dynamics of the two arms was monitored independently on the same molecule (Hohng et al. 2004). Single-molecule three-color FRET experiments have been combined with ALEX, which further allows monitoring the relative donor and acceptor stoichiometry of each FRET pair (Lee et al. 2010c). The implementation of four-color FRET microscopy at the single-molecule level has recently been reported (Lee et al. 2010a; Haga et al. 2011; Stein et al. 2011b). It is however not an easy task to find adequate fluorophores for multicolor FRET studies. The

switchable FRET technique is an alternative to multicolor FRET techniques at the single-molecule level. It uses only two different dyes: one donor label and two or more acceptor labels; the acceptor molecules can be reversibly photoswitched in time so that in average only one of the FRET pairs is active at the same time (Uphoff et al. 2010). This technique thus also allows monitoring multiple distances and correlated behavior.

3.3.5 Quantitative FRET

FRET is often used qualitatively to mark different molecular conformations with different FRET values and is a powerful technique to report on conformation changes and dynamics. FRET has also been used quantitatively to report on distances and obtain structural information on static and dynamic structures. This application of the FRET technique has recently been reviewed in Preus and Wilhelmsson (2012). Using the FRET technique for quantitative studies of the local structure of a molecular complex has the advantage that little material is needed and that molecules can be studied in complex media. The main disadvantage is that the fluorophores' behavior needs to be controlled and modeled. Indeed, the FRET value is linked to a distance between the two fluorophores through Eqs. (3.1) and (3.2) and depends on the donor quantum yield; on the relative orientation of the fluorophores with respect to each other, via κ^2; and on their capability to rotate freely. The choice of the fluorophore, its linker, and position are important for quantitative FRET studies. Indeed fluorophores can interact with and stack on DNA and thus affect a quantitative determination of the FRET value to a distance (Iqbal et al. 2008; Ouellet et al. 2011; Sindbert et al. 2011). Using a probabilistic method to analyze single-molecule FRET data, named the nanopositioning system, quantitative structural information can be obtained from flexible complexes (Muschielok et al. 2008; Muschielok and Michaelis 2011). Quantitative FRET requires careful corrections to and calibrations of the detected fluorescence intensities and particularly the determination of the γ factor in Eq. (3.4) (Lee et al. 2005a, b; Sabanayagam et al. 2005; Edel et al. 2007; Kalinin et al. 2008; McCann et al. 2010).

3.4 Applications to DNA Nanotechnology

Single-molecule FRET microcopy has been used for over a decade to study properties of DNA structures that are also of interest for DNA nanotechnology. There is a significant body of work using this technique on DNA hybridization dynamics (Cisse et al. 2012); DNA flexibility (Vafabakhsh and Ha 2012); DNA secondary structure formation such as hairpins (Deniz et al. 1999), G-quadruplexes (Lee et al. 2005a, b; Kruger et al. 2010), and Holliday junctions (McKinney

et al. 2005; Lee et al. 2010a); and the dynamics of these advanced structures. We will not review this large literature here but instead give a few recent examples of studies combining single-molecule FRET and DNA nanotechnology. We have chosen to highlight two topics: (1) FRET studies of the structural dynamics of advanced DNA structures and (2) the use of DNA nanotechnology to control energy transfer pathways.

3.4.1 Static Structures and Structural Dynamics

Single-molecule FRET studies can elucidate the local structure of individual DNA molecular complexes, also in a sample that exhibits static or dynamic heterogeneity. This can give insights into the function and structure of both static and dynamic DNA molecular devices and motors. A detailed structural view of these molecular complexes can be achieved through quantitative single-molecule FRET studies. This method has been tested using double-stranded DNA rulers, where the donor and acceptor labels have been placed at several positions along the DNA (Clegg et al. 1993; Deniz et al. 1999; Di Fiori and Meller 2010), successfully describing the known DNA structure. Recently, the DNA origami technique has been used to make a more rigid DNA structure where labels can be attached so that they point in the same direction (Stein et al. 2011a). Thus, with the DNA origami rigid ruler, the effect of dye linkers on the donor/acceptor distance is significantly reduced, in contrast to the commonly used double-stranded DNA structures. Detailed structures of DNA molecules such as three-way junctions have been obtained with a combination of quantitative single-molecule FRET and molecular dynamics simulations (Sabir et al. 2011), and different conformations could be resolved.

There are a number of artificial structures that have the possibility of movement, which have been quantified by FRET studies. These structures can have two different states (Mao et al. 1999; Muller et al. 2006; Andersen et al. 2009) or even more states, with the recent report of a DNA actuator structure with 11 different states (Zhang et al. 2011; Kristiansen et al. 2012). Single-molecule FRET has been used to put forward the different conformations and the desired function and heterogeneity of several of these structures including a DNA tweezers structure (Muller et al. 2006).

Single-molecule FRET studies permit to resolve the structure of heterogeneous DNA molecular complexes in solution as discussed above, but it is a powerful tool to follow the movement of dynamic structures. Examples of such studies include revealing the detailed dynamic motion of a bipedal DNA motor (Masoud et al. 2012) and monitoring dynamic switching of a Holliday junction DNA structure with a controlled rate (Buranachai et al. 2006).

3.4.2 Controlled Energy Transfer Pathways

DNA structures can be functionalized at a given position with a large number of possible molecules, including proteins, dyes, and metal nanoparticles (Westerlund and Bjornholm 2009; Sacca and Niemeyer 2011). Thus, they can provide the means to precisely position selected molecules at the nanoscale and to control the distance between these molecules. FRET in this context can be a mechanism to transport light energy at the nanoscale, as exemplified by nature's light-harvesting complexes in photosynthesis. The combination of FRET and DNA nanotechnology can allow controlling the energy transfer distance and pathways and enable the design of DNA-based photonic devices. Double-stranded DNA has been used as scaffolds for dye-based photonic wires, where energy is transferred in a linear fashion over tens of nanometers (Hannestad et al. 2008; Su et al. 2011) including several studies at the single-molecule level (Garcia-Parajo et al. 2005; Tinnefeld et al. 2005; Heilemann et al. 2006; Sanchez-Mosteiro et al. 2006), which revealed heterogeneous energy transfer pathways. The 2D spatial control of energy transfer pathways was demonstrated using a DNA origami tile as motherboard and a single-molecule four-color FRET experiment (Stein et al. 2011b). The energy transferred through a given pathway can be emitted at a different wavelength and at a different location or used for an electron transfer reaction, i.e., converting the energy into an electric charge with eventual subsequent chemical reactions. The combination of DNA motherboards and interconnected photons and chemical and electrical signals may lead to the realization of complex molecular circuits.

3.5 Conclusion and Perspectives

Single-molecule FRET has a unique ability to provide detailed in situ structural dynamic information that is inaccessible with traditional ensemble methods. Here, we have given a short review of the method and of selected work that includes the combination of single-molecule FRET and DNA nanotechnology. We have shown examples where the technique can bring structural and dynamic information to characterize and improve the performance of functional and dynamic DNA devices. But also, we have presented examples where DNA nanotechnology can provide the means to precisely control energy transfer pathways, which could lead to a number of photonic devices.

The single-molecule FRET technique benefits from continuous improvements in our understanding of dye photobleaching and photodynamics (Ha and Tinnefeld 2012) and is thus under continuous development. Single-molecule FRET can also be combined with a number of other techniques including tweezers (Lee et al. 2010b) and more recently plasmons (Acuna et al. 2012), showing that conformational dynamics information can be obtained under a wide variety of conditions. In conclusion, single-molecule FRET is an excellent tool to boost the development of DNA-based technology.

Acknowledgments We would like to acknowledge financial support from the Danish Council for Independent Research's research carrier program Sapere Aude, from the Lundbeck Foundation, and from the Danish National Research Foundation to the Centre for DNA Nanotechnology.

References

Acuna GP, Moller FM, Holzmeister P, Beater S, Lalkens B, Tinnefeld P (2012) Fluorescence enhancement at docking sites of DNA-directed self-assembled nanoantennas. Science 338:506–510

Andersen ES, Dong M, Nielsen MM, Jahn K, Subramani R, Mamdouh W, Golas MM, Sander B, Stark H, Oliveira CLP, Pedersen JS, Birkedal V, Besenbacher F, Gothelf KV, Kjems J (2009) Self-assembly of a nanoscale DNA box with a controllable lid. Nature 459:73–75

Ando T, Uchihashi T, Kodera N, Yamamoto D, Miyagi A, Taniguchi M, Yamashita H (2008) High-speed AFM and nano-visualization of biomolecular processes. Pflugers Arch 456:211–225

Bath J, Turberfield AJ (2007) DNA nanomachines. Nat Nanotechnol 2:275–284

Birkedal V, Dong MD, Golas MM, Sander B, Andersen ES, Gothelf KV, Besenbacher F, Kjems J (2011) Single molecule microscopy methods for the study of DNA origami structures. Microsc Res Tech 74:688–698

Buranachai C, McKinney SA, Ha T (2006) Single molecule nanometronome. Nano Lett 6:496–500

Cisse II, Kim H, Ha T (2012) A rule of seven in Watson-Crick base-pairing of mismatched sequences. Nat Struct Mol Biol 19:623–627

Clegg RM (1992) Fluorescence resonance energy-transfer and nucleic-acids. Methods Enzymol 211:353–388

Clegg RM, Murchie AIH, Zechel A, Lilley DMJ (1993) Observing the helical geometry of double-stranded DNA in solution by fluorescence resonance energy transfer. Proc Natl Acad Sci USA 90:2994–2998

Dave R, Terry DS, Munro JB, Blanchard SC (2009) Mitigating unwanted photophysical processes for improved single-molecule fluorescence imaging. Biophys J 96:2371–2381

Deniz AA, Dahan M, Grunwell JR, Ha TJ, Faulhaber AE, Chemla DS, Weiss S, Schultz PG (1999) Single-pair fluorescence resonance energy transfer on freely diffusing molecules: observation of Forster distance dependence and subpopulations. Proc Natl Acad Sci USA 96:3670–3675

Di Fiori N, Meller A (2010) The effect of dye-dye interactions on the spatial resolution of single-molecule FRET measurements in nucleic acids. Biophys J 98:2265–2272

Edel JB, Eid JS, Meller A (2007) Accurate single molecule FRET efficiency determination for surface immobilized DNA using maximum likelihood calculated lifetimes. J Phys Chem B 111:2986–2990

Endo M, Tatsumi K, Terushima K, Katsuda Y, Hidaka K, Harada Y, Sugiyama H (2012) Direct visualization of the movement of a single T7 RNA polymerase and transcription on a DNA nanostructure. Angew Chem Int Ed Engl 51:8778–8782

Fischer N, Konevega AL, Wintermeyer W, Rodnina MV, Stark H (2010) Ribosome dynamics and tRNA movement by time-resolved electron cryomicroscopy. Nature 466:329–333

Garcia-Parajo MF, Hernando J, Mosteiro GS, Hoogenboom JP, van Dijk E, van Hulst NF (2005) Energy transfer in single-molecule photonic wires. Chemphyschem 6:819–827

Ha T, Tinnefeld P (2012) Photophysics of fluorescent probes for single-molecule biophysics and super-resolution imaging. Annu Rev Phys Chem 63:595–617

Haga T, Sonehara T, Sakai T, Anazawa T, Fujita T, Takahashi S (2011) Simultaneous four-color imaging of single molecule fluorophores using dichroic mirrors and four charge-coupled devices. Rev Sci Instrum 82:023701

Hannestad JK, Sandin P, Albinsson B (2008) Self-assembled DNA photonic wire for long-range energy transfer. J Am Chem Soc 130:15889–15895

Heilemann M, Kasper R, Tinnefeld P, Sauer M (2006) Dissecting and reducing the heterogeneity of excited-state energy transport in DNA-Based photonic wires. J Am Chem Soc 128:16864–16875

Hohng S, Joo C, Ha T (2004) Single-molecule three-color FRET. Biophys J 87:1328–1337

Holden SJ, Uphoff S, Hohlbein J, Yadin D, Le Reste L, Britton OJ, Kapanidis AN (2010) Defining the limits of single-molecule FRET resolution in TIRF microscopy. Biophys J 99:3102–3111

Huang B, Bates M, Zhuang XW (2009) Super-resolution fluorescence microscopy. Annu Rev Biochem 78:993–1016

Iqbal A, Arslan S, Okumus B, Wilson TJ, Giraud G, Norman DG, Ha T, Lilley DMJ (2008) Orientation dependence in fluorescent energy transfer between Cy3 and Cy5 terminally attached to double-stranded nucleic acids. Proc Natl Acad Sci USA 105:11176–11181

Jungmann R, Scheible M, Simmel FC (2012) Nanoscale imaging in DNA nanotechnology. Wiley Interdiscip Rev Nanomed Nanobiotechnol 4:66–81

Kalinin S, Felekyan S, Valeri A, Seidel CAM (2008) Characterizing multiple molecular states in single-molecule multiparameter fluorescence detection by probability distribution analysis. J Phys Chem B 112:8361–8374

Kapanidis AN, Lee NK, Laurence TA, Doose S, Margeat E, Weiss S (2004) Fluorescence-aided molecule sorting: analysis of structure and interactions by alternating-laser excitation of single molecules. Proc Natl Acad Sci USA 101:8936–8941

Krishnan Y, Simmel FC (2011) Nucleic acid based molecular devices. Angew Chem Int Ed Engl 50:3124–3156

Kristiansen M, Kryger MBL, Zhang Z, Voigt NV, Birkedal V, Gothelf KV (2012) Extended DNA tile actuators. Chempluschem 77:636–642

Kruger AC, Raarup MK, Nielsen MM, Kristensen M, Besenbacher F, Kjems J, Birkedal V (2010) Interaction of hnRNP A1 with telomere DNA G-quadruplex structures studied at the single molecule level. Eur Biophys J 39:1343–1350

Lamichhane R, Solem A, Black W, Rueda D (2010) Single-molecule FRET of protein-nucleic acid and protein-protein complexes: surface passivation and immobilization. Methods 52:192–200

Lee JY, Okumus B, Kim DS, Ha TJ (2005a) Extreme conformational diversity in human telomeric DNA. Proc Natl Acad Sci USA 102:18938–18943

Lee NK, Kapanidis AN, Wang Y, Michalet X, Mukhopadhyay J, Ebright RH, Weiss S (2005b) Accurate FRET measurements within single diffusing biomolecules using alternating-laser excitation. Biophys J 88:2939–2953

Lee J, Lee S, Ragunathan K, Joo C, Ha T, Hohng S (2010a) Single-molecule four-color FRET. Angew Chem Int Ed Engl 49:9922–9925

Lee M, Kim SH, Hong SC (2010b) Minute negative superhelicity is sufficient to induce the B-Z transition in the presence of low tension. Proc Natl Acad Sci USA 107:4985–4990

Lee S, Lee J, Hohng S (2010c) Single-molecule three-color FRET with both negligible spectral overlap and long observation time. PLoS One 5:e12270

Mao CD, Sun WQ, Shen ZY, Seeman NC (1999) A nanomechanical device based on the B-Z transition of DNA. Nature 397:144–146

Masoud R, Tsukanov R, Tomov TE, Plavner N, Liber M, Nir E (2012) Studying the structural dynamics of bipedal DNA motors with single-molecule fluorescence spectroscopy. ACS Nano 6:6272–6283

McCann JJ, Choi UB, Zheng LQ, Weninger K, Bowen ME (2010) Optimizing methods to recover absolute FRET efficiency from immobilized single molecules. Biophys J 99:961–970

McKinney SA, Freeman ADJ, Lilley DMJ, Ha TJ (2005) Observing spontaneous branch migration of Holliday junctions one step at a time. Proc Natl Acad Sci USA 102:5715–5720

Muller BK, Reuter A, Simmel FC, Lamb DC (2006) Single-pair FRET characterization of DNA tweezers. Nano Lett 6:2814–2820

Muschielok A, Michaelis J (2011) Application of the nano-positioning system to the analysis of fluorescence resonance energy transfer networks. J Phys Chem B 115:11927–11937
Muschielok A, Andrecka J, Jawhari A, Bruckner F, Cramer P, Michaelis J (2008) A nano-positioning system for macromolecular structural analysis. Nat Methods 5:965–971
Ouellet J, Schorr S, Iqbal A, Wilson TJ, Lilley DMJ (2011) Orientation of cyanine fluorophores terminally attached to DNA via long, flexible tethers. Biophys J 101:1148–1154
Pinheiro AV, Han DR, Shih WM, Yan H (2011) Challenges and opportunities for structural DNA nanotechnology. Nat Nanotechnol 6:763–772
Preus S, Wilhelmsson LM (2012) Advances in quantitative FRET-based methods for studying nucleic acids. Chembiochem 13:1990–2001
Rajendran A, Endo M, Sugiyama H (2012) Single-molecule analysis using DNA origami. Angew Chem Int Ed Engl 51:874–890
Rothemund PWK (2006) Folding DNA to create nanoscale shapes and patterns. Nature 440:297–302
Roy R, Hohng S, Ha T (2008) A practical guide to single-molecule FRET. Nat Methods 5:507–516
Sabanayagam CR, Eid JS, Meller A (2004) High-throughput scanning confocal microscope for single molecule analysis. Appl Phys Lett 84:1216–1218
Sabanayagam CR, Eid JS, Meller A (2005) Long time scale blinking kinetics of cyanine fluorophores conjugated to DNA and its effect on Forster resonance energy transfer. J Chem Phys 123:224708
Sabir T, Schroder GF, Toulmin A, McGlynn P, Magennis SW (2011) Global structure of forked DNA in solution revealed by high-resolution single-molecule FRET. J Am Chem Soc 133:1188–1191
Sacca B, Niemeyer CM (2011) Functionalization of DNA nanostructures with proteins. Chem Soc Rev 40:5910–5921
Sanchez-Mosteiro G, van Dijk E, Hernando J, Heilemann M, Tinnefeld P, Sauer M, Koberlin F, Patting M, Wahl M, Erdmann R, van Hulst NF, Garcia-Parajo MF (2006) DNA-based molecular wires: multiple emission pathways of individual constructs. J Phys Chem B 110:26349–26353
Schoen I, Ries J, Klotzsch E, Ewers H, Vogel V (2011) Binding-activated localization microscopy of DNA structures. Nano Lett 11:4008–4011
Seeman NC (2010) Nanomaterials based on DNA. Annu Rev Biochem 79:65–87
Shih WM, Lin CX (2010) Knitting complex weaves with DNA origami. Curr Opin Struct Biol 20:276–282
Sindbert S, Kalinin S, Hien N, Kienzler A, Clima L, Bannwarth W, Appel B, Muller S, Seidel CAM (2011) Accurate distance determination of nucleic acids via Forster resonance energy transfer: implications of dye linker length and rigidity. J Am Chem Soc 133:2463–2480
Sisamakis E, Valeri A, Kalinin S, Rothwell PJ, Seidel CAM (2010) Accurate single molecule FRET studies using multiparameter fluorescence detection. In: Walter NG (ed) Methods in enzymology, vol 475: Single molecule tools, Pt B: Super-resolution, particle tracking, multi-parameter, and force based methods. Academic, San Diego, pp 455–514
Stein IH, Schuller V, Bohm P, Tinnefeld P, Liedl T (2011a) Single-molecule FRET ruler based on rigid DNA origami blocks. Chemphyschem 12:689–695
Stein IH, Steinhauer C, Tinnefeld P (2011b) Single-molecule four-color FRET visualizes energy-transfer paths on DNA origami. J Am Chem Soc 133:4193–4195
Steinhauer C, Jungmann R, Sobey TL, Simmel FC, Tinnefeld P (2009) DNA origami as a nanoscopic ruler for super-resolution microscopy. Angew Chem Int Ed Engl 48:8870–8873
Su W, Bonnard V, Burley GA (2011) DNA-templated photonic arrays and assemblies: design principles and future opportunities. Chemistry 17:7982–7991
Tinnefeld P, Heilemann M, Sauer M (2005) Design of molecular photonic wires based on multistep electronic excitation transfer. Chemphyschem 6:217–222

Uphoff S, Holden SJ, Le Reste L, Periz J, van de Linde S, Heilemann M, Kapanidis AN (2010) Monitoring multiple distances within a single molecule using switchable FRET. Nat Methods 7:831–836

Vafabakhsh R, Ha T (2012) Extreme bendability of DNA less than 100 base pairs long revealed by single-molecule cyclization. Science 337:1097–1101

Vogelsang J, Kasper R, Steinhauer C, Person B, Heilemann M, Sauer M, Tinnefeld P (2008) A reducing and oxidizing system minimizes photobleaching and blinking of fluorescent dyes. Angew Chem Int Ed Engl 47:5465–5469

Wei B, Dai MJ, Yin P (2012) Complex shapes self-assembled from single-stranded DNA tiles. Nature 485:623–626

Westerlund F, Bjornholm T (2009) Directed assembly of gold nanoparticles. Curr Opin Colloid Interface Sci 14:126–134

Zhang Z, Olsen EM, Kryger M, Voigt NV, Torring T, Gultekin E, Nielsen M, MohammadZadegan R, Andersen ES, Nielsen MM, Kjems J, Birkedal V, Gothelf KV (2011) A DNA tile actuator with eleven discrete states. Angew Chem Int Ed Engl 50:3983–3987

Zhao R, Rueda D (2009) RNA folding dynamics by single-molecule fluorescence resonance energy transfer. Methods 49:112–117

Zhu L, Zhang W, Elnatan D, Huang B (2012) Faster STORM using compressed sensing. Nat Methods 9:721–723

Part II
Design, Creation and Assembly of Sequences that Fold into Well-Defined Structures

Chapter 4
Tile-Based DNA Nano-assemblies

Abhijit Rangnekar and Thomas H. LaBean

Abstract Tile-based DNA nanostructures have played an important role in the evolution of the field of structural DNA nanotechnology over the last three decades. These structures are formed using multiple short synthetic oligonucleotide strands that are specifically designed to self-assemble into desired configurations. Successful assembly of a variety of planar DNA tiles has been demonstrated including crossover tiles, multi-armed tiles, weave tiles, etc. These tiles have then been used to form one- and two-dimensional arrays or lattices. In addition, three-dimensional tile-based structures have been developed using helix bundle tubes, finite-sized closed polyhedral structures, and a three-dimensional crystalline lattice. This chapter chronicles the progress thus far in the design and synthesis of tile-based DNA nano-assemblies. Furthermore, it details the steps involved in the successful design, synthesis, and characterization of such structures. It also reviews the applications of these tiles in molecular computation and in programmed assembly of other nanoscale materials such as proteins, metallic nanoparticles, and aptamers.

Contents

A. Rangnekar • T.H. LaBean (✉)
Department of Materials Science and Engineering, North Carolina State University, Raleigh, NC 27606, USA
e-mail: thlabean@ncsu.edu

J. KJEMS et al. (eds.), *Nucleic Acid Nanotechnology*, Nucleic Acids and Molecular Biology 29, DOI 10.1007/978-3-642-38815-6_4,

4.1 Genesis of DNA Tiles

Nucleic acid strands can be designed such that they hybridize with their complementary sequences and thus fold and assemble into well-defined secondary structures, building blocks, and lattices. This capacity for programmed molecular recognition makes DNA a versatile material with which to design and build nanometer-scale structures. Normal, double-helical DNA is a linear, antiparallel, and unbranched complex of two molecules. It is, however, possible to make DNA structures containing branched junctions; that is, the constituent molecules are linear (i.e., unbranched) but the complex displays a branched topology. For example, a four-arm junction can be made using four individual DNA strands which are complementary to each other in the correct pattern. Using Watson–Crick complementarity, portions of the strands base pair with one another to form two domains of duplex DNA that are linked at one crossover point by exchange of two of the four strands. Such a four-arm junction is an immobile form of the Holliday junction, which is a biologically important structure that exists in cells during homologous recombination (Holliday 1964; Seeman 1982). Topological branch junction structures are an effective strategy for creating multivalent complexes from the normally bivalent and linear DNA double helix. Branched DNA structures have been used to create a wide variety of DNA complexes with useful properties.

In 1982, Nadrian Seeman was the first to propose that DNA building blocks containing branch junctions could be used to construct ordered arrays (Seeman 1982). His vision for this new area of research was to assemble DNA into three-dimensional crystalline lattices to scaffold biological macromolecules, nanodevices, and nanoelectronic components within periodic arrays. After initial experiments involving synthesis of four-arm junctions (Kallenbach et al. 1983; Petrillo et al. 1988) and development of design theories regarding formation of DNA nanostructures (Seeman and Kallenbach 1983), Seeman's group successfully demonstrated the formation of a quadrilateral shape from DNA branched junctions (Chen et al. 1989) followed by five- and six-arm junctions (Wang et al. 1991) and, much later in 2007, of 8- and 12-arm junctions (Wang and Seeman 2007).

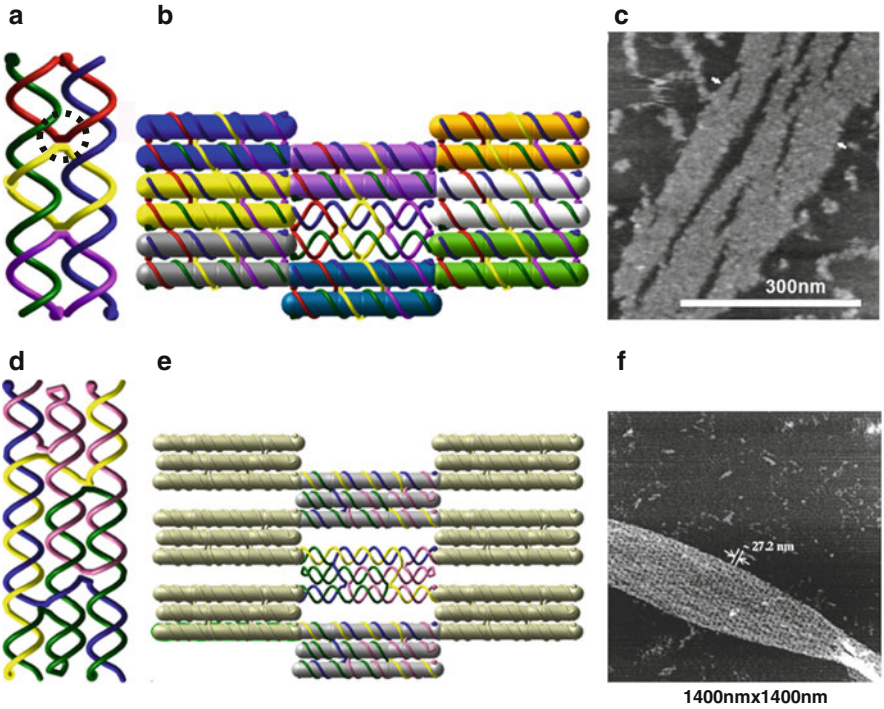

Fig. 4.1 (**a**) A double crossover (DX) tile (shown with vertical helix axes). The two helices are held parallel by crossover junctions (*circled*). (**b**) Sticky ends of a double crossover tile can be suitably programmed to form two-dimensional lattices, shown here with horizontal helix axes. The adjacent tiles are identical but distinctly colored for clarity. (**c**) AFM image of the DX tile array. (**d**) A triple-crossover (TX) tile, which is a planar tile with three parallel helices held together by crossovers. (**e**) Two sets of TX tiles, identified by *color*, appropriately equipped with sticky ends will form two-dimensional arrays as demonstrated in the AFM image in (**f**) (Fu and Seeman 1993; Winfree et al. 1998; LaBean et al. 2000)

4.2 Crossover Tiles with Parallel Helices

In 1993, it was shown for the first time that DNA strands could be designed such that, when annealed, they formed a structure in which the axes of the DNA duplexes were constrained to be parallel and coplanar (Fu and Seeman 1993). This complex is called a double crossover tile (DX tile or simply DX), because it contains two strand-exchange crossover points linking two double helixes (Fig. 4.1a). The main advantage of this design is that the junctions are constrained to a single orientation as opposed to being flexible as observed in the four-arm junction. In such a structure, two strands typically "cross over" from one duplex to the neighboring duplex to hold them together. Such *crossover* motifs, which are the same as immobile Holliday junctions, have since become an integral part of DNA nanostructures (Fig. 4.1a), and joining them together in novel ways with DX-like pairings have generated a large diversity of tile types.

Characterization of DNA nanostructures by atomic force microscopy (AFM) was published for the first time in 1998 (Winfree et al. 1998). Micrometer scale two-dimensional lattices were constructed by equipping DX tiles with sticky ends (Fig. 4.1a–c). This strategy immediately paved the way for the use of DNA as building material for wide ranging nanoscale self-assemblies. Once the success of the strategy was established, research in this direction quickly gained momentum. A number of different structures were reported in the next few years most notably the DNA triple-crossover tile (TX tile), which is a planar tile containing three axially parallel DNA double helices (LaBean et al. 2000) (Fig. 4.1d–f). Additional tile designs include PX (paranemic crossover) and JX_2 (juxtaposed) tiles (Shen et al. 2004). In PX tile, the two helices on one side of the central junction are rotated about a half-turn from their positions when compared to the JX_2 tile. Following this, a few bulkier tiles were also prototyped, including double–double crossover tile (DDX), also known as the quad-crossover (QX), consisting of four parallel DNA double helices (Reishus et al. 2005) and tiles containing 8 and 12 helices (all with parallel and coplanar helix axes) (Ke et al. 2006).

4.3 Multi-armed Tiles

In 1999, Seeman's group designed a two-dimensional DNA lattice from Holliday junction analogues containing two helical domains twisted relative to each other to mimic the approximately 60° angle observed in crystals of individual junctions. Four such junctions were fused to form a rhombus-like tile structure (Mao et al. 1999a). These rhomboid structures were then self-assembled into two-dimensional periodic arrays. This assembly distinguished itself from the assembly of crossover tiles as the lattice growth was achieved in both x and y directions independently (helix stacking in both dimensions) as opposed to the asymmetric growth of the previous lattices (helix stacking only in a single dimension). This concept was further developed when Yan et al. used crossovers in each arm of a four-arm building block giving rise to a cross-tile, also known as the 4×4 tile (Yan et al. 2003a), which also had the characteristic of helix stacking in both x and y directions (Fig. 4.2a). Equipping the tile with sticky ends on both helices in each of the four arms resulted in a beautiful two-dimensional periodic lattice with square aspect ratio (Fig. 4.2b, c). The original 4×4 tile design had some inherent curvature within the tiles, but the effect of this on the overall curvature of the 2D lattice was eliminated by using a corrugation strategy (which involved flipping adjacent tiles).

Mao et al. constructed three-, four- and six-point stars using the same overall design principle but with the added characteristic of symmetric arms (i.e., identical nucleotide sequences on each of the multiple tile arms) (He et al. 2005a, b, 2006). Since the sequences of each arm were identical, this entailed a significant reduction in the number of different DNA strands required per tile type. Moreover, it also ensured that any possible geometric distortions and asymmetric, sequence-specific

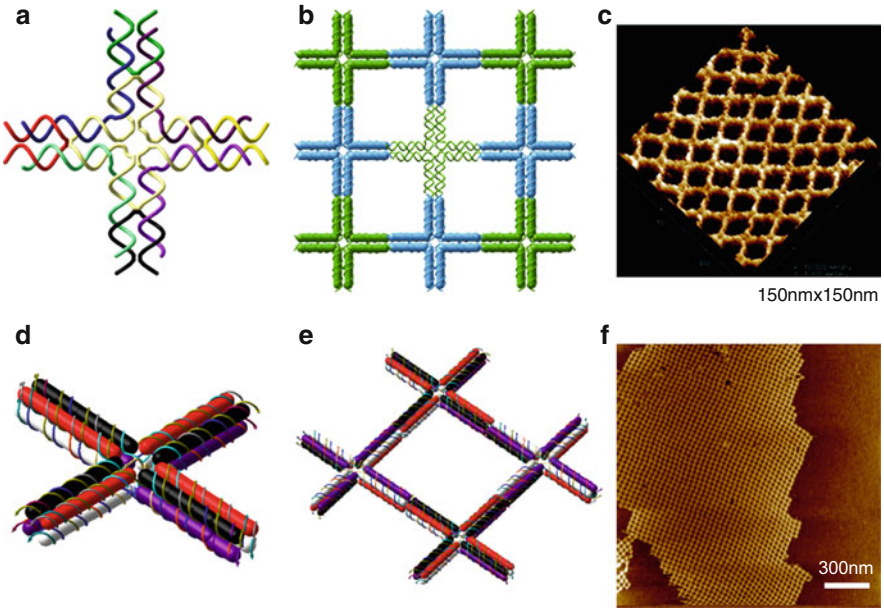

Fig. 4.2 (**a**) 4 × 4 tile with sticky ends. (**b**) Two-dimensional lattice formed by using corrugation strategy with 4 × 4 tiles. Adjacent tiles are flipped such that the same-*colored* tiles face same direction in the array. (**c**) AFM image of the 4 × 4 tile lattice. (**d**) Double-decker tile with sticky ends. All four arms are symmetric. (**e**) Two-dimensional lattice formed by using corrugation strategy with double-decker tiles. (**f**) AFM image of the double-decker lattice with several micrometer in each dimension (Yan et al. 2003a; Majumder et al. 2011)

curvature in the tile would be cancelled out. By adopting sequence symmetry in the cross-tile, it was possible to obtain much larger lattices compared to the asymmetric tiles with edge lengths on the millimeter scale (He et al. 2005b). Double-decker tile is another example of a cross-tile (Majumder et al. 2011). It comprised of two 4 × 4 tiles, lying one on top of the other and linked by two crossovers in each arm perpendicular to the plane of the tile (Fig. 4.2d). The four arms of the double-decker tile were also symmetric, and large two-dimensional lattices of tens of micrometers in size were observed when the corrugation strategy was employed (Fig. 4.2e, f).

4.4 Helix Bundle Tiles

DNA helix bundles constitute another category of DNA tiles. In these tiles, multiple double helices are aligned using crossovers so that they are axially parallel (but not coplanar), and they are typically closed around their circumference. Using this strategy, three-, four- and six-helix bundles have been created (Park et al. 2005;

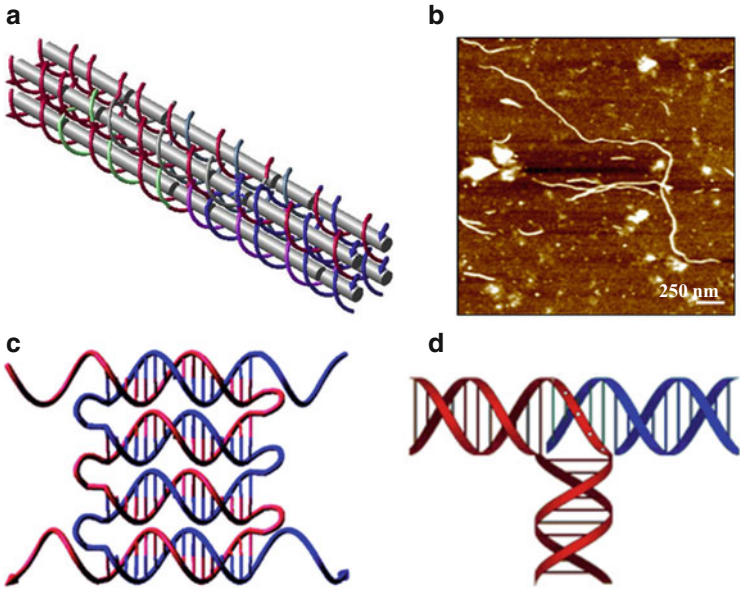

Fig. 4.3 (**a**) DNA four-helix bundle. (**b**) One-dimensional filaments constructed with the four-helix bundle. (**c**) Four-helix weave tile. Adjacent helices are linked via flexible T_4 loops. (**d**) T-junction. Weave tile and T-junction are examples of noncanonical tiles (Rangnekar et al. 2011; Hansen et al. 2010; Hamada and Murata 2009)

Rangnekar et al. 2011; Mathieu et al. 2005). The formation of helix bundle tiles added a new dimension to the field of DNA nanotechnology. When such bundles were attached along their axes using sticky ends, they formed uniform filaments micrometers or tens of micrometers long. By suitable programming of the sticky ends, formation of regular two-dimensional lattices using these bundle tiles was also shown. Figure 4.3a, b illustrates four-helix bundle tile and one-dimensional arrays formed using it (Rangnekar et al. 2011). Later, Seeman's group demonstrated the formation of six- and eight-helix bundles using half-bundle tiles (Kuzuya et al. 2007). They also designed a tile consisting of a six-helix bundle sheath that encompassed a central DNA double helix (Wang et al. 2009).

4.5 Noncanonical Tiles

The presence of multiple crossovers connecting parallel double helices has been repeatedly shown to provide stability and rigidity to tile-based DNA nanostructures. A new building block design, known as the weave tile strategy, was recently reported (Hansen et al. 2010). In this strategy, only two DNA strands are used per tile, rather than the four to nine strands used in the previously discussed tiles. The sequences were designed such that complementary regions weave back and forth to

mimic the strand routing of origami architectures (see Chap. 5), thereby forming a weave-like tile with rigid double-helical domains tethered to neighboring domains by flexible single-stranded T_4 loops (Fig. 4.3c). This strategy avoids the use of crossover junctions, thereby providing greater structural flexibility to the DNA nanostructure without compromising overall stability of the constructs. While weave tiles were only able to assemble into small, somewhat faulty lattices, they were shown to serve as aptamer-display platforms for designing highly effective enzyme inhibitors with substantial anticoagulant activity in blood plasma clotting assays (Rangnekar et al. 2012).

Weave tiles and Holliday junction-based tiles have design limitations affecting the available shapes of DNA nanostructures which are mainly typified by parallel-packed duplexes. However, another DNA branch junction structure known as T-junction motif provides a right angle geometry at the branch point between the connected duplexes (Hamada and Murata 2009). One junction consists of two DNA duplexes. One duplex has a sticky end at the terminus which is complementary to a single-stranded bulge section in the center of the second duplex. After hybridization, the first duplex is inserted into the bulge via its sticky end causing the second duplex to bend at about a 90° angle, thus resulting in an interconnection comprising a branched T-shaped junction (Fig. 4.3d). These T-motifs were used to build nanostructures displaying several different two-dimensional architectures. Rigid triangles from flexible DNA four-arm junctions were also designed using a tensegrity strategy and were then assembled into one- and two-dimensional arrays (Liu et al. 2004).

Recently, Yin et al. (2008) synthesized filaments analogous to DNA helix bundle tiles with monodisperse and programmable circumference. They synthesized "DNA tubes" with circumferences of 4, 5, 6, 7, 8, 10, and 20 DNA helices that displayed increasing stiffness and persistence length with increasing circumference. However, they used single-stranded tiles to build the filaments which involved half-crossovers where only one strand crosses over between helices at the junction points (rather than two strands in the Holliday junction-like crossovers). This single-stranded tile strategy was entirely different from the one adopted by earlier studies using multi-stranded tiles and gave rise to structures with significantly reduced (but tunable) structural rigidity. The structural tunability of the single-stranded tiles was further exploited to create finite but complex and addressable two dimensional shapes as well as three-dimensional structures with sophisticated surface features and intricate interior cavities (Wei et al. 2012; Ke et al. 2012; see Chap. 5 for further details on this type of DNA nanostructures).

4.6 Finite-Sized 3D Structures

Along with two-dimensional structures, Seeman also commenced efforts to build three-dimensional structures. His initial work included construction of a DNA cube (Chen and Seeman 1991) and a DNA-truncated octahedron (Zhang and Seeman

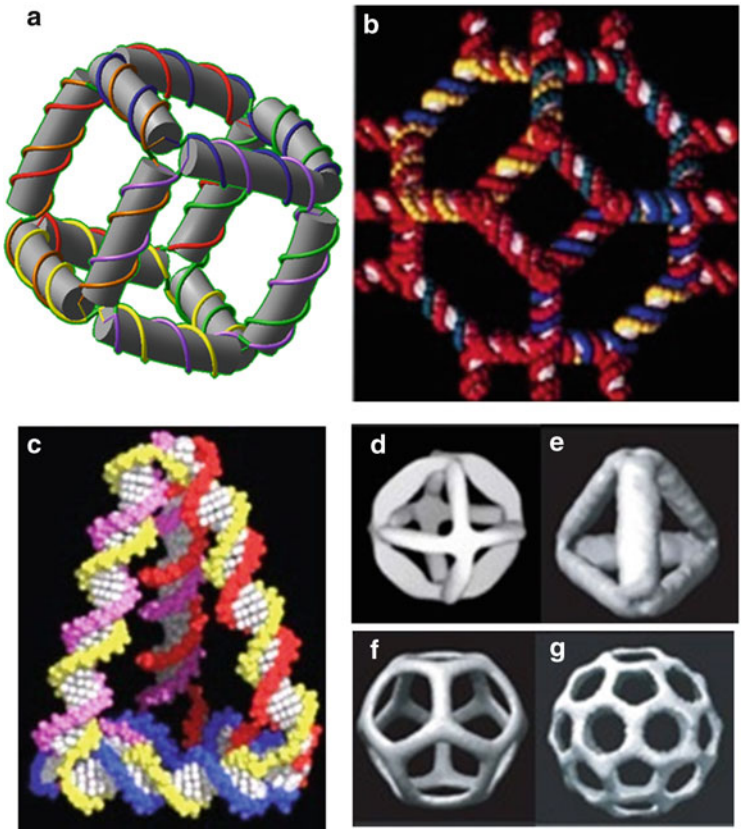

Fig. 4.4 Finite-sized three-dimensional DNA structures. (**a**) DNA cube. (**b**) Truncated octahedron. (**c**) Tetrahedron. (**d**–**g**) Cryo-electron microscopy reconstruction images of (**d**) octahedron, (**e**) tetrahedron, (**f**) dodecahedron, and (**g**) buckyball (Chen and Seeman 1991; Zhang and Seeman 1994; Goodman et al. 2005; Shih et al. 2004; He et al. 2008)

1994). The DNA cube consisted of 12 equal-length double-helical edges arranged about eight vertices (Fig. 4.4a). The vertices were branch points of three-arm junctions. This was the first demonstration of a closed polyhedral structure made from DNA. The truncated octahedron had 36 edges arranged about 24 vertices which were branch points of four-arm junctions (Fig. 4.4b). However, due to the lack of available characterization techniques at the time as well as the extremely small amount of construct synthesized (e.g., on the order of femtomoles), it was impossible to visualize and difficult to conclusively prove the formation of these structures.

In 2004, Shih et al. were able to characterize a three-dimensional DNA nanostructure—a DNA octahedron—by using cryo-electron microscopy (cryo-EM) for the first time (Shih et al. 2004) (Fig. 4.4d). The octahedron was made using a long, specially designed, biosynthesized DNA strand which was

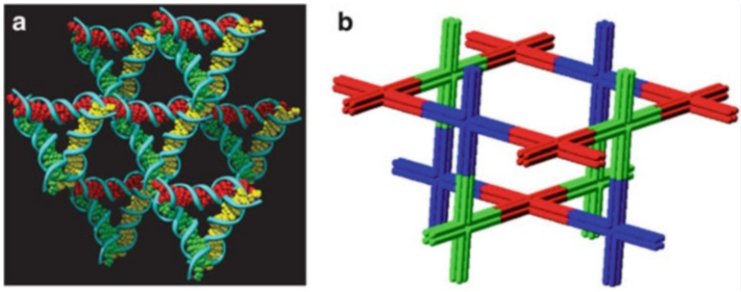

Fig. 4.5 (**a**) Three-dimensional crystal lattice formed by DNA tensegrity *triangles*. The cavities are rhombohedral in shape. (**b**) Double-decker tile can also potentially be used to form three-dimensional lattice structures. The cavities in this case would be cubic and larger than the rhombohedral cavities in (**a**) (Zheng et al. 2009; Majumder et al. 2011)

subsequently folded using a small number of short oligodeoxynucleotide strands. Synthesis of a DNA tetrahedron was also reported later (Goodman et al. 2005) (Fig. 4.4c). More recently, Mao et al. demonstrated the self-assembly and characterization using cryo-EM of tetrahedra, dodecahedra, and buckyball-like structures (He et al. 2008) (Fig. 4.4e–g). The building blocks for all the structures in the Mao study were the three-point stars. Different structures were obtained by assembling three-point star tiles at different concentrations.

4.7 Three-Dimensional Lattices Using DNA Tiles

In 2009, 27 years after founding the field of DNA nanotechnology in an effort to create periodic matter based on DNA crystals, Seeman et al. demonstrated, for the first time, well-ordered macromolecular three-dimensional crystalline lattices using the DNA "tensegrity" triangle (Zheng et al. 2009). As mentioned above, the tensegrity triangle is a rigid DNA motif with threefold rotational symmetry (Liu et al. 2004). The resulting three-dimensional lattice has periodic rhombohedral cavities of approximately 103 nm^3 in size (Fig. 4.5a). Several other DNA tiles have also been proposed for use in the formation of three-dimensional lattices. Sticky ends of the double-decker tile (Majumder et al. 2011) may be programmed to form three-dimensional lattice containing cubic cavities with a periodicity of ~60 nm (Fig. 4.5b). DNA four-helix bundle (Rangnekar et al. 2011) may also be used to form an octahedral structure which could be further assembled into three-dimensional cubic lattice. Triple-crossover tile (TAE tile) (LaBean et al. 2000) and double–double crossover tile (DDX tile) (Reishus et al. 2005) may also be programmed so as to yield periodic arrays in three dimensions, although only the triangle tile crystals have been successfully documented so far.

4.8 Design of DNA Tiles

There are essentially three steps to successfully form any DNA nanostructure—design, experimental assembly, and post-assembly characterization. Nanostructure design includes geometric structure design as well as nucleotide sequence design. Structure design constitutes a positive design paradigm (Dirks et al. 2004) and maximizes the probability of forming the target structure by energy and strain minimization. Sequence design constitutes positive and negative design paradigms (Dirks et al. 2004) and optimizes specificity for the target structure by sequence-symmetry minimization (SSM) and other constraints on the sequences of the participating DNA strands in order to decrease the probability of forming alternative structures.

A major component of many DNA tiles is the crossover junction. Placement within the design and especially spacing between crossovers is of primary importance. A small stretch of DNA double helix can be considered as a rigid cylinder with almost fixed dimensions. The pitch of the B-form DNA double helix is approximately 10.5 bases/turn (Wang 1979). Thus, with the rise of each nucleotide, there is an angular displacement of 34.28° in the plane perpendicular to the helical axis. A starting assumption in calculating the geometry of DNA nanostructures is that all the bases are essentially identical. Given this assumption, the precise positions of the nucleotides can be modeled. The crossovers can then be designed geometrically by determining the locations where the phosphodiester linkage would cross over from one helix to the other.

In 2006, Sherman and Seeman presented a theoretical framework for designing DNA tiles based on the crossover motif, where each double-helical domain is axially parallel and connected to the neighboring domain via Holliday junction-like reciprocal exchanges (Sherman and Seeman 2006). They defined nucleoside end midpoints (NEMids), which are located at the midpoints between consecutive C3′ atoms, and not at the locations of the phosphates (Fig. 4.6). The two linkages in a crossover always flank one NEMid on each of the helices involved. A properly designed crossover does not usually disrupt the base structure since the section of the DNA backbone involved with the crossover is the phosphodiester linkage between two bases. A minimally strained crossover should have the NEMids involved directly on the tangency line between the two helical domains (Fig. 4.6). When nucleosides, instead of the NEMids, are on the tangency line, strand exchange at the crossover would be strained and therefore should be avoided. Crossovers between helices can thus be designed by aligning the helical axes parallel to each other, followed by aligning the NEMids by rotating the individual helices around their axes.

Each arm of a multi-arm tile contains parallel helices bound by crossovers. The arms can then be connected within the core of the tile using single-stranded poly-T regions, for example. The length of the poly-T strand often determines the geometry and shape of the DNA tile. In 4 × 4 tile and six-point star, it is four bases (Yan et al. 2003a; He et al. 2006), whereas in three-point star, it is three bases (He et al. 2005a). Moreover, as mentioned earlier, Mao et al. used three-point star as motif to create several finite-sized three-dimensional structures (He et al. 2008).

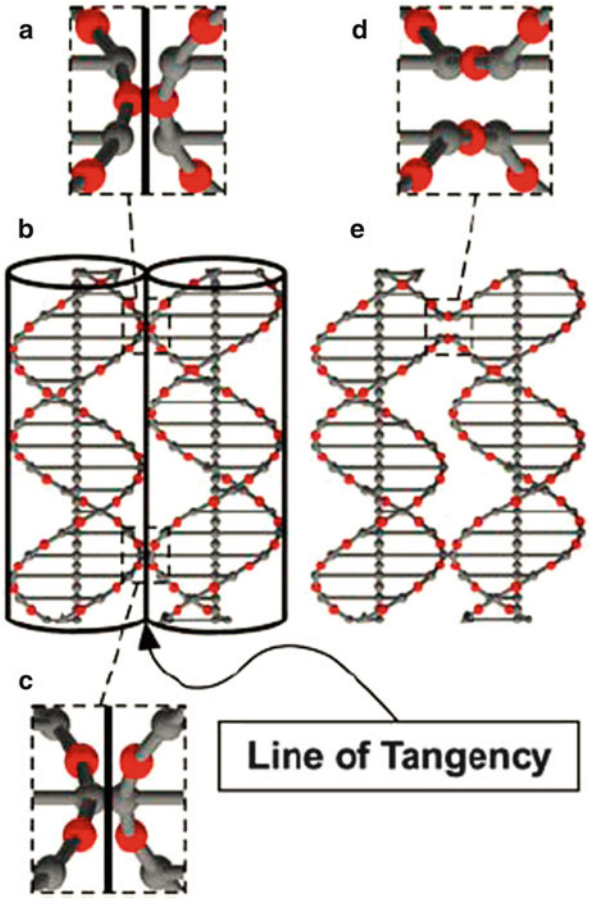

Fig. 4.6 Design of crossover positions. The nucleosides are represented as *gray spheres* and the nucleoside end midpoints (NEMids) are represented as *red spheres*. (**a**) NEMids are aligned in the first step at the line of tangency between two parallel helices as shown in (**b**). (**c**) The point of contact of nucleosides in the adjacent helices at the line of tangency should not be used to design crossover. (**d**) Aligned NEMids are then used to create crossover, where one strand in each helix crosses over to the adjacent helix as shown in (**e**) (Sherman and Seeman 2006)

The shape and size of the resulting structures was dictated by the concentration of the individual three-point star tiles, as well as the length of the poly-T loop at the center of the tile. Flexible poly-T loops may also be used to connect parallel helices in lieu of more rigid crossovers as has been demonstrated in the case of DNA weave tiles (Hansen et al. 2010).

Small DNA tiles are often used to form large lattice structures in one, two and three dimensions. The lattice structures are formed via sticky end cohesion between the tiles. Sticky ends (single-strand DNA) are designed so that they are sufficiently stable in keeping the lattice intact at the characterization temperature. Moreover, the sticky end regions between adjacent tiles must maintain the double-helical twist consistent with the tile design and must not lead to over- or under-winding of the DNA double helix and negatively affect the stability of the target lattice structure. Enthalpic and entropic contributions to the free energy of binding between DX tiles have been measured in order to study the relative effects of rigidity and flexibility in multivalent binding associations (Nangreave et al. 2011).

The next step in DNA tile design is to generate and optimize nucleotide sequences for the component strands. The most important tool to achieve this is SSM (Seeman 1990). SSM means that the sequences are selected with the goal of minimizing sequences with similarities between segments of molecules. Thus, the chances of undesired associations are decreased, and control over secondary structure is improved. The sequence design process assigns sequences that assemble into otherwise unlikely structures by making the maximization of Watson–Crick base-pairing contingent upon their formation. The basic premise underlying this concept is that DNA will form continuous, perfectly paired, double-helical segments in preference to other arrangements.

A "vocabulary element" is defined as the set of nucleotides which is not repeated anywhere else in the structure (Seeman 1990). Depending on the length of the vocabulary element, one can define the maximum number of possible vocabulary elements—64 for trimers, 256 for tetramers, etc. The length of the vocabulary element, in turn, depends upon the size of the structure to be designed. A program called SEQUIN, based on SSM algorithm, was developed by Seeman (1990) in FORTRAN in order to assist with the design of sequences. This program is used to assign sequences to design helices, crossovers, single-stranded loops, connectors, etc. SEQUIN generates adequate sequences, without attempting an exhaustive search for the best possible sequence. The same approach and criteria is extended to the design of sequences for the sticky ends. Additional factors, such as G + C percentage, eschewing runs of poly-G, avoidance of polypurine tracts, may also be taken into consideration while assigning sequences. It is also crucial to ensure the absence of inverted repeats while designing sequences, since these would lead to self-pairing. In case of tiles with symmetric arms, such as three-, four- and six-point stars (He et al. 2005a, b, 2006), the SSM principle is applied to one arm only and the same sequence is then used for all the arms. It must, however, be ensured that the specificity for the target structure is maintained and not affected due to undesired interactions between strands.

4.9 Experimental Synthesis of DNA Tiles

In any tile-based assembly involving multiple strands, ensuring purity and balancing stoichiometry of the participating strands are vitally important. Impure strands may lead to the formation of improperly or partially assembled tiles which would hamper further formation of 1D, 2D, or 3D lattices. Incorrect stoichiometry could also have the same effect. However, in the case of origami-based structures, the staple strands are usually provided in large excess compared to the scaffold strand (see Chap. 5 for further details on origami-based DNA nanostructures). Thus, relative stoichiometry of the staple strands becomes less vital. Moreover, impure strands can also be used under the assumption that in the limit of equilibrium assembly, incorrect strands in the structure would be displaced by the correct strand via strand displacement (Rothemund 2006).

DNA tile and lattice formation in aqueous solution is critically dependent on the presence of counterions. DNA strands have phosphate groups in the backbone thus imbuing them with net negative charge. For DNA strands to bind and form duplex, the electrostatic repulsion between the negatively charged backbones must be offset by the addition of cations in the solution which would act as counterions. DNA tiles containing closely packed helices also benefit from the presence of counterions to reduce the electrostatic repulsion between neighboring duplexes. Mg^{++} is the most commonly used counterion, although Na^{+} and Ni^{++} are also used. Divalent cations bridge neighboring negatively charged phosphate groups within and between helices. Mg^{++} ions are most often used in tris-acetate-EDTA buffer (pH typically between 7.4 and 8.2) for DNA tile assembly. In some experiments, especially in the presence of gold nanoparticles, the presence of Mg^{++} ions may be undesirable, since it can lead to aggregation and precipitation of the colloidal gold. In such cases, monovalent cations, such as Na^{+}, may be used. At such times, Mg^{++} and Na^{+} should be optimized in combination to minimize solubility problems and increase the overall stability of the system components and final target structure (Chandran et al. 2013).

After mixing the participating strands at appropriate stoichiometry in the presence of counterions and buffer, the next step is to assemble the structure. This is achieved by first subjecting the DNA strands to denaturing conditions, so as to destroy any existing secondary structure and then gradually reducing the denaturing conditions so as to form the structure by maximizing Watson–Crick base pairing. Typically, self-assembly is achieved using thermal annealing, wherein, the reaction mixture is first heated to temperatures in excess of 90 °C and then cooled slowly to room temperature. Substrate-assisted annealing has also been done in which the mixture is thermally annealed in the presence of a solid substrate (e.g., mica) which functions as a 2D planar template for maintaining DNA structures near the surface and assists the self-assembly of DNA into the desired 1D or 2D structures (Hamada and Murata 2009).

It may be desirable to assemble the structure at a constant temperature or to use starting solution conditions with greater capacity to denature DNA base pairs. In such cases, the self-assembly of DNA nanostructures can be achieved via isothermal annealing (Jungmann et al. 2008). Here, a denaturing agent (e.g., urea or formamide) is used instead of or along with high temperature to break the secondary structure of the DNA strands. The concentration of denaturing agent in the solution is slowly reduced (by dialysis) to aid the formation of the nanostructure. Although fundamentally similar, there is an important difference between thermal and isothermal annealing strategies. At and near the melting temperature during thermal annealing of the target structure, when the structure formation takes place, the participating strands have much higher kinetic energy owing to elevated temperature. It is possible that such increased local motion could contribute to assembly errors, although this has not been directly tested.

The duration of annealing can also be crucial. Individual tiles do not need long annealing times; the self-assembly can be accomplished by using thermal annealing in 5 min to 2 h. DNA lattices, assembled from individual tiles, often need longer

time periods for annealing. According to design and experimental evidence, the tiles form first during annealing and then the tiles assemble to form the lattice structure. As mentioned earlier, the tile formation takes place mainly at or near its melting temperature. The sticky ends bind to each other at a lower temperature. Tile can be much bulkier than individual strands, thus their motion in solution is far slower than that of individual strands. Moreover, at lower temperature, the kinetic energy of the tile is also less. Hence, it becomes essential to incubate the annealing mixture for longer time periods at lower temperatures in order to form tile-based lattice structures. In such cases, Newton's Law of Cooling (Burmeister 1993) provides an ideal strategy to perform annealing, which is usually done over 16–24 h. The annealing solution is incubated in a hot water bath (temperature $> 90\,^{\circ}\mathrm{C}$), and the water bath is provided sufficient insulation so that it comes down to room temperature in 16–24 h. For tile-based lattice structures, after annealing, the sample is often incubated in the refrigerator (4 °C) overnight to allow the lattice sample to slowly approach its structural equilibrium (Park et al. 2006).

Hierarchical assembly of the DNA nanostructure may also be performed (Park et al. 2006, 2008). This strategy is preferred when more than one type of tile is needed to form the lattice and different tiles share some common strands. It is then desired to assemble individual tiles first followed by mixing and reannealing them. Reannealing is accomplished by heating the mixture to a temperature just above the melting temperature of the sticky ends but well below the melting temperature of the tile so as not to disintegrate and scramble the tiles.

4.10 Characterization of DNA Tiles and Lattices

The next step is the characterization of the assembled DNA nanostructure. For small structures, characterization is usually performed by non-denaturing polyacrylamide gel electrophoresis (PAGE) (see, for example, LaBean et al. 2000). The DNA structures migrate in the gel under applied electric field towards the positive electrode. The speed of migration depends on the molecular weight of the structure as well as some dependence on the overall shape of the complex. More massive, bulkier, and distended structures move slower than smaller, less bulky, and more spherical structures. For larger structures, agarose gel electrophoresis is often employed (Shih et al. 2004). Gel electrophoresis does not provide conclusive structural evidence and thus it becomes essential to either compare the designed structure with a known structure (Mathieu et al. 2005) or to form the structure step by step (by adding one DNA strand at a time) and compare the structures formed after each step (Rangnekar et al. 2011). The latter type of analysis is known as a formation gel.

For large planar structures, such as 1D or 2D lattices, AFM is an invaluable tool in characterization. For AFM imaging, DNA nanostructures are deposited on a substrate surface. The most commonly used substrate is freshly cleaved mica, which is negatively charged (Eaton and West 2010). Thus, the positive counterions,

bound to the DNA structure, aid in the binding of the nanostructure to the mica surface. Imaging is usually performed with tapping mode under a drop of liquid (buffer solution). This ensures that the structure remains stable during the imaging procedure. AFM provides conclusive evidence for formation of the target structures. Fluorescence microscopy can also be used for characterization of very large structures (He et al. 2005b). The annealed structure is treated with a fluorescent dye, which intercalates into the DNA double helix and results in increased fluorescence of the dye. Fluorescence microscopy does not reveal the detailed features. Hence, it is mostly used to determine the approximate size of the nanostructure.

Larger 2D DNA nanostructures may be characterized by transmission electron microscopy (TEM). The annealed structure is negative stained with a heavy metal compound (typically uranyl formate or acetate) which increases the opacity of the sample for the incident electron beam, thus revealing the shape of the DNA structure. TEM of DNA nanostructures does not have as high resolution as AFM; therefore, AFM is usually preferred for 2D nanostructures. Cryogenic transmission electron microscopy (cryo-EM) provides the most convincing evidence for finite-sized 3D nanostructure formation. During cryo-EM, the sample is first frozen to preserve the structural integrity of the nanostructure (Shih et al. 2004). Then TEM is performed, and the images of the structure in different orientation are captured. Software can then be used to combine images and reconstruct a 3D model of the nanostructure. For high-resolution structure determination of 3D crystal lattices, X-ray crystallography has been used (Zheng et al. 2009).

4.11 Applications of DNA Tiles

One of the first applications of DNA tiles was demonstrated in 2000 in the field of molecular computation when the triple-crossover tiles were used to perform computations via algorithmic self-assembly (Mao et al. 2000). The tiles were used to execute four steps of cumulative XOR operations on a string of binary bits. Construction of an aperiodic, patterned lattice displaying barcode information was also reported later using a process of self-assembly by directed nucleation of DX tiles around a scaffold DNA strand (Yan et al. 2003b) (Fig. 4.7a, b). Winfree et al. made DNA crystals that could perform copy operations and also crystals that could count in binary as they grew (Barish et al. 2005). DNA has also been utilized for the construction of functioning molecular devices. The very first such device was a nanomechanical B-Z device made of two DX tiles which could undergo transitions from one conformational state to another based on the solution conditions (Mao et al. 1999b). The switching of DNA between B-form and Z-form and back was shown to cause the structural transition of the device. Later, a PX-JX_2 device was constructed which would undergo transition using DNA strands as the trigger (Yan et al. 2002).

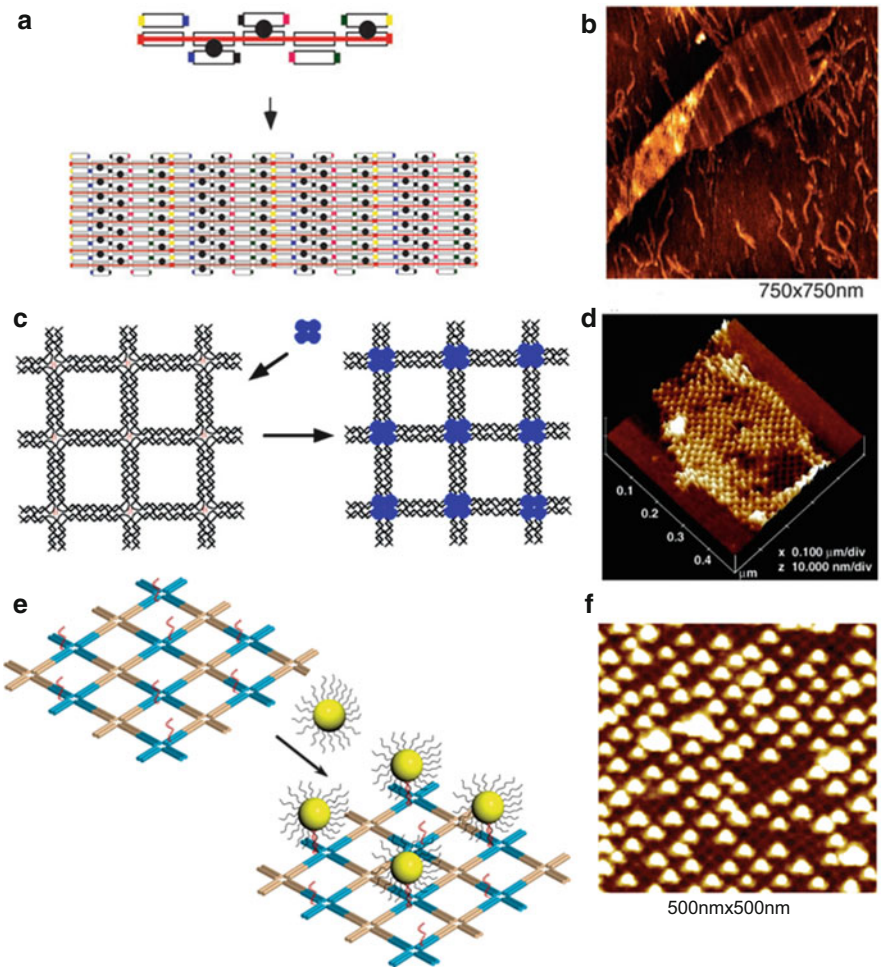

Fig. 4.7 (**a**) Repeating DNA barcode units, made from DX tile array, form a ribbon lattice. *Black circles* represent hairpin loops that serve as topographic marker. (**b**) AFM image of the barcode lattice, where the hairpin stripes act as the readout. (**c**) 4 × 4 tile lattice were functionalized with biotin at the center, which was then used to form periodic assembly of streptavidin molecules (represented as *blue tetramers*). (**d**) AFM image of the streptavidin assembly templated on the lattice. (**e**) The 4 × 4 tile lattice was also constructed with protruding strand at the center of each tile. This strand acted as host for gold nanoparticles conjugated with the complementary strand, resulting in the programmed assembly of the nanoparticles. (**f**) AFM image of the gold nanoparticle arrays (Yan et al. 2003a, b; Zhang et al. 2006)

Self-assembled tile-based DNA lattices have also been used as templates for creating programmable and periodic assembly of other molecules and nanostructures. Implementing existing strategies of DNA-protein conjugation

in vitro on DNA tiles provides opportunities for numerous applications utilizing controlled protein assemblies. The most commonly used strategy for DNA–protein conjugation is the use of biotin-functionalized DNA for binding to streptavidin. A DNA strand can be synthesized with a covalent biotin modification at a desired location, which then acts as the binding site for the streptavidin protein. The biotin–streptavidin binding is one of the strongest known non-covalent interactions (Livnah et al. 1993). One of the first such demonstrations was shown in 2003 when Yan et al. used biotin-functionalized 4 × 4 tile lattice for templated assembly of streptavidin molecules (Yan et al. 2003a) (Fig. 4.7c, d). They further used this strategy to create templated arrays of streptavidin on TX tile arrays (Li et al. 2004). It is possible to fuse other proteins of interest with streptavidin through recombinant DNA technology, and consequently, functional assembly of any protein may be achieved. Covalent coupling of proteins or peptides to DNA by hetero-bifunctional cross-linkers was also exploited to synthesize peptide nanoarrays using DX tile array as scaffold (Williams et al. 2007).

DNA-binding proteins can also bind specifically to the DNA nanostructures without requiring covalent modification of the DNA strand. Proteins which take part in the process of homologous recombination inside the cell have intrinsic binding affinity for Holliday junctions, and therefore they bind to crossovers in DNA nanostructures. One such bacterial recombination protein (RuvA) was used for specific binding to two-dimensional DNA templates to form ordered protein arrays (Malo et al. 2005).

DNA aptamers may also be used for binding proteins to DNA tiles which also do not require any covalent modification to the DNA strand. Aptamers can be incorporated in the DNA tiles at desired locations which then act as the binding site for the specific protein targets of the aptamer. Using this strategy, single-chain antibodies were assembled on DNA arrays (Li et al. 2006). Moreover, it was also demonstrated that two thrombin-binding aptamers could be placed with optimal spacing on a DNA tile to create a bivalent construct for the enhanced binding of thrombin molecule to the DNA nanostructure (Rinker et al. 2008). When four copies of thrombin-inhibiting aptamer were displayed on a weave tile, the resultant anticoagulant activity of the construct was much higher than that of free aptamers (Hansen et al. 2010). The weave tile was used in this case to increase the local concentration of the aptamer, thereby increasing its anticoagulant potential. It was further shown by LaBean et al. that the DNA weave tile can also be used to organize two distinct thrombin-binding aptamers with optimum spacing and orientation (Rangnekar et al. 2012). By judicious engineering of the DNA tile, they created a functional DNA nanostructure which was a multi-aptamer enzyme inhibitor with significantly better anticoagulant activity compared to individual aptamers. They also achieved reversal of thrombin inhibition by using single-stranded DNA antidotes, thus enabling significant control over blood coagulation.

DNA tiles also provide a platform to create programmable assemblies of inorganic nanostructures such as nanoparticles. Yan et al. showed conjugation of 5 nm gold nanoparticles with streptavidin and used biotin–streptavidin conjugation

strategy to achieve linear assembly of gold nanoparticles on a linear TX tile array (Li et al. 2004). The same year, two-dimensional assembly of gold nanoparticles was demonstrated using 2D DNA lattice made from DX tiles (Le et al. 2004). Subsequently, 2D assembly of gold nanoparticles was achieved using 4 × 4 tile lattice by employing three different strategies. In the first strategy, one of the participating strands of the 4 × 4 tile was thiolated and conjugated with a gold nanoparticle followed by annealing resulting into the formation of the lattice with templated nanoparticles (Sharma et al. 2006). In the second approach, 4 × 4 tile lattice was constructed with periodically protruding strands which acted as the host for gold nanoparticles conjugated with the DNA strand complementary to the protruding strands (Zhang et al. 2006) (Fig. 4.7e, f). The third strategy made use of gold-binding peptides covalently fused to DNA strands that were part of the intrinsic 4 × 4 tiles (Carter and LaBean 2011). Seeman et al. used triangular DNA tiles to form two-dimensional assemblies of gold nanoparticles of two different sizes (Zheng et al. 2006). Yan et al. subsequently used gold nanoparticles to fold 2D DX tile array into tubules of various 3D architectures, ranging in shape from stacked rings to single spirals, double spirals, and nested spirals (Sharma et al. 2009). The shape of the tubules was controlled by varying the size of the nanoparticles.

4.12 Conclusion and Future Directions

Tile-based designs have been a popular architectural strategy for assembling molecular constructs within the field of structural DNA nanotechnology. Tile building blocks and lattices formed from them remain useful for forming large, periodic structures such as might be desired as nanoscale metamaterials. Although the addressability of DNA origami as well as its reliable, high-yield assembly has taken some of the interest away from DNA tile assemblies, there remain a number of areas in which tile-based designs cannot easily be replaced. First, the size of origami structures is limited by the size of ssDNA strands available for use as scaffold, so while the largest origami is on the order of a couple hundred nanometers on an edge, tile lattices on the millimeter scale have already been prepared. Second, for medical applications, such as the anticoagulant enzyme inhibitor discussed above, DNA tiles are on the right size scale for binding to individual protein molecules. Finally, for applications in molecular computation, tile-based systems provide the ability to generate tile sets with fairly large numbers of unique tile types without extremely high costs for synthesis of the component strands. Many future applications of DNA tiles are possible both in the realm of electronics nanofabrication as well as designer molecular medicine.

References

Barish RD, Rothemund PWK, Winfree E (2005) Two computational primitives for algorithmic self-assembly: copying and counting. Nano Lett 5:2586–2592. doi:10.1021/nl0520381

Burmeister LC (1993) Convective heat transfer. Wiley, New York

Carter JD, LaBean TH (2011) Organization of inorganic nanomaterials via programmable DNA self-assembly and peptide molecular recognition. ACS Nano 5:2200–2205. doi:10.1021/nn1033983

Chandran H, Rangnekar A, Shetty G, Schultes EA, Reif JH, LaBean TH (2013) An autonomously self-assembling dendritic DNA nanostructure for target DNA detection. Biotechnol J 8:221–227. doi:10.1002/biot.201100499

Chen J, Seeman NC (1991) Synthesis from DNA of a molecule with the connectivity of a cube. Nature 350:631–633. doi:10.1038/350631a0

Chen JH, Kallenbach NR, Seeman NC (1989) A specific quadrilateral synthesized from DNA branched junctions. J Am Chem Soc 111:6402–6407. doi:10.1021/ja00198a063

Dirks RM, Lin M, Winfree E, Pierce NA (2004) Paradigms for computational nucleic acid design. Nucleic Acids Res 32:1392–1403. doi:10.1093/nar/gkh291

Eaton P, West P (2010) Atomic force microscopy. Oxford University Press, Oxford

Fu TJ, Seeman NC (1993) DNA double-crossover molecules. Biochemistry 32:3211–3220. doi:10.1021/bi00064a003

Goodman RP, Schaap IAT, Tardin CF, Erben CM, Berry RM, Schmidt CF, Turberfield AJ (2005) Rapid chiral assembly of rigid DNA building blocks for molecular nanofabrication. Science 310:1661–1665. doi:10.1126/science.1120367

Hamada S, Murata S (2009) Substrate-assisted assembly of interconnected single-duplex DNA nanostructures. Angew Chem Int Ed 48:6820–6823. doi:10.1002/anie.200902662

Hansen MN, Zhang AM, Rangnekar A, Bompiani KM, Carter JD, Gothelf KV, LaBean TH (2010) Weave tile architecture construction strategy for DNA nanotechnology. J Am Chem Soc 132:14481–14486. doi:10.1021/ja104456p

He Y, Chen Y, Liu H, Ribbe AE, Mao C (2005a) Self-assembly of hexagonal DNA two-dimensional (2D) arrays. J Am Chem Soc 127:12202–12203. doi:10.1021/ja0541938

He Y, Tian Y, Chen Y, Deng Z, Ribbe AE, Mao C (2005b) Sequence symmetry as a tool for designing DNA nanostructures. Angew Chem Int Ed 44:6694–6696. doi:10.1002/anie.200502193

He Y, Tian Y, Ribbe AE, Mao C (2006) Highly connected two-dimensional crystals of DNA six-point-stars. J Am Chem Soc 128:15978–15979. doi:10.1021/ja0665141

He Y, Ye T, Su M, Zhang C, Ribbe AE, Jiang W, Mao C (2008) Hierarchical self-assembly of DNA into symmetric supramolecular polyhedra. Nature 452:198–201. doi:10.1038/nature06597

Holliday R (1964) A mechanism for gene conversion in fungi. Genet Res 5:282–304. doi:10.1017/S0016672300001233

Jungmann R, Liedl T, Sobey TL, Shih W, Simmel FC (2008) Isothermal assembly of DNA origami structures using denaturing agents. J Am Chem Soc 130:10062–10063. doi:10.1021/ja8030196

Kallenbach NR, Ma RI, Seeman NC (1983) An immobile nucleic acid junction constructed from oligonucleotides. Nature 305:829–831. doi:10.1038/305829a0

Ke Y, Liu Y, Zhang J, Yan H (2006) A study of DNA tube formation mechanisms using 4-, 8-, and 12-helix DNA nanostructures. J Am Chem Soc 128:4414–4421. doi:10.1021/ja058145z

Ke Y, Ong LL, Shih WM, Yin P (2012) Three-dimensional structures self-assembled from DNA bricks. Science 338:1177–1183. doi:10.1126/science.1227268

Kuzuya A, Wang R, Sha R, Seeman NC (2007) Six-helix and eight-helix DNA nanotubes assembled from half-tubes. Nano Lett 7:1757–1763. doi:10.1021/nl070828k

LaBean TH, Yan H, Kopatsch J, Liu F, Winfree E, Reif JH, Seeman NC (2000) Construction, analysis, ligation, and self-assembly of DNA triple crossover complexes. J Am Chem Soc 122:1848–1860. doi:10.1021/ja993393e

Le JD, Pinto Y, Seeman NC, Musier-Forsyth K, Taton TA, Kiehl RA (2004) DNA-templated self-assembly of metallic nanocomponent arrays on a surface. Nano Lett 4:2343–2347. doi:10.1021/nl048635+

Li H, Park SH, Reif JH, LaBean TH, Yan H (2004) DNA-templated self-assembly of protein and nanoparticle linear arrays. J Am Chem Soc 126:418–419. doi:10.1021/ja0383367

Li H, LaBean TH, Kenan DJ (2006) Single-chain antibodies against DNA aptamers for use as adapter molecules on DNA tile arrays in nanoscale materials organization. Org Biomol Chem 4:3420–3426. doi:10.1039/B606391H

Liu D, Wang M, Deng Z, Walulu R, Mao C (2004) Tensegrity: construction of rigid DNA triangles with flexible four-arm DNA junctions. J Am Chem Soc 126:2324–2325. doi:10.1021/ja031754r

Livnah O, Bayer EA, Wilchek M, Sussman JL (1993) Three-dimensional structures of avidin and the avidin-biotin complex. Proc Natl Acad Sci USA 90:5076–5080. doi:10.1073/pnas.90.11.5076

Majumder U, Rangnekar A, Gothelf KV, Reif JH, LaBean TH (2011) Design and construction of double-decker tile as a route to three-dimensional periodic assembly of DNA. J Am Chem Soc 133:3843–3845. doi:10.1021/ja1108886

Malo J, Mitchell JC, Vénien-Bryan C, Harris JR, Wille H, Sherratt DJ, Turberfield AJ (2005) Engineering a 2D protein–DNA crystal. Angew Chem Int Ed 44:3057–3061. doi:10.1002/anie.200463027

Mao C, Sun W, Seeman NC (1999a) Designed two-dimensional DNA Holliday junction arrays visualized by atomic force microscopy. J Am Chem Soc 121:5437–5443. doi:10.1021/ja9900398

Mao C, Sun W, Shen Z, Seeman NC (1999b) A nanomechanical device based on the B–Z transition of DNA. Nature 397:144–146. doi:10.1038/16437

Mao C, LaBean TH, Reif JH, Seeman NC (2000) Logical computation using algorithmic self-assembly of DNA triple-crossover molecules. Nature 407:493–496. doi:10.1038/35035038

Mathieu F, Liao S, Mao C, Kopatsch J, Wang T, Seeman NC (2005) Six-helix bundles designed from DNA. Nano Lett 5:661–665. doi:10.1021/nl050084f

Nangreave J, Yan H, Liu Y (2011) DNA nanostructures as models for evaluating the role of enthalpy and entropy in polyvalent binding. J Am Chem Soc 133:4490–4497. doi:10.1021/ja1103298

Park SH, Barish R, Li H, Reif JH, Finkelstein G, Yan H, LaBean TH (2005) Three-helix bundle DNA tiles self-assemble into 2D lattice or 1D templates for silver nanowires. Nano Lett 5:693–696. doi:10.1021/nl050108i

Park SH, Pistol C, Ahn SJ, Reif JH, Lebeck AR, Dwyer C, LaBean TH (2006) Finite-size, fully addressable DNA tile lattices formed by hierarchical assembly procedures. Angew Chem Int Ed 45:735–739. doi:10.1002/anie.200503797

Park SH, Finkelstein G, LaBean TH (2008) Stepwise self-assembly of DNA tile lattices using dsDNA bridges. J Am Chem Soc 130:40–41. doi:10.1021/ja078122f

Petrillo ML, Newton CJ, Cunningham RP, Ma RI, Kallenbach NR, Seeman NC (1988) The ligation and flexibility of four-arm DNA junctions. Biopolymers 27:1337–1352. doi:10.1002/bip.360270902

Rangnekar A, Gothelf KV, LaBean TH (2011) Design and synthesis of DNA four-helix bundles. Nanotechnology 22:235601. doi:10.1088/0957-4484/22/23/235601

Rangnekar A, Zhang AM, Li SS, Bompiani KM, Hansen MN, Gothelf KV, Sullenger BA, LaBean TH (2012) Increased anticoagulant activity of thrombin-binding DNA aptamers by nanoscale organization on DNA nanostructures. Nanomedicine: NBM 8:673–681. doi:10.1016/j.nano.2011.08.011

Reishus D, Shaw B, Brun Y, Chelyapov N, Adleman L (2005) Self-assembly of DNA double-double crossover complexes into high-density, doubly connected, planar structures. J Am Chem Soc 127:17590–17591. doi:10.1021/ja0557177

Rinker S, Ke Y, Liu Y, Chhabra R, Yan H (2008) Self-assembled DNA nanostructures for distance-dependent multivalent ligand–protein binding. Nat Nanotechnol 3:418–422. doi:10.1038/nnano.2008.164

Rothemund PWK (2006) Folding DNA to create nanoscale shapes and patterns. Nature 440:297–302. doi:10.1038/nature04586

Seeman NC (1982) Nucleic acid junctions and lattices. J Theor Biol 99:237–247. doi:10.1016/0022-5193(82)90002-9

Seeman NC (1990) *De novo* design of sequences for nucleic acid structural engineering. J Biomol Struct Dyn 8:573–581. doi:10.1080/07391102.1990.10507829

Seeman NC, Kallenbach NR (1983) Design of immobile nucleic acid junctions. Biophys J 44:201–209. doi:10.1016/S0006-3495(83)84292-1

Sharma J, Chhabra R, Liu Y, Ke Y, Yan H (2006) DNA-templated self-assembly of two-dimensional and periodical gold nanoparticle arrays. Angew Chem Int Ed 45:730–735. doi:10.1002/anie.200503208

Sharma J, Chhabra R, Cheng A, Brownell J, Liu Y, Yan H (2009) Control of self-assembly of DNA tubules through integration of gold nanoparticles. Science 323:112–116. doi:10.1126/science.1165831

Shen Z, Yan H, Wang T, Seeman NC (2004) Paranemic crossover DNA: a generalized Holliday structure with applications in nanotechnology. J Am Chem Soc 126:1666–1674. doi:10.1021/ja038381e

Sherman WB, Seeman NC (2006) Design of minimally strained nucleic acid nanotubes. Biophys J 90:4546–4557. doi:10.1529/biophysj.105.080390

Shih WM, Quispe JD, Joyce GF (2004) A 1.7-kilobase single-stranded DNA that folds into a nanoscale octahedron. Nature 427:618–621. doi:10.1038/nature02307

Wang JC (1979) Helical repeat of DNA in solution. Proc Natl Acad Sci USA 76:200–203. doi:10.1073/pnas.76.1.200

Wang X, Seeman NC (2007) Assembly and characterization of 8-Arm and 12-Arm DNA branched junctions. J Am Chem Soc 129:8169–8176. doi:10.1021/ja0693441

Wang Y, Mueller JE, Kemper B, Seeman NC (1991) Assembly and characterization of five-arm and six-arm DNA branched junctions. Biochemistry 30:5667–5674. doi:10.1021/bi00237a005

Wang R, Liu W, Seeman NC (2009) Prototyping nanorod control: a DNA double helix sheathed within a DNA six-helix bundle. Chem Biol 16:862–867. doi:10.1016/j.chembiol.2009.07.008

Wei B, Dai M, Yin P (2012) Complex shapes self-assembled from single-stranded DNA tiles. Nature 485:623–626. doi:10.1038/nature11075

Williams BAR, Lund K, Liu Y, Yan H, Chaput JC (2007) Self-assembled peptide nanoarrays: an approach to studying protein–protein interactions. Angew Chem Int Ed 46:3051–3054. doi:10.1002/anie.200603919

Winfree E, Liu F, Wenzler LA, Seeman NC (1998) Design and self-assembly of two-dimensional DNA crystals. Nature 394:539–544. doi:10.1038/28998

Yan H, Zhang X, Shen Z, Seeman NC (2002) A robust DNA mechanical device controlled by hybridization topology. Nature 415:62–65. doi:10.1038/415062a

Yan H, Park SH, Finkelstein G, Reif JH, LaBean TH (2003a) DNA-templated self-assembly of protein arrays and highly conductive nanowires. Science 301:1882–1884. doi:10.1126/science.1089389

Yan H, LaBean TH, Feng L, Reif JH (2003b) Directed nucleation assembly of DNA tile complexes for barcode-patterned lattices. Proc Natl Acad Sci USA 100:8103–8108. doi:10.1073/pnas.1032954100

Yin P, Hariadi RF, Sahu S, Choi HMT, Park SH, LaBean TH, Reif JH (2008) Programming DNA tube circumferences. Science 321:824–826. doi:10.1126/science.1157312

Zhang Y, Seeman NC (1994) Construction of a DNA-truncated octahedron. J Am Chem Soc 116:1661–1669. doi:10.1021/ja00084a006

Zhang J, Liu Y, Ke Y, Yan H (2006) Periodic square-like gold nanoparticle arrays templated by self-assembled 2D DNA nanogrids on a surface. Nano Lett 6:248–251. doi:10.1021/nl052210l

Zheng J, Constantinou PE, Micheel C, Alivisatos AP, Kiehl RA, Seeman NC (2006) Two-dimensional nanoparticle arrays show the organizational power of robust DNA motifs. Nano Lett 6:1502–1504. doi:10.1021/nl060994c

Zheng J, Birktoft JJ, Chen Y, Wang T, Sha R, Constantinou PE, Ginell SL, Mao C, Seeman NC (2009) From molecular to macroscopic via the rational design of a self-assembled 3D DNA crystal. Nature 461:74–77. doi:10.1038/nature08274

Chapter 5
DNA Origami

Angela Edwards and Hao Yan

Abstract The use of DNA as a building material for designing nanoscale objects is one of the exciting fields of nanotechnology. DNA origami, specifically, has only recently emerged as an extension of smaller folded DNA units since the appearance of immobile junctions and the assortment of structures that followed. DNA origami is the folding of a long single strand of DNA with many short complimentary oligonucleotides that act as "staples," in which hybridization of duplex DNA through Watson–Crick base pairing drives assembly without the use of restriction enzymes or DNA ligase to construct the final two- or three-dimensional form (Rothemund 2006). This technique is valuable primarily due to the multi-nanometer to sub-micrometer scale of the structures produced and their finite nature, which offers greater control over self-assembly within a system in comparison to previously synthesized array structures that had the capacity to extend indefinitely (Mao et al. 1999a). The increasing complexity of structures produced parallels the technological advances in other areas as the availability of computing power and decreasing cost of creating synthetic oligonucleotides gave way to the first true DNA origami structures in 2006 (Rothemund 2006).

Arriving at multidimensional, precise origami assemblies provides a platform for spatial organization of other functional materials. Overhangs of oligonucleotides within the structure can be used as a specific address for heteroelements such as other DNA molecules (Rothemund 2006), RNA (Ke et al. 2008; Zhang et al. 2010; Subramanian et al. 2011; Rinker et al. 2008), proteins (Voigt et al. 2010; Shen et al. 2009), carbon nanotubes (Maune et al. 2010), metallic nanoparticles (Zheng et al. 2012; Ding et al. 2010a, b; Hung et al. 2009; Sharma et al. 2008; Pal et al. 2009), and quantum dots (Stearns et al. 2009; Bui et al. 2010; Tikhomirov et al. 2011) with nanometer precision. The defined and highly stable structure of DNA as a scaffold has great potential for enabling self-assembly of increasingly

A. Edwards (✉) • H. Yan
Department of Chemistry and Biochemistry, The Biodesign Institute of Arizona State University, Tempe, AZ, USA
e-mail: Angela.D.Edwards@asu.edu

J. KJEMS et al. (eds.), *Nucleic Acid Nanotechnology*, Nucleic Acids and Molecular Biology 29, DOI 10.1007/978-3-642-38815-6_5,

intricate systems, with applications that can be extended into almost any field of biochemistry, chemistry, or biophysics. In this chapter we will discuss the principles of designing DNA origami structures, the methods by which nanoscale assembly has been developed with increasing complexity, tools for creating and analyzing DNA structures, and examples of the functional applications of DNA origami.

Contents

5.1 Design of Two-Dimensional Structures

The basis of forming nucleic acid nanostructures lies in the connectivity of the biopolymers. These contacts are achieved through bottom-up fabrication methods, in which the intrinsic properties of molecules and the atoms that comprise them are exploited to self-assemble into the desired structure, rather than deposition of material and subsequent removal of specific portions, as in top-down production protocols. Folding of single-stranded DNA into origami is accomplished by careful design of staple strands that are complimentary to multiple distal regions of the scaffold strand, which undergo spontaneous arrangement into B-form DNA through Watson–Crick base-pairing interactions. A junction is created where the staple connects to the scaffold in different places, acting like multiple strands rather than a single long strand. In 1982, Seeman proposed that synthetic oligonucleotides of specific sequence could be hybridized to create an immobile four-way junction with the structure of a Holliday junction, which would not be subject to branch migration (Fu and Seeman 1993). Further investigations produced different types of junctions, first differentiated by number of helices connected at the junction and second by the orientation of the helical axes around the center of the junction (Du et al. 1992). In origami, the Holliday junction is most commonly utilized in crossover motifs to fold the scaffold. However, single junctions are still subject to a certain amount of migration and flexibility. In order to avoid this phenomenon, a double-crossover motif is frequently used in origami and many other types of DNA nanostructures (Fig. 5.1) (Shih et al. 2004).

Double-crossover molecules can be classified by the orientation of the connected helices to each other as parallel or antiparallel, with the same significance as in DNA polarity nomenclature. Finally, for 2D molecules, the spacing between the

Fig. 5.1 (**a**) A model showing the Holliday junction, a crossover between two parallel helices. (**b**) Positioning two Holliday junctions a full helical turn apart gives the common double-crossover motif molecule. (**c**) Spacing an integer number of helical turns between crossover motifs in adjacent helices gives rise to a planar structure (Reproduced by permission of The Royal Society of Chemistry from Thomas et al. (2011) 40, 12, 5636–5646. Copyright 2011 The Royal Society of Chemistry.)

junctions can be either an even or odd number of helical half-turns (Rothemund 2006). This spacing is paramount to control of curvature between helices, and in origami the antiparallel crossover motif is the most common connectivity used.

Staple strands usually range from 20 to 60 nucleotides in length and thus are obtainable at fairly low cost by automated commercial synthesis. In contrast, one of the primary barriers to the realization of DNA origami structures was the availability of a significantly long scaffold material. Before the origination of origami, one notable attempt at the creation of a long scaffold was demonstrated in 2004 when Shih et al. reported a 1.7 kb single-stranded DNA produced through selective cloning and PCR that self-assembled with five synthetic 40-mer oligonucleotides into an octahedral structure visible by cryo-electron microscopy (Fig. 5.2) (Shih et al. 2004). Prior DNA folding experiments created smaller structures using only synthetic oligonucleotides. Such designs require high precision in stoichiometry and initial purification of all strands involved in order to give the desired product (Fu and Seeman 1993).

A critical step toward the origination of the origami technique came from Yan et al. in 2003 with the assembly of so-called barcode lattice tiles (Yan et al. 2003). These tiles were formed entirely from synthetic oligonucleotide sequences, and attempts to ligate strands into longer scaffold sequences were unsuccessful due to low yields. However, the basic principles of origami were introduced with this method, where the strands formed planar rectangular structures with adjacent helices oriented antiparallel to one another, and the tiles could be polymerized into larger ribbon-like structures by blunt-end stacking effects (Fig. 5.3). In the report, methods to extend scaffold size and prevent stacking where not desired were suggested and later incorporated into DNA origami protocols.

Bridging the gap of structure size between smaller DNA nanostructures such as tiles, hollow polyhedrons, and lattices came with the incorporation of the commercially available viral genomic DNA from bacteriophage M13mp18 (M13). The circular, 7,249-nucleotide single-stranded DNA serves as a much larger, more easily obtained, and inexpensive scaffold than the synthetic oligonucleotides of previous DNA folding methods. The M13 genome has a highly variable sequence containing few secondary structural motifs, with exception to a 73-bp hairpin region that contains a *Bsr*BI restriction site, and is therefore facile to interrupt. Moreover, the use of a molecule with a known sequence further facilitates

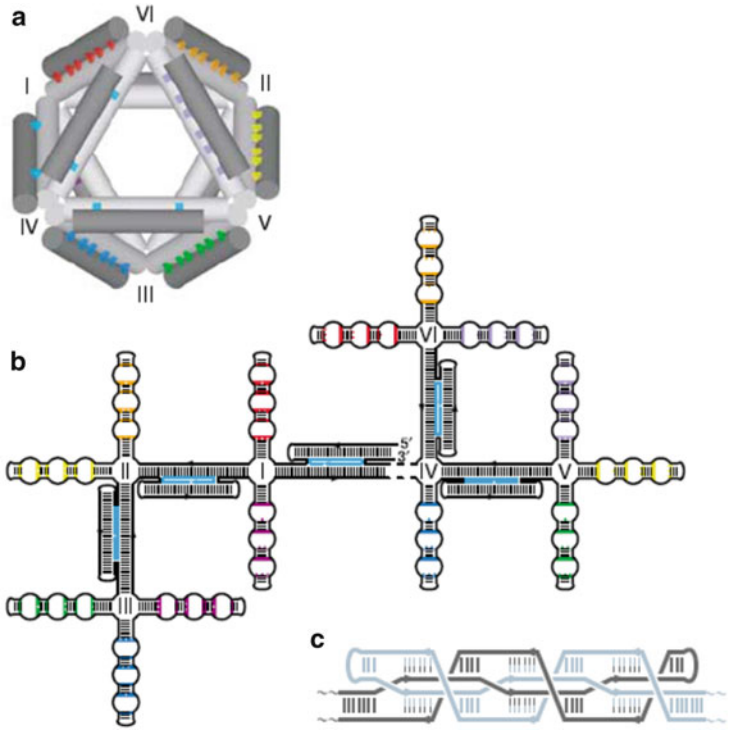

Fig. 5.2 (**a**) Design of a hollow octahedral structure that used a preliminary attempt to extend the length of scaffold previously demonstrated. (**b**) The scaffold is self-complimentary in certain regions and joined by multiple DX crossovers (*cyan*) as well as several PX crossovers, shown in (**c**) (Reprinted by permission from Macmillan Publishers Ltd: Nature, Shih et al. (2004) 427 (6975), 618–621, copyright 2004)

expedient design of origami structures by eliminating the need for complex algorithms to calculate randomized oligomer sequences. Staples are drawn around the M13 scaffold based on the geometric configuration desired, and then sequences complimentary to the corresponding region of M13 DNA can be ordered. In 2006, Rothemund outlined a sequential bottom-up assembly method for the design of 2D origami structures by a raster-fill process (Rothemund 2006). He then utilized M13 DNA to create a number of arbitrarily shaped designs that illustrate the success of this method and provided the first physical examples of DNA origami.

A distinguishing advantage of DNA origami over previous nanostructures is the fidelity of self-assembly, which is contingent upon the ability to mix staples in excess with the scaffold, rather than defined stoichiometry between each component. In his initial report, Rothemund constructed six different origami shapes with dimensions around 100 nm $\times$ 100 nm, each using 200–250 staple oligonucleotides of approximately 30 nt in length in a five- to tenfold excess relative to the scaffold (Fig. 5.4). By mixing all strands in the same reaction, annealing was accomplished by cooling from 90 to 20 °C in 2 h with over 90 % of structures well formed.

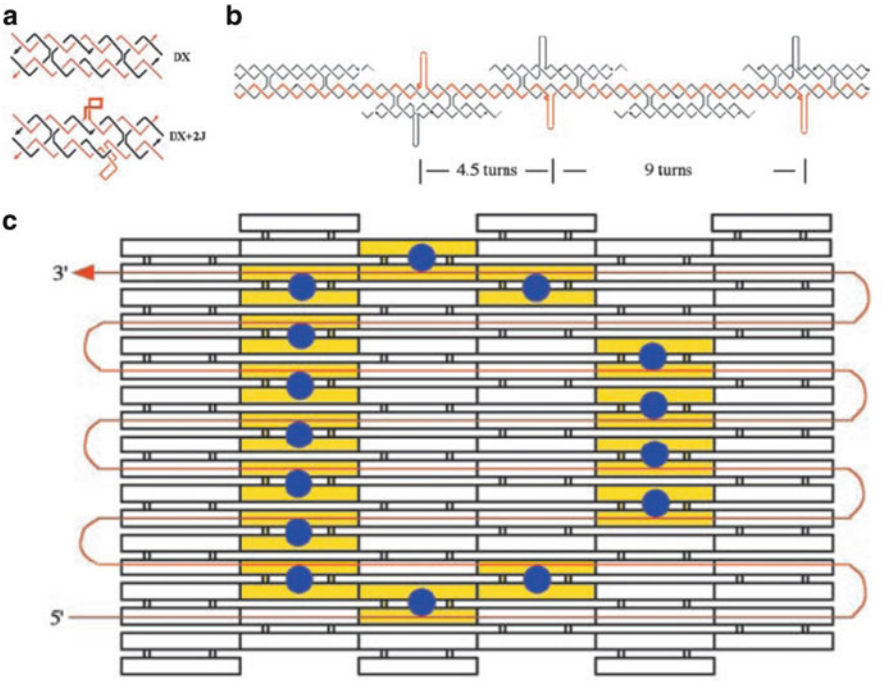

Fig. 5.3 A step toward the conventional DNA origami method achieved by directed nucleation of DX motif tiles and subsequent assembly into a ribbon superstructure. (**a**) Structure of DX and DX + 2J double-crossover motifs used to create (**b**) the full tile. (**c**) A schematic illustration that shows the weaving of a unified scaffold strand through the assembled tile motif from the discussion in the report that predicted the full DNA origami structures to come (Reproduced with permission from Proc. Nat. Acad. Sci. U.S.A., Yan et al. (2003) 100, 14, 1803–1808, Copyright 2003 National Academy of Sciences, USA.)

Previous work had shown that parallel helices in DNA nanostructures do not pack closely, most likely due to electrostatic repulsion between them. In his planar origami designs, Rothemund demonstrated that it is possible to control the packing distance between adjacent helices by crossover spacing. In order to achieve a flat configuration, an integer number of half-helical turns must be used; this was further refined to show that the distance between crossovers controlled helical packing. Raster-fill rectangular origami with 1.5 turns between crossovers gave a distance of 1 nm between parallel helices, and those with 2.5 turns yielded 1.5 nm spacing.

These initial strategies left no bases unpaired, in spite of the regions that appear single-stranded in the schematic (Fig. 5.4), instead creating a bend with a single phosphate group from the phosphodiester bond between covalently attached nucleotides on the scaffold in that region. Though it proved feasible to assemble these forms, Rothemund discovered that the final structures would associate non-specifically at the edges to form aggregates. To ameliorate this, the inclusion of tetrathymidine (T_4) loop regions into staple strands that were non-complimentary to

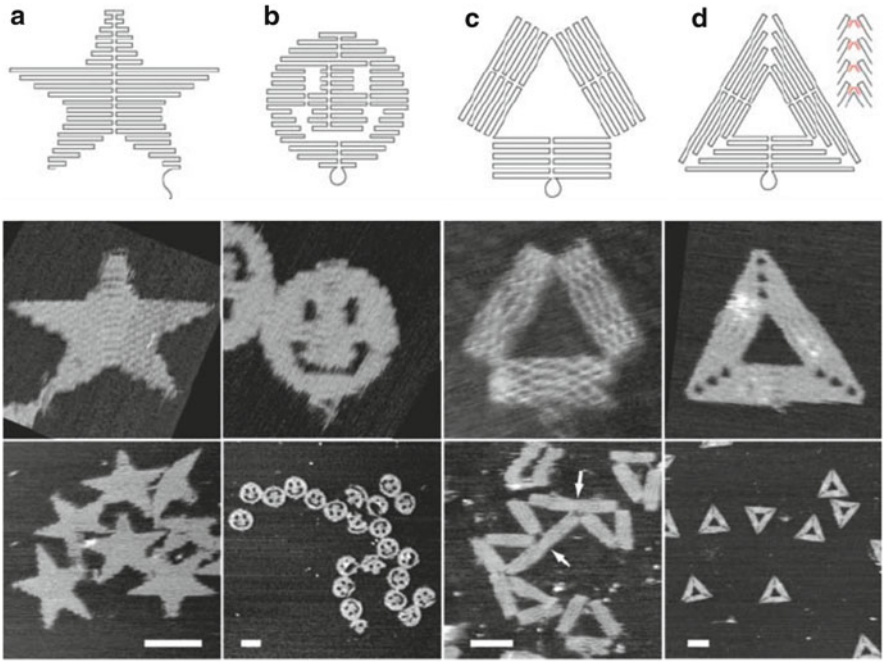

Fig. 5.4 Arbitrarily shaped planar structures with model (*top*) and AFM images (*bottom*) created using the DNA origami method, including (**a**) a five-pointed star, (**b**) disk with three holes, (**c**) triangle made from rectangular domains, and (**d**) triangle with pointed vertices (Reprinted by permission from Macmillan Publishers Ltd: Nature, Rothemund (2006) 440, 297–302, copyright 2006)

the scaffold sequence allowed for the creation of bends between parallel helices that contained a single-stranded loop. The inability of T_4 sequences to hydrogen bond with other T_4 expanses successfully prevents aggregation; accordingly, this technique has been routinely utilized in subsequent origami designs.

5.2 Design of Three-Dimensional Structures

The natural flow of progress to form structures of increasing complexity takes origami from two to three dimensions. The first way in which this was achieved was by constructing hollow architectures of multiple 2D planar origami assemblies, in which the edges of the planes were connected at a perpendicular angle to adjacent planes, enabling a final 3D formation. One example of this was demonstrated by Gothelf, Kjems, and coworkers (Andersen et al. 2009), in which the M13 scaffold was folded into two squares and four rectangles which could then be folded using 59 additional staple strands that spanned the edges of the higher-order cuboid structure (Fig. 5.5a).

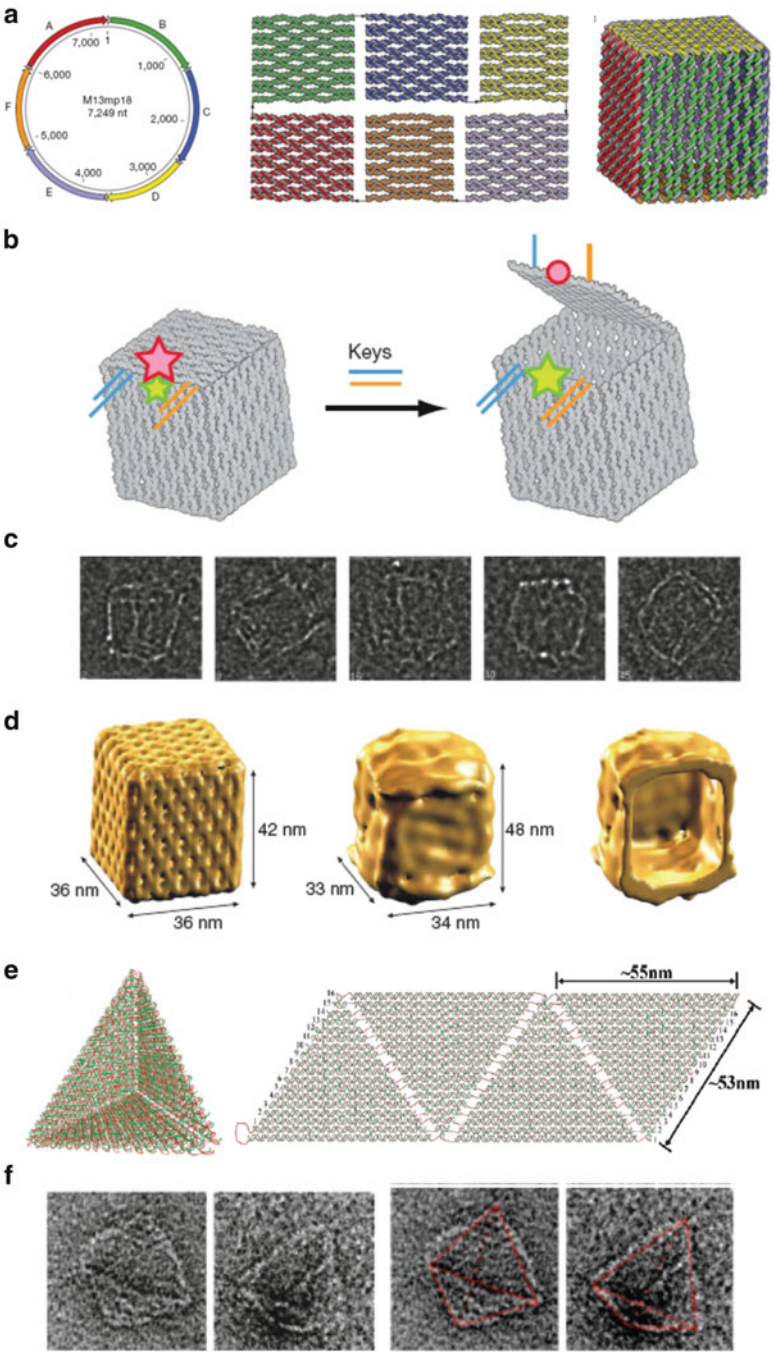

Fig. 5.5 (**a**) Schematic showing the regions of M13mp18 DNA designated to form each side of the box (*left*), with a filled-helix representation (*middle*) of planar origami structures before folding and connection by additional staple strands to form the 3D box structure (*right*) (Andersen et al. 2009). (**b**) Schematic of box lid opening as observed by FRET experiments. Cy3 is

The staples connecting one square face and one rectangular side of the box (Fig. 5.5a) contained a motif that could be induced to dissociate from the origami structure upon addition of "key" oligonucleotides, causing the box "lid" to open. When the lid is closed, it is held together by complimentary staples that are hybridized in a duplex, with the shorter strands extending from the lid and the longer strands extending from the side of the box. Upon addition of sequences complimentary to the overhanging portion of the duplex, the hybridization of the keys into a full duplex with the strands connected to the side of the box displaces the strands from the lid, causing it to open. This toehold displacement action was examined by FRET, where a Cy3 donor molecule was attached to one side of the box and a Cy5 acceptor was connected to the lid. When the box was closed, efficient energy transfer was observed by Cy5 emission. In the open configuration, the dyes were further apart than the upper bound for FRET distance, and only Cy3 emission is observed (Fig. 5.5b).

Similar hollow structure designs were demonstrated shortly after by Kuzuya and Komiyama with a hollow cube and Sugiyama et al. with the creation of various rectangular prism constructs (Kuzuya and Komiyama 2009; Endo et al. 2009). Yan and coworkers also introduced a hollow tetrahedron the same year, in which the folding of the scaffold accomplished the connection of the edges of the origami (Fig. 5.5c) (Ke et al. 2009a). This method was novel in its use of the scaffold strand to span the edges of the 3D structure, rather than requiring one set of staples to fold the planar origami sections and a distinct set to join the structures together on the edges.

While the construction of hollow 3D objects is robust in method via fidelity of formation and ease of assembly, an interesting aspect of these structures was noted by Gothelf and Kjems et al. when examining the box with lid via cryo-EM (Andersen et al. 2009). Instead of having the dimensions expected based on calculated lengths using B-form DNA parameters, the boxes were observed to have a fair amount of curvature along each face (Fig. 5.5d, e). This was later discovered to be a result of the approximations of mean base pairs per helical

Fig. 5.5 (continued) represented as a *green star*, which is small on the left because the emission has spectral overlap with Cy5, the *large red star*, which is the primary emission wavelength observed. When the box is open, Cy5 ceases to emit (*small red circle*), so only Cy3 emission is observed, indicated by the *enlarged green star* (Andersen et al. 2009). (**c**) Cryo-EM images of fully constructed box in closed conformation (Andersen et al. 2009). (**d**) Theoretical dimensions of box based on B-form DNA formation (*left*) and reconstruction of 3D box with observed dimensions (*center*) showing the interior cavity with a cutaway view (*right*) (Andersen et al. 2009). (**e**) 3D model of the tetrahedron (*left*) with 2D schematic of the triangular faces of the tetrahedron showing that the connections at the edges of the faces are from the scaffold strand (*red*) with staples shown in *green*; numbers 1–16 indicate continuous connections of the scaffold strand (*middle*) (Andersen et al. 2009). Reprinted by permission from Macmillan Publishers Ltd: Nature, Andersen (2009) 459, 73–75, copyright 2009. (**f**) TEM images of the formed tetrahedron structures (*left*), with *red lines* highlighting the edges of the structure (*right*) (Reprinted with permission from Ke et al., Nano Lett 9(6):2445–2447. Copyright 2009 American Chemical Society.)

turn of assembled DNA, with the introduction of bent and curved origami structures (Dietz et al. 2009).

The critical change in design principle that allowed for the creation of filled, dense, 3D origami was the variation in spacing between crossovers. In 2009, Shih et al. developed the first solid 3D origami protocols, which were used to make a variety of arbitrary shapes from a hexagonal "honeycomb lattice" (Douglas et al. 2009a). By first approximating 34.3° mean twist per base pair, or 21 bp/two helical turns, they placed crossovers every 7 bp or two-thirds of one helical turn. In a single plane, this causes an alternating zigzag pattern of antiparallel helices that have an angle of 120° between adjacent helices. By designing staples that would further fold these sheets on top of each other, a six-helix repeating unit is arranged that has a six-pointed star shaped hollow space in the middle. Consecutive repeat units form a densely packed lattice that can be adjusted depending on the design to form 3D structures (Fig. 5.6a–d). A variety of structures were produced using the honeycomb lattice, both in the initial report of the design and in subsequent publications (Fig. 5.6e). Although this method can be generalized to form a range of architectures, initial yields were lower than with the planar origami arrangements. Additionally, extremely long thermal ramps are required for assembly, requiring several days up to 172 h, as opposed to the few hours used for simpler structures. As with other folded DNA structures, the solid origami method requires a high concentration of divalent cations, and in the presence of high MgCl2 and low NaCl, the structures below were observed in yields ranging from 7 to 44 % incorporation of the scaffold strand.

In this study, one structure was designed using a novel scaffold strand, the pEGFP-N1 vector sequence. Interestingly, although some folding could be achieved with this scaffold, the efficiency was much lower than with the M13 scaffold DNA. Shih et al. hypothesized that this was due to the high GC content of pEGFP-N1, which is 53 % compared with 43 % in the M13 sequence. The greater stability of GC bonds may lead to misfolding as they can form at a higher temperature than AT bonds. However, as the greatest sequence variability is achieved when the GC content is 50 %, a scaffold that is AT rich may have repetitive sequences, compromising fidelity of folding due to redundancy. Thus, a certain balance of nucleotides must be achieved in selection of a nucleic acid for folding by the DNA origami method.

Yan, Shih, and coworkers reported a square lattice motif for solid 3D origami shortly after the publication of the honeycomb lattice motif. In these designs, four crossover angles set perpendicular to each other (every 90°) are achieved by spacing crossovers between adjacent antiparallel helices every 32 bp, creating a global spacing of 8 bp between crossovers within the assembled structure. This approximates 0.75 turns between crossovers, so it is as if the crossover angle has been rotated 270°, giving a final relative angle of 90° between them (Fig. 5.7a–c) (Ke et al. 2009b).

As with the honeycomb lattice structures, long annealing protocols were required. For the cuboid structures produced, 6 × 12 and 8 × 8 helix designs were observed with a thermal ramp spanning only 48 and 24 h, respectively. However, for the more

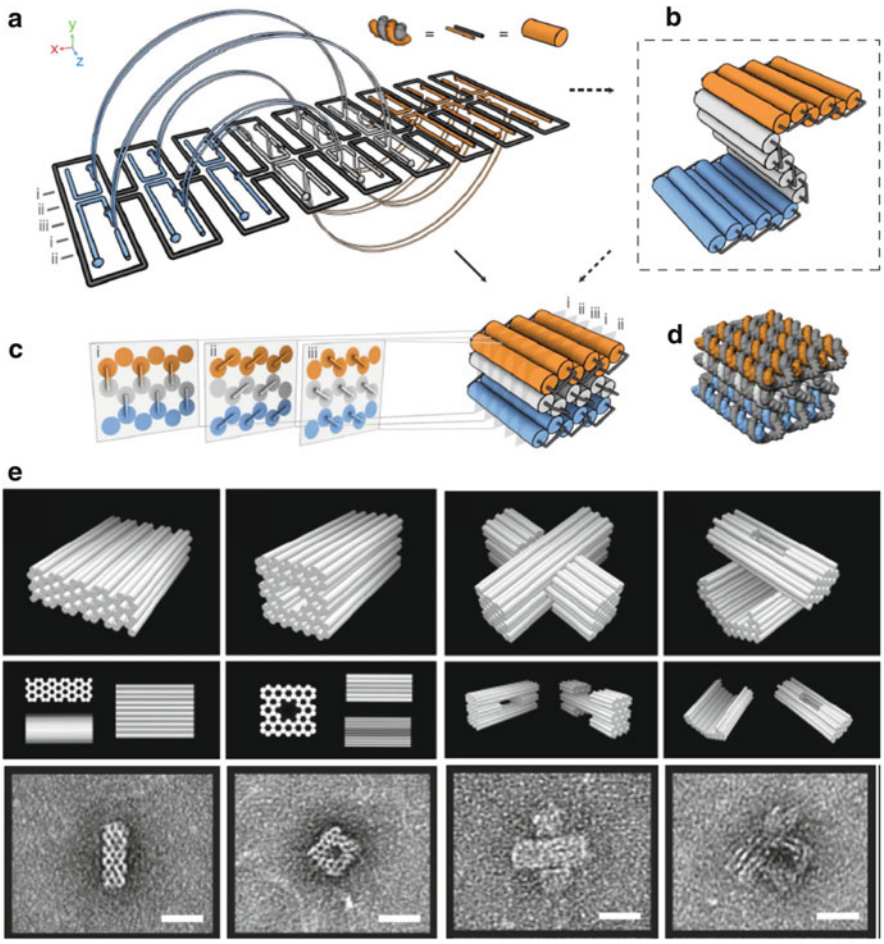

Fig. 5.6 Schematic image of how honeycomb lattice structures are generated. (**a**) The backbone in *black* and staples in *color* show that some staples bridge distant helices to bring them into a stacked conformation. (**b**) An intermediate state of how the curvature begins to take place as the structure forms fully with cross-sectional views (**c**) and a space-filling model (**d**) of the final assembly. The perspectives shown in cross section show that every 7 bp the staples connect the helices at a different angle; the three angles are spaced every 120°. (**e**) Arbitrary shapes created using honeycomb lattice motif: a monolith, square nut, slotted cross, and stacked cross. Computer-generated theoretical structures shown (*top*) and TEM images of assembled particles from different views (*bottom*) (Reprinted by permission from Macmillan Publishers Ltd: Nature, Douglas et al. (2009a) 459 (7245), 414–418, copyright 2009.)

extended 2 × 21 and 3 × 14 architectures, a thermal ramp for 172 h was required to observe successful folding (Fig. 5.7b). The reason for the long annealing times and low yields appears to be the difficulty of staple strand insertion into the center of the structure. If the outer portions of the structure begin to form first, then the helices pack too tightly for staple strands that correspond to core portions of the structure to move

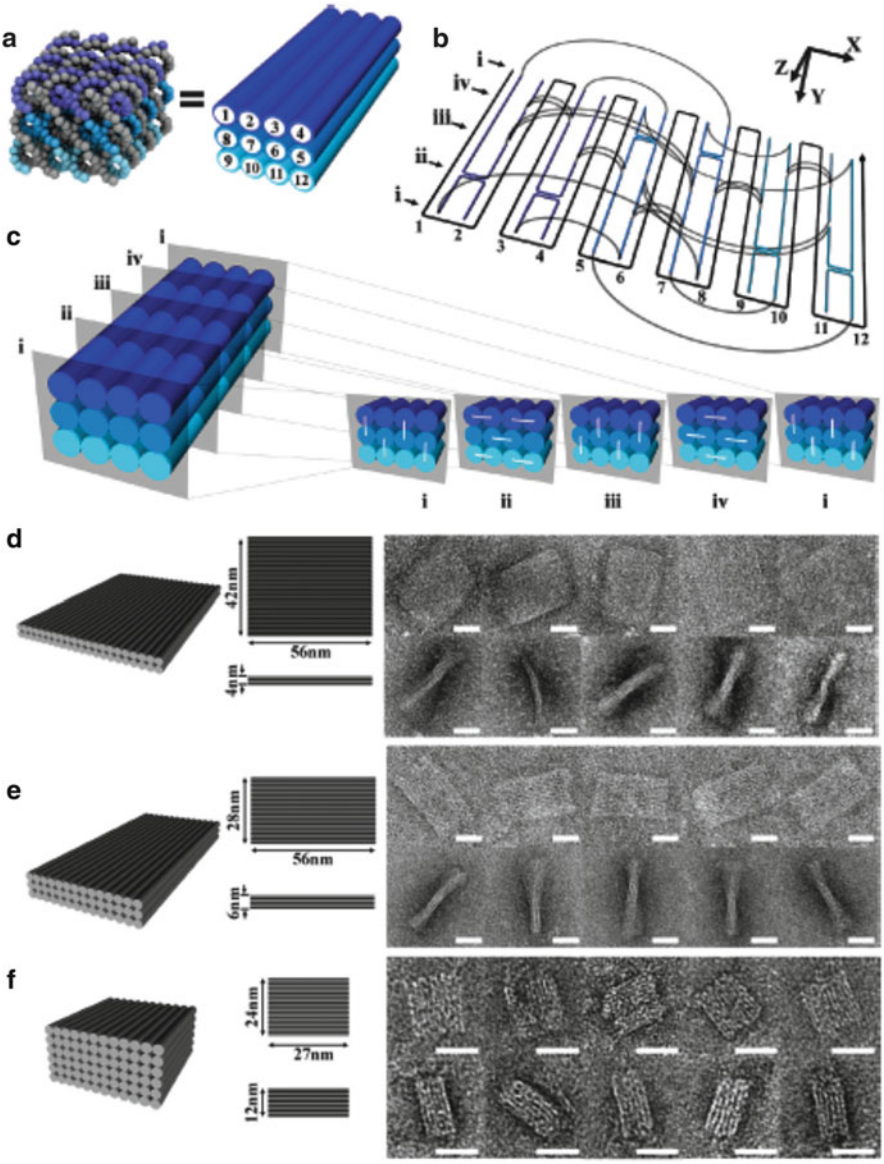

Fig. 5.7 Conceptual design of a 12-helix cuboid structure. (**a**) Shows the layering of helices, each 32 bp long. (**b**) A 2D schematic of the structure with the scaffold strand in a raster-fill pattern in *black*, staples in *color*, and *curved lines* demonstrating bridging staples responsible for the multidimensional stacking of the helices to form layers of the solid structure. In (**c**) Cross sections (i)–(iv) are spaced every 8 bp to show the orientation of crossovers between adjacent helices, with (i) again at the end of the structure, indicating the periodic nature of the pattern. Models (*left*) and AFM images (*right*) of assembled (**d**) 2 × 21, (**e**) 3 × 14, and (**f**) 6 × 12, lattice origami structures (Reprinted with permission from Ke et al., J Am Chem Soc 131(43):15903–15908. Copyright 2009 American Chemical Society.)

through this helical packing. However, without the majority of the strands in proper conformation, the structural integrity is often compromised due to internal instability (Douglas et al. 2009a; Ke et al. 2009b).

5.3 Adding Complexity to Structural Design

One of the main goals of the field of DNA origami is to build structures of ever-increasing complexity. While it had been demonstrated that curvature was possible between parallel helices, both 2D and 3D structures published as of 2009 were still using straight conformations along the axis of each individual double helix. One new design element that has been developed since the introduction of 3D assemblies is the introduction of curvature along the helical axis of the molecules comprising an origami. Previously, curvature between adjacent helices was shown with honeycomb lattices and the bending of planar origami due to the approximations of base pairs per helical turn used to design structures. However, this curvature was not intentional in the design, and deliberate circles or curved edges of 2D origami were only constructed using raster-fill antiparallel helices, rather than creating a bent helix motif. By conceptualizing honeycomb lattice or square lattice DNA motifs as array cell designs, with emphasis on crossover spacing, it is possible to examine the torque induced by small changes in this spacing that can sum to create a global torque in the system. In order to expand the repertoire of origami techniques, Shih and coworkers used this concept to create structures with global twist and bends of various angles in honeycomb array structures (Dietz et al. 2009).

In order to create a global twist on a structure, base pair deletions can be incorporated into a structure, such that it causes a localized overwinding of the helix in which the nucleotides have been removed if there are less than 10.5 bp per turn. This overwinding is compensated for by an overall left-handed torque on adjacent helices in the array. If multiple strands with deletions and the resulting left-handed torque are present within the structure, a global left-handed twist along the helical axes is observed. Similarly, insertion of a base pair into multiple helices of a structure so that there are greater than 10.5 bp/turn induces underwinding in the helices with additional nucleotides. This underwinding forces a right-handed torque on neighboring helices and thus a right-handed twist parallel to the helical axes throughout the structure (Fig. 5.8a–d).

A bend can be formed in the structure by deletions in one portion and cancellation of this global twist by insertions in the other portion of the structure. As the strands with deletions are shortened and those with insertions are lengthened, they comprise the inner and outer portions of the bent molecule, respectively. Many different constructs were assembled to demonstrate the versatility of this method (Fig. 5.8e).

To further expand upon this concept of bending parallel to the helical axis, Yan and coworkers introduced an elegant method for creating rounded, hollow structures that contain both in and out of plane curvature. They first examined creating

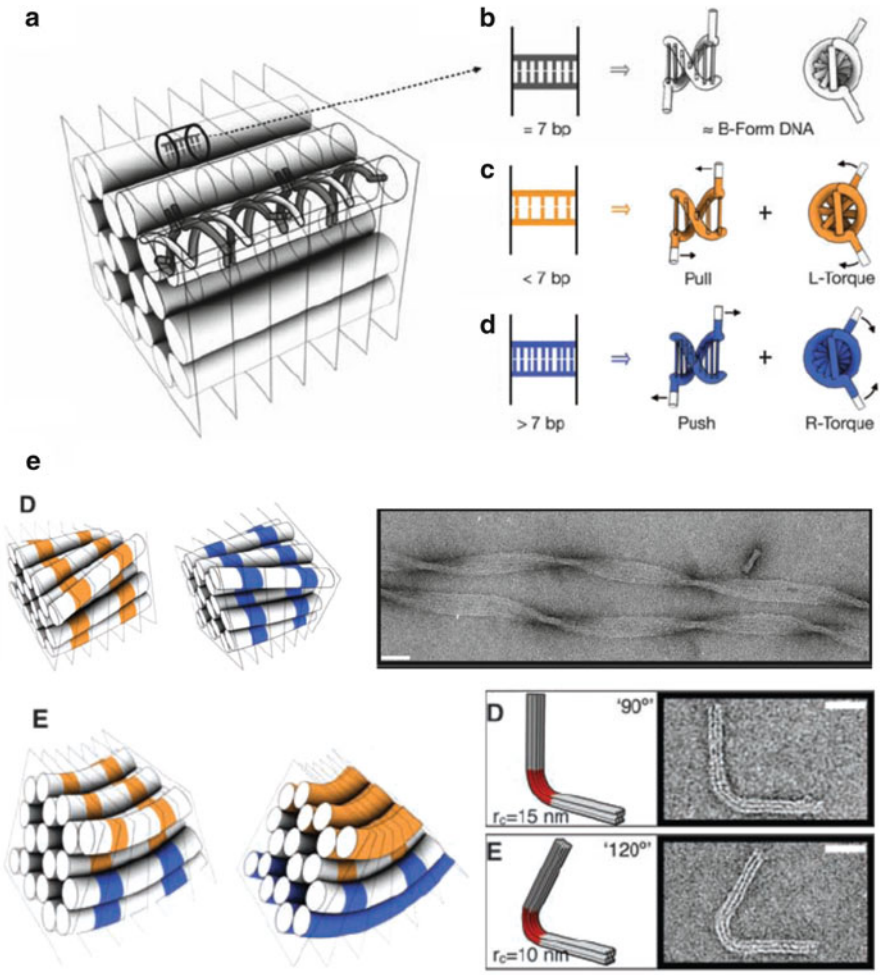

Fig. 5.8 In a honeycomb lattice structure, (**a**) crossover spacings of 7 bp create a neutral structure with no pull or torque on neighboring helices (**b**). Deletion or insertion of base pairs (**c**) exerts both torque and pull on adjacent helices, resulting in twisted structures. (**d**) Shows a conceptual model of global twisting (*left*) with a molecule that is overwound, containing 11 bp per turn (*right*), visualized by TEM. (**e**) By combining both elements into one structure, bending is induced with the helices that have deletions at the inner portion of the bend and those with insertions on the outside as shown in conceptual model (*left*). Degree of bend can be controlled by number of base pairs inserted or deleted, as demonstrated with a 90° bend as well as a 120° bend (*right*) (From Dietz et al. 2009, Science 332:342–346. Reprinted with permission from AAAS.)

curvature of a single helix, which they demonstrated by creating a series of assemblies from concentric ring motifs. By approximating 2.5 nm inter-helical distance from the center of adjacent helices, a typical helical packing distance seen in previous origami designs, they designed the circumference of each ring to maintain

this distance between adjacent rings. They were able to calculate that the circumference of each concentric ring should increase by 48.5 bp for each adjacent ring, which was adjusted to 50 bp for symmetry and ease of design (Fig. 5.9a) (Han et al. 2011).

To introduce the bending into the structure helix by helix, the scaffold strand is woven through the design, and staples are designed so that crossovers occur with a greater number of bases between crossovers in the outer ring than the inner ring. In order to lend symmetry to the structure and increase stability, number of crossovers per ring is designed as a divisor of the change in circumference, Δc, between rings. In the above designs, where Δc is 50 bp, either five or ten crossovers per ring can be selected, so that the number of base pairs between crossovers is uniform throughout each individual helix. By keeping the number of base pairs between crossovers on a single helix an integer multiple of half-turns, the resulting structure is planar, as demonstrated previously in other 2D origami designs. The first assemblies demonstrating this method were planar assemblies of concentric rings (Fig. 5.9b).

By altering the number of base pairs between crossovers between adjacent helices, it is possible to generate out-of-plane curvature in addition to the in-plane curvatures. This principle is the same as previously demonstrated by the honeycomb lattice and square lattice motifs, except that the range of angles possible is greater, with ten possible values between ~34° and ~343°. Some of these angles are shown in the schematic of Fig. 5.9c. By combining these design principles for in- and out-of-plane curvature, hemispherical, spherical, ellipsoid, and other structures were assembled (Fig. 5.9d).

Another interesting tool for 3D structural design was the formation of "tensegrity" structures. Tensegrity, or tensional integrity, is an engineering principle in which rigidity is formed in unusually high proportion to mass and cross-sectional area by combination of elements under tension and those under compression (Snelson 1996). Generally, this takes the form of preloaded rods connected with stress-bearing wires. The first DNA-based structures to use tensegrity design principles formed tensegrity triangles, which were assembled individually and as periodic arrays (Liu et al. 2004; Rothemund et al. 2004). Shih and coworkers (Liedl et al. 2010) introduced an origami version of this structural property by leaving regions of the scaffold single-stranded between honeycomb lattice rods, where they act as entropic springs that hold the rods into a defined position (Fig. 5.10).

The structure maintains integrity unless one of the single-stranded DNA regions is cut, or the origami rods buckle. This has been observed in macroscopic tensegrity constructs and was demonstrated in square "kite" DNA tensegrity structures by variation in the length of the single-stranded DNA wire regions (Liedl et al. 2010). When one wire was lengthened substantially, the other wires were not under sufficient stress, and the structure would distort. Similarly, from overstressing the wires by shortening them, buckling in the origami beams was detected due to the excessive compressive forces, and the structures appeared misfolded. The rigidity of origami beams was investigated by making structures with longer beams, which were observed to buckle significantly as well. Finally, by adding an *EcoRI* restriction site internal to one of the spring elements, mechanical actuation of the structure

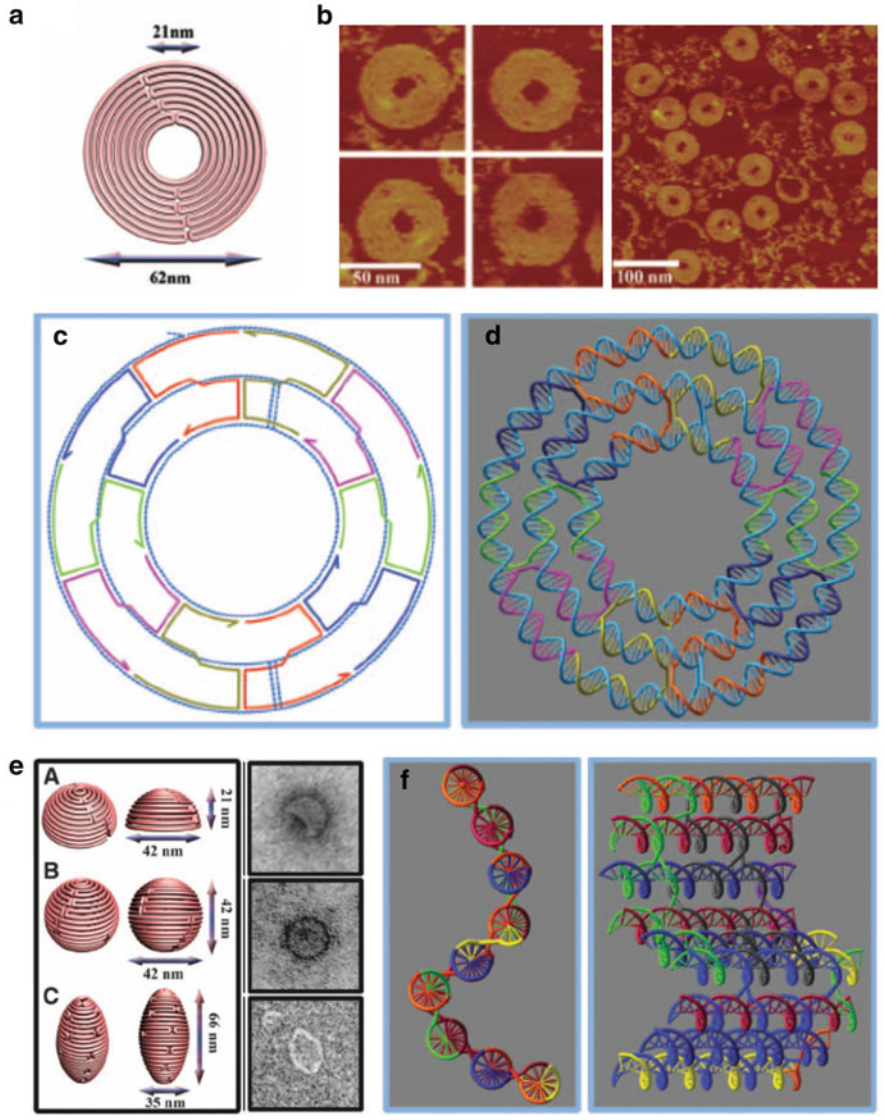

Fig. 5.9 (**a**) A nine-layer concentric ring structure schematic and (**b**) fully assembled, visualized by AFM. (**c**) Conceptual 7 nm structure comprised of three concentric rings. (**d**) The inner ring contains 100 bp, the middle 150, and the outer has 200 (Du et al. 1992). (**e**) Hemispherical, spherical, and ellipsoidal designs (*left*) were assembled and visualized by TEM (*right*). (**f**) Schematic representation of out-of-plane curvature created by varying distances between crossovers: view down helical axes (*left*) and rotated by 135° (*right*) (From Han et al. 2011, Science 325:725–729. Reprinted with permission from AAAS)

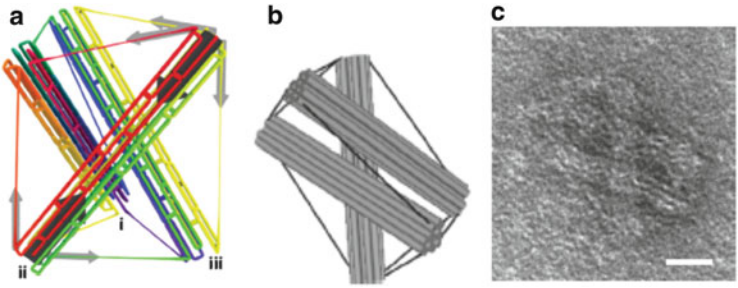

Fig. 5.10 The tensegrity prism, a simple tensegrity structure. (**a**) A schematic showing the scaffold strand pathway through the structure with the staple strands omitted for clarity. (**b**) Model and (**c**) TEM image of assembled prism (Reprinted by permission from Macmillan Publishers Ltd: Nature Nanotechnology, Liedl et al. (2010) 5, 520–524, Copyright 2010.)

from the stretched "kite" form to a parallel beam conformation was achieved when the structures were incubated with EcoRI.

With the tools to create complex 3D structures already well developed, a recent focus in the field of DNA origami has turned toward creating structures with multiple configuration states. One early example of this was the formation of origami with Möbius topology by Yan and coworkers (Han et al. 2010). The Möbius conformation is single-sided and can be easily modeled by taking a circular strip of paper, cutting it, adding a half-twist, and then gluing it back together. This topology has several interesting features that have been the subject of mathematical study. By cutting along the middle of a Möbius strip, it is possible to reconfigure into two interlocked rings, one with a double twist and the other with Möbius conformation. Additionally, it can be cut in a different method to form a larger ring with two full twists.

To create this reconfigurable nanostructure, the Yan group introduced a new technique into the field of DNA origami: DNA kirigami, a "fold-and-cut" process in which the structure is first constructed and then "cut" by strand displacement during additional annealing processes. In order to accomplish the "cutting" of the Möbius origami, the kirigami technique takes advantage of the self-assembled properties of DNA origami. Similar to the strand displacement method seen in the box with controllable lid by Gothelf, Kjems, and coworkers (Andersen et al. 2009), the staples connecting the scaffold at positions that needed to be "cut" were displaced by adding complimentary oligonucleotides (Fig. 5.11).

The initial Möbius origami was created using an 11-helix design, where only six crossovers were necessary per helix as there were only six parallel helices. The design approximated 32 bp for three turns or 10.67 bp per turn, which the DNA readily adopted in spite of the significant twist implied by the models. The molecule has inherent chirality, which would seem to have a preference for the right-handed form due to the global overwinding of greater than 10.5 bp per turn (Dietz et al. 2009), but when assembled only a 1.4:1 excess of the right-handed isomer was observed. This gave insight into the mechanism of origami formation: during the nucleation step, in which the first staples begin to hybridize with the scaffold, the localize twist created

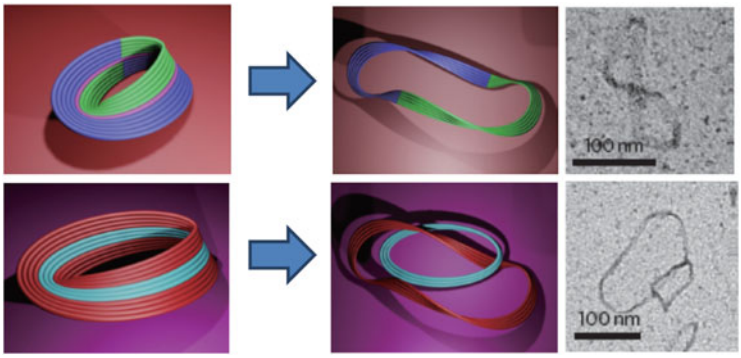

Fig. 5.11 By adding displacement strands to remove extended staple strands on the sixth helix, which is the middle helix, a kirigami ring is produced (*top*). The ring has 720° twist and is no longer a Möbius configuration, as it contains two distinct surfaces. Displacement strands are added to remove the connectivity between the fourth and fifth helices, creating the kirigami catenane (*bottom*). Both structures were examined by TEM (*right*) (Reprinted by permission from Macmillan Publishers Ltd: Nature Nanotechnology, Han et al. (2010) 5, 712–717, Copyright 2010.)

by any given staple is not felt by the others until enough assembly has taken place that the folding path of the scaffold, and thus the chirality of the final object, is fixed. This determination comes from the maximization of base pairing as the dominant free energy driving force, which is equivalent for both right- and left-handed isomer formation. Thus, isomerization in origami formation is a kinetic process that is not determined by overall enthalpy changes (Han et al. 2010).

5.4 Increasing Complexity Through Augmenting Scaffold Size

As many methods for continuing the advance of topological intricacy have been developed, the limitation of scaffold size once again became apparent. While the M13mp18 genome functions robustly as a scaffold for creating origami, the ~7 kb upper bound on size is an inherent barrier to increasing the complexity of DNA nanostructures. Additionally, for creating thinner, branched structures, the M13 scaffold is excessively long, leaving more DNA unfolded than that which is folded within the structure. Several approaches have been utilized to attempt to overcome this, but none has yet been adopted as widely in practice as the initial introduction of M13 DNA by Rothemund with the first origami.

The first attempt to expand the size range of origami was presented by Woolley and coworkers in 2009 (Pound et al. 2009). The group used biotinylated 3′ primers for PCR, which could then be separated from the non-labeled complimentary strand by binding to a streptavidin column under denaturing conditions. They demonstrated the versatility of this technique in its ability to create any sized scaffold strand desired, ranging from 100 to 10,000 nucleotides in length.

Additionally, any source for the scaffold strand can be selected, allowing for the customization of parameters such as GC content or regions of nucleotide repeats as desired. In the report, this was verified by using the 48.5 kb bacteriophage λ DNA as the source in parallel with M13mp18 DNA, which folded reliably into the same origami design by using distinct staples for each scaffold. This method has great potential for future applications, as the scaffold can be designed to fit the origami instead of designing the origami to fit the scaffold. Naturally, if the length of scaffold strand used increases substantially, the required pool of oligo staples will also have to grow proportionately. Labean and coworkers have demonstrated a chip fabrication technique to create oligo pools for this purpose (Saaem et al. 2010).

Using genomic sources of DNA for scaffold material provides a facile route for obtaining longer nucleic acids. However, a challenge for this method is that the majority of genomes are double-stranded. Shih and coworkers (Högberg et al. 2009) addressed this concern by creating a one-pot reaction with two pools of staple strands that used a thermal annealing protocol in tandem with a denaturing formamide gradient. Staples and double-stranded DNA were initially mixed in 40 % formamide and heated, and then during thermal cooling, formamide was gradually removed by dialysis. Using this method, two distinct origami structures were generated by folding the denatured strands separately (Fig. 5.12).

The use of denaturant in folding techniques has interesting implications for the field of DNA origami. Simmel, Shih, and coworkers initially developed this method prior to the report of double-stranded genomic DNA as scaffold material (Saaem et al. 2010). They showed that DNA folding into fully assembled origami structures could be accomplished simply through formamide gradient at constant temperature. Structures produced were indistinguishable in yield and quality from those annealed through thermal ramp protocols. This has prospective utility for functionalization of origami with heteroelements that call for isothermal assembly conditions.

Another method for using genomic double-stranded DNA was devised by Fan and coworkers (Zhang et al. 2012). By amplifying a 26 kb portion of the double-stranded bacteriophage λ genomic DNA, and subsequently producing a single-stranded form through selective enzymatic degradation of one of the strands, they were able to assemble near μm-scale rectangular origami with dimensions of ~100 nm × 200 nm. This technique has several advantages: it does not require modification and successive affinity isolation of one of the strands, PCR is a widely available, high-fidelity technique that can be readily applied to any template source, and the potential to synthesize fully μm-scale scaffold material is obtainable if a non-repetitive DNA sequence of this size can be generated.

The Yan group (Yang et al. 2012) has recently conceived a method for creating "superorigami" structures from the double-stranded λ genome in which both strands are folded to create the assembled structure. Two key design principles introduced in this technique included maximization of folding path asymmetry and periodic crossovers of the single-stranded scaffold DNA. The effective concentrations of both staple and scaffold components were determined to be of critical importance for superorigami formation, as compared with smaller origami structures (Rothemund 2006). This included using a 50:1 M excess of staple strands relative

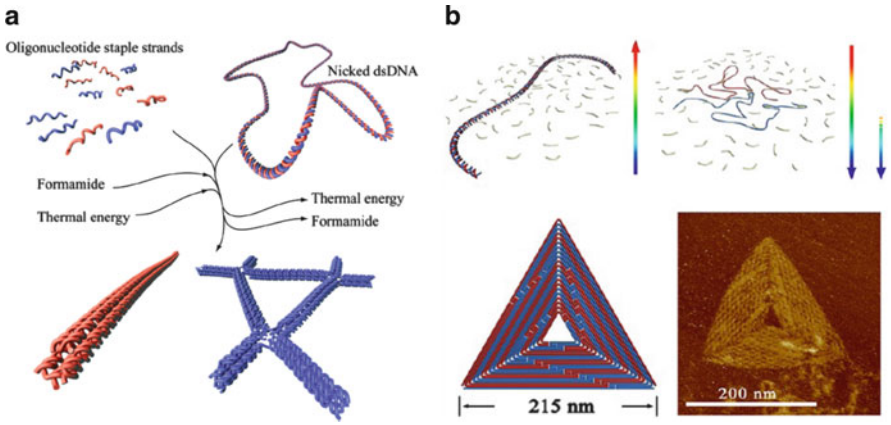

Fig. 5.12 (**a**) Denaturation of genomic dsDNA is accomplished by a combination of formamide and heat in the presence of staple strands, and subsequent renaturation into origami is accomplished by rapid cooling and stepwise dialysis with buffer containing sequentially lower concentrations of formamide (Reprinted with permission from Högberg et al., J Am Chem Soc (2009) 131:9154–9155. Copyright 2009 American Chemical Society.) (**b**) A conceptual model of the annealing process in which the genomic DNA is shown denatured in a pool of staple oligonucleotides (*top*, *left*). The mixture is subjected to two rapid cooling procedures from 90 to 25 °C to denature the scaffold and then from 45 to 4 °C to anneal the staples and assemble the final structure as observed (*top*, *right*). Schematic of a triangular origami design with one strand of the λ scaffold in *blue* and the other in *red* (*bottom*, *left*), with an AFM image of the assembled structure (*bottom*, *right*) (Reprinted with permission from Högberg et al., ACS Nano (2012) 6(9):8209–8215. Copyright 2012 American Chemical Society.)

to the scaffold strand and keeping the overall concentration of scaffold low, as significantly more cross-linked and deformed structures were observed with 5 nm versus 1 nm scaffold concentration. Additional optimization of annealing protocols to reflect thermodynamic requirements of staple lengths used and prevent rehybridization of the scaffold was performed. As the larger scaffold contains more base-pairing interactions than a single-stranded scaffold, it is enthalpically favorable but entropically unfavorable. A thermal ramp protocol as used in previous origami techniques would result in formation of the lowest-energy structure, the double-stranded scaffold. To circumvent this, an annealing protocol that involved multiple heating and rapid cooling steps was designed. From this novel method, discrete superorigami structures reaching 175×175 nm^2 were achieved with assembly yields as high as 85 % (Fig. 5.12).

5.5 Higher-Order Self-Assembly for Larger Nanostructures

Another method for extending origami size is to create structures that use more than one scaffold and thus contain more nucleotides. One successful example of this was reported by Liu and coworkers (Zhao et al. 2010) in which the M13 scaffold was

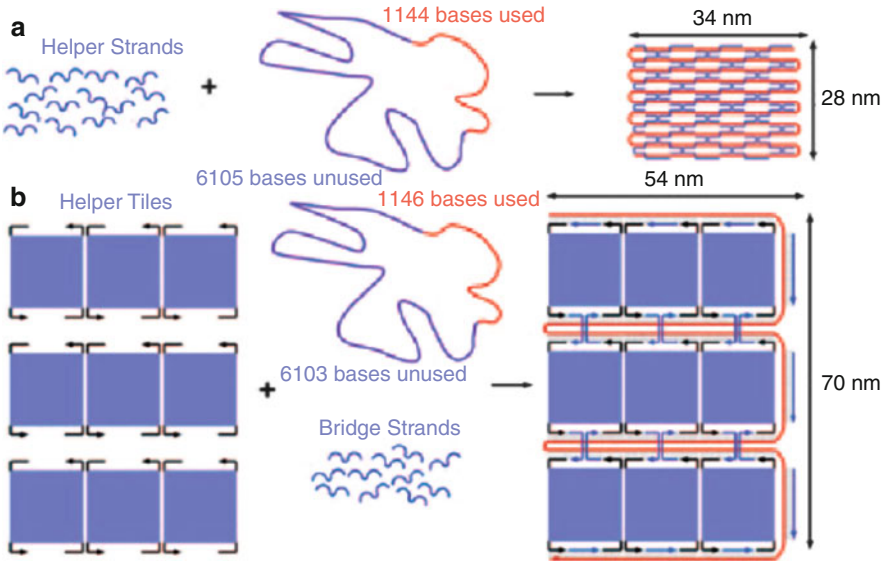

Fig. 5.13 Staples are individually assembled planar origami rectangles (helper tiles) with a raster-fill folding pattern as depicted in (**a**). These helper tiles are then further hybridized with more M13 scaffold strands due to the loops overhanging from their edges that are complimentary to different regions of the scaffold (**b**). Bridge strands are added to stabilize the structure by giving crossovers between antiparallel helices of the scaffold strand (Reproduced with permission from Zhao et al., Angewante Chem. Int. Ed. (2010) 49, 1414–1417, copyright 2010 John Wiley and Sons.)

folded with origami as staples rather than small oligonucleotides. Multiple unique square origami tiles were formed that contained overhanging single-stranded loops on the edges complimentary to different regions of the M13 scaffold (Fig. 5.13). This enabled the formation of origami with greater than 30,000 nucleotides with unique helper sequences throughout the structure, thus retaining the theoretical 4–6 nm resolution of addressability.

A similar method was produced by Sugiyama and coworkers (Endo et al. 2010) through formation of "jigsaw pieces" that could self-assemble into a polymeric structure. The jigsaw pieces were connected via a convex region on one side to a concavity on the adjacent side of the next piece. Through addition of extra helpers, and aided by nonspecific π-stacking interactions at the edges of the pieces where T_4 loops were not included, specific self-assembly was directed after individual origami synthesis. By adding topological features in the form of DNA dumbbell loop patterns to the jigsaw pieces, their unique structures could be identified and correct superstructure assembly yields verified by AFM (Fig. 5.14a). Woo and Rothemund (2011) also introduced a strategy for making origami superstructures that associate based on edge complementarity. Single-stranded loops extended in various places from the edges were given a "1" if the loop was present and "0" for no loop. Edges were then designed to match using the looped regions (Fig. 5.14b).

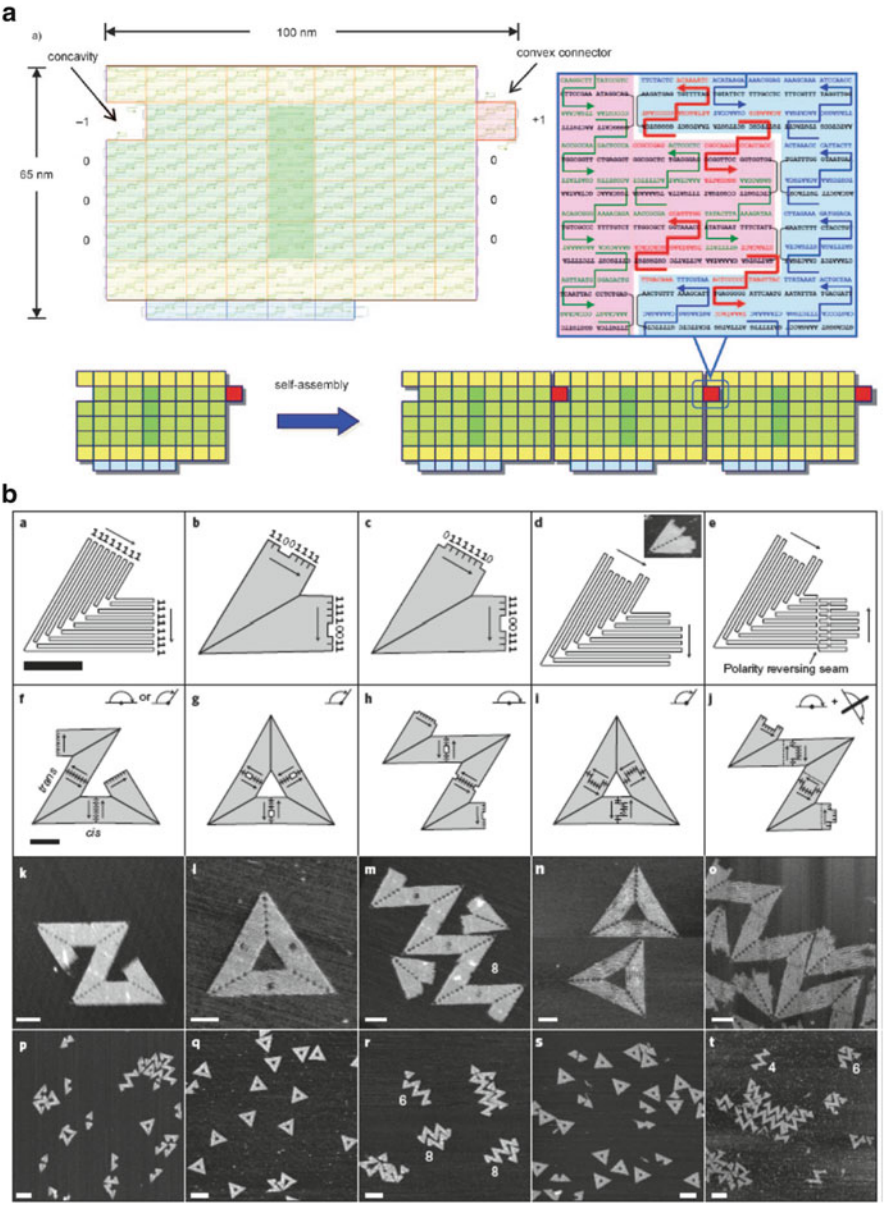

Fig. 5.14 (**a**) Schematic for the design of origami jigsaw pieces from M13 DNA for superstructure assembly (Reprinted with permission from Högberg et al., J Am Chem Soc (2009) 131:9154–9155. Copyright 2009 American Chemical Society.) (**b**) Examples of origami superstructures assembled by complimentary edge shapes with control over *cis–trans* isomerism (Reprinted by permission from Macmillan Publishers Ltd: Nature Chemistry, Woo and Rothemund (2011) 3, 620–627, Copyright 2011.)

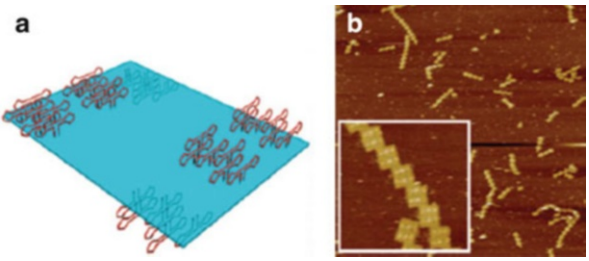

Fig. 5.15 Dumbbell loop extensions from the surface of an origami can be positioned to either reduce or enhance curvature. (**a**) Schematic of a planar rectangular origami that uses dumbbell loops to push opposing corners away from each other, as they tend to curve into each other without the addition of loop features. (**b**) AFM imaging shows assembly of these planar origami tiles into flat ribbons (Reprinted with permission from Liet et al., Langmuir (2012) 28 (4), 1959–1965. Copyright 2012 American Chemical Society.)

Liu, Yan, and coworkers presented another strategy for creating higher-order self-assembly of origami-sized DNA tiles: they introduced a "zigzag" origami tile design that contained dihedral angles of 120° between adjacent antiparallel helices (Li et al. 2010). This was accomplished by spacing crossovers between parallel helices four full turns apart, which was calculated and subsequently visualized by AFM to relieve the deformation produced by the 10.67 bp/turn motif used in the original planar origami structures (Rothemund 2006) that Rothemund reported. This enlarged rectangular tile strategy was designed to promote 2D lattice formation but instead assembled into a variety of 1D arrays. The zigzag motif provides an additional element of flexibility within the plane, which was examined by formation of tubular structures using the same type of tile.

The Yan group recently devised a method to ameliorate the global twist induced in the original rectangular origami design when polymerized into ribbon superstructures (Li et al. 2012). They extended dumbbell-shaped loops from specific locations on the scaffold such that the repulsive forces between them served to position the two corners of the origami that curve up toward each other into a more level conformation or into a configuration in which the corners were curved in the opposite direction. Using this technique they were able to assemble a nearly flat ribbon using the planar rectangle origami (Fig. 5.15). This method adds another tool to DNA nanostructure design principles that may prove to be useful in future assemblies and applications, as it allows for the change of conformation based on higher-level geometries than the secondary structure of the helices through addition of topological features.

Seeman and coworkers reported a successful strategy for assembling origami superstructures by 2D lattice formation. Polymerization of planar origami structures was realized through creating a "braided" structure with two different cross-shaped origami tiles with complimentary ends (Fig. 5.16) (Liu et al. 2011). Perpendicular helical orientation is the crux element in these designs that addressed the design flaws in previous attempts to form 2D lattice structures (Ke et al. 2009b). The ends of helices were designed to exploit the nonspecific stacking interactions

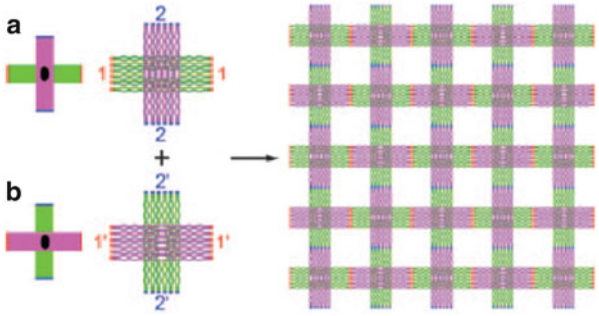

Fig. 5.16 Schematic design for the two cross-shaped tiles used to create a woven 2D lattice. The ends are labeled such that 1 is complimentary to 1′ and 2 is complimentary to 2′. Simplified cartoon depiction (*left*) shows the perpendicular orientation of helices that is critical to yield lattice formation from stacking interactions (Reproduced with permission from Liu et al., Angewante Chem. Int. Ed. (2011) 50, 264–267, copyright 2011 John Wiley and Sons.)

that single-stranded regions are often used to prevent in order to assemble the episodic structure. A similar strategy has been reported for making other periodic arrays in two and three dimensions (Majumder et al. 2011). This technique has the advantage of making very large structures, up to tens of micrometers, which may be useful in the future for capture and assembly-line applications; however, the tradeoff is that the regularity of the repeating motifs within these structures does not allow for full addressability.

A recent method has been developed in which origami is assembled from a modular system that is very straightforward to customize. Rather than combining portions of biological material such as the M13 or other source scaffold with synthetic oligonucleotides, Yin and coworkers (Wei et al. 2012) have devised a "molecular canvas" design in which many short single strands that consist of concatenated sticky ends self-assemble into a planar, rectangular form. Each strand can be treated as a molecular pixel of 3 nm $\times$ 7 nm dimensions. Nanostructures are simply made by choosing to include or omit a pixel and then selecting the corresponding oligonucleotides to mix together in a one-pot reaction (Fig. 5.17).

Shih, Yin, and coworkers (Ke et al. 2012) have extended this method from 2D to 3D with the introduction of "DNA bricks" in which a similar strategy was utilized to fashion modular oligonucleotide bricks that duplex with other bricks to hold an assembled 3D structure together. Each brick is 32 nt long with four 8 nt sticky end domains that can interact with other bricks, and adopt a 16 nt antiparallel helical structure joined by a single phosphate linkage when included in a structure. Using this design, a 1,000 voxel canvas was created, and over 100 unique architectures were formed (Fig. 5.18).

It is likely that this method will be incorporated into future structures and applications, as it demonstrates a robust technique for creating stable 3D structures with completely unique synthetic oligonucleotides and no need for additional purification steps or control over stoichiometry. Additionally, in both reports

Fig. 5.17 (**a**) Method for assembly of a molecular canvas or "brick wall" motif from single-stranded rectangular building blocks (*left*) to make arbitrary shapes such as an eagle head, triangle, or heart (*right*). (**b**) Structures assemble with high fidelity, as seen by AFM imaging of 100 arbitrary shapes created (Reprinted by permission from Macmillan Publishers Ltd: Nature, Wei et al. (2012) 485, 623–627, Copyright 2012.)

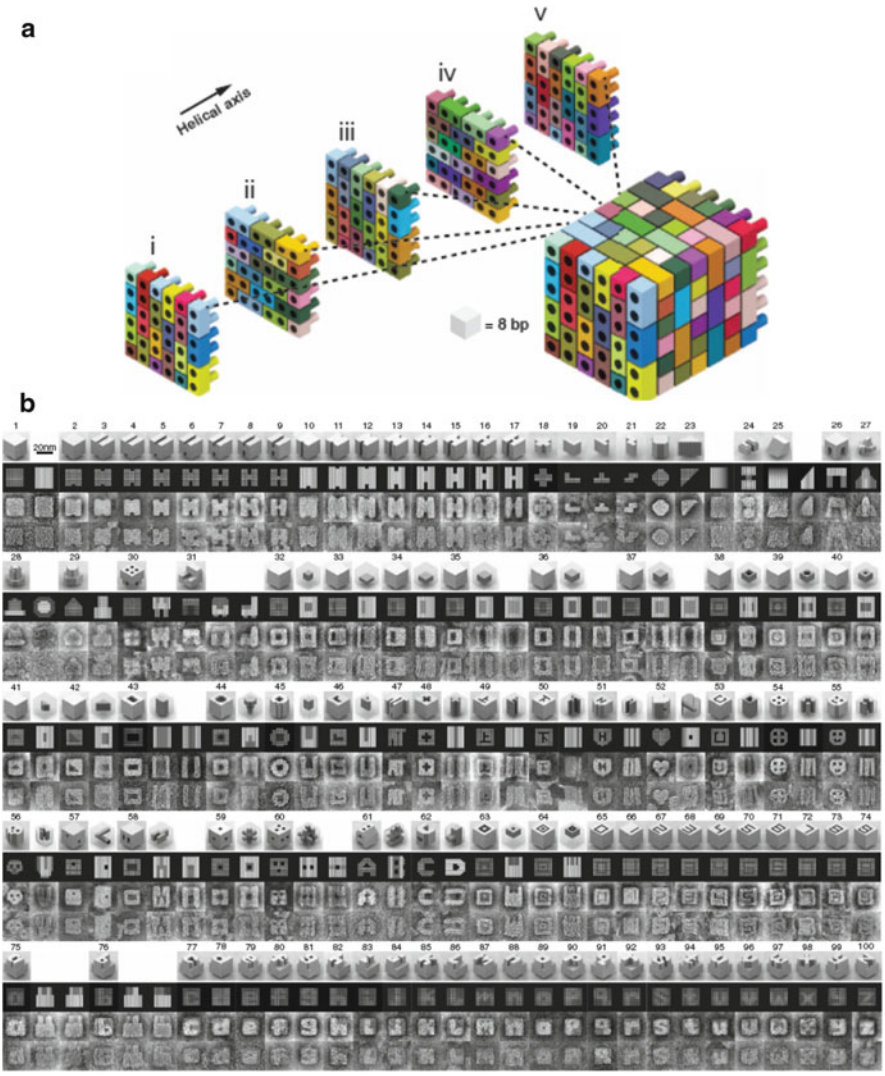

Fig. 5.18 (**a**) Schematic for assembling a cuboid structure from DNA bricks in which each unit is visualized as a LEGO. (**b**) Computer-rendered images of the 100 structures assembled using the DNA brick technique, with corresponding AFM (From Ke et al. 2012, Science 338, 1177–1183. Reprinted with permission from AAAS.)

(Wei et al. 2012; Ke et al. 2012) an automated liquid-handling robot is used to mix the strands from a list generated after design formation in a graphical user interface, thus eliminating sources of human error and streamlining the process for making any arbitrary shape desired.

5.6 Design Software or Origami Design Software

In order to design DNA origami, a variety of ad hoc programs have been created and employed. One common strategy was to draft the structural outline with available software such as Adobe Illustrator and then generate staple sequences with purpose-specific programs that would upload the M13 sequence. This method was time-consuming, and so a few more general software packages were developed and released. For 2D origami, the programs Tiamat (Williams et al. 2009) and an application that functions in the editing program SARSE (Andersen et al. 2008) are commonly used. In Tiamat, the user can add single- or double-stranded DNA molecules one at a time, and join them either along the backbone, or nick the backbone and join across strands to make a crossover molecule. The M13 or other desired scaffold sequence is then added manually into the program, and the corresponding staple strand sequences are generated automatically. The SARSE application works by importing bitmap images and filling them automatically with DNA to create 2D origami shapes. Its utility was demonstrated by the formation of dolphin structures with different tail positions (Andersen et al. 2008). For detailed atomic structures, SARSE files can be rendered in programs such as PyMOL.

One of the most intuitive programs is caDNAno, developed by the Shih laboratory (Douglas et al. 2009b) as a way of generating 3D structures (Fig. 5.19). The initial design of the program only allowed the user to create origami with helices in the honeycomb lattice motif. After selecting the number of helices desired, the user can edit the length of the helices and systematically route the scaffold strand through the design. The program then automatically adds staple strands, which can be adjusted by the user to fit within the desired length and number of crossovers per staple oligo that are desired. The scaffold sequence is assigned last, and the staple sequences are produced subsequently. Recent versions of caDNAno have been released that have a square pattern for helical orientation, allowing for more diverse architectures to be created with the program (Ke et al. 2009b).

Bathe, Dietz, and coworkers (Castro et al. 2011) have developed innovative structural analysis software to operate in tandem with caDNAno: computer-aided engineering for DNA origami (CanDO). CanDO allows the user to calculate a lower bound on the flexibility of an assembled origami in solution by uploading the caDNAno design file. A systematic computation of root-mean-square fluctuations (RMSFs) of each base pair within the structure gives detailed insight into conformational variations visualized in assembled origami (Fig. 5.19c). By enabling prediction of the assembled structure through thermodynamic considerations, applications requiring positional precision to 1–2 nm can be realized with greater fidelity. The original program based calculations on helical bend, stiffness, and canonical twist of dsDNA. The newest version also takes into account nicks, inter-helical repulsive forces, and entropic elasticity of ssDNA regions within the structure (Kim et al. 2012). In addition to forecasting the equilibrium mechanics of DNA origami, CanDO is currently being used to model formation, deformation, and relaxation processes in nanostructures, a feat currently inaccessible by other methods.

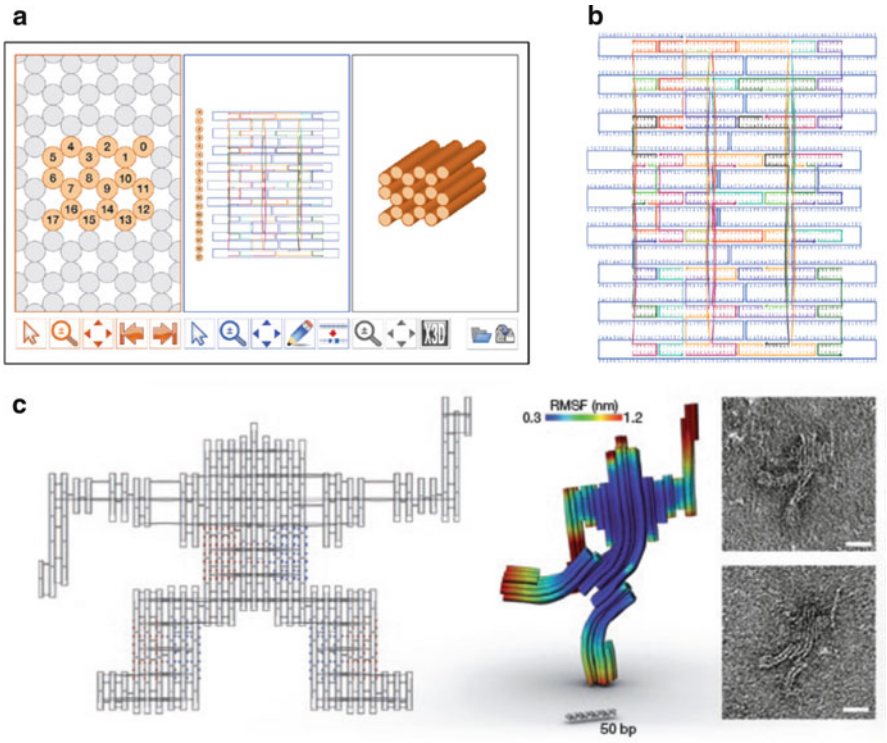

Fig. 5.19 (**a**) Screenshot of caDNAno showing a design that uses the hexagonal honeycomb lattice motif. On the *left*, the user is able to select how many helices to include in the design, viewed looking at the helix axis. In the *middle panel*, the scaffold is shown in *gray* and staple strands in *colors*. On the *right*, a 3D, rotatable model of the structure is generated from the input into the other two panels. (**b**) A desired scaffold sequence can be inserted into the 2D view of the origami and complimentary staples are generated by the program (From Douglas et al, Rapid prototyping of 3D DNA-origami shapes with caDNAno. *Nucleic Acids Research*, (2009) 37, 15, 5001–5006, by permission of Oxford University Press.) (**c**) From a caDNAno design (*left*) the predicted structure and regions of flexibility is presented as a heat map (*middle*) that is consistent with assembled structures visualized by AFM (*right*) (Reprinted by permission from Macmillan Publishers Ltd: Nature Methods, Castro et al. (2011), 8(3), 221–229, Copyright 2011.)

5.7 Functionalization of Origami Structures

Following the development of extensive design principles for static origami structures of increasing complexity, there has been a focus on utilizing origami in various applications as a structural element for nanosystems. Though DNA has somewhat limited inherent chemical properties, it serves as an optimal platform for assembling heteroelements with varied photonic, electronic, and biochemical properties. The most obvious opportunity for using origami nanostructures as a platform for other processes is inherent in the self-assembly mechanism: the

uniqueness of each staple sequence allows for the aforementioned addressability to 4–6 nm resolved pixels. This "molecular pegboard" has been used to conjugate a wide variety of functional moieties such as gold (Ding et al. 2010a, b; Hung et al. 2009; Sharma et al. 2008) and silver nanoparticles (Zheng et al. 2012; Pal et al. 2009), quantum dots (Stearns et al. 2009; Bui et al. 2010; Tikhomirov et al. 2011), fluorophores, aptamers (Liedl et al. 2010; Yang et al. 2012; Zhang et al. 2012; Zhao et al. 2010) and other RNA molecules, repeated (Stein et al. 2011a, b; Steinhauer et al. 2009; Jungmann et al. 2010; Sharonov and Hochstrasser 2006), carbon nanotubes (Maune et al. 2010), streptavidin (Voigt et al. 2010; Kuzyk et al. 2009; Kuzuya et al. 2009; Numajiri et al. 2010a), dendrimers (Liu et al. 2010), virus capsids (Stephanopoulos et al. 2010), and Ni-NTA for binding His-tagged proteins (Shen et al. 2009). All of these binding events are accomplished by modification of staple strands, either during synthesis or through post-synthetic batch-wise enzymatic labeling (Jahn et al. 2011). The staples are then assembled into the complete origami architecture by conventional protocols for subsequent analysis. Since the majority of DNA origami applications use the staple modification techniques discussed below, this section will serve as a survey of DNA origami functionalization. However, the discussed designs only highlight portions of an exciting field replete with novel technological developments. An exhaustive discussion of these applications is beyond the scope of this chapter.

One of the first applications using the DNA origami technique was the development of label-free RNA sensors. Yan and coworkers (Ke et al. 2008) developed rectangular origami designs that had single-stranded V-shaped junctions extended from one side of the molecule by using staple strands that were longer than necessary to form the origami structure. The extended staple regions were complimentary to one of three mRNA sequences selected, and each origami contained only one type of probe. To distinguish between the assembled structures, different patterns of dumbbell loops were positioned on the opposite corner of the origami such that they were a "barcode" readily visible by AFM. Without the target mRNA sequence, the staple extensions were too flexible to be sensed by AFM; however, upon binding the target, the duplex exhibited increased stiffness that was readily detected. When mixed together, the sensors were capable of simultaneous detection of multiple targets within a single reaction (Fig. 5.20a).

A comparable RNA detection technique was developed by Fan and coworkers (Zhang et al. 2010), in which a toehold displacement mechanism allowed for determination of single-nucleotide polymorphisms (SNPs). Staple strands containing a biotin–streptavidin pair extended from the origami, and a matching target strand displaces the biotin–streptavidin, while a mismatched target cannot, giving differential fluorescent patterns. Recently, a different version of this was reported by Seeman and coworkers (Subramanian et al. 2011) in which the SNP detection could be examined at a single-molecule level. A similar toehold mechanism was used in which a strand containing a quencher molecule is displaced by a matching target, leaving a fluorophore capable of giving a fluorescent signal (Fig. 5.20b). The sensor was demonstrated to be effective for detecting a single probe as well as two distinct probes simultaneously, which points toward future

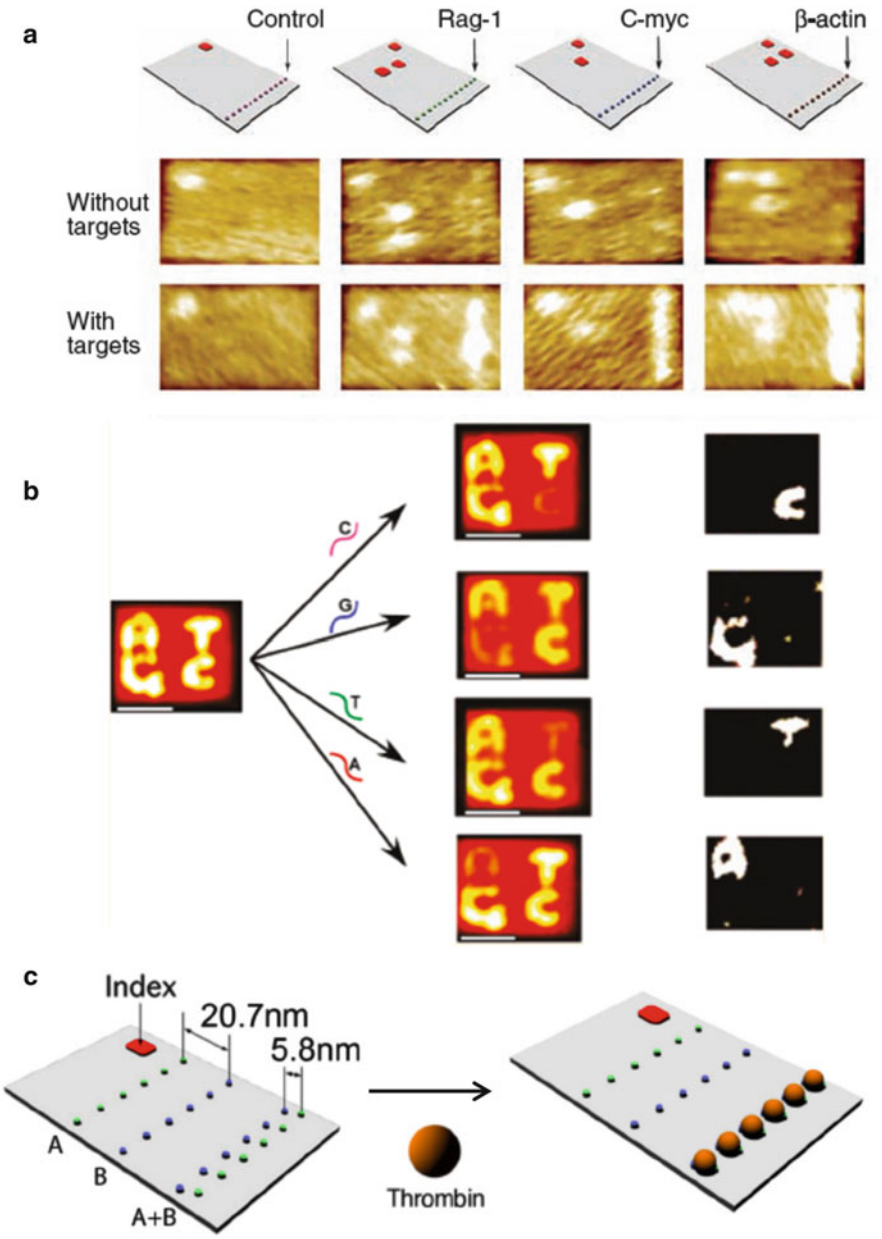

Fig. 5.20 (**a**) Topographical illustration of origami design (*top*). In the *upper left corner* of each origami, the pattern of dumbbell loops identifies the sequence of the probes on the *right* portion of the structure. AFM images of assembled structures without mRNA added (*middle*) and with mRNA/probe hybridization (*bottom*) (From Ke et al. 2008, Science, 319, 180–183. Reprinted with permission from AAAS.) (**b**) The AFM of a tile after strand invasion (*middle*) by an oligonucleotide with the key nucleotide identified as indicated over the *arrow* is subtracted from the AFM of the "full image" (*left*) before any strand invasion has taken place to give the

applications for genomics and proteomics in vivo, as the recognition of separate SNPs exemplifies the case of a diploid organism. Moreover, the water-soluble nature of DNA origami-based systems is advantageous compared with other nanoscale materials for potential biological uses.

The ability to precisely position different molecules with controlled distance between them has been exploited to study binding events. In one report by the Yan group (Rinker et al. 2008), the distance relationship between two aptamers that bind thrombin, a molecule of biological interest, was explored by creating a rectangular structure similar to the previously reported RNA sensor. Aptamer-functionalized staple strands were positioned at regular intervals on the surface of the origami, and thrombin binding was clearly observed by AFM only at the correct spacing between the two aptamers (Fig. 5.20c).

The concept of using DNA origami to study distance relationships between multiple molecules has been extensively employed in the field of super-resolution microscopy. The first example of this was devised by Tinnefeld and coworkers (Steinhauer et al. 2009), in which a nanoscopic ruler was assembled by attaching two fluorophores to the corners of a rectangular DNA origami platform within the distance restraints for Förester resonance energy transfer (FRET). Detection of the fluorescent signal from FRET by most optical techniques is restricted because the distance between the fluorophores is smaller than the diffraction limit. This constraint was bypassed by using total internal reflection fluorescence (TIRF) in combination with several super-resolution techniques. From this experiment, the inter-fluorophore distance was determined to be 88.2 $\pm$ 9.5 nm, opposed to the predicted distance of 89.5 nm based on the origami design (Steinhauer et al. 2009). Similar to previous planar origami assemblies, deformation of flat structures is seen due to approximations made in the design process. This was later circumvented by Liedl and coworkers through the use of a 3 $\times$ 14 square helix motif DNA origami block for related experiments that studied and validated distance-dependent relationships in FRET theory (Stein et al. 2011a).

An additional use of origami for super-resolution methods development was established by Simmel and coworkers (Jungmann et al. 2010), in which the kinetics of individual staple hybridization to DNA origami was examined through a single-molecule fluorescence technique called points accumulation for imaging nanoscale topography (PAINT) (Sharonov and Hochstrasser 2006). The DNA-PAINT technique utilizes the association and dissociation of freely diffusing fluorophores fine-tuned through temperature modulation to avoid common fluorescent labeling issues such as photobleaching and inactive fluorophores. The continual targeting of the

Fig. 5.20 (continued) "subtracted image" (*right*) which shows the identity of the nucleotide (Reprinted with permission from Subramanian et al., Nano Letters (2011) 11, 910–913. Copyright 2011 American Chemical Society.) (**c**) Thrombin binding occurs only when aptamers A and B are displayed on the surface of the origami in close proximity. A distance of 5.8 nm is sufficient for binding, but 20.7 nm is too widely spaced (Reprinted by permission from Macmillan Publishers Ltd: Nature Nanotechnology, Rinker et al. (2008), 3(7), 418–422, Copyright 2008.)

origami to be imaged by dynamic labels improves the TIRF images from being obscured by the diffraction limit in structures with fluorophores affixed directly to the structure into visible, distinct positions with sharp resolution.

Another application of fluorescent molecules and DNA origami from the Tinnefeld group (Stein et al. 2011b) presented a fluorophore network on a rectangular origami in which two pathways of energy transfer were made possible with the addition of a "jumper" fluorophore. The arrangement of four different colored fluorophores gave output from a donor blue fluorophore through either a red or IR fluorophore acceptor, depending on the identity of the jumper fluorophore. This construct was designed to investigate the motion of energy through multiple molecules, a common phenomenon in nature seen in large constructs such as the photosystem proteins. Looking toward the future, the combination of robust DNA origami nanotechnology and single-molecule techniques will likely bring many further advances in the field of plasmonics.

The study of energy transfer pathways and photonics using DNA origami has also been explored through the study of metallic nanoparticles. Specifically, gold (AuNPs) and silver (AgNPs) nanoparticles have been the subject of many studies recently due to their ability to generate high local-field enhancement when excited at their plasmon resonance (Schuller et al. 2010). This potential to circumvent the diffraction limit (Maier et al. 2003) at the nanoscale has led to the proposition of many potential developments for detectors, electronics (Liu et al. 2001; Ozbay 2006), optics (Shipway et al. 2000), spectroscopy, and microscopy (Anker et al. 2008), but a barrier to their creation lies in the need to fabricate materials of nanoscale dimensions (Ozbay 2006). Consequently, the spatial addressability of the origami technique has been recognized as a vital tool in the nascent field of plasmonic nanostructure fabrication.

Similar to other methods of immobilizing heteroelements on origami, the localization of nanoparticles to desired configurations is driven by hybridization of a probe attached to the nanoparticle to a complimentary sequence extended from a staple within the origami construction. The attachment of the oligonucleotides to the nanoparticle is accomplished by using thiol-modified ssDNA, which can be obtained through standard phosphoramidite synthetic chemistry and is commercially available (Fig. 5.21a) (Sharma et al. 2008). Similar techniques have been reported that use chimeric phosphorothioate-modified DNA for using multiple thiol moieties per anchoring domain (Fig. 5.20b) (Pal et al. 2009). In both cases, a soft organic corona is extended from the nanoparticle, which serves the dual purpose of specifying what location on the origami surface the nanoparticle must hybridize to as well as preventing aggregation of the nanoparticles in solution.

Using these techniques for creating ssDNA ligands to metallic nanoparticles, a range of origami-nanoparticle structures have been assembled (Fig. 5.21c–e) (Ding et al. 2010a). Additionally, an interesting method for assembling fluorescent silver nanoclusters was reported by Yan and coworkers, in which sugar-modified staple strands were metallized by use of the Tollens' reagent (Fig. 5.21c) (Pal et al. 2011). Recently, attempts to control more discretely the number of probes attached to each nanoparticle have been reported (Zheng et al. 2012). Nanoparticles are observed to

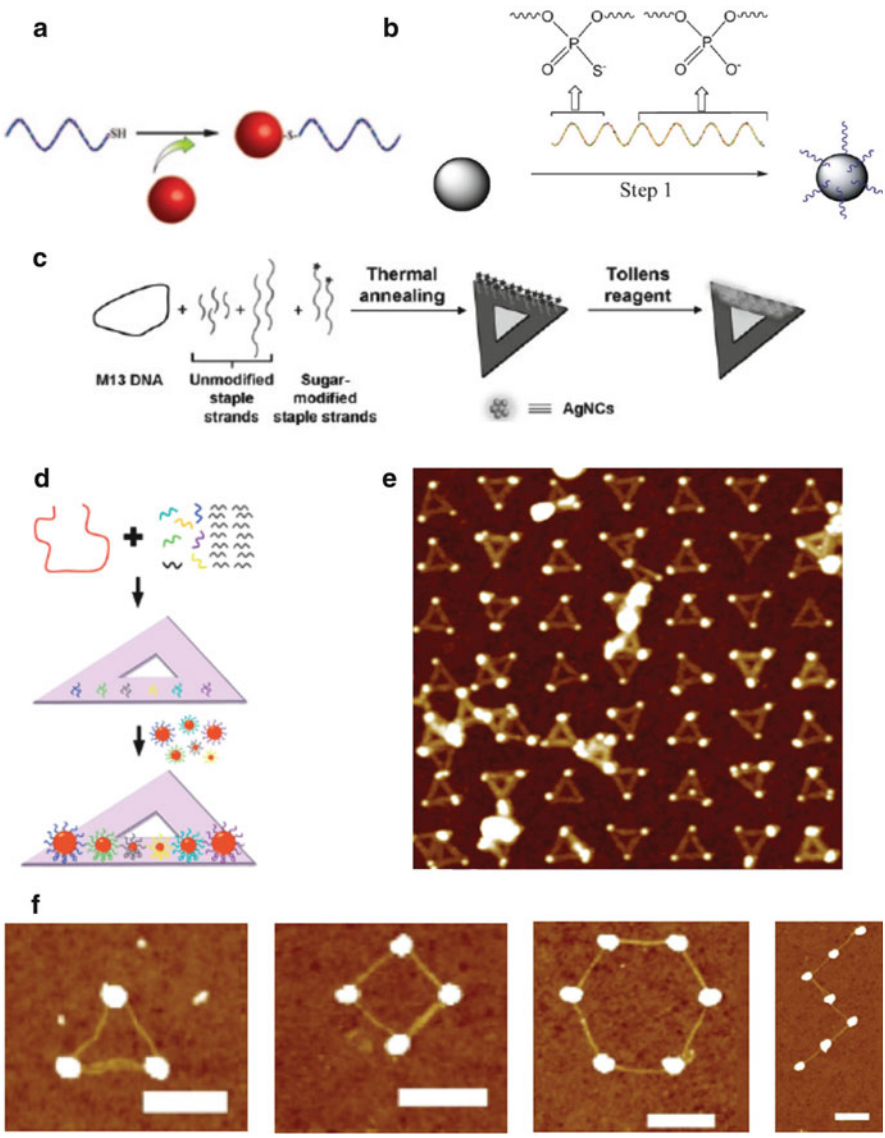

Fig. 5.21 (**a**) Immobilization of thiol-modified ssDNA on an AuNP (Reprinted with permission from Sharma et al., J. Am. Chem. Soc. (2008) 130, 7820–7821. Copyright 2008 American Chemical Society.) and (**b**) phosphorothioate-modified ssDNA for AgNP conjugation (Reproduced by permission of The Royal Society of Chemistry from Pal et al. (2009), 6059–6061. Copyright 2009 The Royal Society of Chemistry.) (**c**) Use of the Tollens' reaction to immobilize silver into nanoclusters on triangular origami containing staples modified with carbohydrate moieties (Reproduced with permission from Pal et al., Angewante Chem. Int. Ed. (2011) 50, 4176–4179, copyright 2011 John Wiley and Sons.) (**d**) Six AuNPs of different sizes were assembled by Yan and coworkers on a triangular origami with precise control over spacing. The schematic shows the different probes on the surface of the DNA and the complimentary sequence on the various AuNPs

form single, sharp bands when subjected to gel electrophoresis; accordingly, higher-resolution electrophoretic techniques can be used to distinguish between the size of nanoparticles with single or multiple ssDNA ligands. By assembling clusters and arrays of nanoparticles of different sizes and plasmonic resonances, novel properties are being created and the methods developed for future construction of devices that harness their desirable electronic and optical characteristics.

In spite of improvements over precise control of functional group orientation relative to each individual origami, a large gap still exists between bottom-up self-assembly methods and top-down processes such as lithography. Technological advances that desire to fully utilize the positional resolution of heteroelements that the DNA origami technique offers will also desire to control the orientation of each origami as deposited on a surface, and thus the process must be approached from both ends. Cha and coworkers (Hung et al. 2009) have begun bridging this gap with a study in which they managed to control deposition of triangular origami on lithographically etched surfaces and subsequently fix the origami through ethanol washing without distorting the structures visibly. Imaging of assembled structures clearly exhibited that this process is useful for controlling the loci of AuNP-functionalized origami, with high assembly yield in nanoparticle to origami conjugation as well as substantial accuracy in regulation of placement of the assembled structures (Fig. 5.21e).

Yan and coworkers (Ding et al. 2010b) also reported a method for combining top-down techniques with self-assembly. Their mechanism was the reverse of the one demonstrated by Cha and coworkers, in that the AuNPs were immobilized via lithographic patterning of a surface and then functionalized with origami nanotube "wires" between the gold islands (Fig. 5.20f). The ability to fine-tune structural deposition from either nucleic acid or heteroelement components holds promise for future utility of these constructs.

Much as structural complexity in DNA origami has steadily increased since its original introduction, the uses and applications of origami methods are also continuing to become ever more intricate. As a nanoscaffold, DNA origami has the ability to organize and assemble an array of other biomolecules. Though the mechanism by which functionalization of DNA origami is accomplished is similar by way of modified staples from one application to the next, DNA origami in shapes that deviate from a planar surface simply used as a molecular pegboard is giving way to novel applications.

Fig. 5.21 (continued) (Reprinted with permission from Ding et al., J. Am. Chem. Soc. (2010a) 132, 3248–3249. Copyright 2010 American Chemical Society.) (**e**) AFM of lithographically patterned triangular origami deposited in alternating orientation and then functionalized with 5 nm AuNPs (Reprinted by permission from Macmillan Publishers Ltd: Nature Nanotechnology, Hung et al. (2009), 5, 121–126, Copyright 2009.) (**f**) Gold islands assembled by conventional surface-patterning lithography techniques are connected by DNA origami nanotubes to create various geometric shapes (Reprinted with permission from Ding et al., Nano Letters (2010b) 10, 5065–5069. Copyright 2010 American Chemical Society.)

One example of this was reported by Shih and coworkers, in which DNA nanotubes were used to inhibit the rotation of membrane proteins giving rise to an anisotropy in the orientation of the proteins for NMR studies (Douglas et al. 2007). The concept of specific positioning of proteins for study was further expanded upon recently with the use of origami to immobilize enzymes that function in a catalytic cascade. By modifying a protein of interest with an ssDNA probe, the protein can be attached to the origami via hybridization with a complimentary probe extended from a staple sequence on the origami. Changing the identity of the staple strand used to capture the protein allows for variation in distance between the proteins, as was demonstrated by Fu et al. (2012a) with a fundamental study of hydration layer effects on substrate channeling using DNA origami as a platform to control enzyme placement precisely (Fig. 5.22a, b).

The ability to examine chemical reactions using a DNA origami platform is not limited to those carried out through enzymatic catalysis. Gothelf and coworkers (Voigt et al. 2010) created a planar origami surface in which individual chemical reactions could be carried out and visualized at the single-molecule level. Different functional groups capable of click chemistry or peptide bond formation were extended from the surface of the origami by staple modification and after incubation steps were performed on mica-immobilized origami. Biotin moieties attached to the reactive groups allowed for streptavidin binding, facilitating the reaction efficiencies to be visualized directly by AFM (Fig. 5.22c).

Just as biotin-modified staples can be used to capture streptavidin, a variety of orthogonal protein targeting schemes have been devised based on affinity interactions. Commercially produced fusion proteins were bound by ligand-modified staples in a report by Niemeyer and coworkers (Sacca et al. 2010), and a similar experiment was conducted by the Komiyama group (Numajiri et al. 2010b) using alkaline phosphatase and horseradish peroxidase. Hexahistidine-tagged proteins can be captured by Ni-NTA-modified staples, as demonstrated by Norton and coworkers (Shen et al. 2009). Opportunities are also available for using DNA-binding moieties with DNA origami due to primary structure. This can be accomplished through sequence-specific pyrrole-imidazole polyamides (Yoshidome et al. 2012; Cohen et al. 2007) or through proteins with DNA-binding domains. A prominent example of using DNA-binding proteins was the binding of human topoisomerase I to probes on a planar DNA origami for AFM analysis by Knudsen and coworkers (Subramani et al. 2010).

The Sugiyama group (Nakata et al. 2012) reported a clever mechanism for binding proteins to DNA origami through the use of zinc finger proteins (ZFPs). Both natural and artificial ZFPs are well characterized, capable of binding a 4-bp sequence in the major groove of dsDNA with nanomolar affinity. From these, two were chosen and modified with fluorescent dyes, biotin or green fluorescent protein, in order to enable detection as well as to demonstrate that addition of a small molecule or fusion with other proteins is possible at both termini with full retention of binding function. The two proteins bind specifically and orthogonally to their respective sequences in a rectangular origami with designed binding cavities (Fig. 5.22d), showing that this method has potential for functionalization of origami with proteins or other molecules in future applications.

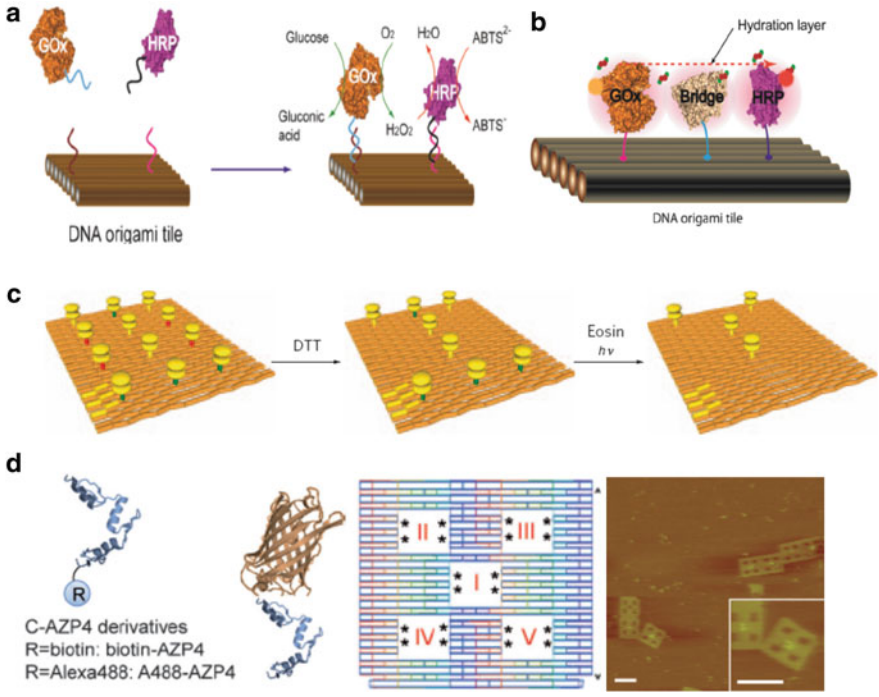

Fig. 5.22 (**a**) Attachment of proteins is driven by hybridization of a covalently linked ssDNA probe on the enzyme to a complimentary sequence of an extended staple in the origami. By placing two enzymes that function in a catalytic cascade in close proximity, it is possible to gain kinetic information. (**b**) Using origami to examine substrate channeling through the hydration layer around proteins by adding a non-catalytic bridge protein in between the enzymes (Reprinted with permission from Fu et al., J. Am. Chem. Soc. (2012a) 134, 5516–5519. Copyright 2012 American Chemical Society.) (**c**) Attachment of streptavidin to various functional groups displayed on a planar origami, which are subsequently cleaved in separate chemical reactions (Reprinted by permission from Macmillan Publishers Ltd: Nature Nanotechnology, Voigt et al. (2010), 5, 200–203, Copyright 2010.) (**d**) The C-AZP4 zinc finger protein with biotin and AlexaFluor488 moieties attached at the N-terminus, as well as GFP attached at the C-terminus (*left*). A rectangular DNA origami with 5 cavities specifying different zinc finger binding sequences was created (schematic, *center*) and examined with AZP4 constructs bound by AFM (*right*) (Reproduced with permission from Nakata et al., Angewante Chem. Int. Ed. (2012) 51, 2421–2424, copyright 2012 John Wiley and Sons.)

Other advances in dynamic systems using DNA origami have been realized in the fields of molecular robotics and DNA computing. DNA origami provides an ideal platform for development of molecular switches (Mao et al. 1999b), placement of functional cargo for transport (Gu et al. 2010), and design of molecular pathways for a nanorobot to follow (Gu et al. 2010; Lund et al. 2010; Wickham et al. 2011). DNA computing and machinery are discussed in detail in the following sections of this text.

RNA nanoengineering has been expanding recently, with the introduction of various structures that utilize non-Watson–Crick interactions between the ribonucleotides (Chworos et al. 2004; Batey et al. 1999). The bulk of applications with DNA origami have so far used short RNA staple extensions as aptamers (Ke et al. 2008; Zhang et al. 2010; Subramanian et al. 2011; Rinker et al. 2008). In contrast with traditional DNA origami design principles, the construction of RNA particles, filaments, and programmable nanostructures (Chworos et al. 2004; Severcan et al. 2009) has been driven by the development of modular RNA motifs (Batey et al. 1999; Severcan et al. 2009; Jaeger 2009), including H-shaped, square-shaped, dimer, and "tecto-RNA" building blocks (Westhof et al. 1996). These conformations are made possible by the rich tertiary structure of RNA due to the additional hydroxyl moiety in ribose compared with deoxyribose, although there are some fidelity and stability concerns due to the more chemically labile nature of RNA compared with DNA (Chworos et al. 2004; Batey et al. 1999; Westhof et al. 1996). There is potential for future applications that utilize both DNA origami and RNA nanostructure formation in tandem (Ko et al. 2010), though there is much foundational work still awaiting the field.

5.8 Perspective and Conclusion

DNA origami has developed rapidly and extensively as a field, as indicated by the expansion from simple planar structures to intricate topologies and functionalized applications within just a 6-year span. However, there are several technical challenges facing the technology that must be overcome, if the trend toward maximizing complexity and utility is to continue at such a brisk pace. The first concern is monetary: augmenting scaffold size while maintaining heterogeneity throughout the structure requires proportionally increasing the number of staple strands. The cost of oligonucleotide synthesis is currently about US $0.10 per base at a 25-nmol scale, which translates into an expense of ~US $700 for creating a new origami structure of the conventional sizes possible through M13mp18 DNA as a scaffold (Pinheiro et al. 2011). In order to create architectures of 10–100 times the current levels of complexity, new synthetic methods are needed that deviate from the classical phosphoramidite chemistry. An emerging technology for "printing" oligonucleotide arrays on high-fidelity microchips has potential for alleviating this concern if used in conjunction with enzymatic amplification (Tian et al. 2009; Kosuri 2010). Use of enzymatic amplification has the additional benefit of scalability for applications that may arise requiring gram to kilogram quantities of an origami structure. Another trial that must be overcome is the absence of kinetic and thermodynamic understanding of how folding occurs during origami formation, such as the order of staple strand association and hybridization rates. Generally, as a structure is increasingly compound, both in size and helical packing as with dense 3D shapes, assembly yields decrease significantly (Douglas et al. 2009a;

Ke et al. 2009b; Yang et al. 2012). Systematic investigations into this area of DNA origami are needed to sustain the advance of structural complexity and achieve finer structural control.

While in vitro methods have been widely applied with great success, it is desirable to develop methods for forming nanostructures in vivo, due to the possibilities for interacting with cellular components, and the ability to produce large quantities of structures by enzymatic means. It has been demonstrated that single-stranded DNA structures using PX crossover motifs can be expressed and folded with fidelity within cells (Fu and Seeman 1993; Lin et al. 2007, 2008). However, few mechanisms exist for creating single-stranded DNA within cells, so techniques such as rolling-circle or reverse-transcription must be used, and to date no full-size origami structures have been produced (Lin et al. 2007, 2008). In contrast, RNA is an attractive option for creating nanostructures in the cell, as it is readily transcribed in single-stranded form (Guo 2010). Controlling tertiary structure is more difficult due to non-Watson–Crick interactions, but some progress has been made by Aldaye and coworkers with assembly of 1D and 2D RNA molecules capable of recruiting proteins and controlling chemical reactions in vivo (Delebecque et al. 2011). Promising results for the stability of DNA nanostructures in vivo have been observed (Douglas et al. 2009b; Mei et al. 2011), so the future of these applications appears to be contingent upon developing more robust methods for their formation.

DNA origami has emerged as an interdisciplinary field, with researchers from different backgrounds contributing to the expedient development of the methods introduced to date. The continued growth will hopefully be aided by the induction of DNA origami techniques into other fields, beyond chemistry, physics, and biology to material sciences, engineering, and computer science. Novel applications have been predicted or are being developed for biomimetic structures, photonics, sensors and diagnostics, targeting and therapeutics, and nano-assembly devices (Pinheiro et al. 2011; Fu et al. 2012b). Looking toward the future, it is clear that DNA origami will be extensively utilized to further the progress of science and technology.

References

Andersen ES, Dong MD, Nielsen MM, Jahn K, Lind-Thomsen A, Mamdouh W, Gothelf KV, Besenbacher F, Kjems J (2008) DNA origami design of dolphin-shaped structures with flexible tails. ACS Nano 2:1213–1218

Andersen ES, Dong M, Nielsen MM et al (2009) Self-assembly of a nanoscale DNA box with a controllable lid. Nature 459:73–75

Anker JN et al (2008) Biosensing with plasmonic nanosensors. Nat Mater 7:442–453

Batey RT, Rambo RP, Doudna JA (1999) Tertiary motifs in RNA structure and folding. Angew Chem Int Ed Engl 38:2326–2343

Bui H, Onodera C, Kidwell C, Tan Y, Graugnard E, Kuang W, Lee J, Knowlton WB, Yurke B, Hughes WL (2010) Programmable periodicity of quantum dot arrays with DNA origami nanotubes. Nano Lett 10:3367–3372

Castro CE, Kilchherr F, Kim DN, Enrique LS, Wauer T, Wortmann P, Bathe M, Dietz H (2011) A primer to scaffolded DNA origami. Nat Methods 8(3):221–229
Chworos A, Severcan I, Koyfman AY, Weinkam P, Oroudjev E, Hansma HG, Jaeger L (2004) Building programmable jigsaw puzzles with RNA. Science 306:2068–2072
Cohen JD, Sadowski JP, Dervan PB (2007) Programming multiple protein patterns on a single DNA nanostructure. J Am Chem Soc 130:402–403
Delebecque CJ, Linder AB, Silber PA, Aldaye FA (2011) Organization of intracellular reactions with rationally designed RNA assemblies. Science 333:470–474
Dietz H, Douglas SM, Shih WM (2009) Folding DNA into twisted and curved nanoscale shapes. Science 325:725–729
Ding B, Deng Z, Yan H, Cabrini S, Zuckermann RN, Bokor J (2010a) Gold nanoparticle self-similar chain structure organized by DNA origami. J Am Chem Soc 132:3248–3249
Ding B, Wu H, Zhao Z, Liu Y, Yu H, Yan H (2010b) Interconnecting gold islands with DNA origami nanotubes. Nano Lett 10:5065–5069
Douglas SM, Chou JJ, Shih WM (2007) DNA-nanotube-induced alignment of membrane proteins for NMR structure determination. Proc Natl Acad Sci USA 104(16):6644–6648
Douglas SM, Dietz H, Liedl T, Hoegberg B, Graf F, Shih WM (2009a) Self-assembly of DNA into nanoscale three-dimensional shapes. Nature 459(7245):414–418
Douglas SM, Marblestone AH, Teerapittayanon S, Vazquez A, Church GM, Shih WM (2009b) Rapid prototyping of 3D DNA-origami shapes with caDNAno. Nucleic Acids Res 37 (15):5001–5006
Du SM, Zhang SW, Seeman NC (1992) Dna junctions, antijunctions, and mesojunctions. Biochemistry 31(45):10955–10963
Endo M, Hidaka K, Kato T, Namba K, Sugiyama H (2009) DNA prism structures constructed by folding of multiple rectangular arms. J Am Chem Soc 131(43):15570–15571
Endo M, Sugita T, Katsuda Y, Hidaka K, Sugiyama H (2010) Programmed-assembly system using DNA jigsaw pieces. Chem Eur J 16:5362–5368
Fu T, Seeman NC (1993) DNA double-crossover molecules. Biochemistry 32(13):3211–3220
Fu J, Liu M, Liu Y, Woodbury NM, Yan H (2012a) Interenzyme substrate diffusion for an enzyme cascade organized on spatially addressable DNA nanostructures. J Am Chem Soc 134:5516–5519
Fu J, Liu M, Liu Y, Yan H (2012b) Spatially-interactive biomolecular networks organized by nucleic acid nanostructures. Acc Chem Res 8:1215–1226
Gu H, Chao J, Xiao SJ, Seeman NC (2010) A proximity-based programmable DNA nanoscale assembly line. Nature 465:202–205
Guo P (2010) The emerging field of RNA technology. Nat Nanotechnol 5:833–842
Han DR, Pal S, Liu Y, Yan H (2010) Folding and cutting DNA into reconfigurable topological nanostructures. Nat Nanotechnol 5:712–717
Han D, Pal S, Nangreave J, Deng Z, Liu Y, Yan H (2011) DNA origami with complex curvatures in three-dimensional space. Science 332:342–346
Högberg B, Leidl T, Shih WM (2009) Folding DNA origami from a double-stranded source of scaffold. J Am Chem Soc 131:9154–9155
Hung AM, Micheel CM, Bozano LD, Osterbur LW, Wallraff GM, Cha JN (2009) Large-area spatially ordered arrays of gold nanoparticles directed by lithographically confined DNA origami. Nat Nanotechnol 5:121–126
Jaeger L (2009) Defining the syntax for self-assembling RNA tertiary architecture. Nucleic Acids Symp Ser 53:83–84
Jahn K, Tørring T, Voigt NV, Sørensen RS, Kodal ALB, Andersen ES, Gothelf KV, Kjems J (2011) Functional patterning of DNA origami by parallel enzymatic modification. Bioconjug Chem 22:819–823
Jungmann R, Steinhauer C, Scheible M, Kuzyk A, Tinnefeld P, Simmel FC (2010) Single-molecule kinetics and super-resolution microscopy by fluorescence imaging of transient binding on DNA origami. Nano Lett 10:4756–4761

Ke Y, Lindsay S, Chang Y, Liu Y, Yan H (2008) Self-assembled water-soluble nucleic acid probe tiles for label-free RNA hybridization assays. Science 319:180–183
Ke Y, Sharma J, Liu M, Jahn K, Liu Y, Yan H (2009a) Scaffolded DNA origami of a DNA tetrahedron molecular container. Nano Lett 9(6):2445–2447
Ke Y, Douglas SM, Liu M et al (2009b) Multilayer DNA origami packed on a square lattice. J Am Chem Soc 131(43):15903–15908
Ke Y, Ong LL, Shih WM, Yin P (2012) Three-dimensional structures self-assembled from DNA bricks. Science 338:1177–1183
Kim D, Kilchherr F, Dietz H, Bathe M (2012) Quantitative prediction of 3D solution shape and flexibility of nucleic acid nanostructures. Nucleic Acids Res 40(7):2862–2868
Ko SH, Su M, Zhang C, Ribbe AE, Jiang W, Mao C (2010) Synergistic self-assembly of RNA and DNA molecules. Nat Chem 2:1050–1055
Kosuri S (2010) Scalable gene synthesis by selective amplification of DNA pools from high-fidelity microchips. Nat Nanotechnol 28:1295–1299
Kuzuya A, Komiyama M (2009) Design and construction of a box-shaped 3D-DNA origami. Chem Commun 28:4182–4184
Kuzuya A, Kimura M, Numajiri K, Koshi N, Ohnishi T, Okada F, Komiyama M (2009) Precisely programmed and robust 2D streptavidin nanoarrays by using periodical nanometer-scale wells embedded in DNA origami assembly. Chembiochem 10:1811–1815
Kuzyk A, Laitinen KT, Torma P (2009) DNA origami as a nanoscale template for protein assembly. Nanotechnology 20:235305
Li Z, Liu M, Wang L, Nangreave J, Yan H, Liu Y (2010) Molecular behavior of DNA origami in higher-order self-assembly. J Am Chem Soc 132(38):13545–13552
Li Z, Wang L, Yan H, Liu Y (2012) Effect of DNA hairpin loops on the twist of planar DNA origami tiles. Langmuir 28(4):1959–1965
Liedl T, Högberg B, Tytell J, Ingber DE, Shih WM (2010) Self-assembly of three-dimensional prestressed tensegrity structures from DNA. Nat Nanotechnol 5:520–524
Lin C, Rinker S, Wang X, Liu Y, Seeman NC, Yan H (2007) Rolling circle enzymatic replication of a complex multi-crossover DNA nanostructure. J Am Chem Soc 129:14475–14481
Lin C, Rinker S, Wang X, Liu Y, Seeman NC, Yan H (2008) In vivo cloning of artificial DNA nanostructures. Proc Natl Acad Sci USA 105:17626–17631
Liu J, Geng Y, Pound E, Gyawali S, Ashton JR, Hickey J, Woolley AT, Harb JH (2001) Metallization of branched DNA origami for nanoelectronic circuit fabrication. ACS Nano 5 (3):2240–2247
Liu D, Wang M, Deng Z, Walulu R, Mao C (2004) Tensegrity: construction of rigid DNA triangles with flexible four-arm DNA junctions. J Am Chem Soc 126(8):2324–2325
Liu H, Tørring T, Dong M, Rosen CB, Besenbacher F, Gothelf KV (2010) DNA-templated covalent coupling of G4 PAMAM dendrimers. J Am Chem Soc 132:18054–18056
Liu W, Zhong H, Wang R, Seeman NC (2011) Crystalline two-dimensional DNA-origami arrays. Angew Chem Int Ed Engl 50:264–267
Lund K, Manzo AJ, Dabby N, Michelotti N, Johnson-Buck A, Nangreave J, Taylor S, Pei R, Stojanovic MN, Walter NG, Winfree E, Yan H (2010) Molecular robots guided by prescriptive landscapes. Nature 465:206–210
Maier SA et al (2003) Local detection of electromagnetic energy transport below the diffraction limit in metal nanoparticle plasmon waveguides. Nat Mater 2:229–232
Majumder U, Rangnekar A, Gothelf KV, Reif JH, LaBean TH (2011) Design and construction of a double-decker tile as a route to three-dimensional periodic assembly of DNA. J Am Chem Soc 133:3843–3845
Mao C, Sun W, Seeman NC (1999a) Designed two-dimensional DNA Holliday junction arrays visualized by atomic force microscopy. J Am Chem Soc 121(23):5437–5442
Mao C, Sun W, Shen Z, Seeman NC (1999b) A nanomechanical device based on the B-Z transition of DNA. Nature 397:144–146

Maune HT, Han SP, Barish RD, Bockrath M, Goddard WA, Rothemund PWK, Winfree E (2010) Self-assembly of carbon nanotubes into two-dimensional geometries using DNA origami templates. Nat Nanotechnol 5:61–66

Mei Q, Wei X, Su F, Liu Y, Youngbull C, Johnson R, Lindsay S, Yan H, Meldrum D (2011) Stability of DNA origami nanoarrays in cell lysate. Nano Lett 11:1477–1482

Nakata E, Liew FF, Uwatoko C, Kiyonaka S, Mori Y, Katsuda Y, Endo M, Sugiyama H, Morii T (2012) Zinc-finger proteins for site-specific protein positioning on DNA-origami structures. Angew Chem Int Ed Engl 51:2421–2424

Numajiri K, Kimura M, Kuzuya A, Komiyama M (2010a) Stepwise and reversible nanopatterning of proteins on a DNA origami scaffold. Chem Commun 46:5127–5129

Numajiri K, Yamazaki T, Kimura M, Kuzuya A, Komiyama M (2010b) Discrete and active enzyme nanoarrays on DNA origami scaffolds purified by affinity tag separation. J Am Chem Soc 132:9937–9939

Ozbay E (2006) Plasmonics: merging photonics and electronics at nanoscale dimensions. Science 311:189–193

Pal S, Sharma J, Yan H, Liu Y (2009) Stable silver nanoparticle-DNA conjugates for directed self-assembly of core-satellite silver-gold nanoclusters. Chem Commun (Camb) (40):6059–6061

Pal S, Varghese R, Deng Z, Zhao Z, Kumar A, Yan H, Liu Y (2011) Site-specific synthesis and in situ immobilization of fluorescent silver nanoclusters on DNA nanoscaffolds by use of the Tollens reaction. Angew Chem Int Ed Engl 50:4176–4179

Pinheiro AV, Han D, Shih WM, Yan H (2011) Challenges and opportunities for structural DNA nanotechnology. Nat Nanotechnol 6(12):763–772

Pound E, Ashton JR, Becerril HA, Woolley AT (2009) Polymerase chain reaction based scaffold preparation for the production of thin, branched DNA origami nanostructures of arbitrary sizes. Nano Lett 9(12):4302–4305

Rinker S, Ke Y, Liu Y, Chhabra Y, Yan H (2008) Self-assembled DNA nanostructures for distance dependent multivalent ligand-protein binding. Nat Nanotechnol 3(7):418–422

Rothemund P (2006) Folding DNA, to create nanoscale shapes and patterns. Nature 440:297–302

Rothemund PWK, Papadakis N, Winfree E (2004) Algorithmic self-assembly of DNA sierpinski triangles. PLoS Biol 2(12):2041–2053

Saaem I, Kuo-Sheng M, Marchi AN, LaBean TH, Tian J (2010) In situ synthesis of DNA microarray on functionalized cyclic olefin copolymer substrate. ACS Appl Mater Interfaces 2:491–497

Sacca B, Meyer R, Erkelenz M, Kiko K, Arndt A, Schroeder H, Rabe KS, Niemeyer CM (2010) Orthogonal protein decoration of DNA origami. Angew Chem Int Ed Engl 49:9378–9383

Schuller JA et al (2010) Plasmonics for extreme light concentration and manipulation. Nat Mater 9:193–204

Severcan I, Geary C, Verzemnieks E, Chworos A, Jaeger L (2009) Square-shaped RNA particles from different RNA folds. Nano Lett 9(3):1270–1277

Sharma J, Chhabra R, Andersen CS, Gothelf KV, Yan H, Liu Y (2008) Toward reliable gold nanoparticle patterning on self-assembled DNA nanoscaffold. J Am Chem Soc 130:7820–7821

Sharonov A, Hochstrasser RM (2006) Wide-field subdiffraction imaging by accumulated binding of diffusing probes. Proc Natl Acad Sci USA 103:18911–18916

Shen W, Zhong H, Neff D, Norton ML (2009) NTA directed protein nanopatterning on DNA origami nanoconstructs. J Am Chem Soc 131:6660–6661

Shih W, Quispe J, Joyce G (2004) A 1.7-kilobase single-stranded DNA that folds into a nanoscale octahedron. Nature 427(6975):618–621

Shipway AN, Katz E, Willner I (2000) Nanoparticle arrays on surfaces for electronic, optical, and sensor applications. Chemphyschem 1:18–52

Snelson K (1996) Snelson on the tensegrity invention. Int J Space Struct 11:43–48

Stearns LA, Chhabra R, Sharma J, Liu Y, Petuskey WT, Yan H, Chaput JC (2009) Template-directed nucleation and growth of inorganic nanoparticles on DNA scaffolds. Angew Chem Int Ed Engl 48:8494–8496

Stein IH, Schüller V, Böhm P, Tinnefeld P, Liedl T (2011a) Single-molecule FRET ruler based on rigid DNA origami blocks. Chemphyschem 12:689–695
Stein IH, Steinhauer C, Tinnefeld P (2011b) Single-molecule four-color FRET visualizes energy-transfer paths on DNA origami. J Am Chem Soc 133:4193–4195
Steinhauer C, Jungmann R, Sobey TL, Simmel FC, Tinnefeld P (2009) DNA origami as a nanoscopic ruler for super-resolution microscopy. Angew Chem Int Ed Engl 48:8870–8873
Stephanopoulos N, Liu MH, Tong GJ, Li Z, Liu Y, Yan H, Francis MB (2010) Immobilization and one-dimensional arrangement of virus capsids with nanoscale precision using DNA origami. Nano Lett 10:2714–2720
Subramani R, Juul S, Rotaru A, Andersen FF, Gothelf KV, Mamdouh W, Besenbacher F, Dong M, Knudsen BR (2010) A novel secondary DNA binding site in human topoisomerase I unravelled by using a 2D DNA origami platform. ACS Nano 4:5969–5977
Subramanian HKK, Chakraborty B, Sha R, Seeman NC (2011) The label-free unambiguous detection and symbolic display of single nucleotide polymorphisms on DNA origami. Nano Lett 11:910–913
Thomas T, Voigt NV, Nangreave J, Yan H, Gothelf KV (2011) DNA origami: a quantum leap for self-assembly of complex structures. Chem Soc Rev 40(12):5636–5646
Tian J, Ma K, Saaem I (2009) Advancing high-throughput assembly of nanoclusters. Mol Biosyst 5:714–722
Tikhomirov G, Hoogland S, Lee PE, Fischer A, Sargent EH, Kelley SO (2011) DNA-based programming of quantum dot valency, self-assembly and luminescence. Nat Nanotechnol 6:485–490
Voigt NV, Tørring T, Rotaru A, Jacobsen MF, Rabnsbæk JB, Subramani R, Mamdouh W, Kjems J, Mokhir A, Besenbacher F, Gothelf KV (2010) Single-molecule chemical reactions on DNA origami. Nat Nanotechnol 5:200–203
Wei B, Dai M, Yin P (2012) Complex shapes self-assembled from single-stranded DNA tiles. Nature 485:623–627
Westhof E, Masquida B, Jaeger L (1996) RNA tectonics: towards RNA design. Fold Des 1: R78–R88
Wickham SF, Endo M, Katsuda Y, Hidaka K, Bath J, Sugiyama H, Turberfield AJ (2011) Direct observation of stepwise movement of a synthetic molecular transporter. Nat Nanotechnol 6:166–169
Williams S, Lund K, Lin C, Wonka P, Lindsay S, Yan H (2009) Tiamat: a three-dimensional editing tool for complex DNA structures. Lect Notes Comp Sci 5347:90–101
Woo S, Rothemund PWK (2011) Programmable molecular recognition based on the geometry of DNA nanostructures. Nat Chem 3:620–627
Yan H, LaBean TH, Feng L, Reif JH (2003) Directed nucleation assembly of DNA tile complexes for barcode-patterned lattices. Proc Natl Acad Sci USA 100(14):1803–1808
Yang Y, Han D, Nangreave J, Liu Y, Yan H (2012) DNA origami with double-stranded DNA as a unified scaffold. ACS Nano 6(9):8209–8215
Yoshidome T, Endo M, Kashiwazaki G, Hidaka K, Bando T, Sugiyama H (2012) Sequence-selective single-molecule alkylation with a pyrrole-imidazole polyamide visualized in a DNA nanoscaffold. J Am Chem Soc 134:4654–4660
Zhang Z, Zeng D, Ma H, Feng G, Hu J, He L, Li C, Fan C (2010) A DNA-origami chip platform for label-free SNP genotyping using toehold-mediated strand displacement. Small 6(17):1854–1858
Zhang H, Chao J, Pan D, Liu H, Huang Q, Fan C (2012) Folding super-sized DNA origami with scaffold strands from long-range PCR. Chem Commun 48:6405–6407
Zhao Z, Yan H, Liu Y (2010) A route to scale up DNA origami using DNA tiles as folding staples. Angew Chem Int Ed Engl 49:1414–1417
Zheng Y, Li Y, Deng Z (2012) Silver nanoparticle-DNA bionanoconjugates bearing a discrete number of DNA ligands. Chem Commun 48:6160–6162

Chapter 6
DNA Nanotechnology: From Biology and Beyond

Chunhua Liu and Andrew D. Ellington

Abstract Over the past three decades, tremendous progress has been made in our understanding of how to use DNA molecules to design and construct intricate nanostructures and nanodevices and how to use these nanoconstructs as versatile tools to functionally arrange a variety of molecules and moieties with nanometer spatial resolution. This chapter summarizes recent development in DNA nanotechnology and addresses its potential applications in drug delivery, analysis and diagnosis, electronics, and photovoltaics.

Contents

C. Liu • A.D. Ellington (✉)
Center for Systems and Synthetic Biology, Institute for Cellular and Molecular Biology, University of Texas at Austin, Austin, TX, USA

Department of Chemistry and Biochemistry, University of Texas at Austin, Austin, TX 78712, USA
e-mail: cl660@utexas.edu; andy.ellington@mail.utexas.edu

J. KJEMS et al. (eds.), *Nucleic Acid Nanotechnology*, Nucleic Acids and Molecular Biology 29, DOI 10.1007/978-3-642-38815-6_6,

Abbreviations

ADP	Adenosine diphosphate
aTAM	abstract Tile Assembly Model
ATP	Adenosine triphosphate
CHA	Catalyzed hairpin assembly
CpG	Cytosine-phosphate-guanine
DX	Double crossover
FRET	Fluorescence resonance energy transfer
GMP	Good manufacturing practice
GOx	Glucose oxidase
HB	Helix bundle
HCR	Hybridization chain reaction
HRP	Horseradish peroxidase
IHF	Integration host factor
JX_2	A topoisomer of PX molecule, one end of JX_2 rotates 180° relative to the PX molecule, producing two juxtaposed duplexes without crossovers in the middle
kTAM	kinetic Tile Assembly Model
LAMP	Loop-mediated isothermal amplification
OLED	Organic light-emitting diodes
PDGF	Platelet-derived growth factor
PX	Paranemic crossover
ssDNA	Single-stranded DNA
SST	Single-stranded tile
STV	Streptavidin
TLR9	Toll-like receptor 9
TX	Triple crossover

6.1 Structural DNA Nanotechnology

Structural DNA nanotechnology refers to use of DNA as a material for the design and construction of objects with topological or geometrical features (Seeman 2003). The discipline was originally devised to facilitate the crystallization of macromolecules, such as proteins (Seeman 1982), by using DNA lattices as scaffolds and intercalating and orienting "guest" molecules in individual units in the lattice. In essence, an organized DNA lattice would have replaced the protein crystal lattice for X-ray determination of protein structures (Seeman 1982, 1999, 2003) (Fig. 6.1), a goal that has yet to be fully realized. Nevertheless, the power of nucleic acid nanotechnology for controlling the structure of matter in 3D to the highest extent (resolution) possible provides a unique means for understanding connections between the organization of matter from the molecular to the macroscopic scale (Seeman 1982).

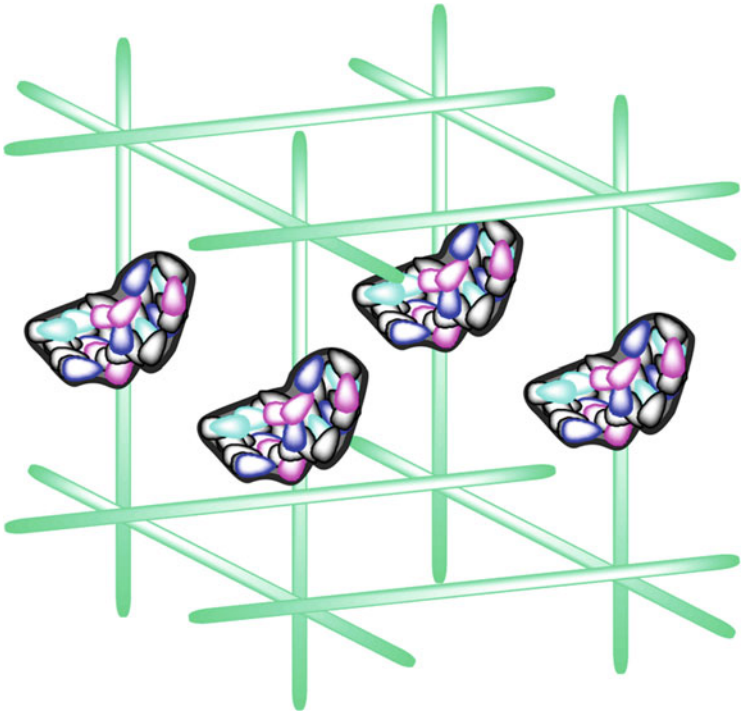

Fig. 6.1 Original proposed application of DNA scaffolds for macromolecular crystallization (Seeman 1982, 1999, 2003). An infinite 3D DNA scaffold assembled from six-armed branched junctions is shown in *green*. The *kidney-shaped objects* represent guest molecules that could be organized in a parallel fashion within each unit of the scaffold for structure determination by X-ray crystallography

6.1.1 Bottom-Up Self-Assembly

The bottom-up assembly of nanostructures proposes the use of smaller elements for the construction of larger and more complex systems, often in an atom-by-atom or molecule-by-molecule manner (Drexler 1981; Drexler and Peterson 1989). One of the most efficient bottom-up strategies is self-assembly, which can be defined as a process in which disordered subunits autonomously organize into ordered structures without external intervention (Lehn 1990; Whitesides and Grzybowski 2002). Bottom-up self-assembly methods usually rely on weak, reversible interactions, such as hydrogen bonding, hydrophobic effects, van der Waals forces, π–π stacking, electrostatic interactions, and/or steric effects (Whitesides et al. 1991; Whitesides and Grzybowski 2002). Relatively weak covalent bonding, such as coordination bonding, is also a possible route to self-assembly (Fyfe and Stoddart 1997; Lehn 2002; Whitesides and Grzybowski 2002).

The advantages of bottom-up self-assembly stem from the power of molecular recognition and complementary interactions, which enable systems to be designed such that assembly is programmable. Programmability has three advantages: first,

there can be virtually atomic precision in the construction of objects; second, the order of assembly can be manipulated so as to progressively yield increasing structural and functional complexity; and finally, if the building process is designed to occur spontaneously, the overall free energy of the objects produced should be minimized, thereby potentially reducing the introduction of defects (Whitesides et al. 1991).

6.1.2 DNA as a Building Block for Nanoconstruction

Nature currently displays the most complex self-assembled constructions. Monomer subunits (such as nucleotides, amino acids, and lipids) are joined to form folded polymers or aggregated assemblies (such as DNA, RNA, proteins, and membranes) which in turn self-assemble or mediate self-assembly into larger functional structures (such as ribosomes, cells, and organisms). However, while nucleic acids are the blueprint for such constructions, DNA per se is not used as the structural building block in most systems. Rather, it is an informational macromolecule that underlies the construction of mostly amorphous objects. While it is possible to use the DNA double helix to create precision nanostructures, DNA nanoconstruction is a decidedly nonnatural process, although many of its principles are inspired by biological networks. Understanding the fundamental chemical, physical, and mechanical mechanisms associated with DNA nanotechnology is thus a wholly new scientific and technological undertaking.

The programmability of Watson–Crick base pairing (Watson and Crick 1953) and sticky-end cohesion (Cohen et al. 1973) has led to the wide use of DNA for building nano-objects. For nanotechnology, it is of great importance to maximize control over the size and shape of nanostructures, in order to obtain tunable and functional nanosystems by rational design. Initially, DNA nanostructures were generated from stiff building blocks that were themselves composed of specific intermolecular interactions that formed predictable local structures (Liu et al. 1994). For example, a variety of rigid linear and branched DNA motifs (e.g., Fu and Seeman 1993; LaBean et al. 2000) have enabled the programmability and self-assembly of well-defined DNA topologies and structures, as we shall further explore below. The advance of DNA nanotechnology has been abetted by ever-improving control over both chemical and enzymatic DNA synthesis and modification.

6.1.2.1 Branched DNA Molecules

The DNA double helix is topologically unbranched, which makes it somewhat incompatible with building complex multidimensional architectures. The design of unconventional DNA motifs for structural and functional purposes has thus been a first goal of paramount importance. While overall the notion of DNA nanotechnology is more chemical than biological, branched DNA motifs can be found at least

transiently in nature, such as the Holliday junction (Holliday 1964) and the Gierer cruciform structure (Gierer 1966). Based on these ephemeral structures, the Seeman group had the key insight that similar, immobile DNA junctions might be designed by minimizing the sequence symmetry so as to preclude branch migration (Seeman 1982; Seeman and Kallenbach 1983). To this end, a sequence-symmetry minimization algorithm was devised (Seeman 1990), and the resultant predicted structures were realized with chemically synthesized oligonucleotides. The construction of branched DNA junctions flanked by different numbers of arms (Ma et al. 1986; Kallenbach et al. 1983; Wang et al. 1991; Wang and Seeman 2007; Yin et al. 2008a) has accordingly been accomplished.

6.1.2.2 Rigid Branched DNA Molecules

Multiarmed, branched DNA molecules are relatively flexible and have therefore proven to be a difficult subunit for higher-ordered constructions, such as the generation of periodic 2D or 3D objects. Fortunately, reciprocal strand exchange (Seeman 2001) opened an opportunity for generating stiffer branched DNA motifs. A general procedure for the derivation of new DNA motifs entails nicking two juxtaposed DNA molecules and then reassociating the nicked strands to create new nodes (Seeman 2001). Different motifs can be obtained by executing different numbers of reciprocal exchanges between the strands of double-stranded DNA molecules. This approach has led to the construction of a variety of base motifs, such as the double crossover (DX) (Fu and Seeman 1993), triple crossover (TX) (LaBean et al. 2000; Liu et al. 2008), and paranemic crossover (PX) molecules (Shen 1999).

These branched DNA motifs have in turn been used to construct a variety of stiffened six- (Mathieu et al. 2005; Wang 2007; Kuzuya et al. 2007), eight- (Wang 2007; Kuzuya et al. 2007), and nine-helix bundles (Wang 2007); tensegrity triangles (Liu et al. 2004a; Zheng et al. 2006; Constantinou et al. 2006); and deltahedra (Shih et al. 2004; Goodman et al. 2005). Ultimately, the surety provided by engineering with rigid structural motifs has proven central to the ability to construct high-dimension nanostructures (Winfree et al. 1998; Shih et al. 2004), nanomechanical devices (Mao et al. 1999a; Yan et al. 2002; Liu et al. 2009, 2012a), and algorithmic patterns (e.g., Winfree 2000; Mao et al. 2000; Rothemund et al. 2004; Fujibayashi et al. 2008).

6.1.3 Self-Assembled Structures and Arrays

6.1.3.1 Regular Nanoconstruction

By combining sticky-end cohesion, enzymatic ligation, and branched DNA motifs, the construction of defined, intricate objects has become routine. For example, a quadrilateral structure could be formed by ligating together four immobile junctions

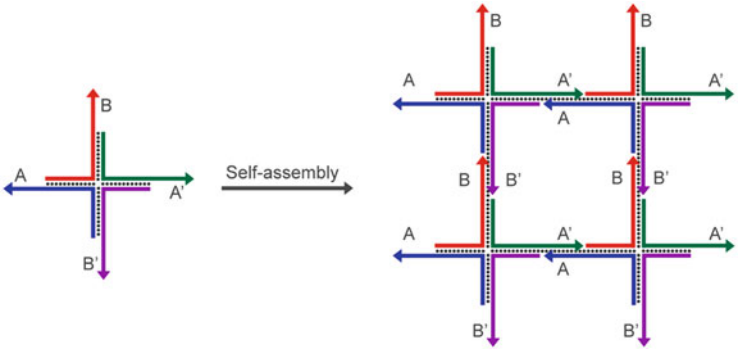

Fig. 6.2 Self-assembly of branched junctions (Seeman 1982, 1991, 2003). An immobile branched junction with sticky ends A, its complement A′, B, and its complement B′ form a quadrilateral through sticky-ended cohesion and ligation. The open valences of the quadrilateral allow it to be extended to 2D or possibly 3D lattices

(Seeman 1982), and that could in turn be organized into 2D or 3D networks via sticky-end assembly (Seeman 1982, 1991, 2003) (Fig. 6.2).

A wide variety of 1D to 3D DNA objects has now been constructed. In the single dimension, organized DNA arrays (Yang et al. 1998b; Mao et al. 1999b; Yan et al. 2003a, b; Liu et al. 2004b; Mathieu et al. 2005; Kuzuya et al. 2007) have been developed, including a 1D DNA tube made from a DX-based single-stranded system (Liu et al. 2006a), a 1D arrangement constructed with PX-JX_2 and PX triangles to characterize the reciprocal motions of the PX-JX_2-containing systems (Liu et al. 2009), and a 1D pattern designed with the sheathing structures of six-helix bundles (6-HBs) connected by a sheathed double helix (Wang et al. 2009).

Periodic or aperiodic 2D DNA lattices have been constructed using various DNA motifs, such as DX (Winfree et al. 1998; Liu et al. 1999; Ding et al. 2004), TX (LaBean et al. 2000), parallelograms (Mao et al. 1999b; Sha et al. 2000, 2002; Feng et al. 2003), 4 × 4 cross-shaped DX (Yan et al. 2003a; Liu et al. 2005a; He et al. 2005a; Park et al. 2006), helix bundles (Mathieu et al. 2005; Wang 2007), three-point stars (He et al. 2005b), five-point stars (Zhang et al. 2009), and six-point stars (He et al. 2006). Artificial 3D DNA constructs have been manufactured involving cubes (Chen and Seeman 1991; Zhang et al. 2009), truncated octahedra (Zhang and Seeman 1994), Borromean rings (Mao et al. 1997), tetrahedra (Goodman et al. 2005; He et al. 2008), trigonal bipyramids (Erben et al. 2007), dodecahedra (He et al. 2008), icosahedra (Zhang et al. 2009), buckyballs (He et al. 2008), sphere-like cages (Zhang et al. 2009), and tubes (Liu et al. 2006a). These objects need not be confined to the nanoscale.

While for the most part these shapes have been constructed from small oligonucleotides, it has also proven possible to program long, single-stranded DNA (ssDNA) to fold into regular structures. For example, an octahedron was generated from a single 1.7 kilobase ssDNA (Shih et al. 2004). This concept was extended to the design and construction of a Holliday junction, a paranemic

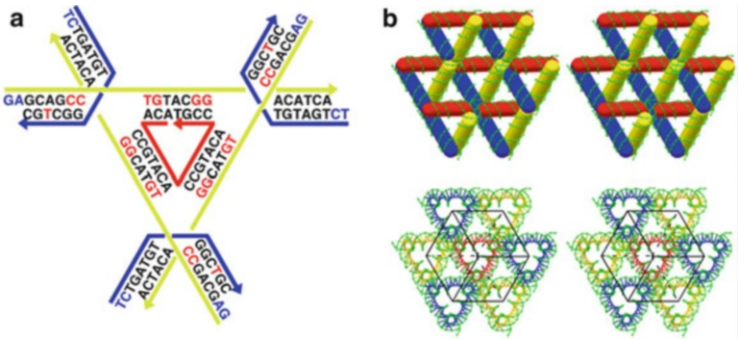

Fig. 6.3 A crystalline 3D lattice formed by *tensegrity triangles* (Zheng et al. 2009). (**a**) The designed structure of the *tensegrity triangle*. *Arrowheads* represent the 3′ ends of the strands. The A-DNA-like nucleotides are displayed in *red characters*. The sticky ends are displayed in *blue*. (**b**) The corresponding self-assembled crystalline 3D lattice. In the *upper panel*, the stereoscopic image shows the surroundings of the *triangle*. The three directions are shown in *blue*, *yellow*, and *red*. The *central triangle* is flanked by six other *triangles*. In the *lower panel*, the stereoscopic image displays a rhombohedral cavity formed by the *tensegrity triangles*. The sketch of the cavity is shown in *black*. Each corner of the rhombohedron contains a *triangle*; seven of the eight *triangles* are shown here. The *rear red triangle* connects through one edge each to the three *yellow triangles* in a plane closer to the viewer. The *yellow triangles* are connected through two edges each to two different *blue triangles* that are even nearer to the viewer. For clarity, the eighth *triangle*, which is the closest to the viewer, is not shown. This figure was generated by GIDEON, a program for designing and analyzing complex DNA structures (Birac et al. 2006)

crossover, and a tetrahedron all from a single length of DNA (Lin et al. 2008; Li et al. 2009). It was also demonstrated that these artificial ssDNA nanostructures can be replicated efficiently in vivo (Lin et al. 2008; Li et al. 2009).

Beyond two dimensions, a 3D crystal (Zheng et al. 2009) (Fig. 6.3a, b) based on the DNA tensegrity triangle (Liu et al. 2004a) was designed, grown, and analyzed by X-ray diffraction (to 4 Å). This was a significant achievement toward the original goal of using DNA lattices as scaffolds for biological macromolecular crystallography (Seeman 1982). However, while defined subunits ultimately yielded crystalline structures, the rigidity and design principles that led to this achievement were not the only route that could have been taken. For example, a 13-nt DNA molecule that could form continuous 3D lattices was identified in a random screen for oligonucleotides that could crystallize (Paukstelis et al. 2004). Interestingly, the individual antiparallel double helices contained mispairs and were linked by parallel homopurine base pairing. Expansions of these 3D DNA lattices were later used as molecular sieves for different size proteins (Paukstelis 2006).

This fortuitous lattice structure emphasizes that conventional Watson–Crick programmability may not be the only route to DNA nanostructures and that many other interactions can potentially be exploited, including reverse Watson–Crick, Hoogsteen, reverse Hoogsteen, wobble, and reverse wobble interactions, embodied in the form of triplex, I-motif, G-quadruplex, A-form duplex, Z-form duplex structures, and so on. In this regard, nanostructures containing a left-handed

Z-DNA (Rich et al. 1984; Mao et al. 1999a) and a pH-sensitive I-motif (Modi et al. 2009) have been generated. The formation of expanded 3D DNA crystals involving noncanonical junctions formed by parallel-stranded homobase pairs has also been demonstrated (Muser and Paukstelis 2012).

6.1.3.2 Irregular Nanoconstruction

Most of the nanostructures discussed so far have relied on an "internal logic" of self-assembly, in which each piece directs the addition of another piece, to make the whole. An alternative approach would be to scaffold the object as a whole in some way. Importantly, such an approach could lead to the production of programmed, aperiodic objects. To this end, an aperiodic 2D lattice was constructed using a long DNA single strand with encoded barcodes for assembly (Yan et al. 2003b). This approach was greatly expanded via the revolutionary DNA origami methods developed by Rothemund (2006) [Fig. 6.4a (i)]. Arbitrary two-dimensional shapes [Fig. 6.4a (ii)] were created by using the 7,249-nt single-stranded genomic DNA from the bacteriophage M13mp18 as a scaffold and then "stapling" together particular sequences within the single-stranded DNA with more than 200 short oligonucleotides (Rothemund 2006). Depending on the oligonucleotides used, the same single-stranded scaffold can be folded into 2D shapes ranging from a map of the Western Hemisphere to a five-pointed star (Rothemund 2006).

The DNA origami approach has since been extended to make both regular and irregular 3D DNA architectures. For example, single-layer origami sheets have been folded to make 6-HBs (Douglas et al. 2007), prisms with different faces (Endo et al. 2009), and 3D cages, such as a DNA tetrahedron with internal cavity of about 1.5×10^{-23} m^3 (Ke et al. 2009a), a DNA box of $42 \times 36 \times 36$ nm^3 in size with a lid (Andersen et al. 2009) [Fig. 6.4b (i), (ii)], and a rectangular container with origami walls (Kuzuya and Komiyama 2009). Theoretically, DNA origami can be designed to create arbitrarily intricate shapes. To this end, templates larger than the M13 bacteriophage are being examined, such as λ-bacteriophage (Keren et al. 2002; Deng and Mao 2003; Guan and Lee 2005; Yang et al. 2012).

Single-layer origami sheets can be folded and stacked upon each other to generate multilayer origami sheets. The cross section of the DNA helices in a multilayer structure can be packed onto a honeycomb lattice (Douglas et al. 2009) [Fig. 6.5a (i), (ii)] or a square lattice (Ke et al. 2009b) [Fig. 6.5b (i)–(iii)]. The multilayer origami sheets can then be further organized into more rigid and complicated 3D shapes. For example, DNA curvature can be controlled by systematically introducing bending and twisting into the assembled nanostructures (Dietz et al. 2009). Right- or left-handed global twists can be created by increasing or reducing the number of base pairs at selected positions along the helical building blocks, and global bending [e.g., Fig. 6.5a (iii)] can be generated by the combination of base-pair deletions and base-pair insertions. Additionally, high curvature DNA nanostructures, such as 3D spherical shells, ellipsoidal shells, and a nanoflask, have been assembled using a different design strategy (Han et al. 2011): by adjusting the number of turns in concentric DNA

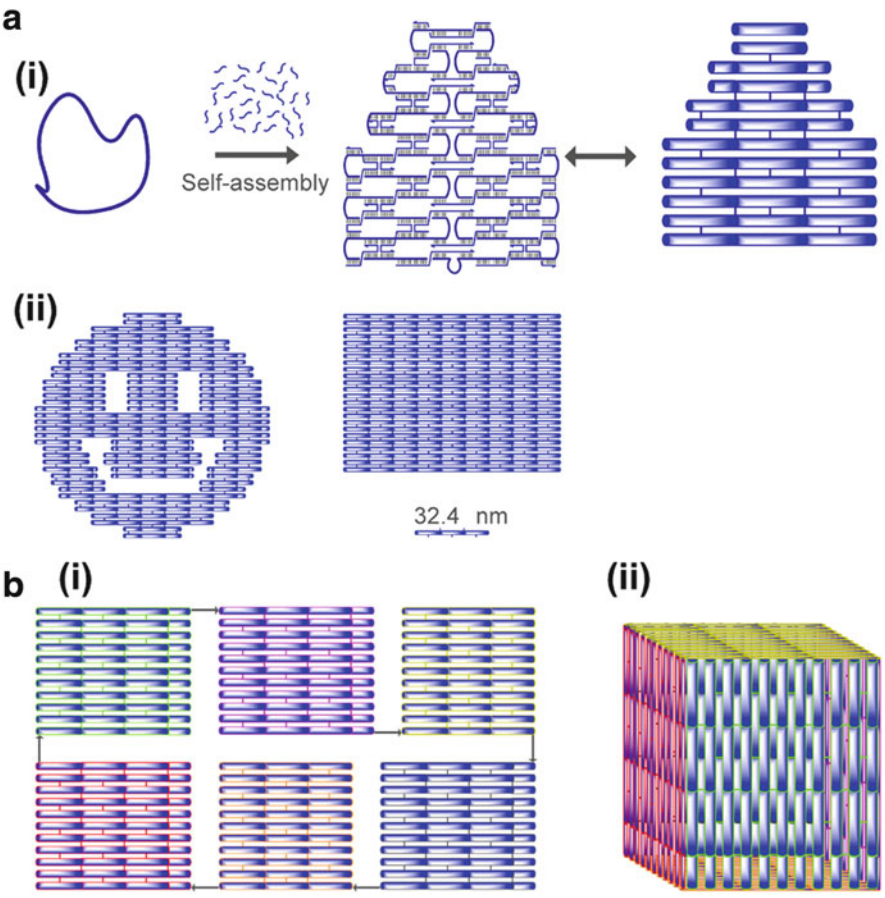

Fig. 6.4 Single-layer DNA origami. (**a**) Scheme and examples of planar, single-layer DNA origami (Rothemund 2006). (**i**) The design principle. A long ssDNA (in *dark blue*) is folded into shapes and held by multiple staple strands (in *light blue*). The folding principle is shown in the *left* and *middle panels*; an abstract model is shown in the *right panel*. (**ii**) Selected examples of the planar, single-layer DNA origami shapes, including a *smiley face* (Rothemund 2006) and a *rectangle* (Rothemund 2006). (**b**) A 3D DNA cube with a controllable lid formed by folding single-layer DNA origami (Andersen et al. 2009). (**i**) An abstract model of the six DNA sheets shown in different colors in a planar fashion. (**ii**) An abstract model of the 3D DNA cube (closed state) with the external size of 42 × 36 × 36 nm^3. All *cylinders* in this figure represent DNA double helices

circles, the in-plane curvature [Fig. 6.5c (i)] can be modulated, while by changing the particular position and pattern of crossovers between adjacent DNA double helices, the out-of-plane curvature [Fig. 6.5c (ii)] can be similarly controlled. Overall, by gradually manipulating the in-plane and out-of-plane curvature, complex 3D DNA nanostructures [e.g., Fig. 6.5c (iii)] can be designed and then built to the design specifications.

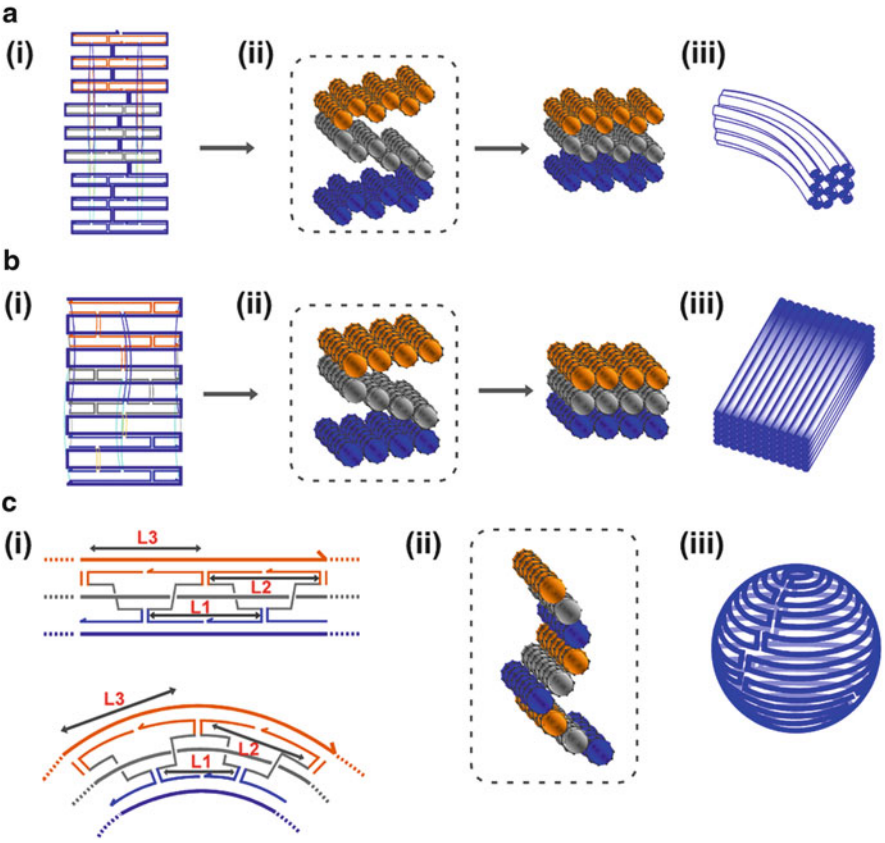

Fig. 6.5 Three-dimensional DNA origami with multiple layers (Douglas et al. 2009; Ke et al. 2009b) or complex curvatures (Han et al. 2011). (**a**) Multilayer DNA origami based on a honeycomb lattice (Douglas et al. 2009). (**i**) A two-dimensional scheme of a three-layer origami with a honeycomb-lattice cross section. This design contains 18 double helices composed of a scaffold (*dark blue*) and staple strands (*orange*, *gray*, *dark blue*). Different layers are connected by crossovers within staple strands shown by *colored arcs*. (**ii**) Molecular models of a 3-by-6 helical bundle. *Left*: an intermediate that is not completely folded. *Right*: the target structure that is fully folded. (**iii**) A selected example showing the bending of a 3-by-6 helical bundle by the combination of base-pair insertions and deletions (Dietz et al. 2009). (**b**) Multilayer DNA origami based on a square lattice (Ke et al. 2009b). (**i**) A two-dimensional scheme of a three-layer origami with a square-lattice cross section. This design contains 12 double helices composed of a scaffold (*dark blue*) and staple strands (*orange*, *gray*, *dark blue*). Different layers are connected by crossovers within staple strands shown by *colored arcs*. (**ii**) Molecular models of a 3-by-4 helical bundle. *Left*: an intermediate that is not completely folded. *Right*: the target structure that is fully folded. (**iii**) A selected example of a 6-by-12 helical bundle ($27 \times 24 \times 12$ nm^3). (**c**) DNA origami with complex curvatures in 3D space (Han et al. 2011). (**i**) Generation of in-plane curvature. *Top*: multiple DNA double helices run parallel to form a straight planar helix bundle. The distances (L1, L2, and L3) between adjacent crossovers connecting neighboring helices remain unchanged and are designed to be the integral number of helical turns. *Bottom*: the straight DNA helix bundle is bent into concentric circles by adjusting the distances L1, L2, and L3 such that the distances between the crossovers in the outer circles are longer than those in the inner circles (L3 > L2 > L1). These distances are not necessarily the integral number of helical turns. (**ii**) Generation of out-of-plane curvature. Multiple DNA double helices are arranged into a *curved shape* by

The use of a templating strand has accelerated progress in the field of DNA nanotechnology. In an interesting and important twist, Yin and coworkers (Yin et al. 2008b; Wei et al. 2012) have further improved this innovation by essentially breaking the template into individual oligonucleotides. These authors developed a single-stranded tile (SST) technique for nanoconstruction that utilizes a large number of 42-nucleotide, unique single-stranded DNA motifs to assemble rationally designed DNA nanostructures by a single-step annealing method. The 42-nucleotide SST motif (Fig. 6.6a) contains four roughly equal-sized domains, each of which can hybridize with four neighboring motifs when folding into a 3 nm $\times$ 7 nm tile (Fig. 6.6b). As with DNA origami, an immense number of objects with different sizes and shapes (e.g., Fig. 6.6c) can be created using the SST strategy. One key advantage of this method is that the same set of SST oligonucleotides can be used to create different shapes by simply including or dropping out sets of oligonucleotide "pixels" at the start of self-assembly.

6.1.3.3 Errors and Their Correction

One concern with using these remarkable DNA nanostructures in practical applications is the limited scale at which they can be generated. This is especially true given that the process of DNA self-assembly is error-prone; understanding the causes of these errors is critical to resolving them and will be extremely important for high scale-up. To date, the best way to understand error rates for self-assembly has been to study algorithmic self-assembly, a way to guide aperiodic DNA 2D crystallization. Two models have been put forth for algorithmic self-assembly: the abstract Tile Assembly Model (aTAM, Winfree 1996, 1998) and the kinetic Tile Assembly Model (kTAM, Winfree 1998). In aTAM, the starting point is a set of square tiles that are similar to mathematical objects known as Wang tiles (Wang 1961, 1962), each containing four labeled edges with associated affinity named strengths. Beginning with a seed structure, the tiles will fill in the spaces next to the existing structure one by one when the combined strength of matched labels reaches at least a certain "temperature," T (Winfree 1998). The limitation of this model is that it ignores the kinetics of reversible tile association and dissociation and thus cannot reflect the effects of environment, such as tile concentration and temperature, on array growth and error rates. kTAM (Winfree 1998) was devised to address this limitation. In this model, free tiles attach to a given position at a rate r_f, which is proportional to their concentration, and the dissociation rate r_r, which depends on

Fig. 6.5 (continued) adjusting the dihedral angles between the planes defined by adjacent double-helical bundles. The dihedral angles are roughly designed to be the integral number of 34°, an angle corresponding to individual nucleotides. (**iii**) A selected example of a 3D sphere (42 $\times$ 42 $\times$ 42 nm^3) constructed by the combination of in-plane and out-of-plane curvatures. All molecular models in this figure were generated by GIDEON (Birac et al. 2006). All *cylinders* in this figure represent DNA double helices

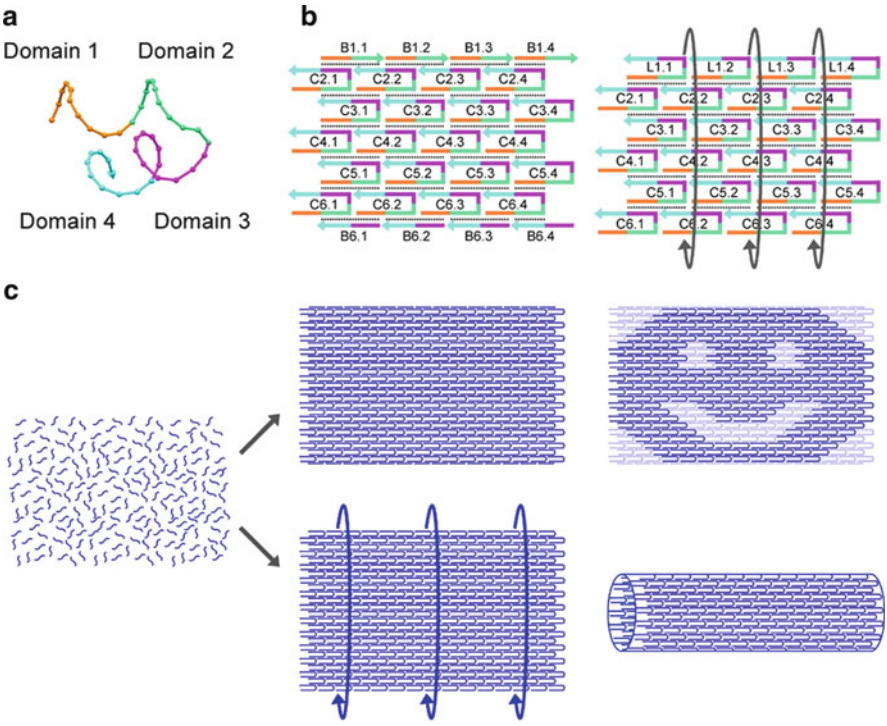

Fig. 6.6 Self-assembly of arbitrary shapes using the single-stranded tile (SST) method (Yin et al. 2008b; Wei et al. 2012). (**a**) SST motif. The 42-nt SST motif contains four domains, each composed of 10 or 11 nt. (**b**) The design principle of a planar structure (*left*) and a tube structure (*right*). Each full tile (42-nt) in the core section of the planar and tube structures is labeled with C. Each half tile (21-nt) in the top and bottom edge sections of a planar structure is labeled with B. Each full tile (42-nt) in the top edge section of a tube structure is labeled with L. (**c**) Selected examples of arbitrary shapes, including a *rectangle*, a *smiley face*, and a *tube* (Wei et al. 2012)

the number and strength of interactions in the array. This model allows for the formation of kinetic traps and predicts a balance between the error rate and the speed of self-assembly (Winfree 1998).

An experimental example of algorithmic self-assembly is the generation of so-called Sierpinski triangles (a type of Wang tile) using DNA, which computationally fulfills all the necessary mechanisms for the molecular implementation of arbitrary cellular automata (Rothemund et al. 2004). In this case, the tiles are represented by DNA DX motifs, and the interacting tile edges are represented by sticky ends. Under slightly supersaturated conditions, algorithmic self-assembly should generate array growth with few errors (Winfree 1998). In practice, though, low error rates have proven to be difficult to achieve. There are at least three types of errors that accumulate during algorithmic self-assembly (Winfree 2006). The first is a growth error that results from incorrect tiles attaching to positions where correct tiles should attach (Winfree and Bekbolatov 2004). The second is a facet

error that results from incorrect tiles attaching to positions where no tiles should attach (Chen and Goel 2004). The final type of error is a nucleation error wherein different tiles attach to each other to form a small array that induces further growth without a programmed seed structure (Schulman and Winfree 2004).

Various strategies for suppressing these errors in DNA tile assembly have been proposed, including design logic based on proofreading (Winfree and Bekbolatov 2004; Chen et al. 2007), self-healing (Winfree 2006; Soloveichik et al. 2008), and nucleation barriers (Schulman and Winfree 2007; Barish et al. 2009). Additionally, environmental controls such as the manipulation of concentration and temperature have been simulated (Schulman and Winfree 2007; Chen and Kao 2011; Chen et al. 2011) and followed up with experimental proofs. For example, the effects of different thermal ramps, divalent-cation concentrations, and monovalent-cation concentrations on origami folding have been examined (Douglas et al. 2009). The reliability of algorithmic DNA tile assembly has greatly improved, with the error rate decreasing from 10 % in 2004 (Rothemund et al. 2004) to 1.4 % in 2008 (Fujibayashi et al. 2008) to 0.13 % in 2009 (Barish et al. 2009) to an astounding 0.05 % in 2010 (Chen and Doty 2012). However, these structures are for the most part derived from algorithmic 2D self-assembly using a limited tile set. The construction of much more intricate DNA nanostructures involves different self-assembly strategies (e.g., hierarchical self-assembly) and tile sets (e.g., 6-HB). Also, the mechanisms underlying 3D nanostructures are more complicated than those for 2D nanostructures, although the strategies used for 2D self-assembly are presumably applicable to 3D self-assembly.

Recently, several empirical rule sets have been developed to optimize self-assembly. For example, a sequence-symmetry strategy has been used to decrease the number of the strands required for self-assembly, in turn reducing assembly error and increasing assembly scale and yield (He et al. 2005a). Similarly, a cost-effective method was generated to construct finite-sized arrays by taking advantage of the geometric symmetry of tile structures (Liu et al. 2005a). Efficient 2D arrays have been constructed by minimizing both the number of steps during hierarchical assembly and the reuse of sticky-end sequences (Park et al. 2006). The ratio of staples to scaffold and the number and length of sticky ends in designed origami folds were also optimized (Rothemund 2006). Likewise, a corrugation strategy was developed in which adjacent tiles alternatively face up and down in the direction of assembly, so as to reduce curvature accumulation and enhance self-assembly scale and yield (Yan et al. 2003a).

From a purely quality control point of view, one potential solution to minimizing error during nanoconstruction is to use enzymatic synthesis to create large amounts of DNA oligonucleotides and DNA templates at low cost. The construction of objects that can be made from a single, long strand, without staples, is especially attractive (Lin et al. 2008; Li et al. 2009), as it reduces the need for purification.

6.1.4 Functional Templating

The ability to truly control matter at nanometer-length scales is a virtually unique advantage of DNA nanotechnology and unsurprisingly has been adapted to the study of other nanoscale systems. A variety of hetero-components, including inorganic, organic, and biological materials, have now been assembled with DNA. For example, metallic nanoparticles, including gold and silver nanoparticles of different diameters, have been successfully incorporated into periodic and aperiodic DNA arrays (Xiao et al. 2002; Le et al. 2004; Pinto et al. 2005; Zheng et al. 2006, 2008; Zhang et al. 2006; Aldaye and Sleiman 2006; Liu et al. 2004b; Sharma et al. 2009; Ding et al. 2010; Shen et al. 2012; Kuzyk et al. 2012; Pal et al. 2010). High local-field enhancements can be obtained by spatially localizing nanoparticles within sub-10 nm of one another via DNA-mediated assembly. DNA has also been used to template the ordered chemical synthesis of small molecules (Gartner et al. 2002), nylon (Zhu et al. 2003; Liu et al. 2006b), and peptide nucleic acids (PNAs) (Heemstra and Liu 2009).

Of particular interest is the use of DNA lattices to organize biological components. This is because biological systems provide mature models for the arrangement of macromolecules with precisely controlled positions, distances, and orientations to maximize their functionality. To this end, DNA lattices have been used to organize proteins, such as streptavidin (Park et al. 2005), thrombin (Liu et al. 2005b), and RuvA (Malo et al. 2005), and to organize nucleic acid enzymes (DNAzymes; Garibotti et al. 2006). Templating can also occur by volume or area, instead of by arrangement, as DNA tetrahedra have been used to encapsulate proteins (Erben et al. 2006; Duckworth et al. 2007).

Because nucleic acid-binding species (aptamers) can be readily added to DNA nanostructures either via co-synthesis or hybridization, it seems natural to incorporate aptamers into DNA nanostructures in order to direct the organization of different protein targets into spatial patterns. 2D DNA tiles associated with a thrombin-binding aptamer (Lin et al. 2006) and an anti-Fc aptamer (Li et al. 2006) have been used to direct the assembly of thrombin and antibodies, respectively. 2D DNA arrays encoded with multiple protein-binding aptamers, such as a human α-thrombin-binding aptamer and a platelet-derived growth factor (PDGF) binding aptamer, have been used to generate high-density addressable protein nanoarrays (Chhabra et al. 2007). DNA helix bundles attached to different aptamers have been used to test the distance dependence of multivalent protein interactions (Rinker et al. 2008). Branched DNA scaffolds linked with bi-specific cell-targeting aptamers have been used to mediate cell–cell interactions (Liu et al. 2011).

Importantly, recent studies have shown that DNA-mediated arrangements of two enzymes or cofactor-enzyme pairs can lead to more efficient catalysis (Niemeyer et al. 2002; Wilner et al. 2009). Examples include scaffolding of NAD(P)H:FMN oxidoreductase and luciferase on a double-stranded DNA scaffold (Niemeyer et al. 2002), an enzyme cascade of glucose oxidase (GOx) and horseradish

peroxidase (HRP) on a 2D hexagonal DNA scaffold or origami (Wilner et al. 2009; Fu et al. 2012), and the measurement of distance-dependent activity of the BMR reductase domain and the BMP porphyrin domain from cytochrome P450 BM3 complexes (Erkelenz et al. 2011). Overall, the activities of assembled enzyme pairs or cofactor-enzyme pairs are increased following assembly. Most impressively, the in vivo organization of the enzyme pair [FeFe]-hydrogenase and ferredoxin has been achieved with engineered RNA scaffolds. Bacterial hydrogen production was increased by up to about 50-fold (Delebecque et al. 2011). Similarly, a recent report has shown that a plasmid DNA scaffold can be used to arrange biosynthetic enzymes into functional metabolic structures in *Escherichia coli* that improve metabolic flux (Conrado et al. 2012). Both of these examples herald a new era when DNA nanotechnology in living structures can be used to rationally modify and control metabolism.

These successes open the door to the use of DNA nanotechnology to greatly enable nanoscale research in general, including understanding and designing nanophotonic systems, creating small chemical factories, developing new multi-component sensor systems, and of course the original goal, crystallography. Many of these potential applications will be explored in Sect. 6.2.

6.1.5 DNA Nanodevices

6.1.5.1 Engineering Conformational Transitions

Beyond stable DNA arrays and objects, it is possible to imagine DNA nanodevices whose conformations can be controlled at the molecular scale. A very simple DNA-based nanomechanical device was constructed as early as 1998 in which adding or removing an intercalator (ethidium) altered supercoiling and in turn resulted in the extrusion of a DNA cruciform and the modulation of the position of a branch point in a four-arm junction (Yang et al. 1998a). Devices predicated on the B–Z structural transition have also been constructed (Mao et al. 1999a). In this case, a run of (CG) dimers between two DX molecules could be induced to fold into the Z-conformer with $Co(NH_3)_6^{3+}$, thereby changing the relative positions of the DX motifs. I-motif nanomachines (Modi et al. 2009), whose conformation can be opened or closed in response to pH changes, have been built and used as pH sensors in living cells. Origami tweezers (Kuzuya et al. 2011) that are controlled by biotin–streptavidin and antibody–antigen, as well as small molecule-nucleic acid interactions, have also been developed (Kuzuya et al. 2011).

A DNA-based device that was driven by the addition of particular sequences was originally developed by Yurke and colleagues (Yurke et al. 2000). The motion of the device, so-called DNA-based tweezers, can be switched between open and closed states using a pair of "fuel" strands that displace one another by branch migration. Following the same methodology, two crossover conformations (PX and JX_2) can be switched back and forth by the alternate addition of the fuel strands (Yan et al. 2002).

Such devices can serve as modular "gears" or "joints" that join and actuate larger nanostructures (Yan et al. 2002). A PX-JX_2 system adapted to a reciprocal format in which the fuel strands leading to the PX state in one device lead to the JX_2 state in the other device and vice versa (Liu et al. 2009) has also been constructed. The PX-JX_2 device was soon incorporated into a 2D DNA array as a robotic arm (Ding and Seeman 2006) and later assembled to control the input for a finite-state machine for DNA computation (Chakraborty 2008). Meanwhile, a DNA translation system (Liao and Seeman 2004), an RNA-controlled DNA rotary nanomachine (Zhong and Seeman 2006), and a three-state DNA nanomechanical device (Chakraborty et al. 2008) based on the PX-JX_2 device have also been demonstrated.

Devices that can respond to proteins have also been designed, although the process is not quite as straightforward as designing devices to respond to sequences. A protein-driven DNA nanodevice was constructed that not only changes its state in response to an external stimulus but also probes the biochemistry of the protein (Shen et al. 2004). In this device, an integration host factor (IHF, Rice et al. 1996) protein triggers a sharp bend in the device of about 160°, leading to the rupture of several base pairs elsewhere in the device. The number of base pairs that can be broken allows investigators to evaluate the amount of work that can be done by the protein binding to DNA (Shen et al. 2004). To measure other protein-mediated distortions of DNA, an open-version TX nanomechanical device (Liu et al. 2012a) has been built to investigate interactions between the SoxR protein and its cognate binding site (Hidalgo and Demple 1994). Upon binding the SoxR protein, the shape of the device changes, leading to the changes in fluorescence resonance energy transfer (FRET) signal between two TX domains labeled with dye molecules. The TX domains amplify the signal from the relatively small distortion of the DNA binding site. The binding free energy for this protein has been estimated to be 3.2–6.1 kcal mol^{-1} using FRET (Liu et al. 2012a). In a similar fashion, DNA-based nanomechanical "scissors" have been used to measure the strength of binding by MutS, a DNA repair protein that recognizes unpaired and bulged bases (Gu et al. 2010b). In principle it is now possible to design sophisticated structured nanodevices that can respond quantitatively at the single-molecule level to different proteins or other stimuli.

6.1.5.2 DNA Walking Devices

Functional biological machines carrying out useful work are ubiquitous in cells. Myosin (Mermall et al. 1998; Mehta et al. 1999; Kinbara and Aida 2005), a well-known molecular motor, can walk along the actin filaments unidirectionally when powered by adenosine triphosphate (ATP) hydrolysis. Kinesins (Svoboda et al. 1993; Yildiz et al. 2004; Carter and Cross 2005) and dyneins (Vale 2003; Gennerich et al. 2007; Carter et al. 2008), also fueled by ATP hydrolysis, vectorially transport molecules along microtubules. Rotary engines such as bacterial flagella (Block et al. 1989; Fahrner et al. 2003; Sowa et al. 2005) composed of more than 40 highly structured protein complexes are driven by proton or ion

pumps and propel bacteria. ATP synthase (Noji et al. 1997; Wang and Oster 1998; Itoh et al. 2004), a molecular waterwheel, makes ATP from adenosine diphosphate (ADP) and phosphate (Pi) by coupling to the energy inherent in a proton gradient.

Given the control over matter that can be exercised using DNA nanotechnology, it is an intrinsically interesting question to determine to what extent similar motors could be designed. To this end, various DNA walker systems driven by the addition of fuel strands have been constructed (Yin et al. 2004; Sherman and Seeman 2004; Shin and Pierce 2004; Tian et al. 2005; Bath et al. 2005; Chhabra et al. 2006; Green et al. 2008; Bath et al. 2009; Yin et al. 2008a; Omabegho et al. 2009; Gu et al. 2010a; He and Liu 2010; Lund et al. 2010). For example, a DNA-based bipedal walker (Sherman and Seeman 2004), consisting of two helices with toeholds as their "feet" and a TX molecule as the "footpath" to be trodden, has been built. This device mimics the locomotion of kinesin and myosin, allowing bidirectional motion along a well-defined track. However, it must be admitted that this device is not autonomous, and the footpath itself is short.

More autonomous walkers that do not require the sequential addition of fuel molecules have also been constructed. An autonomous walker powered by a DNA hairpin has been developed (Yin et al. 2008a); similarly, an autonomous DNA bipedal walker powered by two DNA fuel hairpins showed excellent performance on a one-dimensional DX molecular track (Omabegho et al. 2009). This system involved a ssDNA as the walker, a DX molecule containing two metastable stem-loops as the track, and hairpins as the fuel (Fig. 6.7a). Each leg of the walker was attached to the DX track through hybridization to one strand of the metastable stem-loops, allowing the release of the second strand, which then served as a catalyst for the incoming fuel hairpin (Fig. 6.7a). Initially, the fuel hairpin hybridized to the catalyst and released a sequestered sequence, which could in turn hybridize to the first strand of the metastable stem-loop and desorb the corresponding leg (Fig. 6.7b). The released leg was reattached to the track through hybridization to the next metastable stem-loop. The two fuel hairpins could not directly interact with one another, and thus the release of the second leg depended on the release of the first leg, allowing unidirectional locomotion. The chemical energy provided by the hybridization during strand displacement drove the continuous motion of this walker. Presumably, there is no limitation on the number of the steps this walker could take, given a long enough track.

The walkers can do more than walk, they can also carry cargoes. A DNA walker (Gu et al. 2010a) was built to transport Au nanoparticle cargoes along a 2D DNA origami track. This walker contained seven single-stranded DNAs, four of which were "feet" that attached to the origami track via fuel strands (thus powering forward motion of the walker) and three of which were "hands" that could collect cargoes sequentially attached to the origami tile. Each cargo could be programmed to be either grabbed or bypassed as the walker traversed the track. Various combinations of Au nanoparticles were transported and dropped off over 11 steps. In addition, an autonomous walker powered by a DNAzyme has been developed (Tian et al. 2005) and used to direct multistep organic synthesis (He and Liu 2010).

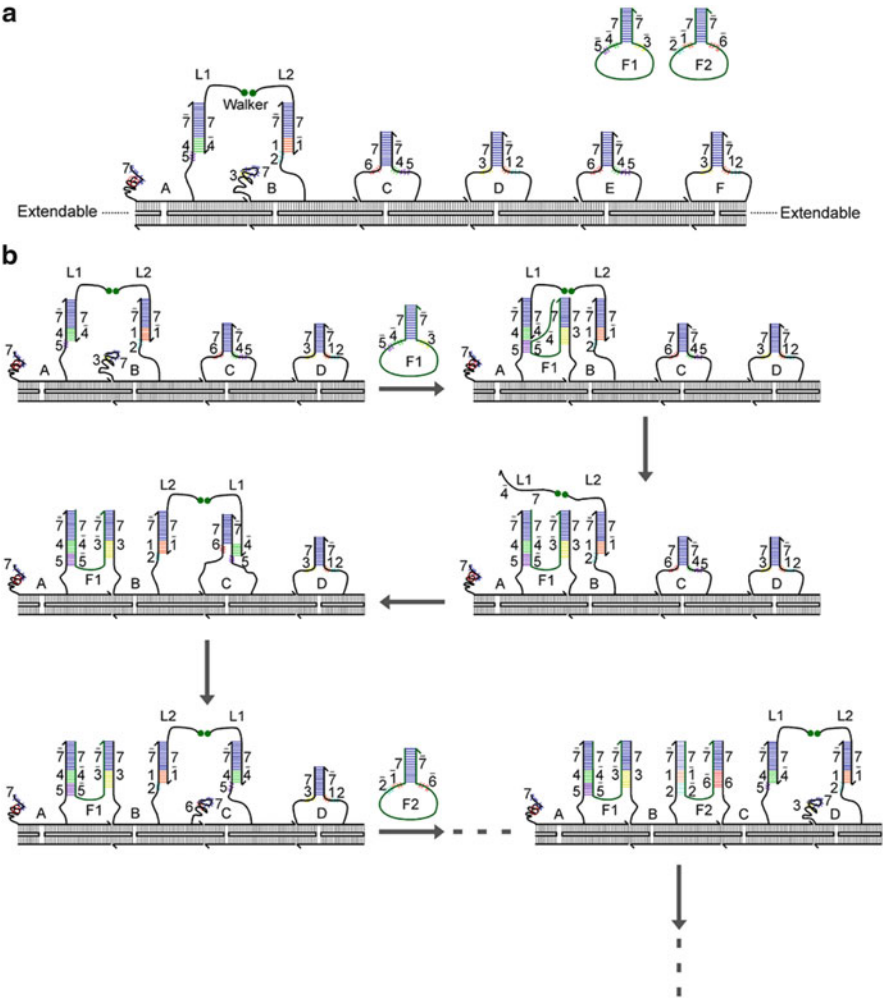

Fig. 6.7 An autonomous, processive, and unidirectional DNA bipedal walker (Omabegho et al. 2009). (**a**) Scheme of the bipedal walker system. The ssDNA walker contains a T16 linker with a 5′, 5′ linkage (shown as *two green dots*) in the *middle*. The extendable DX track contains various metastable stem-loops labeled as A, B, C, D, E, and F. The two fuel hairpins shown as F1 and F2 coexist in the solution, and do not interact with each other. (**b**) Steps of the bipedal walker driven by different fuel hairpins. When fuel hairpin F1 is added, one end of it hybridizes to the free strand of B, and the other end hybridizes to the strand of A holding the left leg L1 of the walker, leading to the release of L1, which moves forward, and held by one strand of C. Hairpin F2 moves the other leg (L2) of the walker from B to D in a similar fashion

A unique spider-like molecular walker composed of streptavidin with four DNA single-stranded legs, three of which are deoxyribozymes that can cleave immobilized RNA substrates, was constructed (Pei et al. 2006). The spider is first attached to an origami track via its non-deoxyribozyme leg; a single-stranded DNA

fuel molecule releases this leg. Further motion occurs as the remaining legs successively (and randomly) cleave the immobilized RNA substrates. Once substrates are exhausted or uncleavable nucleic acids are reached, the spider stops. This walker differs significantly from the others described in that once a leg cleaves a substrate it will more readily dissociate and then will randomly search for the next substrate. Motion is thus much less a deterministic molecular ballet characteristic of all other walkers described above and much more an amorphous set of lurches akin to biological molecular motors. Nevertheless, the spider can move along a predetermined path that includes signals to "start," "follow," "turn," and "stop" (Lund et al. 2010).

6.2 Future Perspectives

Over the years, progress has been made in using DNA nanotechnology to design and manipulate matter at the nanoscale. These advances are now beginning to be implemented for practical applications. Strides are beginning to be made in understanding how DNA nanostructures can uniquely be used to deliver drugs (Sect. 6.2.1), serve as reporters or amplifiers for diagnostics (Sect. 6.2.2), and potentially understand and design energetic materials (Sect. 6.2.3).

6.2.1 DNA Nanostructures for Drug Delivery

Recent reports have suggested that DNA nanostructures can not only deliver drugs but also are uniquely useful in doing so. Their potential application as vaccine adjuvants (Liu et al. 2012b) is very intriguing and may represent one of the first practical applications of these technologies.

First, DNA nanostructures may provide additional stability to nucleic acids that are used for targeting or delivery. For example, DNA origami nanostructures maintained their structural integrity after exposed to cell lysates for 12 h (Mei et al. 2011). Another report has demonstrated that DNA origami structures were not degraded when incubated with T7 exonuclease, *E. coli* exonuclease I, lambda exonuclease, and MseI restriction endonuclease at 37 °C for 1 h (Castro et al. 2011). Tetrahedra are foundational units for the formation of 3D DNA nanostructures: while triangles can be fragile, nucleic acid tetrahedra resist deformation. DNA tetrahedra were shown to be resistant to nucleases with a decay time of 42 h in 10 % fetal bovine serum (Keum and Bermudez 2009). Similarly, 3D DNA tetrahedra were shown to remain substantially intact within cultured human embryonic kidney cells for at least 48 h after transfection (Walsh et al. 2011).

Second, DNA nanostructures provide an opportunity to combine targeting and drug absorption in a single molecule. Folate-labeled DNA nanotubes composed of a 52-nt ssDNA that delivered Cy3 into human cancer cells (nasopharyngeal epidermal

carcinoma KB cells) were developed (Ko et al. 2008). DNA icosahedra were labeled with anti-mucin aptamers and delivered the intercalator doxorubicin, a drug for cancer chemotherapy (Chang et al. 2011). Compared to denatured DNA nanotubes and DNA strands of the same length, the structured DNA nanotubes showed greatly enhanced cellular uptake (Ko et al. 2008). Such increased efficacy of delivery can greatly reduce the side effects associated with drugs. For example, hollow DNA origami tubes covered with up to 62 unmethylated CpG sequences (recognized by Toll-like receptor 9 (TLR9) that activates downstream pathways to induce immunostimulatory effects) stimulated a stronger immune response in freshly isolated spleen cells compared to equal amounts of CpG oligonucleotides associated with a standard carrier Lipofectamine and that the DNA constructs were less toxic than Lipofectamine (Schuller et al. 2011). Similarly, triangular and tubular DNA origami nanostructures were loaded with doxorubicin (via intercalation), leading to increased delivery and killing of otherwise drug-resistant cells relative to intercalation into double-stranded DNA alone (Jiang et al. 2012). This increased efficacy may have been due in part to the more concentrated alkaline drugs modulating the pH of the lysosome and hence the fate of the cargo (Jiang et al. 2012).

Third, the precision of display on DNA nanostructures may be useful for enhancing biological efficacy. 3D DNA tetrahedral nanostructures modified with different numbers of unmethylated cytosine-phosphate-guanine (CpG) motifs significantly improved cellular uptake and immunostimulatory effects than CpG-bearing oligonucleotides, even when the latter are introduced with lipids (Li et al. 2011a). It was further demonstrated that the multivalent 3D DNA tetrahedron can efficiently enter macrophage-like RAW264.7 cells without transfection and that the multivalent CpG motifs greatly enhance the immunostimulatory effect of the nanostructures (Li et al. 2011a). Similarly, a DNA tetrahedron was used to deliver siRNA into tumor cells (Lee et al. 2012). By precisely controlling the size of the DNA nanostructures as well as the spatial orientation and density of cancer-targeting ligands, such as folates, on the DNA tetrahedron surface, these nanoparticles could more efficiently silence target genes in tumors. More recently, a 3D DNA DX tetrahedron was constructed as a platform for assembly of a model antigen, streptavidin (STV), and a representative CpG adjuvant, CPG oligo-deoxynucleotides (mouse-specific ODN-1826) into a synthetic vaccine complex (Liu et al. 2012b). This complex was shown to induce strong antibody responses against the model antigen STV both in vitro and in vivo (Liu et al. 2012b). Compared to branched DNA structures containing STV and CpG, the DX tetrahedron-STV-CpG complex displayed enhanced in vitro cellular uptake of the antigen and improved in vivo induction of antigen-specific antibody (Liu et al. 2012b).

Finally, DNA nanomachines can potentially carry out a number of linked tasks relating to drug delivery. For example, a sophisticated 3D DNA nanorobot was built that could control drug release in the presence of target cells (Douglas et al. 2012). The robot contained cell-specific aptamers at “hinges,” and interactions with particular tumor cells led to the exposure of payloads such as gold nanoparticles and antibodies that could manipulate cell signaling. By changing the hinges, the logic of cargo exposure could be programmed. While it may be that the aptamer

lock is opened by initial binding of the ligands to the unpaired sequences of the inert aptamers—leading to full binding and activity of the aptamer-ligand—it is also likely that spontaneous association-dissociation of the aptamer-blocker allows interaction with the ligand, in turn potentially leading to premature, untriggered access to the antibody cargo.

It can be argued that DNA nanostructures would be expensive devices for drug delivery at their current stage of development. The current prices for constructing a DNA tetrahedron (~250 bp) and a M13-based DNA origami (~7,000 bp) are approximately US $25 and US $700, respectively, based on the current price of US $0.10 per base for 25-nmol oligonucleotide synthesis. Thus, about 10,000 dollars will be required to produce 1 g of DNA for patient treatment. However, technical improvements have begun to dramatically reduce the costs of DNA synthesis. For example, commercially available high-throughput microarrays can be used to synthesize large numbers of oligonucleotides at a current price of less than US $0.001 per base. Similarly, microfluidic oligonucleotide synthesizers can reduce reagent consumption by at least 100-fold relative to parallel solid-phase synthesis of oligonucleotides (Lee et al. 2010). Over the past two decades, the price of oligonucleotide synthesis (including gene synthesis) has been dropping exponentially. Although the scale of these methods is currently not commensurate with patient treatment, the development of high-quality, low-cost enzyme amplification methods (Tian et al. 2009; Kosuri et al. 2010) may eventually provide an alternative means for production. It can be further argued that these advances do not solve the larger problems of purification and quality control that would be associated with good manufacturing practice (GMP) production. However, a similar situation occurred during the initial forays into antisense oligonucleotide therapies and, now, siRNA therapies. While neither of these technologies is yet routine for drug development, the production barriers have been largely overcome.

6.2.2 DNA Nanotechnology for Analysis and Diagnosis

DNA nanotechnology has proven useful both for enhancing analytical methods and for creating novel DNA-based, enzyme-free catalytic devices for diagnostic applications. Analytical tools for labeling or organizing molecules at the nanoscale have proven especially valuable. For example, DNA origami structures have been used as a molecular ruler for the calibration of super-resolution microscopy (Steinhauer et al. 2009). DNA origami nanotubes have also been used to construct detergent-resistant liquid crystals to induce weak alignment of membrane proteins, such as the ζ-ζ transmembrane domain of the T cell receptor (Douglas et al. 2007), and mitochondrial uncoupling protein 2 (Berardi et al. 2011), for NMR structural determinations. DNA kagome lattices of interwoven double helices with p3 symmetry formed by Holliday junctions have been used to arrange target proteins for single-particle electron cryomicroscopy (cryo-EM) structure determination (Malo et al. 2005; Selmi et al. 2011).

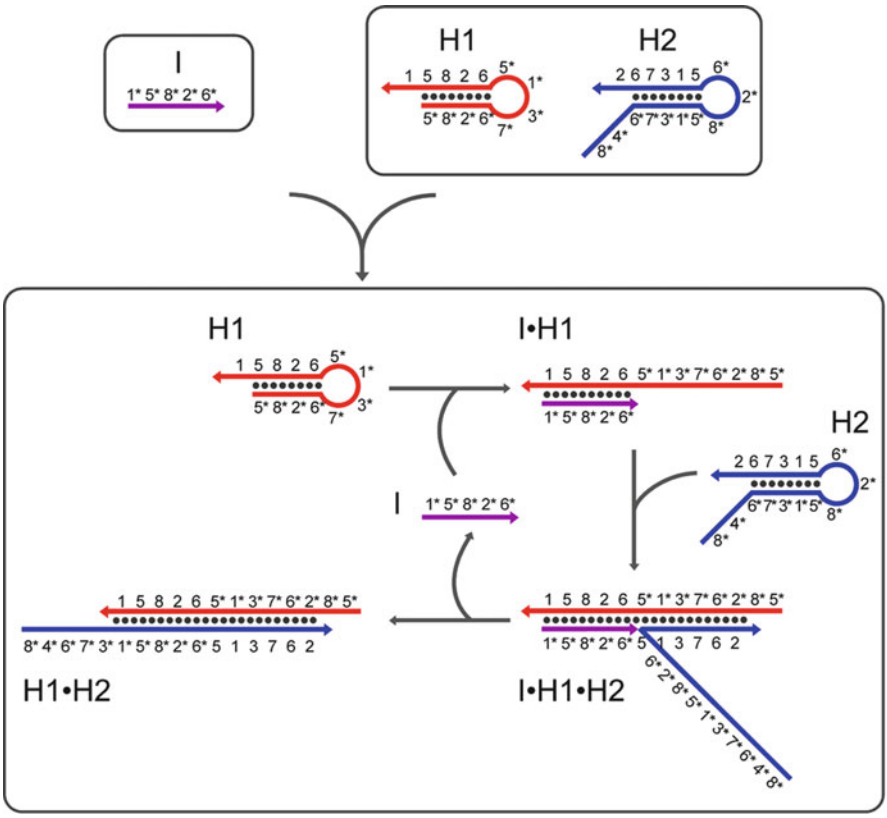

Fig. 6.8 Schematic of catalyzed hairpin assembly (CHA) (Yin et al. 2008a). The *top panel* shows the catalyst (I) and the two kinetically trapped metastable hairpins (H1 and H2). The *bottom panel* describes the reaction steps of the catalyzed hairpin assembly. Domain 1* of catalyst I hybridizes to the toehold 1 of hairpin H1, inducing the opening of H1 and the formation of the product I·H1. The released segment (2*-6*-7*-3*-1*-5*) of H1 serves as the catalyst of hairpin H2: the released 2* of I·H1hybridizes to the toehold 2 of hairpin H2, leading to the opening of H2; H2 then displaces I from H1, producing double-stranded H1·H2. The displaced catalyst I again interacts with additional hairpin molecules. I·H1·H2 represents one of the intermediates formed during branch migration

DNA nanotechnology is often thought to be based on building and manipulating structures at the nanoscale, but there has been a parallel revolution in DNA programming that stems from the same thoughts on guiding self-assembly. For example, the hybridization chain reaction (HCR) (Dirks and Pierce 2004; Venkataraman et al. 2007; Choi et al. 2010), entropy-driven catalysis (Zhang et al. 2007), and catalyzed hairpin assembly (CHA) (Yin et al. 2008a) (Fig. 6.8) were seminal steps toward a general programming language for DNA assembly and have in turn provided interesting platforms for signal amplification and diagnostic detection. The hybridization chain reaction (HCR) (Dirks and Pierce 2004; Choi et al. 2010) has been used to amplify the signals associated with target DNA by 10^5-fold (Wang et al. 2011) and has also been

used to amplify fluorescent signals and multiplexed imaging of mRNA expression in zebrafish embryos (Choi et al. 2010). These imaging advances with DNA circuitry may be further extended by DNA nanostructures. DNA origami has been used to construct a library of 216 distinct sub-micrometer, geometrically encoded fluorescent barcodes, thereby greatly improving the multiplexing capability of fluorescence microscopy, currently limited by the available number of spectrally distinguishable fluorophores (Lin et al. 2012). These DNA barcodes are smaller in size and stiffer in structure compared to most of the currently available fluorescent barcodes (Lin et al. 2012).

CHA is an enzyme-free, "entropy-driven" catalytic DNA circuit originally developed by Yin et al. (2008a) (Fig. 6.8). In general, two kinetically trapped metastable hairpins cannot interact with each other. However, when a DNA single-strand "catalyst" is introduced into the system, it hybridizes to the toehold of one hairpin, triggering the opening of that hairpin via branch migration. A sequestered segment of the first hairpin is released, serving as the "catalyst" for the second hairpin, and initiates the opening of the second hairpin, which can form a longer, more stable double-stranded product with the first hairpin. The original catalyst strand is then displaced and again reacts with additional hairpin molecules. CHA is inherently modular and scalable.

In a recent report (Li et al. 2011b), the kinetics of the CHA reaction has been shown to be fast, with the turnover rate of the catalyst higher than 1 min^{-1}. The uncatalyzed background signal of the CHA reaction was almost undetectable (less than 0.5 M^{-1} s^{-1}) within 1 day, and the signal amplification was about 100-fold within a few hours. A CHA circuit has been combined with a G-quadruplex DNAzyme to make a sensor with a detection limit as low as 0.1 pM (Zheng et al. 2012). CHA reactions can be easily coupled to different analytical methods, such as fluorescence, electrochemistry, colorimetry, and chemiluminescence, with detection limits ranging from 0.1 pM to 1 nM (Li et al. 2011b; Zheng et al. 2012). By combining nonenzymatic transducers such as CHA (Li et al. 2012) with conventional enzyme amplification methods such as the somewhat noise-prone loop-mediated isothermal amplification (LAMP), a sensitive enzymatic, isothermal amplification method (Notomi et al. 2000), it has proven possible to generate paperfluidic diagnostic devices (Allen et al. 2012) that may prove both cheap and easy to use in point-of-care settings.

6.2.3 DNA Nanostructures for Electronics and Photovoltaics

We have already described how DNA nanostructures can be naturally adapted to templating materials and to exploring materials properties (Sect. 6.1.4). Such manipulations may have very practical consequences. The notion that the increasingly tiny distances in modern electronic devices might be generated by a bottom-up (DNA nanotechnology) rather than top-down (photolithography) method has been a goal of this field since the 1980s (Robinson and Seeman 1987). In this regard, it is interesting to note that DNA charge transport can proceed over long

molecular distances (34 nm), surpassing previous reports on molecular wires (Slinker et al. 2011). Higher-order electron transport can also be envisioned by organizing hetero-nanoelectronic components with DNA nanostructures. DNA origami triangles can be integrated into semiconductor surfaces by combining self-assembly with electron beam lithography (Kershner et al. 2009).

Natural photosynthetic systems, such as chloroplasts (Heber and Heldt 1981; Martin et al. 1998; Pfannschmidt et al. 1999), efficiently convert light energy into chemical energy by finely manipulating light-mediated charge separation (McConnell et al. 2010). Human engineers continue to try to mimic or surpass this feat by creating artificial photosynthetic systems, often using complex, covalent supermolecular structures studded with chromophores, electron donors, or acceptors. For the most part, these constructs are both inefficient and costly (Wasielewski 2009). Moreover, these constructs do not have nearly the same degree of spatial control as the natural systems, control which is critical for light-harvesting capacity, charge separation, and transport efficiency. In contrast, DNA nanostructures can be used as an exquisitely defined, completely reconfigurable "breadboard" to arrange the molecular pieces that constitute the light-harvesting complexes.

DNA origami has been used as a template to arrange single-walled carbon nanotubes into 2D architecture (Maune et al. 2010) and to organize various fluorophores into linear paths to achieve multicolor energy transfer not unlike light-harvest complexes (Stein et al. 2011). A 3D self-assembled seven-helix bundle (7HB) has similarly been adapted to organize multiple chromophores with defined positions for efficient harvesting and transport of energy (Dutta et al. 2011). Finally, DNA has been used to organize multivalent quantum dots into branched shapes with high energy transfer efficiencies (Tikhomirov et al. 2011).

DNA may also be useful as a low-activity electronic material for organizing various conductors and semiconductors. Artificial DNA nanostructures appear to have unique physical properties, such as large band gaps and large dielectric constants, when integrated into organic light-emitting diodes (OLED) (Hagen et al. 2006) and solar cells (Lee et al. 2011). DNA-nanostructure-based thin films can function as both an electron blocking layer and a hole transport layer that leads to enhanced power conversion efficiencies (Lee et al. 2011). Overall, by serving as otherwise low-activity substrates for the precise organization of metal nanoparticles/nanorods/nanofilms, semiconductor nanoparticles/nanorods/nanofilms, redox proteins, and organic materials into various charge/energy donor–acceptor pairs (Zhang et al. 2003; Liu et al. 2005c; Clarke and Durrant 2010), DNA nanostructures are likely to play an increasingly important role in the development of a new generation of electronics and photovoltaics.

6.3 Concluding Remarks

DNA nanotechnology is one of the most interesting fields in science and technology. This is because the unique combination of programmability, replicability, and addressability simultaneously enable design, construction, and computation. DNA

nanotechnology remains one of the few ways to truly control matter at the nanoscale and thus has proven to be very valuable in pushing forward nanoscience in general. It is anticipated that this will remain true into the future; indeed, the use of DNA nanotechnology to solve hard problems such as precisely arranging ligands for receptor activation or nanoparticles for generating plasmons will accelerate.

The problem with DNA nanotechnology comes with trying to understand how it might ultimately be commercialized. Unlike other biotechnologies, it is almost uncoupled from cell growth. While proteins can be made at scale and for reasonable prices by cells, most DNA nanostructures cannot (although the first advances in in vivo production are just now occurring). Enzymatic production may be an option, just as in vitro transcription and translation are now becoming workhorses for the production of proteins.

It is often difficult to finely predict the lag time in a technology arc. The polymerase chain reaction was invented after the initial successes of DNA nanotechnology and has of course become not just a commercial success in its own right but has spawned many derivative businesses (e.g., NextGen sequencing). Despite a slow commercial start, it is too early to write off DNA nanotechnology as a business, especially since there are usually multiple "ages" of any given technology; aptamer technology also arose after the initial successes of DNA nanotechnology and has already peaked and declined in the commercial world at least twice since then. It may be the third or fourth age of DNA nanotechnology that finally takes hold in business.

Still, there is a lingering sense that while DNA nanotechnology is the right direction, DNA itself might not be the right material. In this regard, as novel, cheaper materials capable of complexity, complementarity, and self-replication are generated into the future (such as replicable plastics, McHale et al. 2012), the advances of DNA nanotechnology will stand ready as guideposts for development. To date, DNA still remains the only material of any complexity where molecular features can be programmed into distinct shapes that span the nano- to microscales.

Acknowledgments This work was supported by the Welch Foundation (F-1654), the National Security Science and Engineering Faculty Fellowship (FA9550-10-1-0169), and the National Institutes of Health (1 R01 GM094933-02). The content is solely the responsibility of the authors and does not necessarily represent the official views of the funding agencies.

References

Aldaye FA, Sleiman HF (2006) Sequential self-assembly of a DNA hexagon as a template for the organization of gold nanoparticles. Angew Chem Int Ed 45:2204–2209

Allen PB, Arshad SA, Li B, Chen X, Ellington AD (2012) DNA circuits as amplifiers for the detection of nucleic acids on a paperfluidic platform. Lab Chip 12:2951–2958

Andersen ES, Dong M, Nielsen MM, Jahn K, Subramani R, Mamdouh W, Golas MM, Sander B, Stark H, Oliveira CLP, Pedersen JS, Birkedal V, Besenbacher F, Gothelf KV, Kjems J (2009) Self-assembly of a nanoscale DNA box with a controllable lid. Nature 459:73–76

Barish RD, Schulman R, Rothemund PWK, Winfree E (2009) An information-bearing seed for nucleating algorithmic self-assembly. Proc Natl Acad Sci USA 106:6054–6059
Bath J, Green SJ, Turberfield AJ (2005) A free-running DNA motor powered by a nicking enzyme. Angew Chem Int Ed 44:4358–4361
Bath J, Green SJ, Allen KE, Turberfield AJ (2009) Mechanism for a directional, processive, and reversible DNA motor. Small 5:1513–1516
Berardi MJ, Shih WM, Harrison SC, Chou JJ (2011) Mitochondrial uncoupling protein 2 structure determined by NMR molecular fragment searching. Nature 476:109–113
Birac JJ, Sherman WB, Kopatsch J, Constantinou PE, Seeman NC (2006) Architecture with GIDEON, a program for design in structural DNA nanotechnology. J Mol Graph Model 25:470–480
Block SM, Blair DF, Berg HC (1989) Compliance of bacterial flagella measured with optical tweezers. Nature 338:514–518
Carter NJ, Cross RA (2005) Mechanics of the kinesin step. Nature 435:308–312
Carter AP, Garbarino JE, Wilson-Kubalek EM, Shipley WE, Cho C, Milligan RA, Vale RD, Gibbons IR (2008) Structure and functional role of dynein's microtubule-binding domain. Science 322:1691–1695
Castro CE, Kilchherr F, Kim DN, Shiao EL, Wauer T, Wortmann P, Bathe M, Dietz H (2011) A primer to scaffolded DNA origami. Nat Methods 8:221–229
Chakraborty B (2008) Putting DNA to work as nanomechanical, computing and diagnostic devices. Dissertation, New York University
Chakraborty B, Sha R, Seeman NC (2008) A DNA-based nanomechanical device with three robust states. Proc Natl Acad Sci USA 105:17245–17249
Chang M, Yang CS, Huang DM (2011) Aptamer-conjugated DNA icosahedral nanoparticles as a carrier of doxorubicin for cancer therapy. ACS Nano 5:6156–6163
Chen H, Doty D (2012) Parallelism and time in hierarchical self-assembly. In: SODA 2012: Proceedings of the 23rd annual ACM-SIAM symposium on discrete algorithms, pp 1163–1182
Chen H, Goel A (2004) Error free self-assembly using error prone tiles. In: Proceedings of the 10th international meeting on DNA based computers, pp 62–75
Chen H, Kao M (2011) Optimizing tile concentrations to minimize errors and time for DNA tile self-assembly systems. In: Sakakibara Y, Mi Y (eds) DNA computing and molecular programming, vol 6518, Lecture notes in computer science. Springer, Heidelberg, pp 13–14
Chen J, Seeman NC (1991) The synthesis from DNA of a molecule with the connectivity of a cube. Nature 350:631–633
Chen H, Schulman R, Goel A, Winfree E (2007) Reducing facet nucleation during algorithmic self-assembly. Nano Lett 7:2913–2919
Chen H, Doty D, Seki S (2011) Program size and temperature in self-assembly. In: Asano T, Nakano S, Okamoto Y, Watanabe O (eds) Algorithms and computation, vol 7074, Lecture notes in computer science. Springer, Heidelberg, pp 445–453
Chhabra R, Sharma J, Liu Y, Yan H (2006) Addressable molecular tweezers for DNA-templated coupling reactions. Nano Lett 6:978–983
Chhabra R, Sharma J, Ke Y, Liu Y, Rinker S, Lindsay S, Yan H (2007) Spatially addressable multiprotein nanoarrays templated by aptamer-tagged DNA nanoarchitectures. J Am Chem Soc 129:10304–10305
Choi HM, Chang JY, le Trinh A, Padilla JE, Fraser SE, Pierce NA (2010) Programmable in situ amplification for multiplexed imaging of mRNA expression. Nat Biotechnol 28:1208–1212
Clarke TM, Durrant JR (2010) Charge photogeneration in organic solar cells. Chem Rev 110:6736–6767
Cohen SN, Chang ACY, Boyer HW, Helling RB (1973) Construction of biologically functional bacterial plasmids in vitro. Proc Natl Acad Sci USA 70:3240–3244
Conrado RJ, Wu GC, Boock JT, Xu HS, Chen SY, Lebar T, Turnsek J, Tomsic N, Avbelj M, Gaber R, Koprivnjak T, Mori J, Glavnik V, Vovk I, Bencina M, Hodnik V, Anderluh G, Dueber

JE, Jerala R, DeLisa MP (2012) DNA-guided assembly of biosynthetic pathways promotes improved catalytic efficiency. Nucleic Acids Res 40:1879–1889
Constantinou P, Wong T, Kopatsch J, Israel LB, Mao C, Ding B, Sha R, Zhang X, Yang X, Seeman NC (2006) Double cohesion in structural DNA nanotechnology. Org Biomol Chem 4:3414–3419
Delebecque CJ, Lindner AB, Silver PA, Aldaye FA (2011) Organization of intracellular reactions with rationally designed RNA assemblies. Science 333:470–474
Deng ZX, Mao CD (2003) DNA-templated fabrication of 1D parallel and 2D crossed metallic nanowire arrays. Nano Lett 3:1545–1548
Dietz H, Douglas SM, Shih WM (2009) Folding DNA into twisted and curved nanoscale shapes. Science 325:725–730
Ding B, Seeman NC (2006) Operation of a DNA robot arm inserted into a 2D DNA crystalline substrate. Science 314:1583–1585
Ding B, Sha R, Seeman NC (2004) Pseudohexagonal 2D DNA crystals from double crossover cohesion. J Am Chem Soc 126:10230–10231
Ding B, Deng Z, Yan H, Cabrini S, Zuckermann RN, Bokor J (2010) Gold nanoparticle self-similar chain structure organized by DNA origami. J Am Chem Soc 132:3248–3249
Dirks RM, Pierce NA (2004) Triggered amplification by hybridization chain reaction. Proc Natl Acad Sci USA 101:15275–15278
Douglas SM, Chou JJ, Shih WM (2007) DNA-nanotube-induced alignment of membrane proteins for NMR structure determination. Proc Natl Acad Sci USA 104:6644–6648
Douglas SM, Dietz H, Liedl T, Hogberg B, Graf F, Shih WM (2009) Self-assembly of DNA into nanoscale three-dimensional shapes. Nature 459:414–418
Douglas SM, Bachelet I, Church GM (2012) A logic-gated nanorobot for targeted transport of molecular payloads. Science 335:831–834
Drexler KE (1981) Molecular engineering: an approach to the development of general capabilities for molecular manipulation. Proc Natl Acad Sci USA 79:5275–5278
Drexler KE, Peterson C (1989) Nanotechnology and enabling technologies. Foresight Institute. http://www.foresight.org/updates/Briefing2.html. Accessed 20 Sept 2012
Duckworth BP, Chen Y, Wollack JW, Sham Y, Mueller JD, Taton TA, Distefano MD (2007) A universal method for the preparation of covalent protein-DNA conjugates for use in creating protein nanostructures. Angew Chem Int Ed 46:8819–8822
Dutta PK, Varghese R, Nangreave J, Lin S, Yan H, Liu Y (2011) DNA-directed artificial light-harvesting antenna. J Am Chem Soc 133:11985–11993
Endo M, Hidaka K, Kato T, Namba K, Sugiyama H (2009) DNA prism structures constructed by folding of multiple rectangular arms. J Am Chem Soc 131:15570–15571
Erben CM, Goodman RP, Turberfield AJ (2006) Single molecule protein encapsulation in a rigid DNA cage. Angew Chem Int Ed 45:7414–7417
Erben CM, Goodman RP, Turberfield AJ (2007) A self-assembled DNA bipyramid. J Am Chem Soc 129:6992–6993
Erkelenz M, Kuo CH, Niemeyer CM (2011) DNA-mediated assembly of cytochrome P450 BM3 subdomains. J Am Chem Soc 133:16111–16118
Fahrner KA, Ryu WS, Berg HC (2003) Biomechanics: bacterial flagellar switching under load. Nature 423:938
Feng L, Park SH, Reif JH, Yan H (2003) A two-state DNA lattice switched by DNA nanoactuator. Angew Chem Int Ed 42:4342–4346
Fu TJ, Seeman NC (1993) DNA double crossover structures. Biochemistry 32:3211–3220
Fu J, Liu M, Liu Y, Woodbury NW, Yan H (2012) Interenzyme substrate diffusion for an enzyme cascade organized on spatially addressable DNA nanostructures. J Am Chem Soc 134:5516–5519
Fujibayashi K, Hariadi R, Park SH, Winfree E, Murata S (2008) Toward reliable algorithmic self-assembly of DNA tiles: a fixed-width cellular automaton pattern. Nano Lett 8:1791–1797
Fyfe MCT, Stoddart JF (1997) Synthetic supramolecular chemistry. Acc Chem Res 30:393–401

Garibotti AV, Knudsen SM, Ellington AD, Seeman NC (2006) Functional DNAzymes organized into 2D arrays. Nano Lett 6:1505–1507
Gartner ZJ, Kanan MW, Liu DR (2002) Multistep small-molecule synthesis programmed by DNA templates. J Am Chem Soc 124:10304–10306
Gennerich A, Carter AP, Reck-Peterson SL, Vale RD (2007) Force-induced bidirectional stepping of cytoplasmic dynein. Cell 131:952–965
Gierer A (1966) Model for DNA and protein interactions and the function of the operator. Nature 212:1480–1481
Goodman RP, Schaap IAT, Tardin CF, Erben CM, Berry RM, Schmidt CF, Turberfield AJ (2005) Rapid chiral assembly of rigid DNA building blocks form molecular fabrication. Science 310:1661–1664
Green SJ, Bath J, Turberfield AJ (2008) Coordinated chemomechanical cycles: a mechanism for autonomous molecular motion. Phys Rev Lett 101:238101
Gu H, Chao J, Xiao S, Seeman NC (2010a) A proximity-based programmable DNA nanoscale assembly line. Nature 465:202–205
Gu H, Yang W, Seeman NC (2010b) DNA scissors device used to measure MutS binding to DNA mis-pairs. J Am Chem Soc 132:4352–4357
Guan J, Lee LJ (2005) Generating highly ordered DNA nanostrand arrays. Proc Natl Acad Sci USA 102:18321–18325
Hagen JA, Li W, Steckl AJ, Grote JG (2006) Enhanced emission efficiency in organic light-emitting diodes using deoxyribonucleic acid complex as an electron blocking layer. Appl Phys Lett 88:171109
Han D, Pal S, Nangreave J, Deng Z, Liu Y, Yan H (2011) DNA origami with complex curvatures in three-dimensional space. Science 332:342–346
He Y, Liu DR (2010) Autonomous multistep organic synthesis in a single isothermal solution mediated by a DNA walker. Nat Nanotechnol 5:778–782
He Y, Tian Y, Chen Y, Deng ZX, Ribbe AE, Mao C (2005a) Sequence symmetry as a tool for designing DNA nanostructures. Angew Chem Int Ed 44:6694–6696
He Y, Chen Y, Liu H, Ribbe AE, Mao C (2005b) Self-assembly of hexagonal DNA two-dimensional (2D) arrays. J Am Chem Soc 127:12202–12203
He Y, Tian Y, Ribbe AE, Mao C (2006) Highly connected two-dimensional crystals of DNA six-point-stars. J Am Chem Soc 128:15978–15979
He Y, Ye T, Su M, Zhang C, Ribbe AE, Jiang W, Mao C (2008) Hierarchical self-assembly of DNA into symmetric supramolecular polyhedra. Nature 452:198–201
Heber U, Heldt HW (1981) The chloroplast envelope: structure, function, and role in leaf metabolism. Annu Rev Plant Physiol 32:139–168
Heemstra JM, Liu DR (2009) Templated synthesis of peptide nucleic acids via sequence-selective base-filling reactions. J Am Chem Soc 131:11347–11349
Hidalgo E, Demple B (1994) An iron-sulfur center essential for transcriptional activation by the redox-sensing SoxR protein. EMBO J 13:138–146
Holliday R (1964) A mechanism for gene conversion in fungi. Genet Res 5:282–304
Itoh H, Takahashi A, Adachi K, Noji H, Yasuda R, Yoshida M, Kinosita K Jr (2004) Mechanically driven ATP synthesis by F_1-ATPase. Nature 427:465–468
Jiang Q, Song C, Nangreave J, Liu X, Lin L, Qiu D, Wang ZG, Zou G, Liang X, Yan H, Ding B (2012) DNA origami as a carrier for circumvention of drug resistance. J Am Chem Soc 134:13396–13403
Kallenbach NR, Ma R-I, Seeman NC (1983) An immobile nucleic acid junction constructed from oligonucleotides. Nature 305:829–831
Ke Y, Sharma J, Liu M, Jahn K, Liu Y, Yan H (2009a) Scaffolded DNA origami of a DNA tetrahedron molecular container. Nano Lett 9:2445–2447
Ke Y, Douglas SM, Liu M, Sharma J, Cheng A, Leung A, Liu Y, Shih WM, Yan H (2009b) Multilayer DNA origami packed on a square lattice. J Am Chem Soc 131:15903–15908

Keren K, Krueger M, Gilad R, Ben-Yoseph G, Sivan U, Braun E (2002) Sequence-specific molecular lithography on single DNA molecules. Science 297:72–75
Kershner RJ, Bozano LD, Micheel CM, Hung AM, Fornof AR, Cha JN, Rettner CT, Bersani M, Frommer J, Rothemund PWK, Wallraff GM (2009) Placement and orientation of individual DNA shapes on lithographically patterned surfaces. Nat Nanotechnol 4:557–561
Keum JW, Bermudez H (2009) Enhanced resistance of DNA nanostructures to enzymatic digestion. Chem Commun 7:7036–7038
Kinbara K, Aida T (2005) Toward intelligent molecular machines: directed motions of biological and artificial molecules and assemblies. Chem Rev 105:1377–1400
Ko S, Liu H, Chen Y, Mao C (2008) DNA nanotubes as combinatorial vehicles for cellular delivery. Biomacromolecules 9:3039–3043
Kosuri S, Eroshenko N, LeProust EM, Super M, Way J, Li JB, Church GM (2010) Scalable gene synthesis by selective amplification of DNA pools from high-fidelity microchips. Nat Nanotechnol 28:1295–1299
Kuzuya A, Komiyama M (2009) Design and construction of a box-shaped 3D-DNA origami. Chem Commun 28:4182–4184
Kuzuya A, Wang R, Sha R, Seeman NC (2007) Six-helix and eight-helix DNA nanotubes assembled from half-tubes. Nano Lett 7:1757–1763
Kuzuya A, Sakai Y, Yamazaki T, Xu Y, Komiyama M (2011) Nanomechanical DNA origami 'single-molecule beacons' directly imaged by atomic force microscopy. Nat Commun 2:449
Kuzyk A, Schreiber R, Fan Z, Pardatscher G, Roller EM, Hogele A, Simmel FC, Govorov AO, Liedl T (2012) DNA-based self-assembly of chiral plasmonic nanostructures with tailored optical response. Nature 483:311–314
LaBean T, Yan H, Kopatsch J, Liu F, Winfree E, Reif JH, Seeman NC (2000) The construction, analysis, ligation and self-assembly of DNA triple crossover complexes. J Am Chem Soc 122:1848–1860
Le JD, Pinto Y, Seeman NC, Musier-Forsyth K, Taton TA, Kiehl RA (2004) DNA-templated self-assembly of metallic nanocomponent arrays on a surface. Nano Lett 4:2343–2347
Lee CC, Snyder TM, Quake SR (2010) A microfluidic oligonucleotide synthesizer. Nucleic Acids Res 38:2514–2521
Lee KW, Kim KM, Lee J, Amin R, Kim B, Park SK, Lee SK, Park SH, Kim HJ (2011) A two-dimensional DNA lattice implanted polymer solar cell. Nanotechnology 22:375202
Lee H, Lytton-Jean AK, Chen Y, Love KT, Park AI, Karagiannis ED, Sehgal A, Querbes W, Zurenko CS, Jayaraman M et al (2012) Molecularly self-assembled nucleic acid nanoparticles for targeted in vivo siRNA delivery. Nat Nanotechnol 7:389–393
Lehn J-M (1990) Perspectives in supramolecular chemistry – from molecular recognition towards molecular information processing and self-organization. Angew Chem Int Ed 29:1304–1319
Lehn J-M (2002) Supramolecular chemistry and self-assembly special feature: toward complex matter: supramolecular chemistry and self-organization. Proc Natl Acad Sci USA 99:4763–4768
Li H, LaBean TH, Kenan DJ (2006) Single-chain antibodies against DNA aptamers for use as adapter molecules on DNA tile arrays in nanoscale materials organization. Org Biomol Chem 4:3420–3426
Li Z, Wei B, Nangreave J, Lin C, Liu Y, Mi Y, Yan H (2009) A replicable tetrahedral nanostructure self-assembled from a single DNA strand. J Am Chem Soc 131:13093–13098
Li B, Ellington AD, Chen X (2011a) Rational, modular adaptation of enzyme-free DNA circuits to multiple detection methods. Nucleic Acids Res 39:e110
Li J, Pei H, Zhu B, Liang L, Wei M, He Y, Chen N, Li D, Huang Q, Fan C (2011b) Self-assembled multivalent DNA nanostructures for noninvasive intracellular delivery of immunostimulatory CpG oligonucleotides. ACS Nano 5:8783–8789
Li B, Chen X, Ellington AD (2012) Adapting enzyme-free DNA circuits to the detection of loop mediated isothermal amplification reactions. Anal Chem. doi:10.1021/ac301944v

Liao S, Seeman NC (2004) Translation of DNA signals into polymer assembly instructions. Science 306:2072–2074
Lin C, Katilius E, Liu Y, Zhang J, Yan H (2006) Self-assembled signaling aptamer DNA arrays for protein detection. Angew Chem Int Ed 45:5296–5301
Lin C, Rinker S, Wang X, Liu Y, Seeman NC, Yan H (2008) In vivo cloning of artificial DNA nanostructures. Proc Natl Acad Sci USA 105:17626–17631
Lin C, Jungmann R, Leifer AM, Li C, Levner D, Church GM, Shih WM, Yin P (2012) Sub-micrometer geometrically encoded fluorescent barcodes self-assembled from DNA. Nat Chem 4(10):832–839
Liu B, Leontis NB, Seeman NC (1994) Bulged three-arm DNA branched junctions as components for nanoconstruction. Nanobiology 3:177–188
Liu F, Sha R, Seeman NC (1999) Modifying the surface features of two-dimensional DNA crystals. J Am Chem Soc 121:917–922
Liu D, Wang M, Deng Z, Walulu R, Mao C (2004a) Tensegrity: construction of rigid DNA triangles with flexible four-arm DNA junctions. J Am Chem Soc 126:2324–2325
Liu D, Park SH, Reif JH, LaBean TH (2004b) DNA nanotubes self-assembled from triple-crossover tiles as templates for conductive nanowires. Proc Natl Acad Sci USA 101:717–722
Liu L, Guo L, Liu C, Zhang X, Jiang Y (2005a) Intramolecular charge transfer with 1-naphthanilides and 2-naphthanilides. Chin J Chem 23:857–864
Liu Y, Ke Y, Yan H (2005b) Self-assembly of symmetric finite-size DNA nanoarrays. J Am Chem Soc 127:17140–17141
Liu Y, Lin C, Li H, Yan H (2005c) Aptamer directed self-assembly of proteins on a DNA nanostructure. Angew Chem Int Ed 44:4333–4338
Liu H, Chen Y, Yu H, Ribbe AE, Mao C (2006a) Approaching the limit: can one DNA oligonucleotide assemble into large nanostructures? Angew Chem Int Ed 45:1942–1945
Liu Y, Ding L, Sha R, Canary JW, Seeman NC (2006b) Templated synthesis and properties study of nylon-DNA. PMSE Preprints 95:792
Liu W, Wang X, Wang T, Sha R, Seeman NC (2008) PX DNA triangle oligomerized using a novel three-domain motif. Nano Lett 8:317–322
Liu C, Jonoska N, Seeman NC (2009) Reciprocal DNA nanomechanical devices controlled by the same set strands. Nano Lett 9:2641–2647
Liu X, Yan H, Liu Y, Chang Y (2011) Targeted cell-cell interactions by DNA nanoscaffold-templated multivalent bispecific aptamers. Small 7:1673–1682
Liu C, Kim E, Demple B, Seeman NC (2012a) A DNA-based nanomechanical device used to characterize the distortion of DNA by Apo-SoxR protein. Biochemistry 51:937–943
Liu X, Xu Y, Yu T, Clifford C, Liu Y, Yan H, Chang Y (2012b) A DNA nanostructure platform for directed assembly of synthetic vaccines. Nano Lett 12:4254–4259
Lund K, Manzo AJ, Dabby N, Michelotti N, Johnson-Buck A, Nangreave J, Taylor S, Pei R, Stojanovic MN, Walter NG et al (2010) Molecular robots guided by prescriptive landscapes. Nature 465:206–210
Ma R-I, Kallenbach NR, Sheardy RD, Petrillo ML, Seeman NC (1986) Three arm nucleic acid junctions are flexible. Nucleic Acids Res 14:9745–9753
Malo J, Mitchell JC, Vénien-Bryan C, Harris JR, Wille H, Sherratt DJ, Turberfield AJ (2005) Engineering a 2D protein-DNA crystal. Angew Chem Int Ed 44:3057–3061
Mao C, Sun W, Seeman NC (1997) Assembly of Borromean rings from DNA. Nature 386:137–138
Mao C, Sun W, Shen Z, Seeman NC (1999a) A DNA nanomechanical device based on the B-Z transition. Nature 397:144–146
Mao C, Sun W, Seeman NC (1999b) Designed two-dimensional DNA Holliday junction arrays visualized by atomic force microscopy. J Am Chem Soc 121:5437–5443
Mao C, LaBean T, Reif JH, Seeman NC (2000) Logical computation using algorithmic self-assembly of DNA triple crossover molecules. Nature 407:493–496

Martin W, Stoebe B, Goremykin V, Hansmann S, Hasegawa M, Kowallik K (1998) Gene transfer to the nucleus and the evolution of chloroplasts. Nature 393:162–165
Mathieu F, Liao S, Kopatscht J, Wang T, Mao C, Seeman NC (2005) Six-helix bundles designed from DNA. Nano Lett 5:661–665
Maune HT, Han S-P, Barish RD, Bockrath M, Goddard WA III, Rothemund PWK, Winfree E (2010) Self-assembly of carbon nanotubes into two-dimensional geometries using DNA origami templates. Nat Nanotechnol 5:61–66
McConnell I, Li G, Brudvig GW (2010) Energy conversion in natural and artificial photosynthesis. Chem Biol 17:434–447
McHale R, Patterson JP, Zetterlund PB, O'Reilly RK (2012) Biomimetic radical polymerization via cooperative assembly of segregating templates. Nat Chem 4:491–497
Mehta AD, Rock RS, Rief M, Spudich JA, Mooseke MS, Cheney RE (1999) Myosin-V is a processive actin-based motor. Nature 400:590–593
Mei Q, Wei X, Su F, Liu Y, Youngbull C, Johnson R, Lindsay S, Yan H, Meldrum D (2011) Stability of DNA origami nanoarrays in cell lysate. Nano Lett 11:1477–1482
Mermall V, Post PL, Mark S, Mooseker MS (1998) Unconventional myosins in cell movement, membrane traffic, and signal transduction. Science 279:527–533
Modi S, Swetha MG, Goswami D, Gupta GD, Mayor S, Krishnan YA (2009) DNA nanomachine that maps spatial and temporal pH changes inside living cells. Nat Nanotechnol 4:325–330
Muser SE, Paukstelis PJ (2012) Three-dimensional DNA crystals with pH-responsive noncanonical junctions. J Am Chem Soc 134:12557–12564
Niemeyer CM, Koehler J, Wuerdemann C (2002) DNA-directed assembly of bienzymic complexes from in vivo biotinylated NAD(P)H:FMN oxidoreductase and luciferase. Chembiochem 3:242–245
Noji H, Yasuda R, Yoshida M, Kinosita K Jr (1997) Direct observation of the rotation of F_1-ATPase. Nature 386:299–302
Notomi T, Okayama H, Masubuchi H, Yonekawa T, Watanabe K, Amino N, Hase T (2000) Loop-mediated isothermal amplification of DNA. Nucleic Acids Res 28:e63
Omabegho T, Sha R, Seeman NC (2009) A bipedal DNA brownian motor with coordinated legs. Science 324:67–71
Pal S, Deng Z, Ding B, Yan H, Liu Y (2010) DNA-origami-directed self-assembly of discrete silver-nanoparticle architectures. Angew Chem Int Ed 49:2700–2704
Park SH, Yin P, Liu Y, Reif JH, LaBean TH, Yan H (2005) Programmable DNA self-assemblies for nanoscale organization of ligands and proteins. Nano Lett 5:729–733
Park SH, Pistol C, Ahn SJ, Reif JH, Lebeck AR, Dwyer C, LaBean TH (2006) Finite-size, fully addressable DNA tile lattices formed by hierarchical assembly procedures. Angew Chem Int Ed 45:735–739
Paukstelis PJ (2006) Three-dimensional DNA crystals as molecular sieves. J Am Chem Soc 128:6794–6795
Paukstelis PJ, Nowakowski J, Birktoft JJ, Seeman NC (2004) Crystal structure of a continuous three-dimensional DNA lattice. Chem Biol 11:1119–1126
Pei R, Taylor SK, Stefanovic D, Rudchenko S, Mitchell TE, Stojanovic MN (2006) Behavior of polycatalytic assemblies in a substrate-displaying matrix. J Am Chem Soc 128:12693–12699
Pfannschmidt T, Nilsson A, Allen JF (1999) Photosynthetic control of chloroplast gene expression. Nature 397:625–628
Pinto YY, Le JD, Seeman NC, Musier-Forsyth K, Taton TA, Kiehl RA (2005) Sequence-encoded self-assembly of multiple-nanocomponent arrays by 2D DNA scaffolding. Nano Lett 5:2399–2402
Rice PA, Yang SW, Mizuuchi K, Nash HA (1996) Crystal structure of an IHF-DNA complex: a protein-induced DNA U-turn. Cell 87:1295–1306
Rich A, Nordheim A, Wang AH-J (1984) The chemistry and biology of left-handed Z-DNA. Annu Rev Biochem 53:791–846

Rinker S, Ke Y, Liu Y, Chhabra R, Yan H (2008) Self-assembled DNA nanostructures for distance-dependent multivalent ligand-protein binding. Nat Nanotechnol 3:418–422
Robinson BH, Seeman NC (1987) The design of a biochip: a self-assembling molecular-scale memory device. Protein Eng 1:295–300
Rothemund PWK (2006) Folding DNA to create nanoscale shapes and patterns. Nature 440:297–302
Rothemund PWK, Papadakis N, Winfree E (2004) Algorithmic self-assembly of DNA Sierpinski triangles. PLoS Biol 2:2041–2053
Schuller VJ, Heidegger S, Sandholzer N, Nickels PC, Suhartha NA, Endres S, Bourquin C, Liedl T (2011) Cellular immunostimulation by CpG-sequence-coated DNA origami structures. ACS Nano 5:9696–9702
Schulman R, Winfree E (2004) Programmable control of nucleation for algorithmic self-assembly. In: Proceedings of the 10th international meeting on DNA based computers, pp 319–328
Schulman R, Winfree E (2007) Synthesis of crystals with a programmable kinetic barrier to nucleation. Proc Natl Acad Sci USA 104:15236–15241
Seeman NC (1982) Nucleic acid junctions and lattices. J Theor Biol 99:237–247
Seeman NC (1990) De novo design of sequences for nucleic acid structure engineering. J Biomol Struct Dyn 8:573–581
Seeman NC (1991) The use of branched DNA for nanoscale fabrication. Nanotechnology 2:149–159
Seeman NC (1999) DNA engineering and its application to nanotechnology. Trends Biotechnol 17:437–443
Seeman NC (2001) DNA nicks and nodes and nanotechnology. Nano Lett 1:22–26
Seeman NC (2003) Biochemistry and structural DNA nanotechnology: an evolving symbiotic relationship. Biochemistry 42:7259–7269
Seeman NC, Kallenbach NR (1983) Design of immobile nucleic-acid junctions. Biophys J 44:201–209
Selmi DN, Adamson RJ, Attrill H, Goddard AD, Gilbert RC, Watts A, Turberfield AJ (2011) DNA-templated protein arrays for single-molecule imaging. Nano Lett 11:657–660
Sha R, Liu F, Millar DP, Seeman NC (2000) Atomic force microscopy of parallel DNA branched junction arrays. Chem Biol 7:743–751
Sha R, Liu F, Seeman NC (2002) Atomic force measurement of the interdomain angle in symmetric Holliday junctions. Biochemistry 41:5950–5955
Sharma J, Chhabra R, Cheng A, Brownell J, Liu Y, Yan H (2009) Control of self-assembly of DNA tubules through integration of gold nanoparticles. Science 323:112–116
Shen Z (1999) DNA poly-crossover molecules and their applications in homology recognition. Dissertation, New York University
Shen WQ, Bruist MF, Goodman SD, Seeman NC (2004) A protein-driven DNA device that measures the excess binding energy of proteins that distort DNA. Angew Chem Int Ed 43:4750–4752
Shen X, Song C, Wang J, Shi D, Wang Z, Liu N, Ding B (2012) Rolling up gold nanoparticle-dressed DNA origami into three-dimensional plasmonic chiral nanostructures. J Am Chem Soc 134:146–149
Sherman WB, Seeman NC (2004) A precisely controlled DNA biped walking device. Nano Lett 4:1203–1207
Shih WM, Quispe JD, Joyce GF (2004) A 1.7-kilobase single-stranded DNA that folds into a nanoscale octahedron. Nature 427:618–621
Shin J-S, Pierce NA (2004) A synthetic DNA walker for molecular transport. J Am Chem Soc 126:10834–10835
Slinker JD, Muren NB, Renfrew SE, Barton JK (2011) DNA charge transport over 34 nm. Nat Chem 3:228–233
Soloveichik D, Cook M, Winfree E (2008) Combining self-healing and proofreading in self-assembly. Nat Comput 7:203–218

Sowa Y, Rowe AD, Leake MC, Yakushi T, Homma M, Ishijima A, Berry RM (2005) Direct observation of steps in rotation of the bacterial flagellar motor. Nature 437:916–919
Stein IH, Steinhauer C, Tinnefeld P (2011) Single-molecule four-color FRET visualizes energy-transfer paths on DNA origami. J Am Chem Soc 133:4193–4195
Steinhauer C, Jungmann R, Sobey TL, Simmel FC, Tinnefeld P (2009) DNA origami as a nanoscopic ruler for super-resolution microscopy. Angew Chem Int Ed 48:8870–8873
Svoboda K, Schmidt CF, Schnapp BJ, Block SM (1993) Direct observation of kinesin stepping by optical trapping interferometry. Nature 365:721–727
Tian Y, He Y, Chen Y, Yin P, Mao C (2005) A DNAzyme that walks processively and autonomously along a one-dimensional track. Angew Chem Int Ed 44:4355–4358
Tian J, Ma K, Saaem I (2009) Advancing high-throughput gene synthesis technology. Mol Biosyst 5:714–722
Tikhomirov G, Hoogland S, Lee PE, Fischer A, Sargent EH, Kelley SO (2011) DNA-based programming of quantum dot valency, self-assembly and luminescence. Nat Nanotechnol 6:485–490
Vale RD (2003) The molecular motor toolbox review for intracellular transport. Cell 112:467–480
Venkataraman S, Dirks RM, Rothemund PWK, Winfree E, Pierce NA (2007) An autonomous polymerization motor powered by DNA hybridization. Nat Nanotechnol 2:490–494
Walsh AS, Yin H, Erben CM, Wood MJ, Turberfield AJ (2011) DNA cage delivery to mammalian cells. ACS Nano 5:5427–5432
Wang H (1961) Proving theorems by pattern recognition II. Bell Syst Tech J 40:1–42
Wang H (1962) An unsolvable problem on dominoes. Technical report BL-30 (II-15). Harvard Computation Laboratory, Cambridge, MA
Wang T (2007) Structural DNA nanotechnology design and self-assembly of two-dimensional and three-dimensional crystalline lattices. Dissertation, New York University
Wang H, Oster G (1998) Energy transduction in the F_1 motor of ATP synthase. Nature 396:279–282
Wang X, Seeman NC (2007) The assembly and characterization of 8-arm and 12-arm DNA branched junctions. J Am Chem Soc 129:8169–8176
Wang Y, Mueller JE, Kemper B, Seeman NC (1991) The assembly and characterization of 5-arm and 6-arm DNA junctions. Biochemistry 30:5667–5674
Wang R, Liu W, Seeman NC (2009) Prototyping nanorod control: a DNA double helix sheathed within a DNA six-helix bundle. Chem Biol 16:862–867
Wang F, Elbaz J, Orbach R, Magen N, Willner I (2011) Amplified analysis of DNA by the autonomous assembly of polymers consisting of DNAzyme wires. J Am Chem Soc 133:17149–17151
Wasielewski MR (2009) Self-assembly strategies for integrating light harvesting and charge separation in artificial photosynthetic systems. Acc Chem Res 42:1910–1921
Watson JD, Crick FHC (1953) Molecular structure of nucleic acid; a structure for deoxyribose nucleic acid. Nature 171:737–738
Wei B, Dai M, Yin P (2012) Complex shapes self-assembled from single-stranded DNA tiles. Nature 485:623–626
Whitesides GM, Grzybowski B (2002) Self-assembly at all scales. Science 295:2418–2421
Whitesides GM, Mathias JP, Seto CT (1991) Molecular self-assembly and nanochemistry: a chemical strategy for the synthesis of nanostructures. Science 254:1312–1319
Wilner OI, Weizmann Y, Gill R, Lioubashevski O, Freeman R, Willner I (2009) Enzyme cascades activated on topologically programmed DNA scaffolds. Nat Nanotechnol 4:249–254
Winfree E (1996) On the computational power of DNA annealing and ligation. In: Lipton RJ, Baum EB (eds) DNA-based computers. American Mathematical Society, Providence, RI, pp 199–221
Winfree E (1998) Simulations of computing by self-assembly. Technical report CSTR: 1998.22. California Institute of Technology, Pasadena, CA

Winfree E (2000) Algorithmic self-assembly of DNA: theoretical motivations and 2D assembly experiments. J Biomol Struct Dyn 17(Suppl 1):263–270
Winfree E (2006) Self-healing tile sets. In: Chen J, Jonoska N, Rozenberg G (eds) Nanotechnology: science and computation, Natural computing series. Springer, Heidelberg, pp 55–78
Winfree E, Bekbolatov R (2004) Proofreading tile sets: error correction for algorithmic self-assembly. In: Chen J, Reif J (eds) DNA computing and molecular programming, vol 2943, Lecture notes in computer science. Springer, Heidelberg, pp 126–144
Winfree E, Liu F, Wenzler LA, Seeman NC (1998) Design and self-assembly of two-dimensional DNA crystals. Nature 394:539–544
Xiao S, Liu F, Rosen AE, Hainfeld JF, Seeman NC, Musier-Forsyth K, Kiehl RA (2002) Self-assembly of metallic nanoparticle arrays by DNA scaffolding. J Nanopart Res 4:313–317
Yan H, Zhang X, Shen Z, Seeman NC (2002) A robust DNA mechanical device controlled by hybridization topology. Nature 415:62–65
Yan H, Park SH, Finkelstein G, Reif JH, LaBean TH (2003a) DNA-templated self-assembly of protein arrays and highly conductive nanowires. Science 301:1882–1884
Yan H, LaBean TH, Feng L, Reif JH (2003b) Directed nucleation assembly of DNA tile complexes for barcode-patterned lattices. Proc Natl Acad Sci USA 100:8103–8108
Yang X, Vologodskii AV, Liu B, Kemper B, Seeman NC (1998a) Torsional control of double stranded DNA branch migration. Biopolymers 45:69–83
Yang X, Wenzler LA, Qi J, Li X, Seeman NC (1998b) Ligation of DNA triangles containing double crossover molecules. J Am Chem Soc 120:9779–9786
Yang Y, Han D, Nangreave J, Liu Y, Yan H (2012) DNA origami with double-stranded DNA as a unified scaffold. ACS Nano. doi:10.1021/nn302896c
Yildiz A, Tomishige M, Vale RD, Selvin PR (2004) Kinesin walks hand-over-hand. Science 303:676–678
Yin P, Yan H, Daniell XG, Turberfield AJ, Reif JH (2004) A unidirectional DNA walker that moves autonomously along a track. Angew Chem Int Ed 43:4906–4911
Yin P, Choi HM, Calvert CR, Pierce NA (2008a) Programming biomolecular self-assembly pathways. Nature 451:318–322
Yin P, Hariadi RF, Sahu S, Choi HM, Park SH, Labean TH, Reif JH (2008b) Programming DNA tube circumferences. Science 321:824–826
Yurke B, Turberfield AJ, Mills AP Jr, Simmel FC, Newmann JL (2000) A DNA-fuelled molecular machine made of DNA. Nature 406:605–608
Zhang Y, Seeman NC (1994) The construction of a DNA truncated octahedron. J Am Chem Soc 116:1661–1669
Zhang X, Liu C, Liu L, Wu F, Guo L, Sun X, Wang C, Jiang Y (2003) Intramolecular charge transfer with N-benzoylaminonaphthalenes. 1-Aminonaphthalene versus 2-aminonaphthalene as electron donors. Org Biomol Chem 1:728–732
Zhang J, Liu Y, Ke Y, Yan H (2006) Periodic squarelike gold nanoparticle arrays template by self-assembled 2D DNA nanogrids on a surface. Nano Lett 6:248–251
Zhang DY, Turberfield AJ, Yurke B, Winfree E (2007) Engineering entropy-driven reactions and networks catalyzed by DNA. Science 318:1121–1125
Zhang C, He Y, Su M, Ko SH, Ye T, Leng Y, Sun X, Ribbe AE, Jiangh W, Mao C (2009) DNA self-assembly: from 2D to 3D. Faraday Discuss 143:221–233
Zheng J, Constantinou PE, Micheel C, Alivisatos AP, Kiehl RA, Seeman NC (2006) 2D nanoparticle arrays show the organizational power of robust DNA motifs. Nano Lett 6:1502–1504
Zheng J, Lukeman PS, Sherman WB, Micheel C, Alivisatos AP, Constantinou PE, Seeman NC (2008) Metallic nanoparticles used to estimate the structural integrity of DNA motifs. Biophys J 95:3340–3348
Zheng J, Birktoft JJ, Chen Y, Wang T, Sha R, Constantinou PE, Ginell SL, Mao C, Seeman NC (2009) From molecular to macroscopic via the rational design of a self-assembled 3D DNA crystal. Nature 461:74–77

Zheng AX, Li J, Wang JR, Song XR, Chen GN, Yang HH (2012) Enzyme-free signal amplification in the DNAzyme sensor via target-catalyzed hairpin assembly. Chem Commun 48:3112–3114
Zhong H, Seeman NC (2006) RNA used to control a DNA rotary nanomachine. Nano Lett 6:2899–2903
Zhu L, Lukeman PS, Canary JW, Seeman NC (2003) Nylon/DNA: single-stranded DNA with a covalently stitched nylon lining. J Am Chem Soc 125:10178–10179

Part III
DNA-Directed Chemistry

Chapter 7
DNA-Templated Synthesis

Christian B. Rosen, Thomas Tørring, and Kurt V. Gothelf

Abstract In DNA templated synthesis (DTS) the effective local concentration of two or more reactants tethered to oligonucleotide strands is regulated by direct hybridization of the strands or by hybridization to a common template, bringing the reactants in close proximity. This provides efficient DNA-programmed control of chemical reactions at low concentrations. Furthermore, the approach may leave a nucleic acid tag on the reaction product enabling identification by PCR and sequencing. The concept has been applied for a variety of purposes, where control and spatial directionality of chemical reactivity are important, such as for chemical ligation of nucleic acids, nucleic acid detection, construction of macromolecular nanostructures, multistep synthesis, drug discovery, and chemical reaction discovery. In this chapter a selection of pertinent contributions to the field DTS are reviewed.

Contents

C.B. Rosen • T. Tørring • K.V. Gothelf (✉)
Centre for DNA Nanotechnology, Department of Chemistry and iNANO, Aarhus University, Aarhus 8000 C, Denmark
e-mail: kvg@chem.au.dk

J. KJEMS et al. (eds.), *Nucleic Acid Nanotechnology*, Nucleic Acids and Molecular Biology 29, DOI 10.1007/978-3-642-38815-6_7,

7.1 Introduction

DNA-templated synthesis (DTS) has attracted increasing interest since the first report in 1966 (Naylor and Gilham 1966) and hence been adopted by various research areas. The principle of applying DNA as a directing tool in conventional organic chemistry has expanded the scope of synthetic methodology, and today DTS plays a central role in chemistry, chemical biology, and biophysics, here among subfields such as *detection and sensing, polymer formation, drug discovery, and reaction discovery*.

In organic synthesis reactions are normally performed at high concentrations (mM to M) to ensure random collisions between the functional groups participating in an intermolecular reaction. When synthesizing complex organic molecules in several linear steps, the workload increases exponentially through the use of multiple protecting groups and elaborate purifications. Conceptually, this constitutes a fundamental contrast to how nature accommodates chemospecific control. In nature, numerous different reactants are present at the same time, however, in a much lower concentration (nM to μM). At these concentrations random product formation is highly unlikely, however in nature, macromolecules have evolved to act as catalytic templates elevating the local molarity of specific reaction partners. This elegant system provides admirable efficiency and specificity. In several of these biological processes such as DNA replication, DNA transcription into RNA, and translation of RNA into proteins, nucleic acids serve as blueprints. In the attempt to mimic the elegance of nature, we take advantage of the many significant features of DNA that makes it a powerful construct for applications in synthetic chemistry. First of all, the hybridization of DNA is extremely selective owing to the Watson–Crick base pairing between complementary nucleobases. Secondly, owing to its enormous sequence space, DNA can serve as an amplifiable barcode. Finally, automated DNA synthesis is well established making nucleic acids with a plethora of non-natural functionalities commercially available.

The earliest work on the use of nucleic acids for templating chemical reactions in a nonbiological context was aiming at chemically creating the natural phosphodiester unit of the DNA backbone (Naylor and Gilham 1966). Single-stranded DNA (or RNA) was applied as a template to facilitate the formation of phosphodiester bonds, thereby catalyzing the ligation of other nucleic acids or nucleic acid analogues. Today, more sophisticated and highly complex synthetic setups have been implemented and DTS has emerged into a constantly evolving field within natural sciences.

7.2 Nucleic Acid Detection and Sensing Using DTS

The very first example of a DNA-templated synthesis was reported by Naylor and Gilham in 1966 (Naylor and Gilham 1966). They constructed a model system composed of a polyadenosine dodecamer and two polythymine hexamers, one of which was carrying a 5′ phosphate. The model system was incubated with a water-soluble carbodiimide in saline buffer over several days at −3 °C resulting in a thymine dodecamer in poor yield (5 %) (see Fig. 7.1a). The general interest in prebiotic chemistry

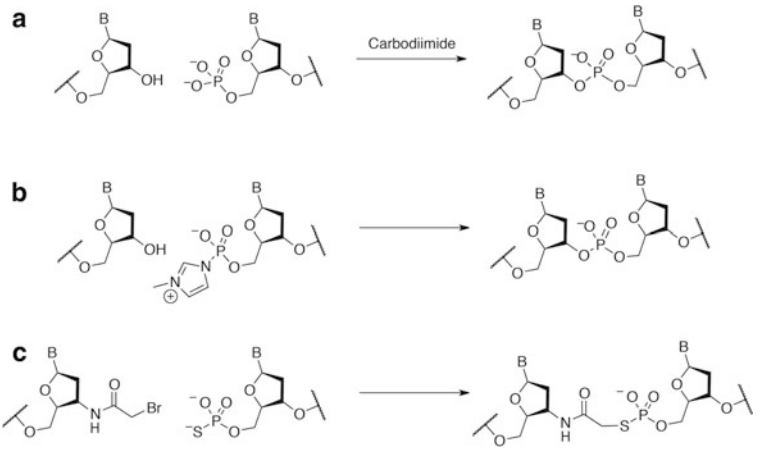

Fig. 7.1 Examples of chemical ligation of DNA strands on a template. (**a**) Using a carbodiimide to make a chemical ligation resulting in a phosphodiester (Naylor and Gilham 1966). (**b**) Chemical ligation using pre-activation (Wu and Orgel 1992). (**c**) Employing phosphorothioates to improve reaction speed and efficiency (Gryaznov and Letsinger 1993)

led Orgel and others to investigate templated, but nonenzymatic creation of nucleic acid. Practically, this was done by incubating a hairpin template with high concentrations of 2-methylimidazole-activated nucleotides and investigating the guided polymerization (Wu and Orgel 1992). The reactions were generally slow, and, in the reaction shown in Fig. 7.1b, even short stretches were not completely polymerized before several days of incubation. In 1993, Gryaznov and Letsinger reported on the much faster ligation between a phosphorothioate and a α-halo acyl moiety (see Fig. 7.1c) (Gryaznov and Letsinger 1993). The templated reaction between two oligonucleotides carrying these modifications resulted in 90 % conversion in only 20 min. Based on this result the authors suggested that such a system could be used as a chemical amplification system. A major issue in using such system for amplification is that the ligation product will normally have increased binding affinity to the template, thereby hampering its ability to act catalytically. A cross-catalytic self-replicating system was reported by Sievers and von Kiedrowski in 1994 (Sievers and von Kiedrowski 1994). Modified trinucleotides with 5′ amines and 3′ phosphates were ligated using a carbodiimide. The products of these ligations could catalyze new ligations. Lynn and coworkers later introduced a ligation mediated by the condensation between an amine and a aldehyde (Luo et al. 1998). A subsequent imine reduction destabilized the duplex, lowered the melting temperature, and diminished the product inhibition.

In 2001, Kool and coworkers published the first DNA-templated detection system for single nucleotide polymorphism (SNP) based on a fluorescent output (Fig. 7.2) (Xu et al. 2001). The output was generated by the autoligation of a 3′ phosphorothioate and a 5′ iodide. The discrimination between such SNP was achieved using short probes of only 7 and 13 bases, wherein the 7-mer would bind to the sequence displaying the SNP. To validate their concept, they first designed radiolabeled

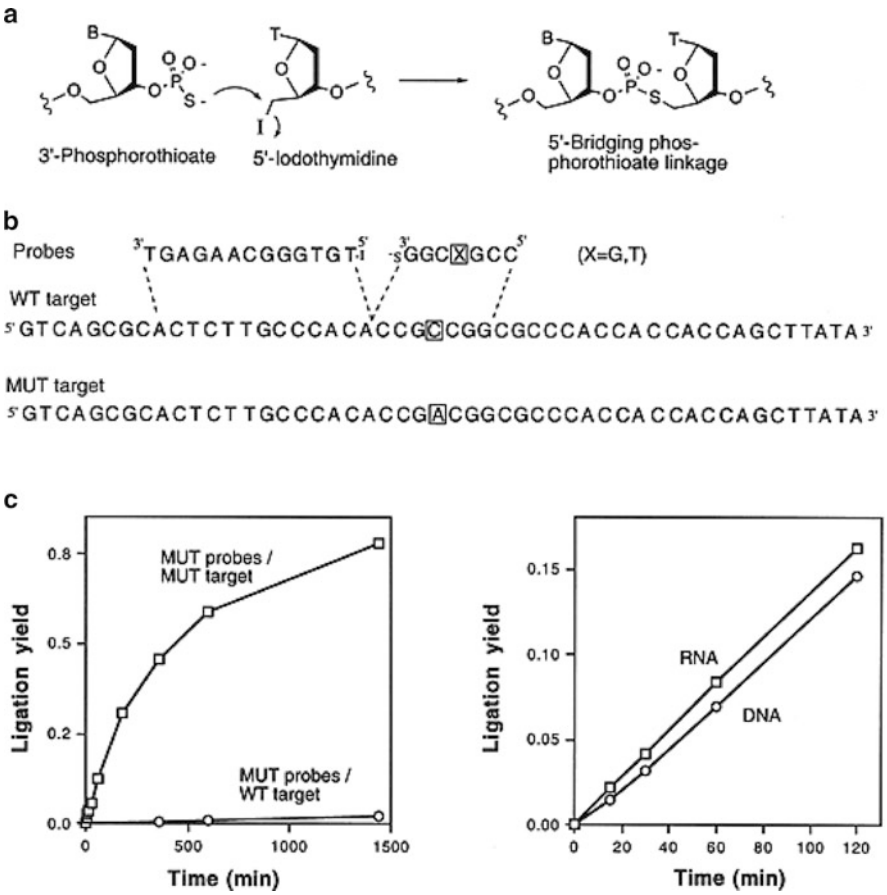

Fig. 7.2 Pioneering work by Kool and coworkers (Xu et al. 2001) on the application of DTS to detect SNPs. (**a**) The phosphorothioate-mediated ligation to a 5′ iodo-oligonucleotide. (**b**) The probe design showing the mutation site in *brackets*. (**c**) The yield of ligation as a function of time, demonstrating the systems ability to detect single base mismatches. Also, the ligation proceeds with both RNA and DNA templates

probes capable of binding a sequence in the H-*ras* protooncogene known to undergo G to T mutations. With a ratio of more than 180-fold, the autoligation showed a clear discrimination between wildtype and mutant target and more surprisingly the system work equally well with a RNA target.

The short sequences employed were also enabling multiple ligations to be catalyzed by the same template. Thus, incubating 10 μM of the probes with only 1 nM of the template resulted in a turnover number of 40, i.e., gaining 280 fmol ligation product from only 7 fmol template. To enable fluorescent detection the researchers employed a three-color system designed to give distinct Förster Resonans Energy Transfer (FRET) signals if either mutant or wild type were present. The donor fluorophore, FAM, was attached to the 13-mer next to the

mutation site, and two different 7-mers were modified with acceptor fluorophores. The probe binding the mutant sequence was modified with ROX giving a red signal and the one binding the wild type sequence was modified with HEX giving a yellow signal. When incubated with a target sequence, the output could be read from solution or after gel electrophoresis.

The past decades have offered several improvements of detection systems based on DNA-templated reactions, but before examining these in closer detail, it is instructive to highlight some aspects of an ideal system. The ideal system should (1) have a stabile dark off-state, (2) discriminate between SNPs, and in particular also the more challenging changes, (3) work in complex media or even live cells, (4) use the template as a catalyst, meaning no significant product inhibition, and (5) give a clear signal upon detection of the analyte.

The first example is a system termed Q-STAR (Staudinger-triggered α-azidoether release) probes developed by the Kool group (Franzini and Kool 2009). The system relies on a DNA probe labeled in one position with a fluorescein fluorophore and in a second position with a Dabsyl quencher bound to the DNA via a relatively stable α-azidoether linker. The second probe is modified with a phosphine capable of reducing the azide to a much more labile hemiaminal ether through a reaction known as the Staudinger reduction. The hemiaminal is readily hydrolyzed in water thereby releasing the bound quencher. The Staudinger reduction consumes the phosphine transforming it into an inert phosphine oxide. The two probes were designed to bind a common target in such a way that the phosphine aligns perfectly with the α-azidoether. As demonstrated in Fig. 7.3, the fluorescein fluorescence increased rapidly in the presence of the phosphine probe and the template. More importantly a template with a single mismatch gave a very low signal allowing the system to discriminate between SNPs. Another design feature was the relative short probe length making the melting temperature of the complex comparable to the incubation temperature of 37 °C. This allowed dynamic exchange of the probes and therefore the template worked in sub-stoichiometric amounts. This was demonstrated with varying amounts of template, 1 eq.–0.01 eq., clearly showing the catalytic nature of the template. To show that the Q-STAR system could be used in a cellular context, the authors prepared a second Dabsyl-quenched probe. The probe bound a target with only one base pair difference, and upon Dabsyl release, the fluorescein would act as a FRET donor to a TAMRA fluorophore also attached to the probe strand. The targets are present in the ribosomal RNA of two bacteria. The fluorescein probe was specific for *E. coli*, whereas the FRET probe was specific for *S. enterica*. The results, presented in Fig. 7.3c, showed that the Q-STAR system effectively discriminated between different cells. In a later report (Franzini and Kool 2011), the authors improved the system by tethering two quenchers to each fluorophore probe. This prevented unspecific loss of a quencher to result in a false positive.

One major constrain when employing nucleic acid-based system for cellular imaging is the inherent impermeability of cell membranes. This normally requires fixating and permeabilizing reagents that the cells seldom survive. To circumvent this and allow imaging of RNA in live cells, Winssinger and coworkers (Pianowski et al. 2009) designed a system composed of guanidine-based peptide nucleic acids

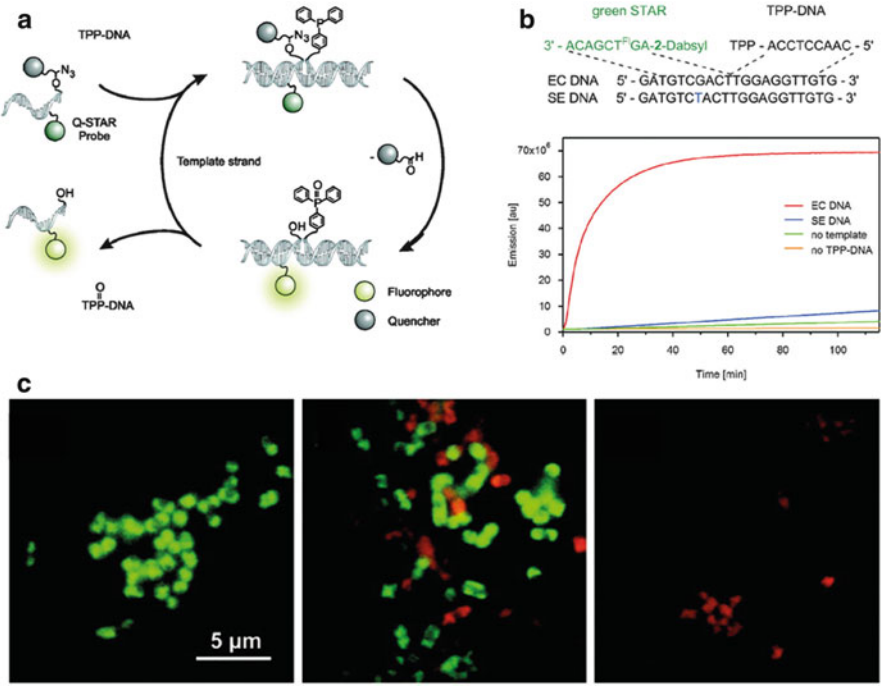

Fig. 7.3 The Q-STAR system developed by Kool and coworkers (Franzini and Kool 2009). (**a**) The catalytic cycle of the Q-STAR system. The template positions the phosphine probe and azide probe in close proximity. This enables a Staudinger reduction that releases the quencher and enables fluorescence. (**b**) Sequence design and fluorescence as a function of time in the presence of target DNA. (**c**) Based on SNP, the probes could be designed to discriminate between *E. coli* and *S. enterica*. All cells were incubated with both probes. *Left*: *E. coli* cells. *Middle*: *E. coli* and *S. enterica*. *Right*: *S. enterica*

(GPNA) previously shown to cross the cell membrane. The system was composed of two GPNA probes, one carrying a phosphine and another carrying an azido-masked rhodamine fluorophore (Fig. 7.4a). The rhodamine fluorescence is dependent on a free amino group and as seen in the previous example, these can be masked as azides and released in a Staudinger reduction. The authors prepared the masked rhodamine as an isocyanate that was readily incorporated in the Fmoc-based solid-phase synthesis of GPNA. The phosphine, being destroyed during the Fmoc cleavage conditions, had to be incorporated in the final step, just before acidic cleavage from the solid support. Initial testing in vitro demonstrated that the designed templated reaction only took place in presence of the template. More importantly, it was shown that the system could discriminate between the fully complementary template and templates with one or two mismatches. Employing the probes in a cellular context also resulted in a successful fluorescence signal. As shown in Fig. 7.4b, incubating the cells with 250 nM of the masked fluorescein probe for

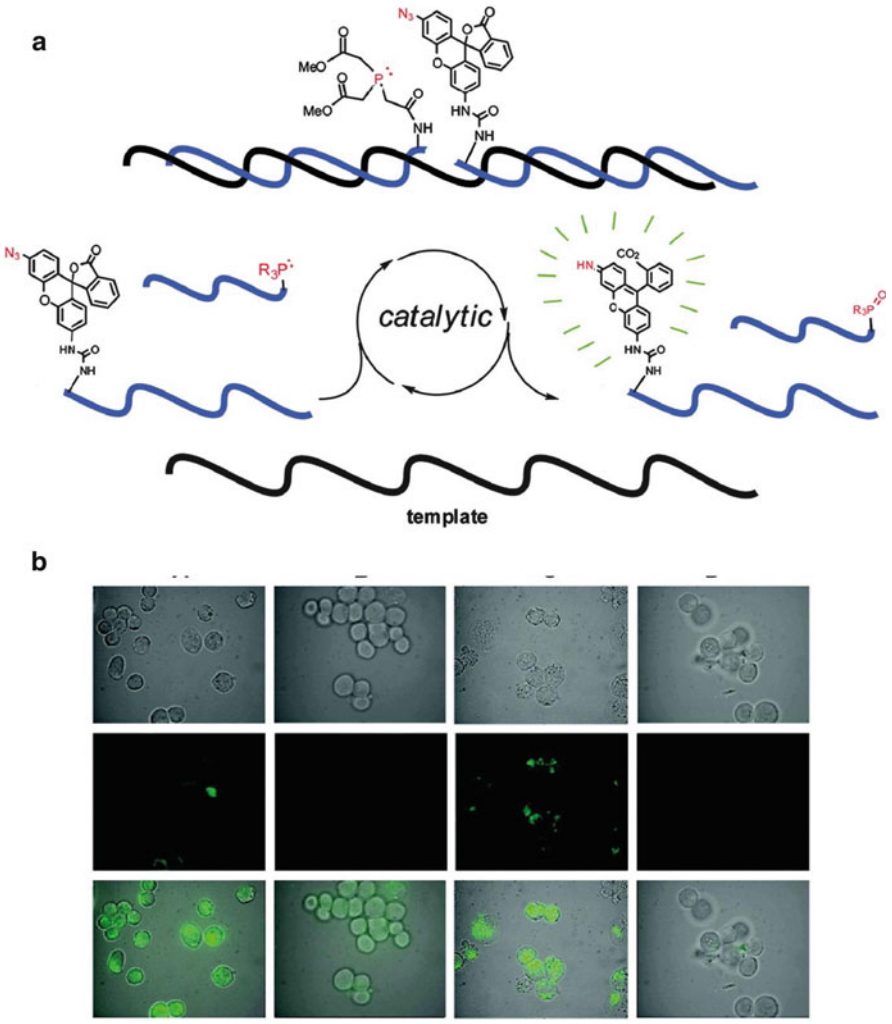

Fig. 7.4 A catalytic demasking of a rhodamine dye based on cell-penetrating GPNA probes and thus applicable to live cells (Pianowski et al. 2009). (**a**) Scheme for the catalytic cycle. (**b**) Live cells incubated with the masked rhodamine probe. *Top row* is white light image, *middle row* is fluorescence, and *bottom row* is an overlay. *First column* has a small molecule azide reductant in large excess. *Second column* is a negative control. *Third column* has the fully matched PNA-conjugated phosphine. *Fourth column* has a mismatched PNA-conjugated phosphine

90 min and then treating with two equivalents of the phosphine probe resulted in fluorescence only in the presence of a fully complementary target.

While the previous two examples have relied on masked or quenched fluorophores, the Seitz group chose a different strategy (Chen et al. 2012). They designed a templated reaction resulting in the de novo synthesis of a fluorophore. Instead of synthesizing the fluorophore through ligation, which could lead to product inhibition, they employed a

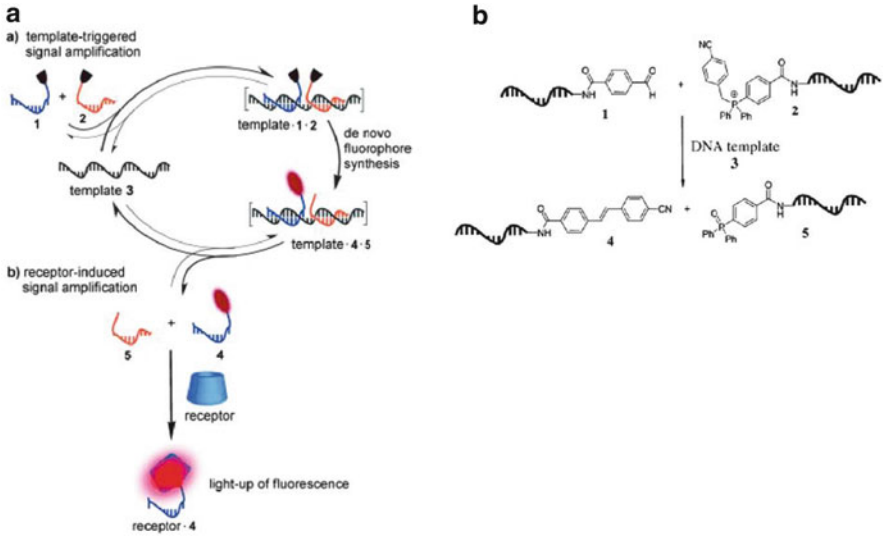

Fig. 7.5 The catalytic DNA-templated synthesis of a fluorophore reported by Seitz and coworkers (Chen et al. 2012). (**a**) Scheme portraying the catalytic formation of a fluorophore. The synthesized fluorophore can act as a guest in a host–guest complex greatly increasing its fluorescence. (**b**) A Wittig reaction resulting in the *trans*-stilbene fluorophore

Wittig reaction in the transfer of a benzylidene group to a benzaldehyde. The resulting stilbene product is fluorescent and principally by synthesizing the fluorophore instead of demasking it should provide a lowered background signal. To amplify the fluorescent signal, Seitz and coworkers combined the system with a receptor capable of binding the formed stilbene and increase its fluorescence output (Fig. 7.5). The combination of template turnover and fluorescence enhancement led to an impressive total signal gain of 336. The Wittig transfer reaction proved stable toward heating, enabling the researchers to challenge a more difficult target, namely double-stranded DNA. Whereas RNA isolated from biological samples mainly is single stranded, albeit with some secondary structure, DNA is dominantly found as the double-stranded species. This poses a significant challenge because the double-stranded form is unlikely to interact with most probes. Heating the sample, denaturing the duplex, and allowing probes to bind can circumvent this problem, but this requires robust chemistry. Incubating their system with a 81-mer duplex and performing several heating cycles to alternately denature and couple the template with the reactive probes, led to a 50 % increase in fluorescence over 3 h in the presence of 4 nM double-stranded target (Fig. 7.5).

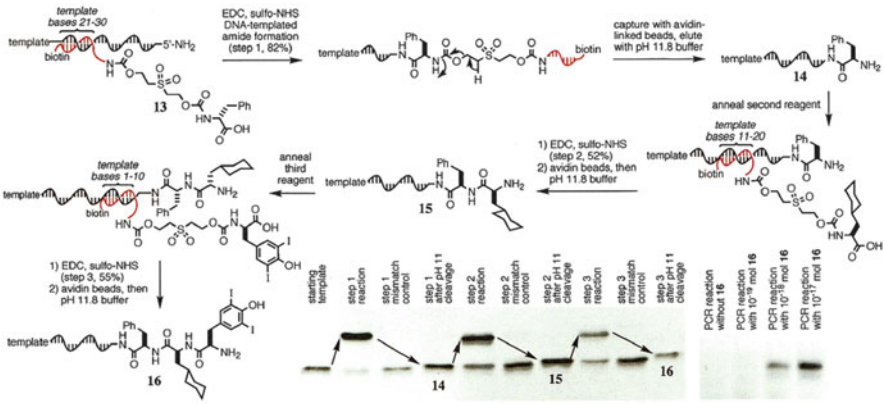

Fig. 7.6 DNA-templated synthesis of a tripeptide utilizing the cleavable sulfone linker construct. The reaction products are purified and isolated by affinity chromatography and analyzed by denaturing PAGE

7.3 Multistep Reactions Using DTS

In order to synthesize complex molecules by DNA-templated synthesis, multiple succeeding steps are required. The discovery of distance-independent regimes for a branch of different chemical reactions performed by DTS (Gartner et al. 2002a), was an important concept in this regard, since it allowed for a single template to be translated into complex organic molecules in a progressive manner. In 2002, David R. Liu and coworkers demonstrated the first examples of multistep synthesis by DTS (Gartner et al. 2002b). For this purpose, they developed different cleavable linkers to connect the reagent oligonucleotide (ON) to the molecular building block of interest. As an example, a linker can be "scarless" in the sense that cleavage of it does not leave any unwanted chemical functionality. An α-amine of an amino acid building block 1 (BB1) was attached to one end of a sulfone linker through a carbamate and likewise a 3′ amine-modified ON was attached to the other end of the linker. Upon hybridization with a 5′ amine-modified ON template, the amino acid BB1 was reacted with the template strand by an amide coupling (Fig. 7.6). A subsequent increase of the pH to 11.8 cleaved the sulfone linker at the carbamate functionality by elimination, hence, liberating an amine group at the 5′ terminal of the now-transferred BB1. This could then be employed in the coupling of a second amino acid building block (BB2) positioned on another reagent ON that is complimentary to a different 10-mer region on the template, following the same procedure. Liu and coworkers designed a method that would allow isolation and purification of the covalent product after each reaction step by installation of a biotin functionality at the 5′ terminal of the reagent ON. The peptide-type product formed through a series of directed reactions of three building blocks was captured and isolated by affinity chromatography, utilizing the strong noncovalent interaction of biotin to streptavidin (STV) beads.

The template was designed with three consecutive 10-mer recognition regions, where each incoming complementary reagent ONs will be closer to the 5′ site of

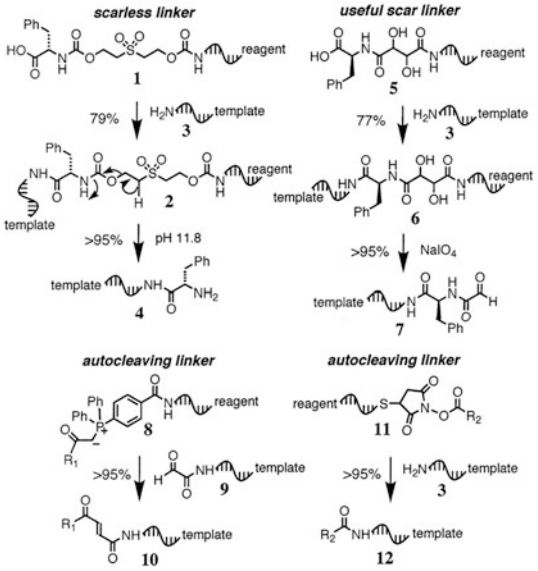

Fig. 7.7 Three types of linker applied for multistep DNA-templated synthesis; the scarless linker, the useful scar linker, and two different examples on autocleaving linkers. R_1 = $NH(CH_2)_2NH$-dansyl; R_2 = biotinyl

reaction and thereby account for the 5′ terminal peptide growth on the template. The yields for the DNA-templated amide formations were ranging from 52 to 82 % determined by denaturing PAGE analysis (Fig. 7.6). An overall yield of the tripeptide resulting from three templated reactions, three linker cleavage steps, and three purification steps was 3 %. In general, the overall yield is usually not as important as for traditional or combinatorial chemistry, since product identification can be achieved through PCR amplification of the template ON (see Sect. 7.4).

In addition to the scarless linker strategy described above, Liu and coworkers developed several other linker constructs. One type, termed the "useful scar linker," contains a vicinal diol moiety, which upon treatment with aqueous sodium periodate ($NaIO_4$) would undergo oxidative cleavage, leaving and aldehyde functionality suitable for further chemical manipulation (Fig. 7.7). Furthermore, they developed different types of linkers that would be automatically cleaved after reaction had occurred, the so-called autocleaving linkers. One example is the Wittig phosphorane reagent, where the DNA-decoding sequence is connected through a triphenylphosphine functionality. While the biotin label on the reagent ON provides an easy and effective purification for both the scarless and the useful scar linker setups, the use of biotin for the autocleaving linker approaches does only allow isolation from unreacted and cleaved reagent ONs and, furthermore, it does not allow separation from unreacted template. Hence, isolation of the product from the template strand has to be accomplished by gel purification or after a subsequent reaction step. Liu and coworkers demonstrated a three-step DNA-templated synthesis applying all of the three mentioned linker constructs. The reaction progress could be followed by PAGE analysis.

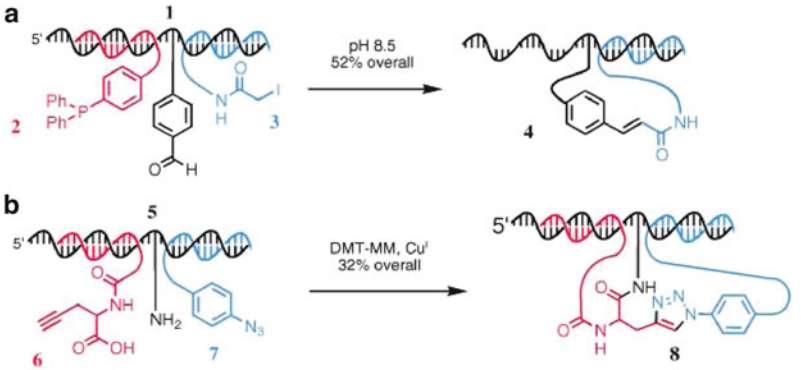

Fig. 7.8 DNA-templated sequential two-step reactions using the T template architecture. (**a**) S_N2 reaction of a 5′ phosphane-linked reagent (*red*) onto a 3′ iodoacetamide-modified reagent (*blue*), followed by Wittig coupling with the corresponding phosphorane and a benzaldehyde functionality on the template (*black*). (**b**) Peptide coupling between a 5′ propargylglycine linked reagent (*red*) and an amine moiety on the template strand (*black*) by activation with DMTMM, followed by copper (I) catalyzed Huisgen–Meldal–Sharpless cycloaddition onto 3′ phenyl azide-linked reagent (*blue*)

In 2003, David Liu and coworkers demonstrated a one pot two-step reaction between three individual reaction partners using DNA-templated chemistry (Gartner et al. 2003). They used a 30-mer T architecture with an aldehyde functionality positioned in the middle of the template strand to sequentially direct the formation of a phosphonium ylide from iodoacetamide, followed by a Wittig coupling to the aldehyde moiety (Fig. 7.8a). The reactions were performed in an overall yield of 52 % of the covalent product. The same principle could be applied to sequence specifically direct the peptide coupling between a 5′ propargylglycine modified ON and an amine-linked T template by the addition of an activating agent (Fig. 7.8b). Subsequent addition of copper (I) allowed for a templated Huisgen–Meldal–Sharpless cycloaddition between an 3′ azide modified oligonucleotide and the alkyne functionality of the propargylglycine, yielding the three-component product in 32 % overall.

One year after, the concept of DNA translation into complex organic molecules was further extended to synthetic *N*-acyloxazolidines (Li et al. 2004). By employment of three coding regions on a T architecture template, Liu and coworkers succeeded in the sequential DNA-templated coupling of three reaction components, beside the amine-modified template (Fig. 7.9a). As an elegant refinement to their initial work (Gartner et al. 2003), different cleavable linkers were introduced in order to achieve the pure *N*-acyloxazolidines product positioned on the encoding template. As the first codon is located further away from the reaction site, the template was designed to hold a so-called Ω region enabling decreased strand flexibility and thereby increase coupling efficiency, resulting in a doubling of the yields to 51 % (Fig. 7.9b). In addition to the three DNA-templated couplings and consecutive purifications steps, a final ring closure was performed, yielding the desired bicyclic structure (Fig. 7.9c).

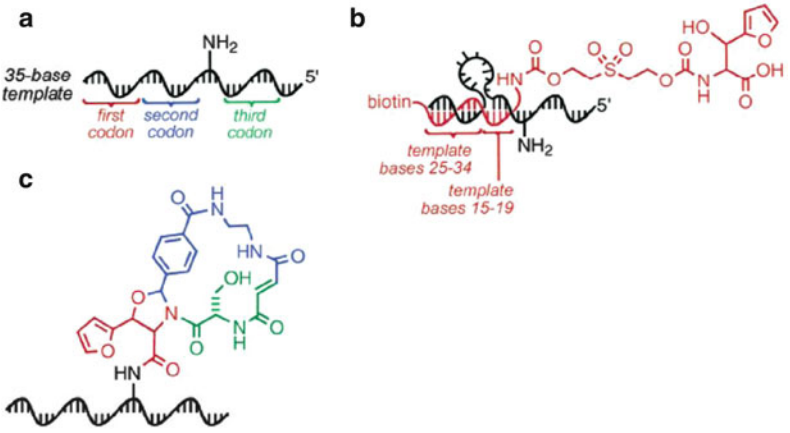

Fig. 7.9 Synthesis of *N*-acyloxazolidines by multistep DTS. (**a**) The amine functionalized T template architecture containing three unique codon regions. (**b**) The Ω architecture formed between the template strand and the first reagent ON. (**c**) The *N*-acyloxazolidine target molecule

7.3.1 DNA-Programmed Assembly of Synthetic Conjugated Nanostructures

DNA-templated synthesis had proven to be a unique and highly reliable technique to fabricate complex organic molecules in a sequential fashion. As reagent concentrations are maintained extremely low during DTS, multiple functional groups of similar reactivity can be present in the same solution, hence protection group chemistry can to some extent be obviated.

Czlapinski and Sheppard published in 2001 a study on DNA-templated assembly of metallosalen–DNA conjugates (Czlapinski and Sheppard 2001). Inspired by this work, Gothelf et al. showed in 2004, how potentially conducting molecular wire constructs could be formed by DNA-directed assembly of several oligo(phenylene ethynylene) (OPE) units, utilizing a so-called end-of-helix architecture (Gothelf et al. 2004). The monomeric OPE units contained terminal salicylaldehydes groups that could be interlinked through covalent manganese–salen complexes (Fig. 7.10).

The monomers were synthesized (Nielsen et al. 2004) with a DMTr-protected primary hydroxyl group on one side chain and with a phosphoramidite functionality at the other. ON fabrication could then be obtained by standard automated oligonucleotide synthesis. The OPE monomers were incorporated at the 16th synthetic DNA cycle, yielding 15-mer ONs of desirable sequences at each side chain. Several modules were annealed and the coupling reaction was performed by incubation of the self-assembled monomers with ethylenediamine and $Mn(OAc)_2$ at 25 °C. The product was analyzed by denaturing PAGE, MALDI-TOF, and DNA-melting temperatures.

In addition to the linear OPE motif, a tripoidal version was synthesized (Fig. 7.10b) and connected to either linear or tripoidal monomers in a DNA-directed fashion,

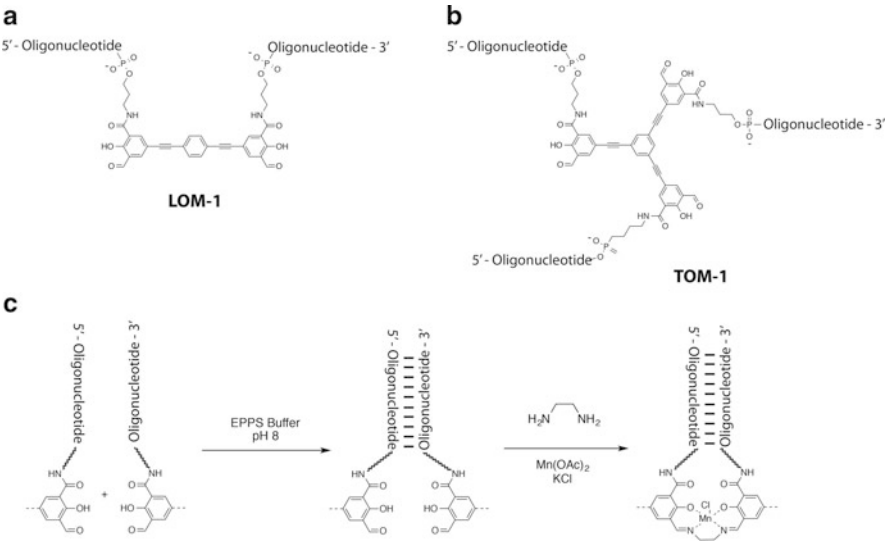

Fig. 7.10 DNA-templated formation of molecular wire constructs. (**a**) The linear oligonucleotide-functionalized module (LOM). (**b**) The tripoidal oligonucleotide-functionalized module (TOM). (**c**) DNA-directed coupling of two salicylaldehydes termini to generate a covalent manganese–salen complex

resulting in branched molecular wire modules of discrete lengths. However, common for both designs were the inability to make larger than tetrameric structures.

As ONs are protruding from the molecules, the covalent wire structure holds the potential to be aligned on a DNA origami surface, resembling an actual circuit. However, the conductivity across a manganese–salen complex has not been confirmed.

Gothelf and coworkers have studied several other DNA-templated approaches for the fabrication of molecular wire constructs, many of which relied on the promising metallosalen complex strategy. These include insertion of disulfide bonds in between the ONs and the monomer side chains, which could be cleaved upon reduction with TCEP (Brown et al. 2004; Nielsen et al. 2005), and synthesis of elongated linear OPE frames (Blakskjær and Gothelf 2006) that could covalently dimerize by the addition of a dual-coding template (Andersen et al. 2008). In 2011, Gothelf and coworkers reported on a new strategy (Ravnsbaek et al. 2011) to obtain fully conjugated molecular wire structures by DNA-directed synthesis. The molecular framework resembles the previous OPE modules, however, contained terminal acetylene functionalities instead of salicylaldehydes. After annealing of the side chain ONs, the acetylenes could be covalently interlinked by Glaser–Eglinton reactions. Utilizing this method, rigid and fully conjugating molecular wires of desirable lengths of up to 8 nm was fabricated. Nevertheless, also for this setup no larger than tetrameric structures were obtained.

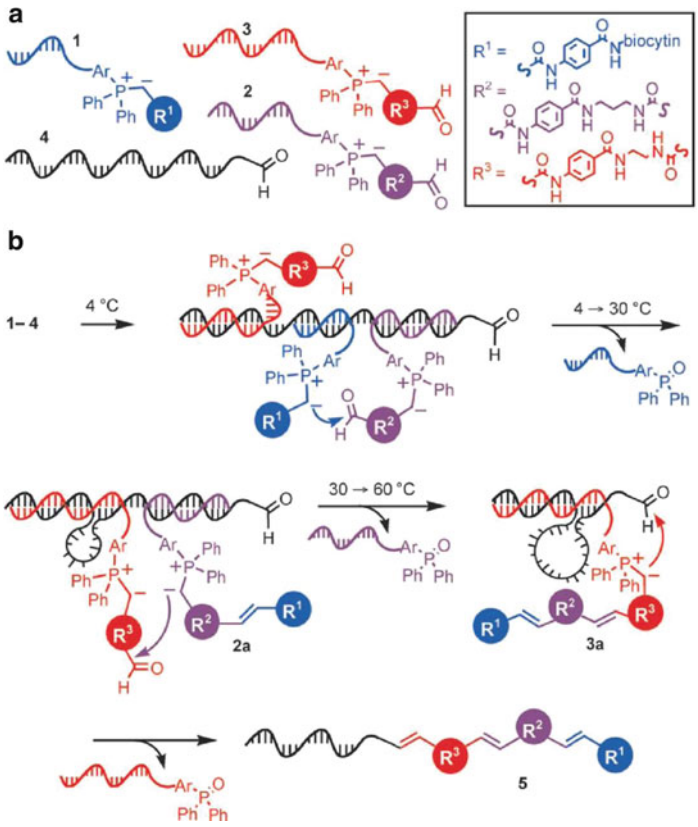

Fig. 7.11 One-pot temperature-controlled synthesis of ordered triolefins by DNA-templated chemistry. (**a**) The three reaction partners 1–3 and the template 4. (**b**) Complete reaction scheme of the formation of triolefins in an ordered manner by fixing the temperature at 4, 30, and 60 °C

7.3.2 Ordered Multistep Synthesis in One Solution

It has been a big challenge to obtain ordered multistep synthetic compounds in a single solution where all reagents are present simultaneously. Liu and coworkers presented in 2005 (Snyder and Liu 2005) a DTS strategy to produce triolefins and tripeptides utilizing temperature control as the sole parameter that is changed throughout the reaction progress.

The three DNA-linked reaction partners (**1**, **2** and **3**) and a 3′ aldehyde-terminated template **4** (Fig. 7.11a) were annealed at 4 °C resulting in a stable DNA duplex structure (Fig. 7.11b). The aldehyde reaction partners (**2**) and (**3**) hold similar reactivity toward the ylide substrate (**1**), however, enforced by the rigidity of the double-stranded DNA, only the (**1**) and (**2**) are in sufficient spatial proximity to enable a chemical reaction, forming the DNA-linked mono-olefin (**2a**). The ylide substrate (**1**) has the shortest DNA sequence (9 bases) and thereby the lowest

melting temperature (T_m), whereas (**2**) is a 12-mer and (**3**) a 25-mer. When the reaction temperature is elevated to 30 °C, the short duplex sequence between ON (**1**) and the template melts, and the residual DNA-linked triphenylphosphine oxide species will spontaneously dissociate, leaving a single-stranded template region between substrate (**3**) and the mono-olefin product. As (**3**) is designed with an ON extension that is complementary to a template sequence near the DNA-linked mono-olefin (**2a**), a Ω-loop is formed, changing the secondary structure of the DNA in a sequence-programmed fashion. A selective Wittig reaction can now occur between the ylide functionality of (**2a**) and the aldehyde of (**3**), generating (**3a**). The temperature was subsequently raised to 60 °C, which likewise caused dissociation of the resulting triphenylphosphine oxide, allowing for a final Wittig coupling to the terminal template aldehyde. Substrate (**1**) contains a terminal biotin functionality, which facilitates easy purification by affinity chromatography using immobilized STV, and isolation of the pure ordered triolefins in 24 % overall yields. By PAGE analysis, truncated products could be estimated to only 10 % of the isolated materials. To confirm the order of the olefin fragments in the isolated product, control reactions were performed, where different aldehyde functionalities were absent, affording intermediate products instead, that were validated by MALDI-TOF analysis. As a proof for the correct order as being a direct result of sequence-programmed changes in the DNA structure and not an effect of intrinsic reactivity differences, the reactive groups of (**R2**) and (**R3**) were exchanged, which led to the expected triolefin product (**R2**-**R3**-**R1**). A similar setup was used for the construction of ordered tripeptides, using DNA-linked NHS-ester-activated amino acids, though with minor modifications in the DNA design.

7.3.3 Autonomous Multistep Synthesis by DTS

In 2010, Liu and coworkers reported a DNA-walker (He and Liu 2010), as the first example of a completely automated mechanism for the fabrication of relatively complex small molecules by DTS. The system proceeds with no external input and produces the desired products significantly faster (a few hours) and more efficient than by previously reported systems (up to 45 % over three couplings). The system mimics the ribosome machinery and allows sequential amine acylation as the walker strand progresses along the track (Fig. 7.12).

The system consists of a template with four 21-mer codons collectively constituting the DNA track (T). The DNA walker (W) is a 38-mer consisting of a DNA sequence (D2′) and a 3′ amino-modified DNA region (D1′) separated by a RNA-cleaving DNAzyme sequence. Finally, the three substrates (S1, S2, and S3) each consist of a unique anticodon sequence complementary to C1, C2, and C3, respectively. Furthermore, they share a common region (D1), complementary to D1′ of W, and have two central RNA nucleotides in the DNA sequence (green dots). S1, S2, and S3 contain a NHS-ester functionality connected to a small molecule, whereas only S1 and S2 have a 3′ amine moiety. Initially, T can self-assemble with S1, S2, and S3 to form a stable duplex structure. When W and S0 are then added to the solution,

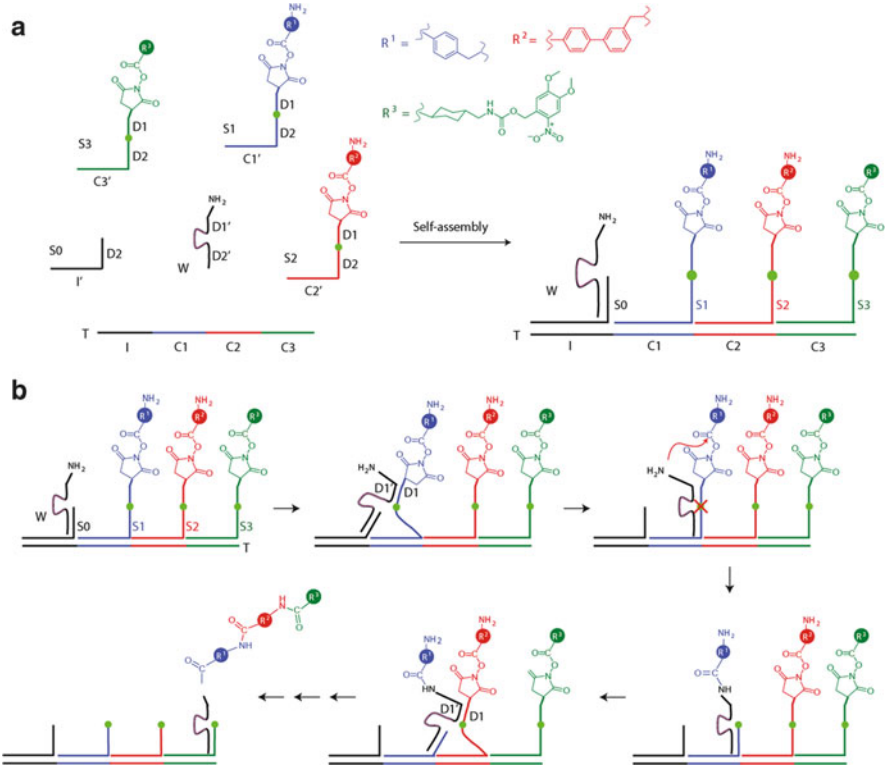

Fig. 7.12 DNA walker construct for tripeptide synthesis without external interference. (**a**) Self-assembly of the reagent strands S1–S3, initiator strand S0, single-stranded DNA track T, and the DNA walker strand W. (**b**) The DNA walker W spontaneously travels along the track T. Each step involves a peptide coupling and a subsequent RNA cleavage, hereby assuring a single-directional movement

they will hybridize to the I region as shown in Fig. 7.12. The D1′ region on W will now spontaneously hybridize with the D1 region of the nearest reagent station (S1) and react with the corresponding NHS-ester functionality, yielding a 3′ amino functionalized peptide containing the R1 moiety. The RNA-cleaving DNAzyme sequence of W subsequently cleaves the ribonucleotide linkage of S1, liberating the reagent. This is repeated at S2 and S3, generating the tripeptide product without external interference of the system.

The reagent stations are separated by approx. 7 nm (two helix turns) to avoid unwanted intramolecular reactions between stations when the walker is not present. Again, the setup has certain limitations in terms of the chemistry that can be applied.

In 2010, the labs of Andrew J. Turberfield and Rachel O'Reilly (McKee et al. 2010) contributed to the field of DNA-templated oligomer synthesis, presenting a new approach to obtain molecular structures with a defined length. Similar to the work by David Liu, they used Wittig olefin chemistry to achieve a tetrameric product through three successive coupling reactions. In contrast to previous work, they applied an end-of-helix architecture, where each templated product was transferred

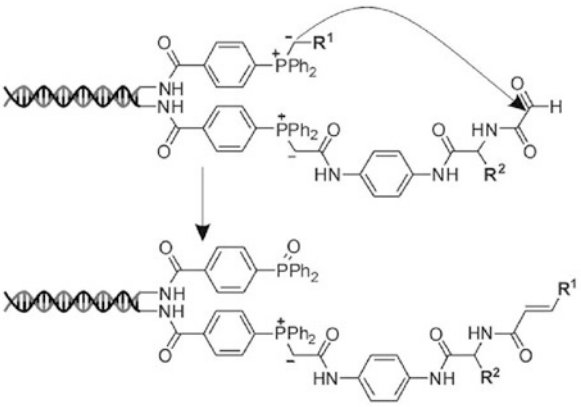

Fig. 7.13 DNA-templated olefin Wittig coupling, where R^1 is transferred to the aldehyde-containing adaptor component. A second incoming adaptor can subsequently react with the ylide functionality on the first adaptor after strand displacement

to the incoming reagent strand upon coupling reaction. All reagent ONs were designed with their reactive phosphine functionality positioned in close proximity to the DNA sequence through a so-called DNA adaptor unit (Fig. 7.13). This would assure a constant intramolecular reaction distance, and the yields would thereby not be affected by an increased macrocyclic reaction intermediate. Additionally, since the formed product is repeatedly transferred to the incoming aldehyde-containing reagent ON, no cleavable linker constructs were needed for this setup.

The three-step DNA-templated synthesis was performed in a single solution through a sequential stand displacement procedure. Each reagent ON contained a unique single-stranded overhang, allowing for a controlled consecutive strand exchange, as illustrated in Fig. 7.14. Finally, the desired tetrameric product could be isolated using a biotinylated DNA strand.

Two years later, Turberfield and O'Reilly extended this concept to produce synthetic 10-mers (McKee et al. 2011) in a one-pot procedure and studied other structurally differing setups to achieve hexameric macromolecules (McKee et al. 2012). Additionally, in 2011, David Liu demonstrated a one-pot DNA-templated synthesis of a hexapeptide through sequential strand displacement (He and Liu 2011).

7.4 Drug Discovery Using DTS

The concept of DNA-templated synthesis provides a powerful strategy to build highly complex organic molecules and synthetic nanostructures with only minor concerns about implementation of protecting groups. Depending on the chemistry applied, multistep syntheses can be performed in a sequential fashion determined by the design of the coding regions. Earlier examples were using a constant template sequence to allow hybridization of a single building block to each coding region, aiming at forming a single and structurally well-defined product. Additionally, it would be desirable if a similar setup could be applied for the introduction of diversity in the molecular motifs and thereby function as a rapid and simple method for the discovery of new protein modulators. Already in 2004 (Gartner et al. 2004), Liu and

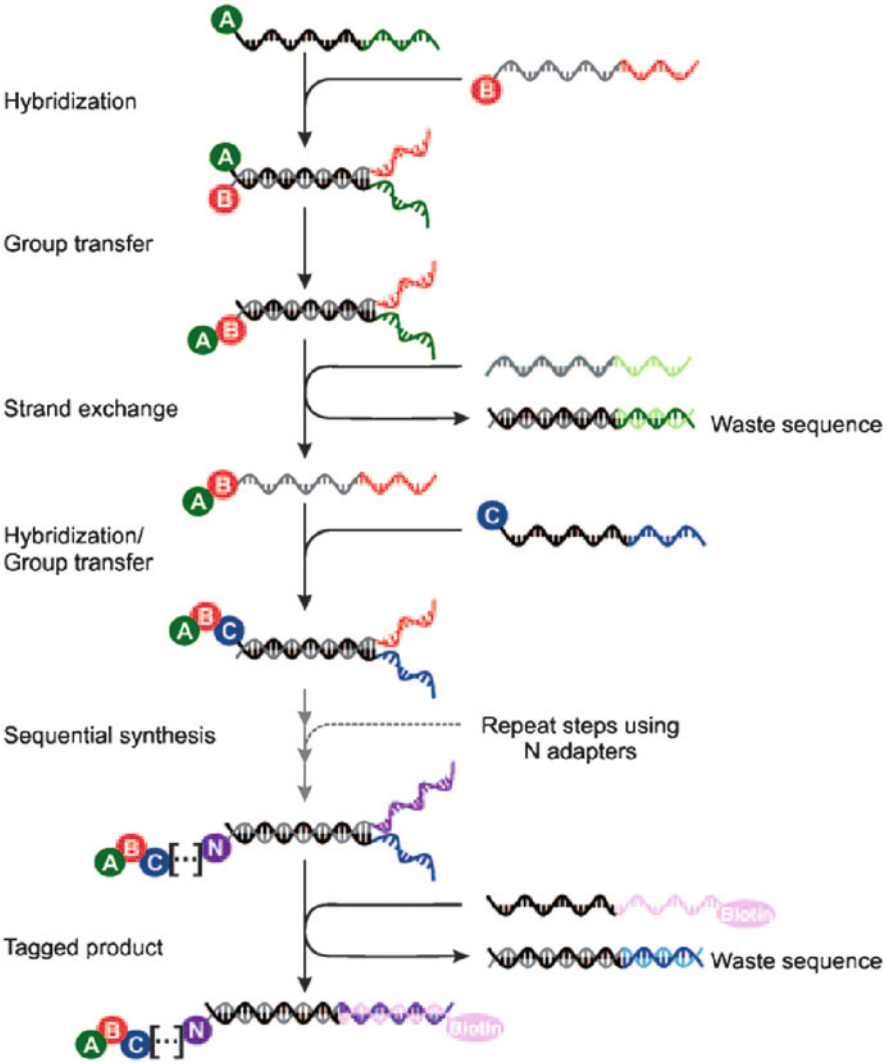

Fig. 7.14 Strand displacement procedure for the one-pot ordered synthesis of oligomers by Wittig chemistry. DNA hybridization allows for functional group transference. After strand displacement a second reaction can take place following the same procedure. Upon several rounds of reactions, the desired oligomer product can be purified by affinity chromatography using a biotin-modified oligonucleotide

coworkers published the first example of such a system, where a small library of macrocycles could be achieved through DNA-templated synthesis, by partly randomizing the coding regions to match multiple DNA-linked building blocks.

DNA-templated chemistry allows for the direct translation of DNA-encoding regions into an organic small molecule. Furthermore, it enables selection-based

purification and PCR amplification from a diverse library of DNA-linked molecules. In 2010, Liu and coworkers (Kleiner et al. 2010) demonstrated the in vitro selection of a library of over 13,000 macrocyclic structures synthesized using DNA-templated chemistry (Fig. 7.15).

For these experiments were used a 3′ amino-modified template strand consisting of two constant terminal primer recognition sites applicable for PCR amplification. Eight different chemical groups (D), defined by a unique scaffold codon, were attached to the amino terminal. Each template contained three individual 10-mer coding regions (Fig. 7.15a; red, blue, and green), where each coding region was partly scrambled to hold a unique sequence complimentary to 1 of 12 different DNA-linked reagents (Fig. 7.15b). Sequential annealing followed by covalent coupling and linker cleavage of the three sequence-defined reagents to a mixture of templates resulted in a large library of the macrocyclic compounds. Since both the scaffold codon and the three reagent codons exclusively correspond to a specific building block, the macrocyclic molecular composition could be directly identified through DNA sequencing after traditional PCR amplification. Finally, the DNA-linked products were selected against 36 biomedically relevant protein targets by incubation with the immobilized protein. The library members that exhibited the strongest binding affinity to the proteins of interest were identified based on the DNA barcodes. These small-molecule macrocycles could then subsequently be synthesized by conventional solid-phase peptide synthesis (SPPS) in milligram scale and used for further studies.

The Danish company Vipergen ApS has, in collaboration with Gothelf's lab, employed a different approach for the development of molecular combinatorial libraries (Hansen et al. 2009). They have used a DNA three-way junction, constituting the so-called DNA YoctoReactor®, to encode the synthesis of 100 different pentapeptide sequences (Fig. 7.16). The reactor platform is made up of three major reaction components and a helper oligo to stabilize the secondary DNA structure under the first amide coupling. Each component is provided with an amino acid or a short peptide reagent (colored dots) and a corresponding unique DNA barcode region (colored lines). Analogous to Liu's setup, the individual barcodes are directly translated into a small-molecule product upon PCR amplification. After each reaction step the desired product was gel purified, followed by a ligation step, where the two reagent templates are covalently connected. Furthermore, the blue and red reaction partners were cleaved from their corresponding barcode templates, thereby allowing for a single attachment site to the resulting ligated template containing all three coding regions. The final library was then subjected to two rounds of affinity selection against a relevant immobilized target protein.

The platform described above was developed in 2009 and holds the potential to produce molecular libraries containing up to 10^{12} different products. Vipergen ApS has further advanced the procedure to compose also four- and five-way junctions, thereby increasing the structural diversity of the small-molecule outcome.

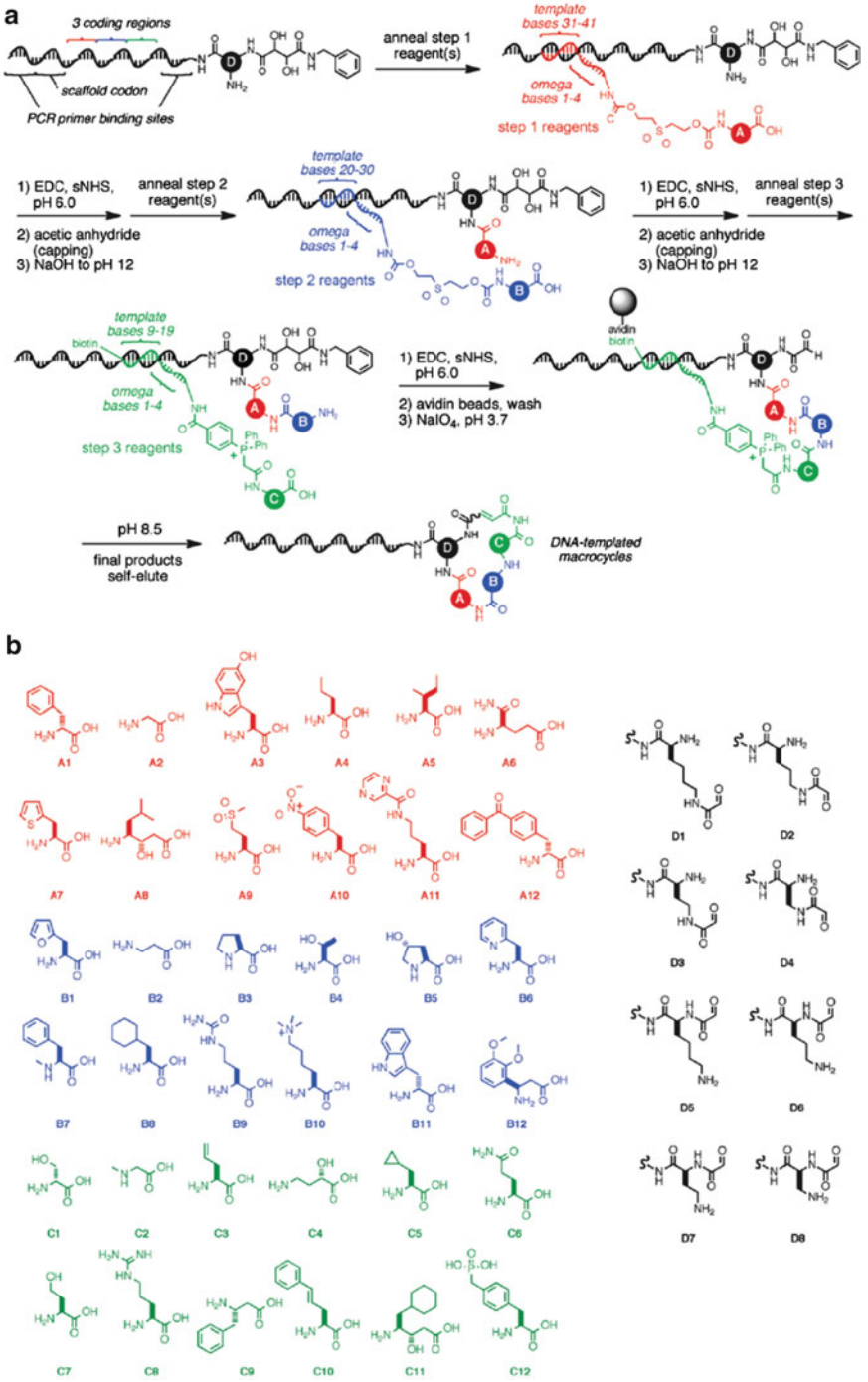

Fig. 7.15 DNA-templated synthesis of a library of macrocyclic compounds for in vitro selection. (**a**) D represents eight different functional groups, whereas A, B, and C individually represents 12 different chemical moieties. Each functionality (A, B, C, and D) is defined by a unique DNA barcode sequence. (**b**) The different DNA-linked reagents

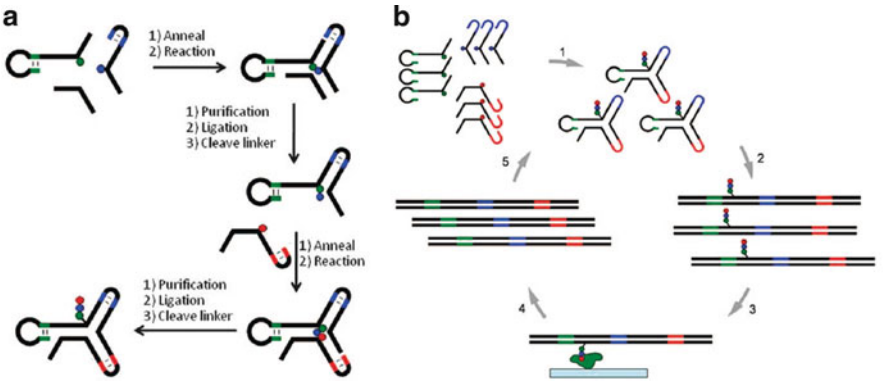

Fig. 7.16 The three-way junction YoctoReactor® used to generate a library of around 100 different pentapeptides. (**a**) Each molecular building block (represented as *colored dots*) is characterized by a unique DNA barcode region (*colored lines*). (**b**) The peptide library is subjected to affinity selection through evolution cycles. The enriched DNA library is PCR amplified and subjected to a second cycle after rolling translation

7.5 Reaction Discovery Using DTS

Similar to using DTS for making combinatorial drug discovery, the lab of David Liu has invented a method for discovering new chemical reactions (Kanan et al. 2004). Typically new reactions are discovered based on retrosynthetic analysis, e.g., by predicting precursors to a wanted target structure and then screening conditions that are likely to facilitate such a reaction. However, Liu and coworkers argued that this approach was unlikely to find unpredictable reactions and that a certain degree of randomness in a high-throughput setup would enable new and useful reactions to be discovered. The central feature is once again the ability to rationally modulate the effective concentration of certain reaction partners by clever DNA design. This allowed the researchers to screen more than a hundred different reagent pairs for bond-forming reactions in a single droplet of buffer.

The system was designed as outlined in Fig. 7.17 and composed of two subsets, A and B. Each component in a subset represents 13 different species; A5 for example is representative for 13 different DNA strands, one for each reaction partner in the B subset and one designed for homodimerization. Mixing all components in the two subsets therefore gave a total of 168 different reagent pairs. In addition to different binding regions, each strand in subset A also carried a unique barcode for PCR amplification.

To validate the fidelity of their system, they mixed the two subsets and added a Cu (I) source. Since one of the 168 reagent pairs was an azide and a terminal alkyne, the substrates for the Huisgen–Meldal–Sharpless cycloaddition, this should give a positive readout. The reaction mixture was incubated for 10 min at 25 °C and then streptavidin beads were used to capture all of the small molecule components from subset B. This was done in a way ensuring that only DNA strands from subset A that successfully

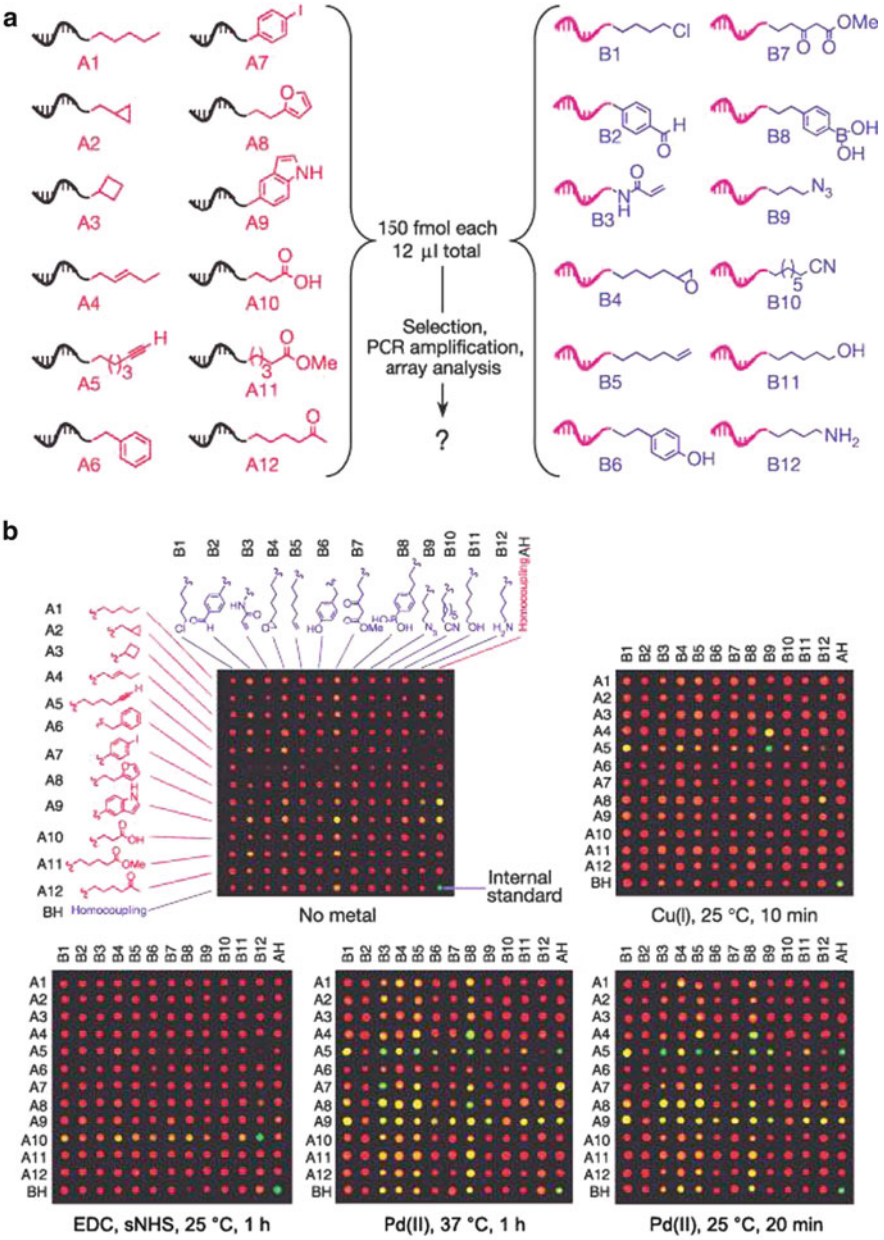

Fig. 7.17 The DNA-templated reaction discovery platform developed by the Liu lab (Kanan et al. 2004). (**a**) The substrate subsets used in the screening process. (**b**) High-throughput analysis of bond-forming reactions. *Red* is no reaction and *green* is a possible bond-forming reaction

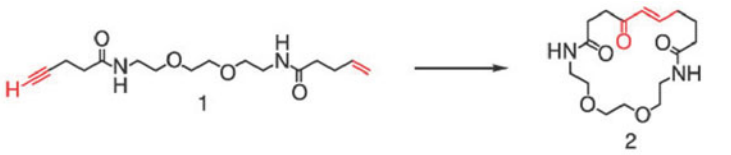

Entry	Metal(s)	Solvent	Conditions	Isolated yield
a	1 equiv. Na_2PdCl_4	1 M NaCl in H_2O	25 °C, 15 h	86%
b	5 mol% Na_2PdCl_4 1 equiv. $CuCl_2$	100 mM NaCl in H_2O	25 °C, 2 h	90%
c	5 mol% Na_2PdCl_4 1 equiv. $CuCl_2$	9:1 THF: H_2O	25 °C, 4 h	91%
d	15 mol% Na_2PdCl_4 1 atm O_2	9:1 THF: H_2O	25 °C, 14 h	73%
e	1 equiv. $CuCl_2$	100 mM NaCl in H_2O	25 °C, 4 h	0%
f	1 equiv. CuCl	100 mM NaCl in H_2O	25 °C, 4 h	0%

Fig. 7.18 Optimization of the palladium-catalyzed enone formation (Rozenman et al. 2007)

participated in bond-forming reactions were isolated. The unique coding sequence on isolated subset A members could then be PCR amplified and the result visualized on a DNA array where red was a negative and green was a positive. As seen in Fig. 7.17, the only combination resulting in a positive result was the azide and alkyne (A5B5) validating the method's capabilities in discovering bond-forming reaction. Furthermore, the researchers validated the system using reaction conditions known to facilitate the amide formation between a carboxylic acid and an amine.

Having validated their system, they subjected the system to a simple Pd(II) salt at 37 °C for an hour. The DNA array, shown in Fig. 7.17b, produced five strong positives and four weaker positives. Some of the results were expected as they correlated with known palladium-catalyzed reaction, such as a Heck reaction when combining an aryl iodide (A7) and acrylamide (B3), but others were not. All nine combinations were tested in isolated DTS reactions and analyzed by denaturing PAGE. This confirmed that all five strong positives and two of the weaker positives resulted from genuine bond-forming reactions. To narrow the selection even further, they decreased reaction time and temperature leading to only a few positives. The more significant of these seemed to be the reaction between a terminal alkene and a terminal alkyne possible forming an enone. Having identified a novel reaction, the researchers designed a small molecule substrate capable of cyclizing through the bond-forming alkyne–alkene reaction (see Fig. 7.18). Reaction condition optimization demonstrated that the reaction proceeded in excellent yield with catalytic amounts of the palladium if copper was used in stoichiometric amounts. Furthermore the reaction proceeded in both water and a mixture of water and THF. The method allowed screening of more than

840 different reactions by one researcher in only 2 days. Each library member had to be synthesized, but as stated by the researchers the amount used for each screening is so low that one batch will allow more than a thousand screenings.

A later study aimed at circumventing the requirement for reaction conditions compatible with DNA hybridization in reaction discovery. Most organic reactions are performed in organic solvent, while DNA hybridization requires water and high salinity. In a paper by Rozenman et al. (2007) the system was improved by enzymatically ligating the two reagent strands prior to reaction. This ligation obviates the need for hybridization, and the researchers validated the system by demonstrating that bond-forming reactions were proceeding both at elevated temperatures (25–95 °C) and in solvent mixtures with low water content (9:1 MeCN:H_2O). Subjecting a mixture of 224 different reagent pairs to a Au(III) source in a MeCN:H_2O mixture (9:1) resulted in the discovery of a new gold-mediated Markovnikov-type addition between an indole and styrene. Further optimization of the initial discovery led to the findings that such reaction could be carried out in excellent yield using triflic acid instead of gold, and dichloromethane instead of acetonitrile/water mixtures. Later, the biocompatible reduction of azides to amines catalyzed by light and ruthenium was also discovered using the same method (Chen et al. 2011).

References

Andersen CS, Yan H, Gothelf KV (2008) Bridging one helical turn in double-stranded DNA by templated dimerization of molecular rods. Angew Chem Int Ed 47:5569–5572

Blakskjær P, Gothelf KV (2006) Synthesis of an elongated linear oligo(phenylene ethynylene)-based building block for application in DNA-programmed assembly. Org Biomol Chem 4: 3442–3447

Brown RS, Nielsen M, Gothelf KV (2004) Self-assembly of aluminium-salen coupled nanostructures from encoded modules with cleavable disulfide DNA-linkers. Chem Commun (13):1464–1465

Chen Y, Kamlet AS, Steinman JB, Liu DR (2011) A biomolecule-compatible visible-light-induced azide reduction from a DNA-encoded reaction-discovery system. Nat Chem 3: 146–153

Chen X-H, Roloff A, Seitz O (2012) Consecutive signal amplification for DNA detection based on de novo fluorophore synthesis and host-guest chemistry. Angew Chem Int Ed 51:4479–4483

Czlapinski JL, Sheppard TL (2001) Nucleic acid template-directed assembly of metallosalen-DNA conjugates. J Am Chem Soc 123:8618–8619

Franzini RM, Kool ET (2009) Efficient nucleic acid detection by templated reductive quencher release. J Am Chem Soc 131:16021–16023

Franzini RM, Kool ET (2011) Two successive reactions on a DNA template: a strategy for improving background fluorescence and specificity in nucleic acid detection. Chem Eur J 17: 2168–2175

Gartner ZJ, Kanan MW, Liu DR (2002a) Expanding the reaction scope of DNA-templated synthesis. Angew Chem Int Ed 41:1796–1800

Gartner ZJ, Kanan MW, Liu DR (2002b) Multistep small-molecule synthesis programmed by DNA templates. J Am Chem Soc 124:10304–10306

Gartner ZJ, Grubina R, Calderone CT, Liu DR (2003) Two enabling architectures for DNA-templated organic synthesis. Angew Chem Int Ed 42:1370–1375

Gartner ZJ et al (2004) DNA-templated organic synthesis and selection of a library of macrocycles. Science 305:1601–1605
Gothelf KV, Thomsen A, Nielsen M, Cló E, Brown RS (2004) Modular DNA-programmed assembly of linear and branched conjugated nanostructures. J Am Chem Soc 126:1044–1046
Gryaznov SM, Letsinger RL (1993) Chemical ligation of oligonucleotides in the presence and absence of a template. J Am Chem Soc 115:3808–3809
Hansen MH et al (2009) A yoctoliter-scale DNA reactor for small-molecule evolution. J Am Chem Soc 131:1322–1327
He Y, Liu DR (2010) Autonomous multistep organic synthesis in a single isothermal solution mediated by a DNA walker. Nat Nanotechnol 5:778–782
He Y, Liu DR (2011) A sequential strand-displacement strategy enables efficient six-step DNA-templated synthesis. J Am Chem Soc 133:9972–9975
Kanan MW, Rozenman MM, Sakurai K, Snyder TM, Liu DR (2004) Reaction discovery enabled by DNA-templated synthesis and in vitro selection. Nature 431:545–549
Kleiner RE, Dumelin CE, Tiu GC, Sakurai K, Liu DR (2010) In vitro selection of a DNA-templated small-molecule library reveals a class of macrocyclic kinase inhibitors. J Am Chem Soc 132:11779–11791
Li X, Gartner ZJ, Tse BN, Liu DR (2004) Translation of DNA into synthetic N-acyloxazolidines. J Am Chem Soc 126:5090–5092
Luo P, Leitzel JC, Zhan Z-YJ, Lynn DG (1998) Analysis of the structure and stability of a backbone-modified oligonucleotide: implications for avoiding product inhibition in catalytic template-directed synthesis. J Am Chem Soc 120:3019–3031
McKee ML et al (2010) Multistep DNA-templated reactions for the synthesis of functional sequence controlled oligomers. Angew Chem Int Ed 49:7948–7951
McKee ML et al (2011) Peptidomimetic bond formation by DNA-templated acyl transfer. Org Biomol Chem 9:1661–1666
McKee ML et al (2012) Programmable one-pot multistep organic synthesis using DNA junctions. J Am Chem Soc 134:1446–1449
Naylor R, Gilham PT (1966) Studies on some interactions and reactions of oligonucleotides in aqueous solution. Biochemistry 5:2722–2728
Nielsen M, Thomsen AH, Cló E, Kirpekar F, Gothelf KV (2004) Synthesis of linear and tripoidal oligo(phenylene ethynylene)-based building blocks for application in modular DNA-programmed assembly. J Org Chem 69:2240–2250
Nielsen M, Dauksaite V, Kjems J, Gothelf KV (2005) DNA-directed coupling of organic modules by multiple parallel reductive aminations and subsequent cleavage of selected DNA sequences. Bioconjug Chem 16:981–985
Pianowski Z, Gorska K, Oswald L, Merten CA, Winssinger N (2009) Imaging of mRNA in live cells using nucleic acid-templated reduction of azidorhodamine probes. J Am Chem Soc 131: 6492–6497
Ravnsbaek JB, Jacobsen MF, Rosen CB, Voigt NV, Gothelf KV (2011) DNA-programmed Glaser-Eglinton reactions for the synthesis of conjugated molecular wires. Angew Chem Int Ed 50:10851–10854
Rozenman MM, Kanan MW, Liu DR (2007) Development and initial application of a hybridization-independent, DNA-encoded reaction discovery system compatible with organic solvents. J Am Chem Soc 129:14933–14938
Sievers D, von Kiedrowski G (1994) Self-replication of complementary nucleotide-based oligomers. Nature 369:221–224
Snyder TM, Liu DR (2005) Ordered multistep synthesis in a single solution directed by DNA templates. Angew Chem Int Ed 44:7379–7382
Wu T, Orgel LE (1992) Nonenzymic template-directed synthesis on hairpin oligonucleotides. 2. Templates containing cytidine and guanosine residues. J Am Chem Soc 114:5496–5501
Xu Y, Karalkar NB, Kool ET (2001) Nonenzymatic autoligation in direct three-color detection of RNA and DNA point mutations. Nat Biotechnol 19:148–152

Part IV
DNA as a Nanomechanical System

Chapter 8
Mechanical DNA Devices

Zhen-Gang Wang and Baoquan Ding

Abstract Natural molecular machines have been playing very significant roles in the world, which stimulated numerous efforts on the artificial molecular machines. DNA ambiguously is an ideal building block for the nanomechanical devices, because of many intriguing features. In this chapter, we first introduce the fundamental elements for understanding and implementing DNA-based nanomachines, such as fuels, dynamic behaviors, and the characterization methods. Furthermore, we describe the development of DNA nanomachines from simple constructs and operations to the sophisticated machinery systems concerning the coherent activation of multiple devices and configurational complexity. In the end, some important applications of DNA mechanical devices are discussed, including molecular transporting, organic synthesis, molecular sensing, and controlled drug delivery. Through this chapter, we aim to promote the fast advancement of the field of the nanomachines, which may push forward the multidisciplinary and interdisciplinary researches.

Contents

Z.-G. Wang • B. Ding (✉)
National Center for Nanoscience and Technology, Beijing, China
e-mail: dingbq@nanoctr.cn

J. KJEMS et al. (eds.), *Nucleic Acid Nanotechnology*, Nucleic Acids and Molecular Biology 29, DOI 10.1007/978-3-642-38815-6_8,

Mechanical motions of human being, such as running, jumping, carrying, and lying, play significant roles in our daily life, representing the continuation of life and the evolution of nature. As the counterpart to the macroscopic mechanics in the microscopic world, the molecular machine, sized in the order of nanometers, has attracted much attention in recent years. Although not visible to the human eye, a huge amount of molecular machines exist in nature, carrying out molecular-level motions and driving nature to perform its function. Examples are biological molecular machines, such as the motor protein myosin (Sweeney and Houdusse 2010), which drives the contraction of muscle fibers; kinesin (Fisher and Kolomeisky 2001); and dynein (Vallee 1993) transporting cargo along polar microtubule through the cell. Natural molecular machines of green plants also display powerful abilities. For example, they harness chemical or light energy to synthesize a great tonnage of organic compounds. The existing system of natural molecular machines is the result of 4.5-billion-year natural evolution. We can even say that we, as human beings, are driven by the molecular machines, and the world is actually composed of nanometer-scale factories.

The intriguing properties of natural molecular machines drive the research of the artificial counterparts to fall in the scope of scientists. Biological molecular machines are the most common natural species, the functions of which are the object to be mimicked by the synthesized molecular machines. What have we learned from the biological molecular machines? First, how can we make the machines run? Speaking of machines, we are reminded of the law of energy conversion. To drive the machine to realize linear or rotary motion, there must be an energy resource to be consumed, named as "fuel." For the biological machines, it is the process of energy conversion, from chemical to mechanical energy (e.g., the motor protein system) or from solar to chemical energy (e.g., the photosynthetic system). The fuel is what drives the molecular machine to do mechanical work repetitively. The second is the complexity and intelligence of the system. All the molecular machines perform their respective biological functions cooperatively to generate a variety of behaviors of an organism, originating from the complex structure of the biological machines and the smart signal system by which signals are produced, transferred, and sensed as required. Despite the functions and the capabilities of the biological machines, they suffer from a key disadvantage which is their inherent instability that potentially restricts their application in many situations in vitro.

It's clear that the scientific goal is to develop artificial machines which, like biological molecular machines, can sense and respond to environmental changes (i.e., absorb one form of energy and convert it to another form) and which can tolerate more versatile conditions than biological machines and offer considerable

advantages in the development of complex nanomachinery system. From the biological machines we have learned that there are three critical points for the operation of a molecular machine: the scaffold, the sensing, and the responsive capability. It seems that the disadvantages of the biological machines are easy to prevent because of the enhanced stability of the synthetic machines, while the simulation of the complex and intricate functions is not an easy job. It requires a step-by-step and continuous endeavor in this field. So far, a wide range of artificial molecular machines have been constructed, through organic synthesis (Saha and Stoddart 2007), bottom-up assembly (Beissenhirtz and Willner 2006), or genetic recombination (van den Heuvel and Dekker 2007). Triggered by a variety of external stimuli (light, chemical, thermal, etc.), the developed artificial molecular machines are capable of performing diverse motions that mimic both macroscopic and microscopic machines, such as scissoring, sliding, rotating, and even stepwise walking. The artificial molecular machines also possess some simple functionalities, like molecular switching, computing, propelling, molecular shuttling, and even cancer cell targeting and attacking. More interestingly, the molecular machines have been immobilized onto solid surfaces and have carried out unidirectional rotary motion (van Delden et al. 2005) or performed macroscopic motion, such as translocation of liquids on the surface (Berna et al. 2005). The current artificial molecular machines mainly involve small organic molecules [azobenzene (Beharry and Woolley 2011), spiropyran (Fukushima et al. 2007), etc. (von Delius et al. 2010)], macromolecules [organic polymers (Fang et al. 2010), DNA (Beissenhirtz and Willner 2006), protein (van den Heuvel and Dekker 2007), etc.], transition metal complexes (Champin et al. 2007), and the conjugation of different species (Zhou et al. 2010; Yuan et al. 2011). The exciting progress in the development of man-made molecular machines is, however, followed by several challenges. One challenge is how to fabricate the sophisticated molecular machines in a simple way? This question is raised since many of the artificial molecular machines, including the well-known monomolecular devices and proteins, required great synthesis skills to meet the structural features. The complex fabrication process slows down further functionalization and the development of high-level machinery systems capable of more sophisticated functions, such as cooperative activation. In the past decade, the progress in DNA nanotechnology entered the field of the mechanical molecular devices. Compared with the above disadvantage in some of the current molecular devices, such as the engineered protein motor and photochromic molecules, the advantages of DNA—including the automated technique of large-scale DNA synthesis, the strict rules of base pairing, the predictability of self-assembly, the high diversity of the structural patterns, the highly specific recognition to a wide range of molecules/ions, and the ease of modification—make DNA a great building block for construction of molecular machines with high controllable complexity.

DNA and its derivatives have shown to be powerful molecules for the assembly of nanostructures with dictated shapes and geometries. The structural DNA nanotechnology, started by Nadrian C. Seeman, has enabled scientists to prepare complex and intricate DNA crystals with high yield. These nanostructures include

various two-dimensional extended nanostructures and three-dimensional self-closed nanostructures with well-defined shape and scale. Especially, the appearance of DNA origami initiated a "revolution" for the moderate-resolution (~6 nm) organization of DNA information into one, two, and three dimensions (Seeman 2010). The origami technique, developed by Paul Rothemund, through folding of a long single-stranded viral DNA aided by hundreds of short "staple" strands, can result in various shapes including a smiley face (Rothemund 2006), a coarse map of China (Qian et al. 2006), along with many three-dimensional structures, such as nanotubes (Ding et al. 2010), a locked/unlocked box (Andersen et al. 2009), a reconfigured Möbius strip (Han et al. 2010), and even 3D spherical shells (Han et al. 2011), ellipsoidal shells (Han et al. 2011), and a nanoflask (Han et al. 2011). Structural DNA nanotechnology provides significant fundamentals for building the scaffolds of DNA machines. The specific recognition of DNA to the heteromolecules and to various ions makes it also an ideal component for sensing devices. Moreover, the conformation of a DNA motif tends to change upon environmental variation (i.e., fluctuation of analyte concentration), indicating the inherent dynamic properties of single-stranded and double-stranded DNA, which allows the dynamic, controlled dehybridization, and rehybridization of nucleic acid structures. Therefore, the technology of assembling the scaffold, the sensitivity to the environmental change, along with the dynamic functions can make DNA well qualified for constructing versatile functional molecular machines. If the multiplex sensing feature of DNA structures is integrated with the energetically favored directional migration of DNA strands, more complex operations can be implemented in a multimachinery system, such as inter-unit cooperation or cascade activation. However, one significant question is unanswered: how to monitor the machinery activation and function? Fortunately, this is one of the intrinsic advantages of DNA. For example, DNA is very easily modified to bear luminescent group that can be measured by photometer or to carry markers that can be imaged by microscopy. Another advantage is that some molecules become detectable once interacting with a specific DNA motif. All these properties pave the way for turning DNA nanomechanical models into the actually occurring devices.

Generally speaking, DNA machines refer to two classes of structures. DNA can be manipulated by various natural enzymes, employed as biocatalytic "nano-tools," for example, the joining of two DNA fragments, the replication and transcription of polynucleotide sequence against a nucleic template strand, the elongation of a single strand, and the scission of a sequence-specific domain in double-stranded DNA using ligases, polymerases, telomerases, and endonucleases/exonucleases. These biocatalytic transformations not only produce new DNA structures but also generate new versatile components containing sticky ends that act as secondary assembly units. These processes are very efficient and usually autonomous, but they are also inherently instable, difficult to be controlled, and irreversible. Alternatively, structures are constructed through the "bottom-up" assembly of DNA strands, which makes full use of the mobility and flexibility of DNA, and the diversity is multiplied by the infinite imagination of the scientists, pioneered by Nadrian C. Seeman in the late 1980s. By means of appropriate predesign of the

scaffolds and triggered by chemical, light, or electric inputs, the DNA structural devices duplicate "macroscopic machine-like" functions that perform linear or rotary motion, act as walkers, or function as motor, rotors, or switches. The recent decades, especially the last 10 years, have witnessed the development of DNA machines. For example, mono-mobile DNA junctions were developed into a spiderlike DNA walking system, and the movement of a DNA unit was upgraded to the concurrent activation of multiple DNA machines. As well, so far, DNA machines can not only capture and release nanoscale objects but also create tiny products of their own on a nanoassembly line. Moreover, the concept of "computing" is introduced into the construction and operation of the DNA machines, thereby improving their functionalities. Numerous advancements in this field can be exemplified. In this chapter, we will describe the exciting success in the area of nanomechanical DNA devices, concentrating on the concepts, constructs, and working mechanisms. Some applications will also be depicted. Finally, we will highlight some challenges and prospectives. The functions and the operation complexity together with the type of the fuel will be discussed. Through this chapter, we wish not only to help you understand the synthetic biological molecular machines but to dig out the notable features of the past significant progress. Additionally, the intentions are to boost the growth of the field of the mechanical molecular devices and to enhance the applications in area of biology and chemistry, such as molecular transporting, organic synthesis, molecular sensing, and controlled drug delivery.

8.1 Fuels, Dynamics, and Characterization

The fuels are the matters that the nucleic acid strands recognize and interact with. They include macro- or small molecules, nucleic acid strands, metal ions, and also protons. The term fuel originates from the fact that upon interaction with the fuel, the conformation of the nucleic acid motifs usually changes and some of the conformational switches are reversible. For example, in DNA aptamers, single-stranded DNA with sequence-specific binding of, e.g., cocaine or adenosine monophosphate (AMP) folds itself to form hairpins when exposed to the corresponding molecules. Upon addition of the hydrolysis enzyme to an AMP–DNA complex, the fuel that can affect the molecular structure of AMP and the interaction between AMP and the aptamer will be disrupted, resulting in the conformational recovery of the nucleic acid strands. Heavy metal ions, such as Hg^{2+} or Ag^{+}, have similar effect on the DNA conformation [Fig. 8.1a (Lee et al. 2008)]. The exposure of the DNA-Hg^{2+}/or Ag^{+} complex to molecules containing a thiol group (e.g., cysteine) results in the preferential interaction between the ions and the thiol group. Alternatively, addition of the pairing fuels can switch the DNA strands between two conformations. Another well-known example is the base pairing between DNA strands, leading to the recognition between complementary strands and the formation of a stable duplex. However, the concept of the word "stable"

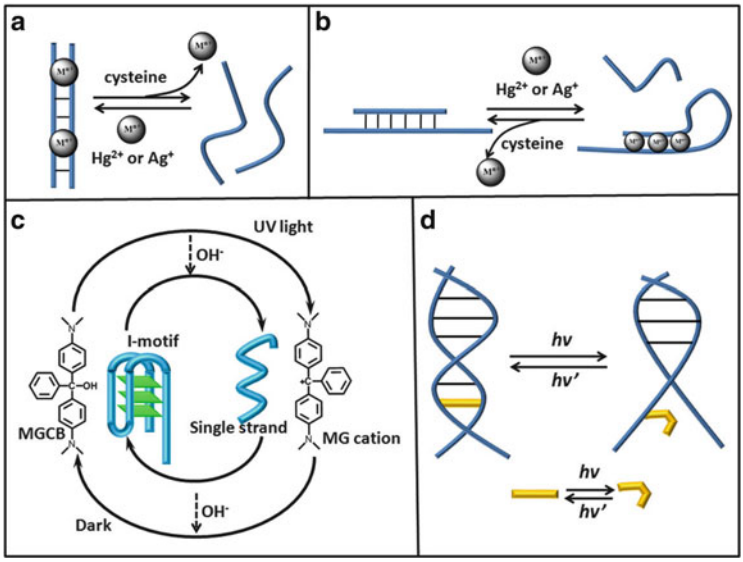

Fig. 8.1 (**a**) Reversible formation and deformation of DNA duplex triggered by heavy metal ions (M^{n+})/cysteine (Lee et al. 2008). (**b**) Example of DNA motif conversion (heavy metal ions/cysteine as exemplified fuels) (Li et al. 2008). (**c**) Light-induced conformational change of cytosine-rich strands (Liu et al. 2007). (**d**) Formation and denaturing of duplex by light-triggered configuration change of tethered photochromic molecules (Asanuma et al. 2007)

here should be discussed in particular. If one of the strands has higher affinity to other molecules, like nucleic acids, an aptamer substrate, or heavy metal ions as referred to as fuel above, the duplex will be transformed into a different DNA structure. However, it could switch back to the duplex in the presence of the "antifuel" [exemplified in Fig. 8.1b (Li et al. 2008)]. The power introduced by the fuel involves chemical, light, and electrochemical energy. The way of powering can be direct or indirect. For example, cytosine-rich nucleic acid strands are responsive to the protons; thus, the strand folds up into an i-motif structure when the solution is acidified (Liu and Balasubramanian 2003). Instead of the direct chemical stimulation, a photo-sensitive molecule, e.g., malachite green carbinol base, is able to release OH^- when exposed to UV light, thus increasing the pH and inducing the formation of single stranded DNA (Liu et al. 2007) (Fig. 8.1c). Alternatively, a strategy of electrooxidization/reduction process has also been used to release and uptake protons, thereby switching pH between acidic and neutral value and vice versa. By doing so, the ability to activate and deactivate i-motif-bridged DNAzyme reversibly was demonstrated (Frasconi et al. 2010). Photochromic molecules with light-dependent configuration was applied to tailor the stability of DNA duplex, which was denatured and renatured due to the change of the wavelength of the incident light (Asanuma et al. 2007) (Fig. 8.1d).

The fuels trigger the inherent dynamics and mobility of the DNA strands, which is the basis for mechanical DNA devices. The possibility of the fuels to power DNA

structures is the matter of thermodynamics. Accurate prediction of DNA secondary structure and hybridization requires a database of thermodynamic parameters for different motifs (e.g., Watson–Crick base pairs, internal mismatches, terminal dangling ends, hairpins, i-motifs) and for the interactions between the nucleic acid strands and a series of substrates. Empirical equations and tools for determining the influence of monovalent cations and magnesium ions on the thermodynamics have been developed for predictions under a variety of salt conditions, and they are generally used to design sequences with maximal probability of forming the desired structures and complexes at equilibrium. On the other hand, at the level of DNA machines, the thermodynamics are related to the energy stored in the machinery system. "The principle of minimum total potential energy" allows ranking of the stability of the different states of the system with the help of thermodynamic predictions for the design of appropriate architecture of nanomachines. To drive a machine, thermodynamic theory only provides the feasibility. How fast, and what mechanism the machine will exert, relies on the kinetics, which has been a hot research topic in nanomechanics. Most of the mechanical DNA devices have been designed to use DNA strand-displacement mechanism, which was already used in a variety of DNA devices, including DNA circuits, catalytic amplifiers, and reconfigurable nanostructures. The strand-displacement mechanism is a process through which two strands with partial or full complementarities hybridize to each other, displacing one or more pre-hybridized strands. So far, the mathematical models developed for chemical reactions have allowed us to simulate various strand-displacement reactions using DNA as the fuel, followed by estimating the rate constants. The review by Zhang et al. showed a detailed story of DNA-fuelled strand-displacement reactions (Zhang and Seelig 2011). It has been demonstrated that many stimuli affecting the stabilities of DNA motifs can lead to the strand-displacement reactions. The reaction kinetics is simulated using appropriate models and the methods of characterization have also been developed. In brief, the thermodynamic and kinetic studies are the solutions to the questions whether the motion of the machine can be initiated and controlled, respectively. Moreover, they are used to engineer the programmed mechanical devices and to instruct the nature of the motion, e.g., the direction of walking and rotation or the automation of the operation.

Monitoring the motions of the mechanical nanodevices is a more technical exercise, which is essential to study the dynamic behaviors. Profiling the optimal methods of characterization for each research object is strongly dependent on the properties of the devices. So far, numerous instruments have been developed for imaging in nanotechnology, and many of them can be adapted for the mechanical DNA devices. The most economical method is the electrophoresis, which utilizes the electrostatic properties of the nucleic acid strands [exemplified in Fig. 8.2a (Yin et al. 2004)]. This method indicates the configurations of the device, according to their different mobility in the gel; the complex or subtle motion is usually not revealed by electrophoresis. Another commonly used method is fluorescence quenching and de-quenching. Since 1996, when the first DNA molecular beacon was reported (Tyagi and Kramer 1996), the fluorophore and the quencher-labeled

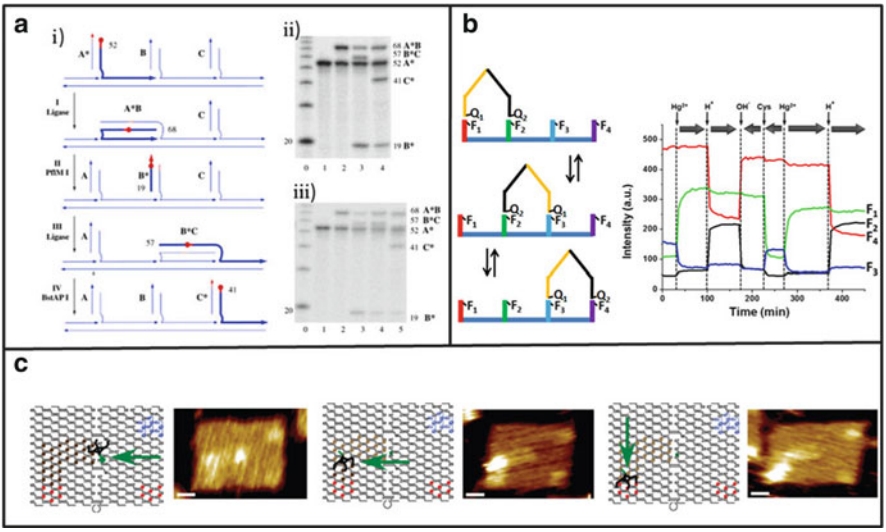

Fig. 8.2 Methods for characterizations of DNA mechanical devices. (**a**) Gel electrophoresis: (**i**) an example of DNA walking device with four-step motion, and the walking element is labeled with radioactive reagent (*red*); (**ii**) denaturing *polyacrylamide gel electrophoresis* (*PAGE*) analysis of autonomous motion of the walker; and (**iii**) PAGE analysis of the stepwise motion of the walker (adapted with permission from John Wiley & Sons, Inc. (Yin et al. 2004)], copyright 2004). (**b**) Monitoring of fuel-instructed motion of the walker using fluorescence quenching and dequenching. In the *left*, the four footholds are labeled with four different fluorophores, the walking feet with two different quenchers. In each walking step, two fluorophores are quenched and the other two exhibit high fluorescence intensity, as shown on the *right* [the *right graph*. Reprinted with permission from Wang et al. (2011). Copyright (2011) American Chemical Society]. (**c**) AFM imaging of the movement of a DNA walking element along a designed track on the 2D surface [reprinted by permission from Macmillan Publishers Ltd: [Nature] (Lund et al. 2010), copyright (2010)]

nucleic acids have been used as important probes for the machinery motions. By spatially positioning the fluorophores and the quenchers, it is possible to monitor both the static and dynamic behaviors of the machines.

The fluorescence method has great advantages over the electrophoresis, e.g., precise and dynamic imaging of the machines, as well as more available access to the dynamic parameters of the machinery system [an example in Fig. 8.2b (Wang et al. 2011)]. Moreover, the technique of DNA labeling has been commercialized; however, it is much more money- and time consuming than the gel electrophoresis because of the labeling process. Despite convenience and consolidation of the methods, the evidence obtained by the above methods is indirect, and in most of cases, control experiments are required to analyze the configuration or the yield of the motions. Atomic force microscopy (AFM) in the liquid mode, which has been developed in the recent decade, has been proved to provide images of well-retained DNA nanostructures. Recently, it has been used to monitor the directional walking [examples in Fig. 8.2c (Lund et al. 2010)] and programmed assembly of the

nano-objects (Gu et al. 2010). Equipped with a fast-scanning apparatus, the real-time monitoring and imaging of the mechanical motion will be possible.

With the mechanical properties of the devices (i.e., dynamics) demonstrated, the manners to monitor the mechanical motion established, and the "fuels" ready for the devices, the next issue will be the versatile constructions and the operations of the DNA mechanical devices, from simplicity to complexity.

8.2 Mobility of Nucleic Acid Motifs and Construction of DNA Nanodevices

Similar to the macroscopic devices, a complex nanomechanical device is actually activated by the cooperative motion of the subunits. It has been a scientifically important job to develop the responsive DNA motifs and to study their mobility. The motifs are not only required to be activated but also to implement switchable motions. Various mobile DNA motifs have been produced, but the most interesting ones are those that are sequence dependent, so that a number of them can be addressed individually in the same physical context.

Generally speaking, the mobile DNA motif can be divided into two categories according to retention of the molecular structure. The first is that molecular structure of the DNA motif is retained when the conformational conversion occurs, while in the other case, the motion of the motif is accompanied by variations of the molecular structure of the DNA motif. The latter category is more popular for constructing complex and intricate nanomachinery system; however, the former case was reported earlier and has shown unique and interesting mechanical as well as optical properties. A typical example is B to Z conformational transition of a DNA duplex with a specific sequence rich of cytosine and guanine bases, e.g., $(CG)_n$ (Jovin et al. 1987). B-DNA and Z-DNA are the only conformations of DNA that have been directly observed in functional organisms. Their major difference in the structure is the helical winding direction, in addition to parameters such as diameter, number of bases per turn, and turn of helix. B-form DNA adopts a right-handed helical structure and Z-form DNA forms a left-handed structure. It was reported that at high concentration of salt or some cations (e.g., Hg^{2+}), conformation transitions from B-form to Z-form occurred (Gruenwedel and Cruikshank 1991; Gruenwedel 1994). Especially, upon removal of Hg^{2+} by a complexing reagent, the helicity of the DNA was recovered, so that the helical inversion was switchable between right- and left-handedness using Hg^{2+} and the complexing reagent as the fuels. The B–Z transition was expanded by Nadrian C. Seeman to a supramolecular mechanical device, consisting of two rigid DNA "double-crossover" (DX) molecules connected by 4.5 double-helical turns, Fig. 8.3 (Mao et al. 1999). One domain of each DX molecule was attached to the connecting helix. The two unconnected domains of the DX molecule lay on the same side of the central axis in a conformation favoring B-DNA, while in Z-DNA promoting

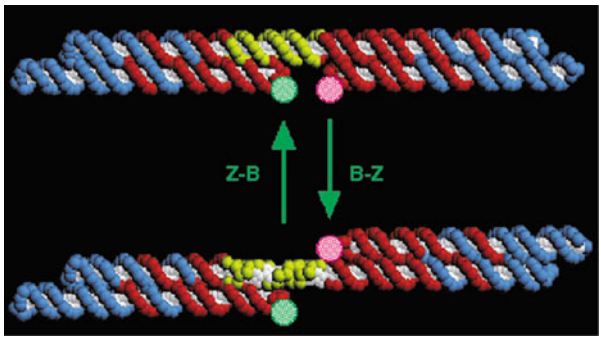

Fig. 8.3 A DNA nanomechanical device based on the B-Z transition. The device consists of two DX molecules connected by a helix (*yellow section*) that can undergo the B-Z transition. When this occurs, the *bottom* domain of the *right* DX molecule swings from the *bottom* to the *top* through a rotary motion [reprinted by permission from Macmillan Publishers Ltd: [Nature] (Mao et al. 1999), copyright (1999)]

conditions, these domains switched to opposite sides of the helix. Each tile (the free end) of the DX molecules carried a fluorophore and the relative proximity of which is measured to detect the relative repositioning of the domains by means of fluorescence resonance energy transfer (FRET). When the B–Z transition occurs, FRET measurements showed an increase in the separation between the fluorophores, consistent with the expected relative rotation of the tiles by ~3.5 turns. In another example, Seeman et al. converted changes in the twist of DNA into linear motion by torsional control of double-stranded DNA branch migration (Yang et al. 1998). The device was composed of a circular double-stranded DNA, which was formed by joining opposite arms of the branched junction. The branched junction can migrate by breaking identical base pairs in one pair of opposite arms and relocating them in the other pair. The conformational change within the circular junction was triggered by the addition of ethidium bromide, which intercalated with adjacent base pairs, lengthening and partially unwinding the double helix. The circle was relaxed by branch migration: by shortening the protruding arms of the junction, the circle was allowed to lengthen without changing the total number of twists within it.

Besides the switch of duplex motif, the high flexibility of single-stranded DNA has been studied extensively. Single-stranded DNA exists in most cases in random-coil configuration. However, for some strands with specific sequence, they are able to form well-ordered configurations under appropriate conditions. For example, guanine-rich sequence exposed to ions (e.g., monovalent, divalent) can fold into quadruplex structures. When the divalent ions were added and then removed by the chelating agent, the pinched quadruplex structure was formed and broken, respectively (Fahlman et al. 2003). If a coordination unit (2,2′-bipyridine) was used to link two GGGG fragments, then the addition and removal of the divalent metal ions proved to switch G-quadruplex from parallel to antiparallel conformation because of the rotation of the bipyridine unit (Miyoshi et al. 2007).

As a complementary sequence to G-quadruplex, cytosine-rich (appropriately spaced) single-stranded DNA indicates two distinct motifs depending on the environment pH: random coil and i-motif. In the i-motif structure, the protonated forms a noncanonical base pair with an non-charged C (i.e., a $C:C^+$ base pair), and these base pairs interdigitate to form a compact quadruple helix that is stable under slightly acidic conditions, as proven by circular dichroism. The unique feature of this sequence is the energetic competition between the i-motif and a double helix that is formed by hybridization of two strands (i-motif and a partially complementary strand). Thermodynamic calculation showed that the i-motif structure is favored energetically compared with the extended duplex structure at acidic pH. Kinetic experiments proved a fast process between the compact and extended configurations by changing the pH (Liu and Balasubramanian 2003). The i-motif to duplex transition was used to do mechanical work. The arrays of nucleic acid strands rich of cytosine bases, coating a silicon cantilever, can exert a compressive surface stress, which bent down the cantilever, at acidic pH that favored the formation of i-motif (Fig. 8.4a) (Shu et al. 2005). The bending process is reversible by switching the conformation of DNA motif. The origin of the surface stress was attributed mainly to electrostatic repulsions between the i-motif strands, and the authors suggested that both inter- and intramolecular repulsions of the compact i-motif structure were higher than the duplex form. Thus the duplex to i-motif transition would induce the bending of the cantilever to increase the available surface area. This is the first work that certified that the mobile DNA motifs could apply a cooperative dramatic force to drive a macroscopic object. Changing pH can also be implemented by light-controlled release and uptake of OH^-, electrochemical redox reactions, and chemical oscillator (Liedl et al. 2006), which all were used to dominate the formation of i-motif structures and the corresponding switches. In addition to switching of the i-motif, the processes of protonation and deprotonation of C bases also resulted in reversible formation and dissociation of a DNA-triplex containing C^+G-C triplets, by changing the solution pH between pH 5.0 and 8.0. Using this mechanism, a DNA nanomachine, constructed by Mao et al., was switched between "open" and "closed" configurations (Chen et al. 2004a) (Fig. 8.4b).

The conformational change of single-stranded DNA can also be tailored by direct photoregulation, different from the photon-induced pH change. Tan and his coworkers covalently tethered azobenzene, a photoresponsive molecule, to the backbone of a single-stranded DNA (Fig. 8.4c) (Kang et al. 2009). When the azobenzene moiety took trans conformation under visible light irradiation, the structural change of DNA displayed a contraction (closed hairpin) configuration and an extension (opened strand) when azobenzene took cis conformation under UV-light irradiation. The process of FRET demonstrated the conformational change of the DNA, by labeling the ends of DNA with a fluorophore-quencher pair. In similar fueling mechanism, Ogasawara et al. demonstrated the successful photoregulation of G-quadruplex formation through isomerization of a photochromic nucleobase, ^{8FV}G, incorporated in aptamers (Ogasawara and Maeda 2009). In a slightly different way of interaction, Zhou et al. used the isomerization of a

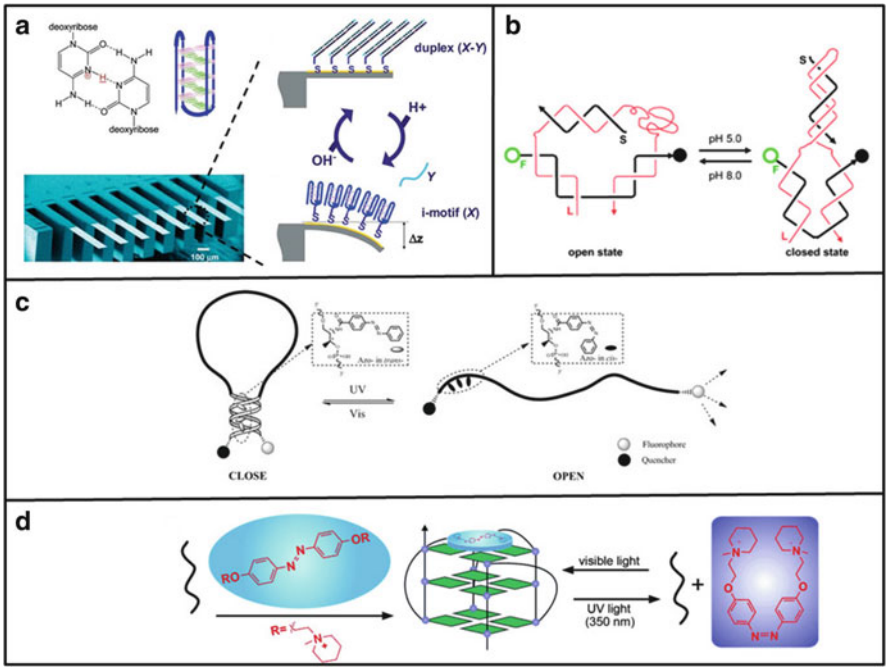

Fig. 8.4 (**a**) Duplex to i-motif conformation conversion exerting force to a microcantilever. At high pH the duplex forms on the surface. At low pH, the strand self-folds into i-motif and induces repulsive in-plane forces (compressive surface stress) to bend down the cantilever [reprinted with permission from Shu et al. (2005). Copyright (2005) American Chemical Society]. (**b**) Operation of the DNA machine based on a duplex–triplex transition induced by pH change [reprinted with permission from John Wiley & Sons, Inc. (Chen et al. 2004a), copyright 2004]. (**c**) Photoswitching of DNA motif between closed and open state by photon-induced conformational change of tethered azobenzene moieties [reprinted with permission from Kang et al. (2009). Copyright (2009) American Chemical Society]. (**d**) Reversible folding and stretching motion of the G quadruplex induced by the photoresponsive azobenzene-derived compound [reprinted with permission from John Wiley & Sons, Inc. (Wang et al. 2010a), copyright 2010]

specially designed azobenzene, which was not covalently attached to the nucleotide, to induce reversible folding and stretching motion of the G-quadruplex (Fig. 8.4d) (Wang et al. 2010a). Briefly, the azobenzene was designed and synthesized to be tethered to positively pendent groups on the ends. They suggested that the trans isomer displayed a planar azobenzene core, participating in π–π stacking with the guanine quartets, and the positively charged side groups displayed a high degree of relaxation and approached the phosphate backbone. The isomerization reduced the stacking and the rotary flexibility of the side chain, thus failed to effect a conformational change.

The metal ions, pH, and photo-fuelled motions are considered to generate removable wastes, which cannot be accumulated and poison the system. However, such motors require the nucleic acid strand either to be encoded with specific

sequences (i.e., i-motif, Z-form DNA) or having high skills for organic synthesis (e.g., pyridine-tethered azobenzene). In fact, so far, the most common mechanism for the DNA motions has been recognized as the strand displacement. The fuel could be DNA strands, metal ions, pH, or aptamer substrates. The DNA motor using strand displacement fell into the first category, in which the base composition (e.g., duplex-single strand-duplex conversion) varied in the process that also involves the compact–extended duplex transition of DNA motifs. An example is the single-molecule DNA nanomotor developed by Tan et al. (Li and Tan 2002). In that system, the DNA motor adopted two distinct conformations: an intramolecular tetraplex and an intermolecular duplex. Through strand-displacement reactions, the nanomotor was enabled to perform an "inchworm" like extending–shrinking motion, which was imaged by FRET. The functions were demonstrated both in solution and on nanoparticle surfaces. In the next part, the strand displacement will be described through the operation of the DNA machines.

8.3 Enhanced Complexity of the Machinery System

A subject of the current research is to mimic the macroscopic machine and to function efficiently in the nanoscale world. Walkers, tweezers, gears, rotators, and metronome (Buranachai et al. 2006) have all been used as examples for constructing the nanosized counterparts. Some other operations are also implemented by the various nanomachines.

8.3.1 Tweezers

The reason that the tweezers are the first to be described is that the molecular tweezers built out of nucleic acid strands was the beginning of complex DNA nanomachines by DNA hybridization. The tweezers, constructed by Yurke and coworkers in 2000 (Yurke et al. 2000), contained three strands: A, B, and C. B and C partially hybridized with A, respectively, to form two rigid double-stranded arms (Fig. 8.5a). Strand A acted as a hinge so that the two arms—AB and AC—can rotate. The DNA strand, referred to as the fuel (F), was able to hybridize with single-stranded tails extended from the free ends of both arm, and this process pulled the arms of the device shut. A section of the fuel strand remained to serve as a toehold for hybridization of a complementary antifuel strand ($\overline{F}$) that released the fuel strand from the arms by strand displacement. This generated a double-stranded waste and reset the device to the initial open configuration. The device could be opened and closed through many cycles by repeated sequential addition of fuel and

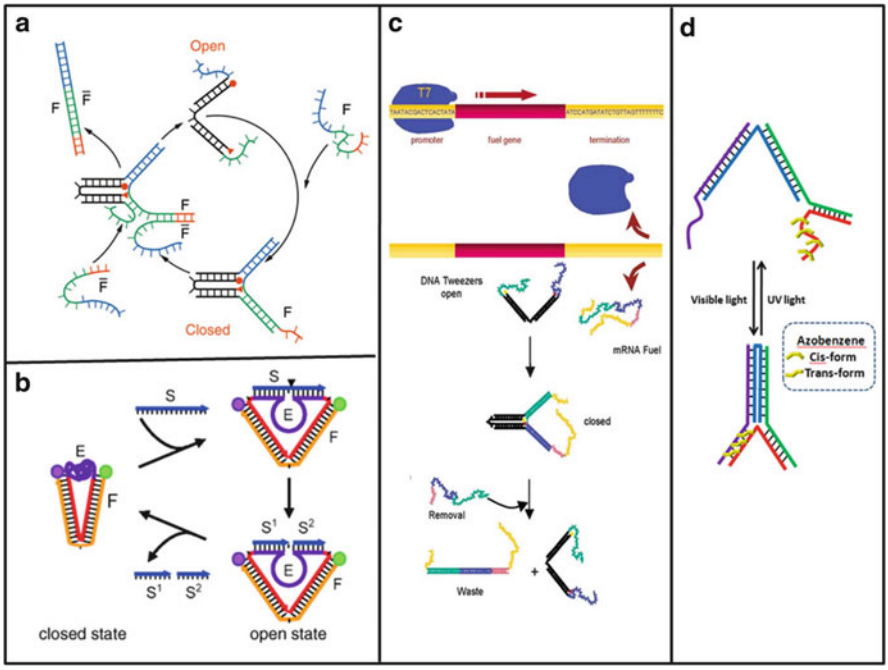

Fig. 8.5 (**a**) Operation of molecular tweezers fuelled by nucleic acid strands, F and $\overline{F}$ [reprinted by permission from Macmillan Publishers Ltd: (Nature) (Yurke et al. 2000), copyright (2000)]. (**b**) Switching of the tweezers between closed and open states by autonomous catalytic cleavage of RNA substrate (reprinted with permission from John Wiley & Sons, Inc. (Chen et al. 2004b), copyright 2004). (**c**) Closing of DNA tweezers controlled by mRNA produced by transcription and subsequent opening of tweezers by a removal strand [reprinted with permission from Dittmer and Simmel (2004). Copyright (2004) American Chemical Society]. (**d**) Photonic control of DNA tweezers tethering azobenzene on the arm

antifuel strands. Operation of the DNA tweezers was characterized using single-molecule FRET measurement through labeling the two arms with a fluorophore and a quencher.

The duplication of "tweezers" by DNA hybridization was further extended by varying the fueling mechanisms, functions, and the number of co-activated tweezers. Mao and coworkers constructed an autonomous DNA tweezers and demonstrated the cyclic operation by means of a biocatalytic reaction (Fig. 8.5b) (Chen et al. 2004b). The tweezers arms consisted of two double-stranded DNA domains that were joined at their open sites by a single-stranded DNA, consisting of a catalytic loop that hydrolyzed RNA. The DNAzyme was bound to the RNA substrate through Watson–Crick base pairing and cleaved the RNA into two short fragments. In absence of the substrate (a DNA-RNA chimera), the single-stranded DNAzyme collapsed into a closed coil as a result of entropic forces. Thus, the overall conformation of the DNA machine was quite compact, i.e., closed configuration. When a DNA–RNA chimera substrate was added, the single-stranded

DNAzyme formed a bulged duplex with the substrate and pushed the two helical domains of the DNA machine apart, leading to an "open configuration." Furthermore, upon binding, the catalytic DNA loop cleaved its substrate into two short fragments, in the presence of Mg^{2+} ions. The resulting fragments dissociated from the machine, which consequently returned to the closed configurations. Consequently, the nanomachine could initiate the cycling of substrate binding, cleavage, and dissociation, resulting in the open and closed configurations. The open sites were labeled by a donor–acceptor pair, and the FRET measurements recorded the opening and closing process of the tweezers. While the free energy released from RNA hydrolysis was used to activate the DNA machines, Simmel et al. used the power of DNA transcription into RNA to control the machine (Fig. 8.5c) (Dittmer and Simmel 2004). A DNA tweezers was switched from the open to the closed conformation by an mRNA fuel strand, which was biocatalytically generated by reverse transcription from a template DNA strand encoding the mRNA. This approach was further refined by placing the gene encoding the RNA fuel strand under the control of either a negative (LexA) or a positive regulator (LacI). Both concepts relied on bacterial expression control systems, in which the presence of an outside effector molecule either stopped (LexA) or started (LacI) transcription of a gene. The template DNA was designed to contain the respective binding sites for the regulator molecules of the fuel gene. In the presence of the positive and the absence of its negative regulator, a much higher percentage of tweezers adopted the closed structure. The reopening of a closed tweezers was reliant upon the manual addition of an opening strand that was complementary to the fuel strand.

Instead of using biological fuel, light-triggered activation of a molecular pair of tweezers was carried out by Ogura et al. (Fig. 8.5d) (Ogura et al. 2009). The use of light as fuel is based on the results in the last section, stating that the formation and dissociation of a DNA duplex can be reversibly photo-regulated by cis–trans isomerization of the azobenzene. The photoisomerizing azobenzene was tethered to a region extended from the double-stranded arms of the tweezers, which was designed similarly to the abovementioned. Under visible light irradiation, the tweezers adopted an open configuration, an energetically more stable configuration because of the trans form of the azobenzene unit. Upon exposure to UV-light irradiation, the azobenzene adopted a cis form. This resulted in the hybridization of the azobenzene-tethered region to the complementary sequence extending from another rigid arm of the tweezers. By switching the wavelength between UV and visible bands, the tweezers were closed and opened, which was monitored by fluorescence measurements.

The complexity of the tweezers system was enhanced significantly through cooperation of multimachinary units by Willner's group. Realizing each tweezers can present two states, i.e., open and closed configurations, an idea was formulated that a larger number of configurations could be realized by the coupling of two tweezers, in the way that communication was established between the two tweezers. The operations of the tweezers are characterized by FRET efficiency, and the open configuration was presented by lower FRET efficiency and higher fluorescence, while the closed configuration was indicated by low fluorescence. It will be easier to use the digital number "1" and "0" to represent the high and low

fluorescence outputs, indicating the open and closed structure configurations respectively. Co-activation of two tweezers can result in a maximum of four configurations: (1,1), (0,0), (0,1), and (1,0), using the fuels as inputs. Such operation of the system requires strict consideration of the energetics inside each tweezers unit, according to which the nucleic sequences of the tweezers arms are carefully designed. Based on the specific recognition of DNA aptamer to adenosine monophosphate (AMP) molecule, Willner's group constructed a two-tweezers system, in which one tweezers (tweezers A) can capture the target DNA strand through hybridization and become closed, in the absence of AMP. Then the other tweezers (tweezers B) arms were empty and adopted the open configuration [state I (0,1)] (Fig. 8.6a) (Elbaz et al. 2009a). Upon addition of AMP, the free strands on tweezers A arms showed stronger affinity toward AMP than the target strand, which was then released for tweezers B. This resulted in the opening of the tweezers A and the closure of tweezers B [state II (1,0)]. Thereafter, by the treatment of adenosine deaminase, AMP was transformed to inosine monophosphate (IMP), which was not recognizable by the aptamer sequence. Consequently, the target strand returned to tweezers A, resulting in tweezers A and tweezers B adopting the closed and open conformations, respectively.

Thermal inactivation of the enzyme and re-addition of AMP released the target strand from the tweezers B. Repeated addition of AMP and adenosine deaminase activated the tweezers A and B concurrently. There were several energetic premises to consider in designing the free strands of the arms of tweezers A and B: (i) the target strand hybridized to the free strands of tweezers A stronger than tweezers B in the absence of AMP; (ii) the aptamer sequence on the arms of tweezers A preferred to bind the substrate AMP than the target strand; and (iii) the target strand formed the stable duplex with the free strands on the arms of tweezers B, closing it. Furthermore, the activation of the two states I and II by the two inputs, AMP and adenosine deaminase, represented a SET-RESET logic operation, according to the truth table. However, the introduction of the enzyme was followed by a significant imperfection, as the thermal activation could induce the subsequent disintegration of the DNA construct. Upon cooling the system, the construct of the tweezers was reformed. The stabilization of the tweezers' structure was a prerequisite for the continuous operation of the tweezers system. The two-tweezers system was improved by Willner's group, by adopting the strategy of operating the tweezers under isothermal conditions (Elbaz et al. 2009b). Briefly, a sequence, which folds into i-motif conformation under acidic conditions was introduced onto the arms of one of the tweezers. The i-motif-encoded tweezers competed with another tweezers in capturing the target DNA strand energetically, thus leading to the coherent activation of two tweezers by switching the pH between acidic and neutral values, at room temperature.

In the following research examples, the two-tweezers system was upgraded to a more complex mechanical system by Willner's group, including three tweezers α, β, and γ, instructed by six fuels (also called logic inputs), i.e., pH-acidic or basic environment, Hg^{2+} ions or cysteine ligand complexing Hg^{2+} ions, and two complementary single-stranded nucleic acids (Wang et al. 2010b). The fuels were used

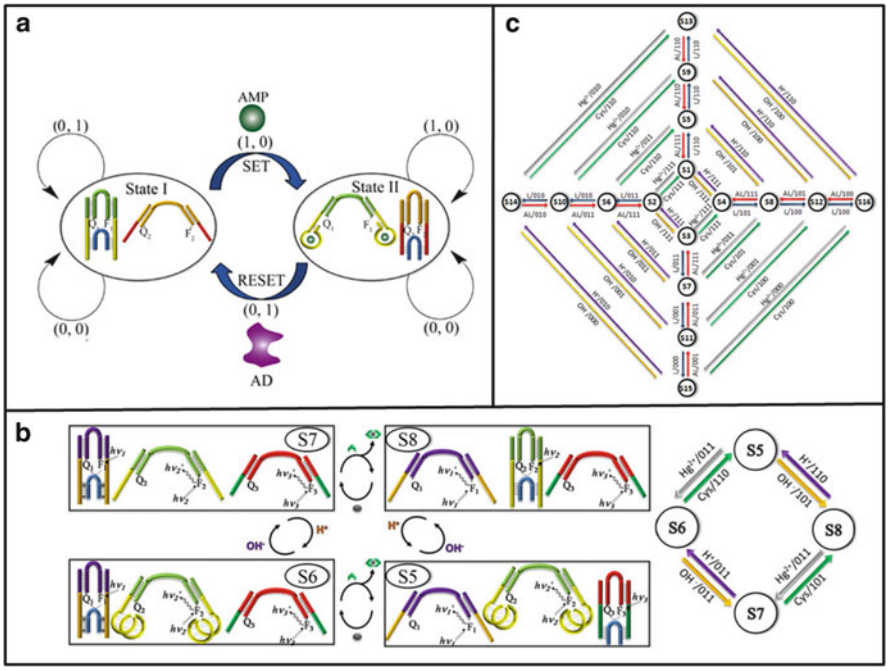

Fig. 8.6 (**a**) Coherent activation of two tweezers by AMP and adenosine deaminase (AD), acting as a SET-RESET logic device [reprinted with permission from John Wiley & Sons, Inc. (Elbaz et al. 2009a), copyright 2009]. (**b**) Concurrent activation of three tweezers using one equivalent of the linker that can close any of the tweezers, instructed by the added fuels (Hg^{2+}, cystein, H^+, or OH^-). The operation results in the automata with four possible states [reprinted with permission of PNAS from Wang et al. (2010b)]. (**c**) Scheme of all 16 states of the automaton, established by a three-tweezers system with six kinds of fuels (Hg^{2+}, cystein, H^+, OH^-, or complementary linker strands) [reprinted with permission of PNAS from Wang et al. (2010b)]

pairwisely and each of which acted reversely for the tweezers. The three tweezers system was designed in such a way that the pairing Hg^{2+} ions/cysteine fueled the opening and closing of tweezers α and pH controlled the configurations of tweezers β, while the fuel strands opened and closed all the three tweezers. In addition, the configurations of tweezers γ were also dependent on tweezers α and β. When the fuels were alternatively applied to the three tweezers system, the mechanical motions of tweezers were activated cooperatively (Fig. 8.6b). Each tweezers were labeled with the respective fluorophore-quencher pair at the ends of the arms. The configurations of the tweezers were investigated as well as the outputs of the system were recorded. As a result, a finite-state automaton system, with 16 states (configurations), eight outputs, and six inputs, was constructed on the basis of the operation of three tweezers (Fig. 8.6c). The system exhibited a memory because each current state and output depended not only on the source configuration but also on past states and inputs. Through integration of the concept of a DNA machine

with the logic computation using new chemical stimuli and appropriate sequence design, Willner's group implemented the first enzyme-free all-DNA automaton experimentally.

8.3.2 Walkers

Walking is one of the most important mechanical motions which biomolecular and macroscopic machines perform. The operation of nanoscale walking devices is obviously more sophisticated than the macroscopic counterparts. Luckily, the motor protein represents an excellent example for designing and running the artificial molecular walking devices. However, whether the direction of the movement is controlled is evidently a challenging problem. Nature has clearly found a solution for the biological machines, e.g., kinesin, which is fueled by ATP to walk along a microtubule. It is exciting that the scientists also have succeeded in the activation and directional control of artificial walking devices, constructed by self-assembly of DNA strands. So far, the structures of nearly all the DNA walking devices, also known as DNA walkers, have been mimicking that of natural nanomotor kinesin. In brief words, a nucleic walking unit with a monoped or multiped is attached to footholds on a DNA-assembled track. The track has been developed from one dimension to two dimensions. The manners of walking vary, but in essence the association/dissociation is driven by hybridization of complementary single strands of DNA to form double helix. The second law of thermodynamics requires the expenditure of energy to achieve unidirectional motion. The fuels have involved the nucleic strands, Mg^{2+}, Hg^{2+}/cysteine, pH, ligase/nicking enzyme, etc. The movement can be unidirectional or two way.

Progress in this area was first reported by the group of Seeman. The reported concept of the biped taking a step is illustrated in Fig. 8.7a (Sherman and Seeman 2004). The device consisted of several all-DNA components, including a "footpath" (dark blue), two "legs" (brown, connected to each other by three flexible linkers) that bear single-stranded "feet" (foot 1 pink, foot 2 orange), and "footholds" A (turquoise) and B (green). Complementary sequences are shown having the same color. The biped started with F1 on foothold A and foot 2 in foothold B. This is called state 1A, 2B. In panel b, the unset strand was introduced to remove foot 2 from foothold B. First, the unset strand grabed the unmated bases in set strand 2B (shown as a gray square). Then, as shown in panel c, the unset strand completely binded to the set strand, removing it from the complex. The bound set/unset strands can then be removed from the solution via the use of magnetic streptavidin beads, which binded the biotins on the ends of the unset strands (shown as blue circles). Once foot 2 was detached, it could be placed on foothold C, which brought the biped to state 1A, 2C, as shown in panel d (this is also the state illustrated in the 3D drawing at left). When unset strand 1A was introduced into the system, foot 1 was detached from foothold A as shown in panel e. Then foot 1 could be attached to foothold B, as shown in panel f. Over the course of this step,

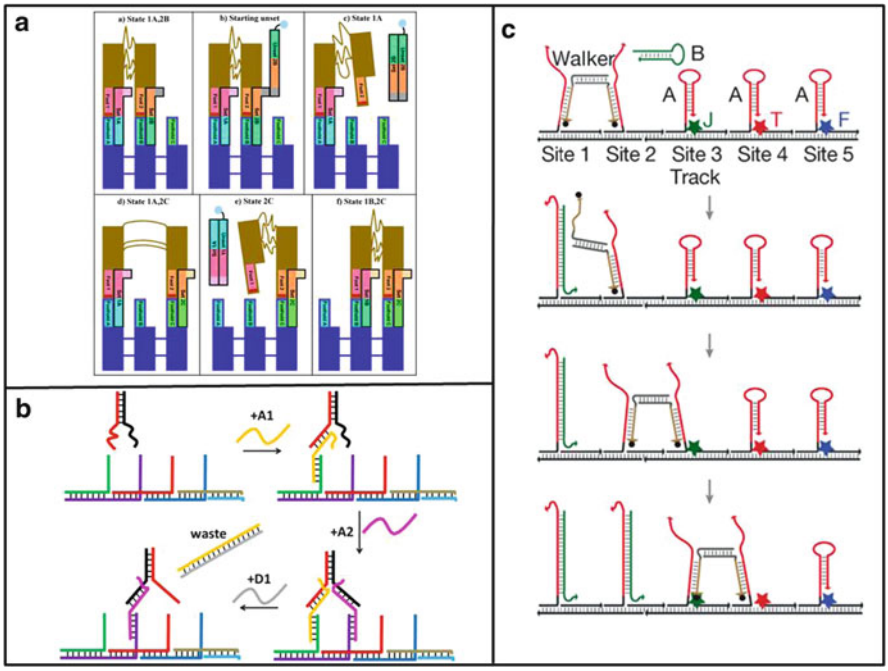

Fig. 8.7 (**a**) A DNA walker triggered by the addition of set and unset strands. The unset strands yield duplex waste and are modified with biotin to facilitate their removal from the reaction mixture [reprinted with permission from Sherman and Seeman (2004). Copyright (2004) American Chemical Society]. (**b**) A DNA walker on a four-foothold track triggered by hybridization and dehybridization. (**c**) The processive and autonomous locomotion of a DNA walking device (reprinted by permission from Macmillan Publishers Ltd: [Nature] (Yin et al. 2008), copyright (2008)]

the biped traveled approximately 2 nm. Because the rise and fall of each foot was precisely controlled by the specific base sequences of the set and unset strands, the step was completely reversible, and the biped could walk back to where it started. Each foot of the biped had a psoralen on the bottom. When exposed to UV light, psoralen covalently linked the foot to the foothold it stood upon. The state of the biped could then easily be monitored using chromatography to separate out the largest covalently linked structures. However, the range of this walker was limited to one or two steps, far different from the natural motors and behind what was required.

Pierce et al. took a step further by demonstrating a processive bipedal DNA nanomotor that moved by advancing the trailing foot to the lead at each step (Shin and Pierce 2004). Compared with the previous work using two feet and two footholds that was incapable of directional motion, the system built by Pierce et al. included two feet and four foot holds and succeeded in efficiently achieving two-way motion (Fig. 8.7b). The fuel DNA strands had to be added by the operator to intervene the system to drive and direct the movement. The implementation of the system automation was first reported by Pierce and his coworkers in 2008

(Fig. 8.7c) (Yin et al. 2008). They developed a walker that moved autonomously and directionally, but with intrinsically limited processivity (about 50 % chance that the motion is terminated at every step). Turberfield's group then reported in their system that the footholds overlapped in such a way that when the leading foot landed, it catalyzed the detachment of the trailing foot (Green et al. 2008). The design proposed and tested a mechanism for autonomous, processive, and directional walker. It also showed the admirable economy: there was no portion of the track that was not used as a foothold.

Subsequently, Seeman's group published an example of an autonomous DNA biped with coordinated feet (Omabegho et al. 2009). Their system consisted of a rigid track and a biped with two different single-stranded feet (A and B). The track was a ~49 nm double-crossover (DX) DNA structure decorated in a directionally polar manner with different metastable DNA stem–loop motifs (each consisting of one "signaling" and one "foothold" strand). The walker comprised two different single-stranded feet that were not joined by a covalent 5′,5′ linkage. Overall, processivity was guaranteed by signaling strands that mediated the interaction between feet and fuel strands as only one foot could detach from the track. Directionality was achieved through the hybridization of metastable hairpin fuel strands to the track (a "burnt-bridges" mechanism). Seeman and coworkers demonstrated a full walking cycle of their device by covalently cross-linking a radioactively labeled walker (32P) to its track in successive walking states and observing fragments with characteristic mobilities during autoradiogram analysis of denaturing PAGE.

Instead of using DNA strands as fuels, biocatalytic energy was also used to drive the autonomous DNA walker. Yan, Turberfield, and Reif et al. constructed a DNA walking device, with a configuration (walking element and the track) similar to the common device, while the movement of the walking element was accomplished by the sequential action of a ligase and two restriction enzymes (Yin et al. 2004). T4 ligase accomplished the set function and created, at the same time, a recognition site for restriction endonucleases (PflM I, BstAP I) that subsequently operated as an unset function. The self-assembled track contained three single-stranded footholds (Fig. 8.2a). The lower part of each foothold was a single-stranded hinge region, while the upper part was a double-stranded segment with a single-stranded overhang acting as a sticky end. At each step the walking element was ligated to the next foothold and then cut from the previous one by the restriction endonuclease. Each ligation created a new restriction site, and each scission broke the previous restriction site. The motion of the walker was unidirectional: the product of ligation between two neighboring footholds could only be cleaved such that the walker moved onto the downstream foothold. The operation of the motor was verified by tracking the radioactively labeled walker in gel electrophoresis.

Thereafter, Turberfield and coworkers reported the design and operation of an autonomous "burnt-bridges" walker that achieved directionality by consuming the track as it moved forward (Fig. 8.8a) (Bath et al. 2005). The single-stranded walking element, a restriction enzyme, and a track composed of the system. The operation was started by the recognition of a particular sequence in a walker-foothold duplex and then catalyzed hydrolysis of the foothold strand. Due to

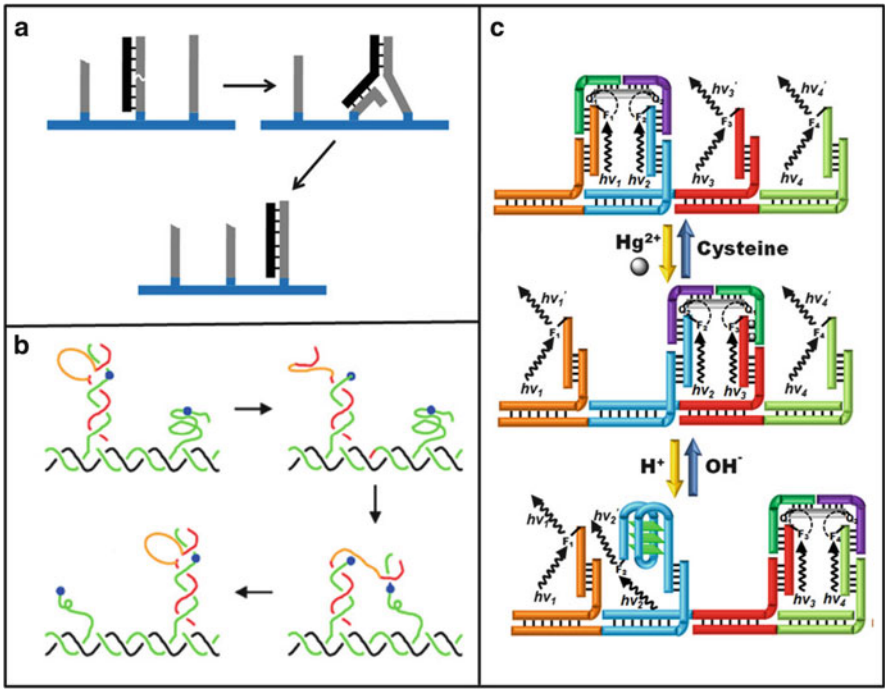

Fig. 8.8 (**a**) An autonomous DNA walker fueled by a nicking enzyme using the strategy of "burned bridges." (**b**) A DNA "walker" on a RNA track triggered by DNAzyme scission and strand migration [reprinted with permission from John Wiley & Sons, Inc. (Tian et al. 2005), copyright 2005]. (**c**) A bipedal DNA walker fueled by ions and cysteine to control the directional walking [adapted with permission from Wang et al. (2011). Copyright (2011) American Chemical Society]

instability, the terminus of the nicked foothold was then released from the duplex region. Thereby, the walker element possessing a toehold region could reach and attach to the second foothold because of the competitive hybridization. A backward step was impossible because attachment to the longer footholds was extremely unstable. The process was then repeated so that the walker eventually was located on the third foothold. It was not cleaved by the enzyme since restriction site was absent. The successful operation of this elegantly simple system was demonstrated on a three-stator test track using fluorescence labeling.

A conceptually similar burnt-bridges walker was published by Mao and his coworkers in the same year (Fig. 8.8b) (Tian et al. 2005). However, the artificial DNAzyme replaced the natural protein enzyme, and RNA was the fuel. The track was constructed of duplex DNA with four evenly spaced slightly different footholds consisting of RNA nucleotides. The walker was a DNAzyme capable of cleaving RNA strands with sequence specificity. Once the walking element was assembled, a cascade reaction was initiated that is almost identical as the one described by the Turberfield et al., regarding both the walking manner and directionality (Bath et al. 2005). One notable difference is that in Mao's system all footholds were

susceptible to recognition by the DNAzyme, so that the final foothold also was hydrolyzed. Moreover, Mao's system included inherently catalytically active unit that triggered directional motion, in contrast with the previous system requiring addition of unset restriction enzymes.

In a very recent research report, Willner's group operated a bipedal walker on a linear track through DNA-ion recognition and competitive strand hybridization (Fig. 8.8c) (Wang et al. 2011). Generally, Hg^{2+} ions, cysteine, H^+, and OH^- were adopted as the fuels. The track contained two footholds with their respective single-stranded sticky ends. One of the sticky ends was designed so that its hybridization of one foot of the bipedal walking element was enhanced by bisthymine-Hg^{2+} coordination, while another one included cytosine-rich sequence folded up to an i-motif upon environment acidification. The ligand complexing Hg^{2+} and OH^- were added to counteract the effect of Hg^{2+} and acidic pH, so that walking direction of the motor was controlled flexibly. The thermodynamic rules was fully used in the design of the walking device, which strictly followed the energetic ranking between the foothold-walker duplex during the movement. The walker system was imaged by labeling the sticky end of each foothold with a fluorophore, and the two sides of the walking element was equipped with quenchers to turn on and off the fluorophore emission. In extension of this research, it was shown that the ends of the linear track were linked covalently and the clockwise or counterclockwise motion of the walker was triggered, termed as "DNA stepper."

The operation of above walking devices was all accomplished on 1D linear track, on which single-pedal or bipedal walker elements moved. In 2010, the dimension and the configuration of the walking element together with motional fashion became more sophisticated, one step closer to creating molecular robots, as reported by the groups of Stojanovic, Walter, Winfree, and Yan (Lund et al. 2010). The technology of DNA origami was used to make a flat surface, on which a molecular spider, comprising a streptavidin molecule as an inert body and three deoxyribozymes as catalytic legs, was positioned. The spider carried out autonomous elementary robotic behaviors such as "start," "follow," "turn," or "stop" when interacting with a precisely defined environment. The construct and operation of the molecular spider are illustrated in Fig. 8.9a. The spider was fueled by the chemical interactions, and its single-stranded DNA "legs" were attached to the origami surface. In order to take a "step," the legs first cleaved a DNA strand on the surface, weakening its interaction with the origami surface. This encouraged the spider to move forward, pulled toward the intact surface, where its interactions were stronger. The spider stopped when it bound to a part of the origami surface which it was unable to cleave. The behavior of the spiders on 48 and 90 nm pathways on the origami landscape was analyzed by AFM and real-time total internal reflection fluorescence microscopy. Statistical analysis of the AFM data showed that on the 90 nm track, 70 % of the spiders reached the "STOP" site within 60 min. Very few spiders were found on a control site on the origami tile, illustrating the processivity of the walker locomotion.

On a similar surface, a rectangular DNA origami, the groups of Sugiyama and Turberfield assembled a 100-nm-long DNA track and showed that a DNA walking unit loaded at one end of the track moved autonomously and at a constant average

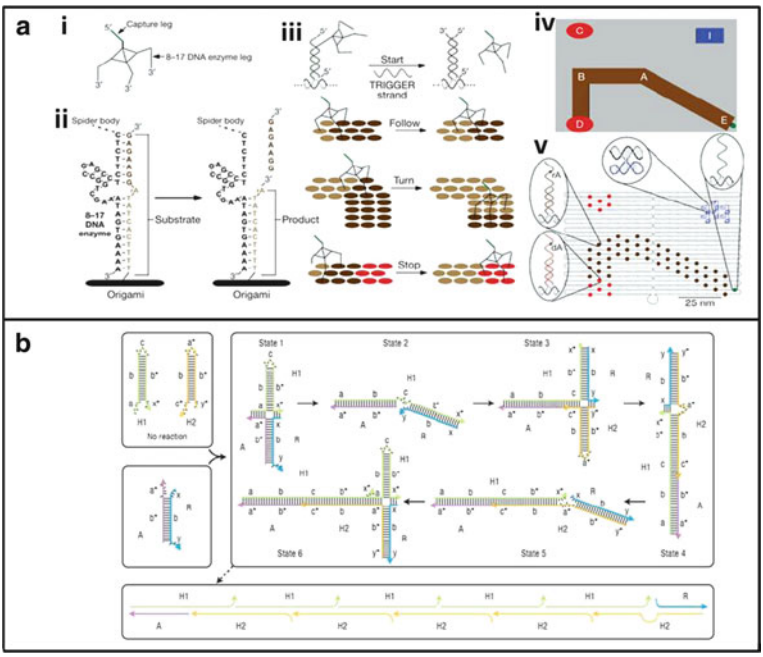

Fig. 8.9 (**a**) A molecular spider with three DNAzyme legs displaying autonomous robotic behavior on a DNA origami landscape. (**i**) The spider consists of a streptavidin core, a single-stranded capture DNA positioning the spider in the beginning, and three DNAzyme legs. (**ii**) Cleavage of the DNAzyme substrate creates two shorter strands, allowing legs to bind with the next substrate. (**iii**) The spider performs the robotic behaviors instructed by the foothold sequence, e.g., following the substrate track, turning and continuing to the stop site. (**iv**) Schematic of the track EABD with positions A to E labeled. (**v**) A representative origami landscape showing the "START" position, the substrate track, STOP and the CONTROL sites, and a topographical imaging marker [reprinted by permission from Macmillan Publishers Ltd: [Nature] (Lund et al. 2010), copyright (2010)]. (**b**) An autonomous polymerization motor. The metastable fuel hairpins (H1 and H2) do not interact in the absence of the A-R complex. Upon mixing, H1 binds to the sticky ends of A-R (State 1), initiating a four-way branch migration (State 2). H2 then hybridizes to the new sticky ends (State 3), initiating a four-way migration (State 4). Then a H1 hairpin binds and begin the next fuel cycle (State 6), continuing the hybridization chain reaction. The R strand is passed back and forth between H1 and H2 hairpins at the living end of the growing polymer, moving away from the A strand, remaining bound the initial H1 hairpin [reprinted by permission from Macmillan Publishers Ltd: [Nature Nanotechnology] (Venkataraman et al. 2007), copyright (2007)]

speed along the full length of the track, a journey comprising 16 consecutive steps for the motor (Wickham et al. 2011). A highlight of this research is that real-time AFM was adequately used for direct observation of the movement of the single element, revealing mechanistic details of its motion.

Another type of track-anchoring walker was recently developed by the group of Turberfield. The track was designed into a branched configuration, and the monopeded walking element was instructed by a set of fuel hairpins to determining

its destination, for example, to turn left or right at a junction in the track (Muscat et al. 2011).

The walkers described have already left huge impression due to the motor that physically walks, the fuel that provides the power resource, and the track that prescribes the direction of motion. There are also other devices engineered to perform the locomotion function. Pierce's group presented an interesting motor, which operated by polymerizing a double-helical DNA tail (Fig. 8.9b) (Venkataraman et al. 2007). The concept was inspired by bacterial pathogen such as *Rickettsia rickettsii* that propel themselves through host cells by polymerizing protein "comet tails." They demonstrated the autonomous and processive locomotion of a motor, powered by the free energy of DNA hybridization.

8.3.3 Other Mechanical Devices

As summarized in this chapter, great efforts have been devoted to the mechanical devices duplicating the function of tweezers and walkers. If careful attention is paid, the common configurations are interchangeable between the tweezers and the walking devices to some extent. It could, e.g., be envisioned that two flexible tiles extending from each double arms of the tweezers were anchored to a pair of sticky ends on a double-stranded linear track. Furthermore, if each tile was programmed with different functional sequence, then a bipedal walker was constructed and could be operated by varying the interaction between the tiles and the track and vice versa. This exemplifies the intriguing inherent conversion properties of DNA motif in deriving various styles of DNA mechanical devices. In principle, the flexible combination of DNA hybridization and versatile motifs together with appropriate design can result in any machinery construct. Therefore, so far, a wide diversity of DNA mechanical devices have been constructed and operated, in addition to the well-known tweezers and walking devices. In this section we will introduce some of the DNA devices playing mechanical tricks.

8.3.3.1 Molecular Gears

As described by Pierce et al., a bipedal DNA walker was constructed and driven by DNA fuel strands. Although we usually study the walking behaviors of the motor on the track, the motions are interactive between the track and the walking elements. In other words, the track "walks" in the opposite direction of the walking element. The concept inspired such imagination that if the walker and the track are designed with circular configuration, their interactive motion will result in the molecular gears: A pair of DNA circles rolls against each other, reported by Mao et al. (Tian and Mao 2004). The relative rolling of the pairing circles was fuelled in "strand displacement" mechanism, based on DNA hybridization and dehybridization.

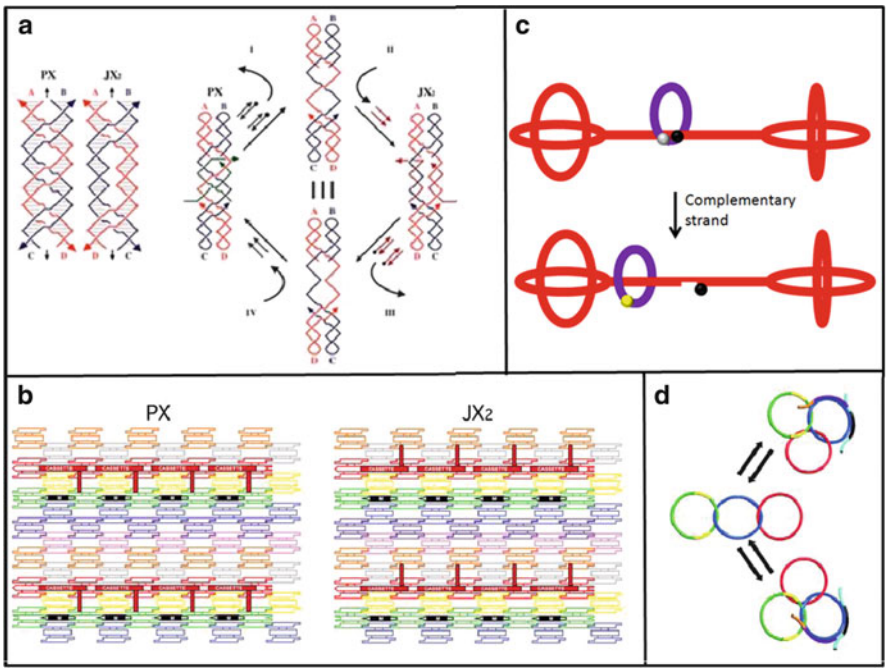

Fig. 8.10 (**a**) The machinery cycle of a PX–JX_2 device through process I–IV [reprinted by permission from Macmillan Publishers Ltd: (Nature) (Yan et al. 2002), copyright (2002)]. (**b**) Insertion of a device cassette into a 2D array, which indicates two states PX and JX_2. The eight TX tiles are shown in different colors. The cassette and reporter helix are shown as *red-filled components*; the *black marker tile* is labeled "M" and is shown with a *black-filled rectangle* representing the domain of the tile that protrudes from the rest of the array. Both the cassette and the marker tile are rotated about 103° from the other components of the array (three nucleotides rotation). The PX arrangement is shown at the *left* and the JX_2 arrangement is on the *right*. Note that the reporter *hairpin* points toward the marker tile in the PX state but points away from it in the JX_2 state [from Ding and Seeman (2006). Reprinted with permission from AAAS]. (**c**) Triggered release of the fluorophore-labeled macrocycle, the movement of which is limited by the *spherical* stoppers on both ends. (**d**) Programmed and reversible reconfiguration of three-rings DNA catenane topologies [reprinted with permission from John Wiley & Sons, Inc. (Elbaz et al. 2012), copyright 2012]

8.3.3.2 Molecular Rotors

More complex mechanical motion than tweezers-related structure was discovered in the "PX–JX_2" device that was driven by DNA hybridization, performing 180° rotations. PX refers to a paranemic crossover structure. This device was based on an interchange between two different DNA topologies, PX and JX_2, that can be used as components for a device, shown in Fig. 8.10a (Yan et al. 2002). The PX motif consisted of two double helices (one red and one blue) wrapped around each other, leading to crossovers between the helical domains at every possible point. In contrast, the JX_2 motif lacked two crossovers in the middle. This difference resulted

in that the two strand pairs were inter-wrapped 1.5 times in the PX structure shown and only once in the JX_2 structure. Interconversion between these two structures was the basis for the device. Starting with the PX state, the green set strands were removed by their complements (process I) to leave an unstructured frame. The addition of the yellow set strands (process II) converted the frame to the JX_2 state, in which the top and bottom domains rotated a half-turn relative to their arrangement in the PX conformation. Processes III and IV reversed this process to return to the PX structure. Gel electrophoresis and AFM were used to demonstrate the action of this device. Seeman et al. advanced the system using RNA in place of DNA to control the device, to enable the machine to respond to signals generated by transcriptional logic circuits, etc. (Zhong and Seeman 2006). In another research, Seeman et al. introduced a PX–JX_2 cassette into eight-tile triple crossover (TX) lattice (Fig. 8.10b) (Ding and Seeman 2006). Using double-stranded "reporter molecules" attached to the cassettes, the switching between the PX and JX_2 states could be demonstrated as the reporter arm changed its orientation relative to a marker tile (black), visualized by AFM.

8.3.3.3 Molecular Rotaxanes and Catenanes

Rotaxanes and catenanes are topologically nontrivial molecular architecture, interlocked mechanically. A rotaxane consists of a dumbbell-shaped molecule threaded through a macrocycle. The most impressive feature is that the macrocycle can move freely along the axle, but the unthreading (dissociation) is prevented by the ends of the dumbbell (stoppers). That means, the macrocycle is kinetically trapped and can only perform intramolecular movement, since the stoppers are larger than the diameter of the ring and the covalent bonds required are significantly distorted. Famulok et al. reported for the first time the assembly and the intramolecular movement of the DNA rotaxane, Fig. 8.10c (Ackermann et al. 2010). In the rotaxane nanostructure, the dumbbell-shaped molecule and the macrocycle were made of double-stranded DNA, and the axle of the dumbbell was threaded through the macrocycle by base pairing. The process involved the locking of the macrocycle to the axle to form pseudorotaxane and the ligation of the stopper molecules to the axle leading to dumbbell topology. With appropriate design of the stoppers, including the size and the structure, the mechanical sliding of the macrocycle, released by oligonucleotides, could be finely tuned.

A catenane consists of two or more interlocked macrocycles. The interlocked rings cannot be separated without breaking the covalent bonds of the macrocycles. The topologies of DNA catenane were first identified in natural cellular processes (Hudson and Vinograd 1967), and substantial research efforts were directed toward the synthesis of artificial nucleic acid-based catenanes (Han et al. 2010; Liu et al. 2008; Schmidt and Heckel 2011). Willner's group advanced the area of DNA catenanes by introducing mechanical concept of "programmed dynamic reconfiguration" (Elbaz et al. 2012), through the synthesis and operation of more flexible single-stranded catenanes. The catenanes were designed so that specific

domains were included in one of the rings for recognizing and hybridizing with another ring. This resulted in mechanical movement of the catenane. Moreover, the configurations of the "paths" could be adjusted, blocked, or de-blocked, through strand displacement, so that the direction of the translocation of the moving rings could be controlled and thus programmed (Fig. 8.10d). The most intriguing feature of the catenanes was that they could undergo programmed and reversible reconfiguration across defined topologies.

In addition to the mentioned devices, a DNA nanoactuator capable of autonomous internal motion (Marini et al. 2011) and a dynamically programmed DNA nanotransporter (Wang et al. 2012) were also reported very recently. Due to the flexibility of DNA self-assembly, theoretically, numerous DNA nanomechanical devices with various functions can be generated. In the future, more research efforts will be laid on the applications of the mechanical devices.

8.4 Applications

Nature has offered prototypes which have provided inspiration in the design of artificial mechanical devices. However, in the case of DNA devices, due to the inherent intriguing properties of nucleic acids, their functions should not be limited to those of natural biological machines. DNA is a biological macromolecule composed of chemical units. Therefore, the research of DNA mechanical devices started with potential progress in many fields. So far, great advancements in DNA mechanical devices have provided successful examples in finding the applications not only in environment sensing but also in the microsynthesis, nano-objects transportation, controlled release, as well as the regulation of surface properties. These applications reveal perfect use of the intrinsic properties of the mechanical devices: unique recognition and responsive mechanics. In the following, some shining progress will be exemplified.

8.4.1 Sensors

As aforementioned, the foundation for constructing DNA mechanical devices is the responsive inherence of DNA motif, which in other words can be seen as the combination of the recognition and the corresponding structural change. The unique recognition of DNA to molecular or ionic targets and the established labeling and characterization methods allow the mechanical devices to function as sensors with high selectivity and sensitivity. The dynamic properties of DNA devices have been used to construct sensors for a series of chemical or biological analytes. The sensitivity not only depends on the characterization but also on the configurations of the devices and the dynamical sensing process, which has been well demonstrated in the amplified biosensing by the autonomous mechanical

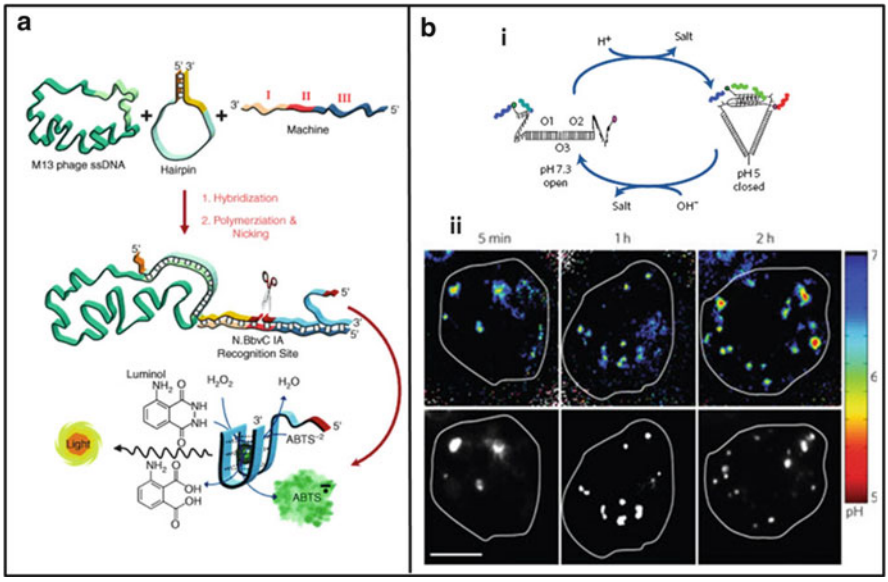

Fig. 8.11 Examples of sensing functions of DNA mechanical devices. (**a**) Amplified analysis of M13 phage ssDNA by enzymes-triggered DNA machine [adapted with permission from John Wiley & Sons, Inc. (Weizmann et al. 2006), copyright 2006]. (**b**) A DNA nanomachine sensing pH changes inside living cells: (**i**) activation of the machine in the open state at high pH and in the closed state at low pH and (**ii**) pseudocolor D/A map of hemocytes pulsed with the machinery switch at the indicated chase times [adapted with permission from Macmillan Publishers Ltd: [Nature Nanotechnology] (Modi et al. 2009), copyright (2009)]

devices. Willner's group invoked the concept that DNA-related catalytic reactions are coupled to the amplification of the signal. The concept was realized by starting with the detection of M13 phage DNA, shown in Fig. 8.11a (Weizmann et al. 2006). The machine track contained three main parts: a primer-binding region (I), a nicking enzyme recognition site (II), and a reporter sequence (II) that included the region complementary to the HRP-mimicking DNAzyme. A fraction of M13 DNA hybridized with a DNA hairpin. Upon opening the hairpin, one of the stem regions served as the primer for the hybridization to the recognition domain of the DNA machine track. Then, the duplex generated between the primer and the track initiated the replication of the track in the presence of a DNA polymerase. The polymerase chain reaction resulted in a duplex structure that included the nick site to be cut by the nicking enzyme. The cleavage of the replicated strand opened a new site for the replication of the track, displacing the previously synthesized strand. The displaced fragment was engineered with the DNAzyme sequence, complexing the hemin to become a HRP-mimicking DNAzyme. The catalysis generated the amplified colorimetric or chemiluminescence signal of the analyte, and the autonomous generation of the catalyst enabled the detection of the target viral DNA with a sensitivity of 10^{-6} M. The research was expanded by engineering the binding domain of the track to recognize cocaine (Shlyahovsky et al. 2007) or Hg^{2+}

(Li et al. 2008). Signal detection was then implemented by lighting a molecular beacon or HRP-mimicking DNAzyme catalysis, respectively, to obtain low detection limit of cocaine or Hg^{2+} ions. Also, Thrombin was sensed by using a similar concept but with an adaption of the detection mechanism as binding of thrombin inhibited the turnover of the DNA machine (Zhu et al. 2009).

As is known, the cytosine-rich DNA sequence is responsive in conformation to a range of pH from acidic to neutral. Tracking of changes of pH is very important and challenging as it is associated to many physiological phenomena inside living organisms such as development of embryo, secretion, and cell–cell fusion. The group of Krishnan therefore built a pH-triggered autonomous DNA mechanical device that could sense changes in pH inside cell organelles (Fig. 8.11b) (Modi et al. 2009). The nanomachine was made of two DNA duplexes connected by a flexible hinge. Each end of the duplex had cytosine-rich strands, which bound to each other to form i-motif structure when pH was acidic and remained apart when it was neutral. Additionally, two fluorophore molecules were attached one to each end of the duplex such that their interaction was directly proportional to the distance between them. Hence, change in pH was directly reflected in the efficiency of energy transfer between the two fluorophores which could be monitored outside the organism. The nanodevice was injected in the nematode *Caenorhabditis elegans*, where it entered the specialized cells called coelomocytes and was trapped in endosomes. Endosomes are known to undergo a series of maturation stages each of which is associated with a change of pH. Each stage of endosome maturation could be tracked by monitoring the FRET of the nanomachine.

A DNA origami-deriving mechanical device was developed recently by Kuzuya et al. to sense the chemical and biological targets at single-molecular resolution (Kuzuya et al. 2011). The device consisted of two levers ~170 nm at a fulcrum, with different relative alignment that could detect single molecules from protein from metal ions. The shape transition of DNA pliers, imaged by the AFM and the fluorescence of the fluorophores, was triggered by three mechanisms: pinching, zipping, and unzipping, in presence of the corresponding targets.

8.4.2 Templated Synthesis

DNA serves as an efficient template for a broad range of chemical transformations. It is well-known DNA templates enzymatic reactions such as polymerase chain reaction (replication) and the formation of phosphodiester bonds of nucleic acids backbones. This encourages researchers to discover the ability of DNA-templated reactions to direct the creation of structures unrelated to the nucleic acid backbone. The complementarities between DNA strands and the availability of nucleotide modifications provide more natural chances for translation of DNA templates into increasingly sophisticated and diverse synthetic molecules. The key point for the DNA-templated synthesis (DTS) concept is when the oligonucleotides bearing chemical groups are held in close proximity by means of hybridization, the reactive species are confined to the same region, resulting in the increase of the effective

molar concentration and acceleration of the reactivity (Gartner and Liu 2001). When the reactants are sufficiently dilute, the rate enhancement is sufficient so that the cross talks can be neglected between the reactive molecules on unconnected oligonucleotides. DNA mechanical devices have showed great advantage in the creation of molecules requiring multistep synthesis and even complex protecting group steps in traditional synthetic chemistry.

An example is the DNA-templated sequential synthesis of ordered functional oligomers, using multiple strand-displacement system that provided the same reaction environment at each step, as reported by the groups of Turberfield and O'Reilly (McKee et al. 2010). The general mechanism is depicted in Fig. 8.12a. The complementary oligonucleotide adapters, functionalized at the 5′ or 3′ end, hybridized to each other to bring their reactive groups into close proximity. Each adapter also included a unique "toehold" to displace it from the active intermediate once the reaction was completed, by addition of a fully complementary "remover" DNA strand. The oligometric product grew and transferred to the incoming adapter. After removal of the spent adapter, the active adapter bearing the growing chain could hybridize and reacted with the next adapter strand to allow the cycle to be repeated. Using this strand-displacement mechanism, a series of olefin 4-mers were synthesized using three sequential DNA-templated Witting reactions. The feature of this research lied in that successive coupling reactions could take place in almost the same environments, independent of the number of coupling steps. That means, the final product length was only decided by the yield of each step. The group of Liu developed the sequential strand displacement producing DNA-templated coupling reactions by adopting a "toehold displacement" strategy (He and Liu 2011). The multistep synthesis mediated a six-step DNA template reaction that proceeded in 35 % overall yield.

A different but even more exciting example is the autonomous synthesis of oligomers through the DNA walking device by the group of Liu (He and Liu 2010). The DNA walker was designed similar to that reported by Mao's group (Tian et al. 2005): the walking element can move along the track autonomously and processively by cleavage of RNA substrates and the subsequent dissociation of RNA fragments. The system is illustrated in Fig. 8.12b. Three substrates (S1–S3) and an initiator (S0) could hybridize on a single-stranded DNA track (T). Each substrate had an amino acid NHS ester at its 5′ end and two ribonucleotides in the middle of its DNA sequence. The DNA walker (W) contained a 3′ amine group and an RNA-cleaving DNAzyme that could cleave the ribonucleotide in the substrates. Initially, all component strands hybridized into a double-stranded construct, except the walking element and initiator strands. Upon addition of the walking element S0 and the initiator W, the template-bound walking element hybridized with the nearest D1. This induced the favorable translocation of W to S0 and triggered DNA-templated acylation of the walking element's amine group with the NHS ester of S1, resulting in the transfer of the first amino acid building block from S1 to W. The loop of the DNAzyme in the walking element cleaved the ribonucleotide linkage in S1, allowing the 5′ fragment of S1 to dissociate. Then the system state was identical to the starting state. Two subsequent cycles of walking element translocation, DNA-templated amine acylation, DNAzyme-catalyzed cleavage,

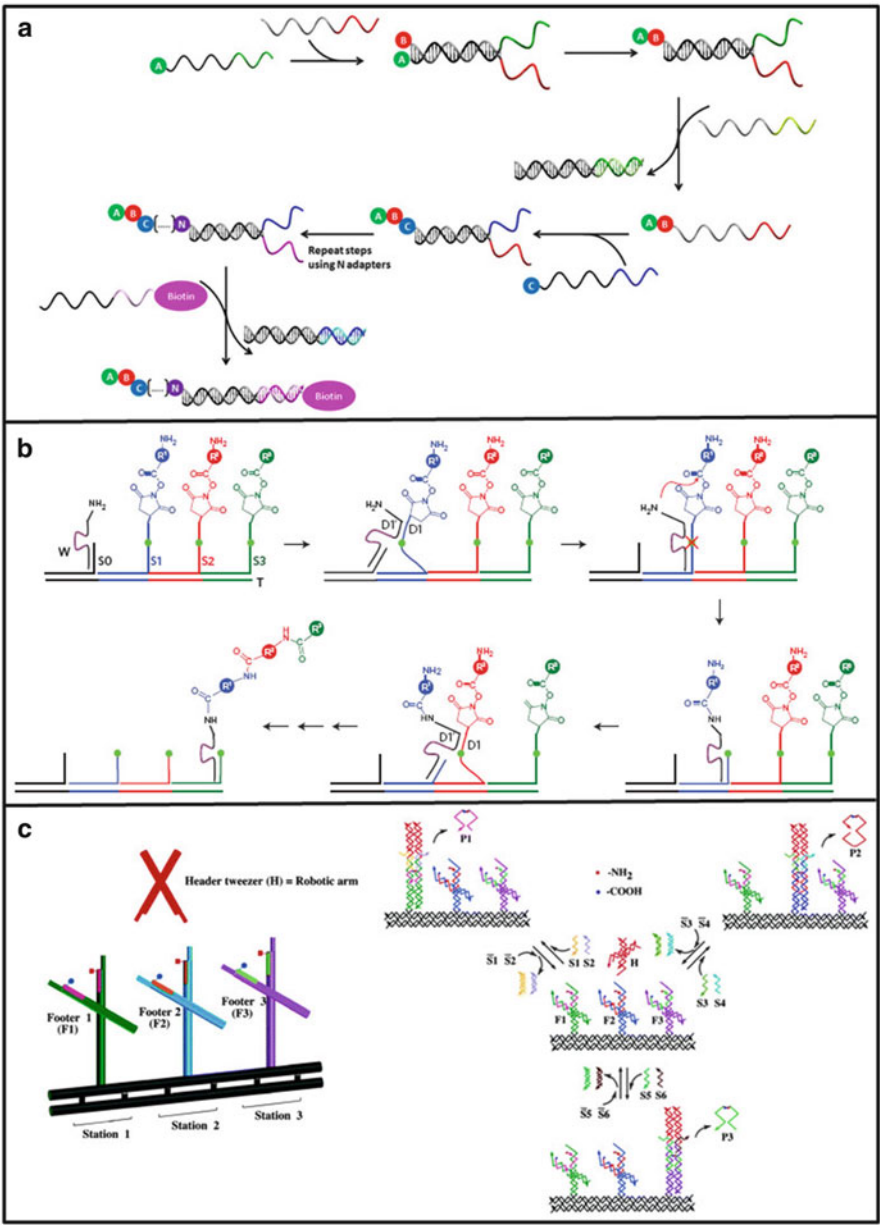

Fig. 8.12 DNA-templated organic synthesis. (**a**) Oligomer synthesis through strand displacement. Hybridization pulls reactive groups into close proximity allowing the group to transfer from the first to the second adapter. Subsequent cycles of strand exchange and rehybridization achieve sequential synthesis. A biotin-tagged strand is used to isolate the final product from the reaction mixture. (**b**) Autonomous multistep synthesis of a triamide product by a DNAzyme-mediated walker [reprinted with permission from Macmillan Publishers Ltd: [Nature Nanotechnology] (He and Liu 2010), copyright (2010)]. (**c**) (*Left*) An array of tweezers bearing –COOH and

and dissociation of the 5′ fragment of the expended substrate resulted in the walking strand covalently linked to the final reaction product (a triamide containing three amino acid building blocks in a specific T-programmed order). Since the walking was driven by the continuous and spontaneous hydrolysis of RNA, the entire reaction sequence proceeded autonomously, in an isothermal condition and no interference from the surrounding. Moreover, the automated mechanical system enabled the efficient generation of target product, since each activated amino acid could only react with the nascent product and any of possible undesired reactions between reactants could be prevented.

Templated organic reactions were also performed on addressable DNA tweezers array (Chhabra et al. 2006). Three tweezers, each bearing two coupling reactants, were self-assembled on a linear DNA track. A fourth tweezer floating freely in solution could be brought to any one of the tweezers and close them by the addition of a unique pair of fuel DNA strands. The coupling reactions happened when the tweezers were closed, and this could be controlled sequentially from one tweezers to another (Fig. 8.12c).

8.4.3 Transportation and Assembly of Cargos

Transportation of objects is ambiguously a basic function of a DNA nanorobot, which could be easily made by DNA walking devices. How machines are designed and operated to work as assembly line is still a challenging topic. A DNA walker was able to transport a molecule and to create new molecule at each step autonomously (He and Liu 2010). In a very recent research, the group of Seeman has constructed a robot-like DNA machine to assemble cargos as it moves (Fig. 8.13) (Gu et al. 2010). The assembly line was implemented by the combination of three DNA-based components: A DNA origami tile, providing the framework and also the track for the assembly process; three DNA machines, or cassettes, serving as programmable cargo-donating devices; a DNA walker, moving along the track from device to device, stopping at the DNA machines to collect and carry the DNA cargo. The walker was fuelled by single strands of DNA that instructed the walking element to move past an "assembly line" of three DNA-made loading devices, each containing a cargo, i.e., gold nanoparticle. Each loading device could be programmed to either donate its cargo to the passing walker ("ON" state) or be in "OFF" state, where no transfer occurred, such that the walker could be controlled to receive anywhere from zero to three particles along its ~200 nm journey, to fabricate eight different products obtained with three two-state devices. AFM was adequately used to visualize and monitor the process steps.

Fig. 8.12 (continued) $-NH_2$ groups (*left*). (*Right*) The amide bond coupling reactions based on the set strands-specific header–footers hybridization [adapted with permission from Chhabra et al. (2006). Copyright (2006) American Chemical Society]

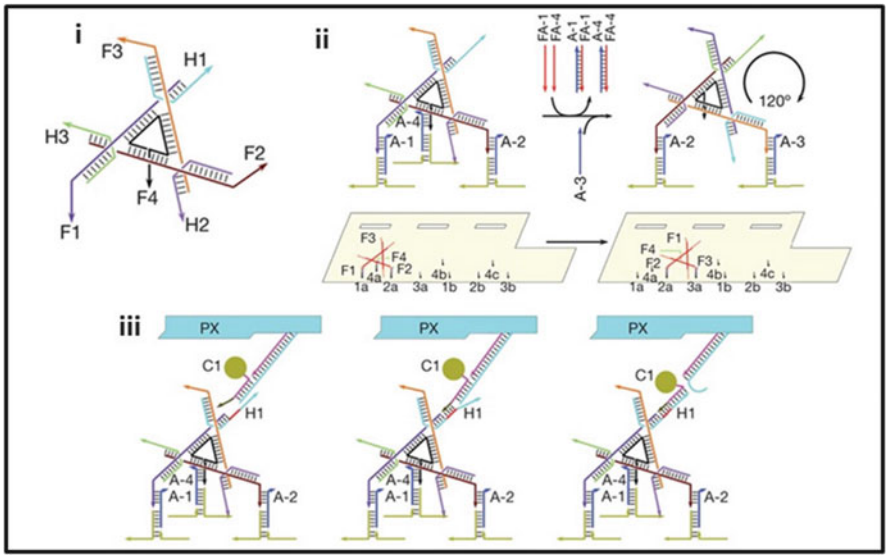

Fig. 8.13 Assembly and transportation of nanoscale objects by DNA mechanical devices. The molecular assembly line. (**i**) The construct of the walking element, including three hands (H1–H3) and four feet (F1–F4). (**ii**) Walking reactions (*upper images*): one stride of the walking element requires the sequential addition of two fuel strands and on anchor strand (walker rotated by 120°). Movement of the walking element on the DNA origami track showing the interaction between the feet and the binding sites. (**iii**) Transfer of gold nanoparticle from the machine to the walking element [adapted by permission from Macmillan Publishers Ltd: [Nature] (Gu et al. 2010), copyright (2010)]

The mechanics of DNA hybridization was also used to transport nanosized objects, reported by Gaub et al. (Kufer et al. 2008). However, different from the previous machines made out of DNA, the mechanical device reported by them was the integration of the two approaches: the precise operation of an instrument and the selective hybridization of DNA. Functional units coupled to DNA oligomers were picked up from a depot area by a complementary DNA strand bound to an AFM tip. These units were transferred to and deposited on a target area to create desired patterns, assembled from different functional units. Each of the cut-and-paste steps was demonstrated by single-molecule force spectroscopy and single-molecule fluorescence microscopy.

8.4.4 Nanocontainer and Releaser

Structural DNA nanotechnology has enabled the construction of scaffolds for encapsulation of nanoscale objects. Meanwhile, the development of mechanical devices provides chances for controlled inclusion and release. The process could be based on the cyclic establishment and the dissociation of the substrate–target

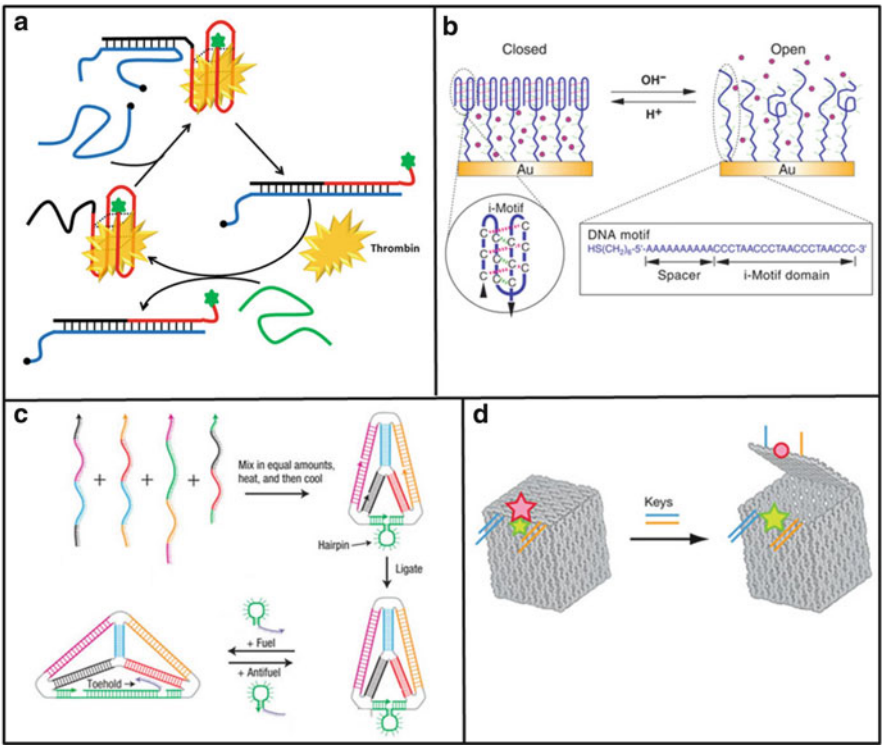

Fig. 8.14 Nano-objects contained and released mechanical devices. (**a**) The operation cycle of the aptamer-based molecular machine in the presence of thrombin. (**b**) Switchable DNA nanocontainer triggered by pH change [reprinted with permission from Mao et al. (2007), copyright 2007, Oxford Journals]. (**c**) A DNA tetrahedron with a single reconfigurable edge. Four strands are combined to form tetrahedron. The edge is extended by adding a fuel hairpin and contracted by the antifuel hairpin [adapted with permission from Macmillan Publishers Ltd: [Nature Nanotechnology] (Goodman et al. 2008), copyright (2008)]. (**d**) The controlled opening of the box lid using a specific DNA key [reprinted by permission from Macmillan Publishers Ltd: [Nature] (Andersen et al. 2009), copyright (2009)]

complexes by external triggers or just by the variation of the container volume to physically breathing in and out of the targets. The first strategy was used by Simmel to grab or release the human blood-clotting factor, α-thrombin, using the DNA aptamer-based machine, Fig. 8.14a (Dittmer et al. 2004). One fuel strand could disrupt the interaction between the aptamer (G-quadruplex) and the thrombin by energetically favored hybridization, and the other fuel strand had higher affinity to the "disrupting" strand, reforming the thrombin–aptamer complex. In the operation, the thrombin-binding DNA aptamer was mechanically switched between a binding and nonbinding form. In another study, pH was used to switch the DNA motif to release a telomere DNA-binding protein by acidification that recognized specifically the duplex structure or a small molecule TMPyP4 by pH neutralization (Xu et al. 2007).

The example of the second strategy is a forest of DNA motors immobilized on the surface, reported by Liu and his group (Fig. 8.14b) (Mao et al. 2007). Each device unit was composed of a motor part containing i-motif sequence on the upper domain and a single-stranded spacer on the lower domain. The spacers provided a low-density packing area, behaving as a container. When pH was acidified or neutralized, the packing density of motor domain could be switched between high (closed container) and low (open container) states. At open state, small molecules were released from the spacer domains, while at closed state, these molecules were included in the nanocontainer sealed on the upper domain by the densely packed DNA motor forest. Instead of on the surface, Liu and his group encapsulated nanoscale objects, gold nanoparticles, into the acidified DNA hydrogel (Cheng et al. 2009). Upon the increase of pH, the nanomotor consisting of i-motifs was extended and the gel was melted, leading to the fast release of the nanoparticles.

Although not yet performing the functions, two attractive devices for controlled trapping and release of nanocargos were constructed by the groups of Turberfield and of Gothelf and Kjems, respectively. The first is a reconfigurable tetrahedral DNA cage (Fig. 8.14c) (Goodman et al. 2008). By fueling the tetrahedral with the required complementary DNA segment, the cage was able to expand. Conversely, when the antifuel strands were added, the fuel strands were pulled away from the edge of the cage, which was contracted again. A tetrahedron with two different-length edges were also made, and they could independently change the volume of the cage. Recently, Turberfield et al. further demonstrated that the tetrahedral DNA cages could enter and survive inside living cells (Walsh et al. 2011). Together with the results in which a single molecule was encapsulated in the DNA cage, these provided the great potential for the molecular cage of DNA being operable in entrapping and performing targeted delivery of biological molecules. The second device was a three-dimensional DNA box built using the DNA origami method, which could be dynamically manipulated, reported by the group of Gothelf and Kjems, Fig. 8.14d (Andersen et al. 2009). The lid was functionalized with a dual "lock-key" system composed of DNA duplexes that included a sticky toehold for the displacement caused by the externally added "key" strands. The opening process of the DNA lid was monitored by FRET process, since two fluorophores with overlapped fluorescence-absorption spectra were inserted into adjacent positions of the box.

8.4.5 Responsive Surface

Most of the functions of DNA mechanical devices are studied in solution. However, if the devices are immobilized on solid surface, it will be an interesting question whether the mechanical motion of the devices can be transformed into the switchable surface properties. Liu and Zhou et al. actuated reversibly an array of gold surface-immobilized DNA nanomotors by switching the solution between slightly acidic and basic pH, resulting in the conformation change between an

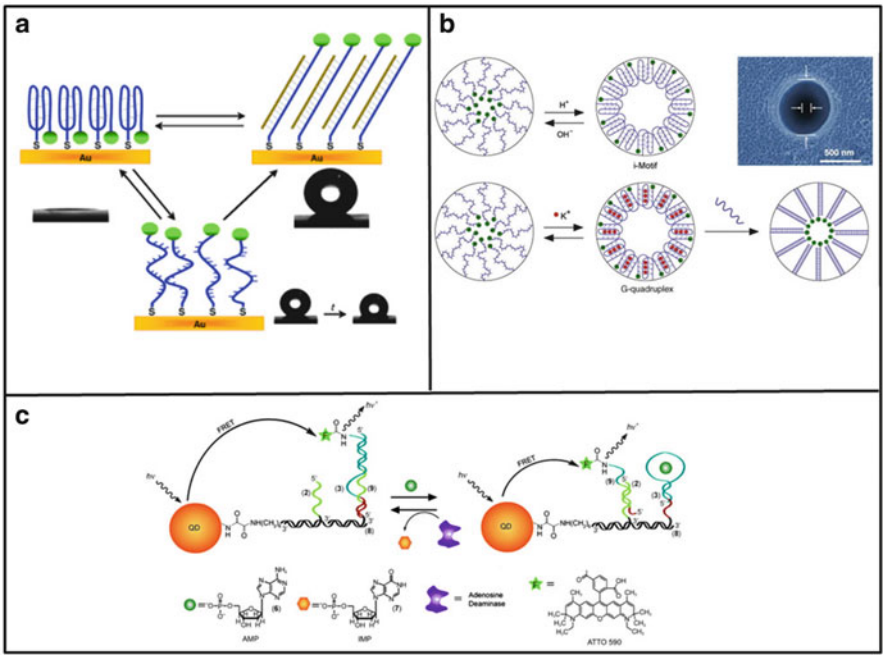

Fig. 8.15 Surface tailored by DNA mechanical devices. (**a**) A responsive surface switched between stable superhydrophilic, metastable superhydrophobic, and stable superhydrophobic states by complementary nucleic strand/pH resulting in DNA motif change [reprinted with permission from John Wiley & Sons, Inc. (Wang et al. 2007), copyright 2007]. (**b**) Nucleic acid machines immobilized inside of etched nanopores. Ion permeability is allowed by either pH-induced unfolding of i-motif (*upper*) or extending of G-quadruplex by removal of K^+. The addition of complementary DNA renders the nanopores into K^+-unresponsive state by forming the duplex (*bottom*). SEM image of a nanopore without immobilized DNA (*right upper*) [reprinted from Current Opinion in Biotechnology, 21, Teller C., Willner, I. Functional nucleic acid nanostructures and DNA machines, 376–391, copyright (2010), adapted with permission from Elsevier]. (**c**) Switchable translocation of a fluorophore-labeled nucleic acid on a DNA track immobilized on a CdSe/ZnS quantum dot, resulting in the change of fluorescence resonance energy transfer [reprinted with permission from John Wiley & Sons, Inc. (Elbaz et al. 2009c), copyright 2009]

i-motif and duplex structure (Liu et al. 2006). One end further away from the surface of the DNA was labeled with a fluorophore. By the mechanical work of the DNA, the fluorophore was lifted up and brought down toward the gold surface, and the motion was transduced into an optical "on–off" nanoswitch of the surface patterns.

Liu and his group adapted this concept to switch the surface wettability (Fig. 8.15a) (Wang et al. 2007). The single-stranded DNA containing i-motif sequence was immobilized on the gold surface through Au-S bond on one end of the strand, while the other end of the DNA was functionalized with a hydrophobic Bodipy-type fluorophore. At low pH, DNA motors were folded into the closed

states and the hydrophilic phosphate backbones of the strands were exposed on the surface, leading to a hydrophilic surface. When the pH was neutralized, the i-motif structures were unfolded into single strands and the hydrophobic groups migrated to the top of the surface, increasing the hydrophobicity of the surface. However, the surface gave a metastable hydrophobic state, observed by a dynamic spreading process of the water droplet, due to the relatively loose arrangement of flexible single-stranded DNA resulting in entropy-driven molecular rearrangement of DNA motors at the interface. The addition of complementary DNA strands formed the closed packed duplex DNA structures on the surface, and the spreading process was prevented. In this case, the surface was in a stable hydrophobic state. The surface wettability was switched back to the hydrophilic state by a slow DNA dehybridization and i-motif refolding process.

The functions of DNA mechanical devices were also used for regulation of the access of molecules to the surface, e.g., controlling ion permeability through pores of a membrane (Fig. 8.15b). i-motif contained strands were attached to the interior of the conical pores, with diameter of 50–500 nm, produced by etching of a polymer membrane. When pH of the solution was basic, the DNA strands existed in a random-coiled state, allowing the ions diffuse freely to and from the underlying electrode through the nanopores. The decrease of pH to an acidic value resulted in the folding of strands into the compact i-motif quadruplex structure, blocking the diffusion of the ions through the pores and thus switching off the ion current (Xia et al. 2008). Increasing the pH again allowed "switching on" of the ion current through the nanopores again. Similarly, guanine-rich strands were also attached to the interior of the nanopores, and K^+-simulated organization of G-quadruplexes was used to control the opening and closing of the pores, thus switching on and off the ion permeability (Hou et al. 2009).

Besides the pore surface, a DNA machine with switchable motion was immobilized on the surface of a quantum dot by the group of Willner (Fig. 8.15c) (Elbaz et al. 2009c). The motional element included the anti-adenosine monophosphate (AMP) sequence-specific aptamer and labeled with a fluorophore. Sequential addition of AMP and its hydrolysis enzyme (adenosine deaminase) resulted in the reversible translocation of the moving strand along the track, leading to the change of FRET efficiency between the fluorophore and the quantum dot surface.

8.5 Prospective

The unique self-assembly and stimuli-responsive features of the nucleic acid strands make DNA a highly exciting material for molecular machines. The complexity of the devices has been enhanced from single-molecular motors to, e.g., an autonomous multi-leg spider, and the applications have been expanded from sensing to autonomous creation of new compounds and even the programmed assembly of nano-objects. However, compared with natural molecular machines and looking

toward the future, the current development cannot disregard the fact that DNA machines are still preliminary, and whatever the constructs and the functions are, they are at the conceptual stage. For example, a dream of DNA nanotechnology is to fabricate a robot. The construct and the intelligence of behavior of this robot are obviously far ahead of the current various DNA "robots" which are just encoded with very simple programs. There still remain many challenges confronting the field. The first is the productivity scale of DNA strands, which limits the mechanical devices especially with enhanced complexity, e.g., DNA origami-based devices, in the laboratory-scale construction and operation. The second is that the current DNA devices are still very primitive, including the fueling system, the automation, the cooperativity between DNA machinery components, and the reliability and the reusability of the machinery devices. The third originates from the chemical structure of the DNA backbones, which leads to the incompatibility of DNA with a lot of species and environments. An example is the difficulty of operations in organic solution. The fourth is the inefficient incorporation of DNA machines into the solid surface, together with the difficulty of imaging the motions on the surface with high resolution. Although researchers have succeeded in immobilization of single-molecule nanomotor onto the surface to regulate the surface functions, the difficulties in complex nanomachines are predictable, regarding the characterization and the operation. These are just some issues of the predicted challenges.

It's impossible to predict the progress within the area of mechanical DNA devices. But the enhancement of complexity of mechanical devices and focus on the machinery functions will be some of the directions. Examples are more diverse environments, smarter system with fast and synchronous functions of sensing, responding, analyzing, memory, feedback, instructing, or DNA machine-made DNA machines. The exciting progress of the devices, witnessed in the past decade, anticipates the fascinating development in this field, and it can be believed that DNA mechanical devices will play a very significant role in future nanoscience and nanotechnology.

References

Ackermann D, Schmidt TL, Hannam JS, Purohit CS, Heckel A, Famulok M (2010) A double-stranded DNA rotaxane. Nat Nanotechnol 5:436–442

Andersen ES, Dong M, Nielsen MM, Jahn K, Subramani R, Mamdouh W, Golas MM, Sander B, Stark H, Oliveira CLP, Pedersen JS, Birkedal V, Besenbacher F, Gothelf KV, Kjems J (2009) Self-assembly of a nanoscale DNA box with a controllable lid. Nature 459:73–76

Asanuma H, Liang X, Nishioka H, Matsunaga D, Liu M, Komiyama M (2007) Synthesis of azobenzene-tethered DNA for reversible photo-regulation of DNA functions: hybridization and transcription. Nat Protoc 2:203–212

Bath J, Green SJ, Turberfield AJ (2005) A free-running DNA motor powered by a nicking enzyme. Angew Chem Int Ed Engl 44:4358–4361

Beharry AA, Woolley GA (2011) Azobenzene photoswitches for biomolecules. Chem Soc Rev 40:4422–4437

Beissenhirtz MK, Willner I (2006) DNA-based machines. Org Biomol Chem 4:3392–3401

Berna J, Leigh DA, Lubomska M, Mendoza SM, Perez EM, Rudolf P, Teobaldi G, Zerbetto F (2005) Macroscopic transport by synthetic molecular machines. Nat Mater 4:704–710
Buranachai C, McKinney SA, Ha T (2006) Single molecule nanometronome. Nano Lett 6:496–500
Champin B, Mobian P, Sauvage JP (2007) Transition metal complexes as molecular machine prototypes. Chem Soc Rev 36:358–366
Chen Y, Lee SH, Mao C (2004a) A DNA nanomachine based on a duplex-triplex transition. Angew Chem Int Ed Engl 43:5335–5338
Chen Y, Wang MS, Mao CD (2004b) An autonomous DNA nanomotor powered by a DNA enzyme. Angew Chem Int Ed Engl 43:3554–3557
Cheng EJ, Xing YZ, Chen P, Yang Y, Sun YW, Zhou DJ, Xu LJ, Fan QH, Liu DS (2009) A pH-triggered, fast-responding DNA hydrogel. Angew Chem Int Ed Engl 48:7660–7663
Chhabra R, Sharma J, Liu Y, Yan H (2006) Addressable molecular tweezers for DNA-templated coupling reactions. Nano Lett 6:978–983
Ding B, Seeman NC (2006) Operation of a DNA robot arm inserted into a 2D DNA crystalline substrate. Science 314:1583–1585
Ding BQ, Wu H, Xu W, Zhao ZA, Liu Y, Yu HB, Yan H (2010) Interconnecting gold Islands with DNA origami nanotubes. Nano Lett 10:5065–5069
Dittmer WU, Simmel FC (2004) Transcriptional control of DNA-based nanomachines. Nano Lett 4:689–691
Dittmer WU, Reuter A, Simmel FC (2004) A DNA-based machine that can cyclically bind and release thrombin. Angew Chem Int Ed Engl 43:3550–3553
Elbaz J, Moshe M, Willner I (2009a) Coherent activation of DNA tweezers: a "SET-RESET" logic system. Angew Chem Int Ed Engl 48:3834–3837
Elbaz J, Wang ZG, Orbach R, Willner I (2009b) pH-Stimulated concurrent mechanical activation of two DNA "tweezers". A "SET-RESET" logic gate system. Nano Lett 9:4510–4514
Elbaz J, Tel-Vered R, Freeman R, Yildiz HB, Willner I (2009c) Switchable motion of DNA on solid supports. Angew Chem Int Ed Engl 48:133–137
Elbaz J, Wang ZG, Wang F, Willner I (2012) Programmed dynamic topologies in DNA catenanes. Angew Chem Int Ed Engl 51:2349–2353
Fahlman RP, Hsing M, Sporer-Tuhten CS, Sen D (2003) Duplex pinching: a structural switch suitable for contractile DNA nanoconstructions. Nano Lett 3:1073–1078
Fang L, Olson MA, Benitez D, Tkatchouk E, Goddard WA, Stoddart JF (2010) Mechanically bonded macromolecules. Chem Soc Rev 39:17–29
Fisher ME, Kolomeisky AB (2001) Simple mechanochemistry describes the dynamics of kinesin molecules. Proc Natl Acad Sci USA 98:7748–7753
Frasconi M, Tel-Vered R, Elbaz J, Willner I (2010) Electrochemically stimulated pH changes: a route to control chemical reactivity. J Am Chem Soc 132:2029–2036
Fukushima K, Vandenbos AJ, Fujiwara T (2007) Spiropyran dimer toward photo-switchable molecular machine. Chem Mater 19:644–646
Gartner ZJ, Liu DR (2001) The generality of DNA-templated synthesis as a basis for evolving non-natural small molecules. J Am Chem Soc 123:6961–6963
Goodman RP, Heilemann M, Doose S, Erben CM, Kapanidis AN, Turberfield AJ (2008) Reconfigurable, braced, three-dimensional DNA nanostructures. Nat Nanotechnol 3:93–96
Green SJ, Bath J, Turberfield AJ (2008) Coordinated chemomechanical cycles: a mechanism for autonomous molecular motion. Phys Rev Lett 101:238101
Gruenwedel DW (1994) The mercury(II) and high-salt-induced conformational B-Z transitions of Poly[d(G-m5C).d(G-m5C)] as studied by non-polarized (ultraviolet) and circularly-polarized (CD) ultraviolet spectroscopy. Eur J Biochem 219:491–496
Gruenwedel DW, Cruikshank MK (1991) Changes in poly[D(T-G).D(C-A)] chirality due to Hg (II)-Binding – circular-dichroism (CD) Studies. J Inorg Biochem 43:29–36
Gu HZ, Chao J, Xiao SJ, Seeman NC (2010) A proximity-based programmable DNA nanoscale assembly line. Nature 465:202–205

Han DR, Pal S, Liu Y, Yan H (2010) Folding and cutting DNA into reconfigurable topological nanostructures. Nat Nanotechnol 5:712–717

Han DR, Pal S, Nangreave J, Deng ZT, Liu Y, Yan H (2011) DNA origami with complex curvatures in three-dimensional space. Science 332:342–346

He Y, Liu DR (2010) Autonomous multistep organic synthesis in a single isothermal solution mediated by a DNA walker. Nat Nanotechnol 5:778–782

He Y, Liu DR (2011) A sequential strand-displacement strategy enables efficient six-step DNA-templated synthesis. J Am Chem Soc 133:9972–9975

Hou X, Guo W, Xia F, Nie FQ, Dong H, Tian Y, Wen LP, Wang L, Cao LX, Yang Y, Xue JM, Song YL, Wang YG, Liu DS, Jiang L (2009) A biomimetic potassium responsive nanochannel: G-Quadruplex DNA conformational switching in a synthetic nanopore. J Am Chem Soc 131:7800–7805

Hudson B, Vinograd J (1967) Catenated circular DNA molecules in Hela cell mitochondria. Nature 216:647–652

Jovin TM, Soumpasis DM, Mcintosh LP (1987) The transition between B-DNA and Z-DNA. Annu Rev Phys Chem 38:521–560

Kang HZ, Liu HP, Phillips JA, Cao ZH, Kim Y, Chen Y, Yang ZY, Li JW, Tan WH (2009) Single-DNA molecule nanomotor regulated by photons. Nano Lett 9:2690–2696

Kufer SK, Puchner EM, Gumpp H, Liedl T, Gaub HE (2008) Single-molecule cut-and-paste surface assembly. Science 319:594–596

Kuzuya A, Sakai Y, Yamazaki T, Xu Y, Komiyama M (2011) Nanomechanical DNA origami 'single-molecule beacons' directly imaged by atomic force microscopy. Nat Commun 2:1–8

Lee JS, Ulmann PA, Han MS, Mirkin CA (2008) A DNA-gold nanoparticle-based colorimetric competition assay for the detection of cysteine. Nano Lett 8:529–533

Li JWJ, Tan WH (2002) A single DNA molecule nanomotor. Nano Lett 2:315–318

Li D, Wieckowska A, Willner I (2008) Optical analysis of Hg^{2+} ions by oligonucleotide-gold-nanoparticle hybrids and DNA-based machines. Angew Chem Int Ed Engl 47:3927–3931

Liedl T, Olapinski M, Simmel FC (2006) A surface-bound DNA switch driven by a chemical oscillator. Angew Chem Int Ed Engl 45:5007–5010

Liu DS, Balasubramanian S (2003) A proton-fuelled DNA nanomachine. Angew Chem Int Ed Engl 42:5734–5736

Liu DS, Bruckbauer A, Abell C, Balasubramanian S, Kang DJ, Klenerman D, Zhou DJ (2006) A reversible pH-driven DNA nanoswitch array. J Am Chem Soc 128:2067–2071

Liu HJ, Xu Y, Li FY, Yang Y, Wang WX, Song YL, Liu DS (2007) Light-driven conformational switch of i-motif DNA. Angew Chem Int Ed Engl 46:2515–2517

Liu Y, Kuzuya A, Sha RJ, Guillaume J, Wang RS, Canary JW, Seeman NC (2008) Coupling across a DNA helical turn yields a hybrid DNA/organic catenane doubly tailed with functional termini. J Am Chem Soc 130:10882-+

Lund K, Manzo AJ, Dabby N, Michelotti N, Johnson-Buck A, Nangreave J, Taylor S, Pei RJ, Stojanovic MN, Walter NG, Winfree E, Yan H (2010) Molecular robots guided by prescriptive landscapes. Nature 465:206–210

Mao CD, Sun WQ, Shen ZY, Seeman NC (1999) A nanomechanical device based on the B-Z transition of DNA. Nature 397:144–146

Mao YD, Liu DS, Wang ST, Luo SN, Wang WX, Yang YL, Qi QY, Lei J (2007) Alternating-electric-field-enhanced reversible switching of DNA nanocontainers with pH. Nucleic Acids Res 35:e33

Marini M, Piantanida L, Musetti R, Bek A, Dong MD, Besenbacher F, Lazzarino M, Firrao G (2011) A revertible, autonomous, self-assembled DNA-origami nanoactuator. Nano Lett 11:5449–5454

McKee ML, Milnes PJ, Bath J, Stulz E, Turberfield AJ, O'Reilly RK (2010) Multistep DNA-templated reactions for the synthesis of functional sequence controlled oligomers. Angew Chem Int Ed Engl 49:7948–7951

Miyoshi D, Karimata H, Wang ZM, Koumoto K, Sugimoto N (2007) Artificial G-wire switch with 2,2′-bipyridine units responsive to divalent metal ions. J Am Chem Soc 129:5919–5925
Modi S, Swetha MG, Goswami D, Gupta GD, Mayor S, Krishnan Y (2009) A DNA nanomachine that maps spatial and temporal pH changes inside living cells. Nat Nanotechnol 4:325–330
Muscat RA, Bath J, Turberfield AJ (2011) A programmable molecular robot. Nano Lett 11:982–987
Ogasawara S, Maeda M (2009) Reversible photoswitching of a G-quadruplex. Angew Chem Int Ed Engl 48:6671–6674
Ogura Y, Nishimura T, Tanida J (2009) Self-contained photonically-controlled DNA tweezers. Appl Phys Express 2:025004
Omabegho T, Sha R, Seeman NC (2009) A bipedal DNA brownian motor with coordinated legs. Science 324:67–71
Qian LL, Wang Y, Zhang Z, Zhao J, Pan D, Zhang Y, Liu Q, Fan CH, Hu J, He L (2006) Analogic China map constructed by DNA. Chin Sci Bull 51:2973–2976
Rothemund PWK (2006) Folding DNA to create nanoscale shapes and patterns. Nature 440:297–302
Saha S, Stoddart JF (2007) Photo-driven molecular devices. Chem Soc Rev 36:77–92
Schmidt TL, Heckel A (2011) Construction of a structurally defined double-stranded DNA catenane. Nano Lett 11:1739–1742
Seeman NC (2010) Structural DNA nanotechnology: growing along with nano letters. Nano Lett 10:1971–1978
Sherman WB, Seeman NC (2004) A precisely controlled DNA biped walking device. Nano Lett 4:1203–1207
Shin JS, Pierce NA (2004) A synthetic DNA walker for molecular transport. J Am Chem Soc 126:10834–10835
Shlyahovsky B, Li D, Weizmann Y, Nowarski R, Kotler M, Willner I (2007) Spotlighting of cocaine by an autonomous aptamer-based machine. J Am Chem Soc 129:3814–3815
Shu WM, Liu DS, Watari M, Riener CK, Strunz T, Welland ME, Balasubramanian S, McKendry RA (2005) DNA molecular motor driven micromechanical cantilever arrays. J Am Chem Soc 127:17054–17060
Sweeney HL, Houdusse A (2010) Structural and functional insights into the myosin motor mechanism. Annu Rev Biophys 39:539–557
Tian Y, Mao CD (2004) Molecular gears: a pair of DNA circles continuously rolls against each other. J Am Chem Soc 126:11410–11411
Tian Y, He Y, Chen Y, Yin P, Mao CD (2005) Molecular devices-A DNAzyme that walks processively and autonomously along a one-dimensional track. Angew Chem Int Ed Engl 44:4355–4358
Tyagi S, Kramer FR (1996) Molecular beacons: probes that fluoresce upon hybridization. Nat Biotechnol 14:303–308
Vallee R (1993) Molecular analysis of the microtubule motor dynein. Proc Natl Acad Sci USA 90:8769–8772
van Delden RA, ter Wiel MKJ, Pollard MM, Vicario J, Koumura N, Feringa BL (2005) Unidirectional molecular motor on a gold surface. Nature 437:1337–1340
van den Heuvel MGL, Dekker C (2007) Motor proteins at work for nanotechnology. Science 317:333–336
Venkataraman S, Dirks RM, Rothemund PWK, Winfree E, Pierce NA (2007) An autonomous polymerization motor powered by DNA hybridization. Nat Nanotechnol 2:490–494
von Delius M, Geertsema EM, Leigh DA (2010) A synthetic small molecule that can walk down a track. Nat Chem 2:96–101
Walsh AS, Yin HF, Erben CM, Wood MJA, Turberfield AJ (2011) DNA cage delivery to mammalian cells. ACS Nano 5:5427–5432

Wang ST, Liu HJ, Liu DS, Ma XY, Fang XH, Jiang L (2007) Enthalpy-driven three-state switching of a superhydrophilic/superhydrophobic surface. Angew Chem Int Ed Engl 46:3915–3917

Wang XL, Huang J, Zhou YY, Yan SY, Weng XC, Wu XJ, Deng MG, Zhou XA (2010a) Conformational switching of G-quadruplex DNA by photoregulation. Angew Chem Int Ed Engl 49:5305–5309

Wang ZG, Elbaz J, Remacle F, Levine RD, Willner I (2010b) All-DNA finite-state automata with finite memory. Proc Natl Acad Sci USA 107:21996–22001

Wang ZG, Elbaz J, Willner I (2011) DNA machines: bipedal walker and stepper. Nano Lett 11:304–309

Wang ZG, Elbaz J, Willner I (2012) A dynamically programmed DNA transporter. Angew Chem Int Ed Engl 51(18):4322–4326

Weizmann Y, Beissenhirtz MK, Cheglakov Z, Nowarski R, Kotler M, Willner I (2006) A virus spotlighted by an autonomous DNA machine. Angew Chem Int Ed Engl 45:7384–7388

Wickham SFJ, Endo M, Katsuda Y, Hidaka K, Bath J, Sugiyama H, Turberfield AJ (2011) Direct observation of stepwise movement of a synthetic molecular transporter. Nat Nanotechnol 6:166–169

Xia F, Guo W, Mao YD, Hou X, Xue JM, Xia HW, Wang L, Song YL, Ji H, Qi OY, Wang YG, Jiang L (2008) Gating of single synthetic nanopores by proton-driven DNA molecular motors. J Am Chem Soc 130:8345–8350

Xu Y, Hirao Y, Nishimura Y, Sugiyama H (2007) I-motif and quadruplex-based device that can control a protein release or bind and release small molecule to influence biological processes. Bioorg Med Chem 15:1275–1279

Yan H, Zhang XP, Shen ZY, Seeman NC (2002) A robust DNA mechanical device controlled by hybridization topology. Nature 415:62–65

Yang XP, Vologodskii AV, Liu B, Kemper B, Seeman NC (1998) Torsional control of double-stranded DNA branch migration. Biopolymers 45:69–83

Yin P, Yan H, Daniell XG, Turberfield AJ, Reif JH (2004) A unidirectional DNA walker that moves autonomously along a track. Angew Chem Int Ed Engl 43:4906–4911

Yin P, Choi HMT, Calvert CR, Pierce NA (2008) Programming biomolecular self-assembly pathways. Nature 451:318–322

Yuan Q, Zhang YF, Chen Y, Wang RW, Du CL, Yasun E, Tan WH (2011) Using silver nanowire antennas to enhance the conversion efficiency of photoresponsive DNA nanomotors. Proc Natl Acad Sci USA 108:9331–9336

Yurke B, Turberfield AJ, Mills AP, Simmel FC, Neumann JL (2000) A DNA-fuelled molecular machine made of DNA. Nature 406:605–608

Zhang DY, Seelig G (2011) Dynamic DNA nanotechnology using strand-displacement reactions. Nat Chem 3:103–113

Zhong H, Seeman NC (2006) RNA used to control a DNA rotary nanomachine. Nano Lett 6:2899–2903

Zhou MG, Liang XG, Mochizuki T, Asanuma H (2010) A light-driven DNA nanomachine for the efficient photoswitching of RNA digestion. Angew Chem Int Ed Engl 49:2167–2170

Zhu CF, Wen YQ, Li D, Wang LH, Song SP, Fan CH, Willner I (2009) Inhibition of the In vitro replication of DNA by an aptamer-protein complex in an autonomous DNA machine. Chemistry 15:11898–11903

Part V
Therapeutic Nucleic Acid

Chapter 9
Nano-encapsulation of Oligonucleotides for Therapeutic Use

Eveline Edith Salcher and Ernst Wagner

Abstract Oligonucleotides got more and more into focus for therapeutic purposes. Administration of such molecules is a challenge, as surviving the bloodstream passage and passing the barrier cell membrane are almost insuperable tasks. Although successful clinical studies have been conducted with naked oligonucleotides, such as antisense agents or siRNA, poor cellular uptake and low cellular persistence reveal the need for adequate carriers.

Delivery of the undamaged oligonucleotide to its site of action has been explored with manifold systems. However, these systems all have one aim: protection of the cargo during the bloodstream passage, facilitation of cellular uptake, and, finally, payload release into the cytosol. Size plays also an important role for the physiological pathway, as particles, if their size is suboptimal, may either clog blood vessels, be removed by the reticuloendothelial system, or undergo rapid renal clearance.

Therefore, research in this field takes advantage of natural nucleic acid encapsulation systems (viruses) or aims at mimicking virus-like features with nonviral carriers. This review focuses on the principles of oligonucleotide encapsulation or packaging with different classes of carrier molecules towards therapeutic use.

Contents

E.E. Salcher (✉) • E. Wagner
Pharmaceutical Biotechnology, Ludwig Maximilians University Munich, Munich, Germany

Center for System-Based Drug Research, Ludwig Maximilians University Munich, Munich, Germany

Center for Nanoscience (CeNS), Ludwig Maximilians University Munich, Munich, Germany

Nanosystems Initiative Munich (NIM), Munich, Germany
e-mail: e.salcher@yahoo.de

J. KJEMS et al. (eds.), *Nucleic Acid Nanotechnology*, Nucleic Acids and Molecular Biology 29, DOI 10.1007/978-3-642-38815-6_9,

9.1 Introduction

Inaccurate processes on cellular level are the origin of various severe diseases. Depending on the nature of the genetic disorder, two main therapeutic strategies can be pursued. One possibility to adjust the life machinery is the replacement of missing or defective genes by introduction of correspondingly encoding DNA into cells.

Alternatively, inaccurate or overexpressed genes with pathological consequences can be deactivated. This latter strategy has an interesting history. More than 30 years ago, the first steps were made towards knocking down genes by the antisense approach using single-stranded oligonucleotides (Zamecnik and Stephenson 1978), but only 13 years ago, the RNA interference pathway was discovered (Fire et al. 1998). Silencing of target genes may take place by small-interfering RNA (siRNA)-mediated mRNA degradation (Hannon 2002; Meister and Tuschl 2004; Zamore and Haley 2005).

Two main possibilities of utilizing the RNAi pathway for therapeutic purposes exist. One is based on the discovery that extracellularly applied artificial double-stranded siRNAs, 20–24 nucleotides long, as soon as taken up into the cell, can enter the RNAi pathway through cytosolic RISC incorporation (Elbashir et al. 2001). The other approach is based on plasmid-based intranuclear expression of short-hairpin RNA (shRNA) (Brummelkamp et al. 2002), which is processed by the cell after entering the cytosol into the corresponding siRNA. This method leads to stable gene silencing, while artificial siRNA attains only transient knockdown, as it is diluted and lost during cell division.

Another naturally occurring class of double-stranded oligonucleotides, namely, microRNAs (miRNAs), utilize RNA interference for regulation of many targets at the same time (Bartel 2004). Deregulation of microRNA expression in tumors (overexpression of oncomiRs, loss of expression of suppressor miRs) suggests their role as either therapeutic targets or therapeutic agents (Lu et al. 2005; Gregory and Shiekhattar 2005).

However, before acting on intracellular level, oligonucleotides have to reach the target tissue and enter the cells, which is a challenging task. Systemic application involves several risks for “naked” oligonucleotides, such as enzymatic degradation during blood circulation and rapid renal clearance. Another challenge is reaching the target tissue and passing the barrier cell membrane before reaching the site of

action. So as to overcome these challenges, accurate protection of the nucleotide cargo by chemical modification and/or packaging into viral or nonviral nanocarriers is mandatory and has been widely studied during the last decades.

This review presents the latest developments of oligonucleotide encapsulation and packaging methods and their potential for therapeutic use.

9.2 Nucleic Acid Encapsulation and Packaging Methods

Reaching the target tissue and entering cells without loss of activity is, as already mentioned, an insuperable challenge for systemically applied naked oligonucleotides. The size of such particles is a very important issue. Large particles may get stuck in tight blood vessels and lead to tissue hypoxia or even death. Capture and inactivation by the reticuloendothelial system is another undesired outcome. If nanoparticles are too small, like naked oligonucleotides, they may be subjected to rapid renal clearance without having the possibility of systemic circulation sufficient to reach the target tissue.

As the natural ideal nucleic acid carriers, namely, viruses, have a size between 20 and 300 nm, the same range is valid for particles formed with nonviral vectors and the nucleic acid. Carriers for plasmid DNA-based gene delivery have been evaluated for decades now, but unfortunately the requirements for the delivery of oligonucleotides or siRNA are not exactly the same (Scholz and Wagner 2012; Kwok and Hart 2011). Still, since the discovery of RNA interference in *C. elegans* (Fire et al. 1998) and in mammalian cells (Elbashir et al. 2001), research in this field has tremendously advanced towards therapeutic application in humans.

Already in the 1990s, antisense oligonucleotides were developed for clinical application, and siRNA for local treatment of CMV retinitis was successfully tested in clinical trials (Azad et al. 1993; Crooke 1998; Grillone and Lanz 2001). However, short in vivo half-life and transient transfection hamper the use of naked oligonucleotides. Therefore, packaging methods and delivery strategies have been developed in order to overcome these drawbacks.

9.3 Viral Vectors for Oligonucleotide Delivery

Viruses are natural carrier systems for the delivery of any kind of nucleic acid optimized in host interactions over very long time. They are programmed by nature to reach the target tissue, enter cells, and set free the nucleic acid for their own replication. Therefore, it seems rightly reasonable that these highly specific natural shuttles, due to their ability to adapt to changing environmental conditions, found application as nucleic acid vectors with very promising therapeutic potential. Different viral vector systems have been evaluated during the past years for oligonucleotide delivery. Replication-defective adeno-associated viruses (AAV)

packaging their genome into pure protein capsids, and also lentiviruses (LV), a subclass of retroviruses, containing the nucleic acid/protein capsid within a lipid envelope, showed high efficiency combined with the best safety profiles (Couto and High 2010; Sliva and Schnierle 2010). These vectors are able of transducing both dividing and nondividing cells, thus allowing high gene transfer rates.

For persistent intracellular siRNA activity, a DNA-based method for sustained intracellular siRNA expression was developed (Brummelkamp et al. 2002; Paddison et al. 2002). Plasmid DNA cassettes encoding for the corresponding shRNA are transcribed in the nucleus and further processed in the cytosol, leading to sustained gene knockdown. Thus, in a further step, such shRNA-encoding cassettes were encapsulated in viral vectors for targeted delivery. Beverly Davidson used adeno-associated viruses (AAV) for therapeutic use by shRNA expression (Xia et al. 2004). This strategy was further pursued and evaluated in mouse models, aiming at treatment of various diseases such as prion disease or Huntington's disease, viral infections like HBV, HCV, and HIV (Couto and High 2010). AAV were also used for the delivery of shRNA for eradication of prostate cancer xenografts (Sun et al. 2010).

Furthermore, Anderson et al. (2007) combined three anti-HIV RNAs in one lentiviral vector. In a xenograft mouse model, by the simultaneous delivery of shRNA, TAR decoy, and anti-CCR5 ribozyme into human CD34+ cells, T cells with maintained functionality but HIV resistance were generated. This threefold combination vector is used at the moment in a clinical trial for AIDS/lymphoma patients (DiGiusto et al. 2010).

Viral vectors can also be used for substituting downregulated suppressor miRNAs in tumors. Kota et al. (2009) have shown that systemic administration of an AAV vector expressing the suppressed miRNA in a mouse liver cancer model dramatically reduced tumor progression.

Although the results achieved with viral vectors in RNAi are very promising, this application for therapeutic purposes is still accompanied by a few challenges. shRNA expressed by viral vectors, for instance, can induce immune responses such as interferon (IFN) induction (Kenworthy et al. 2009; Fish and Kruithof 2004) or toxicity can occur due to oversaturation of the RNAi pathway (Grimm et al. 2006). Another significant drawback is the safety issues related to viral vectors, such as their potential of immune response induction or the risk of insertion mutagenesis. Furthermore, low loading capacity and difficult large-scale production may limit therapeutic application (Tomanin and Scarpa 2004; Devroe and Silver 2004).

9.4 Synthetic Carriers for Oligonucleotide Delivery

The research work dedicated to development and optimization of nonviral nucleic acid formulations is motivated out of the hope for a virus-like high transfection efficiency with minimal or no side effects. Viral features, though, can be considered and imitated, as viruses represent natural examples of most effective carrier system.

Several classes of synthetic carriers have evolved out of this aim. Like in viruses, the formulation of siRNA or other oligonucleotides may follow significantly different rules depending on the chemical (lipid-free or lipid-based) composition of the carrier.

In the following sections, different classes of synthetic formulations used for oligonucleotide encapsulation for therapeutic purpose will be described.

9.5 Natural Cationic Polymers

Natural cationic polymers such as chitosan, atelocollagen, or protamine have the advantage of being biodegradable and nontoxic. Packaging of the oligonucleotide occurs via electrostatic interactions between the positively charged polymer and the negatively charged backbone of the cargo, thus forming nano-sized polyplexes, usually bearing a positive surface charge. Furthermore, encapsulation of siRNA has already been shown to enable biocompatible and efficient gene silencing.

Atelocollagen-siRNA polyplexes, for instance, were used for tumor growth inhibition in a germ cell tumor xenograft mouse model (Minakuchi et al. 2004). Also, vascular endothelial growth factor inhibition achieved with such polyplexes suppressed tumor angiogenesis and growth (Takei et al. 2004).

The natural, arginine-rich cationic polypeptide protamine has the ability for efficient condensation of nucleic acids. Complexes consisting of a cell-penetrating peptide derived from natural arginine-rich protamine and siRNA suppress tumor growth in a mouse hepatocarcinoma model (Choi et al. 2010) without induction of immunostimulatory effects.

Nanoparticles formed with the natural cationic polysaccharide chitosan, for instance, were shown to mediate effective gene silencing after either intravenous (Pille et al. 2006) or intraperitoneal (Howard et al. 2009) administration while at the same time displaying favorable safety profiles.

Cyclodextrin-based oligocations have also proven their capability of acting as biocompatible and efficient nucleic acid carriers. Targeted siRNA-cyclodextrin nanoparticles, with transferrin as targeting ligand and polyethyleneglycol (PEG) for shielding, have been used in mouse models for treatment of metastatic Ewing's sarcoma (Hu-Lieskovan et al. 2005). Such nanoparticles were also intravenously administered to patients with solid tumors in a clinical trial (Davis et al. 2010), achieving specific gene inhibition.

9.6 Synthetic Cationic Polymers

A synthetic polymer-based backbone offers the possibility for a wide spectrum of modifications with regard to optimization for a given cargo. One of the leading synthetic polycation for pDNA delivery is the "gold standard" polyethylenimine

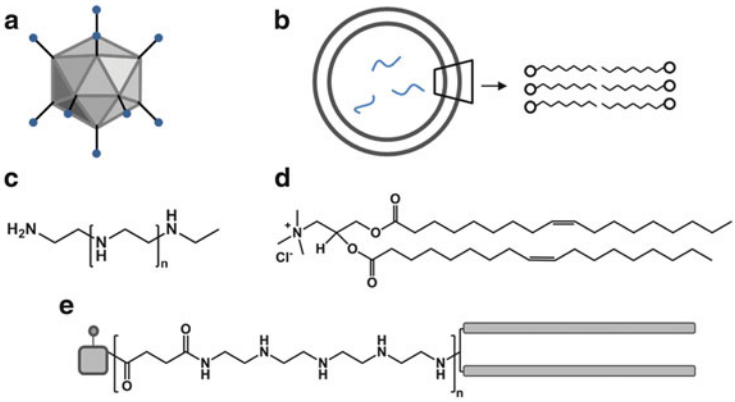

Fig. 9.1 Examples of carriers used for oligonucleotide encapsulation. (**a**) Adenovirus. (**b**) Liposome consisting of a bilayer membrane with the lipid tails clustered together. (**c**) Linear PEI. (**d**) DOTAP. (**e**) Exemplified structure of sequence-defined polymers consisting of a cross-linking domain, a succinoyl tetraethylene pentamine unit and a bis (fatty acid) tail

(PEI) (Fig. 9.1c). PEI has outstanding features like excellent interaction with nucleic acids, pronounced endosomal buffering capacity, which is important for the endosomal escape, and high accessibility for modification (Boussif et al. 1995; Akinc et al. 2005). Therefore, it seemed reasonable that PEI, either linear or branched, might be useful for oligonucleotide and siRNA delivery. In order to avoid toxicity after systemic administration (Moghimi et al. 2005), various modifications of PEI were investigated, such as PEGylation (modification with polyethylene glycol; PEG) (Tsai et al. 2011; Beyerle et al. 2011), introduction of targeting moieties or lytic domains (Kwon et al. 2008), deacylation (Thomas et al. 2005), alkylation (Fortune et al. 2011), or succinoylation (Zintchenko et al. 2008). PEI modified with stearic acid was used as cationic counterpart for the formation of siRNA polyplexes for induction of tumor apoptosis in a melanoma cell line (Alshamsan et al. 2010).

Schaffert et al. (2011b) combined different domains in one carrier, each for fulfilling another task, for delivery of the apoptosis, and for immune response inducing double-stranded RNA polyinosinic:polycytidylic acid, poly(I:C). Branched 25 kDa PEI was modified with PEG as a shielding domain, the tumor cell targeting moiety epidermal growth factor (EGF), and melittin for enhancing endosomal escape. The group could show growth retardation of human A431 xenograft tumors in mice.

The polypeptide polylysine (PLL) was also used as a cationic polymer for siRNA delivery. PLL on its own does not mediate efficient transfection and additionally has been shown by Symonds et al. to induce apoptosis in three different human cell lines (Symonds et al. 2005). Therefore, it was modified by Meyer et al. with different moieties, each responsible for facilitating a step in the delivery pathway, all together resulting in a very efficient delivery construct (Meyer et al. 2008, 2009).

9.7 Precise and Sequence-Defined Synthetic Carriers

Most of the polymers mentioned above and also others developed up to now have a significant drawback, which is polydispersity of the carrier. This negative feature hampers precise conclusions on structure–activity relationships, as the efficiency or also toxic effects cannot be traced back to one single compound. Also, large-scale GMP production requires identical reproducible batches; polydispersity impedes achieving this aim.

Development of dendritic polymers was a step towards solving this drawback. Different synthetic strategies enable the development of branched three-dimensional molecules with a well-defined structure and a narrow polydispersity range. The options for modification and improvement are very broad and have been widely investigated for gene delivery. Dendritic gene carriers such as polyamidoamine (PAMAM), polypropylenimine (PPI), or dendritic polylysine (PLL) with different surface and internal modifications have been investigated for delivery of antisense nucleotides, siRNA, and DNAzymes. A more detailed overview is given in Ravina et al. (2010).

In contrast to polymers, peptides designed for oligonucleotide and siRNA delivery (Andaloussi et al. 2011; Ezzat et al. 2011; Leng and Mixson 2005) benefit from precise sequence-defined assembly by solid-phase-supported synthesis (SPS). Hartmann and Börner took first advantage of this methodology for the generation of precise, sequence-defined poly(amidoamines) (Hartmann et al. 2006). These compounds were shown to efficiently condense pDNA (Hartmann et al. 2008).

Schaffert et al. (2011a) further developed this strategy by the generation of precise cationic oligo(aminoethane)-based building blocks suitable for SPS, thus enabling fast and parallel synthesis of structural variations. The oligoamino acid building blocks were designed to contain the 1,2-diaminoethane motif (Wagner 2012) which is part of a series of very effective polycationic carriers such as PEI or related degradable carriers (Miyata et al. 2012). In a subsequent publication, an excerpt was given over selected compounds out of a library of more than 300 structures with differing topologies and containing activity-enhancing moieties such as cysteines or fatty acids (Fig. 9.1e). These precise oligomers did not only show efficient transfection for pDNA, reaching levels equivalent to PEI, but also knockdown of the target gene down to approximately 10 % with very good maintenance of cell viability and low in vivo cytotoxicity (Schaffert et al. 2011c). Structure–activity relationships of these carriers with siRNA were further evaluated in vitro and in vivo (Frohlich et al. 2012). Apart from linear topologies, also branched structures such as four-arms and the influence of various different building blocks were tested (Salcher et al. 2012). Also, novel constructs generated by SPS containing of PEG moieties and targeting ligands such as folic acid could efficiently complex and deliver siRNA and knock down the target genes (Dohmen et al. 2012; Martin et al. 2012).

9.8 Cationic Lipids and Liposomes

Synthetic lipids containing a polar head group and a lipid tail have the ability to form so-called liposomes (Fig. 9.1b). Hydrophilic structures like oligonucleotides can be encapsulated in the aqueous core of such liposomes. Encapsulation may take advantage of inclusion of cationic lipids in the bilayer. Electrostatic interactions between the cationic lipids and the negatively charged nucleic acid strongly enhance the encapsulation efficiency. Alternatively, cationic liposomes may also form complexes (lipoplexes) with nucleic acid without encapsulation into the interior of lipid bilayer membranes. In both types of the formed particles, the lipidic structures can provide oligonucleotide cargo protection after systemic delivery. Moreover, a crucial advantage is the interaction of the cationic lipid with anionic lipids in the cellular and endosomal membrane, thus facilitating cell entry and endosomal escape as basis for cargo release into the cytosol.

The cationic lipid DOTMA (*N*-[1-(2,3-Dioleyloxy)propyl]-*N,N,N*-trimethyl-ammoniumchlorid chloride) was the first synthetic lipid used for gene delivery to mammalian cells and was presented in 1989 (Felgner and Ringold 1989), followed by the delivery of antisense oligonucleotides and ribozymes (Akhtar et al. 2000; Hughes et al. 2001). Since then, these promising vectors were further improved and evaluated for oligonucleotide delivery. The cationic lipid DOTAP (Fig. 9.1d), for instance, was used for siRNA encapsulation and subsequent melanoma inhibition (Tran et al. 2008).

Cationic lipids were also commercialized, such as Lipofectamine 2000 (Invitrogen) and i-FECT (Neuromics), and widely used for siRNA encapsulation and transfection (Yokota et al. 2007; Kumar et al. 2006). Additionally, Lipofectamine was used for inhibiting HIV-I expression by transfection of encapsulated locked nucleic acid (LNA)-modified antisense oligonucleotides and DNAzymes (Jakobsen et al. 2007).

Particle stability is also a crucial issue concerning systemic delivery. Hence, stable nucleic acid lipid particles (SNALPs) got more and more into focus. SNALPs are PEG-lipid-coated liposomes consisting of different cationic and fusogenic lipids. The coating provides particle stability during formulation and also hampers undesired interactions with blood components.

In vivo studies conducted by Morrissey et al. (2005) showed inhibition of HBV replication by the administration of anti-HBV siRNA-SNALP complexes. Furthermore, systemic delivery of siRNA-SNALP formulation targeting apolipoprotein B (ApoB) in nonhuman primates led to efficient protein reduction lasting for 11 days after injection (Zimmermann et al. 2006; Frank-Kamenetsky et al. 2008). The SNALP formulation contained the lipids 3-*N*-[(methoxypoly(ethylene glycol)) carbamoyl]-1,2-dimyristyloxy-propylamine (PEG-C-DMA), 1,2-dilinoleyloxy-*N*, *N*-dimethyl-3-aminopropane (DLinDMA), and 1,2-distearoyl-sn-glycero-3-phosphocholine (DSPC) and cholesterol at specified ratios.

Highly effective guinea pig postexposure protection from the lethal Zaire Ebola virus was shown by treatment with SNALP-encapsulated siRNA (Geisbert

et al. 2006). In a subsequent study, a combination of SNALP-embedded siRNAs targeting the expression of three viral proteins was used for preventing macaques from lethal hemorrhagic fever induced by the Ebola virus (Geisbert et al. 2010). Due to their high efficiency and positive safety profile, SNALPs are currently being evaluated in clinical trials (Burnett and Rossi 2012).

Semple et al. used the ionizable cationic lipid 1,2-dilinoleyloxy-3-dimethylaminopropane (DLinDMA) as a base substance for the design of a library of 1,200 lipid nanoparticle compounds. These were screened for siRNA delivery, and the best performer was used for SNALP formulation and characterization. Gene silencing was tested in rodents and nonhuman primates with a successful outcome at low-dose application (Semple et al. 2010).

PEGylation of cationic lipoplexes (Sonoke et al. 2008) leads to increasing plasma concentration of the lipoplex and also to a higher accumulation in tumor. However, PEGylation also hampers cellular uptake and endosomal escape. Hatakeyama and colleagues therefore introduced between PEG and their multifunctional envelope-type nano-device (MEND) an enzymatically cleavable bond which should release the PEG moiety and thus facilitate cellular uptake. The molecule was further modified with the pH-sensitive fusogenic peptide GALA for enhanced endosomal escape, and encapsulated siRNA showed efficient knockdown after intratumoral delivery compared to unmodified MEND (Hatakeyama et al. 2009).

Toxicity, though, is an issue with cationic lipid particles, as has been reported both in vitro and in vivo (Ma et al. 2005; Lv et al. 2006; Akhtar and Benter 2007). The use of neutral lipids for encapsulation and delivery of siRNA should help to avoid toxicity associated with positively charged polymers. Peer et al. (2008) developed liposomes (neutral) coated with hyaluronan for stabilization and covalently attached monoclonal antibody on the surface. Condensed CyD1-siRNA was loaded into these particles, and efficient gene silencing in an intestinal inflammation murine model after IV application could be shown. In another study, siRNA targeting oncoprotein EphA2 encapsulated into neutral liposome 1,2-dioleoyl-sn-glycero-3-phosphatidylcholine (DOPC) (Landen et al. 2005) led to inhibited tumor growth in mice bearing ovarian tumors.

In order to circumvent undesired side effects caused by synthetic lipid structures, natural lipid analogs such as cardiolipin were evaluated for siRNA delivery (Chien et al. 2005; Pal et al. 2005).

A large library of lipid-like materials, so-called lipidoids, was developed and tested for the ability to transfect siRNA in vitro (Akinc et al. 2008), thus finding a leading structure for in vivo formulations. Further studies with this leading structure encapsulating siRNA showed efficient and sustained gene silencing in lung and liver targets in mice, rats, and cynomolgus monkeys (Akinc et al. 2008; Frank-Kamenetsky et al. 2008; Epiphanio et al. 2008).

Saw and colleagues loaded oligodeoxynucleotides complexed with cell-penetrating peptide (CPP) into CPP surface-modified liposomes (anionic) for successfully sensitizing glioblastoma cells to the effects of chemotherapeutic agent paclitaxel (Saw et al. 2010).

Another class of lipid-based vectors are solid lipid nanoparticles (SLN) consisting of natural or synthesized lipids, resulting in biocompatible and biodegradable lipid systems (zur Muhlen et al. 1998) which were primarily used for gene delivery (del Pozo-Rodriguez et al. 2007; Pan et al. 2009; Choi et al. 2008). SLN were also used for encapsulation of anti-microRNA oligonucleotides (AMO) in order to decrease human lung cancer cell functions related to microRNA-21 (Shi et al. 2012).

9.9 Conclusion and Prospects

Oligonucleotides possess a great therapeutic potential, as their gene sequence specificity can be exploited for finding the best strategy for disease treatment at its genetic origin. Delivery of oligonucleotides for therapeutic purposes has made vast progress during the last decades. Different strategies have been evaluated, all pursuing one aim—treating humans suffering of severe disorders. Nevertheless, appropriated shuttles have to be found for target cell transfection. Suitable encapsulation protects the cargo during blood circulation, mediates cellular uptake, and, depending of the payload nature, can lead to a sustained effect on the target gene.

Various encapsulation methods offer several options, all still bearing advantages but also drawbacks, though. Viruses, for instance, are the perfect nucleic acid carriers designed by nature. Thus, their outstanding properties concerning cargo protection and delivery were widely exploited for therapeutic purposes. Nevertheless, despite the highly promising results achieved with viral vectors, safety issues still hamper establishment as therapeutic agents. Therefore, nonviral oligonucleotide encapsulation methods and delivery strategies are getting more and more into focus. Either synthetic or natural polymers, cationic or neutral lipids have been evaluated for their therapeutic potential. The type of delivery system also has to be well chosen, though, as cationic lipids and polymers may have an impact on siRNA-caused immune stimulation and undesired off-target effects (Akhtar and Benter 2007; Hollins et al. 2007; Omidi et al. 2003, 2005). Even so, other features such as a positive safety profile, low production costs, and high loading capacity have led such carrier systems towards clinical trials, thus marking the first steps towards curing genetically based disorders by tackling the problem at its origin.

References

Akhtar S, Benter I (2007) Toxicogenomics of non-viral drug delivery systems for RNAi: potential impact on siRNA-mediated gene silencing activity and specificity. Adv Drug Deliv Rev 59 (2–3):164–182. doi:10.1016/j.addr.2007.03.010

Akhtar S, Hughes MD, Khan A, Bibby M, Hussain M, Nawaz Q, Double J, Sayyed P (2000) The delivery of antisense therapeutics. Adv Drug Deliv Rev 44(1):3–21

Akinc A, Thomas M, Klibanov AM, Langer R (2005) Exploring polyethylenimine-mediated DNA transfection and the proton sponge hypothesis. J Gene Med 7(5):657–663

Akinc A, Zumbuehl A, Goldberg M, Leshchiner ES, Busini V, Hossain N, Bacallado SA, Nguyen DN, Fuller J, Alvarez R, Borodovsky A, Borland T, Constien R, de Fougerolles A, Dorkin JR, Narayanannair Jayaprakash K, Jayaraman M, John M, Koteliansky V, Manoharan M, Nechev L, Qin J, Racie T, Raitcheva D, Rajeev KG, Sah DW, Soutschek J, Toudjarska I, Vornlocher HP, Zimmermann TS, Langer R, Anderson DG (2008) A combinatorial library of lipid-like materials for delivery of RNAi therapeutics. Nat Biotechnol 26(5):561–569. doi:10.1038/nbt1402

Alshamsan A, Hamdy S, Samuel J, El-Kadi AO, Lavasanifar A, Uludag H (2010) The induction of tumor apoptosis in B16 melanoma following STAT3 siRNA delivery with a lipid-substituted polyethylenimine. Biomaterials 31(6):1420–1428. doi:10.1016/j.biomaterials.2009.11.003

Andaloussi SE, Lehto T, Mager I, Rosenthal-Aizman K, Oprea II, Simonson OE, Sork H, Ezzat K, Copolovici DM, Kurrikoff K, Viola JR, Zaghloul EM, Sillard R, Johansson HJ, Said Hassane F, Guterstam P, Suhorutsenko J, Moreno PM, Oskolkov N, Halldin J, Tedebark U, Metspalu A, Lebleu B, Lehtio J, Smith CI, Langel U (2011) Design of a peptide-based vector, PepFect6, for efficient delivery of siRNA in cell culture and systemically in vivo. Nucleic Acids Res 39(9):3972–3987. doi:10.1093/nar/gkq1299

Anderson J, Li MJ, Palmer B, Remling L, Li S, Yam P, Yee JK, Rossi J, Zaia J, Akkina R (2007) Safety and efficacy of a lentiviral vector containing three anti-HIV genes – CCR5 ribozyme, tat-rev siRNA, and TAR decoy – in SCID-hu mouse-derived T cells. Mol Ther 15 (6):1182–1188. doi:10.1038/sj.mt.6300157, 6300157 [pii]

Azad RF, Driver VB, Tanaka K, Crooke RM, Anderson KP (1993) Antiviral activity of a phosphorothioate oligonucleotide complementary to RNA of the human cytomegalovirus major immediate-early region. Antimicrob Agents Chemother 37(9):1945–1954

Bartel DP (2004) MicroRNAs: genomics, biogenesis, mechanism, and function. Cell 116 (2):281–297

Beyerle A, Braun A, Merkel O, Koch F, Kissel T, Stoeger T (2011) Comparative in vivo study of poly(ethylene imine)/siRNA complexes for pulmonary delivery in mice. J Control Release 151 (1):51–56. doi:10.1016/j.jconrel.2010.12.017

Boussif O, Lezoualc'h F, Zanta MA, Mergny MD, Scherman D, Demeneix B, Behr JP (1995) A versatile vector for gene and oligonucleotide transfer into cells in culture and in vivo: polyethylenimine. Proc Natl Acad Sci USA 92(16):7297–7301

Brummelkamp TR, Bernards R, Agami R (2002) A system for stable expression of short interfering RNAs in mammalian cells. Science 296(5567):550–553. doi:10.1126/science.10689991068999 [pii]

Burnett JC, Rossi JJ (2012) RNA-based therapeutics: current progress and future prospects. Chem Biol 19(1):60–71. doi:10.1016/j.chembiol.2011.12.008

Chien PY, Wang J, Carbonaro D, Lei S, Miller B, Sheikh S, Ali SM, Ahmad MU, Ahmad I (2005) Novel cationic cardiolipin analogue-based liposome for efficient DNA and small interfering RNA delivery in vitro and in vivo. Cancer Gene Ther 12(3):321–328. doi:10.1038/sj.cgt.7700793

Choi SH, Jin SE, Lee MK, Lim SJ, Park JS, Kim BG, Ahn WS, Kim CK (2008) Novel cationic solid lipid nanoparticles enhanced p53 gene transfer to lung cancer cells. Eur J Pharm Biopharm 68(3):545–554. doi:10.1016/j.ejpb.2007.07.011

Choi YS, Lee JY, Suh JS, Kwon YM, Lee SJ, Chung JK, Lee DS, Yang VC, Chung CP, Park YJ (2010) The systemic delivery of siRNAs by a cell penetrating peptide, low molecular weight protamine. Biomaterials 31(6):1429–1443. doi:10.1016/j.biomaterials.2009.11.001, S0142-9612(09)01198-3 [pii]

Couto LB, High KA (2010) Viral vector-mediated RNA interference. Curr Opin Pharmacol 10 (5):534–542. doi:10.1016/j.coph.2010.06.007

Crooke ST (1998) Vitravene – another piece in the mosaic. Antisense Nucleic Acid Drug Dev 8 (4):vii–viii

Davis ME, Zuckerman JE, Choi CH, Seligson D, Tolcher A, Alabi CA, Yen Y, Heidel JD, Ribas A (2010) Evidence of RNAi in humans from systemically administered siRNA via targeted nanoparticles. Nature 464(7291):1067–1070. doi:10.1038/nature08956

del Pozo-Rodriguez A, Delgado D, Solinis MA, Gascon AR, Pedraz JL (2007) Solid lipid nanoparticles: formulation factors affecting cell transfection capacity. Int J Pharm 339 (1–2):261–268. doi:10.1016/j.ijpharm.2007.03.015

Devroe E, Silver PA (2004) Therapeutic potential of retroviral RNAi vectors. Expert Opin Biol Ther 4(3):319–327. doi:10.1517/14712598.4.3.319

DiGiusto DL, Krishnan A, Li L, Li H, Li S, Rao A, Mi S, Yam P, Stinson S, Kalos M, Alvarnas J, Lacey SF, Yee JK, Li M, Couture L, Hsu D, Forman SJ, Rossi JJ, Zaia JA (2010) RNA-based gene therapy for HIV with lentiviral vector-modified CD34(+) cells in patients undergoing transplantation for AIDS-related lymphoma. Sci Transl Med 2(36):36ra43. doi:10.1126/scitranslmed.3000931

Dohmen C, Edinger D, Frohlich T, Schreiner L, Lachelt U, Troiber C, Radler J, Hadwiger P, Vornlocher HP, Wagner E (2012) Nanosized multifunctional polyplexes for receptor-mediated SiRNA delivery. ACS Nano 6(6):5198–5208

Elbashir SM, Harborth J, Lendeckel W, Yalcin A, Weber K, Tuschl T (2001) Duplexes of 21-nucleotide RNAs mediate RNA interference in cultured mammalian cells. Nature 411 (6836):494–498

Epiphanio S, Mikolajczak SA, Goncalves LA, Pamplona A, Portugal S, Albuquerque S, Goldberg M, Rebelo S, Anderson DG, Akinc A, Vornlocher HP, Kappe SH, Soares MP, Mota MM (2008) Heme oxygenase-1 is an anti-inflammatory host factor that promotes murine plasmodium liver infection. Cell Host Microbe 3(5):331–338. doi:10.1016/j.chom.2008.04.003

Ezzat K, El Andaloussi S, Zaghloul EM, Lehto T, Lindberg S, Moreno PM, Viola JR, Magdy T, Abdo R, Guterstam P, Sillard R, Hammond SM, Wood MJ, Arzumanov AA, Gait MJ, Smith CI, Hallbrink M, Langel U (2011) PepFect 14, a novel cell-penetrating peptide for oligonucleotide delivery in solution and as solid formulation. Nucleic Acids Res 39(12):5284–5298. doi:10.1093/nar/gkr072, gkr072 [pii]

Felgner PL, Ringold GM (1989) Cationic liposome-mediated transfection. Nature 337 (6205):387–388. doi:10.1038/337387a0

Fire A, Xu S, Montgomery MK, Kostas SA, Driver SE, Mello CC (1998) Potent and specific genetic interference by double-stranded RNA in Caenorhabditis elegans. Nature 391 (6669):806–811

Fish RJ, Kruithof EK (2004) Short-term cytotoxic effects and long-term instability of RNAi delivered using lentiviral vectors. BMC Mol Biol 5:9. doi:10.1186/1471-2199-5-9

Fortune JA, Novobrantseva TI, Klibanov AM (2011) Highly effective gene transfection in vivo by alkylated polyethylenimine. J Drug Deliv 2011:204058. doi:10.1155/2011/204058

Frank-Kamenetsky M, Grefhorst A, Anderson NN, Racie TS, Bramlage B, Akinc A, Butler D, Charisse K, Dorkin R, Fan Y, Gamba-Vitalo C, Hadwiger P, Jayaraman M, John M, Jayaprakash KN, Maier M, Nechev L, Rajeev KG, Read T, Rohl I, Soutschek J, Tan P, Wong J, Wang G, Zimmermann T, de Fougerolles A, Vornlocher HP, Langer R, Anderson DG, Manoharan M, Koteliansky V, Horton JD, Fitzgerald K (2008) Therapeutic RNAi targeting PCSK9 acutely lowers plasma cholesterol in rodents and LDL cholesterol in nonhuman primates. Proc Natl Acad Sci USA 105(33):11915–11920. doi:10.1073/pnas.0805434105, 0805434105 [pii]

Frohlich T, Edinger D, Klager R, Troiber C, Salcher E, Badgujar N, Martin I, Schaffert D, Cengizeroglu A, Hadwiger P, Vornlocher HP, Wagner E (2012) Structure-activity relationships of siRNA carriers based on sequence-defined oligo (ethane amino) amides. J Control Release 160(3):532–541. doi:10.1016/j.jconrel.2012.03.018

Geisbert TW, Hensley LE, Kagan E, Yu EZ, Geisbert JB, Daddario-DiCaprio K, Fritz EA, Jahrling PB, McClintock K, Phelps JR, Lee AC, Judge A, Jeffs LB, MacLachlan I (2006) Postexposure

protection of guinea pigs against a lethal ebola virus challenge is conferred by RNA interference. J Infect Dis 193(12):1650–1657. doi:10.1086/504267

Geisbert TW, Lee AC, Robbins M, Geisbert JB, Honko AN, Sood V, Johnson JC, de Jong S, Tavakoli I, Judge A, Hensley LE, Maclachlan I (2010) Postexposure protection of non-human primates against a lethal Ebola virus challenge with RNA interference: a proof-of-concept study. Lancet 375(9729):1896–1905. doi:10.1016/S0140-6736(10)60357-1

Gregory RI, Shiekhattar R (2005) MicroRNA biogenesis and cancer. Cancer Res 65 (9):3509–3512. doi:10.1158/0008-5472.CAN-05-0298

Grillone LR, Lanz R (2001) Fomivirsen. Drugs Today (Barc) 37(4):245–255

Grimm D, Streetz KL, Jopling CL, Storm TA, Pandey K, Davis CR, Marion P, Salazar F, Kay MA (2006) Fatality in mice due to oversaturation of cellular microRNA/short hairpin RNA pathways. Nature 441(7092):537–541. doi:10.1038/nature04791

Hannon GJ (2002) RNA interference. Nature 418(6894):244–251. doi:10.1038/418244a

Hartmann L, Krause E, Antonietti M, Borner HG (2006) Solid-phase supported polymer synthesis of sequence-defined, multifunctional poly(amidoamines). Biomacromolecules 7 (4):1239–1244

Hartmann L, Hafele S, Peschka-Suss R, Antonietti M, Borner HG (2008) Tailor-made poly (amidoamine)s for controlled complexation and condensation of DNA. Chemistry 14 (7):2025–2033

Hatakeyama H, Ito E, Akita H, Oishi M, Nagasaki Y, Futaki S, Harashima H (2009) A pH-sensitive fusogenic peptide facilitates endosomal escape and greatly enhances the gene silencing of siRNA-containing nanoparticles in vitro and in vivo. J Control Release 139 (2):127–132. doi:10.1016/j.jconrel.2009.06.008, S0168-3659(09)00418-0 [pii]

Hollins AJ, Omidi Y, Benter IF, Akhtar S (2007) Toxicogenomics of drug delivery systems: exploiting delivery system-induced changes in target gene expression to enhance siRNA activity. J Drug Target 15(1):83–88. doi:10.1080/10611860601151860

Howard KA, Paludan SR, Behlke MA, Besenbacher F, Deleuran B, Kjems J (2009) Chitosan/siRNA nanoparticle-mediated TNF-alpha knockdown in peritoneal macrophages for anti-inflammatory treatment in a murine arthritis model. Mol Ther 17(1):162–168. doi:10.1038/mt.2008.220

Hughes MD, Hussain M, Nawaz Q, Sayyed P, Akhtar S (2001) The cellular delivery of antisense oligonucleotides and ribozymes. Drug Discov Today 6(6):303–315

Hu-Lieskovan S, Heidel JD, Bartlett DW, Davis ME, Triche TJ (2005) Sequence-specific knockdown of EWS-FLI1 by targeted, nonviral delivery of small interfering RNA inhibits tumor growth in a murine model of metastatic Ewing's sarcoma. Cancer Res 65(19):8984–8992. doi:10.1158/0008-5472.CAN-05-0565

Jakobsen MR, Haasnoot J, Wengel J, Berkhout B, Kjems J (2007) Efficient inhibition of HIV-1 expression by LNA modified antisense oligonucleotides and DNAzymes targeted to functionally selected binding sites. Retrovirology 4:29. doi:10.1186/1742-4690-4-29

Kenworthy R, Lambert D, Yang F, Wang N, Chen Z, Zhu H, Zhu F, Liu C, Li K, Tang H (2009) Short-hairpin RNAs delivered by lentiviral vector transduction trigger RIG-I-mediated IFN activation. Nucleic Acids Res 37(19):6587–6599. doi:10.1093/nar/gkp714, gkp714 [pii]

Kota J, Chivukula RR, O'Donnell KA, Wentzel EA, Montgomery CL, Hwang HW, Chang TC, Vivekanandan P, Torbenson M, Clark KR, Mendell JR, Mendell JT (2009) Therapeutic microRNA delivery suppresses tumorigenesis in a murine liver cancer model. Cell 137 (6):1005–1017. doi:10.1016/j.cell.2009.04.021

Kumar P, Lee SK, Shankar P, Manjunath N (2006) A single siRNA suppresses fatal encephalitis induced by two different flaviviruses. PLoS Med 3(4):e96. doi:10.1371/journal.pmed.0030096

Kwok A, Hart SL (2011) Comparative structural and functional studies of nanoparticle formulations for DNA and siRNA delivery. Nanomedicine 7(2):210–219. doi:10.1016/j.nano.2010.07.005, S1549-9634(10)00239-X [pii]

Kwon EJ, Bergen JM, Pun SH (2008) Application of an HIV gp41-derived peptide for enhanced intracellular trafficking of synthetic gene and siRNA delivery vehicles. Bioconjug Chem 19 (4):920–927

Landen CN Jr, Chavez-Reyes A, Bucana C, Schmandt R, Deavers MT, Lopez-Berestein G, Sood AK (2005) Therapeutic EphA2 gene targeting in vivo using neutral liposomal small interfering RNA delivery. Cancer Res 65(15):6910–6918. doi:10.1158/0008-5472.CAN-05-0530

Leng Q, Mixson AJ (2005) Small interfering RNA targeting Raf-1 inhibits tumor growth in vitro and in vivo. Cancer Gene Ther 12(8):682–690

Lu J, Getz G, Miska EA, Alvarez-Saavedra E, Lamb J, Peck D, Sweet-Cordero A, Ebert BL, Mak RH, Ferrando AA, Downing JR, Jacks T, Horvitz HR, Golub TR (2005) MicroRNA expression profiles classify human cancers. Nature 435(7043):834–838. doi:10.1038/nature03702

Lv H, Zhang S, Wang B, Cui S, Yan J (2006) Toxicity of cationic lipids and cationic polymers in gene delivery. J Control Release 114(1):100–109. doi:10.1016/j.jconrel.2006.04.014

Ma Z, Li J, He F, Wilson A, Pitt B, Li S (2005) Cationic lipids enhance siRNA-mediated interferon response in mice. Biochem Biophys Res Commun 330(3):755–759. doi:10.1016/j.bbrc.2005.03.041

Martin I, Dohmen C, Mas-Moruno C, Troiber C, Kos P, Schaffert D, Lachelt U, Teixido M, Gunther M, Kessler H, Giralt E, Wagner E (2012) Solid-phase-assisted synthesis of targeting peptide-PEG-oligo(ethane amino)amides for receptor-mediated gene delivery. Org Biomol Chem 10(16):3258–3268. doi:10.1039/c2ob06907e

Meister G, Tuschl T (2004) Mechanisms of gene silencing by double-stranded RNA. Nature 431 (7006):343–349. doi:10.1038/nature02873

Meyer M, Philipp A, Oskuee R, Schmidt C, Wagner E (2008) Breathing life into polycations: functionalization with pH-responsive endosomolytic peptides and polyethylene glycol enables siRNA delivery. J Am Chem Soc 130(11):3272–3273

Meyer M, Dohmen C, Philipp A, Kiener D, Maiwald G, Scheu C, Ogris M, Wagner E (2009) Synthesis and biological evaluation of a bioresponsive and endosomolytic siRNA-polymer conjugate. Mol Pharm 6(3):752–762. doi:10.1021/mp9000124

Minakuchi Y, Takeshita F, Kosaka N, Sasaki H, Yamamoto Y, Kouno M, Honma K, Nagahara S, Hanai K, Sano A, Kato T, Terada M, Ochiya T (2004) Atelocollagen-mediated synthetic small interfering RNA delivery for effective gene silencing in vitro and in vivo. Nucleic Acids Res 32 (13):e109. doi:10.1093/nar/gnh093

Miyata K, Nishiyama N, Kataoka K (2012) Rational design of smart supramolecular assemblies for gene delivery: chemical challenges in the creation of artificial viruses. Chem Soc Rev 41 (7):2562–2574

Moghimi SM, Symonds P, Murray JC, Hunter AC, Debska G, Szewczyk A (2005) A two-stage poly(ethylenimine)-mediated cytotoxicity: implications for gene transfer/therapy. Mol Ther 11 (6):990–995

Morrissey DV, Lockridge JA, Shaw L, Blanchard K, Jensen K, Breen W, Hartsough K, Machemer L, Radka S, Jadhav V, Vaish N, Zinnen S, Vargeese C, Bowman K, Shaffer CS, Jeffs LB, Judge A, MacLachlan I, Polisky B (2005) Potent and persistent in vivo anti-HBV activity of chemically modified siRNAs. Nat Biotechnol 23(8):1002–1007. doi:10.1038/nbt1122

Omidi Y, Hollins AJ, Benboubetra M, Drayton R, Benter IF, Akhtar S (2003) Toxicogenomics of non-viral vectors for gene therapy: a microarray study of lipofectin- and oligofectamine-induced gene expression changes in human epithelial cells. J Drug Target 11(6):311–323. doi:10.1080/10611860310001636908

Omidi Y, Hollins AJ, Drayton RM, Akhtar S (2005) Polypropylenimine dendrimer-induced gene expression changes: the effect of complexation with DNA, dendrimer generation and cell type. J Drug Target 13(7):431–443. doi:10.1080/10611860500418881

Paddison PJ, Caudy AA, Bernstein E, Hannon GJ, Conklin DS (2002) Short hairpin RNAs (shRNAs) induce sequence-specific silencing in mammalian cells. Genes Dev 16 (8):948–958. doi:10.1101/gad.981002

Pal A, Ahmad A, Khan S, Sakabe I, Zhang C, Kasid UN, Ahmad I (2005) Systemic delivery of RafsiRNA using cationic cardiolipin liposomes silences Raf-1 expression and inhibits tumor growth in xenograft model of human prostate cancer. Int J Oncol 26(4):1087–1091

Pan X, Chen L, Liu S, Yang X, Gao JX, Lee RJ (2009) Antitumor activity of G3139 lipid nanoparticles (LNPs). Mol Pharm 6(1):211–220. doi:10.1021/mp800146j

Peer D, Park EJ, Morishita Y, Carman CV, Shimaoka M (2008) Systemic leukocyte-directed siRNA delivery revealing cyclin D1 as an anti-inflammatory target. Science 319 (5863):627–630

Pille JY, Li H, Blot E, Bertrand JR, Pritchard LL, Opolon P, Maksimenko A, Lu H, Vannier JP, Soria J, Malvy C, Soria C (2006) Intravenous delivery of anti-RhoA small interfering RNA loaded in nanoparticles of chitosan in mice: safety and efficacy in xenografted aggressive breast cancer. Hum Gene Ther 17(10):1019–1026. doi:10.1089/hum.2006.17.1019

Ravina M, Paolicelli P, Seijo B, Sanchez A (2010) Knocking down gene expression with dendritic vectors. Mini Rev Med Chem 10(1):73–86

Salcher EE, Kos P, Frohlich T, Badgujar N, Scheible M, Wagner E (2012) Sequence-defined four-arm oligo(ethanamino)amides for pDNA and siRNA delivery: impact of building blocks on efficacy. J Control Release 164(3):380–386

Saw PE, Ko YT, Jon S (2010) Efficient liposomal nanocarrier-mediated oligodeoxynucleotide delivery involving dual use of a cell-penetrating peptide as a packaging and intracellular delivery agent. Macromol Rapid commun 31(13):1155–1162. doi:10.1002/marc.200900861

Schaffert D, Badgujar N, Wagner E (2011a) Novel Fmoc-polyamino acids for solid-phase synthesis of defined polyamidoamines. Org Lett 13(7):1586–1589. doi:10.1021/ol200381z

Schaffert D, Kiss M, Rodl W, Shir A, Levitzki A, Ogris M, Wagner E (2011b) Poly(I:C)-mediated tumor growth suppression in EGF-receptor overexpressing tumors using EGF-polyethylene glycol-linear polyethylenimine as carrier. Pharm Res 28(4):731–741. doi:10.1007/s11095-010-0225-4

Schaffert D, Troiber C, Salcher EE, Frohlich T, Martin I, Badgujar N, Dohmen C, Edinger D, Klager R, Maiwald G, Farkasova K, Seeber S, Jahn-Hofmann K, Hadwiger P, Wagner E (2011c) Solid-phase synthesis of sequence-defined T-, i-, and U-shape polymers for pDNA and siRNA delivery. Angew Chem Int Ed Engl 50(38):8986–8989. doi:10.1002/anie.201102165

Scholz C, Wagner E (2012) Therapeutic plasmid DNA versus siRNA delivery: common and different tasks for synthetic carriers. J Control Release 161(2):554–565. doi:10.1016/j.jconrel.2011.11.014, S0168-3659(11)01044-3 [pii]

Semple SC, Akinc A, Chen J, Sandhu AP, Mui BL, Cho CK, Sah DW, Stebbing D, Crosley EJ, Yaworski E, Hafez IM, Dorkin JR, Qin J, Lam K, Rajeev KG, Wong KF, Jeffs LB, Nechev L, Eisenhardt ML, Jayaraman M, Kazem M, Maier MA, Srinivasulu M, Weinstein MJ, Chen Q, Alvarez R, Barros SA, De S, Klimuk SK, Borland T, Kosovrasti V, Cantley WL, Tam YK, Manoharan M, Ciufolini MA, Tracy MA, de Fougerolles A, MacLachlan I, Cullis PR, Madden TD, Hope MJ (2010) Rational design of cationic lipids for siRNA delivery. Nat Biotechnol 28 (2):172–176. doi:10.1038/nbt.1602

Shi SJ, Zhong ZR, Liu J, Zhang ZR, Sun X, Gong T (2012) Solid lipid nanoparticles loaded with anti-microRNA oligonucleotides (AMOs) for suppression of microRNA-21 functions in human lung cancer cells. Pharm Res 29(1):97–109. doi:10.1007/s11095-011-0514-6

Sliva K, Schnierle BS (2010) Selective gene silencing by viral delivery of short hairpin RNA. Virol J 7:248. doi:10.1186/1743-422X-7-248

Sonoke S, Ueda T, Fujiwara K, Sato Y, Takagaki K, Hirabayashi K, Ohgi T, Yano J (2008) Tumor regression in mice by delivery of Bcl-2 small interfering RNA with pegylated cationic liposomes. Cancer Res 68(21):8843–8851. doi:10.1158/0008-5472.CAN-08-0127, 68/21/8843 [pii]

Sun A, Tang J, Terranova PF, Zhang X, Thrasher JB, Li B (2010) Adeno-associated virus-delivered short hairpin-structured RNA for androgen receptor gene silencing induces tumor eradication of prostate cancer xenografts in nude mice: a preclinical study. Int J Cancer 126 (3):764–774. doi:10.1002/ijc.24778

Symonds P, Murray JC, Hunter AC, Debska G, Szewczyk A, Moghimi SM (2005) Low and high molecular weight poly(L-lysine)s/poly(L-lysine)-DNA complexes initiate mitochondrial-mediated apoptosis differently. FEBS Lett 579(27):6191–6198. doi:10.1016/j.febslet.2005.09.092, S0014-5793(05)01237-8 [pii]

Takei Y, Kadomatsu K, Yuzawa Y, Matsuo S, Muramatsu T (2004) A small interfering RNA targeting vascular endothelial growth factor as cancer therapeutics. Cancer Res 64 (10):3365–3370. doi:10.1158/0008-5472.CAN-03-2682

Thomas M, Lu JJ, Ge Q, Zhang C, Chen J, Klibanov AM (2005) Full deacylation of polyethylenimine dramatically boosts its gene delivery efficiency and specificity to mouse lung. Proc Natl Acad Sci USA 102(16):5679–5684. doi:10.1073/pnas.0502067102, 0502067102 [pii]

Tomanin R, Scarpa M (2004) Why do we need new gene therapy viral vectors? Characteristics, limitations and future perspectives of viral vector transduction. Curr Gene Ther 4(4):357–372

Tran MA, Gowda R, Sharma A, Park EJ, Adair J, Kester M, Smith NB, Robertson GP (2008) Targeting V600EB-Raf and Akt3 using nanoliposomal-small interfering RNA inhibits cutaneous melanocytic lesion development. Cancer Res 68(18):7638–7649. doi:10.1158/0008-5472.CAN-07-6614

Tsai LR, Chen MH, Chien CT, Chen MK, Lin FS, Lin KM, Hwu YK, Yang CS, Lin SY (2011) A single-monomer derived linear-like PEI-co-PEG for siRNA delivery and silencing. Biomaterials 32(14):3647–3653. doi:10.1016/j.biomaterials.2011.01.059

Wagner E (2012) Polymers for siRNA delivery: inspired by viruses to be targeted, dynamic, and precise. Acc Chem Res 45(7):1005–1013. doi:10.1021/ar2002232

Xia H, Mao Q, Eliason SL, Harper SQ, Martins IH, Orr HT, Paulson HL, Yang L, Kotin RM, Davidson BL (2004) RNAi suppresses polyglutamine-induced neurodegeneration in a model of spinocerebellar ataxia. Nat Med 10(8):816–820. doi:10.1038/nm1076

Yokota T, Iijima S, Kubodera T, Ishii K, Katakai Y, Ageyama N, Chen Y, Lee YJ, Unno T, Nishina K, Iwasaki Y, Maki N, Mizusawa H, Akari H (2007) Efficient regulation of viral replication by siRNA in a non-human primate surrogate model for hepatitis C. Biochem Biophys Res Commun 361(2):294–300. doi:10.1016/j.bbrc.2007.06.182

Zamecnik PC, Stephenson ML (1978) Inhibition of Rous sarcoma virus replication and cell transformation by a specific oligodeoxynucleotide. Proc Natl Acad Sci USA 75(1):280–284

Zamore PD, Haley B (2005) Ribo-gnome: the big world of small RNAs. Science 309 (5740):1519–1524. doi:10.1126/science.1111444

Zimmermann TS, Lee AC, Akinc A, Bramlage B, Bumcrot D, Fedoruk MN, Harborth J, Heyes JA, Jeffs LB, John M, Judge AD, Lam K, McClintock K, Nechev LV, Palmer LR, Racie T, Rohl I, Seiffert S, Shanmugam S, Sood V, Soutschek J, Toudjarska I, Wheat AJ, Yaworski E, Zedalis W, Koteliansky V, Manoharan M, Vornlocher HP, MacLachlan I (2006) RNAi-mediated gene silencing in non-human primates. Nature 441(7089):111–114. doi:10.1038/nature04688

Zintchenko A, Philipp A, Dehshahri A, Wagner E (2008) Simple modifications of branched PEI lead to highly efficient siRNA carriers with low toxicity. Bioconjug Chem 19(7):1448–1455. doi:10.1021/bc800065f

zur Muhlen A, Schwarz C, Mehnert W (1998) Solid lipid nanoparticles (SLN) for controlled drug delivery – drug release and release mechanism. Eur J Pharm Biopharm 45(2):149–155

Chapter 10
Cell-Specific Aptamers for Nano-medical Applications

Günter Mayer, Monika Pofahl, Katia M.U. Schöler, and Silvana Haßel

Abstract This chapter describes cell-type specific aptamers and their use in diagnostics and therapy. Aptamers are single-stranded oligo(deoxy)nucleotides that selectively bind to their target molecules with high affinity. Cell-type specific aptamers in particular can be identified via SELEX using isolated surface proteins or whole cells as targets.

Cell-type specific aptamers have been mostly selected targeting cancer cells, which essentially take into account that about 20 % of the deaths worldwide are due to cancer and cancer-related diseases. In the early stages of cancer, circulating cancer cells are very rare. Cancer cell-targeting aptamers allow the identification of these rare circulating cells, thereby providing new tools for early cancer detection and diagnosis. Furthermore, they can be easily synthesized with a variety of modifications. In this regard tumor cell-targeting aptamers are employed as potential delivery vehicles, whereas they are equipped with various cargo molecules, such as toxins, chemotherapeutics, or siRNA molecules, that allow for the development of cell-specific treatment regimens and the decrease of unwanted side effects.

Contents

G. Mayer (✉) • M. Pofahl • K.M.U. Schöler • S. Haßel
Life and Medical Sciences Institute, University of Bonn, Gerhard-Domagk-Str. 1, 53121 Bonn, Germany
e-mail: gmayer@uni-bonn.de

J. KJEMS et al. (eds.), *Nucleic Acid Nanotechnology*, Nucleic Acids and Molecular Biology 29, DOI 10.1007/978-3-642-38815-6_10,

10.1 Cell-Specific Aptamers

Aptamers were first described in 1990 by Ellington and Szostak (1990) and Tuerk and Gold (1990a). Since then they have become an invaluable research tool and demonstrated a broad application prospected in fundamental research, drug development, clinical diagnosis, and therapy. Basically, aptamers (Latin *aptus* fitting; Greek *meros* particle) are single-chained oligo(deoxy)nucleotides that selectively bind to respective target molecules with high affinity. They form complex 3D structures, which may include stems, loops, bulges, hairpins, pseudoknots, junctions and quadruplexes, or combinations thereof (Stoltenburg et al. 2007; Cruz and Westhof 2011). The conformation of aptamers is often adapted to their specific targets, and selective binding is mediated by structure compatibility, stacking of aromatic rings, electrostatic and van der Waals interactions, hydrogen bonds, or from a combination of these (Hermann 2000). The identification of aptamers is achieved through an iterative process termed systematic evolution of ligands by exponential enrichment (SELEX). In general, four main steps are repeated several times: (a) incubation of a oligo(deoxy)nucleotide library with the target molecule, (b) partitioning of unbound from bound nucleic acids, (c) elution of the binder, and (d) amplification and generation of single-stranded oligo(deoxy) nucleotides (Fig. 10.1).

To date, diverse target structures, such as small molecules [e.g., ethanolamine (Mann et al. 2005)], antibiotics [e.g., neomycin (Wallis et al. 1995)], peptides, and proteins [e.g., APC (Müller et al. 2009)], were used as ligands in SELEX approaches. To increase their chemical diversity and stability, aptamers can be modified before or after the SELEX process. Modifications at the phosphate-ribose backbone or at the nucleobases (Orr 2001; Bouchard et al. 2010) are known, for example, the substitution of the 2′-position with fluoride or methoxy groups (Bouchard et al. 2010). The recent years has seen a tremendous increase of aptamers that target a distinct or a series of cells and cell subtypes (Table 10.1). These aptamers have gained emerging interest since they are applicable and adaptable to various biomedical applications. Especially, the fabrication of nanodevices seems to be a promising task using cell-type-selective aptamers. Aptamers targeting distinct cells can be identified by different approaches. The most convenient one seems to be the direct use of a target cell during an in vitro selection process. Several studies describe cell-SELEX protocols (Raddatz et al. 2008; Cerchia et al. 2009). However, the molecular target of such approaches needs to be determined post-selectively (Shamah et al. 2008; Meyer et al. 2011).

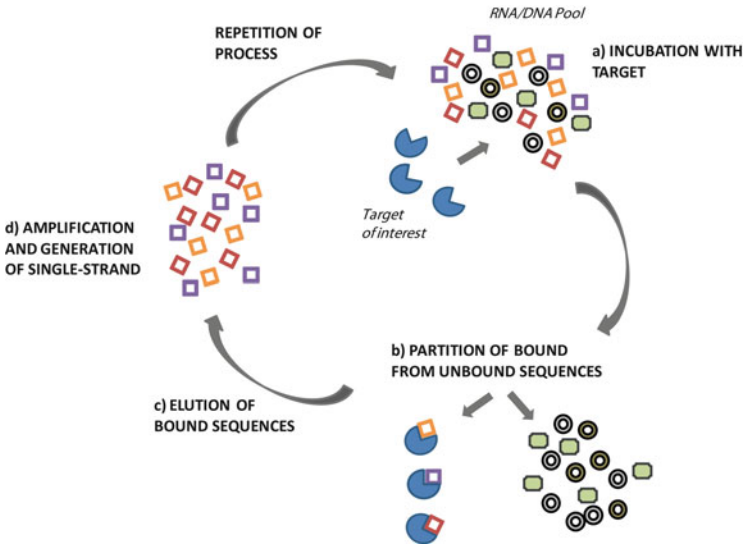

Fig. 10.1 Systematic evolution of ligands by exponential enrichment (SELEX) is used to select aptamers. This multistep process, composed of (a) incubation of the starting RNA or DNA pool with the target of interest, (b) partitioning of unbound from bound nucleic acids, (c) elution of the binder from the target, and (d) its amplification and single-strand generation, is repeated several times until an enriched population of aptamers is evolved

A target-driven approach can be achieved by recombinant expression of extracellular domains of cell-type-specific receptors or transmembrane proteins. Aptamers that have been generated against those proteins, through so-called classical SELEX protocols, need then to be analyzed afterwards regarding their potential to recognize the target when embedded in its natural environment. Also a combination of both approaches has been described (Hicke 2001). Alternatively, the target molecule can be expressed in cells that do not naturally bear the designated receptor. These cells can be used for selection experiments, whereas the non-expressing cell might be suitable for pre- or counterselection steps.

The first example of complex targets used in SELEX experiments was published in 1998 (Morris et al. 1998). In that membrane, preparations of red blood cells (RBC), so-called RBC ghosts, were addressed, and aptamers were enriched targeting two distinct membrane proteins. Besides, Morris and coworkers were able to isolate one of the aptamer's targets, namely, transferrin receptor monomer (CD71), by specific aptamer-based cross-linking experiments.

Since then, many cell-SELEX strategies were described, which are improved and optimized regarding minimization of high background binding of nucleic acids to the cell surface (Cerchia et al. 2005; Ohuchi et al. 2006). In addition, different cell-SELEX methods can be used to gain the desired biological activity of the aptamer. Our group reported an elegant, albeit elaborated, method to monitor the enrichment of putative cell-specific binder in 2008 (Raddatz et al. 2008). Here,

Table 10.1 List of complex-target-specific aptamers

Target	DNA/RNA	References
Viruses		
HIV	RNA	Tuerk et al. (1992)
RSV	RNA	Pan et al. (1995)
HPV16	RNA	Nicol et al. (2011)
Bacteria		
Anthrax spores	DNA	Bruno and Kiel (1999)
Campylobacter jejuni	DNA	Dwivedi et al. (2010)
M-type *Streptococcus pyogenes*	DNA	Hamula et al. (2011)
Pseudomonas aeruginosa	DNA	Wang et al. (2010)
Parasites		
Trypanosome brucei	RNA	Homann and Göringer (1999)
Trypanosome cruzi	RNA	Ulrich (2002)
Mammalian cells		
Pigpen endothelial cells	DNA	Blank (2001)
Murine pheochromocytoma cells	RNA	Cerchia et al. (2005)
Human red blood cells	DNA	Morris et al. (1998)
Human glioblastoma cells	RNA	Hicke (2001)
Human prostate cancer cells	RNA	Lupold et al. (2002)
Human B cells	DNA	Wu et al. (2003)
Human breast cancer cells	RNA	Chen (2003)
Human glioma cells	RNA	Cerchia et al. (2009)
Human epidermoid carcinoma	RNA	Li et al. (2011)

fluorescent-activated cell sorting (FACS) was implemented into the selection process to separate bound from unbound nucleic acids and, more importantly, dead from living cells. Dead cells are prone to nonspecifically take up nucleic acids what is counteracting on the enrichment process. In 2006, Ohuchi et al. published the so-called target expressed on cell surface-SELEX (TECS-SELEX) (Ohuchi et al. 2006). Here, the target of interest, namely, transforming growth factor-β type III receptor (TGF-β III receptor), was expressed on Chinese hamster ovary (CHO) cells, and thereby specific RNA aptamers were enriched. Furthermore, Cerchia et al. (2005) showed that a negative- or counter-SELEX step using a non-mutated or mutated target-expressing cell line captures unspecific binders. Cerchia and coworkers obtained rearranged during transfection (RET) receptor tyrosine kinase-specific RNA aptamers by using murine pheochromocytoma (PC12) cells, which express either no RET or different domains of RET. Thus, they drive the selection towards the human RET receptor mutated in the extracellular domain, which is published to be involved in multiple endocrine neoplasia syndrome 2A and familial medullary thyroid carcinoma (Jhiang 2000). Based on their investigations in 2005, Cerchia and coworkers proceed in whole-cell SELEX: in 2009, they generated aptamers, which specifically discriminate cells within the same tumor type (Cerchia et al. 2009). The clinical outcome of cancer is often hardly to tell, because of the heterogeneity of malignant cells. Cerchia et al. (2009) enriched aptamers that discriminate human U87MG glioma cells from less

malignant T98G cells and path the way for individual-specific cancer treatment. In 2001 Hicke et al. published a crossover approach: first, they performed nine rounds of selection-targeting tenascin-C-expressing U251 glioblastoma cells and then further enriched the sequences by incubation for two additional selection rounds with purified tenascin-C protein (Hicke 2001).

The significant step further in generating tumor-specific aptamers was described recently as a sole in vivo approach. Here, the physiological target conformation, conditioned by the target's microenvironment, is not impaired, and, thus, the naturally in situ condition of the target molecule is maintained. Mi et al. described a first in vivo selection experiment in 2009 (Mi et al. 2009). They focused on a mouse model, which bears intrahepatical colorectal cancer metastases. The starting modified RNA pool was administered intravenously into the tail vain. After circulation the mice were sacrificed and the tumor tissue resected. Subsequently, the tumor-associated RNA molecules were isolated, amplified, and prepared for the next in vivo selection cycle. In this way, a tumor-specific aptamer was identified after 14 rounds of selection. Further investigations revealed that the aptamer targets the p68 RNA helicase, which has been previously reported to be overexpressed on colorectal tumors (Abdelhaleem 2005). Cell-surface proteins represent accessible targets for developing novel therapies and diagnostics. The importance of potential cell-surface binders is shown by the fact that a large number of human diseases are linked to alterations maintained in these proteins (Sanders and Myers 2004; Josic et al. 2008). Aptamers that specifically target cell-surface molecules therefore have the potential to serve as therapeutic agonists, antagonists, or diagnostic agents. Selective aptamers may block the proliferation or metastatic induction of cell-surface receptors, either by acting directly on these or through the delivery of conjugated toxins to explicitly decimate tumor cell populations. They are also useful as imaging tools for diseases or stage-specific markers in diagnostics. By discrimination between cell types, aptamers allow the enrichment and purification of stem cells (Guo et al. 2006a) or the visualization of differentiated and non-differentiated cells (Berezovski et al. 2008). Studies in mammals revealed low immunogenicity and toxicity of aptamers, which is of utmost importance to conduct conclusive animal studies or applications in humans in later developmental stages. For example, Drolet et al. (2000) demonstrate the absence of severe side effects after administration of the anti-vascular endothelial growth factor (VEGF) aptamer NX1838, later known as EYE001 or macugen®, to rhesus monkeys. In addition, the administration of 1,000-fold higher doses of aptamers than required clinically immunogenicity was found to be absent or limited (Drolet et al. 2000; Eyetech Study Group 2002). In comparison to humanized antibodies, aptamers are devoid of residual sequences from other species and therefore are not prone to elicit human immune response. In the following sections, the applications of cell-specific aptamers in diagnostic and therapeutic settings will be discussed.

10.2 Aptamers in Cellular Diagnostics

Cell-specific aptamers have been mostly selected for cancer cells, which mainly takes into account that about 20 % of the deaths worldwide are due to cancer and cancer-related diseases (Alberts et al. 2008; Kumar et al. 2007). Cancer arises from a single cell, in which genetic or epigenetic changes occurred, resulting in excessive and unregulated proliferation independent of physiologic growth stimuli (Alberts et al. 2008; Kumar et al. 2007). However, transformation from healthy to cancer cells requires a number of independent mutations in proto-oncogenes and tumor suppressor genes (Alberts et al. 2008). Such mutations may occur in the germline or in somatic cells (Alberts et al. 2008). Germline mutations result in a hereditary predisposition to cancer, whereas mutations in somatic cells contribute to sporadic tumors (Alberts et al. 2008; Kumar et al. 2007; Knudson 2002). Overall, there are more than 100 distinct types of cancers, arising from various underlying molecular mechanisms (http://www.who.int/mediacentre/factsheets/fs297/en/). Early detection of cancer is thought to considerably increase the success of available treatment regimens. Therefore, comprehensive diagnosis is performed to detect cancer, even long before symptoms may occur (http://www.who.int/cancer/detection/en/). In this way preventive diagnostic approaches are available for breast cancer, cervical carcinoma, and colorectal cancer (http://www.who.int/cancer/detection/variouscancer/en/index.html). Early-stage cancer sees less than 100 circulating cancer cells in 1 ml of patient blood, which also bears approximately 5×10^9 other cells (Cristofanilli et al. 2004). This illustrates that diagnostic assays are required to specifically and with utmost sensitivity detect cancer cells. Commonly, diagnostic assays shall fulfill some prerequisites, such as robustness, sensitivity, and affordability. Cell-specific aptamers have entered the stage and proven to be well suited for diagnostic applications. Since aptamers are oligonucleotides, which fold into a specific three-dimensional structure, they can be denatured and refolded (Ellington and Szostak 1990). Hence, their binding is reversible; diagnostic assays based on aptamers can thus be recycled (Tuerk and Gold 1990b). The major challenge in aptamer-based biosensors is to convert the binding event of an aptamer to its target into a detectable signal (Fig. 10.2a). A multitude of different ways have been employed to achieve this conversion. Examples are fluorophores; nanoparticles, in particular, gold or iron; and quantum dots which were developed for detection purposes (Fig. 10.2b). Overall, aptamer-based diagnosis can be distinguished into two different setups: in solution or on chip (Fig. 10.2c).

10.2.1 Detection of Tumor Cells with Aptamers by Fluorescence Imaging

Fluorescence-based detection is the most common type of imaging in biological and medical applications (López-Colón et al. 2011). Aptamers can be easily

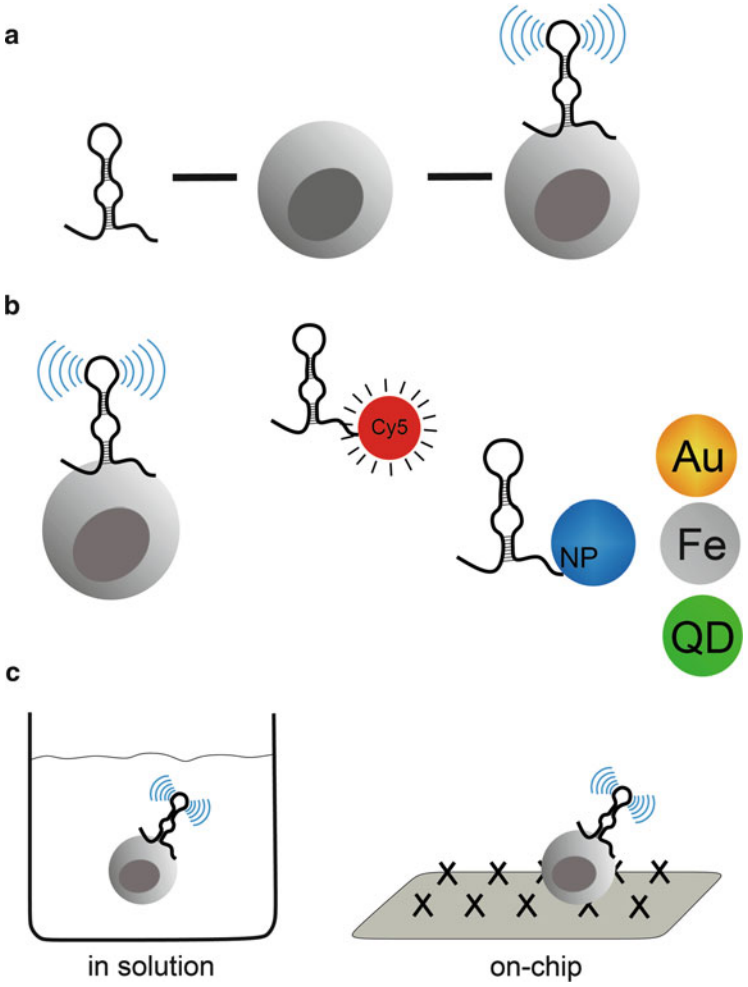

Fig. 10.2 Aptamers are selected either against a known specific biomarker on target cells or against an unknown receptor on the cell surface. (**a**) The binding of cell aptamers needs to be converted into a detectable signal. (**b**) A multitude of different ways have been employed to achieve this conversion, such as fluorophores; nanoparticles, in particular, gold (Au) or iron (Fe); and quantum dots (QD). (**c**) Aptamers have been mainly used in two different setups either in solution or on-chip

modified with fluorescent dyes. Upon target recognition the fluorescent signal can be detected by various fluorescence imaging systems, offering different resolutions depending on the employed fluorophore and overall aptamer performance (Weissleder and Ntziachristos 2003; Weissleder and Pittet 2008). By this means, aptamer–cell interactions can be validated by fluorescently labeled aptamers and cytometry, fluorescence, or confocal microscopy (Shangguan et al. 2006, 2008;

Tang et al. 2007; Sefah et al. 2009). Labeled aptamers targeting leukemia cells, such as acute T-cell leukemia (CEM), Burkitt's lymphoma (Ramos), and non-Hodgkin's B-cell lymphoma (Toledo), were shown to allow specific detection of leukemia cells in patient samples (Shangguan et al. 2006; Tang et al. 2007; Sefah et al. 2009). Even though significant progress has been made in ex vivo applications, aptamer-based in vivo noninvasive imaging is still quite rare. In vivo imaging is essential to localize primary tumor sites and, more importantly, metastases. Visualization is not only relevant for initial detection of tumors, but it is furthermore implicated when controlling tumor regression during therapy or in recognizing cancer relapse. In comparison to relatively large antibodies, aptamers are excellently suited for in vivo applications. Their small size facilitates rapid diffusion into the targeted tissues and interaction with the target molecules. However, aptamer half-life in blood is rather short, due to nuclease degradation, renal excretion, and hepatobiliary clearance (Charlton et al. 1997; Dougan et al. 2003). The circulation time of aptamers can be increased by chemical modifications, such as the introduction of locked nucleic acids (LNAs) or by polyethylene glycol (PEG) (Kurreck 2002; Healy et al. 2004). TD05, an aptamer selected against Burkitt's lymphoma cells, was successfully tested by this means in a xenograft nude mice model (Shi et al. 2010).

Fluorophore-based assays have disadvantages, resulting in a need for different detection methods. Biosensors employing optical signals are prone to background interference in complex biological samples, resulting in a reduction of detection capability. Therefore, other signaling moieties are employed, namely, nanoparticles.

10.2.2 Nanoparticles

Nanoparticles (NPs) are chemically designed materials sizing from 5 to 200 nm, which are used in various biomedical applications (Shi et al. 2010). Several fabrications of NPs are yet available with varying properties but adaptable to aptamer technology.

Quantum dots (QDs) are single crystals with only a few nanometers diameter. Their dimension can be controlled by applying defined temperature, duration, and presence of ligands during synthesis protocols (Jaiswal et al. 2002; Michalet 2005). QDs have several advantages over fluorophores; they show higher photostability, increased brightness, and narrow fluorescent spectra (Murray et al. 1993; Alivisatos 1996; Peng et al. 2000). Cell-targeting aptamers equipped with QDs have been used in cell imaging approaches. Prostate cancer is the second leading cause of cancer death in American man (Greenlee et al. 2001). In 2002, Lupold et al. selected two aptamers, A9 and A10, against the PSMA-expressing prostate tumor cell line LNCaP (Lupold et al. 2002). A9 was modified with QDs to specifically detect and label prostate cancer cells (Chu et al. 2006a). In this study, the aptamers were biotinylated and coupled to the streptavidin-coated quantum dots by

biotin–streptavidin interaction. The A9 aptamer:QD conjugates specifically recognized PSMA on live and fixed cells (Chu et al. 2006a). Bagalkot et al. (2007) took the next step by constructing a QD equipped with the PSMA aptamer to synchronously visualize and treat cancer cells in vitro (Section 10.3.1).

Gold nanoparticles (AuNPs) can be employed in reflectance imaging, since a single gold nanoparticle produces a signal, which is 10^6 times stronger than the signal generated by organic fluorophores (Smith et al. 2007; Bamrungsap et al. 2012). Furthermore, AuNPs are not prone to photo-bleaching opposed to organic dyes. For these reasons, cell-targeting aptamers have been functionalized via thiol chemistry with gold nanoparticles for in vitro imaging purposes. AuNPs were equipped with an aptamer towards platelet-derived growth factor (PDGF) (Huang et al. 2008) via thiol chemistry as described in 1998 by Storhoff et al. (1998). The AuNPs are visualized using the reflecting mode of a confocal microscope. Gold NPs are well suited for in vivo applications, since they have been shown to be less cytotoxic compared to organic dyes. Next to diagnostic applications, aptamer-modified AuNPs have been used as multimodal-targeting platform, combining diagnostic and therapy (Jaiswal et al. 2002; Michalet 2005).

Fluorescence imaging has been used in vivo even though the tissue-penetrating depth is fairly limited. Deep tissue penetration is only achievable using infrared light. Magnetic resonance imaging (MRI) is free of this limitation. It allows three-dimensional imaging of the whole human body. Nowadays, MRI is employed to differentiate between regular tissue and a solid tumor; however, MRI gains no molecular information. Smart MRI contrast agents, equipped with a targeting unit, are required to achieve this goal. Cell-specific aptamers can be employed to supply specificity to MRI contrast agents, such as iron oxide NPs. In 2007, Smith et al. functionalized iron oxide NPs with either an aptamer towards Burkitt's lymphoma, CCRF-CCM, or Toledo cells. These NPs were shown to magnetically extract the desired target cells from a cell mixture (Smith et al. 2007). Nair et al. developed the so-called nanosurgeon by functionalizing magnetic NPs with the aptamer GB-10, which targets tenascin-C on glioma cells. The nanosurgeons were shown to differentiate between glioma and normal cells. After its binding to the cells, a three-dimensional rotating magnetic field was applied, resulting in surgical action and, thus, in removal of the glioma cells (Nair et al. 2010). The major advantage of the nanosurgeon is based in its ability to differentiate between tumor and healthy cells, resulting in the selective removal of the tumor cells without damaging the surrounding healthy tissue.

10.2.3 On-Chip-Based Approaches

As mentioned previously, the number of circulating cancer cells is low in cancer patients who are in the early state of disease (Oita et al. 2010). Thus, new techniques

need to be developed for efficient capturing and enriching of cancer cells and their subsequent sensitive detection.

On-chip assays have to fulfill two essential prerequisites to be applicable in routine clinical diagnostics: they need to have a high capture efficiency combined with excellent purity of the enriched cell populations. On-chip assays have three major advantages compared to other biosensor systems. First, on-chip assays offer a favored ratio of aptamer to the solution under investigation. A bigger volume of solution can be analyzed while requiring fewer detection reagents. Second, the resident time for cell separation is short. Third, due to the nature of aptamers, on-chip aptamer assays can be efficiently recycled what may reduce costs significantly; aptamers are much more stable to heat, pH, and organic solvents than antibodies and can be denaturated and renatured multiple times without significant loss of activity. Phillips et al. (2009) were able to enrich cancer cells in a microfluidic channel modified with sgc8 aptamer to capture CCRF-CEM cells. About 80 % of the cells of interest were captured (capture efficiency) and the purity was 97 % (Phillips et al. 2009). However, since the throughput is too low and the detection not yet optimal, the assay is not applicable for patient samples (Phillips et al. 2009). In a follow-up paper, Xu et al. demonstrated that a microfluidic device subdivided into three regions, each region modified with one type of aptamer (TD05, sgd5, sgc8) specific to one of three leukemia cell lines (Ramos, Toledo, CCRF-CEM), is able to differentiate between the cancer cell lines (Xu et al. 2009). In 2009, Dharmasiri et al. developed a microfluidic device, with PSMA aptamer as a ligand, to isolate and enumerate LNCaP cells (which were used as a model for rare circulating cancer cells) from whole blood. The captured cells were released by trypsination. Both recovery (90 %) and purity (100 %) of cell populations were agreeable with subsequent applications (Dharmasiri et al. 2009). However, despite promising in vitro results, none of the microfluidic devices were tested with clinical samples yet.

Next to enriching cancer cells, it is highly desired to recover viable and physiologically intact cells, which enables cellular analysis by a pathologist. Circulating cancer cells were found to be more susceptive to mechanical stress than cancer cell lines (Liu et al. 2011). Therefore, detaching captured circulating cancer cells using a nondestructive method is necessary for diagnosis in clinical practices (Wan et al. 2011). Cell-specific aptamers, which show temperature-dependent binding, can release their captured targets upon temperature change (Bunka et al. 2010; Sullenger and Gilboa 2002). In this way, an anti-epidermal growth factor receptor (EGFR) aptamer was selected by Ellington et al. in 2010 (Li et al. 2010) and applied for cancer cell isolation followed by microscopic cytology (Wan et al. 2010). Since EGFR is strongly upregulated in a large variety of cancers, this provides a broadly applicable setting to analyze EGFR-dependent cancer cells (Singh and Harris 2005).

Even though a variety of the aptamer-based cell diagnostics are actually designed for clinical applications, none of them is yet used in clinical diagnostics. Aptamers are not limited to detection, but they can furthermore be employed in theragnostic, an approach combining diagnostic and therapy.

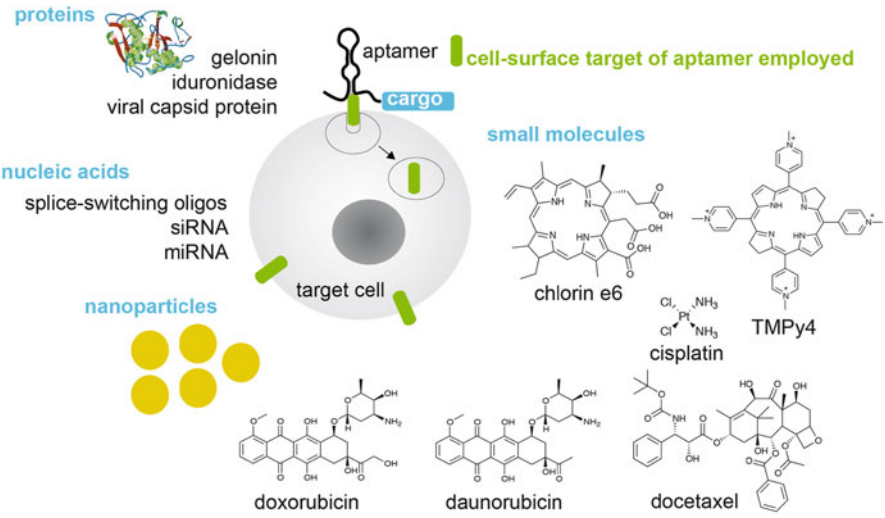

Fig. 10.3 Aptamer-mediated cell—import of various cargo molecules: cell-specific aptamers that are internalized into cells upon target recognition were used as delivery tools for the directed import of various polar molecules. Aptamers have been modified with cargos by covalent bonding, hybridization, or physical conjugation. A variety of cargos like proteins, functional nucleic acids, small molecules, and molecules for photodynamic therapies were successfully delivered via aptamers in a cell-specific manner. Furthermore, aptamer-functionalized nanoparticles were employed as platforms for directed import of multiple molecules. For references see text

10.3 Aptamers as Transport Vehicles

The therapeutic applications of highly polar molecules, such as siRNA, are limited, what is mainly due to their inefficient uptake by cells. A variety of lipids, peptides, and proteins have yet been examined as potential delivery vehicles to overcome this limitation and to facilitate the translocation of polar molecules into cells. For example, siRNAs have been covalently modified with cholesterol (Wolfrum et al. 2007), transferrin (Cardoso et al. 2007), and antibodies (Song et al. 2005) or non-covalently assembled with delivery vehicles, such as folate-conjugated phage RNAs (Guo et al. 2006b). However, most of these targeting molecules lack cellular specificity, and some of them are expensive and time consuming in respect of synthesis. Hence, there is a great demand on delivery molecules combining high specificity and straightforward chemical synthesis. Aptamers combine most of these requirements and consequently have been employed as potential delivery molecules in the recent years. Several groups succeeded in identifying cell-specific aptamers, thereby targeting a plethora of cell-surface receptors. Some of these aptamers have been shown to be actively internalized upon binding to their respective receptor on the cell surface. Therefore, aptamers are highly suitable for the transport of a variety of cargos into specific target cells (Fig. 10.3).

10.3.1 The PSMA Recognizing Aptamer

The most-established and best-characterized aptamers for delivery purposes are the prostate-specific membrane-antigen (PSMA) aptamers A9 and A10, identified by Lupold et al. in 2002 (Lupold et al. 2002). Overexpression of PSMA is correlated with prostate cancer and, thus, is of importance as a diagnostic marker. This integral membrane glycoprotein becomes internalized by endocytosis and, hence, can be used as a protein target for delivery purposes. Farokhzad et al. provided the first report of an aptamer-targeted delivery in 2004, using aptamer-decorated nanoparticles (Farokhzad et al. 2004). They synthesized a functionalized nanoparticle composed of a release polymer coupled to an amine-modified PSMA aptamer (A10) via a carbodiimide coupling on the surface of nanoparticles. As a model drug they encapsulated rhodamine-labeled dextran within those nanoparticles. These nanoparticle–aptamer conjugates significantly are taken up by PSMA-expressing prostate cancer epithelial LNCaP cells. Inversely, they did not enter PSMA-negative PC3 cells. In 2006, this system was taken a significant step further by the same group (Farokhzad et al. 2006). This time, A10-modified nanoparticles loaded with the chemotherapeutic docetaxel (Dtxl) were employed, resulting in a significantly enhanced in vitro cellular toxicity as compared to nontargeted nanoparticles lacking the targeting PSMA aptamer. Furthermore, injection of Dtxl-loaded nanoparticle–aptamer conjugates in subcutaneous prostate cancer xenograft mice resulted in a reduction of the tumor size in vivo. The following years have seen the PSMA aptamer to be continuously used for the cellular delivery of other molecules, such as proteins and siRNA molecules. Chu et al. (2006b) reported the successful delivery of gelonin, a small N-glycosidase protein, which causes cell death by disrupting protein synthesis through cleaving a specific glycosidic bond in rRNA. Aptamer–gelonin conjugates not only showed specific internalization but also decreased toxicity of gelonin. In 2006, two groups independently published the cell-specific import of siRNA molecules using PSMA aptamers. Levy and colleagues modularly assembled siRNA–aptamer–streptavidin complexes via biotin chemistry. The ternary complexes were incubated with prostate cancer cells resulting in a siRNA-mediated inhibition of gene expression of lamina A/C or GAPDH. The efficiency of this aptamer-based import was comparable with the use of conventional lipid-based transfection reagents (Chu et al. 2006c). However, immunogenicity may limit the use of streptavidin as a delivery molecule. Therefore, Giangrande et al. developed an approach to covalently append the PSMA aptamer A10 with the sense strand of a siRNA molecule specific for Bcl-2 mRNA (McNamara et al. 2006). Consequently, a chimeric molecule could be generated, which bears a targeting (aptamer) as well as a silencing (siRNA) moiety. The resulting aptamer–siRNA chimera specifically targets prostate cancer cells (LNCaP) and, additionally, acts as a substrate for Dicer resulting in cell-type-specific silencing of antiapoptotic genes, both in vitro and in vivo. Addition of a two-nucleotide overhang at the 3′ end or swap of the guide and passenger strands results in an optimized chimera with improved silencing and therapeutic efficacy

(Dassie et al. 2009). Wullner et al. (2008) designed a bivalent aptamer-eukaryotic elongation factor 2 (EEF2) targeting siRNA chimera. The design of a chimera with two anti-PSMA aptamers resulted in an increased cellular uptake of siRNAs and an induced EEF2-siRNA-mediated cytotoxicity to prostate cancer cells. During the last years, the interest in aptamer-directed delivery of nanoparticles increased extremely. In 2007, a quantum dot–aptamer–doxorubicin (Dox) conjugate was reported (Bagalkot et al. 2007). The anthracycline intercalates into the double-stranded stem of the aptamer A10, resulting in changes of its fluorescent behavior. Based on this evidence, a donor acceptor system for fluorescence resonance energy transfer (FRET) was developed to sense the release and import of Dox into PSMA-positive prostate tumor cells. The fluorescence of the nanoparticle is quenched when Dox was intercalated, but upon Dox release, the fluorescence of the nanoparticle can be restored (Bagalkot et al. 2007). Farokhazad et al. went a step further and engineered a multifunctional nanoparticle–aptamer conjugate. In this version, the intercalated Dox-aptamer assembly was coupled to docetaxel (Dtxl) nanoparticles. This approach enables the co-delivery of two drugs at the same time (Zhang et al. 2007). In a similar approach, Zhang and coworkers enabled cellular delivery of Dox with A10-modified superparamagnetic iron oxide nanoparticles, allowing treatment and prostate cancer imaging simultaneously (Wang et al. 2008). In 2010, Kim et al. constructed multicomponent nanoplatforms for the co-delivery of small hairpin RNA (shRNA) targeting the antiapoptotic Bcl-2 mRNA combined with Dox (Kim et al. 2010). Therefore, polyplexes were designed that consist of the PSMA aptamer, intercalated Dox, and shRNA. This nanoplatform efficiently and selectively delivered shRNA and the anticancer drug doxorubicin into LNCaP cells. Similarly, an engineered self-assembled nanoparticle allowing the co-delivery of cisplatin and Dtxl to prostate cancer cells was described by Farokhazad and coworkers, which revealed synergistic cytotoxic effects (Kolishetti et al. 2010). However, the use of aptamers for site-specific delivery of anthracyclines in vivo was so far not reported (Fig. 10.4).

10.3.2 Targeting HIV-Infected Cells: The Case of gp120-Binding Aptamers

In 2002, James and coworkers reported the selection of a specific 2′-F-modified RNA aptamer targeting the glycoprotein 120 (gp120) of HIV strain HXB2 (Sayer et al. 2002). This protein plays an important role for the entry of HIV-1 into host cells, whereas it interacts with CD4 and supports the HIV infection by mediating the fusion of the viral with the host cell membrane. Besides Zhou et al. described different aptamers recognizing the HIV-1 glycoprotein of the R5 strain (Khati et al. 2003). Besides their high affinity, these aptamers were also able to inhibit HIV-1 infection of human peripheral blood mononuclear cells (Khati et al. 2003). A few years later, aptamer-siRNA chimeras were generated (Zhou et al. 2009),

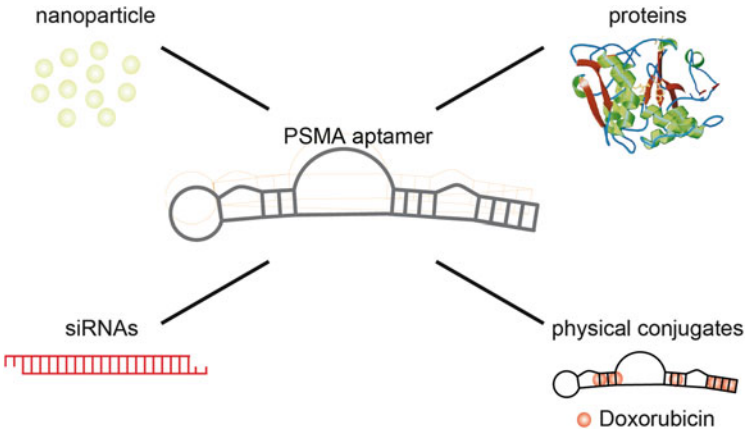

Fig. 10.4 The PSMA aptamer as delivery tool: an RNA aptamer against the prostate membrane antigen (PSMA) serves as delivery vehicle for the import of polar molecules such as doxorubicin (Bagalkot et al. 2006). The PSMA receptor gets internalized via endocytosis, transporting the bound aptamer gelonin (Chu et al. 2006b) complex into the cells (figure modified from Hosur et al. 1995), siRNA (McNamara et al. 2006) against a variety of target mRNAs, or nanoparticles (Farokhzad et al. 2004) to prostate cancer cells

employing gp120 aptamers and HIV-1-specific siRNA molecules. In this approach, aptamer–siRNA chimeras were produced from corresponding double-stranded DNA templates by in vitro transcription, and the functional siRNA duplex was obtained through hybridization with a cognate RNA strand. The anti-gp120-siRNA chimera was not only effective in inhibiting HIV infection of host cells but also Dicer-processed the siRNA domain. Therefore, this chimera represents a dual function molecule in which the aptamer and siRNA portion have potent anti-HIV activities. The group of Rossi selected different aptamers targeting the gp120 protein (Zhou et al. 2009). Based on two of these, they created a series of anti-gp120 aptamer–siRNA chimeras with dual inhibitory function through introduction of a sticky sequence to the aptamer. These sticky sequences were used to modularly conjugate various siRNA molecules (e.g., HIV-1 tat/rev, CD4, and transportin 3-targeting siRNA). The use of Chinese hamster ovary (CHO) cells stably expressing the precursor protein of gp120 (gp160) revealed that these conjugates were internalized into HIV-gp160-positive cells. The siRNA portion was processed by Dicer what results in inhibition of HIV-1 replication and, thus, reducing the infectivity of T cells and primary blood mononuclear cells (PBMCs). Antiviral activity of the gp120 aptamer–siRNA chimera was further analyzed in humanized mouse models. The treatment with either the anti-gp120 aptamer or the aptamer–siRNA, respectively, suppressed HIV-1 replication, whereas the aptamer–siRNA chimera shows a better inhibition and a significantly longer antiviral effect (Neff et al. 2011). To further investigate the adaptability of the anti-gp120 aptamers for the import of various siRNA molecules, Zhou et al. (2011) designed chimeric RNA nanoparticles containing the aptamer coupled to the

packing RNA (pRNA) of the bacteriophage phi29 DNA-packaging motor. These pRNA molecules are able to form dimers, trimers, or hexamers through interaction of interlocking loops. The fusion of the aptamer with pRNA does not affect the ability of the aptamers to bind to its target and, more importantly, inhibit viral replication.

10.3.3 Nucleolin-Targeting G-Quadruplexes

Unlike other cell-specific aptamers, AS1411 was not evolved using SELEX but discovered by testing the possibility of triplex-forming oligodeoxynucleotides to modulate expression of specific genes (Choi et al. 2009). AS1411 is a quadruplex-forming DNA aptamer that recognizes nucleolin and, thus, promotes internalization into cancer cells through hyperstimulation of macropinocytosis (Reyes-Reyes et al. 2010). Once taken up into the cell, AS1411 has been shown to cause a reduction of tumor growth in vitro and in vivo (Ireson and Kelland 2006). As anticancer agent, AS1411 was in clinical trials for the treatment of acute myeloid leukemia (Choi et al. 2009). The target protein of AS1411 is nucleolin, a bcl-2 mRNA-binding protein involved in cell proliferation. The group of Fernandas (Soundararajan et al. 2008) was able to show that AS1411 inhibits the stabilization of the antiapoptotic bcl-2 mRNA and thereby promotes bcl-2 mRNA degradation, which in turn leads to apoptosis. Additionally, AS1411 was reported to alter the localization of the protein arginine methyltransferase 5 (Teng et al. 2007) and to inhibit the activation of nuclear factor-kappaB (Girvan et al. 2006). In 2009, Cao et al. developed an AS1411 aptamer–liposome conjugate, which was able to deliver the chemotherapy drug cisplatin to nucleolin-expressing cancer cells (Cao et al. 2009).

Photodynamic therapy approaches were also realized with AS1411 (Shieh et al. 2010). For that, AS1411 was conjugated with porphyrin-derived molecules, as used during photodynamic therapy regimens, and treatment of MCF-7 breast cancer cells with these conjugates lead to an increased accumulation when compared to nontargeted control cells. Beyond this, nanoparticles were also functionalized with AS1411. As such, the group of Kumar used PLGA–lecithin–PEG nanoparticles coated with AS1411 for the import of the mitotic inhibitor paclitaxel into cancer cells (Aravind et al. 2012). Kim et al. (2012) developed a nanoparticle platform functionalized with AS1411 for the delivery of a microRNA221-molecular beacon, whereas very recently Sullenger et al. described the delivery of so-called splice-switching oligonucleotides to the nucleus of cancer cells (Kotula et al. 2012). They show that these assemblies were delivered to the nucleus and therefore modulate pre-mRNA splicing. Advantageously, AS1411 was not trapped by the endosomal pathway (Kotula et al. 2012). These studies illustrate that AS1411 has been proven to be a useful tool for the delivery of a variety of molecules to tumor cells.

10.3.4 MUC1-Targeting Aptamer

Mucins are glycoproteins expressed by various epithelial cell types protecting the cell surface physicochemically from adverse conditions (Kufe 2009). Additionally, some membrane-associated mucins serve as cell-surface receptors for ligands like lectins, adhesion molecules, or bacteria. Cancer cells revealed differential glycosylation and overexpression of mucins (Hollingsworth and Swanson 2004). These mucins are postulated to protect cancer cells from adverse growth conditions and to control the local molecular microenvironment during invasion and metastasis (Hollingsworth and Swanson 2004). For example, the hydrophobic environment created by increased glycosylation inhibits the ability of some chemotherapeutics to access cancer cells. Furthermore, the interaction of mucins with tumor suppressor proteins, such as p53 (Wei et al. 2005) or Akt (Raina et al. 2004), results in inhibition of apoptosis. Beyond the use as tumor marker, the glycoprotein MUC1 becomes internalized as a result of a recycling processes. Ferreira et al. selected aptamers that bind to MUC1, and in a follow-up study, the aptamers were employed for the specific delivery of chlorin e6 (Ferreira et al. 2009). Chlorin e6 is a natural product of the algae chlorella and used as a photosensitizer during photodynamic therapy. Upon irradiation, an increased toxicity due to produced singlet oxygen species of MUC1-positive cancer cells was observed, when treated with aptamer–chlorin e6 conjugates. Minko and coworkers developed a quantum dot system using the same aptamer for the directed import of Dox into cancer cells, where Dox was coupled to the aptamer via a hydrazone bond (Savla et al. 2011). This arrangement enabled the release of Dox inside the target cells and lead to a higher toxicity when compared with free Dox.

10.3.5 Epidermal Growth Factor Receptor-Targeting Aptamer

The EGF receptor has been shown to be involved in many types of cancer (Singh and Harris 2005). After activation and receptor dimerization, it becomes internalized in a clathrin-dependent manner (Madshus and Stang 2009). Ellington and coworkers selected the RNA aptamer J18, which binds EGFR with high affinity (Li et al. 2010). To prove its delivery properties, the aptamer was coupled to gold nanoparticles. Therefore, a complementary capture oligonucleotide covalently attached on the gold surface was used to attach the aptamer onto the nanoparticle. Using flow cytometry, the aptamer J18 was found to specifically and quantitatively direct the delivery of gold nanoparticles to EGFR-expressing cells. Another aptamer, namely, E07, targeting EGFR was reported in 2011 (Li et al. 2011). This aptamer competes with EGF binding and also inhibits cell proliferation of epidermal carcinoma cells (A431). The human epidermal growth factor receptor 2 (HER-2) was also used as a target for the selection of RNA aptamers. Giangrande

et al. developed a specific SELEX approach for the generation of internalized cell-specific aptamers (Thiel et al. 2012). Consequently, the resultant aptamers were able to deliver siRNA, which targets the antiapoptotic gene Bcl-2 into HER-2-positive cells. In this way, aptamer–siRNA-mediated bcl-2 silencing resensitizes the cells to cisplatin.

10.3.6 Transferrin Receptor Aptamer

As a cell membrane-associated glycoprotein, the transferrin receptor is involved in cellular uptake of iron and the regulation of cell growth (Daniels et al. 2006). This provides potential for the transferrin-mediated delivery of anticancer drugs into cells that express the transferrin receptors (Kratz et al. 1998). However, the production of transferrin conjugates is a laborious task. Therefore, alternative targeting molecules are needed that recognize the transferrin receptor and which can be easily modified. Consequently, RNA and DNA aptamers targeting the extracellular domain of the mouse transferrin receptor were identified (Chen et al. 2008), and in a proof-of-concept study, the uptake into fibroblasts of the aptamer was shown. In further experiments, the aptamer was conjugated to a lysosomal enzyme (Iduronidase) (Chen et al. 2008). In lysosomal storage diseases, the lack of lysosomal enzymes leads to an accumulation of their respective substrates. Consequently, the delivery of functional lysosomal enzymes with specific aptamers leads to a reduction of substrates in the lysosome and, thus, provides a basis for developing novel treatments (Winchester et al. 2000). Very recently, Levy et al. selected 2′ fluoro-modified RNA aptamers against the human transferrin receptor (CD71), which were readily internalized by human cells (Wilner et al. 2012). In order to assess the potential of the aptamers for delivery approaches, they generate aptamer-functionalized stable nucleic acid lipid particles (Wilner et al. 2012).

10.4 Outlook

Aptamers recognizing cells represent very promising tools for biomedical research. The results and studies described in this book chapter illustrate that cell targeting in general and with aptamers in particular is an emerging field. Aptamers thereby unify chemical and biomedical access and application. The ease by which aptamers can be adapted to various regimens is certainly a strong advantage compared to other targeting ligands, such as antibodies. Chemical modifications of aptamers are nowadays widely used, employed to enhance stability and pharmacological profiles and to facilitate detection and monitoring of aptamers in vivo and in vitro. These results promise a broad future for aptamer-based applications, which however will be only met when robust processes become available for the routine generation of

aptamers even without the in-depth knowledge of an aptamer expert. We believe that due to their sophisticated properties, aptamers will finally make their way into diagnostic and therapeutic areas.

References

Abdelhaleem M (2005) RNA helicases: regulators of differentiation. Clin Biochem 38:499–503
Alberts B et al (2008) Molecular biology of the cell. Garland, New York
Alivisatos AP (1996) Semiconductor clusters, nanocrystals, and quantum dots. Science 271:933–937
Aravind A et al (2012) AS1411 aptamer tagged PLGA-lecithin-PEG nanoparticles for tumor cell targeting and drug delivery. Biotechnol Bioeng. doi:10.1002/bit.24558
Bagalkot V, Farokhzad OC, Langer R, Jon S (2006) An aptamer–doxorubicin physical conjugate as a novel targeted drug-delivery platform. Angew Chem Int Ed Engl 45:8149–8152
Bagalkot V et al (2007) Quantum dot–aptamer conjugates for synchronous cancer imaging, therapy, and sensing of drug delivery based on bi-fluorescence resonance energy transfer. Nano Lett 7:3065–3070
Bamrungsap S et al (2012) Pattern recognition of cancer cells using aptamer-conjugated magnetic nanoparticles. ACS Nano 6:3974–3981
Berezovski MV, Lechmann M, Musheev MU, Mak TW, Krylov SN (2008) Aptamer-facilitated biomarker discovery (AptaBiD). J Am Chem Soc 130:9137–9143
Blank M (2001) Systematic evolution of a DNA aptamer binding to rat brain tumor microvessels. Selective targeting of endothelial regulatory protein pigpen. J Biol Chem 276:16464–16468
Bouchard PR, Hutabarat RM, Thompson KM (2010) Discovery and development of therapeutic aptamers. Annu Rev Pharmacol Toxicol 50:237–257
Bruno JG, Kiel JL (1999) In vitro selection of DNA aptamers to anthrax spores with electrochemiluminescence detection. Biosens Bioelectron 14:457–464
Bunka DH, Platonova O, Stockley PG (2010) Development of aptamer therapeutics. Curr Opin Pharmacol 10:557–562
Cao Z et al (2009) Reversible cell-specific drug delivery with aptamer-functionalized liposomes. Angew Chem Int Ed Engl 48:6494–6498
Cardoso ALC et al (2007) siRNA delivery by a transferrin-associated lipid-based vector: a non-viral strategy to mediate gene silencing. J Gene Med 9:170–183
Cerchia L et al (2005) Neutralizing aptamers from whole-cell SELEX inhibit the RET receptor tyrosine kinase. PLoS Biol 3:e123
Cerchia L, Esposito CL, Jacobs AH, Tavitian B, de Franciscis V (2009) Differential SELEX in human glioma cell lines. PLoS One 4:e7971
Charlton J, Sennello J, Smith D (1997) In vivo imaging of inflammation using an aptamer inhibitor of human neutrophil elastase. Chem Biol 4:809–816
Chen CH (2003) Inhibition of heregulin signaling by an aptamer that preferentially binds to the oligomeric form of human epidermal growth factor receptor-3. Proc Natl Acad Sci USA 100:9226–9231
Chen CB et al (2008) Aptamer-based endocytosis of a lysosomal enzyme. Proc Natl Acad Sci USA 105:15908–15913
Choi EW, Nayak LV, Bates PJ (2009) Cancer-selective antiproliferative activity is a general property of some G-rich oligodeoxynucleotides. Nucleic Acids Res 38:1623–1635
Chu TC et al (2006a) Labeling tumor cells with fluorescent nanocrystal–aptamer bioconjugates. Biosens Bioelectron 21:1859–1866
Chu TC et al (2006b) Aptamer: toxin conjugates that specifically target prostate tumor cells. Cancer Res 66:5989

Chu TC, Twu KY, Ellington AD, Levy M (2006c) Aptamer mediated siRNA delivery. Nucleic Acids Res 34:e73
Cristofanilli M et al (2004) Circulating tumor cells, disease progression, and survival in metastatic breast cancer. N Engl J Med 351:781–791
Cruz JA, Westhof E (2011) Sequence-based identification of 3D structural modules in RNA with RMDetect. Nat Methods 8:513–519
Daniels TR, Delgado T, Rodriguez JA, Helguera G, Penichet ML (2006) The transferrin receptor part I: biology and targeting with cytotoxic antibodies for the treatment of cancer. Clin Immunol 121:144–158
Dassie JP et al (2009) Systemic administration of optimized aptamer-siRNA chimeras promotes regression of PSMA-expressing tumors. Nat Biotechnol 27:839–846
Dharmasiri U et al (2009) Highly efficient capture and enumeration of low abundance prostate cancer cells using prostate-specific membrane antigen aptamers immobilized to a polymeric microfluidic device. Electrophoresis 30:3289–3300
Dougan H et al (2003) Evaluation of DNA aptamers directed to thrombin as potential thrombus imaging agents. Nucl Med Biol 30:61–72
Drolet DW et al (2000) Pharmacokinetics and safety of an anti-vascular endothelial growth factor aptamer (NX1838) following injection into the vitreous humor of rhesus monkeys. Pharm Res 17:1503–1510
Dwivedi HP, Smiley RD, Jaykus L-A (2010) Selection and characterization of DNA aptamers with binding selectivity to Campylobacter jejuni using whole-cell SELEX. Appl Microbiol Biotechnol 87:2323–2334
Ellington AD, Szostak JW (1990) In vitro selection of RNA molecules that bind specific ligands. Nature 346:818–822
Eyetech Study Group (2002) Preclinical and phase 1A clinical evaluation of an anti-VEGF pegylated aptamer (EYE001) for the treatment of exudative age-related macular degeneration. Retina 22:143–152
Farokhzad OC et al (2004) Nanoparticle-aptamer bioconjugates. Cancer Res 64:7668
Farokhzad OC et al (2006) Targeted nanoparticle-aptamer bioconjugates for cancer chemotherapy in vivo. Proc Natl Acad Sci USA 103(16):6315–6320
Ferreira CSM, Cheung MC, Missailidis S, Bisland S, Gariépy J (2009) Phototoxic aptamers selectively enter and kill epithelial cancer cells. Nucleic Acids Res 37:866–876
Girvan AC et al (2006) AGRO100 inhibits activation of nuclear factor-kappaB (NF-kappaB) by forming a complex with NF-kappaB essential modulator (NEMO) and nucleolin. Mol Cancer Ther 5:1790–1799
Greenlee RT, Hill-Harmon MB, Murray T, Thun M (2001) Cancer statistics, 2001. CA Cancer J Clin 51:15–36
Guo K-T et al (2006a) A new technique for the isolation and surface immobilization of mesenchymal stem cells from whole bone marrow using high-specific DNA aptamers. Stem Cells 24:2220–2231
Guo S, Huang F, Guo P (2006b) Construction of folate-conjugated pRNA of bacteriophage phi29 DNA packaging motor for delivery of chimeric siRNA to nasopharyngeal carcinoma cells. Gene Ther 13:814–820
Hamula CLA, Le XC, Li X-F (2011) DNA aptamers binding to multiple prevalent M-types of streptococcus pyogenes. Anal Chem 83:3640–3647
Healy JM et al (2004) Pharmacokinetics and biodistribution of novel aptamer compositions. Pharm Res 21:2234–2246
Hermann T (2000) Adaptive recognition by nucleic acid aptamers. Science 287:820–825
Hicke BJ (2001) Tenascin-C aptamers are generated using tumor cells and purified protein. J Biol Chem 276:48644–48654
Hollingsworth MA, Swanson BJ (2004) Mucins in cancer: protection and control of the cell surface. Nat Rev Cancer 4:45–60

Homann M, Göringer HU (1999) Combinatorial selection of high affinity RNA ligands to live African trypanosomes. Nucleic Acids Res 27:2006–2014
Hosur MV et al (1995) X-ray structure of gelonin at 1.8 A resolution. J Mol Biol 250:368–380
Huang Y-F, Lin Y-W, Lin Z-H, Chang H-T (2008) Aptamer-modified gold nanoparticles for targeting breast cancer cells through light scattering. J Nanopart Res 11:775–783
Ireson CR, Kelland LR (2006) Discovery and development of anticancer aptamers. Mol Cancer Ther 5:2957–2962
Jaiswal JK, Mattoussi H, Mauro JM, Simon SM (2002) Long-term multiple color imaging of live cells using quantum dot bioconjugates. Nat Biotechnol 21:47–51
Jhiang SM (2000) The RET proto-oncogene in human cancers. Oncogene 19:5590–5597
Josic D, Clifton JG, Kovac S, Hixson DC (2008) Membrane proteins as diagnostic biomarkers and targets for new therapies. Curr Opin Mol Ther 10:116–123
Khati M et al (2003) Neutralization of infectivity of diverse R5 clinical isolates of human immunodeficiency virus type 1 by gp120-binding 2′ F-RNA aptamers. J Virol 77:12692–12698
Kim E et al (2010) Prostate cancer cell death produced by the co-delivery of Bcl-xL shRNA and doxorubicin using an aptamer-conjugated polyplex. Biomaterials 31:4592–4599
Kim JK, Choi KJ, Lee M, Jo M, Kim S (2012) Molecular imaging of a cancer-targeting theragnostics probe using a nucleolin aptamer-and microRNA-221 molecular beacon-conjugated nanoparticle. Biomaterials 33(1):207–217, http://www.sciencedirect.com/science/article/pii/S0142961211010647
Knudson AG (2002) Cancer genetics. Am J Med Genet 111:96–102
Kolishetti N et al (2010) Engineering of self-assembled nanoparticle platform for precisely controlled combination drug therapy. Proc Natl Acad Sci USA 107:17939–17944
Kotula JW et al (2012) Aptamer-mediated delivery of splice-switching oligonucleotides to the nuclei of cancer cells. Nucleic Acid Ther 22:187–195
Kratz F et al (1998) Transferrin conjugates of doxorubicin: synthesis, characterization, cellular uptake, and in vitro efficacy. J Pharm Sci 87:338–346
Kufe DW (2009) Mucins in cancer: function, prognosis and therapy. Nat Rev Cancer 9:874–885
Kumar V, Abbas AK, Fausto N, Mitchell RN (2007) Robbins basic pathology. Elsevier, Philadelphia, PA
Kurreck J (2002) Design of antisense oligonucleotides stabilized by locked nucleic acids. Nucleic Acids Res 30:1911–1918
Li N, Larson T, Nguyen HH, Sokolov KV, Ellington AD (2010) Directed evolution of gold nanoparticle delivery to cells. Chem Commun (Camb) 46(392–394)
Li N, Nguyen HH, Byrom M, Ellington AD (2011) Inhibition of cell proliferation by an anti-EGFR aptamer. PLoS One 6:e20299
Liu W, Wei H, Lin Z, Mao S, Lin J-M (2011) Rare cell chemiluminescence detection based on aptamer-specific capture in microfluidic channels. Biosens Bioelectron 28:438–442
López-Colón D, Jiménez E, You M, Gulbakan B, Tan W (2011) Aptamers: turning the spotlight on cells. Wiley Interdiscip Rev Nanomed Nanobiotechnol 3:328–340
Lupold SE, Hicke BJ, Lin Y, Coffey DS (2002) Identification and characterization of nuclease-stabilized RNA molecules that bind human prostate cancer cells via the prostate-specific membrane antigen. Cancer Res 62:4029–4033
Madshus IH, Stang E (2009) Internalization and intracellular sorting of the EGF receptor: a model for understanding the mechanisms of receptor trafficking. J Cell Sci 122:3433–3439
Mann D, Reinemann C, Stoltenburg R, Strehlitz B (2005) In vitro selection of DNA aptamers binding ethanolamine. Biochem Biophys Res Commun 338:1928–1934
McNamara JO et al (2006) Cell type-specific delivery of siRNAs with aptamer-siRNA chimeras. Nat Biotechnol 24:1005–1015
Meyer C, Hahn U, Rentmeister A (2011) Cell-specific aptamers as emerging therapeutics. J Nucleic Acids 2011:1–18
Mi J et al (2009) In vivo selection of tumor-targeting RNA motifs. Nat Chem Biol 6:22–24

Michalet X (2005) Quantum dots for live cells, in vivo imaging, and diagnostics. Science 307:538–544
Morris KN, Jensen KB, Julin CM, Weil M, Gold L (1998) High affinity ligands from in vitro selection: complex targets. Proc Natl Acad Sci USA 95:2902–2907
Müller J et al (2009) An exosite-specific ssDNA aptamer inhibits the anticoagulant functions of activated protein C and enhances inhibition by protein C inhibitor. Chem Biol 16:442–451
Murray CB, Norris DJ, Bawendi MG (1993) Synthesis and characterization of nearly monodisperse CdE (E = sulfur, selenium, tellurium) semiconductor nanocrystallites. J Am Chem Soc 115:8706–8715
Nair BG et al (2010) Aptamer conjugated magnetic nanoparticles as nanosurgeons. Nanotechnology 21:455102
Neff CP et al (2011) An aptamer-siRNA chimera suppresses HIV-1 viral loads and protects from helper CD4(+) T cell decline in humanized mice. Sci Transl Med 3:66ra6
Nicol C, Bunka DHJ, Blair GE, Stonehouse NJ (2011) Effects of single nucleotide changes on the binding and activity of RNA aptamers to human papillomavirus 16 E7 oncoprotein. Biochem Biophys Res Commun 405:417–421
Ohuchi SP, Ohtsu T, Nakamura Y (2006) Selection of RNA aptamers against recombinant transforming growth factor-β type III receptor displayed on cell surface. Biochimie 88:897–904
Oita I et al (2010) Microfluidics in macro-biomolecules analysis: macro inside in a nano world. Anal Bioanal Chem 398:239–264
Orr RM (2001) Technology evaluation: fomivirsen. Isis Pharmaceuticals Inc/CIBA vision. Curr Opin Mol Ther 3:288–294
Pan W et al (1995) Isolation of virus-neutralizing RNAs from a large pool of random sequences. Proc Natl Acad Sci USA 92:11509–11513
Peng XG et al (2000) Shape control of CdSe nanocrystals. Nature 404:59–61
Phillips JA, Xu Y, Xia Z, Fan ZH, Tan W (2009) Enrichment of cancer cells using aptamers immobilized on a microfluidic channel. Anal Chem 81:1033–1039
Raddatz ML et al (2008) Enrichment of cell-targeting and population-specific aptamers by fluorescence-activated cell sorting. Angew Chem Int Ed Engl 47:5190–5193
Raina D, Kharbanda S, Kufe D (2004) The MUC1 oncoprotein activates the anti-apoptotic phosphoinositide 3-kinase/Akt and Bcl-xL pathways in rat 3Y1 fibroblasts. J Biol Chem 279:20607–20612
Reyes-Reyes EM, Teng Y, Bates PJ (2010) A new paradigm for aptamer therapeutic AS1411 action: uptake by macropinocytosis and its stimulation by a nucleolin-dependent mechanism. Cancer Res 70:8617–8629
Sanders CR, Myers JK (2004) Disease-related misassembly of membrane proteins. Annu Rev Biophys Biomol Struct 33:25–51
Savla R, Taratula O, Garbuzenko O, Minko T (2011) Tumor targeted quantum dot-mucin 1 - aptamer-doxorubicin conjugate for imaging and treatment of cancer. J Control Release 153:16–22
Sayer N, Ibrahim J, Turner K, Tahiri-Alaoui A, James W (2002) Structural characterization of a 2′ F-RNA aptamer that binds a HIV-1 SU glycoprotein, gp120. Biochem Biophys Res Commun 293:924–931
Sefah K et al (2009) Molecular recognition of acute myeloid leukemia using aptamers. Leukemia 23:235–244
Shamah SM, Healy JM, Cload ST (2008) Complex target SELEX. Acc Chem Res 41:130–138
Shangguan D et al (2006) Aptamers evolved from live cells as effective molecular probes for cancer study. Proc Natl Acad Sci USA 103:11838–11843
Shangguan D et al (2008) Identification of liver cancer-specific aptamers using whole live cells. Anal Chem 80:721–728
Shi H et al (2010) In vivo fluorescence imaging of tumors using molecular aptamers generated by cell-SELEX. Chem Asian J 5:2209–2213

Shieh YA, Yang SJ, Wei MF, Shieh MJ (2010) Aptamer-based tumor-targeted drug delivery for photodynamic therapy. ACS Nano 4:1433–1442
Singh AB, Harris RC (2005) Autocrine, paracrine and juxtacrine signaling by EGFR ligands. Cell Signal 17:1183–1193
Smith JE et al (2007) Aptamer-conjugated nanoparticles for the collection and detection of multiple cancer cells. Anal Chem 79:3075–3082
Song E et al (2005) Antibody mediated in vivo delivery of small interfering RNAs via cell-surface receptors. Nat Biotechnol 23:709–717
Soundararajan S, Chen W, Spicer EK, Courtenay-Luck N, Fernandes DJ (2008) The nucleolin targeting aptamer AS1411 destabilizes Bcl-2 messenger RNA in human breast cancer cells. Cancer Res 68:2358–2365
Stoltenburg R, Reinemann C, Strehlitz B (2007) SELEX – A (r)evolutionary method to generate high-affinity nucleic acid ligands. Biomol Eng 24:381–403
Storhoff JJ, Elghanian R, Mucic RC, Mirkin CA, Letsinger RL (1998) One-pot colorimetric differentiation of polynucleotides with single base imperfections using gold nanoparticle probes. J Am Chem Soc 120:1959–1964
Sullenger BA, Gilboa E (2002) Emerging clinical applications of RNA. Nature 418:252–258
Tang Z et al (2007) Selection of aptamers for molecular recognition and characterization of cancer cells. Anal Chem 79:4900–4907
Teng Y et al (2007) AS1411 alters the localization of a complex containing protein arginine methyltransferase 5 and nucleolin. Cancer Res 67:10491–10500
Thiel KW et al (2012) Delivery of chemo-sensitizing siRNAs to HER2+-breast cancer cells using RNA aptamers. Nucleic Acids Res 40:6319–6337
Tuerk C, Gold L (1990) Systematic evolution of ligands by exponential enrichment: RNA ligands to bacteriophage T4 DNA polymerase. Science 249:505–510
Tuerk C, MacDougal S, Gold L (1992) RNA pseudoknots that inhibit human immunodeficiency virus type 1 reverse transcriptase. Proc Natl Acad Sci USA 89:6988–6992
Ulrich H (2002) In vitro selection of RNA aptamers that bind to cell adhesion receptors of Trypanosoma cruzi and inhibit cell invasion. J Biol Chem 277:20756–20762
Wallis MG, von Ahsen U, Schroeder R, Famulok M (1995) A novel RNA motif for neomycin recognition. Chem Biol 2:543–552
Wan Y et al (2010) Surface-immobilized aptamers for cancer cell isolation and microscopic cytology. Cancer Res 70:9371–9380
Wan Y et al (2011) Velocity effect on aptamer-based circulating tumor cell isolation in microfluidic devices. J Phys Chem B 115:13891–13896
Wang AZ et al (2008) Superparamagnetic iron oxide nanoparticle-aptamer bioconjugates for combined prostate cancer imaging and therapy. ChemMedChem 3:1311–1315
Wang K-Y, Zeng Y-L, Yang X-Y, Li W-B, Lan X-P (2010) Utility of aptamer-fluorescence in situ hybridization for rapid detection of Pseudomonas aeruginosa. Eur J Clin Microbiol Infect Dis 30:273–278
Wei X, Xu H, Kufe D (2005) Human MUC1 oncoprotein regulates p53-responsive gene transcription in the genotoxic stress response. Cancer Cell 7:167–178
Weissleder R, Ntziachristos V (2003) Shedding light onto live molecular targets. Nat Med 9:123–128
Weissleder R, Pittet MJ (2008) Imaging in the era of molecular oncology. Nature 452:580–589
WHO. Cancer. http://www.who.int/mediacentre/factsheets/fs297/en/
WHO. Early detection of cancer. http://www.who.int/cancer/detection/en/
WHO. Screening for various cancers. http://www.who.int/cancer/detection/variouscancer/en/index.html
Wilner SE et al (2012) An RNA alternative to human transferrin: a new tool for targeting human cells. Mol Ther Nucleic Acids 1:e21
Winchester B, Vellodi A, Young E (2000) The molecular basis of lysosomal storage diseases and their treatment. Biochem Soc Trans 28:150–154

Wolfrum C et al (2007) Mechanisms and optimization of in vivo delivery of lipophilic siRNAs. Nat Biotechnol 25:1149–1157

Wu CCN et al (2003) Selection of oligonucleotide aptamers with enhanced uptake and activation of human leukemia B cells. Hum Gene Ther 14:849–860

Wullner U et al (2008) Cell-specific induction of apoptosis by rationally designed bivalent aptamer-siRNA transcripts silencing eukaryotic elongation factor 2. Curr Cancer Drug Targets 8:554–565

Xu Y et al (2009) Aptamer-based microfluidic device for enrichment, sorting, and detection of multiple cancer cells. Anal Chem 81:7436–7442

Zhang L et al (2007) Co-delivery of hydrophobic and hydrophilic drugs from nanoparticle-aptamer bioconjugates. ChemMedChem 2:1268–1271

Zhou J et al (2009) Selection, characterization and application of new RNA HIV gp 120 aptamers for facile delivery of Dicer substrate siRNAs into HIV infected cells. Nucleic Acids Res 37:3094–3109

Zhou J, Shu Y, Guo P, Smith DD, Rossi JJ (2011) Dual functional RNA nanoparticles containing phi29 motor pRNA and anti-gp120 aptamer for cell-type specific delivery and HIV-1 inhibition. Methods 54:284–294

Part VI
Application in Nanobiosensors

Chapter 11
Nucleic Acid Sequencing and Analysis with Nanopores

Slaven Garaj

Abstract It has recently been recognized that solid-state nanopores in single-atomic-layer graphene membranes can be used to electronically detect and characterize single long charged polymer molecules. We have now fabricated nanopores in single-layer graphene that are closely matched to the diameter of a double-stranded DNA molecule. Ionic current signals during electrophoretically driven translocation of DNA through these nanopores were experimentally explored and theoretically modeled. Our experiments show that these nanopores have unusually high sensitivity (0.65 nA/Å) to extremely small changes in the translocating molecule's outer diameter. Such atomically short graphene nanopores can also resolve nanoscale-spaced molecular structures along the length of a polymer, but they do so with greatest sensitivity only when the pore and molecule diameters are closely matched. Modeling confirms that our most closely matched pores have an inherent resolution of $\leq$0.6 nm along the length of the molecule.

Contents

S. Garaj (✉)
Department of Physics, National University of Singapore, 2 Science Drive 3, Singapore 117542, Singapore

Department of Bioengineering, National University of Singapore, 9 Engineering Drive 1, Singapore 117576, Singapore

Graphene Research Center, National University of Singapore, Singapore 117456, Singapore

Nanoscience & Nanotechnology Initiative (NUSNNI), National University of Singapore, 2 Engineering Drive 3, Singapore 117581, Singapore
e-mail: slaven@nus.edu.sg

J. KJEMS et al. (eds.), *Nucleic Acid Nanotechnology*, Nucleic Acids and Molecular Biology 29, DOI 10.1007/978-3-642-38815-6_11,

11.1 Introduction

Probably one of the most important advances that will define the scientific progress in the first quarter of the twenty-first century is the development of methods for reliable, inexpensive, and fast readout of the nucleic acid sequences and large-scale deciphering of the genetic codes. Fifty years after the discovery of the DNA structure, the systematic effort to read out individual human genome, Human Genome Project (HGP), was finalized (Human Genome Sequencing Consortium I 2004) in 2004 after 15 years of concentrated efforts and the expenditure approaching three billion US dollars. Since then, the torrent of technological developments lowered the price of full mammalian genome sequencing by several orders of magnitude (http://www.genome.gov/sequencingcosts/). The continuous increase in affordability made the DNA sequencing tools available to the general scientific community, revolutionizing biomedical and agricultural sciences, anthropology, history, and many other scientific endeavors. It shaped our view of us as humans and on our place within the natural order (Human Genome Sequencing Consortium I 2004; Green et al. 2010; Krause et al. 2010).

The next revolution arising from DNA sequencing will happen when the full-genome sequencing technology becomes affordable enough to make a step from the research laboratories to hospitals, for use in health care, predictive, and personalized medicine. To achieve this, according to National Human Genome Research Institute (Schloss 2008), the price tag for full-genome de novo sequencing should reach of US $1,000. Current cutting-edge technologies (for example, by Illumina or Life Technologies) are still ~2 orders of magnitude more expensive than required. To overcome the price gap, it will not suffice to incrementally improve on the current technologies, but it will require development of new methods based on untapped science. The history of the sequencing industry is a case study of such disruptive technologies, where a technological lifetime of a state-of-art method can be only few years.

Nanopore sequencing is a major contender that could dominate the next cycle of sequencing technologies. The method was proposed (Kasianowicz et al. 1996) already in 1995, and since then the field expanded from the exploratory research to the commercial platform development. The method relies on pulling a long strand of DNA molecule trough a nanometer-scaled pore and the electrical detection of sequential nucleobases as they pass through the sensing part of the nanopore. It promises a nondestructive, single-molecule sequencing of long strands of ~10^5 nucleobases, and it is highly parallelizable to achieve the whole mammalian genome sequencing in a matter of hours. With all these advantages, several companies are developing nanopore-sequencing platforms, most notably Oxford Nanopore Technologies.

The nanopores are also an important scientific method, releasing a plethora of scientific research in physics, chemistry, and biology of nucleic acids and proteins, as well as in nanofluidics and surface chemistry. With this overview, our aim is to introduce a general reader to the science of nanopore, the most important ideas with direct consequences to nanopore sequencing, and present the outstanding challenged to be solved. Since the nanopore sequencing is highly interdisciplinary research field with constant influx of new ideas, we hope this short review will incited a reader to contribute to the unresolved scientific and technological questions with a fresh look from her/his research field.

11.2 Nanopore Sensor

A nanopore sensor consists of two chamber filled with aqueous salt solution (usually potassium chloride solution), separated by a thin membrane. The membrane is perforated with a single nanometer-scaled pore, which comprises the only path the ions and molecules can use to move between the two reservoirs (Fig. 11.1a). As we apply the bias between the two Ag/AgCl electrodes in opposing reservoirs, the flow of ions through the nanopore is recorded as baseline ionic current.

When a negatively charged DNA molecule is introduced in the negatively bias chamber ("cis-chamber"), it will diffuse through the reservoir until it approaches close enough to the mouth of the nanopore to be captured by its electric field. The combination of the electric field gradient and drag forces linearizes the DNA molecule and it threads through the pore in a single file fashion (Fig. 11.1b). The translocating DNA molecule physically blocks the pore, reducing the area of the nanopore available for ionic flow, which leads to a characteristic transient drop in recorded ionic current ("current blockade"). As the DNA molecule fully translocates into the opposing chamber (trans-chamber), the ionic current through unobstructed pore is reverted to its baseline value (Fig. 11.1c).

The instantaneous value of the current blockade during the DNA translocation is a very sensitive measure of the physical and chemical properties of the section of the DNA molecule that is residing within the pore at that given instant. In the first report of the DNA translocation through a pore in 1996, Branton, Deamer, and coworkers (Deamer and Branton 2002) already proposed that nanopores could be used to detect individual nucleobases in their native sequence by carefully observing their fingerprint in the current blockade. In their pioneering experiment, they used α-hemolysis protein channel in a lipid bilayer membrane as a nanopore to detect many single-stranded DNA molecules.

While the biological nanopores (biopores) still remain in a focus of vibrant research efforts, a solid-state equivalent to biological pores was reported (Li et al. 2001) in 2001—they are pore drilled in insulating silicon nitride (SiN_X)-freestanding membrane. While being chemically and mechanically very robust, solid-state nanopores can be fabricated in a large variety of the dimensions and

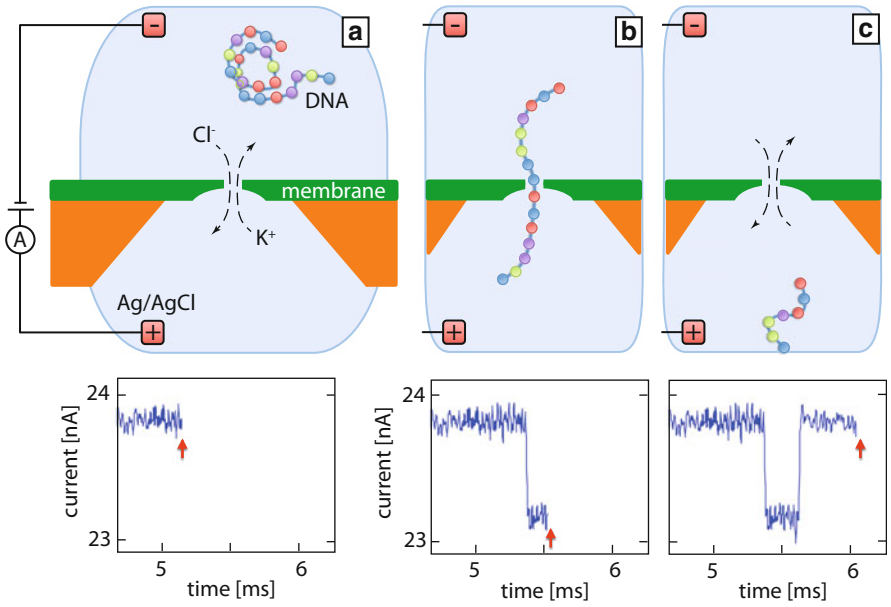

Fig. 11.1 DNA detection by nanopores—schematics: (**a**) nm-scaled pore in a thin membrane is the only connection between two reservoirs filled with aqueous salt solution. As the voltage is applied between the reservoirs, baseline ionic current through nanopore is detected. (**b**) DNA molecule is introduced in negatively bias chamber, and it is electrophoretically driven towards and through the nanopore. As DNA passes through the nanopore in single-file fashion, it physically blocks the flux of ions through the nanopores, resulting in characteristic drip of observable ionic current ("current blockade"). (**c**) When the DNA molecule fully translocates through the nanopore, the ionic current is reverted to its baseline value

shapes, so to be used for variety of applications outside the reach of biopores—including detection of double-stranded DNA molecules (dsDNA), proteins, etc. Finally, a new class of graphene nanopores was reported (Garaj et al. 2010; Schneider et al. 2010; Merchant et al. 2010) in 2010, with rather unique properties: (a) graphene nanopore is formed in atomically thin membrane; (b) the ultrathin structure leads to enhanced ionic flow close to the graphene edges (Garaj et al. 2013) and leads to steep increase in sensitivity; (c) graphene is electrically conductive, so it could be used not only as a membrane material but also as electrical sensor or electrode.

To achieve reproducible sequencing, all nanopore-based platforms, regardless of their nature, need to fulfill the same basic set of requirements (Fig. 11.2):

1. *Robustness*: Every DNA sequencing system has to be durable and robust within its operational conditions; it should have viable, reproducible, and scalable fabrication route.
2. *Sensitivity*: The detector has to have sufficient contrast to distinguish the signals from different types of nucleotides.

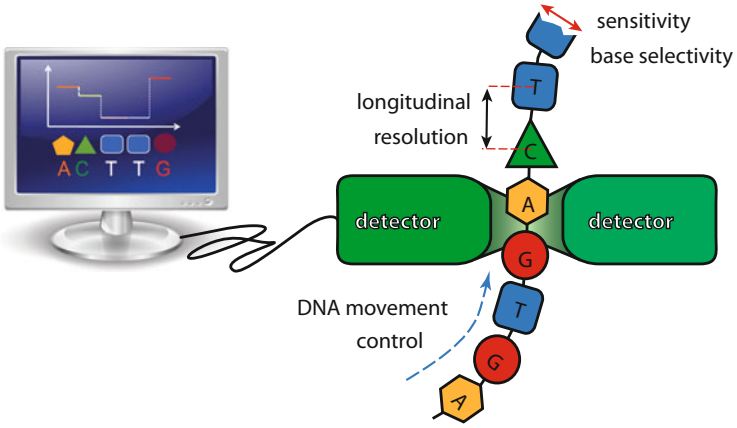

Fig. 11.2 Any successful nanopore-based sequencing platform, regardless of its specifics, has to meet four crucial challenges: (1) nanopore/detector system should be robust and stable in its operating environment, and it should be easily and inexpensively fabricated; (2) sensitivity—detectable and reproducible contrast in signals from different types of nucleobases should be achieved; (3) longitudinal resolution—the detector should be able to resolve individual nucleobases along the length of the molecule; (4) DNA movement control is required to slow down the DNA passage through the pore and to suppress effects of Brownian motion of the molecule

3. *Longitudinal resolution*: The active part of the detector has to have sufficient spatial resolution along the length of the molecule to distinguish a signal from individual nucleotide, without interference from neighboring nucleotides.
4. *DNA movement control*: Freely translocating DNA molecule passes through the nanopore so quickly that individual nucleobases do not dwell within the active part of the detector for long enough time to be properly identified. Furthermore, Brownian motion can thug the molecule back at random times, leading to uncontrolled multiple reads of the same nucleobase (Lu et al. 2011). To avoid these pitfalls, a robust scheme for the controllable ratcheting of the DNA molecule along the active part of the detector is required.

General approach is to tackle all those challenges separately, and the solutions will be combined in the final sequencing device. In the following sections we will introduce different nanopore types in more details and discuss how do they fare against those challenges.

11.3 Biological Nanopores

Biological nanopores (biopores) are self-assembles proteins channels perforating a lipid bilayer membrane. The transmembrane proteins are naturally found in cell membranes; they are responsible for transport of ions or molecules across the membrane or act as lysis-causing cell toxins. Figure 11.3 shows cross section of

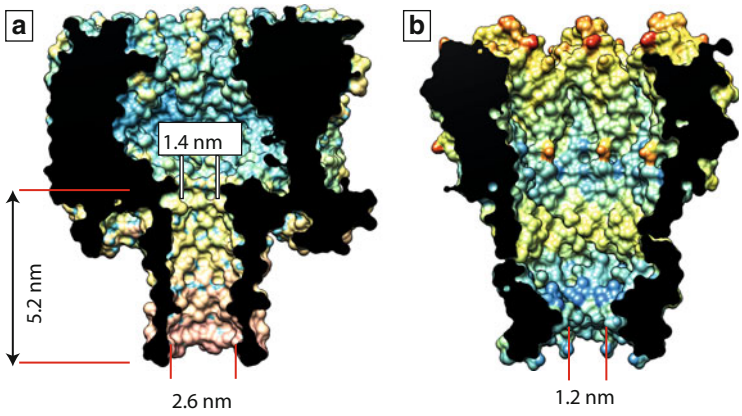

Fig. 11.3 Cross section of the translocation channel for two commonly used protein pores: (**a**) α-hemolysin pore and (**b**) MspA pore. Both pores are incorporated in a lipid membrane separating two reservoirs with analytes. In a typical translocation experiments, the ssDNA molecule enters the nanopore channel from the top

the atomic structure of the two types of biopores that are most widely used in DNA translocation experiments: α-hemolysin and MspA. The shape of self-assembled protein pores is well defined and reproducible to the level of individual atoms, and their structure is deduced with angstrom precision using X-ray crystallography methods. Furthermore, a biopore's sensitivity and selectivity to the translocating DNA molecules can be controlled by modifying electrical charge or hydrophobicity of individual chemical sites on proteins, using modern genetic engineering techniques.

The *α-hemolysin* transmembrane proteins, which occur naturally as an exotoxins excreted by *Staphylococcus aureus* bacteria, were used in the first, pioneering demonstration of ssDNA and RNA translocation through a nanopore (Kasianowicz et al. 1996). The mushroom shaped protein consists of a wide vestibule connected to a narrow β-barrel that perforates the cell membrane. The 5-nm long *β*-barrel has inner diameter of 2.6 nm, but the tightest constriction is at the barrel-vestibule connection, and it is only 1.4 nm wide. The tight constriction in biopores allows only translocation of the ssDNA molecules and excludes dsDNA and other thicker biopolymers. The barrel-shaped geometry of the *α-hemolysin* pore is detrimental to the longitudinal resolution of the biopores sensor: when a long DNA strain spans the nanopore, at least 10–15 nucleobases within the barrel contribute to the averaged ionic-current signal (Meller et al. 2001). The translocation of RNA homopolymers (poly-A and poly-C) reveals the clear difference in the current blockade signal from purine and pyrimidine ribounucleotides, but the difference was attributed to the RNA homopolymers' secondary structure and not the intrinsic nucleotide contrast of the biopores (Akeson et al. 1999). Equivalent experiments with translocation of various DNA homopolymers revealed negligible difference in the resulting ionic current signals from different nucleobases (Meller et al. 2000).

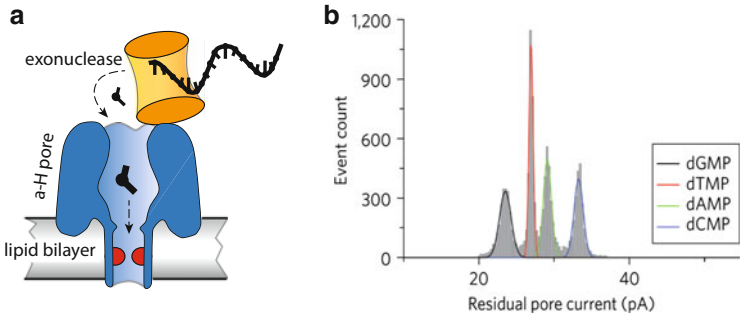

Fig. 11.4 (**a**) Exonuclease sequencing scheme employs an enzyme attached to the mouth of the pore, which is cutting individual nucleotides as it processes a ssDNA molecule. The detached mononucleotides are electrophoretically captured by the pore, and detected individually, thus solving the issue of longitudinal resolution and DNA translocation control. (**b**) Distributions of current blockades associated with different mononucleotides show sufficient contrast for reliable sequencing. The unreliable capture success rate of the digested mononucleotides remains a serious flaw of this method. Figure (**b**) is reproduced with the permission of publishers

All those experiments confirm that the unmodified *α-hemolysin* biopores lacks the required sensitivity and longitudinal resolution for DNA sequencing.

Exonuclease sequencing method is an interesting approach to solving all the above challenges: the scheme involves covalently attaching an exonucluease enzyme at the mouth of the pore, digesting a strand of DNA molecule (Fig 11.4a)—as a mononucleotide is cleaved from the strand, it is electrophoretically captured and driven into the pore. Bayley and coworkers demonstrated that aminocyclodextrin adapter can be covalently attached within *α-hemolysin* barrel, restricting further the narrowest constriction within the pore, and leading to well-defined contrast in detecting unlabeled nucleobases (Astier et al. 2006; Wu et al. 2007), with 99 % of readout confidence (Fig. 11.4b). The combination of the exonuclease cleaving of mononucleotides and their subsequent detection by cyclodextrin-decorated *α-hemolysin* would be poised to solve the challenges of movement control, sensitivity, and longitudinal resolution if it were not for a possibly fatal flaw of this method: the mononucleotide capture success of the pores is incomplete, leading to unacceptably high sequencing error rate.

As *α-hemolysin* pore falls short in terms of resolution and sensitivity, a new type of a proteins pore, *Mycobacterium smegmatis* porin A (MspA), comes into focus. The MspA has a shape of the tapered cone with the smallest constriction of 1.2 nm at the bottom of the cone (Fig 11.3b). Its advantageous geometry alone indicates good sensitivity and resolution. Gundlach and coworkers performed a series of experiments (Derrington et al. 2010; Manrao et al. 2011) with MspA, immobilizing ssDNA oligomer of interest by attaching it to a molecular anchor consisting of a larger biotin–NeutrAvidin complex or dsDNA section. The molecular anchor is too wide to pass through the pore and remains jammed in the upper, wider section of the MspA, whereas ssDNA overhang extends into the pore's active constriction causing the current blockade. Placing different homopolymer ssDNA overhangs within

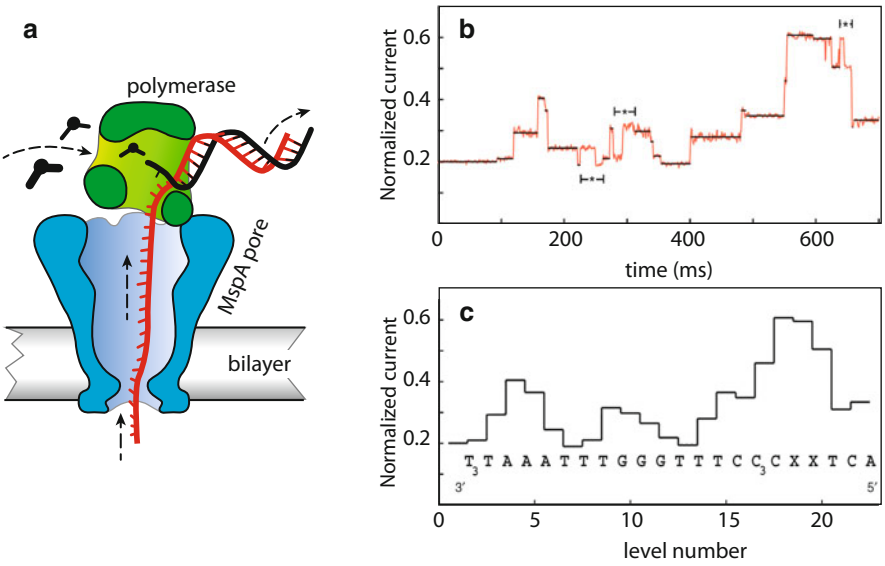

Fig. 11.5 (**a**) Strand sequencing method exploits a polymerase (phi29) enzyme at the nanopore entrance to control the DNA translocation. With a step-wise incorporation of mononucleotides into the double strand, the single-stranded overhang is pulled up through the MspA pore. (**b**) Current trace of a passage of a section of ssDNA molecule in the previously discussed configuration reveals well-separated current levels associated with different nucleobases. (**c**) Mean current of levels extracted from the previous plot, plotted with the associated DNA sequence. Despite its unmatched sensing properties, MspA pore still has longitudinal resolution of ~3 nucleobases, as every current level in influenced by the combined contribution of a nucleotide in the central part of the pore and its two nearest neighbors. Figures (**b**) and (**c**) are reproduced with the permission of publishers

the MspA constriction, they demonstrated extraordinary nucleotide contrast (Derrington et al. 2010), several times more enhanced than in the case of cyclodextrin-decorated *α-hemolysin* pore Next, using engineered overhang homopolymers (i.e., poly-A) with a single nucleotide substitution (i.e., dT) at the varying position along the length of the polymer, they have demonstrated that the longitudinal resolution of MspA pore is ~3 nucleotides (Manrao et al. 2011).

The DNA translocation control via molecular anchor was useful to test the sensing properties of biopores, but it is impractical for DNA sequencing. The alternative strand-sequencing scheme involves coupling enzyme motor (phi29 polymerase) to the biopores (Lieberman et al. 2010; Olasagasti et al. 2010), making it possible to controllably ratchet the ssDNA molecule through the nanopore one nucleotide at the time (Cherf et al. 2012), with current-blockade readout at each step (Fig. 11.5a). Combining phi29 polymerase with MspA pore leads to the impressive readout of a DNA sequence (Fig. 11.5b, c). While the resolution of MspA is far from ideal single-nucleotide resolution, it is not necessary restrictive for DNA sequencing, provided a multiple current-blockade signal levels could be

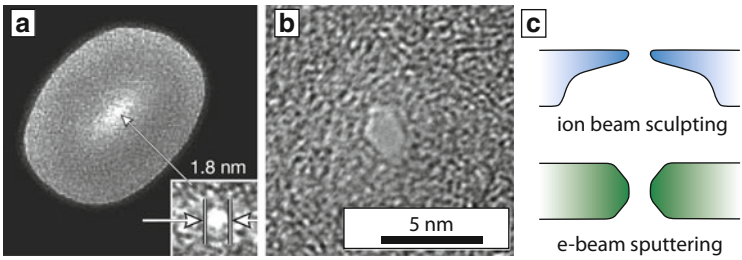

Fig. 11.6 Transmission electron micrographs of solid-state nanopores fabricated by (**a**) ion beam sculpting (Li et al. 2001) and (**b**) electron beam sputtering in TEM (Storm et al. 2003). (**c**) Cross section profile comparison between the nanopores fabricated by the two methods. Figures (**a**) and (**b**) are reproduced with the permission of publishers

distinguished, each corresponding to different combinations of the three nucleotides within the active MspA constriction. If this would be possible with the current MspA pores remains to be seen, while additional mutations of MspA pore could increase the longitudinal resolution even further.

11.4 Solid-State Nanopores

The solid-state equivalents of the protein nanopores were first demonstrated (Li et al. 2001) in 2001 by Golovchenko and coworkers, who fabricated nanometer-sized pores in thin silicon-nitride (SiN_X) membranes using ion-beam sculpting method. The method consists of sputtering a larger pore using focused ion beam and subsequent exposing the pore to lower energy argon ions to induce surface flow of the membrane material, controllably shrinking the pores to the desired size. Currently, the method of choice for nanopore fabrication is the sputtering with the focused electron beam in transmission electron microscope (TEM), which was first applied for DNA analysis by Dekker and coworkers (Storm et al. 2003, 2005). The nanopores fabricated by the two methods (Fig. 11.6) have different cross section, but for most parts they exhibit the equivalent DNA sensing properties. The other methods for nanopore fabrication have been developed since, including conformal closing of the larger pores using atomic layer deposition (Chen et al. 2004), or feedback controlled etching of along the induced defect path through an insulating solid-state membrane (Park et al. 2007).

Advantages of solid-state nanopores, compared to protein pores, are their superior chemical and thermal stability and mechanical durability. Using established micro/nano-fabrication techniques, the solid-state nanopores can be incorporated into versatile sensing platforms that could include additional optical or electrical sensors and actuators, expanding their biosensing applications. Those DNA sequencing schemes will be discussed in more details later.

Whereas the dimensions of the biopores are limited by the properties of their constituting proteins, with pore constriction not exceeding 1.5 nm in diameter, the

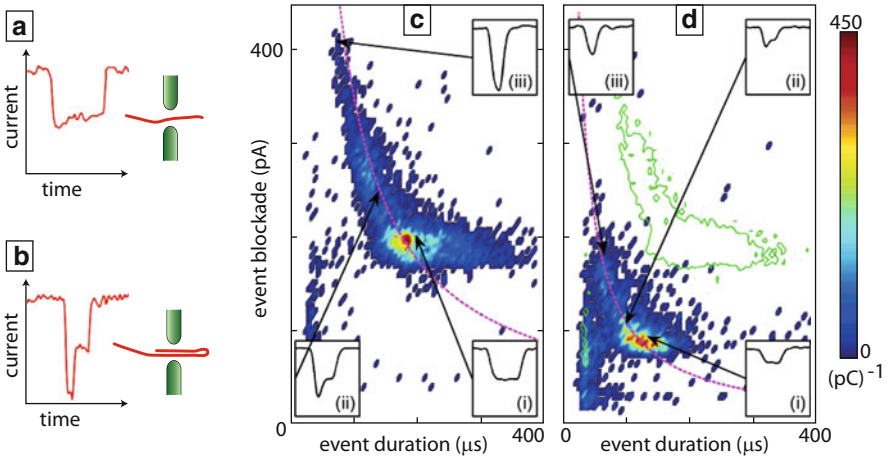

Fig. 11.7 (**a**) Translocation of a fully extended and linearized DNA molecule leads to a current blockade event with well-defined and reproducible current level. (**b**) If a pore is wide enough, a DNA molecule can fold onto itself while entering the pore, leading to stepwise doubling of the current blockade level. (**c**) Distribution of dsDNA translocation events as a function of the translocation time and average current blockade (Fologea et al. 2005). The *color* scheme represents density of events in a given bin. Folded events are clustered in the region of faster translocations and larger blockade. (**d**) Distribution of ssDNA translocation events for the same pore as in (**c**). Figures (**c**) and (**d**) are reproduced with the permission of publishers

solid-state nanopores can be fabricates with a wide range of diameters. Larger nanopore diameters permit detection of dsDNA molecules (Li et al. 2003) (molecular diameter ~2 nm), proteins (Han et al. 2006; Talaga and Li 2009), and DNA–protein complexes (Hall et al. 2009; Raillon et al. 2012); they also allow investigation of the DNA polymer dynamics and confirmations. If a nanopore is wide enough, a folded molecule could be pulled into the pore, leading to the two-step current blockade signal (Fig. 11.7a, b): the current blockade signal doubles during the time a double-folded portion of the molecule resides within the nanopore.

Figure 11.7c shows the distribution of many DNA translocation events through a nanopore defined by their translocation time τ (event duration) and averaged current blockade ΔI_B (event blockade), where the color scale represents a number of translocation events in a given bin. Although folded events have the double average current blockade, they translocate faster such that the total electric charge deficit (ecd $= \Delta I_B \times \tau$) is conserved. Figure 11.7d shows the translocation events through the same pore when the dsDNA is denatured into ssDNA segments by increasing pH of the solution. The distribution for ssDNA events shifts now towards smaller current blockades, mirroring reduced cross section of the denatured DNA molecules. The hyperbolic shape along the constant *ecd* line for dsDNA and ssDNA event distributions indicate that both types of molecules translocate freely through the nanopore, without any interactions with the walls of the nanopore.

The observed velocity of free translocation of DNA molecule is ~15 mm/s (Fig. 11.7c), meaning that each nucleobase resides on average within the pore no longer then 20 ns. This period is insufficient to characterize the base and extract the genetic code. Devising a solid-state method for controllable movement of the molecule throughout the pore is a crucial challenge that has to be solved in order to make solid-state nanopores a viable sequencing technique. Stolovitzky and coworkers from IBM suggested a scheme for controllable DNA movement using very narrow electrodes incorporated within the nanopore (Luan et al. 2010). Applying alternating voltage across the electrodes should controllably ratchet DNA molecules through the nanopore. Numerical calculations suggested that such "DNA chip" scheme should be feasible in principle, but it has not been demonstrated experimentally yet.

The top-down fabrication method for solid-state nanopores offers larger versatility in applications then for biopores, but at the same time it leads to poorer reproducibility of the nanopore geometry. Atomic-level size control found in biopores remains elusive for solid-state nanopores, but it will have to be achieved eventually to make solid-state nanopores a viable candidate for DNA sequencing. Understanding local surface chemistry of solid-state nanopores and achieving controllable surface modification and functionalization, will be crucial to attain sufficient nucleobases selectivity and to avoid stochastic DNA–surface interactions. One possible future route is combination some aspects of biopores with solid-state nanopores, such as coating solid-state nanopores with lipid bilayer (Yusko et al. 2011) or wedging a protein pore within a larger solid-state nanopore (Hall et al. 2010).

11.5 Graphene Nanopores

Graphene is isolated, single atomic layer thin lattice of sp^2-bonded carbon with remarkable physical and chemical properties and high mechanical durability. Large-scale fabrication techniques are able to produce meter-sized sheets of single-layer graphene of high crystallinity. Being the thinnest material possible, graphene is the ultimate membrane for a nanopore detector, with possibly single-nucleotide longitudinal resolution.

As grown graphene membrane, suspended over a window in SiN_X/Si chip and inserted between two electrolyte reservoirs, is an excellent barrier to flow of ions, despite being a single atomic layer thick (Garaj et al. 2010). The membrane remains stable and well sealing even when a voltage in excess of 250 mV is applied between the reservoirs. When a single nanometer pore is fabricated by focusing electron beam in TEM (Fig. 11.8a–d), ionic current across the membrane increases significantly. The resulting ionic conductance of graphene nanopores has a distinctive linear dependence on nanopore diameter (Garaj et al. 2010), as expected for a very thin pore whose resistance to ionic flow is dominated by access resistance (in contrast, thicker SiN_X pores have quadratic diameter dependence). The effective

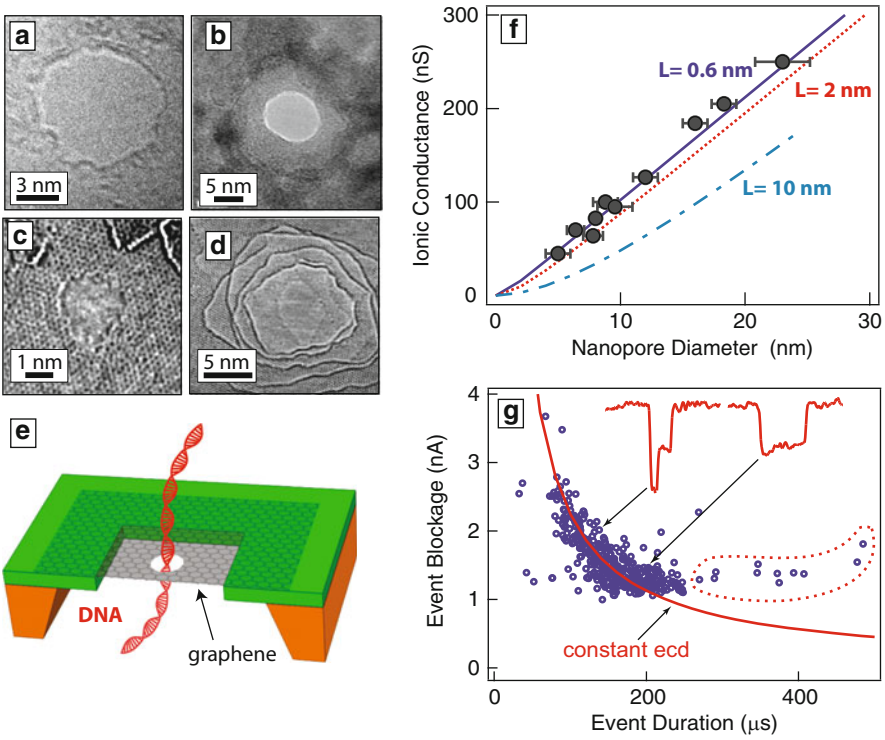

Fig. 11.8 (**a**–**d**) Transmission electron micrograph of different graphene nanopores: (**a**) graphene nanopore fabricated in single-layer graphene membrane by focused electron beam sputtering (Garaj et al. 2010); (**b**) nanopore fabricated in graphene membrane coated with ~8 nm of aluminum oxide (Venkatesan et al. 2012); (**c**) edge-grown graphene nanopore with single-atom control of size (Russo and Golovchenko 2012); (**d**) electron beam sculpted pore at high temperatures (Song et al. 2011), with controllable faceting of nanopore edges. (**e**) Schematics of a nanopore in a single-layer graphene sheet stretched over a window in freestanding SiN_X membrane. (**f**) Linear dependence of ionic conductance vs. the nanopore diameter implies sub-nm effective thickness of graphene membrane in the ionic solution. (**g**) Distribution of translocation events (Garaj et al. 2010) along the curve of constant ecd indicates suppressed of the interaction between the graphene nanopore and DNA molecules at high ionic salt conditions (3 M KCl, pH10). All figures are reproduced with the permission of publishers

thickness of only $L = 0.6$ nm for graphene membrane in electrolyte is deduced from those measurements. The other concurrent studies (Schneider et al. 2010; Merchant et al. 2010) found the much smaller conductance of their graphene nanopores, with square diameter dependence, indicating that their membranes are order of magnitude thicker than expected, probably due to intentional coating of graphene with a polymer intended to reduce DNA sticking or unintentional contamination during the fabrication process.

At high salt concentration (3 M KCl), dsDNA translocates through graphene nanopores uninhibited by interaction with graphene, as seen by the hyperbolic

distribution of the translocation event diagram along ecd line (Fig. 11.8g). The observed mean translocation speed of ~50 bases/μs makes direct readout of bases impossible at this time, but numerical calculation, based on the measured graphene effective thickness, reveals the longitudinal resolution of $\delta z = 0.35$ nm, which is comparable to base separation in DNA molecule. Very recent experiments on the translocation of DNA molecules through small, tightly fitting graphene nanopores (Garaj et al. 2013), reveal that such pores have extremely high sensitivity on the small variation of the diameter of the translocating molecule. Thus, the graphene nanopore can likely achieve the base selectivity required for the DNA sequencing, provided pores' sizes and shapes can be controlled with the atomic precision.

Generally, graphene nanopores are fabricated by sputtering of carbon atoms (Garaj et al. 2010; Schneider et al. 2010; Merchant et al. 2010; Fischbein and Drndic 2008; Girit et al. 2009) with TEM beam at high acceleration voltage (200 kV). This method has insufficient control over nanopore diameter and often leads to asymmetric pore shapes. However, when the drilling process is performed at elevated temperatures in TEM (>600 °C), mobile carbon ad-atoms on the graphene surface controllably repair any electron-induced damage on the carbon surface and lead to pores with well-defined edge facets (Song et al. 2011). Recently, it was demonstrated the graphene pores could be controllably grown atom-by-atom (Russo and Golovchenko 2012) from an induced defect site, by irradiating it with electron beam in energy range that allows it to knock out carbon atom from an edge, but not from the bulk graphene.

A defining property of the graphene membrane, the one that makes graphene nanopores very distinctive from solid-state nanopore, is its high electrical in-plane conductivity. The conductivity is very sensitive to the local chemical and electrostatic environment, due to π orbitals protruding out of the graphene plane, making it ideal electrical sensor. The graphene's sensing properties are the basis of several proposed DNA sequencing scheme that will be discussed in the next section.

11.6 Other Sequencing Methods

Many nanopore sequencing architectures employ ionic current modulation through the nanopore for reading out the localized bases, but there are other, possibly better, or complementary ways for nucleobase identification. A nanopore can be used only to localizing individual nucleobases in a well-defined space, in sequential order, but the nucleotide recognition can be employed using some other method, such as nanopore-integrated electrical sensors or in some cases optical detection of dye-modified bases (see Fig. 11.9). Compared to ionic current detection, such methods often offer larger detection speed, higher signal-to-noise ratio, simple multiplexing, increased longitudinal resolution, etc. In other cases, they might offer in additional readout channel to be combined with ionic current measurements to improve nucleobase recognition.

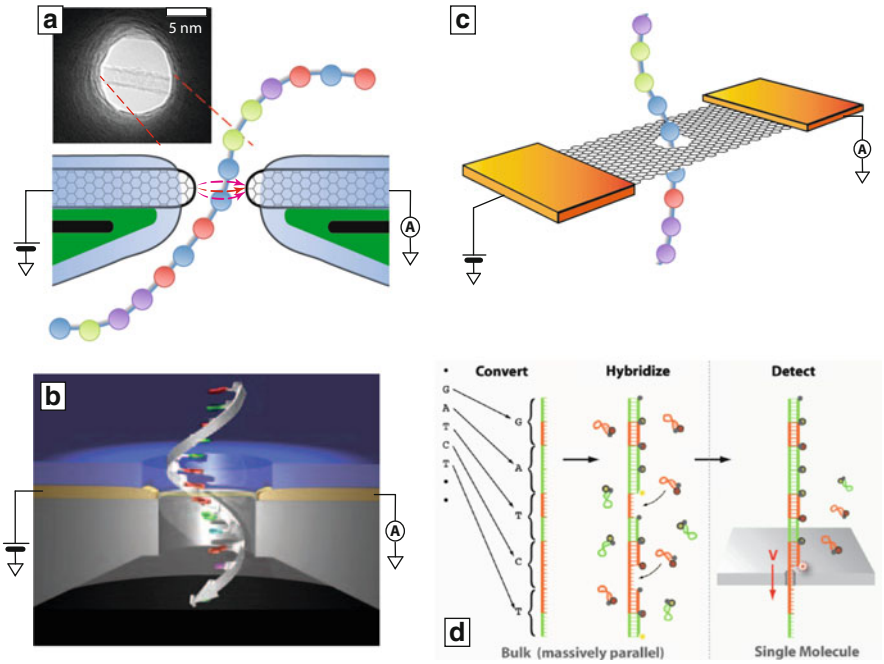

Fig. 11.9 Proposed DNA sequencing schemes based on electrical or optical sensors integrated with the nanopore platform. (**a**) Electrically addressable carbon nanotube, aligned across the nanopore with sub-nanometer precision, can act as field-effect or tunneling sensor for the DNA molecules threading the nanopore (Sadki et al. 2011) (*inset*: TEM image of a nanotube-articulated nanopore). (**b**) Nanopore with embedded two metallic electrodes, separated by 1 nm gap, acting as a tunneling detector (Tsutsui et al. 2010). (**c**) Proposed graphene electrical sensor: translocating DNA molecule modifies transverse electrical current in graphene nanoribbon perforated with a nanopore (Nelson et al. 2010). (**d**) Optopore sequencing: each base of a DNA molecule is biochemically converted into a longer sequence equipped with different optical reporters corresponding to a given nucleobases type. As the sequence is unzipped while passing through a narrow nanopore, the released dies are optically detected (McNally et al. 2010). Figures (**a**), (**c**) and (**d**) are reproduced with the permission of publishers

One class of electrical nanopore detectors is based on integrating gapped electrodes made of carbon nanotubes (Sadki et al. 2011), metal (Ivanov et al. 2011), or graphene (Postma 2010) within the nanopore, and subsequently detecting the variation of the electrical tunneling current between the opposing electrodes during the DNA translocation (Fig. 11.9a, b). In proof-of-principle scanning tunneling experiments, tunneling current signatures from different nucleotide types show discernible contrast (Huang et al. 2010). The integrations of nanotube (Sadki et al. 2011) and metallic (Ivanov et al. 2011) electrodes with nanopores were reported, but integrated nucleotide detection has not been achieved yet. One of the main challenges for the tunneling sensor is its dependence of small geometrical variations that can swap any nucleotide-specific contrast—the current

strongly depends on small variation in distance and orientation of the nucleobases from the electrodes.

11.7 Outlook

With all the exciting development in last years, it is fair to say that the nanopore DNA sequencing is behind the corner. The challenges in DNA sequencing with biopores are solved or they are close to be so; any remaining issues are technical in nature, and there are no basic scientific principles that should prevent nanopore sequencing. Strong nucleotide contrast is achieved with MspA pores (Derrington et al. 2010; Manrao et al. 2012), and robust DNA translocation control has been demonstrated last year using phi29 polymerase motor (Cherf et al. 2012). It still remains an open question if the demonstrated longitudinal resolution of ~3 nucleotides by MspA pore is sufficient for reliable sequencing (Manrao et al. 2011). To distinguish all the combination of three different nucleotides, maximum 64 current levels need to be resolved (the actual number is probably less, since the correlational statistics can be employed). In the case that the current levels of some of the nucleotide-trio combinations are degenerate, the multiple resequencing will not eliminate the resulting systematic error—additional efforts will be needed to increase the longitudinal resolution of the biopores.

Graphene nanopores, as well as some of the electrical sequencing schemes, have a potential for achieving single-nucleotide longitudinal resolution, which is currently lacking in biopores. However, solid-state and graphene nanopores are still far behind biopores in other aspects, lacking in the departments of reproducible and scalable fabrication, translocation control, and nucleotide contrast. Following the current research development and extrapolating future trends, the solid-state and graphene nanopores are on a good trajectory to become a viable second-generation nanopore sequencing technology and to replace biopores in the future on the grounds of price, scalability, and speed.

Acknowledgments We would like to acknowledge financial support from the Singapore National Research Foundation (grant NRF-NRFFOO1-131).

References

Akeson M, Branton D, Kasianowicz JJ et al (1999) Microsecond time-scale discrimination among polycytidylic acid, polyadenylic acid, and polyuridylic acid as homopolymers or as segments within single RNA molecules. Biophys J 77:3227–3233. doi:10.1016/S0006-3495(99)77153-5

Astier Y, Braha O, Bayley H (2006) Toward single molecule DNA sequencing: direct identification of ribonucleoside and deoxyribonucleoside 5′-monophosphates by using an engineered protein nanopore equipped with a molecular adapter. J Am Chem Soc 128:1705–1710. doi:10.1021/ja057123

Chen P, Mitsui T, Farmer DB et al (2004) Atomic layer deposition to fine-tune the surface properties and diameters of fabricated nanopores. Nano Lett 4:1333–1337. doi:10.1021/nl0494001

Cherf GM, Lieberman KR, Rashid H et al (2012) Automated forward and reverse ratcheting of DNA in a nanopore at 5-Å precision. Nat Biotechnol 30:344–348. doi:10.1038/nbt.2147

Deamer DW, Branton D (2002) Characterization of nucleic acids by nanopore analysis. Acc Chem Res 35:817–825. doi:10.1021/ar000138m

Derrington IM, Butler TZ, Collins MD et al (2010) Nanopore DNA sequencing with MspA. Proc Natl Acad Sci USA 107:16060–16065 doi:10.1073/pnas.1001831107

Fischbein MD, Drndic M (2008) Electron beam nanosculpting of suspended graphene sheets. Appl Phys Lett 93:113107. doi:10.1063/1.2980518

Fologea D, Gershow M, Ledden B et al (2005) Detecting single stranded DNA with a solid state nanopore. Nano Lett 5:1905–1909. doi:10.1021/nl051199m

Garaj S, Hubbard W, Reina A et al (2010) Graphene as a subnanometre trans-electrode membrane. Nature 467:190–193. doi:10.1038/nature09379

Garaj S, Liu S, Golovchenko JA, Branton D (2013) Molecule-hugging graphene nanopores. Proc Natl Acad Sci USA - July 8 Early Edition. doi:10.1073/pnas.1220012110

genome.gov. DNA sequencing costs. http://www.genome.gov/sequencingcosts/. Accessed 25 Mar 2013

Girit CO, Meyer JC, Erni R et al (2009) Graphene at the edge: stability and dynamics. Science 323:1705–1708. doi:10.1126/science.1166999

Green RE, Krause J, Briggs AW et al (2010) A draft sequence of the neandertal genome. Science 328:710–722. doi:10.1126/science.1188021

Hall AR, van Dorp S, Lemay SG, Dekker C (2009) Electrophoretic force on a protein-coated DNA molecule in a solid-state nanopore. Nano Lett 9:4441–4445. doi:10.1021/nl9027318

Hall AR, Scott A, Rotem D et al (2010) Hybrid pore formation by directed insertion of α-haemolysin into solid-state nanopores. Nat Nanotechnol 5:874–877. doi:10.1038/nnano.2010.237

Han A, Schürmann G, Mondin G et al (2006) Sensing protein molecules using nanofabricated pores. Appl Phys Lett 88:093901. doi:10.1063/1.2180868

Huang S, He J, Chang S et al (2010) Identifying single bases in a DNA oligomer with electron tunnelling. Nat Nanotechnol 5:868–873. doi:10.1038/nnano.2010.213

Human Genome Sequencing Consortium I (2004) Finishing the euchromatic sequence of the human genome. Nature 431:931–945. doi:10.1038/nature03001

Ivanov AP, Instuli E, McGilvery CM et al (2011) DNA tunneling detector embedded in a nanopore. Nano Lett 11:279–285. doi:10.1021/nl103873a

Kasianowicz J, Brandin E, Branton D, Deamer D (1996) Characterization of individual polynucleotide molecules using a membrane channel. Proc Natl Acad Sci USA 93:13770–13773

Krause J, Fu Q, Good JM et al (2010) The complete mitochondrial DNA genome of an unknown hominin from southern Siberia. Nature 464:894–897. doi:10.1038/nature08976

Li J, Stein D, McMullan C et al (2001) Ion-beam sculpting at nanometre length scales. Nature 412:166–169

Li J, Gershow M, Stein D et al (2003) DNA molecules and configurations in a solid-state nanopore microscope. Nat Mater 2:611–615. doi:10.1038/nmat965

Lieberman KR, Cherf GM, Doody MJ et al (2010) Processive replication of single DNA molecules in a nanopore catalyzed by phi29 DNA polymerase. J Am Chem Soc 132:17961–17972. doi:10.1021/ja1087612

Lu B, Albertorio F, Hoogerheide DP, Golovchenko JA (2011) Origins and consequences of velocity fluctuations during DNA passage through a nanopore. Biophys J 101:70–79. doi:10.1016/j.bpj.2011.05.034

Luan B, Peng H, Polonsky S et al (2010) Base-by-base ratcheting of single stranded DNA through a solid-state nanopore. Phys Rev Lett 104:238103. doi:10.1103/PhysRevLett.104.238103

Manrao EA, Derrington IM, Pavlenok M et al (2011) Nucleotide discrimination with DNA immobilized in the MspA nanopore. PLoS One 6:e25723. doi:10.1371/journal.pone.0025723
Manrao EA, Derrington IM, Laszlo AH et al (2012) Reading DNA at single-nucleotide resolution with a mutant MspA nanopore and phi29 DNA polymerase. Nat Biotechnol 30:349–353. doi:10.1038/nbt.2171
McNally B, Singer A, Yu Z et al (2010) Optical recognition of converted DNA nucleotides for single-molecule DNA sequencing using nanopore arrays. Nano Lett 10:2237–2244. doi:10.1021/nl1012147
Meller A, Nivon L, Brandin E et al (2000) Rapid nanopore discrimination between single polynucleotide molecules. Proc Natl Acad Sci USA 97:1079–1084. doi:10.1073/pnas.97.3.1079
Meller A, Nivon L, Branton D (2001) Voltage-driven DNA translocations through a nanopore. Phys Rev Lett 86:3435–3438. doi:10.1103/PhysRevLett.86.3435
Merchant CA, Healy K, Wanunu M et al (2010) DNA translocation through graphene nanopores. Nano Lett 10:2915–2921. doi:10.1021/nl101046t
Nelson T, Zhang B, Prezhdo OV (2010) Detection of nucleic acids with graphene nanopores: ab initio characterization of a novel sequencing device. Nano Lett 10:3237–3242. doi:10.1021/nl9035934
Olasagasti F, Lieberman KR, Benner S et al (2010) Replication of individual DNA molecules under electronic control using a protein nanopore. Nat Nanotechnol 5:798–806. doi:10.1038/nnano.2010.177
Park SR, Peng H, Ling XS (2007) Fabrication of nanopores in silicon chips using feedback chemical etching. Small 3:116–119. doi:10.1002/smll.200600268
Postma HWC (2010) Rapid sequencing of individual DNA molecules in graphene nanogaps. Nano Lett 10:420–425. doi:10.1021/nl9029237
Raillon C, Cousin P, Traversi F et al (2012) Nanopore detection of single molecule RNAP–DNA transcription complex. Nano Lett 12(3):1157–1164. doi:10.1021/nl3002827
Russo CJ, Golovchenko JA (2012) Atom-by-atom nucleation and growth of graphene nanopores. Proc Natl Acad Sci USA 109:5953–5957. doi:10.1073/pnas.1119827109
Sadki ES, Garaj S, Vlassarev D et al (2011) Embedding a carbon nanotube across the diameter of a solid state nanopore. J Vac Sci Technol B 29:053001-1–053001-4. doi:10.1116/1.3628602
Schloss JA (2008) How to get genomes at one ten-thousandth the cost. Nat Biotechnol 26:1113–1115. doi:10.1038/nbt1008-1113
Schneider GF, Kowalczyk SW, Calado VE et al (2010) DNA translocation through graphene nanopores. Nano Lett 10:3163–3167. doi:10.1021/nl102069z
Song B, Schneider GF, Xu Q et al (2011) Atomic-scale electron-beam sculpting of near-defect-free graphene nanostructures. Nano Lett 11:2247–2250. doi:10.1021/nl200369r
Storm A, Chen J, Ling X et al (2003) Fabrication of solid-state nanopores with single-nanometre precision. Nat Mater 2:537–540. doi:10.1038/nmat941
Storm A, Chen J, Zandbergen H, Dekker C (2005) Translocation of double-strand DNA through a silicon oxide nanopore. Phys Rev E Stat Nonlin Soft Matter Phys 71(5 Pt 1):051903. doi:10.1103/PhysRevE.71.051903
Talaga DS, Li J (2009) Single-molecule protein unfolding in solid state nanopores. J Am Chem Soc 131:9287–9297. doi:10.1021/ja901088b
Tsutsui M, Taniguchi M, Yokota K, Kawai T (2010) Identifying single nucleotides by tunnelling current. Nat Nanotechnol 5:286–290. doi:10.1038/nnano.2010.42
Venkatesan BM, Estrada D, Banerjee S et al (2012) Stacked graphene-Al_2O_3 nanopore sensors for sensitive detection of DNA and DNA–protein complexes. ACS Nano 6:441–450. doi:10.1021/nn203769e
Wu H-C, Astier Y, Maglia G et al (2007) Protein nanopores with covalently attached molecular adapters. J Am Chem Soc 129:16142–16148. doi:10.1021/ja0761840
Yusko EC, Johnson JM, Majd S et al (2011) Controlling protein translocation through nanopores with bio-inspired fluid walls. Nat Nanotechnol 6:253–260. doi:10.1038/nnano.2011.12

Chapter 12
Application of Nanomaterials for DNA Sensing

Alfredo de la Escosura-Muñiz and Arben Merkoçi

Abstract DNA sensing technology is taking advantage of the latest developments in materials science and in particular from the nanomaterial field. Because of the outstanding optical, electrical, and electrochemical qualities of nanomaterials, significant developments in the design of novel DNA sensing systems are being undertaken in the last years. Properties of nanoparticles such as light absorption and dispersion are bringing interesting DNA sensing alternatives. Electrochemical sensing techniques are also taking advantage of electrical properties of nanoparticles. In most cases nanoparticle-based DNA sensing systems are being offered as excellent screening and better alternatives to existing conventional strategies/assays with interest for point-of-care clinical analysis, food quality, safety, and security applications.

Future investigations in this area are directed to the searching of novel high sensitive and integrated platforms that include lateral-flow and lab on a chip-based sensing systems.

A. de la Escosura-Muñiz
ICN2 - Institut Catala de Nanociencia i Nanotecnologia, Campus UAB, 08193 Bellaterra (Barcelona), Spain

A. Merkoçi (✉)
ICN2 - Institut Catala de Nanociencia i Nanotecnologia, Campus UAB, 08193 Bellaterra (Barcelona), Spain

ICREA - Institucio Catalana de Recerca i Estudis Avançats, 08010 Barcelona, Spain
e-mail: arben.merkoci@icn.cat

J. KJEMS et al. (eds.), *Nucleic Acid Nanotechnology*, Nucleic Acids and Molecular Biology 29, DOI 10.1007/978-3-642-38815-6_12,

Contents

12.1 General Introduction

The identification and quantification of specific DNA sequences is of crucial importance for many fields being the medical diagnostics one of the most important ones. For example, the detection of DNA mutations is already correlated to specific diseases. The most frequent of these mutations are single-nucleotide polymorphisms (SNPs), the change of just one base in a DNA sequence which can provoke serious damages to the organisms. Environmental control is other of the fields which has interest in DNA analysis. Food and water contamination can be monitored by the detection of specific DNA sequences which are indicators of pathogens. Forensic applications also need to be fast and specific so as to correlate DNA sequences with person's identification. In this context the development of sensitive, specific, easy to use, fast, and cheap DNA biosensors is of extremely importance (Sassolas et al. 2008; Pérez-López and Merkoçi 2011).

Nanomaterial (NMs)-based DNA sensing consists in the detection of the DNA sequence of interest using single-stranded DNA (ssDNA) as bioreceptor and optical or electrochemical transducing, where the NMs is used as either transducer modifier or signal producer (label). DNA sensing systems use to take advantage of the electrochemical and optical properties of the nanostructured materials, directly related with their nanometric size.

Nanoparticles have been demonstrated to be an emerging alternative to other labels (i.e., fluorescence dyes and enzymes) for DNA detection (Merkoçi et al. 2005a). Nanoparticles possess characteristic properties such as the large fraction of surface atoms, high surface energy, spatial confinement, and reduced imperfections which are not present in the bulk materials and that make them interesting for DNA sensing systems (Merkoçi 2010; De la Escosura-Muñiz et al. 2010).

In addition to nanoparticles the application of other nanostructured materials such as carbon nanotubes in sensors (Merkoçi et al. 2005b) and analytical methods (Merkoçi 2006) with interest for DNA detection has been also reported. Of special interest is also the use of single nanochannels and nanoporous membranes for DNA analysis, opening the way to simple DNA sequencing devices (De la Escosura-Muñiz and Merkoçi 2012).

Gold nanoparticles (AuNPs) are the most used NPs in biosensing not only of nucleic acids but also of other biomolecules. AuNPs have unique features such as easy synthesis and functionalization, good biocompatibility, surface plasmon resonance effect, and electrocatalytic activity. The functionalization of AuNPs is generally done through the Au–S bond, using biomolecules modified with thiol groups. Beside AuNPs other types of NPs such as semiconductor NPs (the so-called quantum dots), silver NPs (AgNPs), and bimetallic/core-shell NPs with advantageous properties such as paramagnetism also have been reported. In general all the mentioned NPs act as labels or carriers of other labels while being employed in DNA detection. AuNPs, besides few other metallic NPs, are also used as modifiers of the transducers in order to enhance the biosensing system performance (i.e., electron transference).

12.2 Optical DNA Sensing Using Nanomaterials

The intrinsic optical properties (UV–vis light absorption and autofluorescence properties) of NPs and also their ability to change optical properties of sensor surfaces (i.e., in surface plasmon resonance and scattering light-based devices) have been approached for their sensible detection in DNA hybridization assays while being used as labels. These advantageous properties of NPs applied in the main optical DNA sensing methodologies are summarized in the following subsections. Due to the fact that the vast majority of optical applications are based on the use of AuNPs, the subsections are classified regarding the optical methods used for the NP detection.

12.2.1 UV–Vis Light Absorption-Based Detection

AuNPs have an extraordinarily high extinction coefficient, emanating from the inherent plasmonic properties (Storhoff et al. 2000). Their optical properties are strongly dependent on the interparticle separation distance and aggregation that cause a massive shift in the extinction spectrum, giving rise to a color change of AuNPs suspensions from red to purple (Faraday 1857). The clearly distinguishable color shifts allow a very simple monitoring that can even be performed by the naked eye. The use of controllable aggregation of AuNPs for biosensing applications was pioneered by Mirkin's group (Mirkin et al. 1996; Storhoff et al. 1998). Most nanoparticle-based colorimetric sensors are designed in such a way that of the

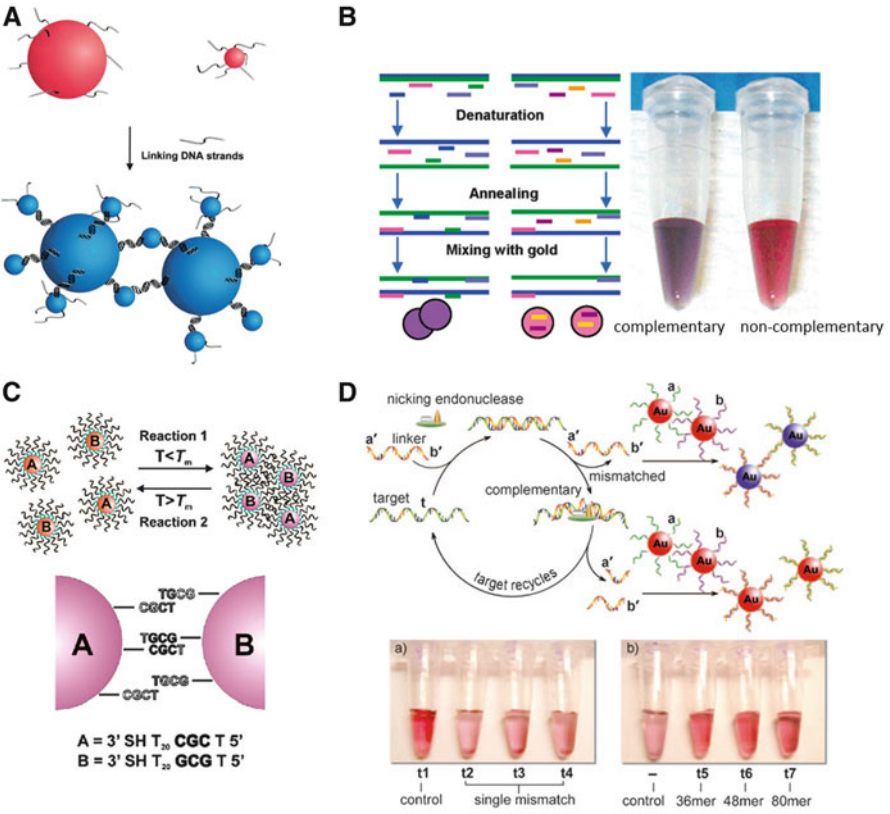

Fig. 12.1 UV–vis light absorption-based DNA detections. (**A**) General scheme of the principle of the DNA detection based on the change in the absorption spectra due to the AuNPs aggregation. (**B**) Application of the principle for the identification of PCR-amplified DNA sequences. (**C**) Scheme of the proposed two types of hybridizations engaged by curved particles: normal base-pairing interactions and "slipping" interactions through non-Watson–Crick-type base-pairing interactions. (**D**) Scheme of the nicking endonuclease-assisted nanoparticle amplification (NEANA) proposed for target DNA detection. Adapted with permission from Mirkin (2000), Li and Rothberg (2004), Hill et al. (2009), and Xu et al. (2009)

recognition of an analyte causes particle aggregation and consequently a colorimetric response (Stewart et al. 2008). For example, AuNPs suspension previously modified with a probe ssDNA can be hybridized with a target ssDNA (complementary in its two ends with ssDNA), producing in this way NPs aggregation with the consequent change in color, applied for the detection of DNA characteristic of anthrax, a biological warfare agent (Mirkin 2000) (Fig. 12.1A).

Based on these principles, Li and Rothberg (2004) used the aggregation of unmodified AuNPs as a hybridization indicator (Fig. 12.1B). The analytes, PCR product without additional processing, are hybridized with probes under normal

physiological conditions prior to exposure to the AuNPs. The color change is detected with the naked eye, avoiding the use of any instrumentation.

Although extensively applied for DNA sensing, the exact nature of the DNA base interactions contained within the AuNP/DNA structures is not well known yet. A step forward in this context has been done by Mirkin and coworkers (Hill et al. 2009) which described experiments that suggest that the curved particles can be engaged in two types of hybridizations, one that involves complementary strands and normal base-pairing interactions and a second "slipping" interaction, which can stabilize the aggregate structures through non-Watson–Crick interactions (Fig. 12.1C). A slipping interaction in this case is defined as a secondary base-pairing motif (not necessarily Watson–Crick and partial complementarity) that contains fewer total base interactions than the primary and stronger interaction (normal Watson–Crick and full complementarity) of the system, while still imparting a measure of stability onto the nanoparticle aggregate systems.

This metal-nanoparticle-based homogeneous colorimetric detection of oligonucleotides holds great promise for low-cost, low-volume, and rapid readout of target DNA sequence. Despite these advantages, a number of notable challenges associated with this detection system such as relatively low sensitivity and the need for stringent control over melting temperatures for the detection of a single-base mismatch in DNA still exist. In addition, this system is generally limited to the detection of short ssDNA.

Two recent approaches that improve the performance of the classical colorimetric detection deserve to be highlighted in this chapter. The first one has been reported by Xu et al. (2009) who described a homogeneous colorimetric DNA detection by a novel nicking endonuclease-assisted nanoparticle amplification (NEANA) process that is capable of recognizing long ssDNA with single-base mismatch selectivity and a high signal amplification. The main innovation here consists in the fact that the target ssDNA also serves as a linker strand that triggers particle aggregation and a color change. It is known that the colorimetric detection limit is directly associated with the minimum number of the linkers required to initiate particle aggregation that can be visualized with the naked eye. To increase the sensitivity of this homogeneous nanoparticle-based assay, a detection system that contains an additional oligonucleotide strand as linker, and a nicking endonuclease (an enzyme that recognizes specific nucleotide sequences in dsDNA and cleaves only one of the two strands), is introduced. If the linker DNA is noncomplementary to the target ssDNA, particle aggregation will occur (Fig. 12.1D).

The second approach highlighted here is the very recent one described by Yan et al. (2012) that consists in a new class of stimulus-responsive DNA-functionalized AuNPs that incorporate azobenzene-modified oligonucleotides. Beyond the classic directed assembly and sensing behaviors associated with oligonucleotide-modified NPs, these particles also exhibit reversible photoswitching of their assembly behavior. They observed that exposure to UV light induces a trans-cis isomerization of the azobenzene which destabilizes the DNA duplex, resulting in dissociation of the NP assemblies. The isomerization is reversible upon exposure to blue light,

resulting in rehybridization and reassembly of the DNA-linked NP obtaining a sensing system even able to discriminate single-base mismatches.

12.2.2 Surface Plasmon Resonance-Based Detection

Surface plasmon resonance (SPR) offers a flow-through biosensing technology able to measure very small changes in refractive index on noble metal surfaces when binding of an analyte to that surface occurs. In a typical SPR measurement, one of the biomolecules (the receptor) is immobilized onto a thin gold film. The biorecognition of the analyte by the immobilized receptor causes a refractive index change at the surface layer, which is detected through SPR angle change of the reflected light.

The sensitivity of these label-free SPR-based biosensing systems can be greatly enhanced by using, for example, AuNP tags through the electronic coupling interaction between the localized surface plasmon (LSP) of the NPs and the surface plasmon wave associated with the SPR gold film, as reported by He et al. (2000). Another example of a novel optical biosensing technology which takes advantage of plasmonic consists in the building of nanoparticle-enhanced diffraction gratings (NEDG) (Wark et al. 2007), where the optical properties of the planar surface plasmons generated on gold diffraction gratings are combined with those of the adsorbed AuNP tags. This principle can be extended not only for DNA hybridization assays but also for aptamer-based assays and immunoassays approaching also the properties of different-shaped AuNPs (spheres and rods) (Fig. 12.2a) (Wark et al. 2010).

The coupling of microfluidics and nanoparticle-based SPR amplification is also a very interesting approach which has been mainly focused on the combination of continuous-flow microfluidic devices and AuNPs labels (Luo et al. 2008). As recently reported by Malic et al. (2011), the microfluidic platforms can be also modified using electron-beam lithography to integrate arrays of periodic gold nanostructures so as to enhance the SPR signal and improve the sensitivity of the DNA detection (Fig. 12.2b).

Many other approaches have been reported in the last years, taking advantage of the recent advances in the nanoscience and nanotechnology. A recent trend consists in the possibility of chemical synthesis and engineering of novel NP structures. For example, plasmonic properties of metal-based core–shell NPs with varying compositions have been theoretically studied and experimentally applied for the enhancement in the sensitivity of SPR biosensing systems. In this context, a high enhancement on the sensitivity obtained using AuNPs has been very recently achieved using Au@SiO2 core–shell nanoparticle tags (Moon et al. 2012).

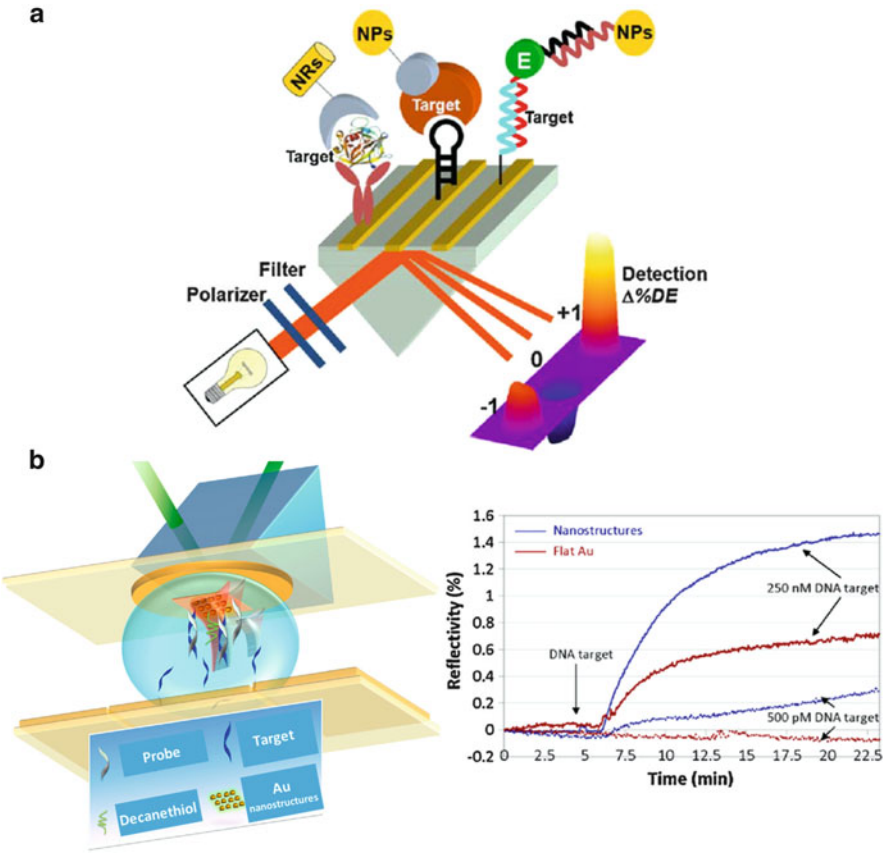

Fig. 12.2 Surface plasmon resonance-based DNA detections. (**a**) Schematic of nanoparticle-enhanced diffraction grating setup for DNA detection and other biosensing assays. (**b**) Scheme of the coupling of microfluidics and SPR analysis for DNA hybridization detection, amplified using Au nanostructures integrated on the microfluidic platform (*left*) and graphic of the enhancement on the SPR signal due to the nanostructures in comparison with flat gold platforms. Adapted with permission from Wark et al. (2010) and Malic et al. (2011) respectively

12.2.3 Light-Scattering and Surface-Enhanced Raman Spectroscopy-Based Detection

Light scattering (LS) is another optical property of metal NPs (mainly of AuNPs) that is of great interest for DNA sensing. Metal NPs of different compositions and sizes have the ability to scatter light of different wavelengths according to their different surface plasmon resonances. It is known that the light-scattering cross section of an AuNP with a diameter of 60 nm is 200–300 times stronger than that of a polystyrene bead of the same size and 4–5 orders of magnitude stronger than that

of a strong fluorescence dye (Jain et al. 2006). Based on this principle, a DNA array imaging technique using oligonucleotide-functionalized nanoparticles was pioneered by Mirkin's group in 2001 (Taton et al. 2001) and followed and improved by others (Dai et al. 2008), even taking advantage of the properties of gold nanorods (anisotropic configuration and unique optical properties), instead of the traditional spheres (He et al. 2008). This method is sensitive, selective, and allows a multicolor labeling for DNA array and can also be extended to several other applications like those based on "spot-and-read" colorimetric detection (Storhoff et al. 2004) and on silver-plated DNA and AuNPs assemblies (Bonham et al. 2007). An important characteristic of these systems is that individual NPs and their dimers or oligomers can be differentiated directly according to their distinct scattering spectra. This differentiation allows the DNA sensing based on counting individual color-coded plasmonic NPs using an ordinary dark-field microscope coupled with a color charge-coupled device (CCD) camera as recently reported by Xiao and coworkers (Xiao et al. 2010).

On the other hand, it deserves to be also highlighted the use of the surface-enhanced Raman scattering (SERS) microscopy as very sensitive technique for the detection of DNA, taking advantage of the use of NPs. SERS of molecules on or close to the surface of metallic nanostructures that can support localized surface plasmon resonances is measured. An organic dye (Raman tag) is necessary here to get the Raman signal, and NPs can play different roles to increase this signal and thus improve the sensitivity of the assays (Koegler et al. 2012). For example, AuNPs can be used as platforms for the detection of DNA measuring the signal coming from a Raman tag. Consequently, DNA hybridization event can be monitored by immobilizing a probe ssDNA on the surface of AuNPs and letting it react with the complementary target ssDNA modified with a Raman tag (i.e., tetramethylrhodamine—TAMRA) as done by Huh et al. (2009) in a microfluidic device (Fig. 12.3A, a). The distance dependence of LSPR between a NP and the Raman label is the basis of an alternative detection configuration. It consists in the immobilization on the AuNPs platform of a DNA hairpin structure modified with the Raman dye. The process of hybridization with complementary target disrupts the loop configuration, increasing the distance of the Raman active molecule and thus reducing the SERS signal (Fig. 12.3A, b) (Fabris et al. 2007). Alternatively, AuNPs can also enhance the SERS signal acting as carriers of Raman tags in DNA hybridization assays performed on gold substrates as done by Yuan et al. (2009) (Fig. 12.3B), observing a high increase in the SERS signal and consequently an improvement in the detection limit of the target DNA, from nM to fM levels. Furthermore, the well-known ability of AuNPs to catalyze the silver reduction and hence to form a silver coating allows these NPs to act as SERS promoters for the dye-labeled particles that have been captured by target molecules in a microarray format as pioneered by Mirkin's group (Cao et al. 2002). Both configurations (nanostructures as platforms and as carriers of Raman tags) can be combined as recently reported by Kim's group (Kang et al. 2010) where gold nanowires (AuNWs) have been used as support of the DNA hybridization assay and AuNPs (sphere shaped) have been modified with the reported DNA labeled

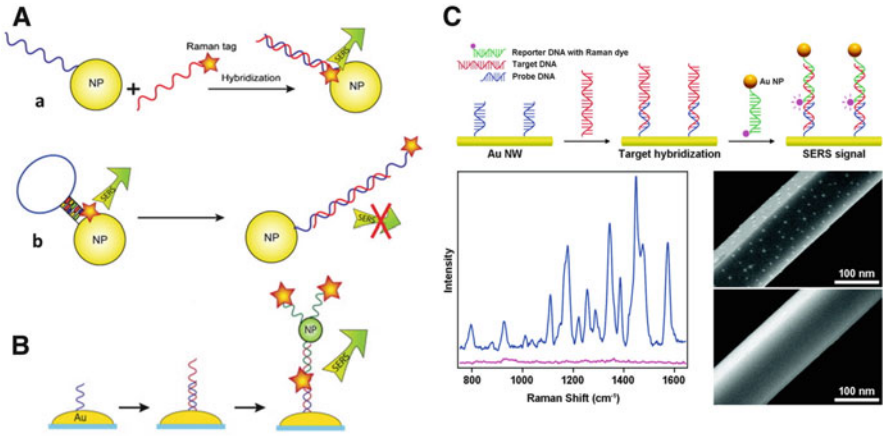

Fig. 12.3 Schematic representation of SERS-based DNA detection designs using NPs. (**A**) AuNPs platforms for DNA hybridization detection using (**a**) a Raman tag labeled complementary target ssDNA and (**b**) a probe ssDNA hairpin structure modified with the Raman tag. (**B**) AuNPs labels as carriers of the Raman tag. (**C**) Combination of AuNWs platforms and AuNP carriers of Raman tags. The *graph* shows the SERS spectra obtained for the assay performed with the specific target (*blue spectrum*) and for a noncomplementary one (*magenta spectrum*). SEM images correspond to a typical Au particle-on-wire structure constructed by adding complementary target DNAs (*top*) and a clean NW by noncomplementary target DNAs (*bottom*). Adapted with permission of Koegler et al. (2012) and Kang et al. (2010) respectively

with the Raman dye (Fig. 12.3C), obtaining a high sensitive and multiplex DNA sensor for bacteria detection, enabling diagnostics of infectious diseases.

12.2.4 Fluorescence-Based Detection

Semiconductor nanoparticles, the so-called quantum dots (QDs), possess outstanding optical characteristics which have allowed their use as fluorescent markers (Alivisatos 1996; Murray et al. 1993). Of special interest is the fact that QDs of different diameters exhibit different emission bands when excited by a single wavelength (Han et al. 2001).

The autofluorescence properties of inorganic semiconductor CdSe/ZnS core–shell NPs can also be directly approached in DNA microarrays, as done by Vora et al. (2008) for the sensitive detection of pathogenic organisms. Other core–shell nanoparticles such as magnetic/luminescent Fe_3O_4/Eu:Gd_2O_3 also have been used for the monitoring of DNA hybridization reactions (Son et al. 2007). This kind of core–shell nanoparticles allow a great versatility since these can be synthesized in multiple colors depending on the phosphorescent lanthanide ion (i.e., europium, terbium, and samarium), allowing a multiplex detection of a number of targets.

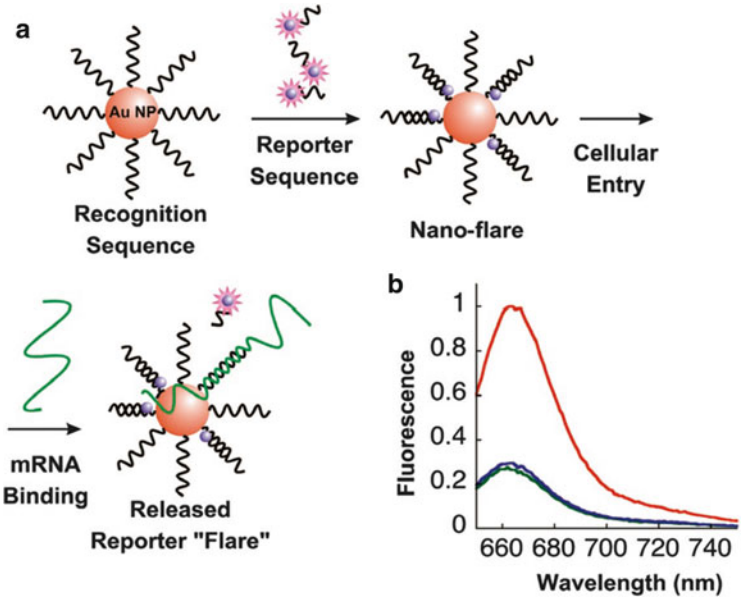

Fig. 12.4 Fluorescent detection based on the "nanoflare" concept. (**a**) AuNPs functionalized with a recognition sequence are hybridized with a short complementary reporter strand labeled with a fluorescent dye which is quenched by the AuNP. This strand is able of being displaced by the mRNA target, releasing the dye and generating the fluorescent emission. (**b**) Fluorescence spectra of 1 nM nano-flares alone (*green*), in the presence of 1 μM target (*red*), and in the presence of 1 μM noncomplementary sequence (*blue*). Adapted with permission from Seferos et al. (2007)

Silica nanoparticles (SiNPs), doped with either magnetic materials or dyes, have also been exploited not only for detection but also for the collection and purification of DNA/RNA (Hilliard et al. 2002; Knopp et al. 2009; Qin et al. 2009).

Other optical properties of NPs that have been approached for the DNA hybridization detection are the ability of AuNPs to act as quenchers of the fluorescence of other markers (Maxwell et al. 2002). An interesting approach based on this property that deserves to be highlighted here is based on the concept of "nano-flares" pioneered by Mirkin's group (Seferos et al. 2007; Prigodich et al. 2009). They demonstrated that oligonucleotide-modified AuNP probes hybridized to fluorophore-labeled complements can be used as both transfection agents and cellular "nano-flares" for detecting mRNA in living cells. This "nano-flares" take advantage of the above-mentioned highly efficient fluorescence quenching properties of AuNPs, the cellular uptake of oligonucleotide NP conjugates without the use of transfection agents, and the enzymatic stability of such conjugates. The presence of target mRNA is indicated by these nanoconjugates through the release of a flare sequence, which generates an increase in fluorescence (Fig. 12.4). Furthermore, multiplexed nano-flares using different probes labeled with different fluorophores have been very recently proposed by the same group (Prigodich et al. 2012) for the simultaneous detection of a variety of mRNAs.

12.2.5 Lateral-Flow Nucleic Acid Assay-Based Detection

Lateral-flow nucleic acid (LFNA) test strips, also called dipstick test strips, are emerging alternatives for nucleic acid detection, being also ideal for point-of-care applications. The concept is based on the well-known immunochromatographic strip technology but with the handicap of the inherent complexity of the DNA hybridization reaction compared with the immunocomplex formation in terms of kinetics or reaction. For this reason, most of these LFNA test strips are based on the formation of hapten–protein (i.e., biotin–streptavidin) or hapten–antibody or complexes (Corstjens et al. 2001; Baeumner et al. 2004). Here the optical properties of AuNPs have been approached for the obtaining of sensitive devices which have been applied for the visual genotyping of single-nucleotide polymorphisms (Litos et al. 2009). Furthermore, the ability of the AuNPs to act also as carrier of enzymatic labels (i.e., horseradish peroxidase—HRP) as pioneered by Liu's group (Mao et al. 2009; He et al. 2011) allows to obtain a final amplified signal which allows to improve the detection limits of human genomic DNA samples up to levels of μg/mL (Fig. 12.5)

These rapid, sensitive, and low-cost tool devices show great promise for in-field and point-of-care diagnosis of genetic diseases and for the detection of infectious agents.

12.3 Electrochemical DNA Sensing Using Nanomaterials

In contrast with the optical applications where the vast majority of DNA sensing systems are based on the use of AuNPs, in the case of the electrochemistry-based ones, there are a wider range of nanomaterials applied, including not only a variety of metal nanoparticles but also other nanostructured platforms such as single nanochannels and nanoporous membranes. For this reason and for a better understanding, this section is divided in different subsections related to the main nanomaterials used for electrochemical DNA analysis.

12.3.1 AuNPs

12.3.1.1 Direct/Catalytic Voltammetric Detection

The excellent electroactivity of metallic AuNPs together with their easy bioconjugation has given rise to their extensive use as labels in electrochemical DNA sensing systems. Several electrochemical routes (voltammetric, potentiometric, conductometric, impedimetric, and scanning electrochemical microscope-based methods) have been exploited for the sensitive detection of these NPs tags

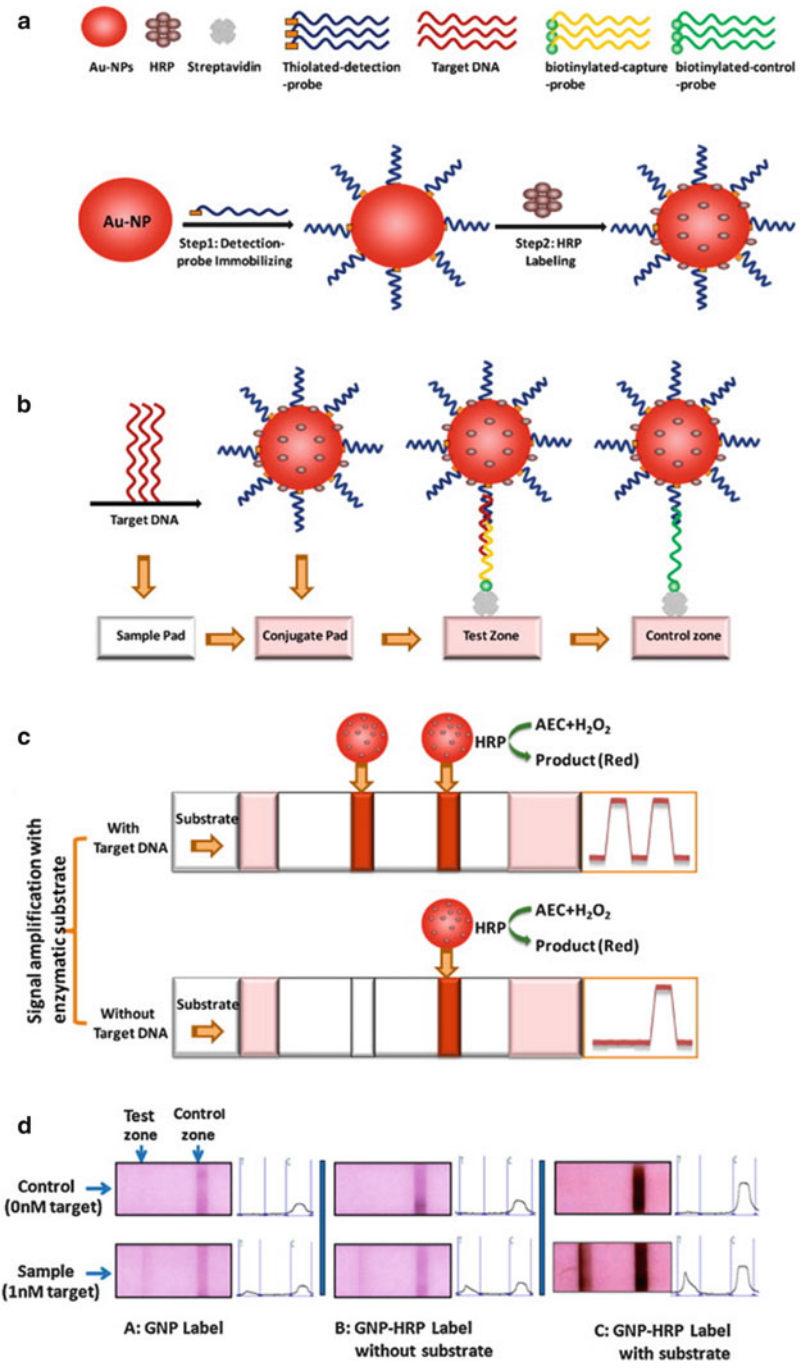

Fig. 12.5 Lateral-flow nucleic acid (LFNA)-based applications. (**a**) Schematic illustration of the preparation of HRP-AuNP-DNA conjugates; (**b**) schematic illustration of capturing HRP-AuNP-DNA conjugates on the test and control zones of lateral-flow nucleic acid biosensor; (**c**) signal

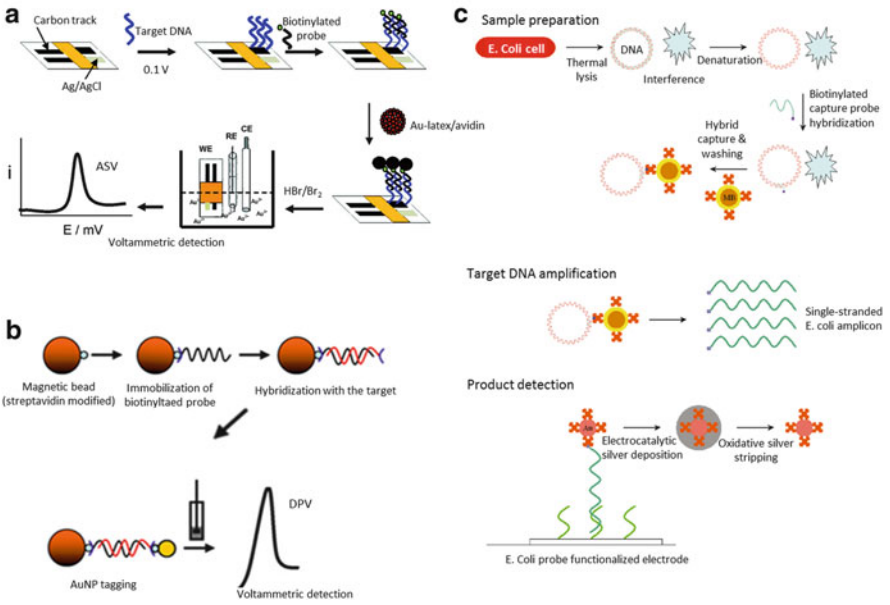

Fig. 12.6 DNA detections based on direct/catalytic voltammetric properties of AuNPs labels. (**a**) Detection of AuNP tags (loaded in latex microspheres) after acidic dissolution and anodic stripping voltammetric quantification of the released Au(III) ions. (**b**) Scheme of a magnetosandwich-type assay using AuNP tags and direct voltammetric detection without previous NPs dissolution. (**c**) Catalytic detection of AuNPs after silver electrocatalytic deposition and oxidative silver stripping applied for the detection of PCR-amplified *Escherichia coli*-related DNA. Adapted with permission from Pinijsuwan et al. (2008), Castañeda et al. (2007) and Yeung et al. (2006) respectively

in bioassays (De la Escosura-Muñiz et al. 2008). In most of the DNA sensing systems, the target ssDNA is detected in sandwich-type assays, using a capture probe ssDNA (generally immobilized on the electrotransducer surface or in other supports such as magnetic beads) that hybridizes first with the DNA target followed by a second hybridization by a signaling DNA probe labeled with the NP.

AuNP labels can be dissolved in an acidic/oxidative solution of HBr/Br_2, releasing Au(III) ions that can be easily detected using voltammetric techniques, as done by Pinijsuwan et al. (2008) who immobilized the capturing probe directly on the electrode and took also advantage of the use of latex microspheres as carriers of the AuNPs labels for achieving detection limits at the fM level (Fig. 12.6a). Alternatively, a 96-well microplate platform for the hybridization assays was

Fig. 12.5 (continued) enhancement of biosensor in the presence of enzymatic substrate. AEC, 3-amino-9-ethylcarbazole. (**d**) Typical photo images and recorded responses of LFNABs using unmodified AuNPs (*left*), AuNPs modified with enzyme before (*center*) and after (*right*) the addition of the specific substrate. Adapted with permission from He et al. (2011)

proposed by Liao et al. (2009) for the detection of a gene associated with papillary thyroid carcinomas at aM levels through the chemical dissolution of AuNP tags and voltammetric detection.

In spite of these examples, the necessity of using such a hazardous oxidative medium has directed the research to alternative detection routes for the AuNP tags like those pioneered by Pumera et al. (2005) consisting in the soft electrochemical oxidation of the AuNPs instead of the strong chemical one (Fig. 12.6b). The same group also took advantage of the use of magnetic beads platforms for the pre-concentration and minimization of matrix effects, achieving in this way a sensitive system for the detection of breast cancer and cystic fibrosis related ssDNA at levels of μg/mL (Castañeda et al. 2007) and able to discriminate noncomplementary DNA as well as DNA containing one- and three-base mismatches, with the consequent interest for future applications in single-nucleotide polymorphisms (SNPs) detection. Following a similar approach, amplified DNA coming from an isothermal amplification can be also detected, achieving detection limits below ng/mL of an isothermally amplified target characteristic of Mycobacterium tuberculosis (Torres-Chavolla and Alocilja 2011).

Furthermore, AuNPs also possess strong catalytic activity towards other reactions which have been approached in various DNA sensing strategies. For example, the well-known catalytic activity of the AuNPs on the silver reduction can be approached to selectively deposit silver on their surface, followed by the electrochemical oxidative dissolution of the silver ions which can be measured and related with the quantity of the AuNPs and consequently with the concentration of the biomolecule of interest in sandwich-type assays. This strategy was followed by Yeung et al. (2006) who integrated the DNA sensor in a microchip for the detection of PCR-amplified *Escherichia coli*-related DNA. All the assay steps are performed here in the chip: the thermal lysis of pathogens, the magnetic particle-based isolation of the target genomes, PCR amplification, and voltammetric detection of the silver ions released after amplification on AuNP labels (Fig. 12.6c).

AuNPs also exhibit catalytic activity on the reduction of chemical compounds such as the reduction of *p*-aminophenol. This product can be then electrooxidized to *p*-quinoneimine starting a redox cycling in the presence of $NaBH_4$ which offers large signal amplification. Using this strategy and taking advantage of magnetosandwich assay, detection limits of around 1 fM of target ssDNA have been achieved (Selvaraju et al. 2008).

12.3.1.2 Indirect Detection: Signal Amplifiers and Carriers of Other Labels

The presence of AuNPs attached to the electrotransducer surface through the DNA hybridization reaction produces an increase in the conductivity of the surface, exerting an amplification effect in detection strategies based in both conductometric and impedimetric measurements. These changes have been very recently approached by Gao et al. (2011) for the DNA detection (Fig. 12.7a). They first

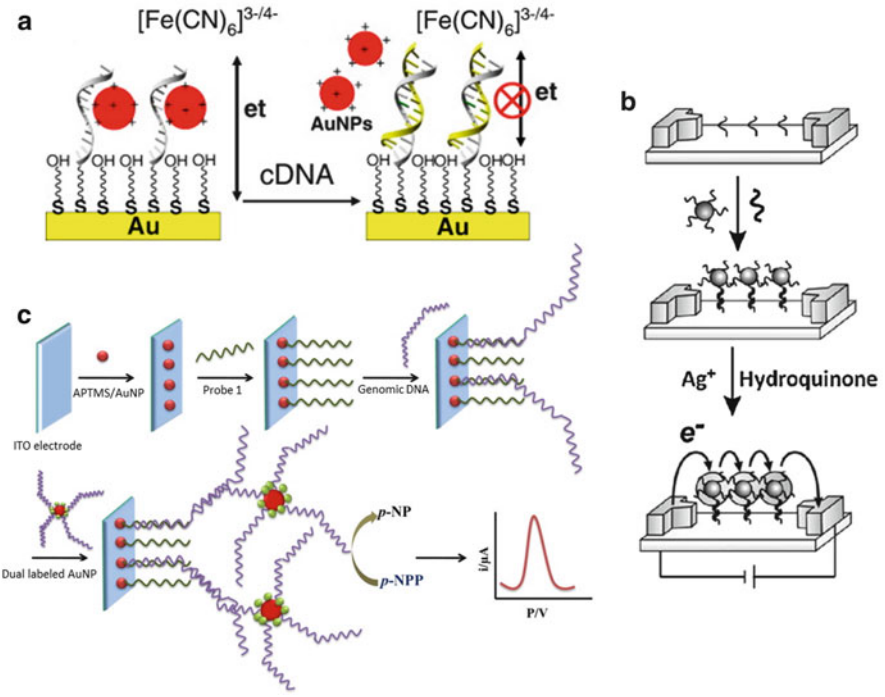

Fig. 12.7 DNA detections based on indirect detection of AuNPs labels. (**a**) Assay based in the increase in the impedance measured on the electrotransducer by displacement of AuNP tags due to the hybridization. (**b**) Assay based in the increase in the conductance due to the presence of AuNP tags and silver enhancement. (**c**) Assay based on the use of AuNPs as carriers of alkaline phosphatase enzyme and final voltammetric measurement of the amplified enzymatic hydrolysis reaction. Adapted with permission from Gao et al. (2011), Park et al. (2002) and Thiruppathiraja et al. (2011) respectively

immobilized a ssDNA on the electrotransducer surface and then attached the AuNPs that in turn decrease the electron transfer resistance. In the presence of the complementary sequence, the AuNPs are displaced resulting in an increase of the impedance, indicating the hybridization event. PCR-amplified DNA was also detected by measuring the changes in the impedimetric response of a carbon electrode by labeling the amplified product with AuNPs (Bonanni et al. 2009), lowering the detection to below fM levels. Silver amplified AuNPs can also be used to improve even more the sensitivity of these conductivity-based DNA sensing systems as done by Mirkin's group (Park et al. 2002) reaching detection limits of ssDNA as low as 500 fM (Fig. 12.7b).

Finally, a representative example of the use of AuNPs as carriers of other electrochemical labels has been very recently reported by Thiruppathiraja et al. (2011). Using AuNPs loaded with alkaline phosphatase enzyme as signal amplifier and voltammetrically measuring the corresponding enzymatic hydrolysis

reaction, they were able to detect genomic DNA reaching detection limits in the order of ng/mL (Fig. 12.7c).

12.3.1.3 Modifiers of Electrotransducer Surfaces

Another important approach is based on the fact that the presence of AuNPs on the electrotransducer surface (mostly by adsorption or included in a composite) promotes the electron transfer and improves potentiometric and conductometric responses. Furthermore, AuNPs are commonly used here for the immobilization of a probe ssDNA improving the efficiency of the hybridization. Examples of these applications are the works reported by Tang's group (Li et al. 2010, 2011a), who immobilized the AuNPs on carbon electrodes taking advantage of different organic films and voltammetrically detected the signal coming from typical redox indicators achieving limits of detection of target ssDNA in the order of 10^{-11} M. Alternatively, dentritic gold nanostructures (Li et al. 2011b) (Fig. 12.8A) or hollow gold nanospheres (Liu et al. 2010) (Fig. 12.8B) can be used in similar approaches.

AuNPs forming nanocomposites with polyaniline fibers (Spain et al. 2011) and even with graphene sheets (Hu et al. 2011) have also been recently reported for the same purpose.

12.3.2 Semiconductor NPs (Quantum Dots) and Other Metallic NPs

The use of semiconductor nanoparticles with different compositions (quantum dots, QDs) has enormous potential in multidetection designs, since each of these materials can give rise to a specific voltammetric signal characteristic of the contained metal (i.e., Pb, Cd, Zn, etc.) after the NP electrodissolution, known as anodic stripping voltammetry technique. Furthermore, the conditions for the electrochemical detection are generally less aggressive (less acidic conditions, lower potentials) which can be advantageous for some biosensing applications.

A pioneering work is reported by Wang in 2003 (Wang et al. 2003) and followed by other authors (Hansen et al. 2006) (Fig. 12.9A). Different QDs (made of zinc sulfide, cadmium sulfide, and lead sulfide) were used as encoding tags to differentiate the signals of three DNA targets related to breast cancer gene. The well-defined and resolved position and size of the stripping voltammetric peaks corresponding to the metals oxidation (after the NPs dissolution and a metal reductive pre-concentration) allow to identify and quantify the corresponding DNA target in sandwich-type hybridization assays performed on magnetic beads platforms.

Amplification methodologies based on the use of polystyrene microbeads as carriers of a high number of CdTe tags also have been reported for the detection of ssDNA related to breast cancer at fM levels (Dong et al. 2010) (Fig. 12.9B).

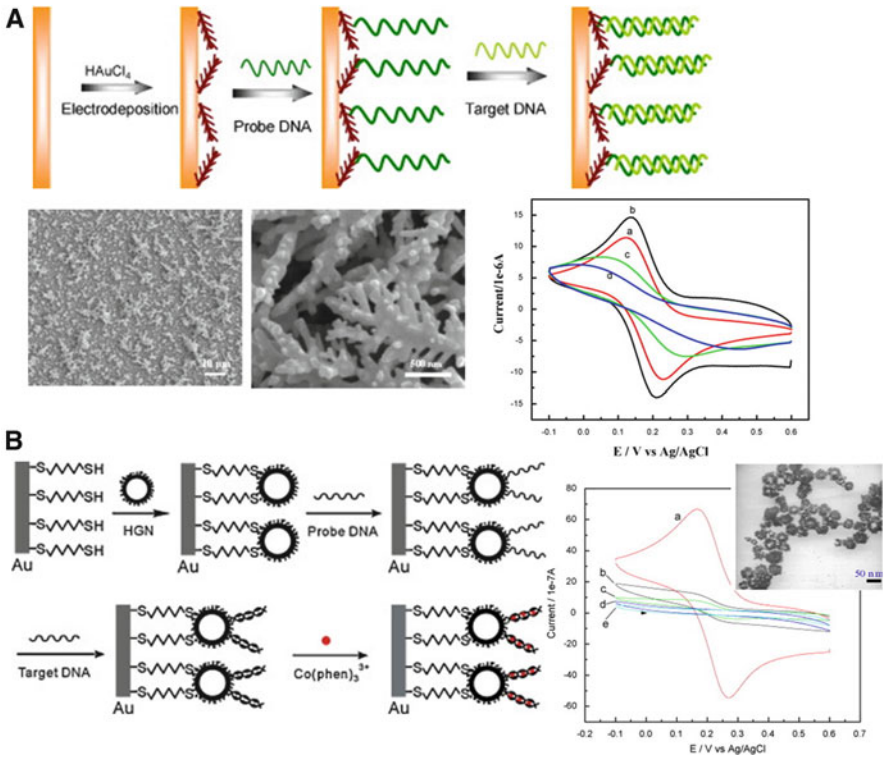

Fig. 12.8 DNA detections based on AuNPs used as modifiers of electrotransducer surfaces. (**A**) Dendritic gold nanostructure used in a planar gold electrode and (**B**) hollow gold nanospheres onto a gold electrode. Schemes of the DNA hybridization assays, SEM images of the nanostructures, and voltammetric signals obtained for the Fe^{2+}/Fe^{3+} system after the different electrode functionalization steps (from "a" to "d" or "e," respectively) are also shown. Adapted from Li et al. (2011b) and Liu et al. (2010) respectively

A double-tagged stem loop immobilized onto multiwalled carbon nanotube-modified carbon electrodes was proposed by Fan and coworkers, labeling on one end with dabcyl and on the other end with PbNPs (Fan et al. 2011) or CdS (Fan et al. 2010). The hybridization event opens the loop and allows the interaction of the dabcyl with the nanotubes (through dabcyl-cyclodextrin interaction) making also possible the stripping voltammetric detection of the QD which is related with target ssDNA levels up to 10^{-10} M. CdTe NPs have also been reported as labels in similar approaches (Kjällman et al. 2010).

Finally, it deserves to be highlighted the methodology reported by our group as alternative to the extensively used NP dissolution prior the stripping voltammetric detection. It consists on the direct detection of CdS NPs tags by simply reducing the Cd(II) to Cd(0) on the electrode surface by applying a soft electrochemical potential followed by the voltammetric reoxidation which generates the peak of currents

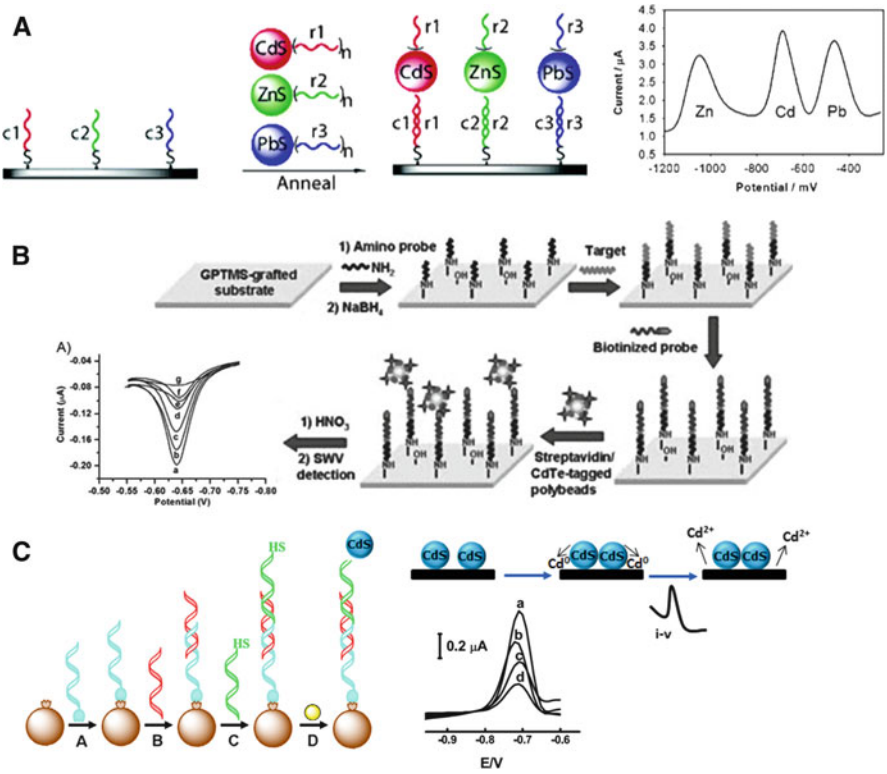

Fig. 12.9 Semiconductor nanoparticles (quantum dots) used in electrochemical DNA assays. (**A**) Multiplex detection using QDs of different compositions (CdS, ZnS, and PbS) and the corresponding voltammetric signals after acidic NPs dissolution. (**B**) Use of polystyrene microbeads as carriers of a high number of CdTe tags and final voltammetric detection after acidic NPs dissolution. (**C**) Magnetosandwich-type DNA hybridization assay with final direct voltammetric detection of the CdS QDs without the need of acidic dissolution. Adapted with permission from Hansen et al. (2006), Dong et al. (2010) and Marín and Merkoçi (2009)

related with the NPs quantity. This method was applied for the detection of cystic-fibrosis-related ssDNA at μg/mL levels using magnetic beads as platforms of the hybridization reactions in a sandwich-type assay (Marín and Merkoçi 2009) (Fig. 12.9C).

Silver nanoparticles (AgNPs) also exhibit excellent electroactivity of high interest for electrochemical biosensing. However, some limitations related to their not easy synthesis and latent toxicity have minimized their extensive use. One of the most remarkable applications of AgNPs in electrochemical DNA sensing is reported by Jiang et al. (2011) who performed a sandwich-type DNA hybridization assay on gold electrodes using biotinylated signaling ssDNA and later labeling with streptavidin-modified AgNPs. The final detection of the target ssDNA at fM concentrations is achieved thanks to the increase in the electron transfer on the

electrode surface due to the presence of the AgNPs, quantified by impedimetric measurements.

Alternatively, AgNPs can be directly generated by reduction of silver ions catalyzed by other tags. For example, detection limits in the fM level have been recently achieved (Kong et al. 2008) performing hybridization assays on the surface of interdigitated microelectrodes and finally measuring the increase in conductance due to the presence of AgNPs, directly generated by reduction of silver ions catalyzed by hematin tags.

The advantageous properties of NPs with other compositions have also been approached, in a minor extent, for the electrochemical detection of DNA. For example, Cu@Au alloy NPs have been proposed as tags in a sandwich-type assay for the detection of ssDNA at pM levels by dissolving the NP and detecting the Cu by anodic stripping voltammetry (Cai et al. 2003).

Fe_2O_3@Au core/shell nanoparticles have also been used taking advantage of the Au for the functionalization with the capture ssDNA and the paramagnetic properties of the Fe_2O_3 for magnetic separation purposes (Li et al. 2011c). In a similar mode magnetic polymer nanoparticles (Pal and Alocilja 2010) and liposomes (Liao and Ho 2009) have been proposed as magnetic platforms and carriers of labels in electrochemical DNA hybridization assays.

12.3.3 Single Nanochannels and Nanoporous Membranes

12.3.3.1 Single Nanochannels

Biosensing devices using single nanochannels are based on the concept of the Coulter counter (Coulter 1953, 1956) which allows detecting of microparticles simply by measuring the changes in the electrical conductance between two chambers separated by a microchannel when the microparticle enters through this channel. Based on this principle, nanochannels have been built for the sensing of biomolecules at nanometric scale, necessary for the detection of DNA (De la Escosura-Muñiz and Merkoçi 2012). Single biological ion channels are generally built by inserting natural proteins, which contain nanochannels in their natural conformation (i.e., α-hemolysin protein), in lipid bilayers. In this way, biomimetic systems which simulate the cell's ion channels are obtained (Bayley et al. 2001; Hou et al. 2011; Siwy and Howorka 2010). The biosensing using these ion channels based on the Coulter counter principle is called stochastic sensing. The specificity of these sensors to a high variety of analytes can be achieved through the insertion of specific receptors using genetic engineering techniques.

The DNA hybridization event can be detected with these sensing systems by covalently attaching inside the nanochannel the probe ssDNA. The DNA duplex formation gives rise to a change in the ionic current between both sides of the lipid bilayer where the channel is inserted (Vercoutere et al. 2003) (Fig. 12.10A),

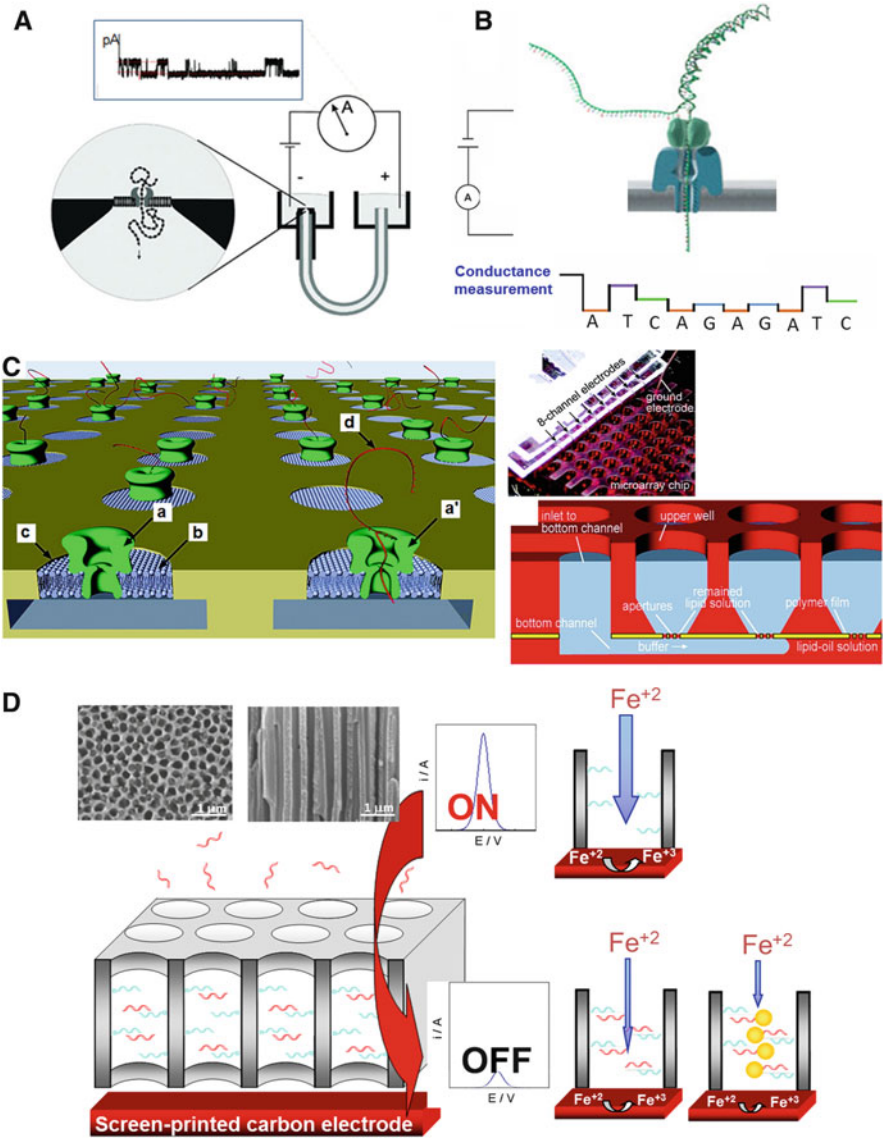

Fig. 12.10 DNA sensing using nanochannels. (**A**) Scheme of a single nanochannel sensor based on the concept of the Coulter counter. (**B**) α-Hemolysin channel as a potential tool for DNA sequencing. The DNA strand enters through the pore (above), and each of the four different bases of DNA could produce characteristic time series recordings (below). (**C**) α-Hemolysin nanochannel array on a bilayer lipid membrane enables detection of multichannel signals. Details of the experimental setup are also shown. (**D**) Array of solid-state nanochannels (Al_2O_3 membrane) used as modifier of an electrotransducer surface and detection of the hybridization event by the blockage in the signal of the Fe^{2+}/Fe^{3+} system, even amplified by the presence of AuNP tags. Front and cross-sectional SEM views of the membrane are also shown. Adapted with permission from Vercoutere et al. (2003), Kasianowicz et al. (2008), Osaki et al. (2009) and De la Escosura-Muñiz and Merkoçi (2010) respectively

allowing the identification of the target ssDNA strand even at single-base resolution (Howorka et al. 2001; Nakane et al. 2004).

Efforts in the development of nanopore-based microRNA deserve to be highlighted here. A very representative work is the recently reported by Wang et al. (2011) where an α-hemolysin pore is used to selectively detect microRNAs at the single molecular level in plasma samples from lung cancer patients without microRNA amplification in a label-free assay. By using oligonucleotide probes, microRNA is captured in the channel generating a target-specific signature signal which allows the quantification of subpicomolar levels of microRNAs related to cancer and distinguishes single-nucleotide differences.

Furthermore, one of the more promising perspectives of the nanochannel-based biosensing systems relies in the potential ability of the α-hemolysin nanochannel for DNA sequencing. The idea consists in the fact that DNA single strands could be electrophoretically driven through the nanochannel and pass in an elongated conformation generating a "fingerprint"-like blocking of the ionic current. The transit time and extent of the current could reveal information about the length of the nucleic acid and its base composition, while the magnitude of the conductance changes could give details about the presence of mismatches in DNA sequences (Kasianowicz et al. 2008; Venkatesan and Bashir 2011; Branton et al. 2008) (Fig. 12.10B). This ideal system could directly detect nucleotides, without reagents or labeling, from a single molecule of ssDNA, in contrast with the established techniques that require the use of fluorescent or luminescent labels after a PCR amplification. Furthermore, this analysis would also be able to do sequencing of much longer strands of DNA. Some companies have recently proposed commercial approaches that take advantage of this sensing principle. Oxford Nanopore Technologies has just presented a commercial system (GridION platform) which combines the α-hemolysin channel (inserted in synthetic materials instead of the traditional lipid bilayer) with the use of enzymes which ratchet DNA through the channel, being able to read many tens of kilobases. This system integrates data analysis algorithms to translate the characteristic electronic signals into DNA sequence data (Clarke et al. 2009).

To improve the efficiency of these nanochannel DNA sensors, Bayley's group (Stoddart et al. 2009) has recently reported the concept of a multibase recognition site in a single α-hemolysin nanopore using two reading heads, so the current signal offers information about two positions in the sequence improving the overall quality of sequencing.

Based on all these principles, third-generation sequencing platforms have recently been commercialized by that and other companies, also taking advantage of labeling technologies (Munroe and Harris 2010).

12.3.3.2 Nanoporous Membranes

Since a single nanochannel can detect only a single molecule at a time, strategies for manufacturing arrays of biological ion nanochannels able to do multidetection

based on the stochastic sensing concept are required. However, the difficulty of the simultaneous measurements in a high number of channels generated on the same membrane has limited this kind of multiplexed detection. One of the few examples of such application has been reported by Osaki et al. (2009) (Fig. 12.10C). They reported a microarray system that allows simultaneous recording of multiple ionic currents through α-hemolysin nanopores inserted at a lipid bilayer, being able to detect translocation events of nucleic acid molecules and opening the way for further high-throughput applications.

Arrays of solid-state/artificial nanochannels embedded in chemically and mechanically robust synthetic membranes have also been proposed for electrochemical DNA sensing, taking advantage of methodologies different to the stochastic sensing one. These approaches are mostly based on the blockage of electrotransducer surfaces due to the formation of the DNA duplex inside the channel. Here, Al_2O_3 nanoporous membranes prepared by anodization of the aluminum metal substrate are the most used materials, due to their advantageous properties (i.e., high pore density and easy bioconjugation) and mass production possibilities. For the electrical measurements, the back layer of aluminum under the membrane can act as working electrode and a polished aluminum rod as the counter electrode as reported by Smirnov's group (Vlassiouk et al. 2005; Takmakov et al. 2006). Our group has recently reported a novel and simpler setup based on the blockage of screen-printed carbon electrodes modified with commercial Al_2O_3 membranes. The analytical signal is obtained measuring the decrease in standard voltammetric signals (Fe^{2+}/Fe^{3+} system) due to the blockage in the diffusion of the electroactive ions through the membranes, thanks to both steric and electrostatic repulsion effects generated by the formation of the DNA duplex. Furthermore, AuNP tags have been used as additional blocking agents, allowing to improve the detection limits of the label-free DNA sensing system up to levels of ng/mL (De la Escosura-Muñiz and Merkoçi 2010) (Fig. 12.10D).This methodology shows excellent perspectives for the analysis of real samples where the nanoporous membrane acts not only as sensing platform but also as filter of micrometric components of the whole blood, allowing minimization of matrix effects (De la Escosura-Muñiz and Merkoçi 2011; De la Escosura-Muñiz et al. 2013).

12.4 Conclusions and Future Perspectives

Nanomaterial-based sensors are showing to be interesting alternative devices for DNA analysis. Nanomaterials are integrated in various ways in both electrochemical and optical-based detection devices. From the various kinds of nanomaterials, nanoparticles such as gold nanoparticles and quantum dots are the most reported for their use as labels including multilabeling technologies. These applications have shown clear advantages in relation to existing technologies. Stability, cost-efficiency, and overall the multiplexing analysis seem to be the most important advantages in relation to nanoparticle application in DNA-based sensors with

interest for clinical monitoring between other applications. Nanochannels have also emerged as interesting materials to improve the DNA sensor performance opening the way to novel DNA sequencing methodologies. In addition emerging of novel nanomaterials such as graphene is being converted to a novel research target for various biosensing applications including DNA detection.

Future trends in this field will be surely focused on the integration of the here reviewed strategies on microchip devices. Microfluidics platforms (lab-on-a-chip or lateral-flow devices) are the excellent avenues for an integrated DNA technology. These platforms are already integrating in a single device all the steps required for the detection of DNA: sample pretreatment, amplification reaction, labeling, pre-concentration, and final detection. Such an integration level is expecting to better approach the DNA technology to point-of-care applications in many places with less resources and lack of specialized personnel to perform such analysis. Solving problems such as the application/use of complicated nanomaterial fabrication and related DNA measuring technologies, not in agreement with mass production and user-friendly idea, so as to bring these novel devices to the end-users represent important challenges in the future research and development in this field.

Acknowledgments We acknowledge MEC (Madrid) for the project MAT2011-25870, the EU's support under FP7 contract number 24651355 "NADINE," and the NATO Science for Peace and Security Programme's support under the project SfP 983807.

References

Alivisatos AP (1996) Perspectives on the physical chemistry of semiconductor nanocrystals. J Phys Chem 100:13226–13229

Baeumner AJ, Pretz J, Fang S (2004) Universal nucleic acid sequence biosensor with nanomolar detection limits. Anal Chem 76:888–894

Bayley H, Cremer PS (2001) Stochastic sensors inspired by biology. Nature 413:226–230

Bonanni A, Pividori MI, Campoy S, Barbé J, del Valle M (2009) Impedimetric detection of double-tagged PCR products using novel amplification procedures based on gold nanoparticles and Protein G. Analyst 134:602–608

Bonham AJ, Braun G, Pavel I, Moskovits M, Reich NO (2007) Detection of sequence-specific protein-DNA interactions via surface enhanced resonance Raman scattering. J Am Chem Soc 129:14572–14573

Branton D, Deamer DW, Marziali A, Bayley H, Benner SA, Butler T, Di Ventra M, Garaj S, Hibbs A, Huang X et al (2008) The potential and challenges of nanopore sequencing. Nat Biotechnol 26:1146–1153

Cai H, Zhu N, Jiang Y, He P, Fang Y (2003) Cu@Au alloy nanoparticle as oligonucleotides labels for electrochemical stripping detection of DNA hybridization. Biosens Bioelectron 18:1311–1319

Cao YWC, Jin R, Mirkin CA (2002) Nanoparticles with Raman spectroscopic fingerprints for DNA and RNA detection. Science 297:1536–1540

Castañeda MT, Merkoçi A, Pumera M, Alegret S (2007) Electrochemical genosensors for biomedical applications based on gold nanoparticles. Biosen Bioelectron 22(9–10):1961–1967

Clarke J, Wu HC, Jayasinghe L, Patel A, Reid S, Bayley H (2009) Continuous base identification for single-molecule nanopore DNA sequencing. Nat Nanotechnol 4:265–270

Corstjens P, Zuiderwijk M, Brink A, Li S, Feindt H, Niedbala RS, Tanke H (2001) Use of up-converting phosphor reporters in lateral-flow assays to detect specific nucleic acid sequences: a rapid, sensitive DNA test to identify human papillomavirus type 16 infection. Clin Chem 47:1885–1893

Coulter WH (1953) Means for counting particles suspended in a fluid. US Patent 2,656,508

Coulter WH (1956) High speed automatic blood cell counter and cell size analyzer. Proc Natl Electron Conf 12:1034

Dai Q, Liu X, Coutts J, Austin L, Huo Q (2008) A One-step highly sensitive method for DNA detection using dynamic light scattering. J Am Chem Soc 130:8138–8139

De la Escosura-Muñiz A, Merkoçi A (2010) Nanoparticle based enhancement of electrochemical DNA hybridization signal using nanoporous electrodes. Chem Commun 46:9007–9009

De la Escosura-Muñiz A, Merkoçi A (2011) A nanochannel/nanoparticle-based filtering and sensing platform for direct detection of a cancer biomarker in blood. Small 7:675–682

De la Escosura-Muñiz A, Merkoçi A (2012) Nanochannels preparation and application in biosensing. ACS Nano 6(9):7556–7583

De la Escosura-Muñiz A, Ambrosi A, Merkoçi A (2008) Electrochemical analysis with nanoparticle-based biosystems. Trends Anal Chem 27:568–584

De la Escosura-Muñiz A, Parolo C, Merkoçi A (2010) Immunosensing using nanoparticles. Mater Today 13:24–34

De la Escosura-Muñiz A, Chunglok W, Surareungchai W, Merkoçi A (2013) Nanochannels for diagnostic of thrombin-related diseases in human blood. Biosens Bioelectron 40:24–31

Dong H, Yan F, Ji H, Wong DKY, Ju H (2010) Quantum-dot-functionalized poly(styrene-co-acrylic acid) microbeads: step-wise self-assembly, characterization, and applications for sub-femtomolar electrochemical detection of DNA hybridization. Adv Funct Mater 20:1173–1179

Fabris L, Dante M, Braun G, Lee SJ, Reich NO, Moskovits M, Nguyen TQ, Bazan QC (2007) A heterogeneous PNA-based SERS method for DNA detection. J Am Chem Soc 129:6086

Fan H, Xing R, Xu Y, Wang Q, He P, Fang Y (2010) A new electrochemical method for DNA sequence detection with homogeneous hybridization based on host–guest recognition technology. Electrochem Comm 12:501–504

Fan H, Zhao K, Lin Y, Wang X, Wu B, Li Q, Cheng L (2011) A new electrochemical biosensor for DNA detection based on molecular recognition and lead sulfide nanoparticles. Anal Biochem 419:168–172

Faraday M (1857) The Bakerian lecture: experimental relations of gold (and other metals) to light. Philos Trans R Soc Lond 147:145–181

Gao Q, Zhang W, Guo Y, Qi H, Zhang C (2011) Highly sensitive impedimetric sensing of DNA hybridization based on the target DNA-induced displacement of gold nanoparticles attached to ssDNA probe. Electrochem Comm 13:335–337

Han M, Gao X, Su JZ, Nie S (2001) Quantum-dot-tagged microbeads for multiplexed optical coding of biomolecules. Nat Biotechnol 19:631–635

Hansen J, Mukhopadhyay R, Hansen JØ, Gothelf KV (2006) Femtomolar electrochemical detection of DNA targets using metal sulfide nanoparticles. J Am Chem Soc 128:3860–3861

He L, Musick MD, Nicewarner SR, Salinas FG, Benkovic SJ, Natan MJ, Keating CD (2000) Colloidal Au-enhanced surface plasmon resonance for ultrasensitive detection of DNA hybridization. J Am Chem Soc 122:9071–9077

He W, Huang CZ, Li YF, Xie JP, Yang RG, Zhou PF, Wang J (2008) One-step label-free optical genosensing system for sequence-specific DNA related to the human immunodeficiency virus based on the measurements of light scattering signals of gold nanorods. Anal Chem 80:8424–8430

He Y, Zhang S, Zhang X, Baloda M, Gurung AS, Xu H, Zhang X, Liu G (2011) Ultrasensitive nucleic acid biosensor based on enzyme–gold nanoparticle dual label and lateral flow strip biosensor. Biosens Bioelectron 26:2018–2024

Hill HD, Hurst SJ, Mirkin CA (2009) Curvature-induced base pair "slipping" effects in DNA-nanoparticle hybridization. Nano Lett 9:317–324
Hilliard L, Zhao X, Tan W (2002) Immobilization of oligonucleotides onto silica nanoparticles for DNA hybridization studies. Anal Chim Acta 470:51–56
Hou X, Guo W, Jiang L (2011) Biomimetic smart nanopores and nanochannels. Chem Soc Rev 40:2385–2401
Howorka S, Cheley S, Bayley H (2001) Sequence-specific detection of individual DNA strands using engineered nanopores. Nat Biotechnol 19:636–639
Hu Y, Hua S, Li F, Jiang Y, Bai X, Li D, Niu L (2011) Green-synthesized gold nanoparticles decorated graphene sheets for label-free electrochemical impedance DNA hybridization biosensing. Biosens Bioelectron 26:4355–4361
Huh YS, Chung AJ, Cordovez B, Erickson D (2009) Enhanced on-chip SERS based biomolecular detection using electrokinetically active microwells. Lab Chip 9:433–439
Jain PK, Lee KS, El-Sayed IH, El-Sayed MA (2006) Calculated absorption and scattering properties of gold nanoparticles of different size, shape, and composition: applications in biological imaging and biomedicine. J Phys Chem B 110:7238–7248
Jiang X, Chen K, Han H (2011) Biosens Bioelectron 28:464–468
Kang T, Min Yoo S, Yoon I, Lee SY, Kim B (2010) Patterned multiplex pathogen DNA detection by Au particle-on-wire SERS sensor. Nano Lett 10:1189–1193
Kasianowicz JJ, Robertson JWF, Chan ER, Reiner JE, Stanford VM (2008) Nanoscopic porous sensors. Annu Rev Anal Chem 1:737–766
Kjällman THM, Peng H, Soeller C, Travas-Sejdic J (2010) A CdTe nanoparticle-modified hairpin probe for direct and sensitive electrochemical detection of DNA. Analyst 135:488–4894
Knopp D, Tang D, Niessner R (2009) Bioanalytical applications of biomolecule-functionalized nanometer-sized doped silica particles. Anal Chim Acta 647:14–30
Koegler P, Clayton A, Thissen H, Nonato G, Santos C, Kingshott P (2012) The influence of nanostructured materials on biointerfacial interactions. Adv Drug Deliv Rev 64 (15):1820–1839
Kong JM, Zhang H, Chen XT, Balasubramanian N, Kwong DL (2008) Ultrasensitive electrical detection of nucleic acids by hematin catalysed silver nanoparticle formation in sub-microgapped biosensors. Biosens Bioelectron 24:787–791
Li H, Rothberg LJ (2004) Label-free colorimetric detection of specific sequences in genomic DNA amplified by the polymerase chain reaction. J Am Chem Soc 126:10958–10961
Li F, Feng Y, Dong P, Tang B (2010) Gold nanoparticles modified electrode via a mercapto-diazoaminobenzene monolayer and its development in DNA electrochemical biosensor. Biosens Bioelectron 25:2084–2088
Li F, Feng Y, Dong P, Yang L, Tang B (2011a) Gold nanoparticles modified electrode via simple electrografting of in situ generated mercaptophenyl diazonium cations for development of DNA electrochemical biosensor. Biosens Bioelectron 26:1947–1952
Li F, Han X, Liu S (2011b) Development of an electrochemical DNA biosensor with a high sensitivity of fM by dendritic gold nanostructure modified electrode. Biosens Bioelectron 26:2619–2625
Li K, Lai Y, Zhang W, Jin L (2011c) Fe2O3@Au core/shell nanoparticle-based electrochemical DNA biosensor for Escherichia coli detection. Talanta 84:607–613
Liao WC, Ho JA (2009) Attomole DNA electrochemical sensor for the detection of Escherichia coli O157. Anal Chem 81:2470–2476
Liao KT, Cheng JT, Li CL, Liu RT, Huang HJ (2009) Ultra-sensitive detection of mutated papillary thyroid carcinoma DNA using square wave stripping voltammetry method and amplified gold nanoparticle biomarkers. Biosens Bioelectron 24:1899–1904
Litos IK, Ioannou PC, Christopoulos TK, Traeger-Synodinos J, Kanavakis E (2009) Multianalyte, dipstick-type, nanoparticle-based DNA biosensor for visual genotyping of single-nucleotide polymorphisms. Biosens Bioelectron 24:3135–3139

Liu S, Liu J, Han X, Cui Y, Wang W (2010) Electrochemical DNA biosensor fabrication with hollow gold nanospheres modified electrode and its enhancement in DNA immobilization and hybridization. Biosens Bioelectron 25:1640–1645

Luo YQ, Yu F, Zare RN (2008) Microfluidic device for immunoassays based on surface plasmon resonance imaging. Lab Chip 8(5):694–700

Malic L, Veres T, Tabrizian M (2011) Nanostructured digital microfluidics for enhanced surface plasmon resonance imaging. Biosens Bioelectron 26:2053–2059

Mao X, Ma Y, Zhang A, Zhang L, Zeng L, Liu G (2009) Disposable nucleic acid biosensors based on gold nanoparticle probes and lateral flow strip. Anal Chem 81:1660–1668

Marín S, Merkoçi A (2009) Direct electrochemical stripping detection of cystic-fibrosis-related DNA linked through cadmium sulfide quantum dots. Nanotechnology 20:055101

Maxwell DJ, Taylor JR, Nie S (2002) Self-assembled nanoparticle probes for recognition and detection of biomolecules. J Am Chem Soc 124:9606–9612

Merkoçi A (2006) Carbon nanotubes in analytical sciences. Microchim Acta 152:157–174

Merkoçi A (2010) Nanoparticles-based strategies for DNA, protein and cell sensors. Biosens Bioelectron 26:1164–1177

Merkoçi M, Aldavert M, Marín S, Alegret S (2005a) New materials for electrochemical sensing V: Nanoparticles for DNA labeling. Trends Anal Chem 24:341–349

Merkoçi A, Pumera M, Llopis X, Pérez B, Del Valle M, Alegret S (2005b) New materials for electrochemical sensing VI: Carbon nanotubes. Trends Anal Chem 24:826–838

Mirkin CA (2000) Programming the assembly of two- and three-dimensional architectures with DNA and nanoscale inorganic building blocks. Inorg Chem 39:2258–2272

Mirkin CA, Letsinger RL, Mucic RC, Storhoff JJ (1996) A DNA-based method for rationally assembling nanoparticles into macroscopic materials. Nature 382:607–609

Moon S, Kim Y, Oh Y, Lee H, Kim HC, Lee K, Kim D (2012) Grating-based surface plasmon resonance detection of core-shell nanoparticle mediated DNA hybridization. Biosens Bioelectron 32:141–147

Munroe DJ, Harris TJR (2010) Third-generation sequencing fireworks at Marco Island. Nat Biotechnol 28:426–428

Murray CB, Norris DJ, Bawendi MG (1993) Synthesis and characterization of nearly monodisperse CdE (E = sulfur, selenium, tellurium) semiconductor nanocrystallites. J Am Chem Soc 115:8706–8715

Nakane J, Wiggin M, Marziali AA (2004) Nanosensor for transmembrane capture and identification of single nucleic acid molecules. Biophys J 87:615–621

Osaki T, Suzuki H, Le Pioufle B, Takeuchi S (2009) Multichannel simultaneous measurements of single-molecule translocation in α-hemolysin nanopore array. Anal Chem 81:9866–9870

Pal S, Alocilja EC (2010) Electrically active magnetic nanoparticles as novel concentrator and electrochemical redox transducer in Bacillus anthracis DNA detection. Biosens Bioelectron 26:1624–1630

Park SJ, Taton TA, Mirkin CA (2002) Array-based electrical detection of DNA with nanoparticle probes. Science 295:1503–1506

Pérez-López B, Merkoçi A (2011) Nanomaterials based biosensors for food analysis applications. Trends Food Sci Technol 1–15

Pinijsuwan S, Rijiravanich P, Somasundrum M, Surareungchai W (2008) Sub-femtomolar electrochemical detection of DNA hybridization based on latex/gold nanoparticle-assisted signal amplification. Anal Chem 80:6779–6784

Prigodich AE, Seferos DS, Massich MD, Giljohann DA, Lane BC, Mirkin CA (2009) Nano-flares for mRNA regulation and detection. ACS Nano 3:2147–2152

Prigodich AE, Randeria PS, Briley WE, Kim NJ, Daniel WL, Giljohann DA, Mirkin CA (2012) Multiplexed nanoflares: mRNA detection in live cells. Anal Chem 84:2062–2066

Pumera M, Castañeda MT, Pividori MI, Eritja R, Merkoçi A, Alegret S (2005) Magnetically trigged direct electrochemical detection of DNA hybridization using Au67 quantum dot as electrical tracer. Langmuir 21:9625–9629

Qin PZ, Niu CG, Zeng GM, Ruan M, Tang L, Gong JL (2009) Time-resolved fluorescence based DNA detection using novel europium ternary complex doped silica nanoparticles. Talanta 80:991–995

Sassolas A, Leca-Bouvier BD, Blum LJ (2008) DNA biosensors and microarrays. Chem Rev 108:109–139

Seferos DS, Giljohann DA, Hill HD, Prigodich AE, Mirkin CA (2007) Nano-flares: probes for transfection and mRNA detection in living cells. J Am Chem Soc 129:15477–15479

Selvaraju T, Das J, Jo K, Kwon K, Huh CH, Kim TK, Yang H (2008) Nanocatalyst-based assay using DNA-conjugated Au nanoparticles for electrochemical DNA detection. Langmuir 24:9883–9888

Siwy ZS, Howorka S (2010) Engineered voltage-responsive nanopores. Chem Soc Rev 39:1115–1132

Son A, Dosev D, Nichkov M, Ma Z, Kennedy IM, Scow KM, Hristov KR (2007) Quantitative DNA hybridization in solution using magnetic/luminescent core–shell nanoparticles. Anal Biochem 370:186–194

Spain E, Kojima R, Kaner RB, Wallace GG, O'Grady J, Lacey K, Barry T, Keyes TE, Forster RJ (2011) High sensitivity DNA detection using gold nanoparticle functionalised polyaniline nanofibres. Biosens Bioelectron 26:2613–2618

Stewart ME, Anderton CR, Thompson LB, Maria J, Gray SK, Rogers JA, Nuzzo RG (2008) Nanostructured plasmonic sensors. Chem Rev 108:494–521

Stoddart D, Maglia G, Mikhailova E, Heron AJ, Bayley H (2009) Multiple base-recognition sites in a biological nanopore: two heads are better than one. Angew Chem Int Ed 48:1–5

Storhoff JJ, Elghanian R, Mucic RC, Mirkin CA, Letsinger RL (1998) One-pot colorimetric differentiation of polynucleotides with single base imperfections using gold nanoparticle probes. J Am Chem Soc 120:1959–1964

Storhoff JJ, Lazarides AA, Mucic RC, Mirkin CA, Letsinger RL, Schatz GC (2000) What controls the optical properties of DNA-linked gold nanoparticle assemblies? J Am Chem Soc 122:4640–4650

Storhoff JJ, Lucas AD, Garimella V, Bao P, Müller UR (2004) Homogeneous detection of unamplified genomic DNA sequences based on colorimetric scatter of gold nanoparticle probes. Nat Biotechnol 22:883–887

Takmakov P, Vlassiouk I, Smirnov S (2006) Sensing DNA hybridization via ionic conductance through a nanoporous electrode. Analyst 131:1248–1253

Taton TA, Lu G, Mirkin CA (2001) Two-color labeling of oligonucleotide arrays via size-selective scattering of nanoparticle probes. J Am Chem Soc 123:5164–5165

Thiruppathiraja C, Kamatchiammal S, Adaikkappan P, Santhosh DJ, Alagar M (2011) Specific detection of Mycobacterium sp. genomic DNA using dual labeled gold nanoparticle based electrochemical biosensor. Anal Biochem 417:73–79

Torres-Chavolla E, Alocilja EC (2011) Nanoparticle based DNA biosensor for tuberculosis detection using thermophilic helicase-dependent isothermal amplification. Biosens Bioelectron 26:4614–4618

Venkatesan BM, Bashir R (2011) Nanopore sensors for nucleic acid analysis. Nat Nanotechnol 6:615–624

Vercoutere WA, Winters-Hilt S, DeGuzman VS, Deamer D, Ridino SE, Rodgers JT, Olsen HE, Marziali A, Akeson M (2003) Discrimination among individual Watson-Crick base pairs at the termini of single DNA hairpin molecules. Nucleic Acids Res 31:1311–1318

Vlassiouk I, Takmakov P, Smirnov S (2005) Sensing DNA hybridization via ionic conductance through a nanoporous electrode. Langmuir 21:4776–4778

Vora GJ, Meador CE, Anderson GP, Taitt CR (2008) Comparison of detection and signal amplification methods for DNA microarrays. Mol Cell Probes 22:294–300

Wang J, Liu G, Merkoçi A (2003) Electrochemical coding technology for simultaneous detection of multiple DNA targets. J Am Chem Soc 125:3214–3215

Wang Y, Zheng D, Tan Q, Wang MX, Gu LQ (2011) Nanopore-based detection of circulating microRNAs in lung cancer patients. Nat Nanotechnol 6:668–674

Wark AW, Lee HJ, Qavi AJ, Corn RM (2007) Nanoparticle-enhanced diffraction gratings for ultrasensitive surface plasmon biosensing. Anal Chem 79:6697–6701

Wark AW, Lee HJ, Kim S, Nayeem S, Lee HJ (2010) Bioaffinity detection of pathogens on surfaces. J Ind Eng Chem 16:169–177

Xiao L, Wei L, He Y, Yeung ES (2010) Single molecule biosensing using color coded plasmon resonant metal nanoparticles. Anal Chem 82:6308–6314

Xu W, Xue X, Li T, Zeng H, Liu X (2009) Ultrasensitive and selective colorimetric DNA detection by nicking endonuclease assisted nanoparticle amplification. Angew Chem Int Ed 48:6849–6852

Yan Y, Chen JIL, Ginger DS (2012) Photoswitchable oligonucleotide-modified gold nanoparticles: controlling hybridization stringency with photon dose. Nano Lett 12:2530–2536

Yeung SW, Lee TMH, Cai H, Hsing IM (2006) A DNA biochip for on-the-spot multiplexed pathogen identification. Nucleic Acids Res 34(18):e118

Yuan W, Ho HP, Lee RKY, Kong SK (2009) Surface-enhanced Raman scattering biosensor for DNA detection on nanoparticle island substrates. Appl Opt 48:4329–4337

Index

J. KJEMS et al. (eds.), *Nucleic Acid Nanotechnology*, Nucleic Acids and Molecular Biology 29, DOI 10.1007/978-3-642-38815-6,